Second Edition

The Drift of Sea Ice

Matti Leppäranta

Springer

PRAXIS

The Drift of Sea Ice
(Second Edition)

Matti Leppäranta

The Drift of Sea Ice

(Second Edition)

Springer

Published in association with
Praxis Publishing
Chichester, UK

PRAXIS

Professor Matti Leppäranta
Department of Physics
University of Helsinki
Helsinki
Finland

SPRINGER-PRAXIS BOOKS IN GEOPHYSICAL SCIENCES
SUBJECT *ADVISORY EDITOR*: Philippe Blondel, C.Geol., F.G.S., Ph.D., M.Sc., F.I.O.A., Senior Scientist, Department of Physics, University of Bath, UK

ISBN 978-3-642-04682-7 e-ISBN 978-3-642-04683-4
DOI 10.1007/978-3-642-04683-4
Springer Heidelberg Dordrecht London New York

Library of Congress Control Number: 2010929859

Cover design: Jim Wilkie
Project copy editor: Rachael Wilkie
Typesetting: Aarontype Limited

Printed on acid-free paper

Springer is part of Springer Science + Business Media (www.springer.com)

Contents

Preface to the first edition

The drift of sea ice, forced by winds and ocean currents, is an essential element in the dynamics of the polar oceans, those essential and fragile components of the world's climate system. Because its structure is almost two-dimensional, the sea ice drift problem is fascinating for theoretical research in geophysical fluid dynamics. Apart from two-dimensionality, this medium is complicated by its granularity, compressibility, and non-linearity.

The drift transports sea ice over long distances, particularly to regions where ice is not formed by thermodynamic processes. The ice transports latent heat and fresh water, and the influence of ice melting on the salinity of the mixed layer is equivalent to a considerable amount of precipitation. The ice cover forms a particular air–sea interface, which is modified drastically by differential ice motion; consequently, sea ice dynamics is a key factor in air–sea interaction processes in the polar oceans. In particular, the opening and closing of leads (open water channels) have a major impact on air–sea heat exchange. Thus the drift of sea ice plays a very important role in high-latitude weather, polar oceanography, and global climate. This is of renewed interest owing to the increasingly growing concern about man-made global warming.

The waters in the region at the ice margin are known for their high biological productivity because of favourable light and hydrographical conditions; therefore, the location of ice margins – to some degree determined by the drift of ice – is of deep concern in marine ecology.

The drift of ice is also a major environmental factor. Pollutants accumulate in the ice sheet, originating from the water body, sea bottom, and atmospheric fallout, and they are transported within the ice over long distances. A particular pollutant question is oil spills. The drift and dispersion of oil in ice-covered seas has become a very important issue; it is a difficult problem, oil being partly transported with ice and partly dragged by ice. There are three major oil exploration areas in the seasonal sea ice zone: offshore Alaska, Barents Sea, and offshore Sakhalin Island in the Sea of Okhotsk.

Sea ice has always been a barrier to winter shipping. For the purpose of sea ice monitoring and forecasting, ice information services have been in operation for about 100 years. The drift of ice shifts the ice edge, opens and closes leads, and forms pressure zones, which are all key points in navigation through an ice-covered sea. Also hummocks and sea ice ridges result in local accumulation of ice volume and strength, causing major problems to marine operations and constructions. Because of ice dynamics, the ice situation may change rapidly; therefore, ice information services work in all ice-covered seas on a daily basis, updating their ice charts and producing ice forecasts. Expansion of the Northern Sea Routes requires ongoing development of sea ice mapping and forecasting services, where sea ice dynamics plays a key role.

This book presents the science of sea ice drift through its 100-year history to the present state of knowledge. Chapter 1 gives a brief historical overview and presents the sea ice drift problem and the subject matter of the book. The material includes geophysical theory, observations from field programmes, and mathematical models. Chapter 2 describes sea ice material and how it needs to be approached from the perspective of the research and modelling of ice drift. Chapter 3 presents methodologies, data analysis, and the outcome of sea ice kinematics measurements and techniques to construct the ice conservation law, a fundamental law in the dynamics of sea ice. The equation of motion is presented and analyzed in Chapters 4 and 5, including the rheology problem, derivation of two-dimensional equations, and magnitude estimation and scaling. In Chapters 6–8, solutions to the ice drift problem are presented, from simple analytical models to full numerical models. The free drift case results in an algebraic equation, while analytical solutions are easily obtained for channel and zonal flows, critically important tools to interpret the results of more complex models. Chapter 9 briefly discusses some applications of the knowledge of sea ice drift. The end matter contains a collection of study problems, the references, and the index.

The underlying idea behind the book has been to include the whole story of sea ice dynamics in a single volume, from material state through the laws of dynamics to mathematical models. There is a crying need for a synthesis of these research endeavours, as sea ice dynamics applications have been increasing and, apart from review papers, no comprehensive book exists on this topic in English.

The author has contributed to research into sea ice dynamics since 1974. In particular, his topics of interest have been (in chronological order): short-term sea ice forecasting, drift stations in the Baltic Sea, MIZEX (Marginal Ice Zone Experiment), sea ice ridging, sea ice remote sensing, seasonal modelling of Baltic Sea ice conditions, scaling problems, and finally sea ice in coastal zones. This book has grown from the author's lectures on sea ice drift, initially at the University of Helsinki, Finland and then at UNIS (Universitetsstudiene i Svalbard), Longyearbyen, Norway, and from visits to various universities, in particular the Cold Regions Research and Engineering Laboratory, Hanover, New Hampshire, USA and Hokkaido University, Mombetsu and Sapporo, Japan.

In the progress of his research the author has learned about sea ice drift from a large number of colleagues. Especially, he wants to thank Professors Erkki Palosuo

and William D. Hibler III, as well as Professors Jan Askne, Robert V. Goldstein, Sylvain Joffre, Zygmunt Kowalik, Sveinung Løset, Anders Omstedt, Sergey N. Ovsienko, Kaj Riska, Hayley H. Shen, Kunio Shirasawa, Peter Wadhams, and Wu Huiding. He is also deeply thankful to his students in sea ice dynamics, in particular Professor Zhang Zhanhai, Dr Jari Haapala, Dr Paula Kankaanpää, and Mr Keguang Wang. His home institutes, the Finnish Institute of Marine Research (1974–1992) and the Department of Geophysics (1992; renamed in 2001 as the Division of Geophysics/ Department of Physical Sciences) of the University of Helsinki, are deeply thanked for good working conditions and support. The scientists and technicians who have participated in the ice dynamics research programmes from these institutes and from several other organizations are gratefully acknowledged. Mr Keguang Wang is also thanked for a careful scientific review of the manuscript. Also, he and Ms Pirkko Numminen provided assistance with some of the graphics. Finally, the author wants to thank the Praxis team – Clive Horwood, Philippe Blondel, and Neil Shuttlewood –for professional guidance and help in getting this book completed, in particular to Dr Blondel for his very careful and excellent review of the whole book.

Matti Leppäranta
Helsinki, 18 June 2004

Preface to the second edition

This second edition has been prepared six years after the first one. There has been much progress in sea ice dynamics during this period, and consequently a revision is well motivated. This edition contains new sections on thermodynamics, ice–ocean dynamic interaction, frequency spectrum of ice drift, spatial structures of ice velocity, and oil spill models in ice-covered waters. In addition, based on comments from several readers and students of the first edition, modifications, restructuring, additions and technical improvements have been made in most sections.

The progress in the research of sea ice drift has been largely connected to the ice thickness problem, scaling issues, ice engineering and climate models. Mapping of sea ice thickness, in particular the dynamic-thermodynamic evolution of ice thickness, is the main problem to be solved before deeper revisions of sea ice dynamics theory and models are feasible. *Cryosat-1*, ESA's satellite designed for mapping the thickness of sea ice and glaciers, was destroyed shortly after launch in 2005, but in 2010 a new era in sea ice science started with *Cryosat-2*. Ice engineering needs for sea ice dynamics models have been largely increasing for oil-spill cleaning, ice forcing on ships and platforms, and operational strategy in oil and gas exploration in ice-covered waters. Also the navigation conditions have been changing in ice-covered seas in the northern hemisphere due to a decrease of ice thickness and extent.

As a whole, the role of cryosphere is coming more and more important in the Earth system science. The World Climate Research Programme (WCRP) established a core project Climate and Cryosphere (CLIC) in 1999, European Geophysical Union (EGU) established a division of Cryospheric Sciences (CR) in 2002, and the International Union of Geodesy and Geophysics (IUGG) established its eighth association, the International Association of Cryospheric Sciences (IACS), in 2007. In addition, International Polar Year (IPY) took place in 2007–2009 with a major cryosphere programme.

The author is grateful to his collaborators in the research of sea ice dynamics. Fruitful contacts have continued with the majority of the colleagues listed in the preface of the first edition. Especially he is thankful to organizers of two major IPY Sea Ice Summer Schools in 2007 for the invitation to give lectures, organized in Shanghai by Professors Zhang Zhanhai and Wu Huiding and in Longyearbyen, Svalbard by Dr Dirk Notz and Professor Frank Nilsen. A joint sea ice research and education programme was also started between the author and Professor Li Zhijun from the Dalian University of Technology in 2007. Others to thank are Professor Knut Høyland, Dr Tuomo Kärnä, Dr Yusuke Kawaguchi, Dr Tarmo Kõuts, Professor Aleksei Marchenko and Professor Achim Stössel. The list of PhD students in sea ice dynamics has increased by MSc Mika Mäkelä, MSc Ioanna Merkouriadi, MSc Annu Oikkonen and MSc Caixin Wang. The author also wants to thank Dr Juha Karvonen and Dr Simon Prinsenberg for help in the preparation of this book. Ms Salla Jokela has helped with the new graphics, and the Praxis team has been of great help as usual. Support to continue sea ice research has been available from the Academy of Finland and Maj and Tor Nessling Foundation, Finland.

Matti Leppäranta
Helsinki, December 2009

Figures

Tables

Symbols

A	Ice compactness
C	Drift ice strength reduction for opening
C_a	Air drag coefficient
C_w	Water drag coefficient
C_{a1}	Linear air drag coefficient
C_b	Bottom drag coefficient
C_{w1}	Linear water drag coefficient
d	Characteristic diameter of an ice floe
D	Continuum length scale
D_1; D_2	Harmonic and biharmonic diffusion coefficients
e	Aspect ratio of elliptic yield curve
E_p	Potential energy
f	Coriolis parameter
F	Force, Yield function
Fr	Froude number
g	Gravity acceleration
h	Ice thickness
h_0	Demarcation thickness
h_c	Cut-off size of ridges
h_d	Thickness of deformed ice
h_h	Thickness of hummocked ice
h_i	Ice floe thickness
h_k	Ridge keel depth
h_R	Mean thickness of ridges
h_s	Ridge sail height
h_u	Thickness of undeformed ice
h'	Freeboard of ice
h''	Draft of ice

H	Heaviside function; ice thickness scale; water depth
i	Imaginary unit
$\mathbf{i}$	Unit vector east
I	Ice function
$\mathbf{I}$	Unit tensor
$\mathbf{j}$	Unit vector north
J	Ice state
k	Thickness multiplicator in ridging
$\mathbf{k}$	Unit vector vertically upward
K	Diffusion coefficient
l_c	Characteristic length of ice on water foundation
L	Length scale
L_{MO}	Monin–Obukhov length
L_R	Length of ridges in a given horizontal area
m	Mass of ice per unit area
M	Mass transport
M_1, M_2	Elastic modulus
$\boldsymbol{n}$	Unit vector normal to a surface
Na	Nansen number
P	Probability density
p_a	Air pressure
P	Ice strength
P^*	Ice strength level constant
q	Ridge porosity; area of floes larger than given size
r	Radius vector
r_e	Radius of the Earth
r_I	Radius of gyration
Ro	Rossby number
S	Surface area of a region
S_f	Surface area if an ice floe
Sr	Strouhal number
S_R	Areal concentration of ridges
t	Time
T	Timescale
T_D	Advective timescale
T_I	Inertial timescale
$\boldsymbol{u} = (u, v)$	Ice velocity
$\boldsymbol{U}_a = (U_a, V_a)$	Wind velocity
$\boldsymbol{U}_{ag}$	Geostrophic wind
$\boldsymbol{U}_w = (U_w, V_w)$	Water velocity
$\boldsymbol{U}_{wg}$	Geostrophic current
w	Vertical velocity
x	East coordinate
X	Friction number
y	North coordinate

Y	Young's modulus of sea ice
z	Upward coordinate
Z	Zenith angle
z_0	Roughness length
α	Wind factor
β	Sea surface slope
γ	Ratio of keel depth to sail height of ridges; ratio of compressive strength to shear strength; free local variable
Γ	Boundary curve; ratio of frictional dissipation to potential energy production in ridging; local free variable
δ	Delta function; differential element
δ_A	Draft aspect ratio
Δ	Strain-rate invariant function connected to elliptic yield curve
Δ_0	Maximum creep rate in viscousplastic sea ice rheology
Δt	Time step
Δx	Grid size
ε	Strain
$\dot{\varepsilon}$	Strain rate
$\dot{\varepsilon}$	Deviatoric strain rate
$\dot{\varepsilon}_{\mathrm{I}}, \dot{\varepsilon}_{\mathrm{II}}$	Strain rate invariants
$\dot{\varepsilon}_1, \dot{\varepsilon}_2$	Principal strain rates
ζ	Bulk viscosity
η	Shear viscosity
θ	Deviation angle between wind and wind-driven ice drift
θ_0	Deviation angle for massless ice
θ_a	Turning angle in atmosphere
θ_w	Turning angle in water
Θ_h	Ice thickness gradient correction for two-dimensional ice stress
θ_w	Turning angle in water
κ	Restitution coefficient in floe collisions; von Karman constant; friction coefficient
λ	Usually local variable; longitude
λ_i	Ice inertial response time
λ_w	Ocean boundary layer inertial response time
Λ	Gradient length scale
μ	Ridge density
ν	Poisson's ratio; kinematic viscosity
ξ	Sea level elevation
π	Spatial density of ice thickness distribution
Π	Cumulative ice thickness distribution
ρ	Ice density
ρ_a	Air density
ρ_w	Water density
ϕ	Latitude, thermodynamic growth rate of ice

σ	Ice stress
σ_t, σ_c	Tensile and compressive strength of sea ice, small scale
σ_Y	Yield strength
$\sigma_{\mathrm{I}}, \sigma_{\mathrm{II}}$	Stress invariants
σ_1, σ_2	Principal stresses
Σ	Total ice stress
τ	Shear stress
τ_a	Air stress on ice surface
τ_w	Water stress on ice bottom
ϕ	Latitude; thermodynamic growth rate of ice
ϕ_A	Thermodynamic growth rate of ice compactness
Φ	Geopotential height
χ_0	Opening rate of leads
χ_d	Rate of ridging and hummocking
ψ	Mechanical deformation function, thickness redistributor derivative $\mathrm{d}\Psi = \mathrm{d}h$
ψ'	Redistributor in ridging (ψ'_- for loss and ψ'_+ for gain)
Ψ	Ice thickness redistributor
ω	Frequency
$\dot{\omega}$	Vorticity, rotation rate
Ω	A region in ice cover; rotation rate of the Earth
φ	Slope angle of ridge sails φ_s and keels φ_k, deformation mode
ϑ	Angle of internal friction

Abbreviations

AARI	Arctic and Antarctic Research Institute
AEM	Airborne electromagnetic method
AIDJEX	Arctic Ice Dynamics Joint Experiment
AVHRR	Advanced very high resolution radiometer
DMSP	Defense Meteorological Satellite Program
EM	Electromagnetic
ERS	European Remote Sensing Satellite
ESA	European Space Agency
GPR	Ground-penetrating radar
GPS	Global positioning system
IABP	International Arctic Buoy Programme
MIZ	Marginal ice zone
MIZEX	Marginal Ice Zone Experiment
MODIS	Moderate resolution imaging spectroradiometer
NASA	National Aeronautics and Space Administration
NOAA	National Oceanic and Atmospheric Administration
NP	North Pole
NSIDC	National Snow and Ice Data Centre
R/V	Research vessel
SAR	Synthetic aperture radar
SCAR	Scientific Committee on Antarctic Research
SIMI	Sea Ice Mechanics Initiative
SMMR	Scanning multichannel microwave radiometer
SP	Severnyi Polyus (North Pole)
SSIZ	Seasonal sea ice zone

SSM/I	Special sensor microwave/imager
SST	Sea surface temperature
VTT	Technical Research Centre of Finland
WMO	World Meteorological Organization
WRCP	World Climate Research Programme

1

Introduction

Sea ice occurs in about 10% of the world ocean's surface, growing, melting, and drifting under the influence of solar, atmospheric, oceanic, and tidal forcing. Most sea ice lies in the Arctic and Antarctic Seas above 60° latitude, but seasonally freezing smaller basins exist further down toward the equator, to even below 40°N in the Bo Hai Sea, China. In sizeable basins, solid sea ice lids are statically unstable and break into fields of ice floes forming *drift ice*. These fields undergo transport as well as opening and closing, which altogether create the exciting sea ice landscape as it appears to the human eye. This book is about the geophysics of the drift of sea ice, and Chapter 1 gives a brief history of the research, introduces the problem with applications, and outlines the subject matter of the book.

People living by freezing seas, such as the Baltic Sea in northern Europe, have known the ice drift phenomenon for a long time and it has traditionally affected everyday life (Figure 1.1). Seal hunting has been based on drifting ice floes for the productive season in spring. In narrow places, the drift of ice may have stopped for a middle winter period and ice bridges have formed, providing ways to cross the sea. For navigation, sea ice formation has introduced a barrier; in particular, the drift of ice has made the management of this barrier difficult. Recently the transport and dispersion of pollutants in sea ice, oil spills in ice-covered waters, and forces on oil and gas platforms by drifting ice have become important research topics.

The history of sea ice dynamics science began in the late 1800s. Karl Weyprecht led the Austro-Hungarian Expedition on the schooner *Tegetthoff* to Franz-Josef Land in 1872–1874 and examined sea ice thickness and morphology (Weyprecht, 1879). He found from empirical data that sea ice thickness is proportional to the square root of the freezing-degree-days, explained by Stefan (1891) using a heat conduction law. Fridtjof Nansen drifted with topsail schooner *Fram*, moored to ice, across the Eurasian Arctic Ocean between 1893 and 1896. The wind-driven drift speed was on average 2% of the wind speed and the drift direction deviated 30º to the right from the wind direction (Nansen, 1902). Ekman (1902) explained this with wind forcing, ice–water drag, and the Coriolis acceleration. In the south, the German

M. Leppäranta, *The Drift of Sea Ice*, Springer Praxis Books,
DOI 10.1007/978-3-642-04683-4_1, © Springer-Verlag Berlin Heidelberg 2011

Figure 1.1 A section of the marine chart by Olaus Magnus Gothus (1539) showing the northern Baltic Sea. Landfast ice bridges and seal hunting from drift ice floes are illustrated. Olaus Magnus Gothus (1490–1557), the last catholic bishop of Sweden, was deeply interested in northern nature and people. He prepared this chart and in 1555 published a book, *The History of the Nordic Peoples*.

ship *Deutschland* drifted with the ice in the Weddell Sea between 1911 and 1912 (Brennecke, 1921). Winter navigation in the seasonal sea ice zone initiated research connected to the development of mapping and forecasting methods for drift ice conditions (Jurva, 1937).

Wind-driven ice drift was further examined for the atmospheric and oceanic drag forces, and Rossby and Montgomery (1935) presented atmospheric and oceanic boundary-layer models for sea ice and discussed the role of the stability of stratification for drag forces. Free drift model was completed by Shuleikin (1938).

In the Soviet Union, development of the Northern Sea Route[1] gave rise to a large number of investigations into the movement of sea ice. First named the Northern Research and Trade Expedition, the Arctic and Antarctic Research Institute (AARI) was established in 1920 in Petrograd (later Leningrad, presently St. Petersburg). A series of *North Pole drifting stations* was commenced in 1937, where scientific teams drifted along with their campsites from the North Pole region to the Greenland Sea. Zubov (1945) further examined the Nansen–Ekman drift law and presented semi-empirical modifications for various particular cases. He was responsible for the isobaric drift law which states that ice drifts along the isobars of atmospheric surface pressure. Zubov also contributed to further development of the Stefan's ice growth model. In Japan, a research programme was begun in the 1940s on the drift of ice in the Sea of Okhotsk (Fukutomi, 1952), and North American scientists worked from ice islands in the Beaufort Sea, in particular from *T-3*, or *Fletcher's ice island*.

The closure of the sea ice dynamics problem was completed in the 1950s as laws for the internal friction of ice and ice conservation were established. Internal friction, already recognized by Nansen (1902), is a major factor in ice drift, and its understanding necessitates a rheological equation or a constitutive law. It smoothes the drift spatially and guides the ice drift to satisfy realistic boundary conditions. The first attempt was by Laikhtman (1958), who considered drift ice as a Newtonian viscous fluid. The ice conservation law was introduced by Nikiforov (1957), allowing time integration and adjustment of the ice mass field to external forcing. This closure was then utilized in the first generation of numerical models of sea ice dynamics (Campbell, 1965; Doronin, 1970). Also, the first numerical models for sea ice thermodynamics were developed (Maykut and Untersteiner, 1971). In the 1960s, remote-sensing satellites started to map the Earth's surface, providing a new look in particular over uninhabited areas. In drift ice research a huge step followed – for the first time it was possible to have a large-scale daily view of the polar oceans and their sea ice cover.

In the 1970s, two major steps were made in sea ice dynamics with the *AIDJEX (Arctic Ice Dynamics Joint Experiment)* programme (Pritchard, 1980a). From a physical basis, plastic rheologies were introduced for drift ice (Coon *et al.*, 1974), and the concept of ice thickness distribution was presented (Thorndike *et al.*, 1975). Plasticity allows the presence of stationary ice under non-zero forcing and the

[1] The seaway from Europe to Far-East Asia along the Eurasian shelf and Bering Strait, also called the 'Northeast passage'.

occurrence of narrow deformation zones. Thickness distribution contains local thickness variations and adds structural information about ice into the ice conservation law. Hibler (1979) employed a viscous–plastic rheology and constructed a computationally very effective sea ice model, which has become a standard reference. In 1969, a coastal radar system was opened in Japan for continuous sea ice monitoring (Tabata, 1972), and in the Baltic Sea it was decided in 1970 to keep the main harbours open all year; that brought more research resources to ice engineering, sea ice remote sensing and sea ice dynamics (Leppäranta, 1981a).

Another approach has been the derivation of a statistical theory for the drift and diffusion of sea ice. This was first based on simple linear models, such as the Nansen–Ekman law, which have since undergone further modifications. The *International Arctic Buoy Programme* (`http://iabp.apl.washington.edu/`) has produced an extensive amount of data, and it is interesting that their statistics show the same numbers as Nansen's data (Thorndike and Colony, 1982). In Antarctic regions, a similar programme is also ongoing (`http://www.ipab.aq/`). The statistical approach was developed into a Markov chain model by Colony and Thorndike (1984). Sea ice drift was taken as the mean field plus a random walk, and drift buoy data were used to estimate the process parameters. The statistical method complements the deterministic dynamics approach since answers can be easily provided to statistical questions, such as the probability of sea ice drifting from the Kara Sea to the Barents Sea.

In the 1980s, the focus was on mesoscale ice–ocean and air–ice interaction studies. New observational data collection campaigns and process-modelling efforts were realized, in particular within the *MIZEX (Marginal Ice Zone Experiment)* programme (Wadhams *et al.*, 1981; Muench *et al.*, 1987). Work was begun with granular flow models to deduce the mechanical behaviour of drift ice from individual ice floe–floe interactions (Shen *et al.*, 1986). Later, numerical discrete particle methods were developed, which resulted in some success in marginal ice zone dynamics (Løset, 1993) and the sea-ice-ridging process (Hopkins, 1994).

The launch of the *ERS-1* satellite by the European Space Agency (ESA) in 1991 initiated an intensive phase in ice kinematics mapping, with the advent of spaceborne synthetic aperture radars (SARs). These instruments became excellent research and routine tools in the 1990s (Fily and Rothrock, 1987; Kwok *et al.*, 1990; Liu *et al.*, 1998; Kondratyev *et al.*, 1996). Utilization of passive microwave satellite imagery was also extended to the extraction of sea ice kinematics information (Agnew *et al.*, 1997; Kwok *et al.*, 1998). Another landmark in the 1990s was a major increase in sea ice dynamics research in Antarctica, accompanied by wintertime expeditions and the first Antarctic drifting station, the US–Russian *Ice Station Weddell-1*, deployed in 1992 in the Weddell Sea (Gordon and Lukin, 1992; see also `http://www.ldeo.columbia.edu/res/fac/physocean/proj_ISW.html`).

The most recent developments in sea ice dynamics concern scaling: from local ice-engineering problems to mesoscale or large-scale geophysics (see Dempsey and Shen, 2001). A mechanics programme, called SIMI (Sea Ice Mechanics Initiative), has studied the Beaufort Sea (Richter-Menge and Elder, 1998). Anisotropic effects have been introduced into sea ice rheology due to the orientation of leads (Coon

et al., 1998). Russia restarted the North Pole drift station programme in 2003 after 12 years of interruption. Methods for remote sensing of sea ice thickness are slowly progressing (e.g., Wadhams, 2000). This is perhaps the most critical point for the future development of the theory and models of sea ice dynamics. Model developments also focus on deep analysis of the physics of model realizations, the improvement of coupled air–ice–ocean models, and the design of data assimilation methodology (Dulière and Fichefet, 2007). There is a large difference in the characteristics of the ice cover in Arctic and Antarctica due to dynamical boundary conditions: almost closed boundary in north and free ocean boundary in south (Figure 1.2).

Drift ice is a peculiar *geophysical medium* with a large horizontal scale and a very small vertical scale. It is *granular*: ice floes are the elementary particles. The drift takes place on the scale of floes and larger. The ice moves on the sea surface plane with no vertical velocity structure; thus, ice drift can be treated as a *two-dimensional* problem. Since the sea surface is almost a constant geopotential surface, packing densities of ice floes may easily change and therefore drift ice must be taken as a *compressible* medium. The rheology of drift ice shows a highly *non-linear* relation between stress and strain rate, much different from the air above and the water

Figure 1.2a A drift ice landscape from the northern Greenland Sea, June 1983; the photograph was taken during MIZEX-83 (Marginal Ice Zone Experiment, 1983), onboard the R/V *Polarbjørn*. The ice field consists of ice floes with hummocks and ridges.

Figure 1.2b A drift ice landscape from Weddell Sea, December 2004; the photograph was taken during transport from Cape Town to Dronning Maud Land, onboard the R/V *Akademik Fyodorov*. The ice field is much less deformed and more open than in the Arctic Ocean.

below. Finally, because of freezing and melting, an *ice source/sink* term is included in the ice conservation law. Being thin, the direct Coriolis effect on the ice is rather weak, in contrast to the atmosphere and ocean.

The full ice drift problem includes the following unknowns: *ice state* (a set of relevant material properties), *ice velocity*, and *ice stress*. The system is closed according to equations for the conservation of ice, the conservation of momentum, and ice rheology. Ice is driven by winds and ocean currents and responds to forcing by its inertia, internal friction, and adjustment of its state field. The Coriolis effect slightly modifies ice movement. The dynamics of sea ice is coupled with thermodynamics, since freezing strengthens and melting weakens the ice, while ice motion influences the further growth or melting of ice via transport and differential motion.

Although the ice drift problem offers quite interesting basic research possibilities, the principal science motivation has come from sea ice introducing a particular air–sea interface. The exchange of momentum, heat, and material between the atmosphere and the ocean takes place in drift ice fields in high latitudes, and this interface experiences transport as well as opening and closing due to ice drift. This is crucially important to both regional weather and global climate. Ice extent, largely

Figure 1.3 Icebreakers have extended navigation season in ice-covered seas since late 1800s. Their operation is sensitive to ice dynamics, due to ice pressure and thick deformed ice formations. Icebreaker *Sisu* assisting a cargo vessel in the Baltic Sea.
Photograph by Mr. Riku Lumiaro, printed with permission.

influenced by ice drift, has a key role in the cryospheric albedo effect. Also, ice transports latent heat and freshwater, while ice melting gives a considerable heat sink and freshwater flux into oceanic surface layer. In the ecology of polar seas, the location of the ice edge and its ice-melting processes is a fundamental boundary condition for summer productivity.

Sea ice and climate have strong coupling, presently a major research area in the drift of sea ice (e.g., Frolov *et al.*, 2009). The amount of ice in polar seas is dictated both by thermal and dynamical forcing. Large negative anomalies, in particular the minimum in 2007, have been observed in summer ice conditions in the Arctic Ocean. A rather new research line for sea ice dynamics is in paleoclimatology and paleoceanography (Bischof, 2000). Marine sediments provide an archive of drift ice and iceberg data, and via its influence on ocean circulation, drift ice has been an active agent in global climate history.

In the practical world, sea ice dynamics is connected with three major questions. First, sea ice models have been applied to guide winter navigation (Figure 1.3) by providing short-term forecasts of ice conditions (e.g., Leppäranta, 1981a). Possible climate warming may largely increase the use of the Northern Sea Route from Europe to Far East (Johannessen *et al.*, 2007). Second, ice engineering is concerned with ice loads on fixed structures and ships, and the dynamics of ice brings risks for ice pressure and ice-structure collisions, which both are difficult to predict. (e.g., Sanderson, 1988). Third, the question of pollutant transport by drifting sea ice has become an important issue (Pfirman *et al.*, 1995). In particular, risk assessment of oil spills and their clean-up require proper oil transport and dispersion models for ice-covered seas (e.g., Ovsienko *et al.*, 1999a).

The theory and models of sea ice dynamics are applicable in general to ice dynamics in large basins (large relative to ice thickness and external forcing). The essential feature is that floating ice breaks into floes and then drifts. This is true in large lakes, such as Lake Ladoga in Russia, Lake Vänern in Sweden, and the Great Lakes of North America (Wake and Rumer, 1983; Leppäranta and Wang, 2008). Even in large rivers (e.g., the Niagara River in North America), the drift of ice floes can be examined with the same models (Shen *et al.*, 1993).

This book presents a treatise on the geophysical theory and empirical knowledge of the drift of sea ice. The objective is to describe ice drift by observational data (Figure 1.4), to introduce the basic ideas and laws of sea ice dynamics, to provide solutions to elementary cases that help us to understand the ice drift geophysics, and to present the status of sea ice dynamics models. Apart from the first edition of this book, earlier books devoted to sea ice dynamics are only available in Russian (e.g., Timokhov and Kheysin, 1987; Gudkovic and Doronin, 2001). Review articles have been written in English by Rothrock (1975b), Hibler (1986), and Leppäranta (1998). Individual chapters about ice drift can be found in sea ice geophysics books by Zubov (1945), Doronin and Kheysin (1975), and Wadhams (2000). Frolov *et al.* (2005) published a book about the history of 100 years of sea ice observations in the Arctic Ocean.

The general structure of the book is the following: Chapters 2–4 present the drift ice medium and its kinematics; in Chapter 5 this medium is inserted into Newton's

Figure 1.4 Deployment of a corner reflector mast for deformation studies by a laser geodimeter, in the Baltic Sea in April 1978. A system with several reflector sites allows accurate monitoring of sea ice kinematics in a 5 km scale array.

2nd law to obtain the equation of motion; and in Chapters 6–8 a solution to the ice drift problem is given. Chapter 2 provides a description of drift ice material, leading to an "ice state", the set of relevant quantities for the mechanical behaviour of drift ice. A section of sea ice thermodynamics is also included. In Chapter 3, ice velocity observations are presented, a theoretical framework is given for ice kinematics analysis, and the ice conservation law is derived. Chapter 4 treats drift ice rheology, a difficult but necessary subject to understand the motion of drift ice. The momentum equation of ice dynamics is derived in Chapter 5, including a discussion of principal external forcings – air and water drag force – and analysis of the equation. Free drift is examined in Chapter 6, and ice drift in the presence of internal friction is the subject of Chapter 7. In both these chapters analytical solutions are presented for particular ice flows. The modern solution to understanding sea ice drift by numerical modelling is given in Chapter 8, and the aim is to help the reader understand how this solution is arrived at, how it reflects the behaviour of real sea ice, and how one should interpret the outcome of numerical sea ice dynamics models. Finally, a brief discussion is given on some consequences of the ice drift phenomenon (Chapter 9). Chapter 10 invites the reader to tackle a collection of study problems. Chapter 11 lists the references. This is followed by the index.

2

Drift ice material

2.1 SEA ICE COVER

This chapter presents the material structure of sea ice from local scale to large scale. Ice floes form granular drift ice fields, for which continuum approximations are used when the scale of interest is much larger than the floe size. These fields are characterized by their ice type, ice compactness, floe size and shape, and ice thickness, as shown in Sections 2.1 and 2.2. Section 2.3 is devoted to thermodynamics of sea ice, which is closely coupled with dynamics and which is a necessary element in sea ice dynamics models. Section 2.4 presents the ice thickness distribution, and Section 2.5 deals with ice ridges, the thickest accumulations of mechanically deformed ice, which have a key role in the mechanical energy budget of drift ice. The chapter ends with Section 2.6 introducing the concept of "ice state" – a set of material properties of drift ice necessary to understand and model its dynamics.

In the world sea ice cover, ice occurs all year in the *perennial sea ice zone*, covering the inner Arctic Ocean north of about 80°N and smaller sections in the Antarctica, mainly the western Weddell Sea. Ice occurs only in winter in an area called the *seasonal sea ice zone* (SSIZ), extending on average down to 60° latitudes.

Table 2.1 and Figure 2.1 show the main sea ice basins, with sizes ranging from 200 km to 3000 km. Southern Ocean sea ice cover is actually a ring, 20,000 km long and with a width ranging from almost zero in summer to 1000 km in winter, centred around Antarctica at 60–70°S. Within freezing seas there are smaller sub-basins, which contain dynamically independent ice packs such as the Gulf of Riga in the Baltic Sea (size $L = 100$ km and typical ice thickness $h = 0.2$ m). The drift ice basin closest to the equator is the Bo Hai Sea (Gulf of Chihli) off the coast of China, located between the latitudes of 37° and 41°N[1].

[1] Sea ice forms occasionally in the Chesapeake Bay estuary on the east coast of USA at similar latitudes but drift ice phenomena are not of concern there.

M. Leppäranta, *The Drift of Sea Ice*, Springer Praxis Books,
DOI 10.1007/978-3-642-04683-4_2, © Springer-Verlag Berlin Heidelberg 2011

Nikolai Nikolaevich Zubov (1885–1960), a great pioneer in the science of sea ice, its physics and its geography. He was the author of the monumental book *L'dy Arktiki [Arctic Ice]*, published in 1945 in Moscow and translated into English in 1963.
Reproduced from Collections of the Russian State Museum of Arctic and Antarctic, St. Petersburg, with permission.

The thickness of ice is 2–5 m in the Arctic Ocean and Greenland Sea, while in the SSIZ it is an order of magnitude less. For an enclosed drift ice basin there is no ice exchange with neighbouring seas, while in an open basin a large part of the ice boundary is toward open water and the mobility of the ice is therefore greater. The ratio $\delta = h/L$, which characterizes the stability of a solid ice sheet in a basin, ranges from 10^{-7} to 5×10^{-6} in sea ice basins where drift ice occurs (Table 2.1). In subarctic medium size lakes ($L \sim 10$ km, $h \sim 0.5$ m), $\delta \sim 5 \times 10^{-5}$, and the ice forms a solid stationary sheet. In Lake Ladoga, the largest lake in Europe, we have $L = 100$ km and $h = 0.5$ m and the ice cover is mobile as suggested by $\delta = 5 \times 10^{-6}$.

2.1.1 Sea ice landscape

A "sea ice landscape" consists of leads and ice floes with ridges, hummocks, and other variable morphological characteristics. *Ice types* have been defined to provide practical standards for observers (WMO, 1970; see also `http://www.aari.nw.ru/` for updates). They originate from shipping activities in ice-covered waters

Table 2.1 The main basins of the world ocean's ice zone. The types, E = enclosed, SE = semi-enclosed and O = open, refer to the ice exchange with neighbouring seas.

Basin	Size L (km)	Type	Ice thickness, h (m)	Stability, h/L ($\times 10^{-6}$)
Central Arctic	3000	SE	2–5	0.7–2
Greenland Sea	1000	O	2–5	2–5
Barents Sea	1000	O	1–2	1–2
Kara Sea	1000	SE	1–2	1–2
White Sea	200	SE	0.1–1	0.5–5
Baltic Sea	500	E	0.1–1	0.2–2
Sea of Azov	200	E	0.1–0.2	0.5–1
Sea of Okhotsk	1000	SE	0.1–2	0.2–4
Bohai Sea	300	E	0.1–0.3	0.3–1.0
Bering Sea	1000	SE	0.1–1	0.1–1
Hudson Bay	500	E	0.5–1	1–2
Gulf of St Lawrence	300	E	0.1–1	0.3–3
Labrador Sea	500	O	0.5–1	1–2
Baffin Bay	500	SE	1–2	2–4
Southern Ocean	1000	O	0.5–2	0.5–2
Weddell Sea	1500	O	0.5–3	0.3–2
Ross Sea	500	O	0.5–1	1–2

and are based on appearance (i.e., how the ice looks to an observer on a ship or in an aircraft: Figures 2.2 and 1.2). This ice-type classification system has worked fairly well and has not suffered from severe subjective biases. The formation mechanism, aging, and deformation influence the appearance. Thus appearance provides information of ice thickness, which is seldom known from direct measurements. Some ice-type names are based on their resemblance to familiar objects (Figure 2.3).

Definitions

Let us now give a brief list of the necessary sea ice nomenclature for dynamics based on internationally agreed standards (Armstrong *et al.*, 1966; WMO, 1970):

Ice in the ocean

- *Sea ice*. Any form of ice found at sea that originates from the freezing of seawater.
- *Ice of land origin*. Ice formed on land or in an ice shelf, found floating in water.

Age of ice

- *New ice*. A general term for recently formed ice.
  - *Frazil ice*. Fine spicules or plates of ice suspended in water.
  - *Nilas*. A thin, elastic crust of ice that easily bends under the action of waves and swell and rafts under pressure (matt surface and thickness up to 10 cm).

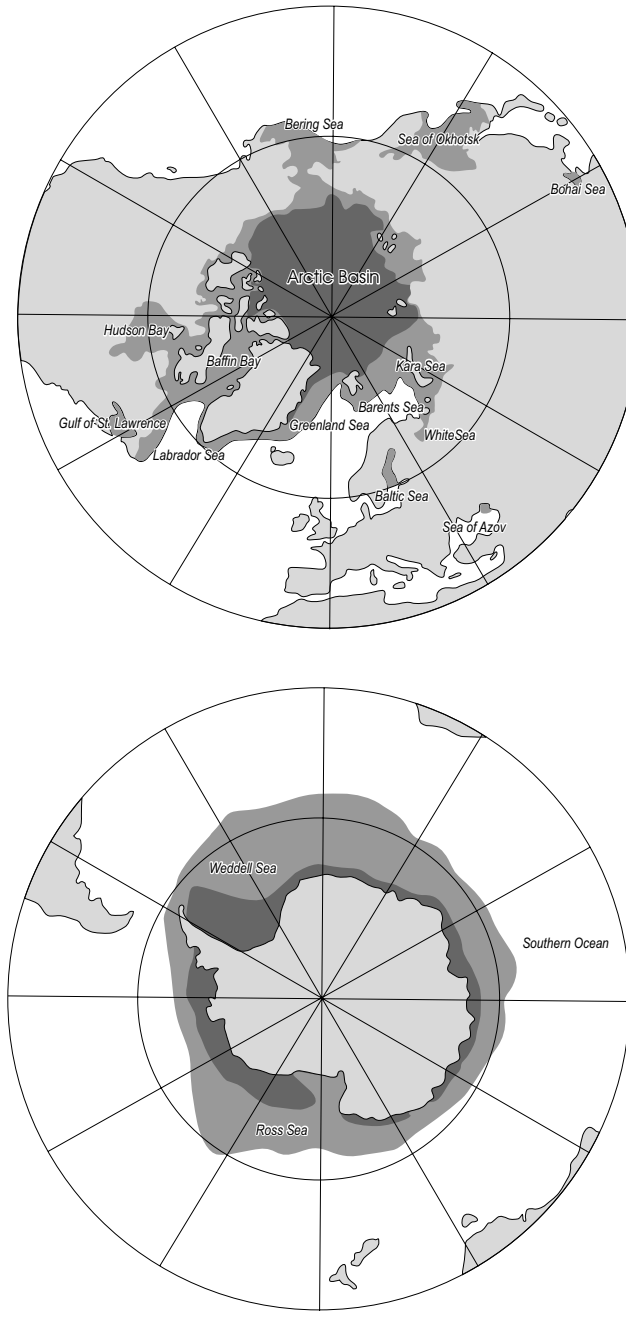

Figure 2.1 The world sea's ice zones in summer and winter. Dark area shows the perennial ice, lighter area shows the seasonal sea ice zone.
From Untersteiner (1984), with modifications for subarctic small basins.

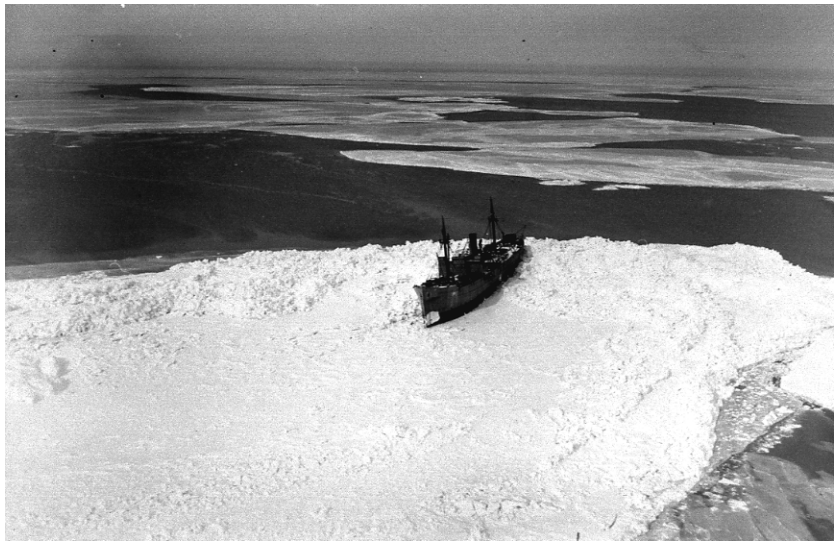

Figure 2.2 Aerial photograph from a Finnish Air Force ice reconnaissance flight in the Central Baltic, winter 1942. Airborne reconnaissance meant a huge step in understanding the morphology and drift of sea ice. The pilot was Erkki Palosuo, who later became a sea ice geophysicist and used his sea ice data from the Second World War for his doctoral thesis (Palosuo, 1953).

Reproduced with permission from Erkki Palosuo.

Figure 2.3 Pancake ice (the ice pieces shown are about 1 m across), also named lotus ice in the Far East, blini ice in Russia, and plate ice in Scandinavia and Finland.

- *Young ice*. Ice in transition between new ice and first-year ice (10–30 cm thick).
- *First-year ice*. Ice with no more than 1 year's growth that develops from young ice (thickness 30 cm to 2 m). Level when undeformed, but where ridges and hummocks occur, it is rough and sharply angular.
- *Multi-year ice*. Ice of more than 1 year's growth (thickness over 2 m). Hummocks and ridges are smooth and the ice is almost salt-free.

Forms of ice

- *Landfast ice*. Sea ice that remains fast along the coast, over shoals, or between grounded icebergs (also called *fast ice*).
- *Grounded ice*. Floating ice that finds itself aground in shoal water.
- *Drift ice*. Term used in a wide sense to include any sea ice other than fast ice (a substitute term is *pack ice*).
- *Ice field*. Area of drift ice at least 10 km across.
- *Pancake ice*. Pieces of new ice, usually approximately circular, about 30 cm to 3 m across and with raised rims due to the pieces striking against each other.
- *Ice floe*. Any relatively flat piece of ice 20 m or more across.
- *Level ice*. Sea ice that is unaffected by deformation (a substitute term is *undeformed ice*).
- *Deformed ice*. A general term for ice that has been squeezed together and in places forced upward and downward (a substitute term is *pressure ice*).
- *Rafted ice*. A form of pressure ice in which one floe overrides another. A type of rafting common in nilas whereby interlocking thrusts are formed – each floe thrusting "fingers" alternatively over and under the other – is known as *finger rafting*.
- *Brash ice*. Accumulations of ice made up of fragments no more than 2 m across (the wreckage of other forms of ice).
- *Hummocked ice*. A form of pressure ice in which pieces of ice are piled haphazardly, one piece over another, to form an uneven surface.
- *Ridge*. A ridge or wall of broken ice forced up by pressure (the upper – above water level – part is called the *sail* and the lower part the *keel*).

Openings in ice cover

- *Ice compactness*. The amount of sea surface covered by ice as a fraction of the whole area being considered (a substitute term is *ice concentration*).
- *Crack*. Any fracture that has not parted more than 1 metre.
- *Fracture*. Any break or rupture in ice resulting from deformation processes (length from metres to kilometres).
- *Lead*. Any fracture or passageway through sea ice that is navigable by surface vessels. Leads are opened by wind or ocean current forcing.
- *Polynya*. Any nonlinear-shaped opening enclosed in ice. Typical forms are *coastal polynyas* driven by persistent offshore winds and *open ocean polynyas* driven largely by upwelling of warm deeper water.
- *Ice edge*. The demarcation between the open sea and sea ice.

Table 2.2 Classification of ice concentration A (WMO, 1970).

Verbal	Numerical	Verbal	Numerical
Ice free	$A = 0\%$	Very open drift ice	$0\% < A < 30\%$
Open drift ice	$30\% \leq A < 50\%$	Close drift ice	$50\% \leq A < 70\%$
Very close drift ice	$70\% \leq A < 90\%$	Compact drift ice	$90\% \leq A \leq 100\%$

Ice compactness or *ice concentration*, denoted by A, is normally given in percentages or tenths and further categorised into six standard classes (Table 2.2; Figure 2.4). Between ice and open water surfaces, apart from melting conditions, there are strong contrasts and satellite remote sensing methods can detect them. Ice compactness is a key dynamic state variable as it tells of the mobility of drift ice fields.

The polar oceans also contain ice of land origin. By the mechanism called *calving*, pieces of ice break away from land ice masses facing the ocean. These pieces are classified (WMO, 1970) according to their size: *icebergs* (top more than 5 m above sea level), *ice islands* (top about 5 m above sea level and area more than few thousand square metres), *bergy bits* (top 1–5 m above sea level and area 100–300 m^2), and *growlers* (smaller than bergy bits). These pieces differ from sea ice floes by their ice quality (fresh water ice), thickness and three-dimensional character.

2.1.2 Sea ice zones

In a given basin, sea ice cover can be divided into zones of different dynamic character (Weeks, 1980): central pack, shear zone, landfast ice, and marginal ice zone. Shear zone and landfast ice form the coastal boundary zone, while the marginal ice zone is the boundary zone toward the open ocean. Very small basins only contain fast ice and the width of the boundary zones – marginal ice zone and shear zone – is of the order of 100 km.

The central pack consists of the interior ice that is free from immediate influence from the boundaries. Changes are smoother there than in the boundary zones and are caused by external forcing. The length scale is the size of the basin itself; but due to the width of boundary zones, the central pack only exists in large seas.

Landfast ice, or *fast* ice, is the immobile coastal sea ice zone, stationary for most of the ice season. The width of this zone depends on the thickness of ice, topography of the sea bottom, and the areal density of islands and grounded forms of ice. Fast ice extent develops stepwise, in an almost discontinuous manner (Jurva, 1937; Divine, 2003). Grounding of sea ice ridges creates fixed support points to stabilize the ice sheet. Because of the size of ridges and ice thickness, in Arctic seas the fast ice zone extends to depths of about 10–20 m (Zubov, 1945; Volkov *et al.*, 2002) while in subarctic seas such as the Baltic Sea the limit is normally close to 10 m (Leppäranta, 1981b). In Antarctic waters, grounded icebergs may act as tie points for fast ice

formation, and therefore the fast ice zone may extend deeper into the ocean as well (e.g., Massom *et al.*, 2003). Off Hokkaido in the Sea of Okhotsk, there are no islands and the depth of the sea increases rapidly with distance from the shoreline. Tides "clean" the ice that forms close to the shore, and as a consequence the fast ice zone is practically non-existent.

The shear zone is the boundary zone of the drift ice field next to the landfast ice (or coast). There the mobility of the ice is restricted by the geometry of the boundary and strong deformation takes place. The width is 10–200 km. A well-developed shear zone is found on the coast of the Beaufort Sea of the Arctic Ocean. Based on deformation data, Hibler *et al.* (1974a) concluded its representative width was around 50 km. At the solid boundary, ice velocity is sensitive to the forcing direction (Goldstein *et al.*, 2009). The velocity is often discontinuous across the boundary, thus modifying local hydrography and circulation. In basins of $\sim$100 km length scale, such as the Bay of Bothnia in the Baltic Sea, the whole ice pack feels the presence of land, and geometric steering by the basin is seen in ice motion.

The marginal ice zone (MIZ) lies along the boundary of open water and sea ice cover. It is loosely characterized as the area of pack ice where the influence of the open ocean is directly observed. MIZ extends to a distance of 100 km from the ice edge (Wadhams, 1980b; Squire, 1998). This distance corresponds to the penetration distance of ocean swell into a drift ice field; this distance also corresponds to the length scale below which the wind fetch over ice is not long enough to build ice ridges. In the MIZ, there is a large temporal and spatial variability of ice conditions and intensive air–ice–sea interaction. Off-ice winds cause MIZ diffusion, while on-ice winds drive the ice to form a sharply compact ice edge (Zubov, 1945). The open sea influence is strongest in a narrow *ice edge zone*, width up to 5 km.

Well-developed MIZs are found along the oceanic ice edge of the polar oceans, and their locations are largely controlled by the polar fronts. At a compact ice edge there is a discontinuity in sea surface velocity and roughness, and possibly a front in temperature and salinity. They affect the mesoscale circulation in the ocean, resulting in eddies and jets as well as ice edge upwelling and downwelling. A front may also form in the atmospheric boundary layer. In smaller, subarctic seas there is usually not time enough for a proper marginal ice zone to develop. In such seas, ice cover extends and retreats a long distance back and forth during a short ice season. Ice edge zones, however, develop quickly and are a common feature at the ice margin under on-ice wind forcing.

In the past, the ice margin used to be considered the border of an unknown ocean where the ice mysteriously transported sand and driftwood from unknown places. And as such drifting sea ice was strange, it inspired the Vikings to name a new land – Iceland – due to the presence of drift ice in its fjords.

2.1.3 Sea ice charting

Sea ice charting began in the late 1800s for navigation in ice-covered waters. Due to the dynamics of sea ice, the charts need daily updating and therefore much is

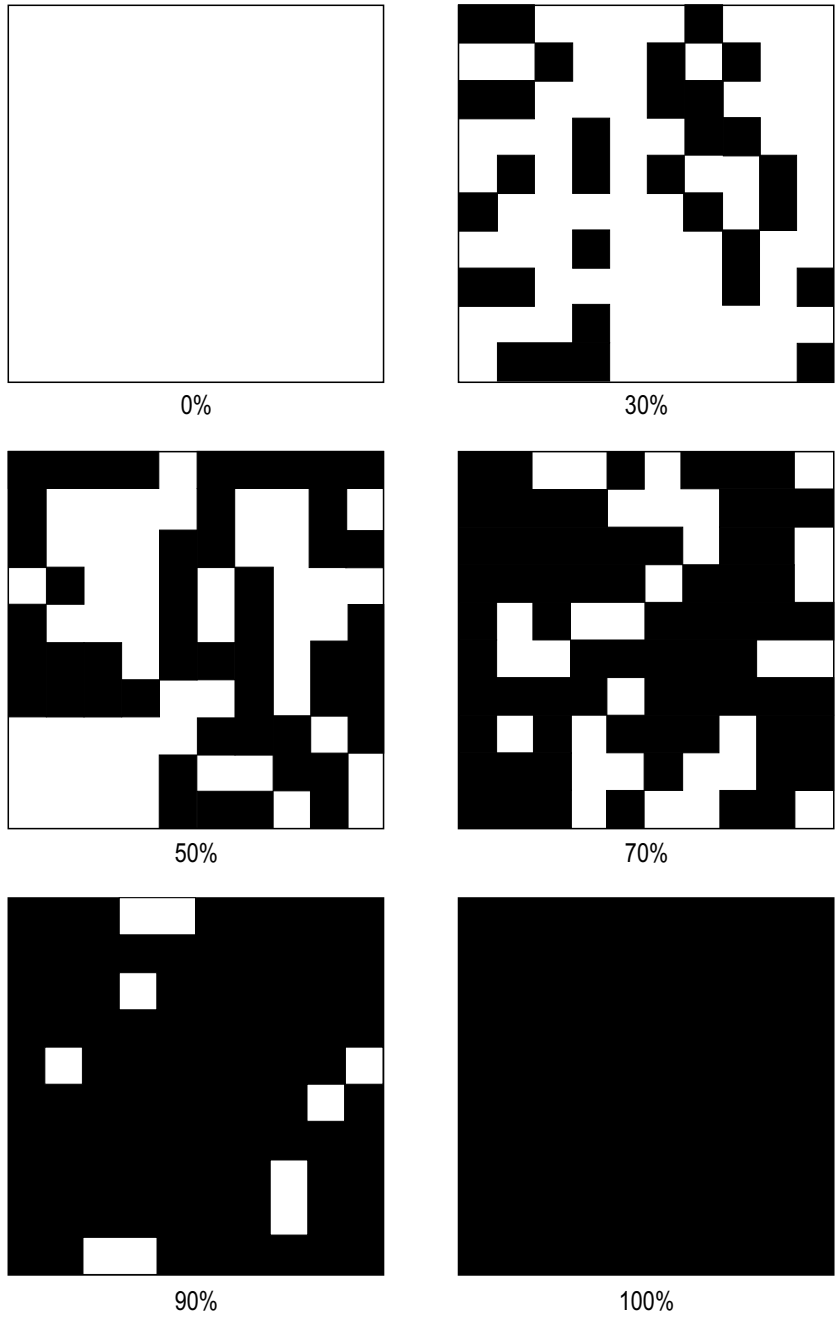

Figure 2.4 Classification of ice concentration (WMO, 1970), with the class boundaries illustrated by random binary charts. From left up to right down: open water, very open drift ice, open drift ice, close drift ice, very close drift ice, compact drift ice.

required of the mapping methods. Before the time of airborne and spaceborne remote sensing, ice charts were based on ship reports and occasional ground truth observations, which provide only limited information. Aerial reconnaissance played an important role until the 1970s, but since then satellite observation technology has been the main method of data collection. Sea ice information is presented according to an international standard (WMO, 2000). However, ships operating in ice conditions also take original satellite images to see detailed ice conditions along a planned route.

Polar orbiting weather satellites, such as the *NOAA AVHRR* series, with optical and infrared channels were taken into ice charting in the 1970s. However, both channels are limited by cloudiness, and the optical channel is further limited by the lack of sunlight in polar winter. Due to the weather limitations, microwave methods have become a critically important complementary tool. Soviet Union *Okean* series satellites produced simultaneous optical–radar image pairs for ice conditions in the Northern Sea Route in the 1980s (e.g., Johannessen *et al.*, 2006). At present, passive microwave mapping is the principal method for regular, global sea ice charting, mainly using US Defense Meteorological Satellite Program (DMSP) special sensor microwave imager (SSM/I) data (Figure 2.5), available via the National Snow and Ice Data Center (NSIDC) in Boulder, Colorado (`http://nsidc.org`) (Cavalieri *et al.*, 1999). This method is weather- and light-independent but limited by low spatial resolution (20–30 km), too small for regional ice charting.

Synthetic aperture radar (SAR) has become an extremely useful complementary tool. The first extensive satellite SAR data set was collected by *ERS-1*, launched by the European Space Agency (ESA) in 1991. A few years later, the *Radarsat* satellite series was started in Canada, commercial satellites designed for sea ice mapping (Stern and Moritz, 2002; Belchansky and Douglas, 2002; `http://www.radarsat2.info/`). SAR technique provides high spatial resolution but has limitations. A balance must be chosen between repeat cycle, swath and spatial resolution (i.e., full coverage of an area is possible with 5-day repeat cycles using lower resolution). Also, interpretation of the radar signal for sea ice information is sometimes problematic. Ice conditions change significantly on a daily basis in the seasonal sea ice zone (Leppäranta, 1981a; Leppäranta *et al.*, 1998), and the relation between sea ice and radar image is not one-to-one (Carsey, 1992; Wadhams, 2000). For example, ice and open water signatures are not always different, and ridges may be mixed with frost flowers on thin ice in narrow leads. Radar is at its best, in mapping ice kinematics.

An example of a sea ice chart over the Arctic is given in Figure 2.6. Ice charts basically present ice compactness and ice type. In subarctic seas with heavy winter traffic, ice charts are invaluable in providing information about the ice thickness and floe size. In the Baltic Sea, each of the nine coastline countries has an ice service for regional ice charting (e.g., `http://www.fmi.fi/weather/index_9.html/` for the Finnish Ice Service). Another way of ice charting is automatic mapping of the ice concentration field, the principal ice quantity manageable by remote sensing. NSIDC provides global ice charts such as that shown in Figure 2.5 on a daily basis. In Hokkaido, Japan, a coastal radar system was used from 1969 to 2005 for mapping

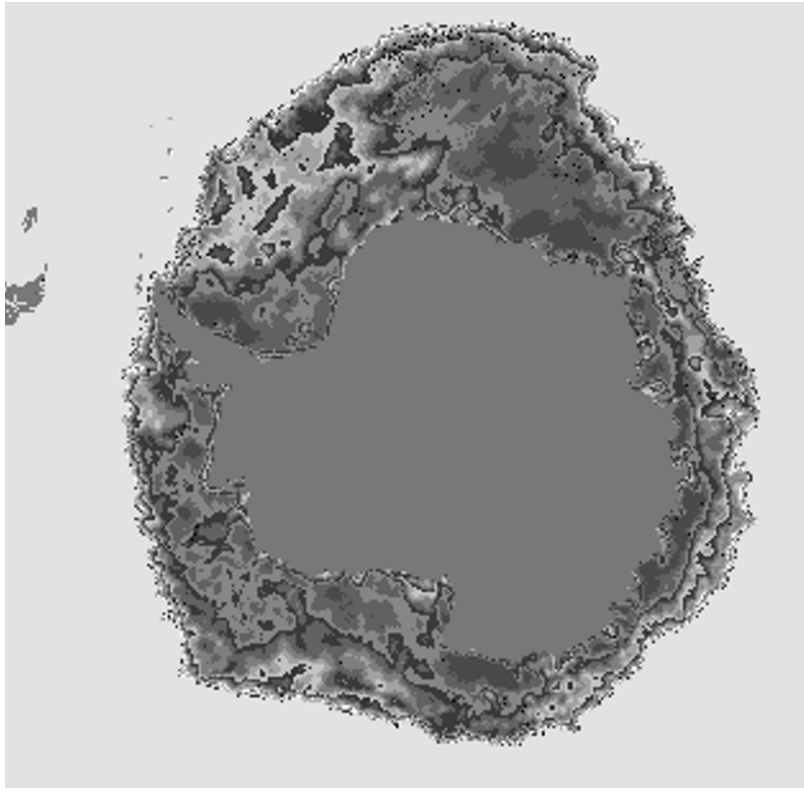

Figure 2.5 Sea ice concentration in the Antarctic based on passive microwave SSM/I data. At the ice edge, compactness increases rapidly to about 80%, while in the inner pack it is mostly 75–90% with a few areas below the 70% level only in the Weddell Sea. NRTSI Product for 2003-10-2 National Snow and Ice Data Center, Boulder, CO.
Reproduced from Cavalieri et al. (1999), with permission from National Snow and Ice Data Center, Boulder, CO.

offshore ice conditions in the Sea of Okhotsk to a distance of 60 km from the coast (`http://www.hokudai.ac.jp/lowtemp/sirl/sirl-e.html`).

The main problem in sea ice charting is how to obtain good ice thickness information – this is also the main problem for the progress of sea ice dynamics theory and modelling.

2.2 ICE FLOES TO DRIFT ICE PARTICLES

2.2.1 Scales

Sea ice mechanics is examined over a wide range of scales. *Microscale* includes individual grains and ice impurities, extending from sub-millimetres to 0.1 m. In the *local scale*, 0.1–10 m, sea ice is a solid sheet, a polycrystalline continuum with a

substructure classified according to the formation mechanism as congelation ice, snow-ice, and frazil ice (Eicken and Lange, 1989). *Ice floe scale* extends from 10 m to 10 km and includes individual floes and ice forms such as rubble, pressure ridges, and fast ice. When the scale exceeds the floe size, the sea ice medium is called drift ice or pack ice and, as in dynamical oceanography, the scales 100 km and 1000 km are *mesoscale* and *large scale*, respectively.

The drift of sea ice takes place on the floe scale and larger. The horizontal structure of sea ice cover is well revealed by optical satellite images (Figure 2.7). The elementary particles are *ice floes*, described by their thickness h and characteristic diameter d. The WMO nomenclature (WMO, 1970) restricts ice floes to those ice pieces with $d > 20$ m; smaller ones are termed *ice blocks*. This is convenient because for ice floes the *aspect ratio* h/d is smaller than about 0.1 and floes included in the definition are flat. The floe size ranges from the lower limit to tens of kilometres. In sea ice dynamics research we consider the drift of individual floes or the drift of a system of ice floes, called a *drift ice field*.

Ice density is taken as a constant ($\rho = 910\,\mathrm{kg\,m^{-3}}$). Therefore, armed with thickness information we can calculate the mass of ice, given as the mass per unit area by $m = \rho h$. In reality, the density varies within $\pm 1\%$ around this reference due to variations in the temperature, salinity and gas content of the ice. Ice floes float

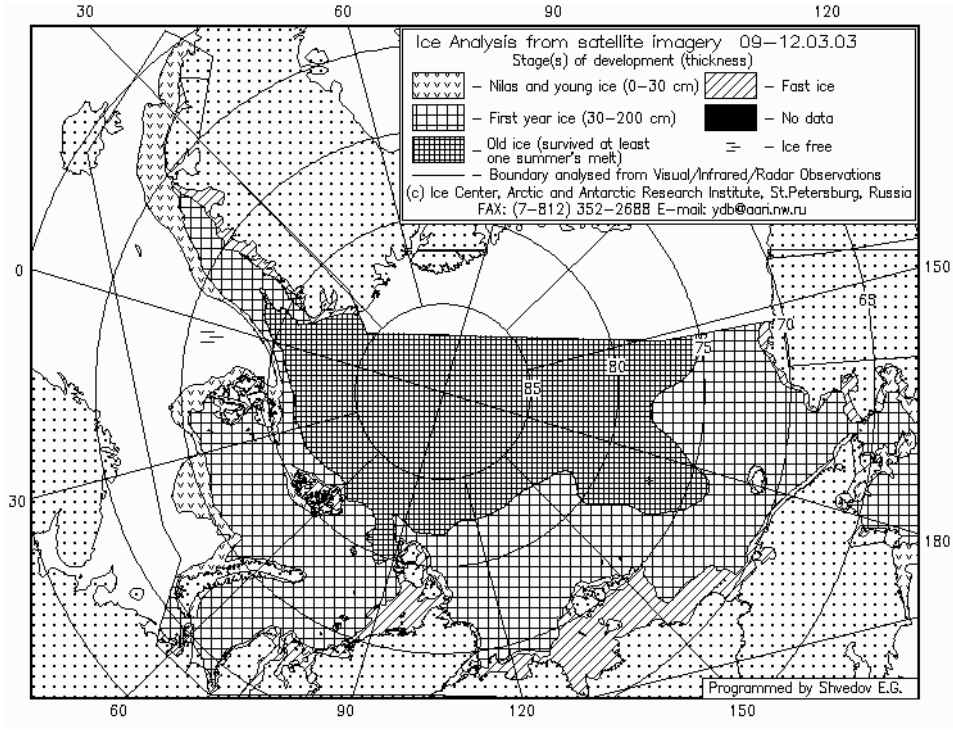

Figure 2.6 Ice chart over the Eurasian side of the Arctic Ocean, 12 March 2003.
Reproduced with permission from Arctic and Antarctic Research Institute, St Petersburg, Russia: htpp://www.aari.nw.ru/

freely, apart from shallow areas where grounding may occur. The portions of an ice floe above and beneath the sea surface are, respectively, *freeboard* (h') and *draft* (h''), $h = h' + h''$. Archimedes' law states that:

$$\frac{h''}{h} = \frac{\rho}{\rho_w} \tag{2.1}$$

where ρ_w is the density of seawater. Since $\rho_w \approx 1028\,\mathrm{kg\,m^{-3}}$ is the density of cold seawater (salinity 35‰, temperature at freezing point), $\rho/\rho_w \approx 0.89$. The potential energy of an ice floe per unit area consists of the freeboard and draft portions, and for floating ice it equals (Rothrock, 1975a):

$$E_p = \rho g \int_0^{h'} z dz - (\rho_w - \rho) g \int_{-h''}^{0} z dz = \frac{1}{2} \frac{\rho(\rho_w - \rho)}{\rho_w} g h^2 \tag{2.2}$$

where $g = 9.8\,\mathrm{m\,s^{-2}}$ is acceleration due to Earth's gravity. For ice not floating but supported from the sea bottom, the right-hand equation of Eq. (2.2) is not true.

The behaviour of a drift ice field depends on its horizontal size L and the thickness and size of ice floes. This gives three length ratios: the floe aspect ratio h/d, granularity L/d, and stability h/L. The number of ice floes is proportional to $(L/d)^2$, and the mechanical breakage of an ice sheet mainly depends on h/L and mode of breakage.

Drift ice particles

A drift ice material particle is a set of ice floes. A particle of size D contains $n \approx (D/d)^2$ floes. For the continuum approximation to be valid n must be large: $n > 100$ or equivalently $D/d > 10$. Additionally, the particle size should be much less than the scale of changes or the gradient scale $\Lambda = Q/|\nabla Q|$ where Q is a property of the ice dynamics field. Summarizing, the scales should satisfy:

$$d \ll D \ll \Lambda \qquad \text{for a continuum} \tag{2.3a}$$

or

$$d \sim D \sim \Lambda \qquad \text{for a discrete system} \tag{2.3b}$$

In the real world, the situation is often intermediate (i.e., $d < D < \Lambda$). Depending on the particular question under examination, $d \sim 10^1$–$10^4\,\mathrm{m}$, $D \sim 10^3$–$10^5\,\mathrm{m}$ and $\Lambda \sim 10^4$–$10^6\,\mathrm{m}$. The gradient scale requirement arises for the linear deformation approach to be applicable. Taylor polynomial[2] shows that, e.g., for displacement or velocity, the ratio of the nonlinear residual to the linear term is $\sim \frac{1}{2}|\boldsymbol{x}|/\Lambda$, where $\boldsymbol{x} = (x, y)$ is the horizontal space coordinate vector. Consequently, the condition $D \ll \Lambda$ needs to be satisfied.

[2] Taylor polynomial is written in one dimension as,

$$f(x) = f(0) + \frac{x}{1!} f'(0) + \frac{x^2}{2!} f''(0) + \cdots + \frac{x^n}{n!} f^{(n)}(0) + R_{n+1}(x),$$

where the residual $R_{n+1}(x)$ is of the order of x^{n+1}; for two dimensions $f^{(n)}$ is replaced by $(\partial_x + \partial_y)^n f$ (e.g., Adams, 1995).

In the continuum theory of drift ice, field variables such as ice velocity are defined for each drift ice particle (cf. fluid parcels in fluid dynamics); but, because of the finite size of the floes, their individual features may play a role in the motion of drift ice fields. Thus the theory includes a basic inaccuracy. As D approaches Λ, discontinuities start to build up, and as D approaches d, a system with a single floe or a few floes appears.

Let $h = h(x, y, t)$ stand for the ice thickness in a given point and time; for open water $h = 0$. Define a function "ice", I, by:

$$I(x, y, h_0)\begin{cases} = 0, & \text{if } h(x, y) \leq h_0 \\ = 1, & \text{if } h(x, y) > h_0 \end{cases} \tag{2.4}$$

where h_0 is the *demarcation thickness*. This definition separates thin ice and is convenient in some theoretical considerations. Consider a region Ω in a sea ice pack – it may be a basin, a drift ice particle, or anything between – whose surface area is S. The packing density, or compactness, of ice is defined as:

$$A = \frac{1}{S}\int_{\Omega} I(x, y; 0)d\Omega \tag{2.5}$$

For uniform circular floes, the most open and dense locked packings are $\pi/4 \approx 0.79$ and $\pi/(2\sqrt{3}) \approx 0.91$, respectively (Figure 2.8). The further below 0.79 the packing goes, so contacts between floes become fewer. Since ice floes float nearly on a geopotential surface[3], compactness may easily change. However, at the locked level, further compression necessitates ice breakage and pressure ice formation. The connection between compactness and mean free path l_w is for uniform circular floes

$$\frac{A}{A_{\max}} \approx \frac{d^2}{(d + l_w)^2} \tag{2.6}$$

where $A_{\max}$ is the densest packing for a given set of floes. For $l_w = d$, we have $A/A_{\max} \approx \frac{1}{4}$: and $A/A_{\max} < 0.8$ for $l_w/d > 0.12$, considered to be already in the low stress regime. For distributed floe sizes $A_{\max}$ is in general larger, and $A/A_{\max}$ can be estimated by using averages of d and $d + l_w$ in Eq. (2.6). As the distribution widens, $A_{\max} \to 1$. Thus an important characteristic of an ice floe field is the uniformity of floe sizes.

The *mean ice thickness* $\tilde{h}$ and the *mean ice floe thickness* $\tilde{h}_i$ are defined by:

$$\tilde{h} = \frac{1}{S}\int_{\Omega} h d\Omega = A\tilde{h}_i \tag{2.7}$$

The mean ice floe thickness is thus the mean thickness of the actual ice floe pieces in Ω, while open water is also included in the mean ice thickness. At times, these different thickness definitions have caused confusion. Clearly, we have $0 \leq A \leq 1$ as well as $0 \leq \tilde{h} \leq \tilde{h}_i$. Ice compactness and mean ice floe thickness are the fundamental quantities for the mechanical properties of drift ice. Other ice quantities are integrated over drift ice particles or any regions in similar ways.

[3] Surface normal to the local gravitational acceleration (true horizontal).

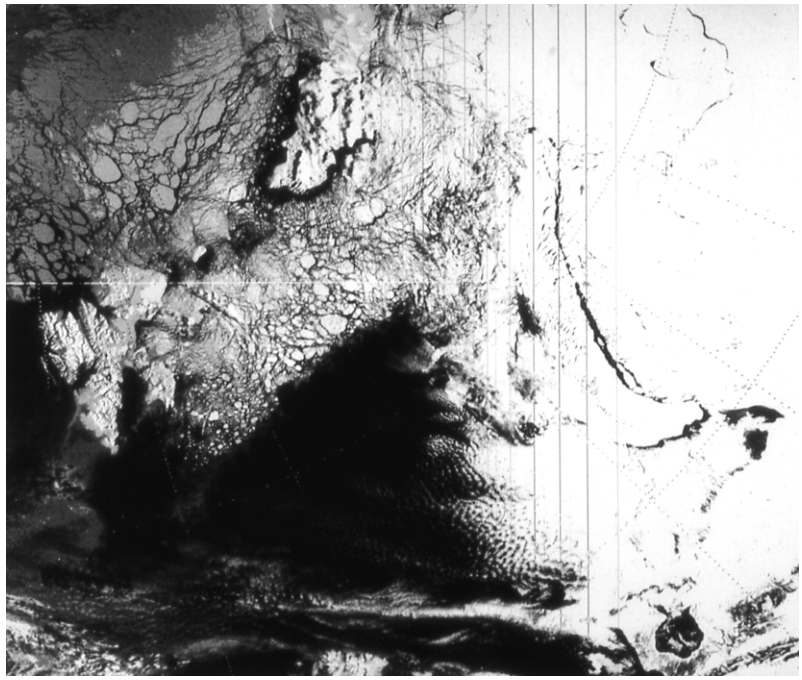

Figure 2.7. An optical channel NOAA–6 image over the Barents Sea and Arctic basin north of it, 6 May 1985. Svalbard is shown on the left, Franz Joseph's land up in the middle, and Novaya Zemlya on the right. The east side is cloudy, but elsewhere drift ice floes can be seen. The image was received at the Tromsø receiving station, Norway.

The granular medium approach was introduced for drift ice in the 1970s, taking ideas from soil mechanics (Coon, 1974), resulting in poly-granular continuum models. More recently, discrete particle models have been used and found to work well in the floe scale (e.g., Løset, 1993; Hopkins, 1994); but for larger scale drift ice problems they have not overcome continuum models. A possible step between discrete and continuum models could be the "particulate medium" approach (Harr, 1977). This is composed of a complex conglomeration of discrete particles, in arrays of varying shapes, sizes and orientations. The laws of mechanics are derived from probabilistic viewpoint.

2.2.2 Size and shape of ice floes

Floe size distribution

Sea ice floes break continuously into smaller pieces, and in the cold season they are at the same time frozen together into larger pieces. Floe size distributions show statistical regularity based on random floe break-up mechanisms. A characteristic floe diameter d can be defined from its surface area S_f as $d = \sqrt{4S_f/\pi}$. For a circle, d

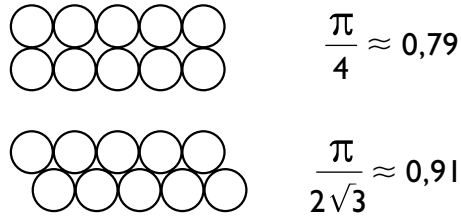

Figure 2.8 Open and dense locked packings of uniform circular ice floes.

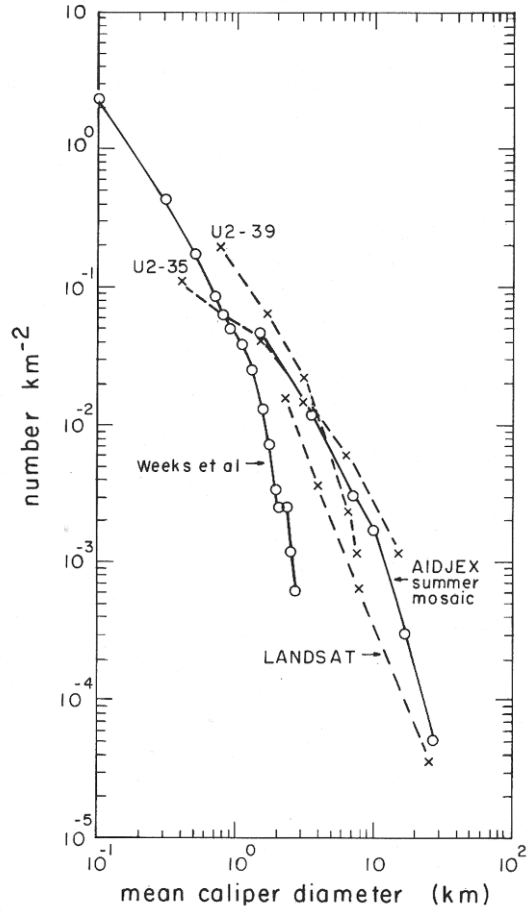

Figure 2.9 Floe size distributions from the Arctic Ocean.
Reproduced from Rothrock and Thorndike (1984), with permission from the American Geophysical Union.

equals the diameter. Rothrock and Thorndike (1984) introduced their mean "caliper diameter", equal to the directional average of the opening the floe goes through. It is approximately equal to the π^{-1} times the perimeter. For a circle, this is therefore equal to the diameter. Actual floe size observations cover a certain range $d_0 \leq d \leq d_1$, where d_0 and d_1 are the minimum and maximum resolution, respectively. Floes are usually examined from satellite images, aerial photographs or ship-borne oblique-angle video records.

The distribution of floe sizes is usually presented using the spatial density $p(d)$ (i.e., number of floes in different size classes). A more preferable way is, however, to consider the areal coverage. The area of the floes larger than size d is:

$$Q(d) = \int_d^\infty r^2 p(r)\, dr \tag{2.8}$$

Then q-fractiles $d^{(q)}$ can be defined through $Q(d^{(q)}) = qQ(0)$ (i.e., floes larger than $d^{(q)}$ cover the fraction of q of the total ice area). A natural representative floe size is $d^{(0.5)}$, the median. In soil mechanics (e.g., Harr, 1977), $d^{(0.1)}$ defines the effective size and the ratio $d^{(0.6)}/d^{(0.1)}$, is known as the uniformity coefficient.

Observed floe size distributions show regular features. The spatial density function steadily falls toward larger values with no local peaks or gaps at least within the observation windows (Figure 2.9), and the shape of the distribution may be derived from rather simple fracturing principles (Figure 2.10). Eq. (2.8) tells us that if the spatial density falls as d^{-2}, the distribution of the areal coverage of ice floes is uniform.

Fractal geometry models lead to *power law* size distributions (e.g., Korvin, 1992). The probability density is:

$$p(d; n) \propto d^n \tag{2.9}$$

In a d-band where n = constant, *self-similarity* holds. Within a self-similar band the geometric structure is independent of the scale, reflected by photographs showing similar floe systems in different scales within the self-similar band, and a measure stick needs to be added for the scale information (Figure 2.11). Such scale invariance is quite common in geophysical data. For all power laws we have $\int_0^\infty x^n dx = \infty$. Floes are smaller than the basin and therefore the integral should be taken from 0 to basin size (L) only. Then the integral is finite for $n > -1$; however, this is not necessary since for a fractal system the number of ice floes is infinite. The necessary condition is that the area of ice floes is finite:

$$\int_0^L x^{n+2} dx < \infty \tag{2.10}$$

which means that $n > -3$. Observations usually suggest that $-3 < n < -1$ for $d > 20$ m (i.e., for ice pieces defined as floes in the WMO, 1970 nomenclature).

Example Take $n = -2$. Then

$$\frac{Q(d)}{Q(0)} = 1 - \frac{d}{d_1}$$

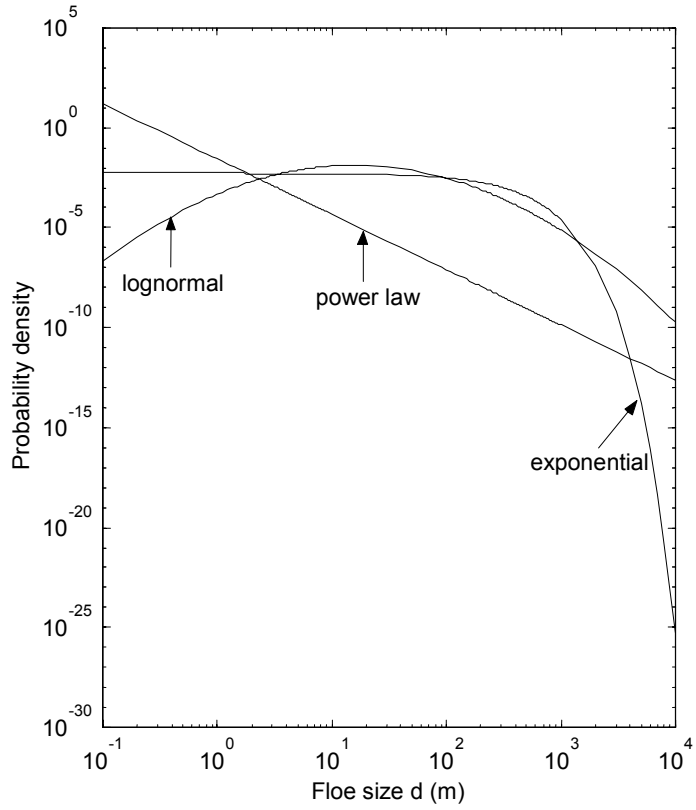

Figure 2.10 The forms of the power law, exponential, and lognormal distributions for the floe size, scaled with median equal to 500 m.

where d_1 is the maximum floe size. The distribution of floe size in terms of areal coverage is uniform from zero to d_1, as sometimes observed (e.g., Leppäranta, 1981b). The median floe size is $d_1/2$, and any q-fractile is given by $d_q = d_1(1-q)$. The uniformity coefficient is $4/9 \approx 0.44$. For $n < -2$ small floes are areally dominant while for $n > -2$ the opposite is true. The exponent obtained from observations therefore illustrates how fractured the ice field is.

In the data of Rothrock and Thorndike (1984) the mean caliper diameter followed the power law ($d > 100$ m) with $-2.5 < n \leq -1.7$. For the spring season in the Baltic Sea, Leppäranta (1981b) obtained $-3 < n < -2$, decreasing in the course of the spring melting season. This illustrates that the area of small floes increases at the cost of large ones. Cases with $n \leq -3$ have been occasionally reported; then the ice floe field must be understood as a multi-fractal where $n \leq -3$ holds in the observation window but as $d \to 0$ the power must go above -3.

A classical *random breakage* model, where the breakage probability is independent of the floe size, gives the *logarithmic normal distribution* (Kolmogorov, 1941).

Then, by definition, $\log d$ is normally distributed, say, with mean M and variance s^2. Define a characteristic floe size d_* by $\log d_* = M$. The probability density then reads:

$$p(d; d_*, s^2) = \frac{1}{ds\sqrt{2\pi}} \exp\left[\frac{-\log(d/d_*)}{2s^2}\right], \quad d > 0 \tag{2.11}$$

The median is then equal to d_*, the mode and mean are $d_* \exp(-s^2/2)$ and $d_* \exp(s^2/2)$, respectively, and the variance is $d_*^2 \exp(s^2)[\exp(s^2) - 1]$ (e.g., Crow and Shimizu, 1988). The parameter s^2 is regarded as the shape parameter of the distribution. It is dimensionless since by definition s^2 is the average of $(\log d - \log d_*)^2 = \log(d/d_*)^2$. The median of the distribution Q for floe coverage becomes $d_* \exp(2s^2)$. The distribution has a positive mode, which is not far from zero and usually not covered in observational data; thus the existence of such a mode in nature is not clear.

Logarithmic normal distribution has been found to fit observations as well as the power law. The reason is likely due to that these two distributions differ remarkably only at very small floe sizes (see Figure 2.10), normally not covered by the observation window.

If the breakage probability is proportional to the floe size, the spatial Poisson process results, leading to the *exponential distribution* of floe size:

$$p(d; \lambda) = \lambda \exp(-\lambda d) \tag{2.12}$$

where λ is the distribution shape parameter. This is analogous to the distribution of waiting times of customers in the theory of temporal Poisson processes. Density can be directly integrated: the relative areal coverage of floes larger than d is $Q(d) = [1 + \lambda d + \frac{1}{2}(\lambda d)^2] \exp(-\lambda d)$. The median of the distribution Q can be numerically solved as $d_{0.5} \approx 2.67\lambda^{-1}$. Exponential distribution is quite different from the other two and is not much supported by observations.

According to the present knowledge, only in the case of small floes can physical mechanisms be found to produce a favourable floe size. An important property of floating ice is its *characteristic length*:

$$l_c = \sqrt{\frac{Yh^3}{12\rho_w g(1 - \nu^2)}} \tag{2.13}$$

where Y is Young's modulus and ν is Poisson's ratio; representative values for them are $Y \approx 3$ GPa and $\nu = 0.3$ (e.g., Mellor, 1986). For $h = 1$ m, we have $l_c = 12.7$ m. The length of flexural waves of an elastic ice beam on water foundation under a point load equals $2\pi l_c$. When ice floes break under rafting the size of pieces is $\frac{1}{4}\pi l_c$ (Coon, 1974).

An eye-striking ice field is *pancake ice* (see Figure 2.3), which is often found in the marginal ice zone when the ice cover is extending in turbulent oceanic surface layer conditions. Frazil crystals join in the surface to plate aggregates, which collide with each other and become rounded. Due to its visual appearance, this ice type is called pancake ice, and the size of the "pancakes" is up to a few metres. They grow by mechanical scavenging and rafting up to thickness of consolidation, which has been reported to be around 60 cm in Antarctic seas (Doble, 2008).

At the ice edge, reflection and penetration of swell takes place (Wadhams, 1978; Squire *et al.*, 1998; Squire, 1998). A penetrating swell becomes damped with distance from the ice edge. The wave energy as a function of distance (x) from the ice edge is:

$$E(x) = E(0)\exp(-x/l_s), \tag{2.14}$$

where l_s is the attenuation distance. Long waves penetrate more easily. In heavy, compact ice, $l_s \approx 1$ km for short waves (100 m) and 5 km for long swells. The dominant wavelength increases exponentially from the ice edge and waves easily break floes down to one-half wavelengths. Consequently, the floe size should increase exponentially from the ice edge, as long as there is enough energy in the wave field for floe breakage. This is observed in the MIZ in a qualitative sense: floes are small, $\sim 10^2$ m and there is general increase in floe size with distance from the ice edge. But no actual e-folding length scales for the floe size have been recorded, the signal being contaminated by strong mixing and the thermo-mechanical decay of ice floes.

Random breakage seems to explain the floe size distributions well, with the breakage probability independent of the floe size, apart from the breaking by waves. Small floes may have preference sizes but their size distributions have not been studied to any great extent. The question is then how to formulate the random breakage probability that would lead to the exact form of the distribution (Lensu, 2003). Ice floes have more or less randomly distributed defects; that is, cracks due to thermal, hydrostatic (from non-uniform ice thickness), tidal, and wind loads.

Shape of ice floes

Sea ice floes are convex. Wintertime ice floes are typically rectangular or pentagonal, while in summer the sharp corners erode and the floes become rounded (Timokhov, 1998).

The shape of a floe can be quantified using its major axis ($d_{\max}$), minor axis ($d_{\min}$), and characteristic diameter (d_*), where $d_{\min}$ is the minor axis corresponding to the smallest opening through which the floe may penetrate, $d_{\max}$ is the length perpendicular to the direction of the minor axis, and d_* is the diameter of the circle with the same surface area as the floe. The shape parameters are:

$$\upsilon = \frac{d_{\max}}{d_{\min}}, \quad \kappa = \frac{d_*^2}{d_{\max} d_{\min}} \tag{2.15}$$

where υ is elongation and κ is shape factor. The latter equals unity for elliptical ice floes and $\pi/4$ for rectangular floes. In a study in the Baltic Sea (Leppäranta, 1981b), elongation was mostly 1–2 and the shape factor was 0.7–1.0. There are not enough floe shape results available to state how typical these Baltic Sea properties are.

Floe information in drift ice mechanics

Granular media consist of grains and voids (e.g., Oda and Iwashita, 1999). Their macroscopic behaviour is determined by the grains, their arrangements, and

interacting forces between the grains. Some efforts have been made for granular medium approach in sea ice dynamics with floes as individual grains, but in essence all mesoscale and large-scale sea ice models are based on the continuum theory. Linkages between floe scale mechanics and continuum mechanics are not clear.

Ice floe information is implicitly included in the continuum theory in that the validity of continuum hypothesis requires that the drift ice particle size should be an order of magnitude greater than the characteristic floe size (see Eq. 2.3). Otherwise, it is not yet clear how useful the floe size and shape information really are in the continuum of sea ice dynamics. The granular medium approach would be the way to link floe scale mechanics and continuum mechanics together as well as to understand properly the physical meaning of continuum model parameters. In local-scale granular models, both floe size and shape influence the results (and in particular, the friction coefficient between ice floes is important).

When ice floes reach their maximum packing density, the nature of material behaviour changes. When compactness is low, floe interactions do not transmit forces well and the level of stress is very small. When the ice pack closes up and the stress increases to a significant level, floes make contact with others, group together, and then lose many of their individual features. Nevertheless, the stress field still depends on the shape of ice floes throughout the total area of contact surfaces. This may be a reason for stress fields being lower in summer conditions. Drag forces between air and ice, and between water and ice depend on the size and shape of ice floes (Zubov, 1945; Andreas *et al.*, 1984). When floes are smaller their number is larger and consequently there are more floe edges to provide form drag. This feature, however, disappears when the floes close up.

Ovsienko (1976) was the first work to include floe size in a drift ice model, but without mechanical interaction. Shen *et al.* (1986) developed a theory based on momentum transfer by floe collisions using uniform and circular ice floes. For such floes a discrete particle model with full floe–floe interaction was studied by Løset (1993). Hopkins and Hibler (1991) and Hopkins (1994) examined the sea ice-ridging process with a discrete particle model and the floes could be of general polygonal shape.

The poor understanding of the role of horizontal floe characteristics is largely due to the fact that in sea ice dynamics the thickness of ice floes is the principal floe property, their horizontal size being given less prominence. However, the size and shape of ice floes show much more regularity than the thickness field, and they can be easily monitored by remote sensing methods. Consequently, floes would be quite useful in sea ice dynamics modelling by adding their evolution laws for examinations by model simulations against observations. The floes would serve as test material and tracers for model ice mechanics.

In applied fields, floe size can be an important property to predict. Loads on structures caused by individual drifting floes depend on the floe size, and drift and dispersion of oil spills in an ice-covered sea are sensitive to ice compactness and floe geometry. Therefore, although the floe size and shape would not exert much influence on the dynamics of ice itself, they can be necessary to be kept in the model as a field, which changes by advection, diffusion, mechanical breakage, and thermodynamics. In short-term forecasting, just advection and diffusion would be a useful approach.

2.3 SEA ICE GROWTH AND MELTING

2.3.1 Freezing of seawater

The freezing point (T_f) of normal seawater is $-1.9°C$, while the temperature of maximum density (T_D) is well below that[4]. Therefore the density of seawater increases throughout the cooling process and vertical convection penetrates to the halocline or, if halocline does not exist, to the sea bottom. Brackish waters behave as fresh water lakes in that $T_f < T_D$. The onset of freezing depends on the external conditions (Weeks and Ackley, 1986; Eicken and Lange, 1989; Weeks, 1998a). In case of weak wind a thin primary ice layer forms first, and then *congelation* ice crystals grow down from the bottom of the primary ice. In windy conditions *frazil ice* crystals are first formed, moving free in the turbulent surface layer and joining into a solid sheet when the buoyancy overcomes the turbulence. This is also the initial stage in pancake ice formation. In shallow and well-mixed waters frazil may also attach into the sea bottom to form *anchor ice*. Snow falls on the top of ice and may form slush to further freeze into *snow-ice*. In Antarctic shelf waters, so-called *platelet ice* forms as glacial melt water rises from bottom of ice shelves, becomes supercooled, and crystallizes onto sea ice bottom as large platelets. Thus a sea ice sheet in general consists of layers of different forms of ice. Good references for sea ice thermodynamics are Maykut and Untersteiner (1971), Makshtas (1984) and Shirasawa *et al.* (2005).

Congelation ice crystals grow down from the ice–water interface, and the crystals are columnar, diameter 0.5–5 cm and height 5–50 cm. The growth is limited by the insulation effect of the ice, and the thicker the ice, the lower the growth rate will be. In the Arctic Ocean, congelation ice is the dominant ice type. Frazil ice forms in open water areas. The crystals are small (1 mm or less). The growth rate can be fast because of intensive heat losses from open water to cold atmosphere and the growth is not strongly limited as long as there is open water present. In Antarctic seas, frazil ice is the dominant ice type. There it is also typical that frazil crystals join in the surface to form pancake ice.

Snow-ice forms on top of the ice from slush, generated by snow and liquid water available from flooding, liquid precipitation or melt water of snow. The crystals are small as in frazil ice. Growth of snow-ice is limited by the presence of snow and availability of liquid water. The most common formation mechanism is flooding, which becomes possible when the snow weight has forced the ice sheet below the water surface level, that is:

$$\frac{h_s}{h} > \frac{\rho_w - \rho}{\rho_s} \tag{2.16}$$

where h_s is snow thickness and ρ_s is snow density. Since $(\rho_w - \rho)/\rho_s \approx 1/3$, the thickness of snow needs to be at least one-third of the thickness of ice for the flooding to occur. Since growth limitation is provided by the ratio h_s/h, snow-ice formation is

[4] $T_f[°C] = -57.5S + 54.0915S^{3/2} - 215.4996S^2 - 7.53 \times 10^{-3}p$ [bar], where S is salinity and p is pressure (UNESCO, 1981).

common in Antarctic first-year ice and in low latitude seas, such as the Baltic Sea and the Sea of Okhotsk, where snow accumulation is large and ice is not too thick.

By thermal processes first-year polar sea ice grows to 1–2 m thickness and multi-year ice to 3–4 m. In the seasonal sea ice zone the thickness is mostly less than 1 m. Thermally grown ice is also called *undeformed ice*, as distinct from *deformed ice* forming in mechanical deformation processes. Sea ice thermodynamics forms a coupled temperature–salinity problem (e.g., Maykut and Untersteiner, 1971), but in thermodynamic models so far salinity has been a prescribed function of time and depth. In sea ice growth heat flow is strongly vertical and transfer of heat through ice is slow. The heat diffusion coefficient is $\approx 1 \times 10^{-6}\,\mathrm{m^2\,s^{-1}}$, which gives the length scale of 4 m in a half year's time. Thus in floe scale or larger scale processes ice growth can be taken as a local vertical process. Melting of sea ice can, on the other hand, take place also laterally, when heat absorbed by leads is transferred to lateral boundaries of ice floes (see Rothrock, 1986).

The sea ice nomenclature (WMO, 1970) connects thicknesses to types of undeformed ice as discussed in Section 2.1. New ice forms grow up to 10 cm, young ice is 10–30 cm, and first year ice is divided into thin (30–70 cm), medium (70–120 cm), and thick (greater than 120 cm) categories. Undeformed first-year ice can be as much as 2 m thick, while the equilibrium thickness of undeformed multi-year ice is 3–4 m (Maykut and Untersteiner, 1971). The terminology is based on ice conditions in the Arctic seas; it is not fully used in subpolar regions because of inconsistencies in the use of common language: for example, in the Baltic Sea, the thickest ice could be "thin first-year ice", and "young ice" could be several months old and as old as any ice there. It is therefore preferable to give the numerical value of thickness.

The impurities of sea ice consist of *brine*, *solid salt crystals*, *gas bubbles* and *sediments*. The first two types result from growing sea ice capturing salts (Weeks, 1998a). They constitute the most important impurities to the physical properties of sea ice; in particular, the mechanical strength of sea ice sheet depends primarily on the brine volume. The volume fraction of gas bubbles is $\nu_a \sim 1\%$, and the bubble size is in the range 0.1–10 mm. Sediment particles originate from the water body, harvested by frazil ice, from sea bottom when anchor ice rises up due to its buoyancy, and from atmospheric fallout accumulating on the ice during the ice season. Sediments may influence the properties of ice and they may also have a significant role in transporting matter, especially pollutants.

2.3.2 Ice growth

Thermodynamic growth of congelation ice is a classical geophysical problem, where approximate analytical solutions are available (Figure 2.12). Weyprecht (1879) showed, based on his data from the Arctic, that sea ice thickness is proportional to the square root of the sum of freezing-degree-days, which is defined as:

$$S_0(t) = -\int_0^t [T_0(t') - T_f]dt' \tag{2.17}$$

(a)

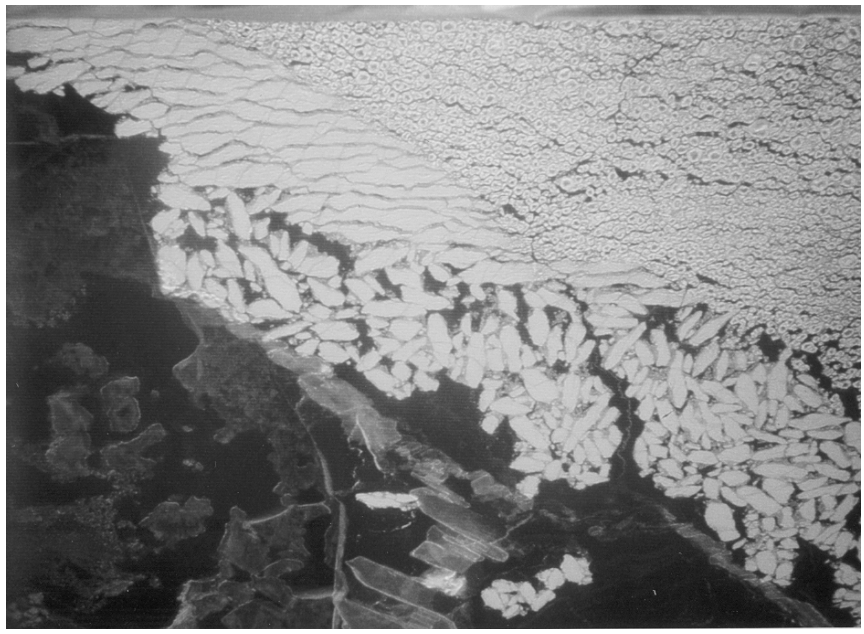

(b)

Figure 2.11 Sea ice floes shown in pictures over different scales. (a) Thin ice floes and rafted ice, altitude 500 m. (b) Oblique angle over ridged ice, altitude 1 km.

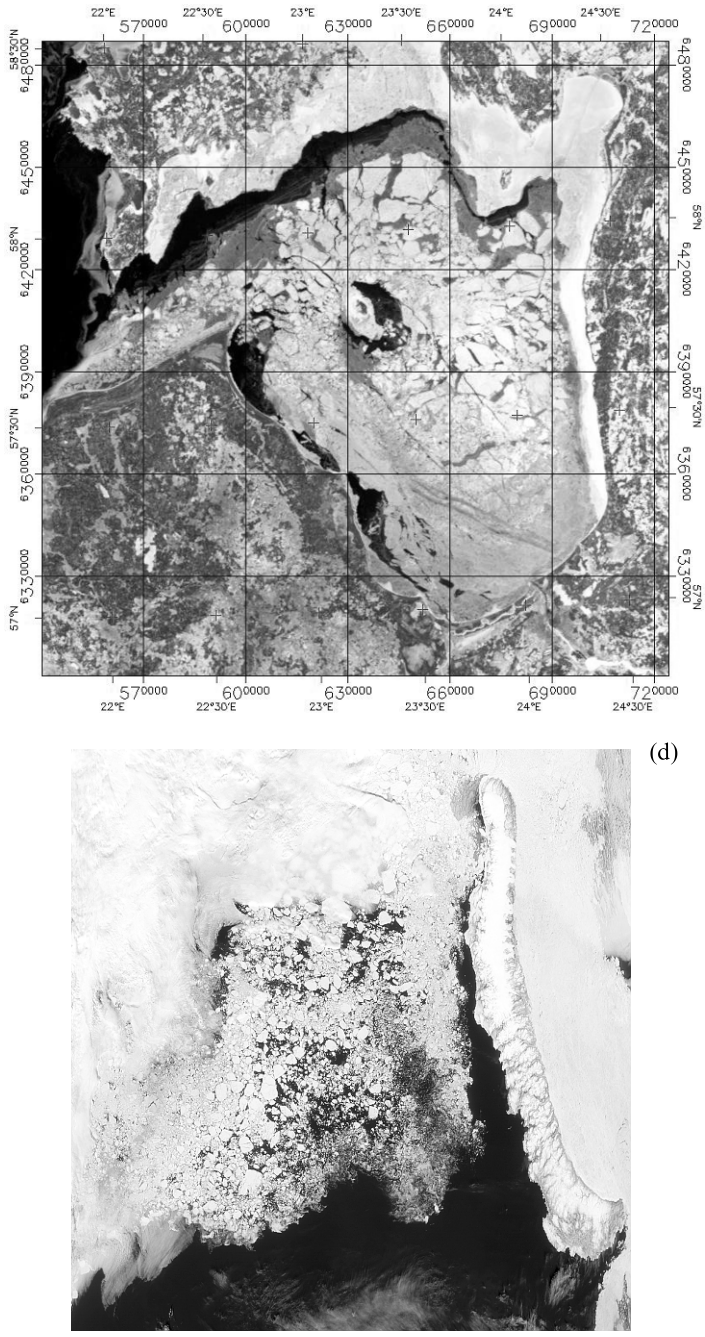

Figure 2.11 (continued). (c) Gulf of Riga, basin size 120 km. (MODIS image of NASA's Terra satellite.) (d) Barents Sea – the length of Novaya Zemlya on the right is about 1000 km (© NASA, Visible Earth Team).

where T_0 is the surface temperature (assuming that $T_0 \leq T_f$). The physics of this result was then explained by Stefan (1891). The thermodynamics of congelation ice follows the Fourier heat conducting law:

$$\frac{\partial}{\partial t}(\rho c T) = \frac{\partial}{\partial z}\left(\kappa \frac{\partial T}{\partial z}\right) + q \tag{2.18}$$

where c is specific heat, κ is thermal conductivity, and q is the absorption of solar radiation within the ice sheet, $q = q(z)$.

Ignoring thermal inertia, solar radiation and heat flux from water to the ice bottom, and assuming constant thermal conductivity, a linear temperature profile results. The slope of this profile gives the conduction of heat, which must correspond to the latent heat release due to congelation ice growth at the bottom of the ice sheet:

$$\rho L \frac{dh}{dt} = \kappa \left.\frac{\partial T}{\partial z}\right|_{z=h^n} = \kappa \frac{T_f - T_0}{h} \tag{2.19}$$

This is the Stefan's model (Stefan, 1891). The thicker the ice, the slower is the conduction, and hence the rate of ice growth decreases when the ice becomes thicker. With initial value $h(0) = 0$, Eq. (2.19) can be directly integrated into $h = a\sqrt{S_0}$, where $a = \sqrt{2\kappa/(\rho L)} \approx 3.3\,\mathrm{cm\,d^{-1/2}\,{}^\circ C^{-1/2}}$ is the growth coefficient. It is also seen that growth of very thin ice rarely would exceed $10\,\mathrm{cm\,d^{-1}}$ and for 1 m thick ice the growth rate is already below $1\,\mathrm{cm\,d^{-1}}$.

A major problem with the Stefan's model is that the surface temperature is required. This is not usually known and therefore the freezing-degree-days S based on air temperature rather than surface temperature is used; i.e., in the integral in Eq. (2.17) $T_0 - T_f$ is replaced by $T_a - T_f$, where T_a is air temperature. Zubov (1945) added air–ice heat exchange to the model, and based on the continuity of heat flow resulted in the pair of equations:

$$\rho L \frac{dh}{dt} = \kappa \frac{T_f - T_0}{h} = K_a(T_0 - T_a), \quad T_0 \geq T_a \tag{2.20a}$$

where K_a is ice–air heat transfer coefficient. Note that we must have here $T_0 \geq T_a$ for the ice to grow (i.e., days $T_0 < T_a$ are ignored). The solution is:

$$h = \sqrt{a^2 S + \delta^2} - \delta \tag{2.20b}$$

where $\delta = \kappa/K_a \approx 10\,\mathrm{cm}$ is the insulation efficiency of the atmospheric surface layer. The classical Stefan's law is recovered by letting $\delta \to 0$, which means physically that the atmosphere can take any heat, which is coming through the ice.

Example 100 days with the air temperature of $-10^\circ\mathrm{C}$ gives $S = 810^\circ\mathrm{C \cdot day}$, and then Zubov's model gives $h = 94.4\,\mathrm{cm}$ and Stefan's model gives 84.9 cm. The square root law describes well how the ice insulates itself from the cold atmosphere during the growth process. Especially when the ice is thin, Stefan's model strongly overestimates the ice growth. For $S = 20^\circ\mathrm{C \cdot day}$, the Zubov and Stefan models give 7.9 cm and

14.8 cm, respectively. Inversely, we can see that since first-year ice thickness is 2 m at highest in the Arctic Ocean, the freezing-degree-days must sum there to 4000°C · day.

The main problem in Zubov's model is the lack of snow. Heat flux through snow is $\kappa_s \Delta T/h_s$, where κ_s is thermal conductivity of snow and ΔT is the temperature difference across the snow layer. This can be added as a new equation into the Zubov's model (Eq. 2.20a), but in general, analytic solutions are no longer possible since the thickness and conductivity of snow depend on time. For illustration, if they are constant, the solution is similar to Zubov's case, but the insulation layer thickness δ is replaced by:

$$\delta^* = \left(1 + \frac{K_a h_s}{\kappa_s}\right)\delta \tag{2.21}$$

Since $\kappa_s/K_a \sim 2$ cm, just a 2-cm snow layer will double the insulation effect of the atmospheric surface layer. The insulation effect of the snow is limited by the buoyancy of ice, since snow accumulation may lead to flooding and further to snow-ice formation (see Eq. 2.16). If snow thickness increases with ice thickness but not enough for slush formation, the maximum insulation effect reduces the ice thickness to half as compared with the growth of snow-free ice (Leppäranta, 1993).

Snow-ice grows from slush on top of the ice. Latent heat released in freezing needs to be conducted through the dry snow above slush only. Also, less latent heat needs to be released than in the growth of congelation ice since the slush already contains ice crystals. The growth equation reads:

$$\rho\nu L \frac{dh_{si}}{dt} = \kappa \frac{T_f - T_s}{h_{si}} = \kappa_s \frac{T_s - T_0}{h_s'} = K_a(T_0 - T_a), \quad T_0 > T_a \tag{2.22}$$

where $\nu \sim 50\%$ is the water content of the slush layer, h_{si} is snow-ice thickness, T_s is temperature at the snow-ice-snow interface and h_s' is the thickness of dry snow above snow-ice–slush layer. This is as Zubov's model except that the latent heat of freezing is reduced by the factor of ν. The fractions of congelation ice and snow-ice depend on snow accumulation history (Figure 2.13). Assume that in an extreme situation, when the slush is produced by flooding, the rate of snowfall is just enough to produce continuous growth of snow-ice and no congelation ice forms. Then the ice thickness becomes 70% of the snow-free congelation ice case (Leppäranta, 1993).

In spring, the day-and-night melting–freezing cycle gives additional growth to the snow-ice layer. Shirasawa *et al.* (2005) reported on average 24 cm snow-ice growth in the melt–freeze cycles in April offshore Sakhalin in the Sea of Okhotsk. Close to the edge of the seasonal sea ice zone liquid precipitation may significantly contribute into the accumulation of the snow-ice layer. For snow-ice formation by melt–freeze cycles or liquid precipitation, the limiting factor is the snow. In the former case the snow-ice layer may grow at most to $(\rho_s/\rho)h_s$, while in the latter case the limit is h_s. When there is no snow left, any water on ice may freeze into surface ice. Together, snow-ice and surface ice are called *superimposed ice*, a term familiar from glaciology.

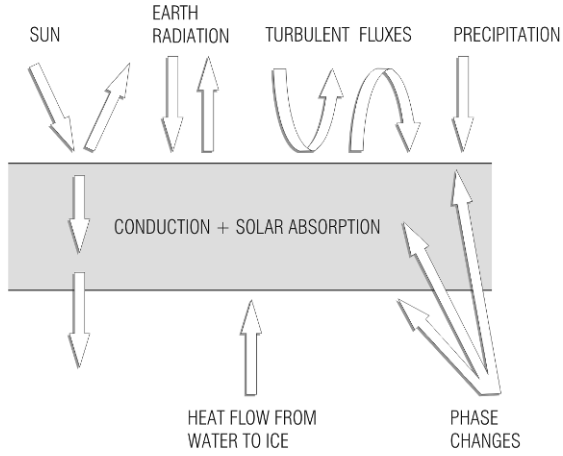

Figure 2.12 Schematic illustration of sea ice thermodynamics. Ice grows and melts at the boundaries and in the interior, forced by heat exchange with air and water and by radiation.

Frazil ice growth is a dynamic-thermodynamic phenomenon. Frazil ice crystals are generated in turbulent open water spots, and they are then transported further by ocean surface layer currents. The rate of production of frazil crystals, h_F is:

$$\frac{dh_{\mathrm{F}}}{dt} = -\frac{Q_n}{\rho L} \tag{2.23}$$

where Q_n (here $Q_n < 0$) is the net heat gain by the ocean surface layer (the full heat budget with net gain will be discussed in Section 2.3.5). Note that the dimension of h_F is length and this quantity can be interpreted as the production of volume over unit surface area. What simplifies the problem is that we can assume $T_0 = T_f$. With low air temperature and moderate or stronger wind, the sensible heat flux is dominating.

Example. If $T_a = -10^{\circ}\mathrm{C}$ and $U_a = 10\,\mathrm{m\,s^{-1}}$, we have $Q_n \sim 200\,\mathrm{W\,m^{-2}}$, which means frazil ice production of $\sim 6\,\mathrm{cm\,day^{-1}}$. The corresponding growth using Zubov's model would be 3.8 cm starting from zero and 2.1 cm starting from 10 cm.

Frazil ice crystals flow in the turbulent boundary layer. They may attach to the bottom of the ice sheet downstream, attach to the sea bottom in shallow areas, or form an ice layer in the opening where they have formed after the buoyancy of ice crystals has overcome the turbulence. Frazil ice layers can be recognized in the ice sheet later on[5]. From sea ice dynamics point of view, frazil ice formation means rapid production of ice and increase of ice mass as well as, in many situations, rapid closing of open water areas. However, if frazil is transported away, open water becomes semi-persistent and continues long time with its high rate of ice production,

[5] Frazil ice and snow-ice crystals are similar in the crystal structure but can be distinguished using oxygen isotope ratios since snow-ice contains fresh precipitation.

as is the case in many polynyas. In turbulent conditions with surface waves, frazil ice formation is the first stage in the development of pancake ice, a common process in Antarctic sea areas (Doble, 2008).

2.3.3 Melting of sea ice

Sea ice melts from the top surface by atmospheric and solar heat fluxes, in the interior by solar radiation, and from the bottom surface by oceanic heat flux. Boundary melting follows simply from a positive heat balance:

$$\frac{dh_0}{dt} = -\frac{Q_n}{\rho L}, \quad \frac{dh_b}{dt} = -\frac{Q_w}{\rho L} \tag{2.24}$$

where Q_w is the oceanic heat flux. Incoming solar radiation, Q_s, is divided into three parts by the sea ice medium: absorption at the surface, penetration through the surface, and reflection and scattering back to atmosphere (see Perovich, 1998). The "surface" is here a very thin top layer where infrared radiation is absorbed. The penetrating part is light: $Q_{s+} = (1 - \alpha)\gamma Q_s$, where α is albedo and γ is the fraction of the optical band in solar radiation. Since the optical thickness of sea ice is 0.5–5 m, depending on the quality of ice, part of sunlight goes through ice into the water. For the light transfer through the ice, the exponential attenuation law is normally employed:

$$\frac{\partial Q_{s+}}{\partial z} = -\lambda Q_{s+} \tag{2.25}$$

where λ is the attenuation coefficient, $\lambda \sim 1\,\mathrm{m}^{-1}$ for congelation ice and $\lambda \sim 10\,\mathrm{m}^{-1}$ for snow-ice (Perovich, 1998). Radiation absorbed inside the ice is used for internal melting. Field data have shown that in lake ice the boundary melting and internal melting are of the same magnitude (Jakkila *et al.*, 2009), and it can be anticipated that for sea ice the internal melting would be as important. What makes the treatment of solar radiation difficult for sea ice thermodynamics is the large space–time variability of optical properties of sea ice during the melting season.

Oceanic heat flux comes from the oceanic boundary layer beneath the ice and can be estimated using the turbulent boundary layer theory (see McPhee, 2008). The bulk formula is written

$$Q_w = \rho_w c_w C_{wH}(T_w - T_f)|\boldsymbol{U}_w - \boldsymbol{u}| \tag{2.26a}$$

where c_w is specific heat of seawater, C_{wH} is ice–water heat exchange coefficient, and T_w and $\boldsymbol{U}_w$ are water temperature and water velocity, respectively. In contrast to atmospheric heating, oceanic heat flux is always positive toward ice and thus it melts ice though the whole year, i.e., heat flows only from water to ice. At the bottom of sea ice we have the boundary condition:

$$\rho L \frac{dh}{dt} + Q_w = \kappa \left.\frac{\partial T}{\partial z}\right|_{z=h^n} \tag{2.26b}$$

In the melting season the right-hand side is zero, and oceanic heat flux is all used for melting of ice.

Much research work has been done on the heat fluxes at the upper surface. But the lower boundary is much less known, due to greater observational difficulties and also due to the uniqueness of the ice–ocean interaction. There was a large interdisciplinary study of the Surface Heat Budget of the Arctic Ocean (SHEBA), consisting of a year-long field experiment from October 1997 through October 1998 in the Chukchi Sea (e.g., Perovich *et al.*, 2003). The oceanic heat flux during the SHEBA summer ranged from 10 to $40\,\mathrm{W\,m^{-2}}$, and the average bottom melt rate during the summer was $0.50\,\mathrm{cm\,d^{-1}}$, equivalent to an average oceanic heat flux of $17.5\,\mathrm{W\,m^{-2}}$ (Perovich *et al.*, 2003). Undeformed landfast ice cover, such as in a lake, lagoon, fjord, bay or in a sheltered coastal region, works as a stable platform for ocean boundary layer investigations, and also there the ice grows mainly by thermodynamics. According to measurements over landfast ice the oceanic heat flux has been found in the range of 1–$100\,\mathrm{W\,m^{-2}}$, which makes a significant contribution to the ice thickness evolution (e.g., Shirasawa *et al.*, 2006). Uusikivi *et al.* (2006) observed very small heat fluxes of $1\,\mathrm{W\,m^{-2}}$ or less in a laminar flow and/or laminar-turbulent transition regime under sheltered coastal landfast ice covers in the Baltic Sea.

The oceanic heat flux Q_w can be included in Zubov's model by adding it to the left term in Eq. (2.20a). The growth equation reads then:

$$\rho L \frac{dh}{dt} + Q_w = \frac{a^2}{2} \cdot \frac{T_f - T_a}{h + d} \quad (T_f > T_a) \tag{2.27}$$

A general analytical solution is no more possible. If $T_a = \text{constant}$, it is seen that there exists an equilibrium solution with $dh/dt = 0$:

$$h_q = \frac{a^2}{2} \cdot \frac{T_f - T_a}{Q_w/\rho L} - d \quad (T_f > T_a) \tag{2.28}$$

If the oceanic heat flux is strong, it may become a limiting factor in ice growth by ice thickness reaching the equilibrium. For example, if $T_f - T_a = -15^\circ\mathrm{C}$ and $Q_w = 30\,\mathrm{W\,m^{-2}}$, we have $h_q = 80\,\mathrm{cm}$.

In sea ice models the oceanic heat flux is normally fixed and often it has been used as a tuning factor. *Maykut and Untersteiner* (1971) employed a constant oceanic heat flux of $6\,\mathrm{W\,m^{-2}}$ to obtain the best-fit equilibrium thickness cycle for multiyear ice in the Arctic Ocean in their classical model. Modelling in the Antarctic seas has indicated that there the heat flux can be one order of magnitude larger. Thus the ice growth may there reach the equilibrium solution (2.28).

Sea ice has not a definite melting point but always warming includes dilution of brine by melting of ice at brine pocket boundaries. In the beginning of the melting season ice is nearly isothermal with temperature close to $0^\circ\mathrm{C}$. Then there is essentially no conduction, and melting can be examined as a process where thickness decreases by melting at the boundaries and by growth of voids in the

interior by solar radiation. Expressing the void volume as thickness equivalent, n, we have:

$$\begin{aligned} \rho L \frac{dh}{dt} &= -(Q_n + Q_w), \quad Q_n \geq 0 \\ \rho L \frac{dn}{dt} &= \lambda Q_{s+} = \lambda(1-\alpha)\gamma e^{-\lambda z} Q_s \end{aligned} \tag{2.29}$$

The net ice volume is $h - n$. At the top surface the snow melts first, then the ice. Snow protects the ice cover due to its high albedo and small optical depth. Thus the internal deterioration starts up only after snow has melted. Internal melting gives rise to structural defects and once the porosity of the ice reaches 0.4–0.5 the ice cannot bear its own weight and breaks into small pieces into the surface water. Then there is a rapid increase in the rate of melting. As an approximation, all melting can be included in the ice thickness when defined as ice volume per unit area, $h^* = h - n$:

$$\frac{dh^*}{dt} = -\frac{1}{\rho L}[Q_n + Q_w + (1-\alpha)\gamma(1 - e^{-\lambda h^*})Q_s], \quad Q_n \geq 0 \tag{2.30}$$

Melting is almost independent of the thickness of ice and dictated by the length of melting season. A heat flux of $30\,\mathrm{W\,m^{-2}}$ would melt the ice vertically by $1\,\mathrm{cm\,day^{-1}}$, and such levels are observed commonly for the net radiation flux in polar summer.

Melting of sea ice takes place also laterally when there is open water between ice floes. Solar radiation is absorbed in leads, and the heat is further transferred to ice floes at their horizontal boundaries. This enhances the solar energy transfer since albedo of water surface is much lower than albedo of ice or snow surface. In addition to influencing the floe size distribution, lateral melting decreases ice compactness.

Consider an ice field of compactness $A < 1$ consisting of uniform floes with thickness h. By simple geometry it is seen that the net energy absorption in leads, Q_n, melts lateral boundaries to decrease the compactness as:

$$\frac{dA}{dt} = -\frac{1}{2} \cdot \frac{Q_n}{\rho L h}(1 - A) \tag{2.31}$$

If the factor $\gamma = Q_n/(2\rho L h)$ is constant, the solution is $A = 1 - (1 - A_0)e^{\gamma t}$. Thus the ice compactness decreases to zero exponentially in time $t = -\gamma^{-1}\log(1 - A_0)$. For $Q_n = 100\,\mathrm{W\,m^{-2}}$ and $h = 1\,\mathrm{m}$, we have $t = 48$ days. In fact, along with lateral melting the ice is melting also vertically, h decreases, and rate of compactness decrease becomes even more accelerated.

Example For a simple illustrative case for the floe size, consider a sea ice field of area S consisting of uniform circular floes with thickness h and diameter d. The energy absorbed by leads is consumed to lateral melting at the floe boundaries and decrease of floe size:

$$Q_n(1 - A)S = -\rho L h N \pi d \frac{\dot{d}}{2}$$

where N is number of floes. Since $AS = N\pi(\frac{1}{2}d)^2$, we have

$$\frac{\dot{d}}{d} = -\frac{1 - A}{2A} \cdot \frac{Q_n}{\rho L h}$$

For $A = \frac{1}{2}$, $h = 1\,\mathrm{m}$ and $Q_w = 100\,\mathrm{W\,m^{-2}}$, the floe size decreases by 1.4% per day. Full integration of this equation needs integration of the compactness (Eq. 2.31) simultaneously, here we get just idea of the scale.

Finally, analytic growth and melting models can be combined for the equilibrium multiyear ice thickness. In one winter sea ice grows to 0.5–2 m thickness while in summer ice melts up to 1 m. Where the summer melt is less than the first year's growth, multi-year ice develops. This is the case in the Central Arctic Ocean and in places in the Southern Ocean, mainly in the Weddell Sea.

Zubov's model is taken as the basis. The thickness of ice after the n'th summer is

$$h_n = \sqrt{h_{n-1}^2 + 2h_{n-1}\delta + \delta^2 + aS} - \delta - \Delta h, \quad n \geq 1 \tag{2.32}$$

where Δh is the summer melting, which is determined by the radiation balance and oceanic heat flux; here we take $\Delta h \approx$ constant (independent of ice thickness). At equilibrium, $h_{n+1} = h_n = h_e$, where h_e is the equilibrium thickness of multi-year ice:

$$h_e = \frac{aS - (\Delta h)^2}{2\Delta h} - \delta \tag{2.33}$$

The condition of multi-year ice is trivial: $h_1 > \Delta h$. For $h_1 = 2\,\mathrm{m}$, $\Delta h = \frac{1}{2}\,\mathrm{m}$ and $\delta = 10\,\mathrm{cm}$, we have $h_e = 3.55\,\mathrm{m}$, but changing the summer melt to 1 m gives us $h_e = 1.3\,\mathrm{m}$, illustrating the high sensitivity to the equilibrium thickness to summer melt.

2.3.4 Numerical modelling of ice thermodynamics

Development of numerical models of sea ice thermodynamics began in the late 1960s. Maykut and Untersteiner (1971) presented a model for congelation ice temperature and thickness based on full heat conduction law. A simplified version was prepared by Semtner (1976) for climate simulations, and snow-ice models were added by Leppäranta (1983) and Saloranta (2000). In numerical modelling the temperature profile and resulting heat flow is solved in a dense grid across the ice sheet. Compared with the analytical models, more realistic boundary conditions can be applied and the thermal inertia of the heat flow through the ice can be included. In these models the salinity of the ice is prescribed and together with the temperature determines the brine volume; a full temperature-salinity model for sea ice has not yet been developed.

Numerical models of sea ice thermodynamics are vertical since the heat transfer is slow to reach any significant distance in the horizontal directions. The equation for heat conduction becomes:

$$\frac{\partial}{\partial t}(\rho c T) = \frac{\partial}{\partial z}\left(\kappa \frac{\partial T}{\partial z} - Q_{s+}\right) \tag{2.34a}$$

$$\textit{Surface}: \kappa \frac{\partial T}{\partial z} = Q_n + m(T)\rho L \frac{dh}{dt} \tag{2.34b}$$

$$\textit{Bottom}: T = T_f, \quad \kappa \frac{\partial T}{\partial z} = Q_w + \rho_i L \frac{dh}{dt} \tag{2.34c}$$

where $m(T) = 1$ for $T = T_f$ or 0 otherwise. Equations (2.34b–c) state that the heat fluxes are continuous through the upper and lower surfaces: conduction into ice equals external heat flux plus heat release or take-up due to phase changes. In the presence of slush, snow-ice forms in the upper layers in a similar way and since slush contains ice crystals less latent heat is released. The thermal properties of sea ice depend on the brine volume, which depends on temperature and salinity (see Maykut and Untersteiner, 1971). Since flow of brine and consequent desalinization depends on its volume, the temperature and salinity of sea ice constitute a coupled problem.

The exchange of mass and heat with the atmosphere and the incoming solar radiation define the boundary conditions at the surface of the ice-sheet. They are given, respectively, as

$$h' = P - E \tag{2.35a}$$

$$Q_n = (1 - \alpha)(1 - \gamma)Q_s + Q_{nL} + Q_c + Q_e + Q_P \tag{2.35b}$$

where P is precipitation and E is evaporation, Q_{nL} is net longwave radiation, Q_c and Q_e are sensible and latent heat fluxes, and Q_P is the heat provided by precipitation. Estimation methods for these heat fluxes are presented, e.g., by Makshtas (1984), Andreas (1998) and Curry and Webster (1999).

Numerical congelation ice models have a passive snow layer, and they were later extended to include an interacting snow model (Leppäranta, 1983; Saloranta, 2000; Shirasawa *et al.*, 2005). The sea ice–snow model consists of four types of layer: snow, slush, snow-ice and congelation ice. These layers are interacting: snow accumulation creates slush and snow-ice depending on the total thickness of ice, while the growth and decay of congelation ice depend on the snow and slush conditions. The snow layer needs its own model. The thickness of snow decreases due to three different reasons: surface melting, compaction, and formation of slush, which further transforms into snow-ice.

The outcome of the Maykut and Untersteiner (1971) model for the annual cycle is shown in Figure 2.14. The equilibrium thickness is sensitive to three factors: oceanic heat flux, snow accumulation and albedo. With zero oceanic heat flux the equilibrium thickness was doubled as compared with the standard case of 6 W m^{-2}. The role of snow is protective since large amounts of snow reduce the summer melt. In the Maykut-Untersteiner model the summer albedo was kept at 0.64, and it was shown that lowering that to 0.44 melted all ice in summer from the Arctic Ocean.

Shirasawa *et al.* (2005) used the congelation ice–snow-ice model in the Sea of Okhotsk (Figure 2.15). Offshore Sakhalin the result was very good but it was worse for offshore Hokkaido, where the ice is thinner. This is a general problem in sea ice thermodynamics that thin ice is difficult to simulate. However, the result in Hokkaido was useful and showed the high sensitivity of ice thickness and stratigraphy to amount and timing of snowfall.

In sea ice dynamics models the grid size is 10–100 km, and thermodynamics act independently in the grid cells. In purely dynamical models thermodynamics is ignored, which is often a reasonable assumption in short-term simulations. The critical limit is the time scale when open water has reached a significant thickness to

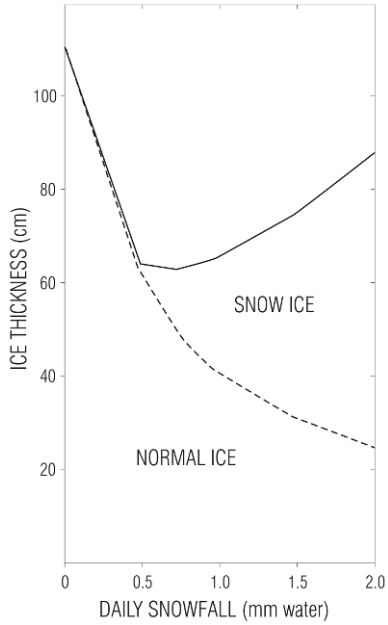

Figure 2.13 The proportions of congelation ice and snow-ice as a function of snow accumulation history for conditions in Oulu, northern Baltic Sea. Air temperature follows climatology and snowfall comes at a fixed rate shown in the *x*-axis.
From Leppäranta (1983).

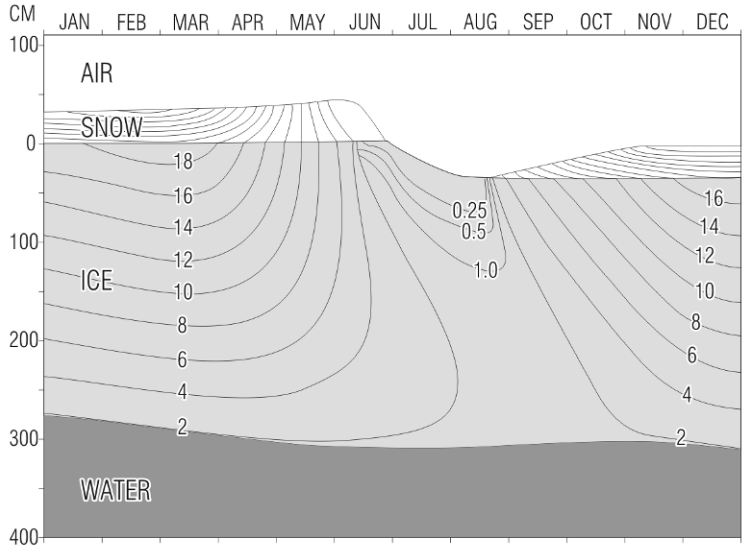

Figure 2.14 Annual cycle of ice temperature (isotherms inside ice and snow in °C) and thickness (scale on the left, cm) of multi-year ice at the equilibrium thickness.
Redrawn from Maykut and Untersteiner (1971).

contribute into the strength of the ice cover. The magnitude of this thickness ranges from 10 cm in SSIZ to 50 cm in the Central Arctic Ocean; using Zubov's model we can see that the corresponding time scale is 3 days in the SSIZ if $T_a = -10°C$ or 15 days in the Central Arctic if $T_a = -20°C$. Formally, when thermodynamics is taken into account, a *growth rate function* $\Phi = \Phi(t, h)$ is added into the ice conservation law, with melting specified by negative growth rates. This growth rate can be taken from climatology or produced using a thermodynamic model, whose complexity level is a question of choice. Thermal growth has the tendency of smoothing the ice field since thin ice grows faster than thick ice, but melting, first of all due to the patchiness of albedo, works to spread the thickness distribution.

2.4 THICKNESS OF DRIFT ICE

2.4.1 Mechanical ice growth

Sea ice thickness is characterized by a very large variability in space and time due to thermal and mechanical processes. The thickness range extends from zero, defining open water as "ice of zero thickness" up to as much as 50 m in the largest pressure ridges. Sea ice thickness is an irregular field and, because of fracturing and new ice growth in leads, it may have discontinuities. In the continuum approach, certain

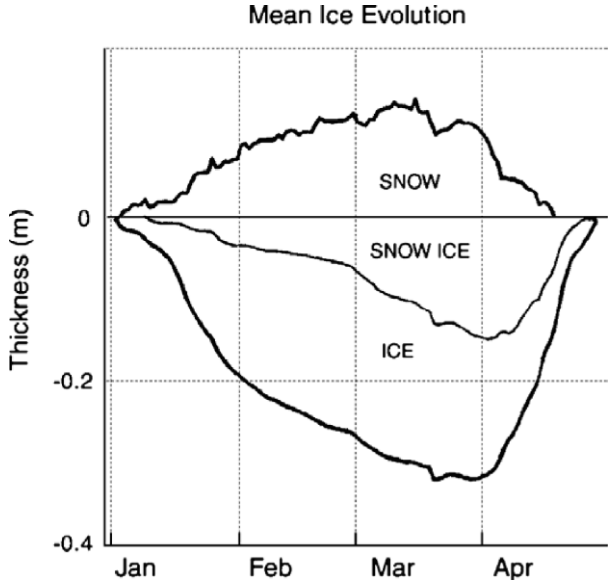

Figure 2.15 Mean modelled thickness of snow, snow-ice and congelation ice layers in Saroma-ko lagoon off in Hokkaido. Snow is shown above the zero line, snow-ice and congelation layers below the zero line.
From Shirasawa *et al.* (2005).

statistics of the thickness field, such as mean thickness, are considered for each continuum particle; these statistics are assumed to be smooth, as required by the theory. In the previous section thermodynamics was considered, and in this section the picture is completed with the presentation of sea ice thickness evolution as a result of mechanics.

Sea ice, which has formed mechanically from broken, thermally grown ice is called *deformed ice*. At a smaller scale, the thickness of deformed ice may vary a lot. A good illustration is provided by upward-looking submarine sonar data (Figure 2.16). Most of the thickness section is quite heavily deformed, which is typical for the Greenland Sea ice conditions. In this section ridge keels penetrate 10–20 m beneath the sea level (there are five ridge keels for this 2-km section). Rothrock (1986) shows a thickness section from the Beaufort Sea with a correlation length scale of the order of 1 km; the standard deviation was 2.4 m and the average was 3 m.

Mechanical deformation produces ice types with a range of thicknesses. Most of the variability in sea ice thickness is caused by mechanics, since pressure ridges form in time scales of several hours. Mechanical thickness changes are asymmetric in that, while mechanical increase of ice thickness takes place, existing deformed ice is not undone mechanically but may disappear only because of melting. This also means that transforming kinetic energy into potential energy in deformation is mechanically irrecoverable. Thus pressure ice build-up while increasing the volume and strength of the ice does not lead to returning forces, in contrast to ocean dynamics.

Thin ice usually undergoes rafting in compression (Figure 2.17). A theoretical formula for the maximum thickness of rafting ice is (Parmerter, 1975):

$$h_{rf} = \frac{14.2(1-\nu^2)}{\rho_w g}\frac{\sigma_t^2}{Y} \tag{2.36}$$

where σ_t is the tensile strength of the ice sheet, a representative value being 0.65 MPa (Mellor, 1986). This gives $h_{rf} = 15$–20 cm. In single rafting the local thickness is doubled. Several layers of rafted ice have been documented (Palosuo, 1953;

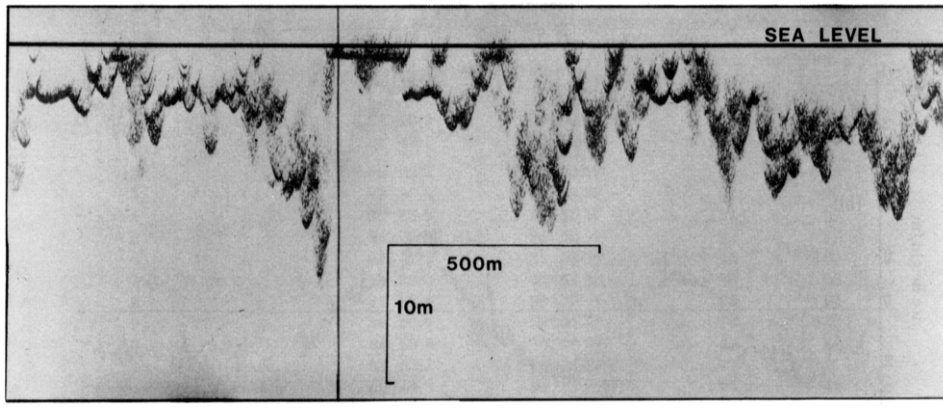

Figure 2.16 A section of ice draft profile in the Greenland Sea from submarine sounding. Reproduced from Wadhams (1981), with permission from the Royal Society of London.

Bukharitsin, 1986). As the ice thickness increases, bending moments as a result of overriding become so large that small pieces break off and start to form hummocks and ridges. When thin ice is compressed against thick ice (in particular, at the fast ice boundary), jammed brash ice barriers form. Contrary to other deformed ice types, these barriers may loosen when the compressive force ceases. Working with predominantly very thin ice, the rafting process would need particular consideration.

Hummocking accumulates ice blocks into layers several times the thickness of the original ice sheet (Figure 1.2a). The thickest forms of drift ice, ridges, may be up to 50 m thick. Fresh hummocks and ridges contain voids (20–40%) between the ice blocks. In cold conditions a consolidated layer grows down from the sea surface level. Thus the ice volume is 0.6–1.0 times the thickness, depending on the degree of consolidation.

Example (*piling*) Piling uniform-sized balls on top of each other results in open and closed locked packings of $\pi/6 \approx 0.52$ and $\sqrt{2} \cdot \pi/6 \approx 0.74$, respectively (corresponding porosities are 0.48 and 0.26). Experience shows that, when piling chopped firewood by randomly throwing one piece on top of each other, porosity will be about 1/3. The closed packing of balls and random firewood piling are well within the range of the observed porosities of new hummocks and ridges.

2.4.2 Measurement methods

To obtain thickness information is very difficult. A lot of effort has been put into this problem in sea ice remote sensing (e.g., Rossiter and Holladay, 1994; Wadhams, 2000). A good solution still does not exist – a major barrier to the progress of knowledge in drift ice dynamics. The basic techniques of sea ice thickness mapping are listed in Table 2.3.

Drilling is the traditional way of determining ice thickness, a direct measurement but not feasible for mesoscale or large-scale monitoring. One specific methodology for thickness mapping is recording from a ship (ice-breaker) the thickness of

Table 2.3 Methods for sea-ice thickness measurement.

Method	Quality	Comments	Reference
Drilling	Excellent	Laborious	Traditional
Submarine sonar	Good	Access problems	Williams *et al.* (1975)
Bottom-moored sonar	Good	Non-real-time	Vinje and Berge (1989)
AEM	Good	Resolution ~ flight altitude	Kovacs and Holladay (1990)
Thermal mapping	Fair	Thin ice OK	Steffen and Lewis (1988)
Airborne laser	Fair	Sea ice ridges OK	Ketchum (1971)
GPR	Poor	Problems with brine	Rossiter *et al.* (1980)
SAR	Poor	Ice types only	Kwok *et al.* (1992)
Passive microwave	Poor	Ice types only	Gloersen *et al.* (1978)

overturned ice blocks (Overgaard *et al.*, 1983). Upward-looking sonar systems are considered the best method for ice thickness mapping by remote sensing. They measure the draft, which provides a very good estimate for total thickness. They are, however, restricted by their high instrumental and logistics costs, and the unavailability of real-time data. Submarine sonars have been routinely used since the 1950s (Lyon, 1961) but their data are normally classified (Figure 2.16 shows an example). Bottom-moored sonars were developed in the 1980s for ice thickness mapping (Vinje and Berge, 1989).

The airborne electromagnetic method (AEM), originally developed for ore prospecting and geological surveys, was introduced in the late 1980s for sea ice thickness mapping (see Rossiter and Holladay, 1994). By emitting electromagnetic fields at frequencies of 1–10 kHz, eddy currents are generated in the conductive seawater. These currents generate a secondary electromagnetic field, and, measuring this field at the receiver, the distance to seawater can be determined. Measuring the distance to the sea ice surface by an altimeter, the sea ice thickness is obtained. AEM is a logistically feasible way for reliable and quick ice thickness mapping. It also provides line data with a resolution of the order of the flight altitude (30–100 m). Thus ridges can be identified for their total cross-sectional area but not for the geometric structure. The accuracy of results depends on the inversion model used (Figure 2.18),

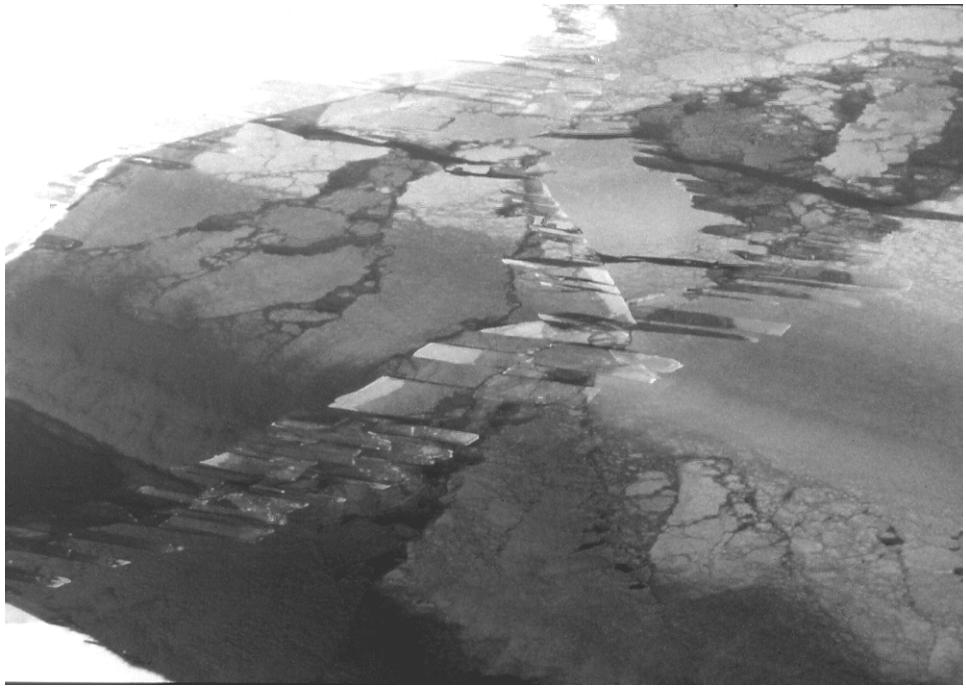

Figure 2.17 Thin ice sheets undergo rafting in compression. The width of the interlocking fingers in the picture varies between 1 and 10 m.

since by adding layers a more realistic conductivity distribution can be taken for the ice. Surface-based or shipborne EM systems have also been introduced (Haas, 1998).

Thermal infrared mapping can be applied to sea ice mapping in cold weather because the surface temperature of sea ice and the eventual snow cover on top depend on the structure and thickness of the ice and snow. It works well for ice thinner than about 50 cm when the air temperature is less than 5°C (Steffen and Lewis, 1988; Leppäranta and Lewis, 2007). Airborne laser profilometers give the upper surface topography (quite widely used since 1970). In principle, surface elevation can be interpreted for total ice thickness using Archimedes' law, but the measurement accuracy and snow cover cause severe problems. However, sea ice ridges are shown in surface topography profiles and constitute the principal aim of laser surveys.

Microwave sea ice mapping is carried out by ground-penetrating radar (GPR), synthetic aperture radar (SAR), and the (passive) radiometer. They are widely used for sea ice mapping but provide only poor results for ice thickness (Rossiter and Holladay, 1994; Kwok *et al.*, 1998; Wadhams, 2000; Karvonen *et al.*, 2005). Radar signals cannot penetrate sea ice because of brine and seawater inclusions, and the direct connection between ice thickness and backscatter is weak. SAR can detect two to four nominal ice types: the most promising is ridged ice, because piled-up ice blocks give strong backscatter. Microwave radiometers (10–100 GHz) can differentiate between open water, first-year ice and, to some degree, multi-year ice (Gloersen *et al.*, 1978; Kondratyev *et al.*, 1996). On the global scale they are by far the most used system for collecting sea ice information (see Figure 2.5).

A particular technique is ship-borne remote sensing. It is limited by the ship's tactical navigation to find the best route and it is therefore biased toward smaller thicknesses; however, the advantages are simplicity and low costs. The methods have included photography and video recording of ice blocks turning as the ice is broken (Overgaard et al. 1983; Shimoda *et al.*, 1997; Lu and Li, 2009), oblique-view laser profilometry (Leppäranta and Palosuo, 1981) and EM surveys.

It is clear that no single method is sufficient for ice thickness mapping; rather, a combination of instruments is needed to cover the whole range from 0 m to 50 m thicknesses. Satellite-derived thickness information results in poor quality, as it is only based on the thermal method or microwaves, both of which are of limited use. In 2010 ESA launched satellite *CryoSat 2*[6], which is designed for mapping thickness of sea ice and glaciers (`http://www.esa.int/esaLP/LPcryosat.html`). The measurement accuracy for polar sea ice is claimed to be good enough to monitor annual variations in sea ice thickness. *CryoSat-2* carries a sophisticated radar altimeter called SIRAL (Synthetic Aperture Radar Interferometric Radar Altimeter). The system measures the freeboard, and the accuracy of the resulting mean thickness is, according to ESA, 1.6 cm for Arctic sea ice areas in the scale of 10^5 km^2 and 0.17 cm in the Antarctica in the area scale of 10^6 km^2. These accuracies are better by a factor of 2–3 as specified by the scientific requirements.

[6] The trial with *CryoSat 1* in 2005 resulted in destruction of the satellite due to launch failure.

2.4.3 Ice thickness distribution

In sea ice dynamics – as well as in sea ice geophysics and engineering in general – sea ice thickness is the primary ice property of ice fields. It determines the volume and strength of ice cover, and is a key ice parameter in estimating ice loads on structures and navigation conditions. The mean sea ice thickness in continuum length scales is 2–8 m in the Central Arctic Ocean. It is lower in the Eurasian Shelf and at its highest off northern Greenland and the Canadian Archipelago (Figure 2.19). Distribution is strongly influenced by the drift of ice. Without dynamics the thickness would be more or less symmetric around the North Pole, but due to ice transport it is lowest (about 2 m) on the Siberian Shelf and 3 m or more in the Beaufort Sea. The highest thicknesses, averaging 8 m, result from the mechanical deformation of ice. In the seasonal sea ice zone the mean thicknesses range in $\frac{1}{2}$–2 m. In the Antarctic sea ice thicknesses are much less than in the Arctic. According to a large ship-borne data set, the long-term mean and standard deviation of total sea ice thickness is reported as 0.87 ± 0.91 m, which is 40% greater than the mean thickness of undeformed ice, 0.62 m (Worby *et al.*, 2008). The correlation length scale was 100–300 km.

In the continuum length scales sea ice thickness is presented using a thickness distribution (Thorndike *et al.*, 1975). With this approach it is possible to include the large thickness variability in the analysis and modelling of ice dynamics. Let $\underline{h} = \underline{h}(x, y; t)$ stand for the actual ice thickness and h represent the ice thickness as the distribution variable. Recalling the ice function I in Eq. (2.4) we have $1 - I(h) = 1$ if $\underline{h} \leq h$ or 0 if $\underline{h} > h$. In a region Ω, the area of ice thinner than or equal to h is:

$$S(h) = \int_{\Omega} [1 - I(h)] \, \mathrm{d}\Omega \tag{2.37a}$$

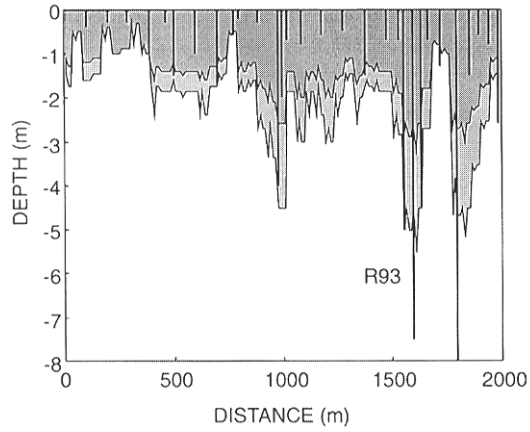

Figure 2.18 AEM calibration for ice thickness in the Baltic Sea, March 1993. The vertical bars show drilling data, dark and light-shaded areas show inversions with one- and two-layer models, respectively (the footprint is 100 m).
From Multala *et al.* (1996).

Thus $S(0)$ is the area of open water and $S(\infty)$ is the total area of Ω. The normalized form of the distribution:

$$\Pi(h) = \frac{S(h)}{S(\infty)} \tag{2.37b}$$

is the spatial ice thickness distribution, analogous to the probability distribution[7]. The derivative (in the generalized sense) of Π, $\pi(h) = \mathrm{d}\Pi/\mathrm{d}h$, is the spatial density of the ice thickness. *Note*: the thickness distribution was originally (Thorndike *et al.*, 1975) chosen continuous from the right (i.e., $S(h)$ equal to the area of ice thinner than h); here it is continuous from the left (i.e., $S(h)$ equal to the area of ice thinner than or equal to h). The current way is also common in probability theory; the difference is academic, though.

The thickness distribution is not continuous[8] everywhere since part of the spatial density mass is concentrated in open water and in homogenous ice patches. These discontinuities can be mathematically handled using the delta function δ and Heaviside function H:

$$\delta(s) = 0, \quad \text{if } s \neq 0, \quad \text{and} \quad \int_{-\infty}^{\infty} \delta(s) f(s) ds = f(0) \tag{2.38a}$$

$$H(s) = \begin{cases} 0, & s < 0 \\ 1, & s \geq 0 \end{cases} \tag{2.38b}$$

where f is for any integrable function. They are connected by the generalized derivative:

$$\frac{dH}{ds} = \delta(s) \tag{2.38c}$$

The spatial (cumulative) distribution function and density can be written as sums of discrete parts and continuous parts:

$$\Pi(h) = \sum_k \pi_k H(h - h_k) + \Pi'(h) \tag{2.39a}$$

$$\pi(h) = \sum_k \pi_k \delta(h - h_k) + \pi'(h) \tag{2.39b}$$

where π_k's are the probabilities of discrete thicknesses h_k, $k = 0, 1, \ldots, \Pi'$ is the continuous component of the distribution, and $\pi' = \mathrm{d}\Pi'/\mathrm{d}h$.

The thickness distribution has the following mathematical properties:

(i) $\Pi(0) = 1 - A$ and $\Pi(\infty) = 1$ by definition.
(ii) The first moment is the mean ice thickness.
(iii) The second moment is proportional to the mean potential energy of the ice (see Eq. 2.2).

[7] Analogous but physically dissimilar; there is no random field embedded, the distribution describes the variability of the real field of ice thickness – as in mechanics of rigid bodies.
[8] For continuity, the left and right limits must exist and be equal.

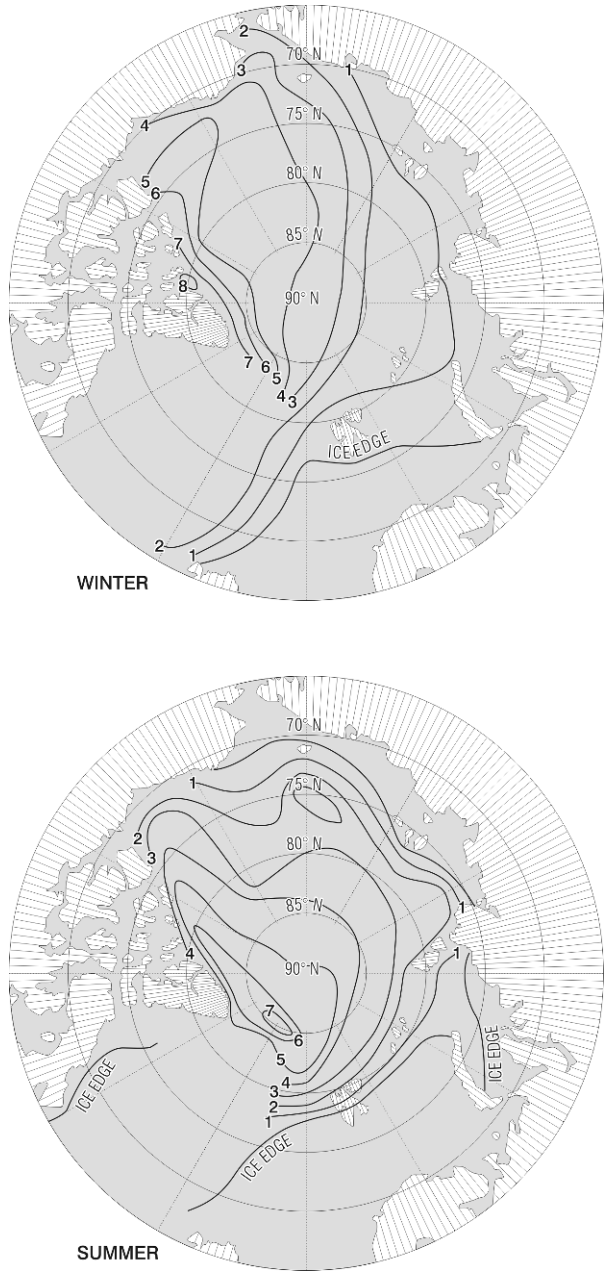

Figure 2.19 Mean sea ice draft in the Arctic Ocean based on submarine data. Since Archimedes' law states that 89% of the ice sheet is beneath the sea surface, the mean sea ice thickness is obtained by multiplying these draft numbers by 1.12.
Reproduced from Bourke and Garret (1987), with permission from Elsevier.

There is no simple general form for the distribution function because of the very large space-time variability of its shape, and therefore discrete histogram approximations are used. However, the upper tail of the spatial density containing deformed ice drops to zero exponentially (Wadhams, 1998). The thickness distribution includes both undeformed and deformed ice but ignores spatial information about the structure of drift ice. Figure 2.20 shows ice thickness distributions from both polar regions. The multi-year peak is well developed only in the Arctic Ocean, and there is much less deformed ice in Antarctica.

2.5 SEA ICE RIDGES

Sea ice ridges are a particular form of deformed ice or pressure ice (Figure 2.21). They are the thickest ice formations, typically 5–30 m, and over large areas their volume may account for up to about one-half of the total ice volume. In sea ice dynamics, ridging is the main sink of kinetic energy in deformation due to friction and production of potential energy (Rothrock, 1975a). Ridges are important hydrodynamic form drag elements at the air–ice and ice–water interfaces. In ice engineering, ridges are of deep concern because (i) they are connected with the highest ice loads on structures within first-year ice fields, (ii) they scour the sea bottom, (iii) they influence shipping conditions, and (iv) they influence on-ice traffic conditions. *In situ* field studies on the structure of ridges are made by drilling, diving and sonar, while their spatial statistics are mapped by remote-sensing methods, primarily airborne laser profilometer, SAR, and submarine upward-looking sonar.

2.5.1 Structure of ridges

Detailed investigations of the structure of sea ice ridges commenced in the 1960s from the needs of polar ocean engineering (Palosuo, 1970; Kovacs, 1971; Weeks *et al.*, 1971). The top part of a ridge is called *the sail* and the lower part is called *the keel;* in the keel there is a *consolidated zone*, which grows downward from the water surface level as the ridge ages. In the sail and lower keel the ice blocks are loose or weakly frozen together. A simple structural model of ridges (Figure 2.21) consists of triangular keel and sail, described by the keel depth h_k, sail height h_s, slope angles φ, and porosity ν; $\varphi \approx 30^\circ$ (keel) or 20° (sail) and $\nu \approx 0.25$ (e.g., Timco and Burden, 1997; Kankaanpää, 1998). The cross-sectional volumes of keel and sail are $h_k^2 \cot \varphi_k$ and $h_s^2 \cot \varphi_s$. A more general model would have a trapezoidal keel.

The structure of a ridge undergoes continuous evolution due to freezing, melting and erosion, becoming smoother with time (Figure 2.22). Erosion of roughness features smoothes the external geometry, and in the interior consolidation takes place in the keel. Contacts freeze between ice blocks, first releasing the latent heat to warm ice blocks in a fresh ridge. The capacity of the blocks to absorb latent heat is

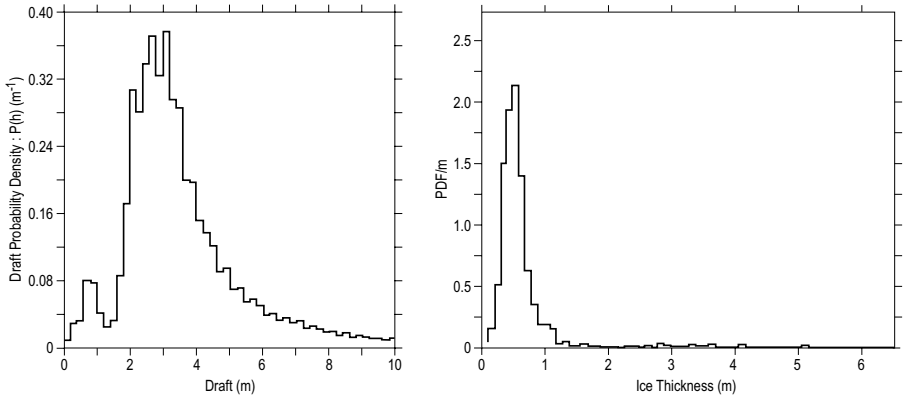

Figure 2.20 Observed ice thickness distributions. Left: Fram Strait (Wadhams, 1980a). Right: Antarctica, Atlantic sector (Wadhams *et al.*, 1987).

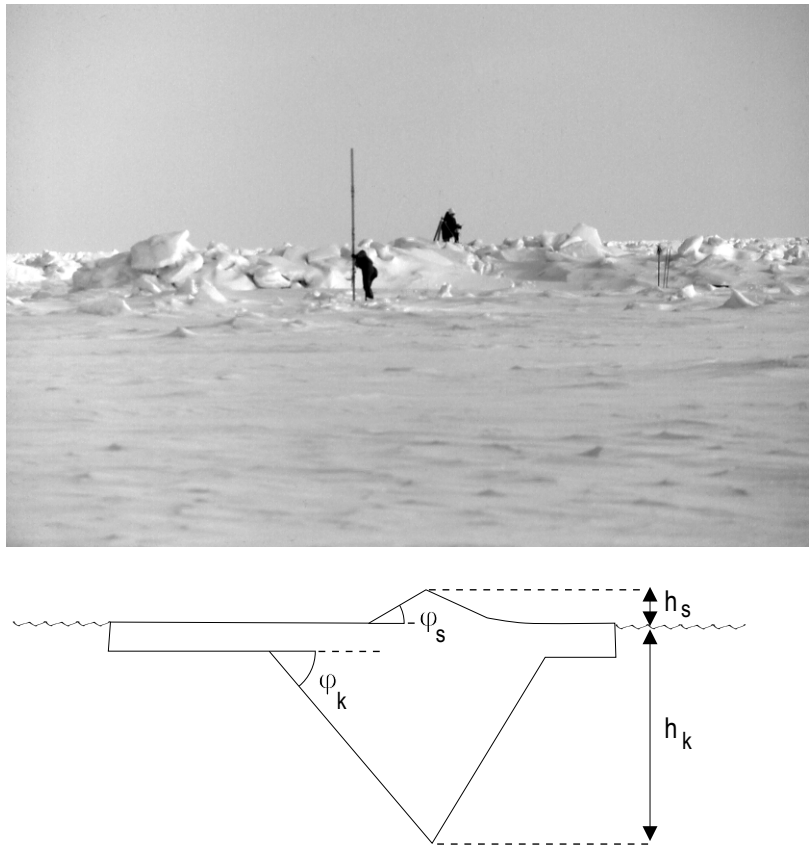

Figure 2.21 An ice ridge shown in a field photograph (Baltic Sea, March 1988) and in a schematic cross-sectional diagram.

not large, and for further consolidation the latent heat must be conducted to the atmosphere. By this way, the consolidation front progresses downward inside the ridge, and the growth rate can be approximated using the Zubov model (see Section 2.3), with the modification that latent heat released in consolidation equals νL. The solution is therefore for the thickness of the consolidated layer:

$$h_F = \sqrt{a^2 \nu^{-1} S + \delta^2} - \delta \tag{2.40}$$

That is, asymptotically, as $h_F \gg \delta$, the thickness of the consolidated layer grows $\nu^{-1/2} \approx 2$ times faster than undeformed ice. This has been well documented in observational data (Leppäranta and Hakala, 1992). Applying equilibrium thickness results (Eq. 2.33) to multi-year ridges, a theoretical limit thickness would be about 15 m as long as there are ice blocks to take into consolidation. But when the blocks are all taken into the solid ridge or melted, the thickness would start to come down toward the equilibrium thickness of undeformed ice. The whole cycle would take, however, several decades, and therefore thick, solid, old multi-year ridges are occasionally observed in the Central Arctic Ocean.

Ice ridges float according to the Archimedes' law (see Eq. 2.1). The ratio of keel depth to sail height $\gamma = h_k/h_s$ is obtained from:

$$(\rho_w - \rho) h_k^2 \cot \varphi_k = \rho h_s^2 \cot \varphi_s \tag{2.41}$$

We have $\gamma = 2.8$ for $\varphi_k = \varphi_s$ and $\gamma = 3.5$ for $\varphi_k = 30^\circ$, $\varphi_s = 20^\circ$. According to observations, for multi-year ridges $\gamma \approx 3$ but for first-year ice ridges $\gamma \approx 4$–5 (Wright *et al.*, 1978). The latter case comes from the keel being steeper than the sail. Wittman and Schule (1966) presented a triangular keel model with $\gamma \approx 3.3$ based on field data. Once the sail height is known, the total cross-section of a ridge can be estimated as $R = k h_s^2$ where the coefficient k represents all structural parameters. For the Baltic Sea, according to Leppäranta and Hakala (1992), $k \approx 17$.

A physical limitation exists for ridge growth (Parmerter and Coon, 1972; Hopkins and Hibler, 1991). When a ridge has grown to a certain vertical size, the ice sheet is too weak to penetrate into the ridge, for further growth. It breaks in front of the ridge, producing lateral growth. This limiting size mainly depends on the thickness of the parent ice sheet (very few ridges grow to this size). The record ridge sizes come from the Beaufort Sea (Wright *et al.*, 1978): a floating ridge with a sail height of 12 m and a keel depth of 45 m, and a grounded ridge with a sail height of 18 m.

In shallow areas where the sea depth is less than the keel depth, grounding takes place and ridges anchor to form fixed ice islands. This is typically observed at the landfast ice boundary. Grounded ridges serve as tie points to the ice and therefore help the fast ice boundary to extend farther away from the coast. Grounded ridges, when moving, scour the ocean bottom, and the keel may penetrate deep, depending on the bottom material (Blondel and Murton, 1997). As a consequence, cables and pipes laid on the floor of shelf waters must be buried deep enough to avoid damage from scouring keels.

2.5.2 Statistical distributions of ridge size and occurrence

Ridges give an impressive feature to the drift ice landscape (Figure 2.23). The spatial distribution of ridging is described in terms of their size and occurrence. The first occurrence data were counts made in reconnaissance flights resulting in a typical level of 5–10 ridges per km, with a maximum of 20 ridges per km (Wittman and Schule, 1966). At present, ridges are usually mapped using airborne laser profilometers for sails (Ketchum, 1971; Hibler *et al.*, 1972; Lewis *et al.*, 1993) and using upward-looking sonar for keels (Williams *et al.*, 1975; Vinje and Berge, 1989).

A cut-off size, h_c, needs to be introduced, since the size of the chosen ridges must be well above the noise level of the measurement system. Also sails should not be mixed with snowdrifts. The cut-off sizes have been 1 m (or 3 feet $\approx$ 0.9 m) for sails and 5 m for the keels in the polar oceans, somewhat lower in smaller subpolar basins

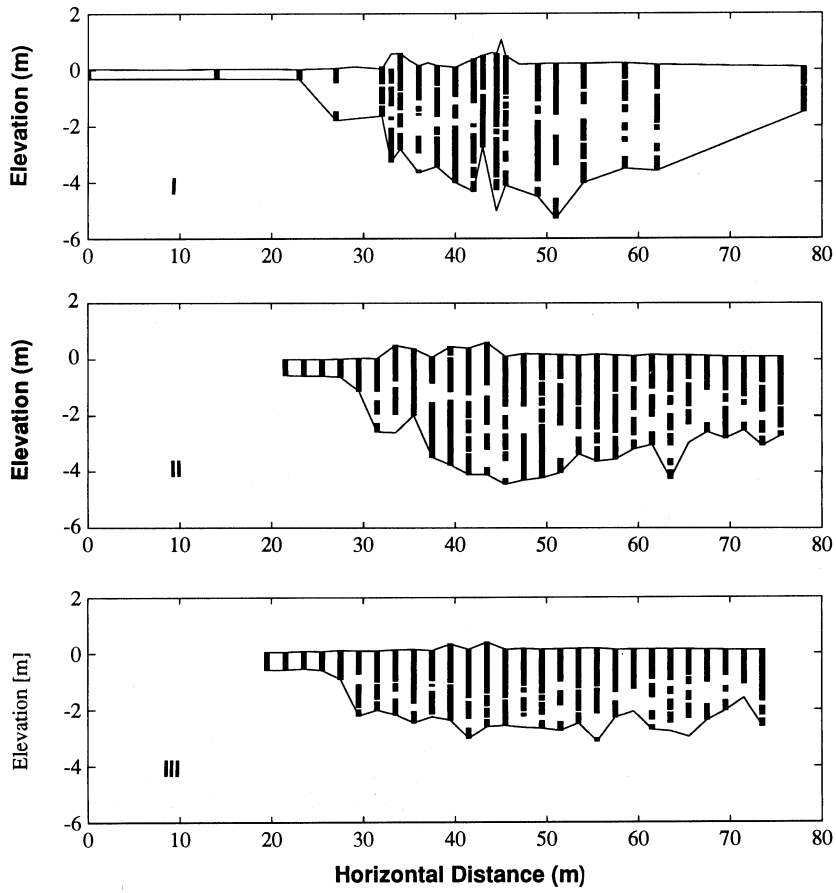

Figure 2.22 The evolution of the cross-sectional profile of one ridge near Hailuoto island, Baltic Sea, winter 1991 (Leppäranta *et al.*, 1995).

such as 0.4 m in the Baltic. Independent sails or keels are taken from observed surface profiles using the Rayleigh criterion: ridges are taken as the local maxima, which are greater than the cut-off height and between which there is a local minimum with elevation less than half of these maxima. The cut-off is more a parameter related to observational technology than to real ice. Visual counts have given about the same number of sails as laser profilometer measurements. This confirms that the cut-off is well tuned to reflect how the ice field looks from above, a situation that is also true of the concept of the significant wave height of wind-driven surface waves.

Ridge size

Sail heights or keel depths follow the exponential distribution:

$$p(h*; h_c, \lambda) = \lambda \exp[-\lambda(h* - h_c)], \quad h* \geq h_c \tag{2.42}$$

where $h*$ represents the sail height or keel depth, and λ is the distribution shape parameter. The mean size is simply $h_c + \lambda^{-1}$ and the standard deviation is λ^{-1}. This distribution was first proposed by Wadhams (1980a) for the Arctic Ocean, and it has been confirmed several times, for sails in the Baltic Sea (Leppäranta, 1981b; Lewis *et al.*, 1993) and in the Antarctic (Weeks *et al.*, 1989; Granberg and Leppäranta, 1999), and for keels in the Arctic by Wadhams and Davy (1986). The first size distribution was proposed by Hibler *et al.* (1972) who arrived at a probability density proportional to $\exp(-h_*^2)$.

The statistical background of the size distribution can be based on a certain random hypothesis concerning the probabilities of the different size arrangements (see Hibler *et al.*, 1972). The exponential distribution comes from assuming that all height arrangements yielding the same total sum are equally probable. Such a hypothesis, however, has no clear physical background. Representative values for the mean sail height and keel depth in the central Arctic Ocean are $\tilde{h}_s \approx 1.2$–1.4 m (cut-off 0.9 m) and $\tilde{h}_k \approx 8$–14 m (cut-off 6.1 m) (Hibler *et al.*, 1972). Therefore the parameter λ^{-1} is 0.3–0.5 m for sails and 2–5 m for keels. In the Baltic Sea the mean sail height was 0.5–0.6 m (cut-off 0.4m) in Lewis *et al.* (1993).

Ridge spacing

Spacings between ridges relate in some way to the size of ice floes, and so we expect similar statistical laws to apply to them (see Section 2.2). In fact, the first model for ridge spacings was the exponential distribution (Hibler *et al.*, 1972). It was later replaced by the logarithmic normal distribution (Wadhams and Davy, 1986; Lewis *et al.*, 1993), giving the impression that new ridges would be randomly born at any point between existing ridges. In the seasonal sea ice zone, as in the Baltic Sea, this may be true. However, in the central Arctic Ocean ridges form in leads and, in turn, the birth of ridges therefore follows the distribution of lead spacings and inherits the logarithmic normal form. The fit is in general not excellent, though, and an attempt was made in Lensu (2003) to improve the distribution model by including a

clustering effect in ridging. Representative values for mean ridge spacing are 5–10 km^{-1} in the Central Arctic Ocean and in the Baltic Sea, but with different cut-off sail heights, 0.9 m and 0.4 m, respectively (Hibler *et al.*, 1972; Lewis *et al.*, 1993).

The inverse mean ridge spacing μ is called the ridge density and is equal to the mean number of ridges per length. It depends on the cut-off size. So, assuming the exponential distribution for ridge size, we have:

$$\mu(h_{c2}) = exp[-\lambda(h_{c2} - h_c)]\mu(h_c) \tag{2.43}$$

where h_c is the original cut-off height and h_{c2} is the new one. With regard to the two-dimensional aspects of spacing, deviations from isotropy occur as one would expect (e.g., Mock *et al.*, 1972; Leppäranta and Palosuo, 1983). However, the isotropy has so far been the main working hypothesis. It simply leads from one to two dimensions through (Mock *et al.*, 1972):

$$\frac{L_R}{S} = \frac{\pi}{2}\,\mu \tag{2.44}$$

where L_R is the total length of ridges in the horizontal area S. For anisotropic cases this equation has been found reasonable when using the directionally averaged ridge density parameter.

2.5.3 Ridging measures

The ridge size and spacing distributions can be combined to form a measure of ridging intensity. Two natural measures arise: $\mu\tilde{h}_*$ and $\mu\tilde{h}_s^2$. The first one is dimensionless and describes the sum of sail heights or keel depths per unit length (with sails it is also proportional to the aerodynamic form drag of ridges: Arya, 1973). The second has the dimension of length and is proportional to the mean thickness of ridges, h_R. This quantity and the areal concentration of ridges (S_R/S) are:

$$h_R = \frac{\pi}{2}\,\mu\tilde{R}, \quad \frac{S_R}{S} = \frac{\pi}{2}\,\mu\tilde{b}_R \tag{2.45}$$

where b_R is the ridge width. If only sail data exist, the cross-section and width of ridges are approximated by $R \approx k h_s^2$ and then $h_R = \frac{1}{2}\pi\mu k\tilde{h}_s^2$ and $b_R = 2\gamma h_s \cot\varphi_k$. Hibler *et al.* (1972) used the formula $h_R = 10\pi\mu\tilde{h}_s^2$ ($k = 30$) to estimate the volume of ridged ice in the Arctic Ocean, while Leppäranta and Hakala (1992) obtained $k = 17$ in the Baltic Sea. The volume of ridged ice is typically 10–40% of total ice volume (Hibler *et al.*, 1974b; Mironov, 1987; Weeks, *et al.*, 1989; Lewis *et al.*, 1993; Granberg and Leppäranta, 1999).

Example In approximate terms, $b_R \approx 3h_k$ and $R \approx \sqrt{3}h_k^2$. Then $S_R/S \approx 5\mu h_k$ and $h_R \approx 3\mu h_k^2$. For representative values, taking $h_k \approx 7.5$ m and $\mu \approx 5\,\mathrm{km}^{-1}$, we have $S_R/S = 19\%$ and $h_R = 84$ cm. These numbers characterize a moderately ridged Arctic region.

In order to describe ridging properly, one needs at least three parameters: cut-off size, mean size, and ridge density. The cut-off size is a free parameter that needs to be "tuned" so that ridge statistics agree with the appearance of the ice field. These parameters can be used to obtain a ridging intensity measure, but the relationship cannot be inverted to obtain the ridge size and spacing from the intensity. However, there are regional regularities (Figure 2.24). In the central Arctic Ocean the size and density of ridges are correlated (Wadhams, 1981), while in the Weddell Sea the mean ridge size shows very small variations and could therefore be considered fixed (Granberg and Leppäranta, 1999). The latter case also holds in the Baltic Sea (Leppäranta, 1981b).

Example (Leppäranta, 1981b) In the Baltic Sea the average sail height is nearly constant, about 20 cm above the cut-off height of 40 cm. The ridge density alone provides a good estimator of the volume of ridged ice: in quantitative terms $h_R = 2.2\,\mathrm{cm}^2\mu \cdot 10^3 \pm 27\%$ (i.e., on average one ridge per kilometre accounts for 2.2 cm in ice thickness).

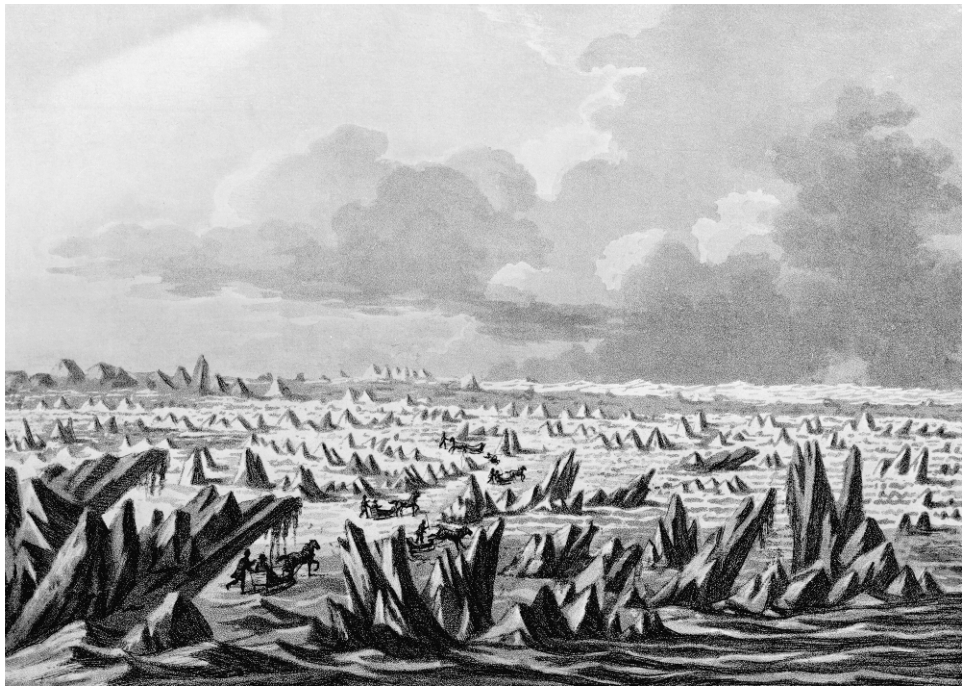

Figure 2.23 The Gulf of Bothnia in winter (Louis Belanger, according to A. F. Skjöldebrand). Travellers across a ridged ice field, a romantic drawing showing the ice landscape in exaggerated linear dimensions to create a fairy-tale atmosphere.
Reproduced from Etienne Bourgelin Vialart, comte de Saint-Morys, Voyage pittoresque de Scandinavie. Cahier de vingt-quatre vues, avec descriptions, 1802, with permission of Collections of Museovirasto, Helsinki, Finland.

2.5.4 Hummocked ice

Not all mechanically deformed ice appears as ridges: in places irregular, hummocked ice fields with no regular geometry are found. Their thickness is less than that of ridges but greater than that of undeformed, level ice. Their existence is well known to icebreaker captains, who consider them a nuisance because they may be hidden beneath the snow cover. Not many direct measurements exist about the spatial distribution of the thickness of hummocked ice. Such a field may be described by the mean and standard deviation of the thickness.

One way to estimate the volume of hummocked ice is to first consider the observation that the exponential distribution for ridge size holds for any manageable cut-off size. This suggests the following hypothesis: The exponential form can be extrapolated down to a zero cut-off height, but at some non-zero level the ridges lose their ridge-like form, which corresponds to the visual appearance of the ice field. The "ridges" beneath a well-chosen cut-off height are then taken to represent hummocked ice. Without any model for the geometry of hummocks, this extrapolation allows us to determine their total volume or the mean thickness h_h:

$$\frac{h_h}{h_h + h_R} = \frac{1}{2} \exp(-\lambda h_c)[1 + (\lambda h_c)^2] \tag{2.46}$$

In most ridge observations $\lambda h_c \sim \frac{1}{2}$, and therefore $h_h/(h_h + h_R) \sim \frac{1}{4}$. Knowing the volume of hummocks is enough for ice budget calculations but it would be desirable to decompose it into mean physical thickness and areal concentration. This would need a geometrical model of hummocked ice.

2.5.5 Total thickness of deformed ice

The mean thickness of deformed ice finally reads:

$$h_d = h_h + h_R \tag{2.47}$$

The spatial distribution of ridges has been traditionally described in terms of areal or volume fraction. Wittman and Schule (1966) reported that in the Canadian Basin the average areal fraction of pressure ice (equivalent to deformed ice) is 0.13–0.18 with a maximum of more than 0.5 in heavy-deformation zones, while according to Kirillov (1957) in the Kara Sea the average volume fraction is 0.28 with a maximum of 0.39.

The degree of ridging and hummocking has also been described by an index from 0 to 5. This index is roughly proportional to the total thickness of deformed ice, with full level 5 corresponding to $h_d/h_u \approx 1.5$–2.5, where h_u is the thickness of undeformed ice, and $h_i = h_u + h_d$ (Gudkovic and Romanov, 1976; Appel, 1989).

Example (*Kirillov's formula*) Kirillov (1957) made the following assumptions for ridges and hummocks: triangular sail and keel cross-sections and $h_k/h_s = 3$, on average $h_k = h_u$, and porosity equal to 0.3. Then $h_d/h_u \approx 2.0 \cdot S_R/S$. Thus observing the area of deformed ice provides an estimate for its volume.

2.6 DRIFT ICE STATE

In the continuum dynamics of sea ice, an ice state J must be defined. It is the set of the material properties of drift ice necessary to solve the dynamics problem. When the number of properties included in J is N we speak of an N-level ice state. Most work in continuum sea ice dynamics has been done by assuming that the ice thickness field is sufficient to describe the state of drift ice. In practice, there are observational limitations to map the thickness field as discussed in Section 2.4.

The first approach is to define ice categories as the ice state variables. Normally these are chosen to be manageable observables, meaning that the ice state is largely based on the information provided by routine ice mapping systems. Recall the function "ice", I, from Eq. (2.4). In a low-level approach it is necessary to define generalized compactness and mean thickness of ice:

$$A(h_0) = \frac{1}{S}\int_\Omega I(x, y; h_0)\, d\Omega \tag{2.48a}$$

$$\tilde{h}(h_0) = \frac{1}{S}\int_\Omega hI(x, y; h_0)\, d\Omega = A(h_0)\tilde{h}_i(h_0) \tag{2.48b}$$

where $\tilde{h}_i(h_0)$ is the mean ice floe thickness over the sub-region $\Omega \cap \{h > h_0\}$. These quantities thus account for all ice thicker than h_0. Very thin ice does not give significant resistance to deformation, and it is preferable to exclude it from the mean thickness for the strength estimator. On the other hand, in remote sensing very thin ice is not well detected, and consequently $A(h_0)$ corresponds better to initialization and validation data. The areal fraction $1 - A(h_0)$ is the concentration of open water and thin ice; ice only grows there thermodynamically. The argument h_0 is no longer shown below but any category may be chosen conditional on $h > h_0$.

Compactness or mean thickness would be natural one-level ice states but they are not used because of too limited information. The minimum feasible ice state is their union, which is in fact the very widely used *two-level ice state* (Nikiforov, 1957; Doronin, 1970):

$$J = \{A, \tilde{h}\} \tag{2.49}$$

or, since $\tilde{h} = A\tilde{h}_i$, the state $J = \{A, \tilde{h}_i\}$ has the same information.

For *three-level ice states*, the decomposition of ice into undeformed ice and deformed ice (Leppäranta, 1981a) is often used:

$$J = \{A, h_u, h_d\} \tag{2.50}$$

The thickness of undeformed ice changes thermodynamically, while undeformed ice is dynamically transformed into deformed ice. This state does not include the areas of undeformed ice and deformed ice, just their thicknesses, and formally accounting for the area also would not be difficult. Lu *et al.* (1989) used another three-level system: ice compactness, first-year ice, and multi-year ice. The timescale was less than 1 month, and therefore these ice categories were independent but very useful

for modelling dynamics because of their different thicknesses and observability. Mechanical deformation may then be correctly limited to first-year ice only.

The ice category approach can be extended to multi-level ice states $J = \{A, j_1, j_2, j_3, \dots\}$. Additional, reasonable, new ice categories are introduced based on their dynamical significance and observability (Haapala, 2000). With a morphological model, more information can be extracted from one category. Leppäranta (1981a) decomposed deformed ice into density and size of ridges, these being controlled visually or with a laser profilometer.

The second approach is to take the *thickness distribution* for the ice state. The question then becomes: How many levels are needed or, in other words, what is the necessary or convenient resolution of the distribution? The thickness classes are fixed, arbitrarily spaced, and their histogram contains the state variables:

$$J = \{\pi_0, \pi_1, \pi_2, \dots, \pi_N\}, \quad \sum_{k=0}^{N} \pi_k = 1 \tag{2.51}$$

The open water fraction is practically always needed and therefore $\pi_0 = 1 - A$ or in general $\pi_0 = 1 - A(h_0)$.

In low-level cases thickness distribution approach is a very crude system in which the actual ice thickness information can easily disappear. Hence, the approach based on ice categories is preferable. The two-level state based on the thickness distribution is not the same as the two-level state based on the ice categories, since in the former case the thickness (or rather the thickness band) is fixed. In new, growing ice, it would need to spread evenly all over the ice band, far from what really happens. Consequently, when choosing the thickness distribution for the ice state the number of thickness classes should be large (of the order of ten). For such a number of levels, the ice category approach becomes cumbersome and the thickness distribution approach becomes preferable.

Example If there are no thermodynamical changes and mechanical changes only concern ice compactness, the two-level ice category and thickness distribution approaches overlap. The former is $J = \{A, \tilde{h} = \text{constant}\}$ and the latter is $J = \{\pi_0, \pi_1 = 1 - \pi_0\}$ (i.e. only $\pi_0 = 1 - A$ and A change).

Also, a combination can be worked out to add more observability to the thickness distribution. One possibility is to divide the thickness distribution into two parts: undeformed and deformed ice. This would allow us to differentiate thermal ice growth from mechanical ice growth.

In principle, the horizontal properties of ice floes can be added to the ice state in a similar way to thickness. Floes possess size and form, and size at least shows statistical regularity (see Section 2.2). In the continuum dynamics of sea ice, floe information has been used only in floe collision models (Shen *et al.*, 1986), there taken as uniform, circular disks. However, when an ice field closes up floes join together to act in groups and their individual signature is lost out from mechanical behaviour of the ice field. Application of discrete particle models to ice mechanics necessitates the detailed knowledge of the size and shape of all ice floes in the study area.

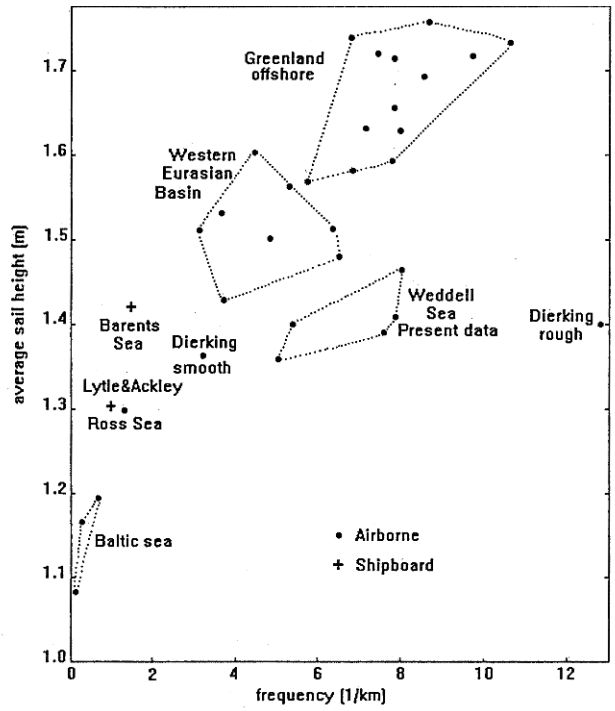

Figure 2.24 Ridge sail height vs. ridge density in different seas. Cutoff is 1 m.
From Dierking (1995), Granberg and Leppäranta (1999), Lytle and Ackley (1991), and Wadhams (1981).

Beginning with sea ice in the world ocean, sea ice types, and sea ice observation systems, the geophysical medium of drift ice has been introduced in this chapter. The drift ice medium appears as a thin, broken film on the sea surface, almost truly 2-dimensional. It consists of ice floes and is regarded as a continuum over length scales much greater than the typical size of floes. The relevant properties of the drift ice continuum for its dynamics are mainly ice compactness and thickness, which vary largely in time and space. The last section presented the concept of an "ice state", which contains information about the drift ice field necessary to understand and model its dynamics. In Chapter 3 observations about the kinematical properties of the drift ice medium are presented.

3

Ice kinematics

3.1 DESCRIPTION OF ICE VELOCITY FIELD

This chapter deals with the methods, data, and physics that relate to sea ice kinematics. It begins with a mathematical description of the two-dimensional motion of a rigid body and a continuum. Then observations of two elements of sea ice kinematics – drift and deformation – are given and analyzed using the mathematical techniques presented. The kinematics approach allows simple but powerful stochastic modelling, which is treated in Section 13.3. In the last section, the ice conservation law is derived for the ice state, linking the ice state from Chapter 2 to its changes due to thermodynamics and kinematics.

In ice kinematics the properties of the velocity field are examined, considering also the correlation of ice velocity with wind and currents. The outcome provides answers to such questions as: How long does it take for the ice to go from point A to point B? What is the typical ice velocity range in a certain sea area? How does the separation distance between two floes evolve? What does the ice velocity spectrum look like? Kinematics data are used in stochastic drift modelling and form the basis in the construction and validation of dynamical sea ice models as well.

Sea ice floats and drifts on the Earth's sea surface, taken as the sphere of radius $r_e = 6370\,\text{km}$. The natural coordinates are the zenith angle Z (latitude is equal to $\pi/2 - Z$) and azimuth (longitude) λ. A local Cartesian coordinate system with x, y and z for the east, north and upward coordinates is usually considered, with the sea surface as the zero reference level (an almost constant geopotential surface). The unit vectors in x, y and z directions are $\boldsymbol{i}$, $\boldsymbol{j}$ and $\boldsymbol{k}$, respectively. The motion of sea ice takes place in the three-dimensional world, but it can be treated as a *two-dimensional* phenomenon on the sea surface. The ice velocity is then given by a two-dimensional vector function of time and the horizontal coordinates $\boldsymbol{u} = \boldsymbol{u}(Z, \lambda; t)$ or, as is more usual, in a local Cartesian system:

$$\boldsymbol{u} = \boldsymbol{u}(x, y; t) \tag{3.1}$$

M. Leppäranta, *The Drift of Sea Ice*, Springer Praxis Books,
DOI 10.1007/978-3-642-04683-4_3, © Springer-Verlag Berlin Heidelberg 2011

Fridtjof Nansen (1861–1930, second from left), a Norwegian polar explorer, with *Fram* in the background. He was the leader of the *Fram* expedition (1893–1896), which drifted across the Arctic Ocean. He was the first to collect sea ice and oceanographic data from the central Arctic Ocean. He showed that the ice drift follows the wind with angular deviation in direction and that the ice flows out to the North Atlantic from the Arctic. Nansen was given the Nobel Peace Prize in 1922 for his help with refugees after the First World War. The photograph is from his book *Fram över Polarhavet* published in 1897 (Finnish translation, 1954).

with u and v, respectively, as the x- and y-components. This is true for two reasons: first, ice lies on the sea surface and does not possess a vertical velocity component; and, second, ice floes move as rigid pieces and the horizontal velocity is independent of the vertical coordinate. In exact terms, with respect to the Earth, the vertical velocity is not zero but given by the boundary condition $w(x, y) = \partial\xi/\partial t$, where ξ is sea level elevation. The slowly changing sea level does not cause any significant inertial effects on the sea ice motion. Then there are small vertical displacements of ice blocks during pressure ice formation; they will be obtained from the ice conservation law presented in Section 3.4.

3.1.1 Motion of a single floe

The dynamics of a single ice floe is examined using classical rigid body mechanics (e.g., Landau and Lifschitz, 1976). This motion has three degrees of freedom consisting of the translational motion $\boldsymbol{U} = (U, V)$ and the rotation rate $\dot{\omega}$ (positive

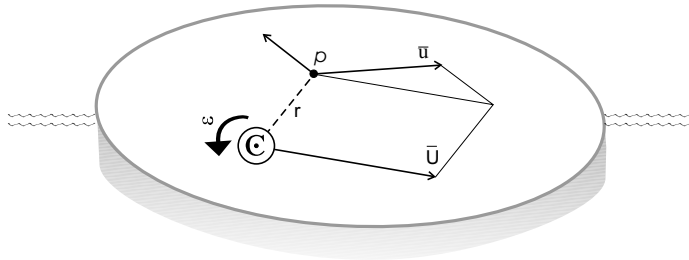

Figure 3.1 Motion of a single ice floe: translation velocity U and angular velocity $\dot{\omega}$ around the mass centre C.

anticlockwise) about the vertical axis (Figure 3.1). For an arbitrary point P in the floe, let $\boldsymbol{r}$ stand for the radius vector from the mass centre of the floe. The velocity at P is:

$$\boldsymbol{u} = \boldsymbol{U} + \dot{\omega}\boldsymbol{k} \times \boldsymbol{r} \tag{3.2}$$

For a circular floe with radius R, the translational kinetic energy is $\frac{1}{2}m|\boldsymbol{U}|^2$ and the rotational kinetic energy is $\frac{1}{4}m(\dot{\omega}R)^2$, their ratio being $2|\boldsymbol{U}|^2/(\dot{\omega}R)^2$. Therefore, if a 1-km size floe is translated by $10\,\mathrm{cm\,s^{-1}}$ the rotation rate must be $\sqrt{2} \times 10^{-4}\,\mathrm{s^{-1}} = 29^\circ\,\mathrm{h^{-1}}$ for the energies to be equal. Such rotation would be exceptionally fast; usually the rotation rate is less than $1^\circ\,\mathrm{h^{-1}}$. Because of the low rotational energy, it is normally sufficient to consider the translational velocity only.

In a granular ice flow, each floe has its own translational and rotational velocities. As long as there are enough free paths around floes, they drift independently. When free paths disappear, floes join into larger and larger groups, and their interaction by collisions and overriding begins. The motion of such a set of ice floes is approximated using purely statistical drift models or continuum flow models.

3.1.2 Continuum deformation

When the size of drift ice particles becomes one order of magnitude larger than the floe size, continuum approximation may be used for the kinematics (see Section 2.2). The continuum approach averages the movements of individual floes to the continuum length scale; the resulting velocity field needs to have continuous spatial derivatives to at least second order to apply continuum mechanics theory to drift ice. The mathematics of general continuum kinematics is presented in detail by Mase (1970) or Hunter (1976), among others.

Strain and rotation

The motion of a drift ice continuum can be decomposed into rigid translation, rigid rotation, and strain. In a horizontal flow, translation has two horizontal components

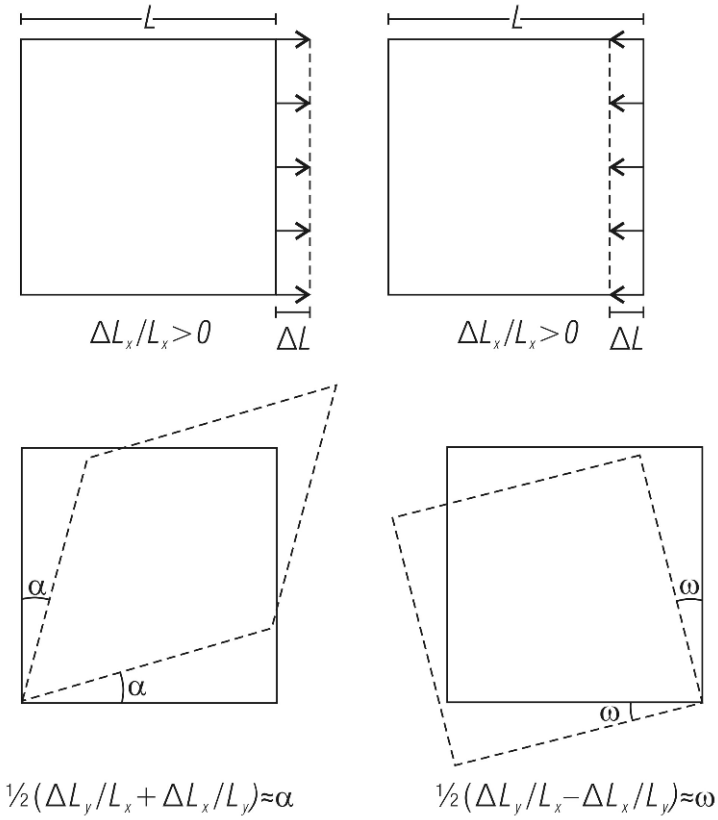

Figure 3.2 Strain modes and rotation, and their measures: upper graphs, extension and contraction; lower graphs, shear and rotation. Note that shear and rotation are drawn for positive signs.

and rotation has one component around the vertical axis, like a rigid single floe has. Strain represents the physical deformation of continuum particles (Figure 3.2). There are three different modes of strain: tensile strain or extension, compressive strain or contraction, and shear strain. The first two modes are normal strains (with opposite signs) that change lengths, while shear strain changes the shape of particles. A tensile strain of 1% means that the material has lengthened by 1%, a compressive strain of 1% means that the material has shortened by 1%, and a shear strain of 1% means that a right angle in the material configuration has changed by 0.01 rad $\approx 0.57°$. Finally, a rotation of 1% corresponds to anticlockwise rotation of the particle by 0.01 rad $\approx 0.57°$.

Strain and rotation are second-order tensors, which can be treated as matrices in Cartesian systems. In two-dimensional theory, any matrix A has four elements:

$$A = \begin{bmatrix} A_{11} & A_{12} \\ A_{21} & A_{22} \end{bmatrix} \tag{3.3}$$

where A_{11}, A_{22} are the diagonal elements, and A_{12} and A_{21} are the off-diagonal elements. The notation $\boldsymbol{A} = (A_{ij})$ is used below. The basic invariants[1] of 2×2 matrices are the trace $\mathrm{tr}\boldsymbol{A} = A_{11} + A_{22}$ and determinant $\det\boldsymbol{A} = A_{11}A_{22} - A_{12}A_{21}$; any functions of them are also invariants. Eigenvalues of a matrix are solutions (λ) of the eigenvalue equation $\det(\boldsymbol{A} - \lambda\mathbf{I}) = 0$ and the corresponding eigenvectors Λ are the solutions (Λ) of $\boldsymbol{A}\Lambda = \lambda\Lambda$. In two dimensions there are two eigenvalues and two corresponding eigenvectors.

Let $\boldsymbol{X}$ stand for a reference configuration of a material particle and consider its change represented by a mapping $\boldsymbol{X} \to \boldsymbol{x}$ (i.e., $\boldsymbol{x} = \boldsymbol{x}(\boldsymbol{X})$). Removing the pure translation, the change in material configuration is given by the *displacement gradient* $\boldsymbol{V} = \boldsymbol{F} - \mathbf{I}$, where $\boldsymbol{F} = \nabla\boldsymbol{x} = (\partial x_i/\partial X_j)$ and $\mathbf{I} = (\delta_{ij})$ is the unit tensor (e.g., Hunter, 1976). In small deformation theory ($|\boldsymbol{V}| \ll 1$) the displacement gradient contains the strain $\boldsymbol{\varepsilon}$ and the rotation $\boldsymbol{\omega}$, given by its symmetric and antisymmetric parts: respectively, $\boldsymbol{\varepsilon} = \frac{1}{2}(\boldsymbol{V} + \boldsymbol{V}^{\mathrm{T}})$ and $\boldsymbol{\omega} = \frac{1}{2}(\boldsymbol{V} - \boldsymbol{V}^{\mathrm{T}})$, where the superscript T stands for the transpose.

Strain-rate and vorticity

Let us consider a drift ice field moving with velocity $\boldsymbol{u}$, consisting of a rigid translation velocity and a differential velocity. The latter is given by the velocity gradient $\nabla\boldsymbol{u}$, where ∇ is the two-dimensional gradient operator, in the Cartesian system $\nabla = \mathbf{i}\partial/\partial x + \mathbf{j}\partial/\partial y$. The velocity gradient is a dyadic (i.e., a second order tensor with four components):

$$\nabla\boldsymbol{u} = \begin{bmatrix} \dfrac{\partial u}{\partial x} & \dfrac{\partial u}{\partial y} \\ \dfrac{\partial v}{\partial x} & \dfrac{\partial v}{\partial y} \end{bmatrix} \tag{3.4}$$

The displacement during a time interval δt equals $\boldsymbol{u}\delta t$. The normal strain along the x-axis is then:

$$\frac{\Delta L_x}{L_x} = \left[\left(u + \frac{\partial u}{\partial x}\,\delta x \right)\delta t - u\delta t \right] \frac{1}{\delta x} = \frac{\partial u}{\delta x}\,\delta t \tag{3.5}$$

Dividing by δt, the rate of normal strain along the x-axis becomes $\partial\boldsymbol{u}/\partial x$. Treating the other strain components in a similar way, it is seen that the velocity gradient is exactly the rate of the displacement gradient. Consequently the symmetric and antisymmetric parts of the velocity gradient tensor:

$$\dot{\boldsymbol{\varepsilon}} = \frac{\partial\boldsymbol{\varepsilon}}{\partial t} = \frac{1}{2}\left[\nabla\boldsymbol{u} + (\nabla\boldsymbol{u})^T\right] \tag{3.6a}$$

$$\dot{\boldsymbol{\omega}} = \frac{\partial\boldsymbol{\omega}}{\partial t} = \frac{1}{2}\left[\nabla\boldsymbol{u} - (\nabla\boldsymbol{u})^T\right] \tag{3.6b}$$

[1] The invariant of a matrix is a function of its elements such that it is not affected by coordinate transformations. Eigenvectors define a coordinate system where a matrix becomes diagonal.

are the *strain-rate* and rotation rate, or *vorticity*, tensors, respectively, and $\nabla \boldsymbol{u} = \dot{\boldsymbol{\varepsilon}} + \dot{\boldsymbol{\omega}}$. Their dimension is 1/time, and their inverses thus define the timescales of strain and rotation.

The strain-rate tensor has three independent components:

$$\left.\begin{aligned} \dot{\varepsilon}_{xx} &= \frac{\partial u}{\partial x} \\ \dot{\varepsilon}_{xy} = \dot{\varepsilon}_{yx} &= \frac{1}{2}\left(\frac{\partial u}{\partial y} + \frac{\partial v}{\partial x}\right) \\ \dot{\varepsilon}_{yy} &= \frac{\partial v}{\partial y} \end{aligned}\right\} \tag{3.7}$$

The strain-rates $\dot{\varepsilon}_{xx}$ and $\dot{\varepsilon}_{yy}$ are the normal strain-rates in the x- and y-directions and $\dot{\varepsilon}_{xy}$ is the shear strain-rate of squares aligned with the x- and y-axes (see Figure 3.2). The total strain-rate is taken as the Frobenius norm of the strain-rate tensor, defined as the square root of the sum of squares of all its components:

$$|\dot{\boldsymbol{\varepsilon}}| = \sqrt{\dot{\varepsilon}_x^2 + \dot{\varepsilon}_{xy}^2 + \dot{\varepsilon}_{yx}^2 + \dot{\varepsilon}_{yy}^2} \tag{3.8}$$

The magnitude of drift ice strain-rate is typically $10^{-6}\,\mathrm{s}^{-1}$, ranging from $10^{-5}\,\mathrm{s}^{-1}$ in active marginal ice zone (MIZ) dynamics (Leppäranta and Hibler, 1987) to $10^{-7}\,\mathrm{s}^{-1}$ in the Central Arctic (Bushuev *et al.*, 1967; Hibler *et al.*, 1973). Note that $10^{-6}\,\mathrm{s}^{-1} = 0.36\%\,\mathrm{h}^{-1} = 8.64\%\,d^{-1}$.

Strain-rates of $10^{-7} - 10^{-5}\,\mathrm{s}^{-1}$ correspond to a timescale of 1–100 days. For $\dot{\varepsilon}_{xx} =$ constant, the line length becomes $L = L_0 \exp(\dot{\varepsilon}_x t)$, and thus the inverse normal strain-rates $|\dot{\varepsilon}_{xx}|^{-1}$ and $|\dot{\varepsilon}_{yy}|^{-1}$ are equal to the e-folding times of the corresponding line lengths. For $\dot{\varepsilon}_{xy} =$ constant, the angles of a square aligned with x- and y-axes change by $\arctan(\dot{\varepsilon}_{xy} t)$, and thus $|\dot{\varepsilon}_{xy}|^{-1}$ equals the time when they have changed by 45º. Positive shear strain means closing the right angle, while negative shear strain means opening it (see Figure 3.2).

Example For a numerical illustration, take the strain-rate magnitude as $10^{-6}\,\mathrm{s}^{-1}$. The deformation timescale is 10 days. Then $\dot{\varepsilon}_{xx} = 10^{-6}\,\mathrm{s}^{-1}$ means that a 10-km line opens in the x-direction by 0.902 km in the first day and $\dot{\varepsilon}_{xy} = 10^{-6}\,\mathrm{s}^{-1}$ (e.g., $\partial u/\partial y = \partial v/\partial x = 10^{-6}\,\mathrm{s}^{-1}$) means that a right angle in x- and y-axis orientations closes by $10^{-1}\,\mathrm{s}^{-1} \approx 5^\circ\,\mathrm{day}^{-1}$.

In a two-dimensional flow, vorticity has only one independent component:

$$\left.\begin{aligned} \dot{\omega}_{xx} &= \dot{\omega}_{yy} = 0 \\ \dot{\omega}_{yx} &= \frac{1}{2}\left(\frac{\partial v}{\partial x} - \frac{\partial u}{\partial y}\right) = -\dot{\omega}_{xy} \end{aligned}\right\} \tag{3.9}$$

The component $\dot{\omega}_{yx}$, denoted usually by $\dot{\omega}$, is the vorticity about the vertical axis (positive anticlockwise), and for a rigid field it is the same as the rigid body rotation rate. A typical magnitude of drift ice vorticity is $10^{-6}\,\mathrm{s}^{-1} = 0.2^\circ\,\mathrm{h}^{-1} = 5^\circ\,\mathrm{d}^{-1}$, which

corresponds to rigid rotation progressing as $\dot{\omega}t$. At time $\dot{\omega}^{-1}$ the rotation has progressed by 1 rad and at time $2\pi\dot{\omega}^{-1} \approx 63$ days one cycle has been completed.

The principal components or the eigenvalues of the strain-rate tensor and the corresponding eigenvectors, normalized to unit length and directions denoted by ϑ_1 and ϑ_2 are:

$$\dot{\varepsilon}_{1,2} = \tfrac{1}{2}\, tr\dot{\boldsymbol{\varepsilon}} \pm \sqrt{(\tfrac{1}{2} tr\dot{\boldsymbol{\varepsilon}})^2 - \det \dot{\boldsymbol{\varepsilon}}} \tag{3.10a}$$

$$\vartheta_1 = \arctan\left(\frac{\dot{\varepsilon}_1 - \dot{\varepsilon}_{xx}}{\dot{\varepsilon}_{xy}}\right), \quad \vartheta_2 = \frac{\pi}{2} + \vartheta_1 \tag{3.10b}$$

where the eigenvalues are chosen so that $\dot{\varepsilon}_1 \geq \dot{\varepsilon}_2$. In the principal axes coordinate system the normal strain-rates are $\dot{\varepsilon}_1$ and $\dot{\varepsilon}_2$, and the shear strain-rate is zero. If $\dot{\varepsilon}_{xy} = 0$, then $\dot{\varepsilon}_{xx}$ and $\dot{\varepsilon}_{yy}$ are the principal values and the x- and y-axes are the principal axes. The particular case $\dot{\varepsilon}_{xx} = \dot{\varepsilon}_{yy}$ and $\dot{\varepsilon}_{xy} = 0$ is spherical deformation. Then the eigenvalues are $\dot{\varepsilon}_1 = \dot{\varepsilon}_2 = \dot{\varepsilon}_{xx}$ and the orientations of the principal axes are arbitrary.

In analyzing strain-rate, the following invariants are often used in drift ice kinematics:

$$\dot{\varepsilon}_{\mathrm{I}} = \dot{\varepsilon}_1 + \dot{\varepsilon}_2 = \operatorname{tr} \dot{\boldsymbol{\varepsilon}} = \dot{\varepsilon}_{xx} + \dot{\varepsilon}_{yy} \tag{3.11a}$$

$$\dot{\varepsilon}_{\mathrm{II}} = \dot{\varepsilon}_1 - \dot{\varepsilon}_2 = \sqrt{(\operatorname{tr} \dot{\boldsymbol{\varepsilon}})^2 - 4 \det \dot{\boldsymbol{\varepsilon}}} = \sqrt{(\dot{\varepsilon}_{xx} - \dot{\varepsilon}_{yy})^2 + 4\dot{\varepsilon}_{xy}^2} \tag{3.11b}$$

The first invariant equals the velocity divergence ($\operatorname{tr} \dot{\varepsilon} = \nabla \cdot \boldsymbol{u}$), while the second invariant is twice the maximum rate of shear. Note that shear deformation on a square depends on the orientation. For a square aligned with the principal axes, there is no shear, and for a square oriented 45º off from the principal axes, shear is at extremum, $\pm\dot{\varepsilon}_{\mathrm{II}}/2$. The Frobenius norm of the strain-rate tensor can be expressed as:

$$|\dot{\boldsymbol{\varepsilon}}| = \sqrt{\dot{\varepsilon}_{11}^2 + \dot{\varepsilon}_{12}^2 + \dot{\varepsilon}_{21}^2 + \dot{\varepsilon}_{22}^2} = \sqrt{(\dot{\varepsilon}_{\mathrm{I}}^2 + \dot{\varepsilon}_{\mathrm{II}}^2/2)} \tag{3.12}$$

The mode of deformation can be thought of as a vector $(\dot{\varepsilon}_{\mathrm{I}}, \dot{\varepsilon}_{\mathrm{II}})/\sqrt{2}$ in the upper half-space (Thorndike *et al.*, 1975)[2]. The proportions of normal and shear deformation are specified by the vector direction φ

$$\tan\varphi = \frac{\dot{\varepsilon}_{\mathrm{II}}}{\dot{\varepsilon}_{\mathrm{I}}}, \quad 0 \leq \varphi \leq \pi \tag{3.13}$$

The angles $\varphi = 0$, $\varphi = \pi/2$ and $\varphi = \pi$ correspond to pure divergence, pure shear and pure convergence, respectively. Also note that the length of the vector provides the magnitude of the total strain-rate (see Eq. 3.12).

[2] The factor $2^{1/2}$ was not included in Thorndike *et al.* (1975) but it is preferable for consistency. It has no effect on the vector direction.

Another useful representation of the strain-rate is its decomposition into the spherical and deviatoric parts $\dot{\boldsymbol{\varepsilon}}_s$ and $\dot{\boldsymbol{\varepsilon}}'$, respectively:

$$\dot{\boldsymbol{\varepsilon}} = \dot{\boldsymbol{\varepsilon}}_s + \dot{\boldsymbol{\varepsilon}}', \quad \dot{\boldsymbol{\varepsilon}}_s = (\tfrac{1}{2}\,\mathrm{tr}\,\dot{\boldsymbol{\varepsilon}})\boldsymbol{I} = (\tfrac{1}{2}\nabla \cdot \boldsymbol{u})\boldsymbol{I} \tag{3.14}$$

The spherical part includes pure compression/dilatation, and the deviatoric part includes pure shear deformation.

There are five specific simple deformation cases:

(i) Spherical strain: $\dot{\boldsymbol{\varepsilon}} = \dot{\boldsymbol{\varepsilon}}_s$.
(ii) Pure shear or, in general, incompressible medium: $\dot{\boldsymbol{\varepsilon}}' = \dot{\boldsymbol{\varepsilon}}$, $\dot{\varepsilon}'_{\mathrm{I}} = 0$
(iii) Uniaxial tension (compression): $\dot{\varepsilon}_{xx} > 0 (\dot{\varepsilon}_{xx} < 0)$, $\dot{\varepsilon}_{xy} = \dot{\varepsilon}_{yx} = \dot{\varepsilon}_{yy} = 0$.
(iv) Uniaxial shear: $\dot{\varepsilon}_{xy} = \dot{\varepsilon}_{yx} = \dfrac{1}{2}\dfrac{\partial u}{\partial y}$, $\dot{\varepsilon}_{xx} = \dot{\varepsilon}_{yy} = 0$.
(v) Zonal flow: $\dfrac{\partial}{\partial y} \equiv 0$; that is $\dot{\varepsilon}_{xx} = \dfrac{\partial u}{\partial x}$, $\dot{\varepsilon}_{xy} = \dfrac{1}{2}\dfrac{\partial v}{\partial x}$, $\dot{\varepsilon}_{yy} = 0$.

Sometimes it is useful to work with curvilinear coordinate systems, in particular with spherical coordinates on the Earth's surface ($r = \text{constant} = r_e$). The strain-rate tensor is then

$$\left.\begin{aligned} \dot{\varepsilon}_{zz} &= \frac{1}{r_e}\frac{\partial uz}{\partial Z}, \quad \dot{\varepsilon}_{\lambda\lambda} = \frac{1}{r_e \sin Z}\frac{\partial u_\lambda}{\partial \lambda} + u_Z \frac{\cot Z}{r_e} \\ \dot{\varepsilon}_{Z\lambda} &= \frac{1}{2}\left(\frac{1}{r_e \sin Z}\frac{\partial u_Z}{\partial \lambda} - u_\lambda \frac{\cot Z}{r_e} + \frac{1}{r_e}\frac{\partial u_\lambda}{\partial Z}\right) \end{aligned}\right\} \tag{3.15a}$$

where Z is zenith angle and λ is longitude. In flows with zonal invariance the derivatives $\partial/\partial\lambda$ are neglected. The curvature effects are then represented by the terms with $\cot Z$. In polar coordinates, the strain-rate is written:

$$\left.\begin{aligned} \dot{\varepsilon}_{rr} &= \frac{\partial u_r}{\partial r}, \quad \dot{\varepsilon}_{\varphi\varphi} = \frac{1}{r}\left(\frac{\partial u_\varphi}{\partial \varphi} + u_r\right) \\ \dot{\varepsilon}_{r\varphi} &= \frac{1}{2r}\left(\frac{\partial u_r}{\partial \varphi} - u_\varphi + r\frac{\partial u_\varphi}{\partial r}\right) \end{aligned}\right\} \tag{3.15b}$$

The deformation of drift ice is particularly asymmetric: leads open and close, pressure ice forms but does not "unform". In pure shear $\dot{\varepsilon}_1 = 0$ and $\dot{\varepsilon}_1 = -\dot{\varepsilon}_2$. This results in opening along the first principal axis and closing along the second principal axis, equal in magnitude. If compactness is initially 1, the rate of opening will be $\dot{\varepsilon}_1$ and the rate of pressure ice production will be $-h\dot{\varepsilon}_2$, even though the total divergence is zero. Therefore, it is necessary to construct a function to describe opening and ridging in a given deformation event. This is made using the angular description (Eq. 3.13) of the mode of strain: open water formation and ridging are given by, respectively, functions $\chi_0(\varphi)$ and $\chi_d(\varphi)$, be specified, times the Frobenius norm of the strain-rate.

Example: estimation of the strain-rate and vorticity from drifter data (Thorndike and Colony, 1980; Leppäranta, 1981b) Drifters[3] are usually irregularly scattered in the study region. Assuming continuum ice flow, the Taylor formula can be used for the velocity field:

$$\boldsymbol{u}(x,y) = \boldsymbol{u}(0,0) + x\left.\frac{\partial \boldsymbol{u}}{\partial x}\right|_{0,0} + y\left.\frac{\partial \boldsymbol{u}}{\partial y}\right|_{0,0} + \boldsymbol{R}$$

where $\boldsymbol{R}$ is a residual of the second order (i.e., for nth order function f, $f(x)/(\delta x)^{n-1} \to 0$ as $\delta x \to 0$). With at least three drifters, we can use linear regression and the above formula to obtain the first-order derivatives of the velocity. With more than three drifters, an estimate of the goodness of fit is obtained for the linear strain field. In a similar fashion, the three second-order derivatives can be added to the Taylor formula. To estimate all, three more drifters are needed.

3.2 OBSERVATIONS

3.2.1 Methods

Drift ice kinematics has been mapped in three different ways. A drifter tracks the trajectory of the floe on which it has been deployed, and imaging airborne or space-borne remote-sensing methods provide displacement fields from sequential mapping. A more recent development is acoustic remote sensing from fixed moorings beneath the ice. The drifter method is Lagrangian, while the acoustic method is Eulerian[4]; the imaging method can be either way.

The drifter method dates back to the drift of *Fram* in the Arctic Basin (Nansen, 1902), followed by *Jermak* and *Maud* in the Arctic and *Deutschland* in the Antarctic. The Soviet North Pole station programme commenced in 1937, with annual stations drifting from the North Pole to the Greenland Sea. In the 1950s and 1960s much research was carried out on Ice Island T-3, also known as Fletcher's Ice Island, drifting in the Beaufort Sea (e.g., Hunkins, 1967). Since the 1970s, automatic tracking methods have been available. *Argos* buoys (Figure 3.3) have produced an extensive data set of the ice kinematics in the Arctic Basin, with a positioning accuracy of 500 m (Thorndike and Colony, 1982). The temporal resolution of the traditional drifter method was at best one to five cycles per day, but spatial information was quite limited. In the Baltic Sea, the Decca Navigator system, a former routine positioning system for ships, was used for ice drift station observations (Leppäranta, 1981b; Leppäranta and Omstedt, 1990).

In the 1960s the mapping of differential ice velocity was commenced in 10–100 km neighbourhood of ice camps. The first field experiment on sea ice deformation was

[3] Sea ice kinematics is traditionally mapped using drifters, buoys or research stations anchored into the ice.
[4] In the Lagrangian approach the paths of physical ice floes are monitored, while in the Eulerian approach instantaneous velocities are observed at fixed points in space. This terminology comes from the Lagrangian and Eulerian formulations in fluid dynamics (e.g., Li and Lam, 1964).

Figure 3.3 Deployment of an *Argos* buoy in Ymer-80 expedition, July 1980, north of Svalbard. *Argos* buoys have provided the fundamental knowledge of the sea ice drift climatology in the polar oceans.

made in 1961 in the Central Arctic by monitoring a square with sides 75–100 km (Bushuyev *et al.*, 1967). In closing up to scales less than 10 km, a high accuracy is required. The methods used include theodolites (Legen'kov, 1977), laser geodimeters (Hibler *et al.*, 1974b; Leppäranta, 1981b), and microwave transponder systems (Leppäranta and Hibler, 1987). Presently the GPS (Global Positioning System) is a natural way to monitor the ice kinematics. The accuracy is excellent, down to metres, and the limiting factor is just the spatial coverage or how many drifters can be deployed in practice. Leppäranta *et al.* (2001) used GPS in a coastal sea ice dynamics experiment, where buoy monitoring and data transmission was taken care of by the local mobile phone network.

The principal properties of a drifter system are the positioning accuracy (δx) and the measurement time interval (δt). From the practical point of view the cost of a single drifter and the realization logistics must also be considered. Taking the positioning error as white noise with variance σ^2, the velocity error in first-order differentiation becomes blue noise[5] with the variance spectrum:

$$\sigma_u^2(\lambda) = \frac{\sigma^2[1 - cos(\lambda\delta t)]}{\pi}, \quad 0 \leq \lambda\delta t \leq \pi \tag{3.16}$$

[5] In white noise the spectral density is constant, while in blue (red) noise there is more variance at higher (lower) frequencies.

where λ is given in radians per time unit δt. The temporal resolution of a drifter system may be taken as the frequency where the measured variance is twice the noise level. To measure the deformation requires more accuracy. Strain-rates are spatial velocity derivatives and estimation adds error from several drifters. Spatial derivative estimated from two drifters at distance L apart has the variance of $2\sigma_u^2/L^2$. The accuracy is improved when several drifters can be used.

Example The *Argos* system is simple to use and the observation system is reliable, but the disadvantages are the cost of drifters, low accuracy (500 m), low data transmission rate (a few hours time interval), and as a consequence a low temporal resolution. Let us take $\delta t = 3\,\text{h}$ and let the variance of the position error be $s^2 = (250\,\text{m})^2$ (accuracy is represented as $2s$). Estimating the ice velocity by first-order differentiation of the drifter positions, the total variance of velocity error is then $2s^2/\delta t^2 \approx 10.7\ (\text{cm/s})^2$ and the Nyquist frequency is $(6\,\text{h})^{-1}$. The standard error of velocity is $0.157\,\text{cm}\,\text{s}^{-1}$ at the frequency of 1 cycle per day, but at the Nyquist frequency, this error is $1.64\ \text{cm}\,\text{s}^{-1}$. For strain-rates in a scale of 100 km and over 1-day time intervals, the standard deviation of error would be $2.2 \times 10^{-6}\,\text{s}^{-1}$, which is too much since the magnitude of deformation rate is typically $10^{-6}\,\text{s}^{-1}$. Thus length scale or time scale of the study must be enlarged.

Sea ice velocity can be extracted from *sequential remote-sensing imagery* by identifying ice floes and then determining the distance travelled (Figure 3.4). This was first done manually using optical imagery (e.g., Gorbunov and Timokhov, 1968; Hibler *et al.*, 1975; Muench and Ahlnäs, 1976). Imaging radars are very good at ice velocity mapping because of their high resolution and weather independence. In particular, along with data obtained by synthetic aperture radar (SAR) satellites, automatic algorithms have been developed based on cross-correlation or feature tracking (Fily and Rothrock, 1987; Vesecky *et al.*, 1988; Kwok *et al.*, 1990; Sun, 1996). Ice kinematics products have been among the most useful sea ice products from SAR satellites.

More recently, algorithms have been developed to extract sea ice motion from satellite passive microwave data using the cross-correlation method (Agnew *et al.*, 1997; Kwok *et al.*, 1998; Liu and Cavalieri, 1998; Kwok, 2001). This approach has the great advantage of the availability of daily data from the *Nimbus-7* scanning multichannel microwave radiometer (SMMR) and DMSP special sensor microwave imager (SSM/I) ever since 1978 for both polar regions (`htpp://nsidc.org/`). Therefore, the results are excellent for climatological investigations.

The drifter method provides temporally dense Lagrangian velocity time series for a limited number of floes, and the satellite or airborne imaging method produces spatially dense Lagrangian displacement fields between consecutive overflights, which are infrequent. Neither is preferable; rather, they are complementary. A high space-time resolution can be provided by fixed remote-imaging stations. A system of three coastal X-band radar stations (Figure 3.5) was used in Hokkaido, Japan from 1969–2005, allowing continuous mapping of the ice cover along a 250-km

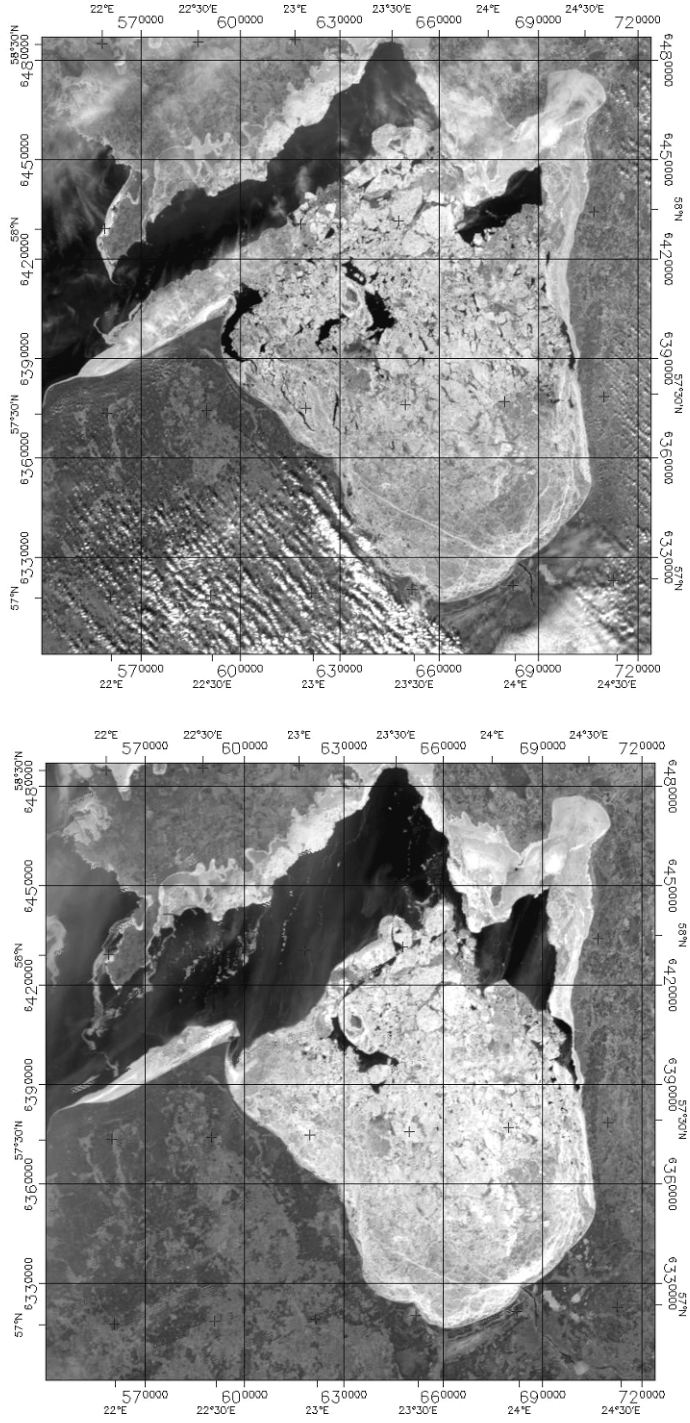
22°E
22°30'E
23°E
23°30'E
24°E
24°30'E
57 0000
60 0000
63 0000
66 0000
69 0000
72 0000
58°30'N
58°N
57°30'N
57°N
648 0000
645 0000
642 0000
639 0000
636 0000
633 0000

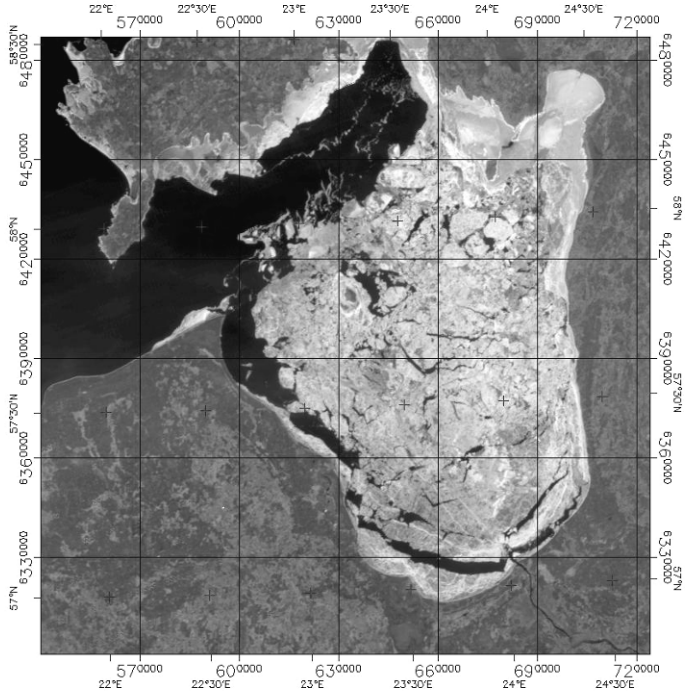

Figure 3.4 Sea ice displacement in the Gulf of Riga, Baltic Sea, seen in consecutive optical moderate resolution imaging spectroradiometer (MODIS) images of NASA's Terra satellite. The size of the basin is 120 km across; note an island at 57°50′N 23°15′E. Dates: March 17, 21 and 28, 2003.

section of coastline out to 60 km from the shore (Tabata, 1972). The system was replaced in 2005 by HF radar system for mapping coastal currents in the open water season and the presence of ice in the ice season (Shirasawa *et al.*, 2010). Figure 3.6 gives an example of sea ice distribution reflecting properties of the kinematics field. As the ice moves along the coast, sometimes eddies can be traced in the coastal current.

Acoustic Doppler Current Profilers (ADCP) are normally used for water velocity measurements. They are based on the acoustic backscatter of suspended particles in natural waters. The ice bottom serves as a good backscatterer, and therefore the method can also be used beneath the ice cover. It has been shown to work in shallow seas (less than 200 m deep) for the ice velocity in the Gulf of St Lawrence (Belliveau *et al.*, 1990). The advantages are the safety of the velocity measurement arrays, a good temporal resolution, and truly Eulerian data series. A major ice–ocean dynamics experiment was performed in winter 2002–2003 offshore Sakhalin based on moorings and ADCP measurements (Fukamachi *et al.*, 2009). Simultaneous data were collected of ice draft, and time-series of ice drift, thickness and transport were obtained.

Figure 3.5 Mombetsu X-band ice radar antenna on top of Mt Oyama (300 m) monitoring the sea ice of the Sea of Okhotsk.

3.2.2 Characteristics of observed sea ice drift

Drift ice speed is of the order of 1–100 cm s^{-1}. Figure 3.7 shows the long-term paths of several drifting stations in the Arctic Ocean. They follow the general sea ice circulation. The Transpolar Drift Stream takes ice from the Siberian Shelf across the Eurasian side and through the Fram Strait into the Greenland Sea, while in the American side ice rotates in the Beaufort Sea Gyre. These two flows meet in

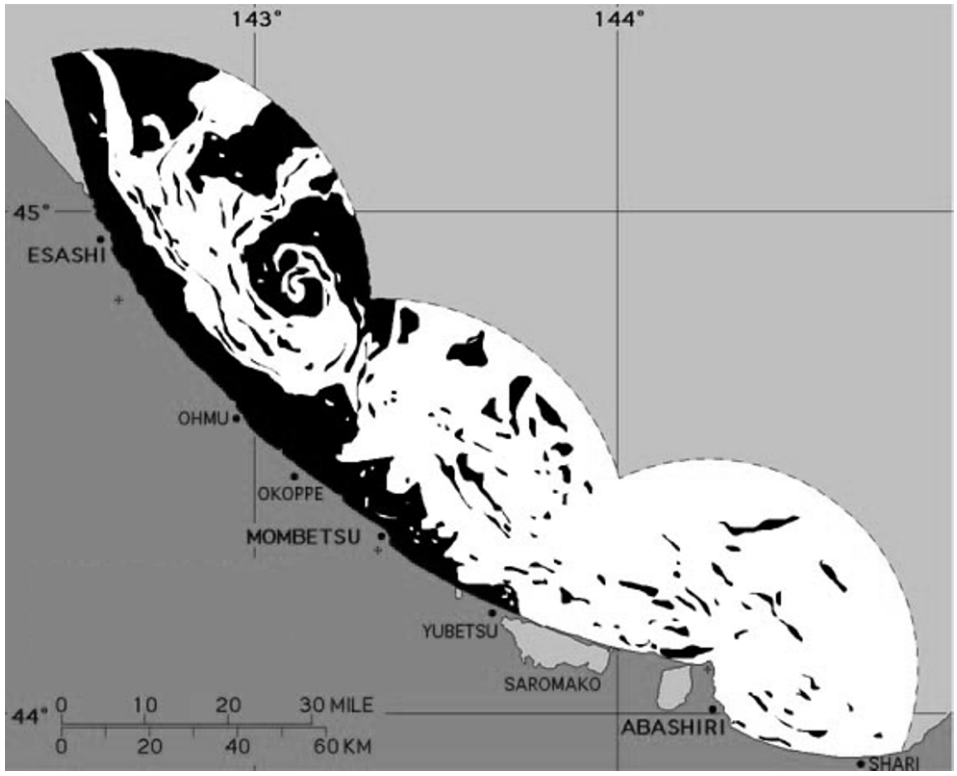

Figure 3.6 Sea ice distribution (ice is white) along the northern coast of Hokkaido on 3 February 2003. The chart is based on three coastal radars mapping the ice up to 60 km from the coastline.

Reproduced with permission from the Sea Ice Research Laboratory, Institute of Low-temperature Science, Hokkaido University.

the central parts of the Arctic Basin where mixing of ice floes between the two ice streams may take place. Average velocities are 1–5 cm s^{-1}, with the higher levels reached when approaching the Fram Strait. The drift pattern follows the ice–ocean linear response to the average atmospheric pressure field over the Arctic Ocean. The time scale of drift pattern is 2–4 years, for the passage from the Siberian shelf to the Greenland Sea or for a circle in the Beaufort Sea gyre. Thus, oldest sea ice is met in the Beaufort Sea, that has done more than one round in the gyre. Undeformed multi-year ice loses a $\frac{1}{2}$-m layer from its surface every summer and grows from its bottom the same amount in the following winter, and all ice is therefore at most about 10 years old in a multi-year ice sheet. Ice older than that may be found in multi-year ridges.

In the Antarctic, the governing features are the westward flow zone close to the continent and eastward drift zone farther out, driven by easterly and westerly winds (Figure 3.8). In places there are meridional movements, which interchange ice floes between the two zones. In particular, the Antarctic Peninsula forces the westward flow

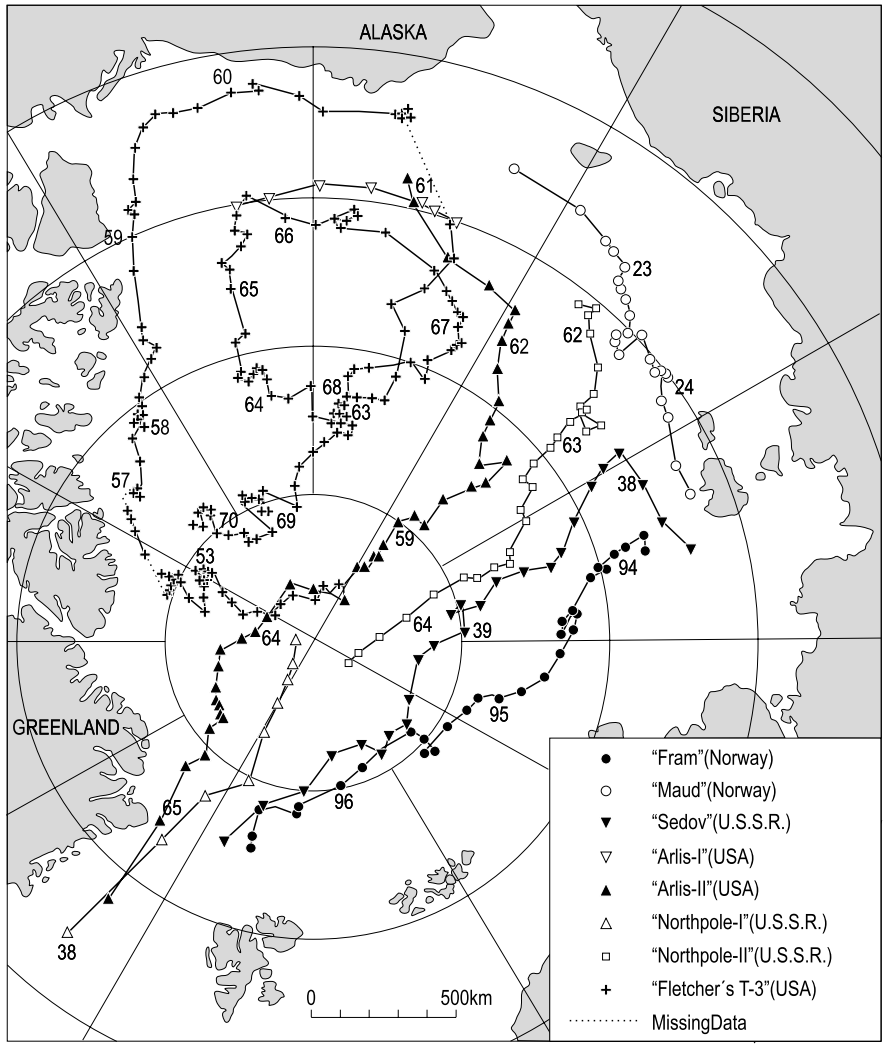

Figure 3.7 Paths of drifting stations in the Arctic Ocean. The numbers show the year (1897–1970) and marks between are at monthly intervals.
Redrawn from Hibler (1980b).

toward the north in the Weddell Sea. In the west wind drift the ice velocity is 10 cm s^{-1}, which sums to 1500 km or along latitude circle 60°S to angular distance of 27°.

Figure 3.9 shows a 1-week time series of hourly sea ice velocity in the Baltic Sea together with wind data. As the ocean current is weak there, the ice followed the wind with essentially no time lag. On average the drift velocity was 2.5% of the wind speed and the direction of ice drift was 20° to the right of the wind direction. However, the ice velocity experienced some remarkable changes, which cannot be

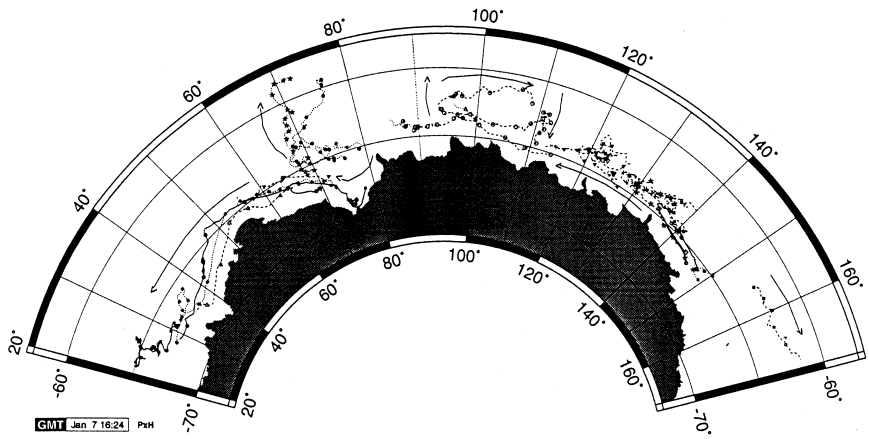

Figure 3.8 Sea ice buoy drifts in the Indian Ocean–eastern Pacific Ocean sector of the Southern Ocean: 1985 (short dashed lines with solid symbols), 1987 (solid line with solid symbols), 1992/93 (solid line with open symbols), 1995/96 (dotted lines) and 1996 (dashed lines). The symbols are plotted at 10-day intervals; arrows show the net drift.
Reproduced from Worby et al. (1998), with permission from the American Geophysical Union.

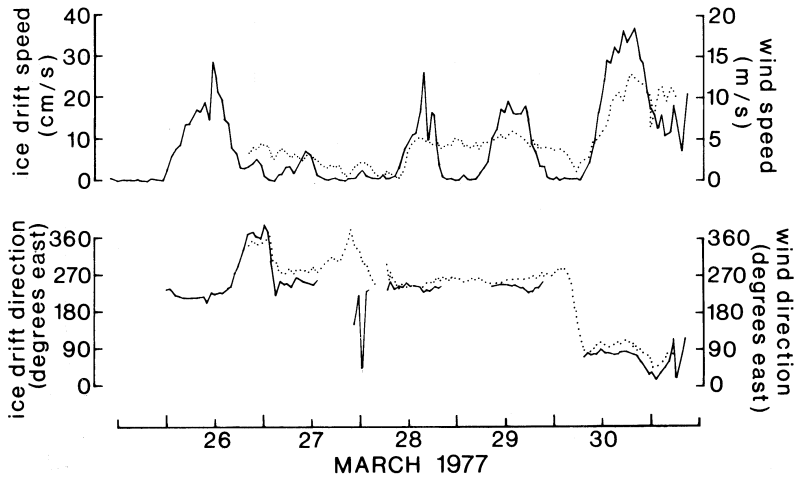

Figure 3.9 Sea ice (solid lines) and wind velocity (dotted lines) time series, Baltic Sea, March 1977.
From Leppäranta (1981a).

explained by a linear wind drift rule: occasionally, the ice nearly stopped during a moderate wind. This behaviour is typical of drifting sea ice: in general there is a good connection with the wind field and ocean currents, but sometimes the ice takes "unexpected" steps, which are due to its internal friction.

In special cases, very high ice velocities (more than $1\ \mathrm{m\ s^{-1}}$) have been observed. Zubov (1945) reported ice velocities up to 2.5 knots as a 1-day average in the

Chukchi Sea; at the time there was wind and a 1-knot current driving the ice. Kuznetsov and Mironov (1986) reported rapid ice movements in transient currents, forced by surface pressure gradients in straits and along the coastline. An extreme and rare case is the *ice river* phenomenon: in coastal regions a narrow ($\approx \frac{1}{2}$ km) band of close pack ice flows at a very high speed, up to $3\,\mathrm{m\,s^{-1}}$, much higher than the surrounding ice field. Kuznetsov and Mironov (1986) described three ice river cases from 1967 to 1977 from the Arctic coast of Russia, based on ship reports. They were sudden and brief; two of them took place during a strong southerly wind.

The *frequency spectra* of ice velocity reach the highest levels on synoptic timescales, and a secondary peak appears at the inertial period (Figure 3.10). In the Arctic Ocean the variance level is lower and the inertial signal weaker in winter than in summer. Apart from the inertial peak, the spectral density falls fast for frequencies higher than 1 cycle per day. The reported spectra of sea ice motion go up to around 5 cycles per day. To obtain very high frequencies the positioning accuracy would need to be of the order of metres.

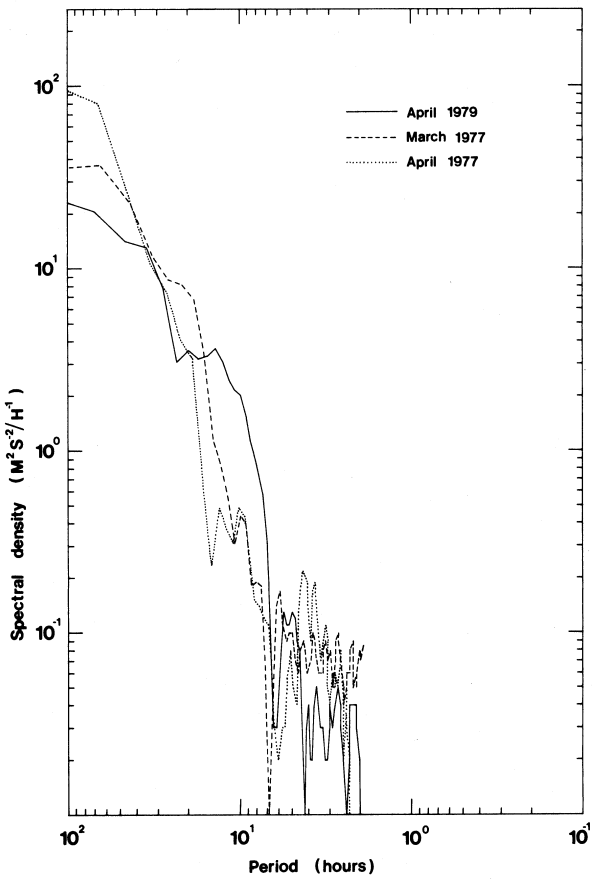

(a)

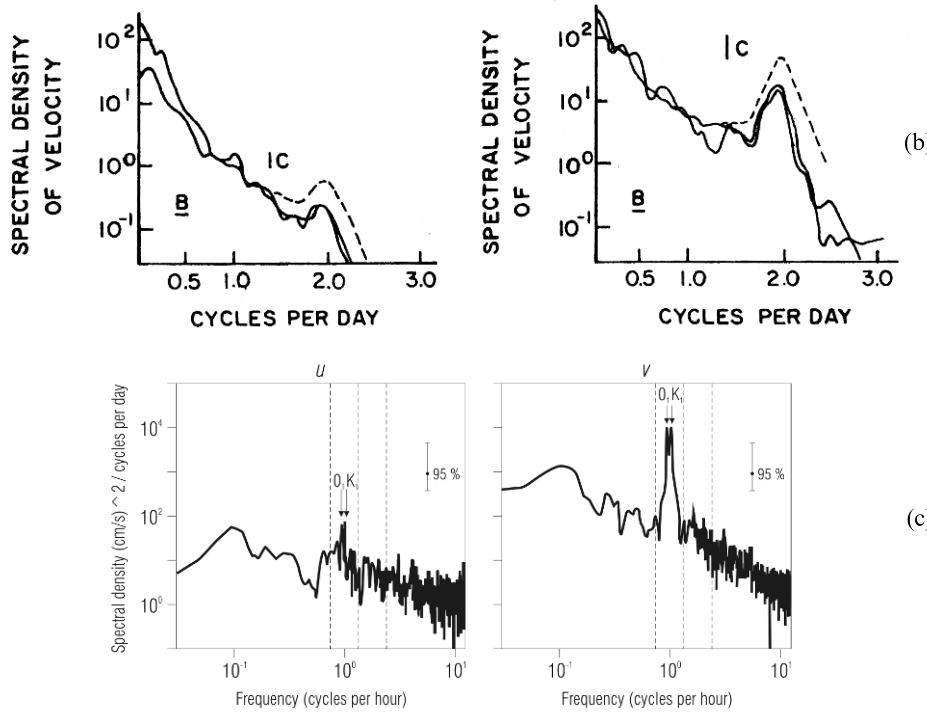

Figure 3.10 Drift ice velocity spectra: (a) Baltic Sea, (b) Arctic Ocean (left: winter; right: summer), and (c) Sea of Okhotsk (left: east component; right: north component). (a) and (b) are Lagrangian and (c) is Eulerian.

(a) From Leppäranta (1981b); (b) Reproduced from Thorndike and Colony, with permission of University of Washington Press; (c) Redrawn from Shevchenko et al. (2004).

An excellent illustration of the ice motion in the Arctic Ocean, tracked by drift buoys, is provided on the website of the International Arctic Buoy Programme (IABP) (`http://IABP.apl.washington.edu/Animations/`). Animations of high-frequency coastal ice motion in the Sea of Okhotsk are available at the Hokkaido University web page (`http://www.hokudai.ac.jp/lowtemp/sirl/sirl-e.html`).

The magnitude of the *rotation rate of ice floes* is usually $10^{-6}\,\mathrm{s}^{-1} = 0.2^\circ\,\mathrm{h}^{-1} = 5^\circ\,\mathrm{d}^{-1}$. According to observations, typically in the Arctic Ocean central pack, $\dot{\omega} \sim 10^{-7}\,\mathrm{s}^{-1}$, $d \sim 10\,\mathrm{km}$ and therefore $\dot{\omega}d \sim 10^{-3}\,\mathrm{m\,s}^{-1}$. In the MIZ, $\dot{\omega} \sim 10^{-5}\,\mathrm{s}^{-1}$ and $d \sim 100\,\mathrm{m}$, and again $\dot{\omega}d \sim 10^{-3}\,\mathrm{m\,s}^{-1}$. Sverdrup (1928) reported a floe rotation rate $2 \times 10^{-6}\,\mathrm{s}^{-1}$ in the Eurasian basin. The results of Legen'kov *et al.* (1974) from the Soviet North Pole station NP-19 showed that the rotation rates of several floes were almost all time less than $10^{-6}\,\mathrm{s}^{-1}$, ice compactness was 0.85–1.00, the floes rotated rather as groups, and the rate increased with decreasing compactness. Leppäranta (1981b) reported a 1.5-km floe in the Baltic Sea rotating at rates below $3 \times 10^{-6}\,\mathrm{s}^{-1}$, ice compactness was about 0.9, and floe rotation correlated well with

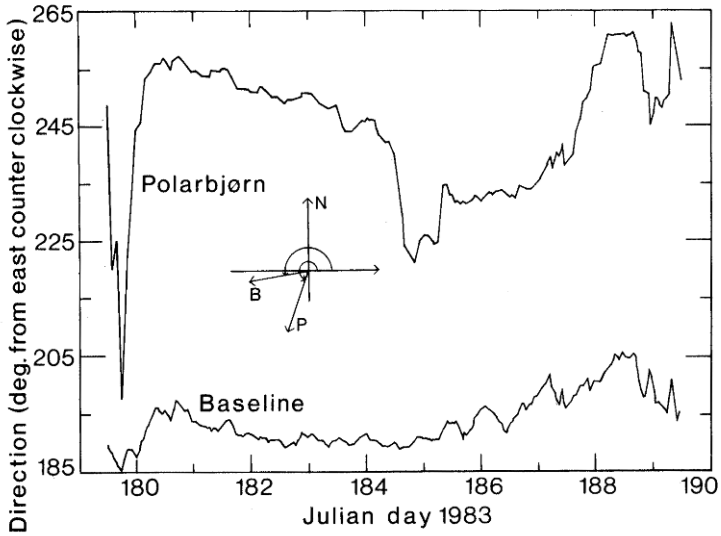

Figure 3.11 Orientation of a drifter array (5 km) baseline and R/V *Polarbjørn* moored to an ice floe in the centre of the array (MIZEX'83 in the Greenland Sea). The large bump for the data of R/V *Polarbjørn* in days 184–185 is non-natural, caused by a necessary correction of the ship's mooring.
From Leppäranta and Hibler (1987).

the local vorticity. Figure 3.11 shows the rotation of a floe together with a 5-km array in the Greenland Sea MIZ. The rates fell within the range 1–10° day^{-1} and correlated well (ice compactness was 0.8–0.9 and floe size was 50–100 m).

Occasionally, floe rotation may be fast. Gorbunov and Timokhov (1968) studied the rotation of floes in the Chukchi Sea. Compactness was rather small, less than 0.8, and floe size was mostly less than 200 m. Their rotation showed very high values: the typical range was ±30° per hour, but on occasion went as high as 100° per hour. Smaller floes had higher rotation rates. The interaction between ice floes had a positive effect on rotation since the rate tended to be higher in close drift ice than in open drift ice. Also floes usually rotated in groups rather than as individuals. During the Marginal Ice Zone Experiment (MIZEX-84) in the Greenland Sea, rotation rates higher than 100° per day were noted by the author when the pack was opening. The very high rotation rates may be caused by ocean eddies or the morphology of the ice floes.

A very particular case is the finding of a new island from ice drift observations. Soviet oceanographer V. Yu. Vize examined the drift of the ship *Svyataya Anna* trapped in drift ice in the Kara Sea and noted an unexpected change in the path. He deduced the presence of an unknown island. Vize was able to estimate quite well the location of the island, confirmed by its actual discovery by Otto Schmidt's expedition in 1930. The island was named Vize Island, located between Franz Josef Land and Severnya Zemlya in the northern Kara Sea.

3.2.3 Strain-rate and vorticity

The 100-km scale

Continuum deformation observation campaigns commenced in the 1960s, along with serious work on sea ice rheology that necessitated knowledge of strain and strain-rate. Bushuyev *et al.* (1967) observed the motion of seven points, four of which formed a rectangle with sides 75–100 km in the central Arctic Ocean. In 22 days, the total translation of the square was about 90 km, while the normal strains along the sides were within 3% in 22 days (i.e., the mean strain-rate was $10^{-8}\,s^{-1}$, or 0.1% day^{-1}). They also measured rotation on an approximately daily basis, and the magnitude was below $10^{-7}\,s^{-1}$ with two general rotation schemes[6]: the Beaufort Sea Gyre ice rotated more or less as a rigid disc; and in the Transpolar Drift Stream there was a maximum speed in the centre and rotation was connected with shear on both sides of the centre.

Long-term sea ice deformation was measured during the main Arctic Ice Dynamics Joint Experiment (AIDJEX) in 1975 (Thorndike and Colony, 1980; Thorndike, 1986) (Table 3.1). The magnitude of strain-rate and rotation was $10^{-7}\,s^{-1}$; the level increased by 50–100% in summer. In winter the divergence was on average 0.07% day^{-1}, which means a total opening of 7% over 100 days, while its standard deviation was 1% day^{-1}. Shear measure (second invariant) is positive and therefore its average is much more than that of divergence, but note that the standard deviations are close. The mean rotation was anticlockwise in winter (as in the Beaufort Sea Gyre) and summed to 30° over 100 days.

The 10-km scale

Hibler *et al.* (1973) monitored mesoscale sea ice deformation in the Beaufort Sea manually, using tellurometers[7] in a 10-km triangle. Short-term (≈ 6 h) deformation events were observed with strain-rate invariants of $10^{-7}\,s^{-1}$, but over intervals of one day or more the level was one order of magnitude less. They also reported good correlation between the strain ellipse and fracturing of the ice. In the next phase a

Table 3.1 Strain-rate and vorticity in AIDJEX 1975 manned array in % per day $\approx 10^{-7}\,s^{-1}$: length scale is 200 km (Thorndike, 1986) – no data provided in the reference.

	Divergence		Maximum shear		Vorticity	
	Mean	St.dev	Mean	St.dev	Mean	St.dev
Winter	0.07	1.0	1.6	1.6	−0.52	2.0
Summer	−0.03	1.6	3.5	2.2	–	–

[6] See Figure 3.17 for a general idea of these rotation fields.
[7] A tellurometer is a geodetic distance meter based on the phase modulation of transmitted radio waves.

laser geodimeter was used for more accurate time series data (e.g., Hibler *et al.*, 1974b). In the shear zone the level of strain-rates was three to five times as much as in the central pack (Hibler *et al.*, 1974a). Therefore, as found by Bushuyev et al. (1967), the Beaufort Sea Ice Gyre is mostly a cohesive wheel with intensive deformation at the boundary of landfast ice. The width of this shear zone was shown to be 50 km.

Legen'kov (1977) analyzed measurements of the Soviet NP-19 drifting station in the Arctic Basin, collected from an ice island using a theodolite and a fixed baseline. The size of the study area was about 5 km. His strain-rates were also $10^{-7}\,s^{-1}$. The temporal stability of the sign of strain-rates was almost always below 24 hours, averaging to about six hours. Therefore, in wind-driven ice dynamics, deformation events are much shorter than the velocity time scale, which is at the synoptic level. The spatial correlation length was also short; although not quantified this was estimated as less than the whole study region for 3-hour strain events. It was also shown that deformation activity increased with decreasing compactness (range of compactness was 0.85–1.0).

In the MIZ the strain-rate level is much larger than in the central pack. Data from the MIZEX-83 experiment in the Greenland Sea, June 1983, showed that the level is as much as $10^{-5}\,s^{-1}$ (5% h^{-1}) in short intensive periods and normally one order of magnitude less (Figure 3.12). For 1% h^{-1} strain-rate, the e-folding time is 100 hours for ice compactness and shear strain on right angle is 45° in 100 hours. However, the deformation was of a back-and-forth nature, and the total change of

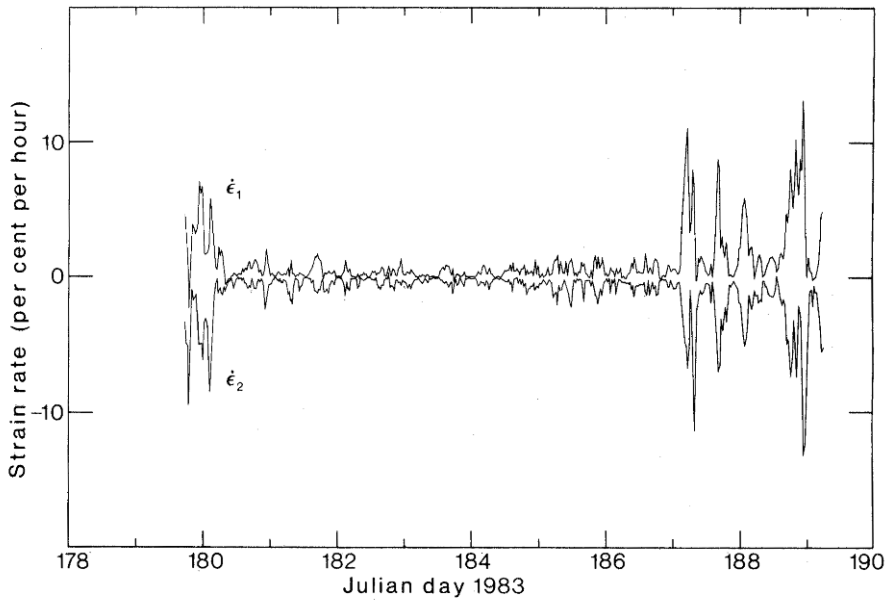

Figure 3.12 Principal strain-rates during the MIZEX'83 experiment. The size of the measurement region was 5 km.
From Leppäranta and Hibler (1987).

the drifter array remained small during the 10-day period of the experiment. In a study by Leppäranta (1981b) in the Baltic Sea, the magnitude of deformation rates was $10^{-6}\,s^{-1}$ and major deformation events lasted 5–10 hours. The statistics over a one-week period for a 5-km array were the following (unit $10^{-6}\,s^{-1}$): $\dot{\varepsilon}_1 = 0.44 \pm 0.66$, $\dot{\varepsilon}_2 = -0.50 \pm 0.55$, with a maximum magnitude of 3; the vorticity was 0.79 ± 0.77 with a maximum of 3.4. Strain-rate of $10^{-6}\,s^{-1}$ gives a total strain of 1% in $10^4\,s \approx 3\,h$, and therefore the ice state undergoes relatively fast changes.

In all reported time series the principal components have mostly opposite signs and are of the same magnitude, which means that their sum (opening/closing of the ice pack) is small and their difference (twice the maximum rate of shear) is large.

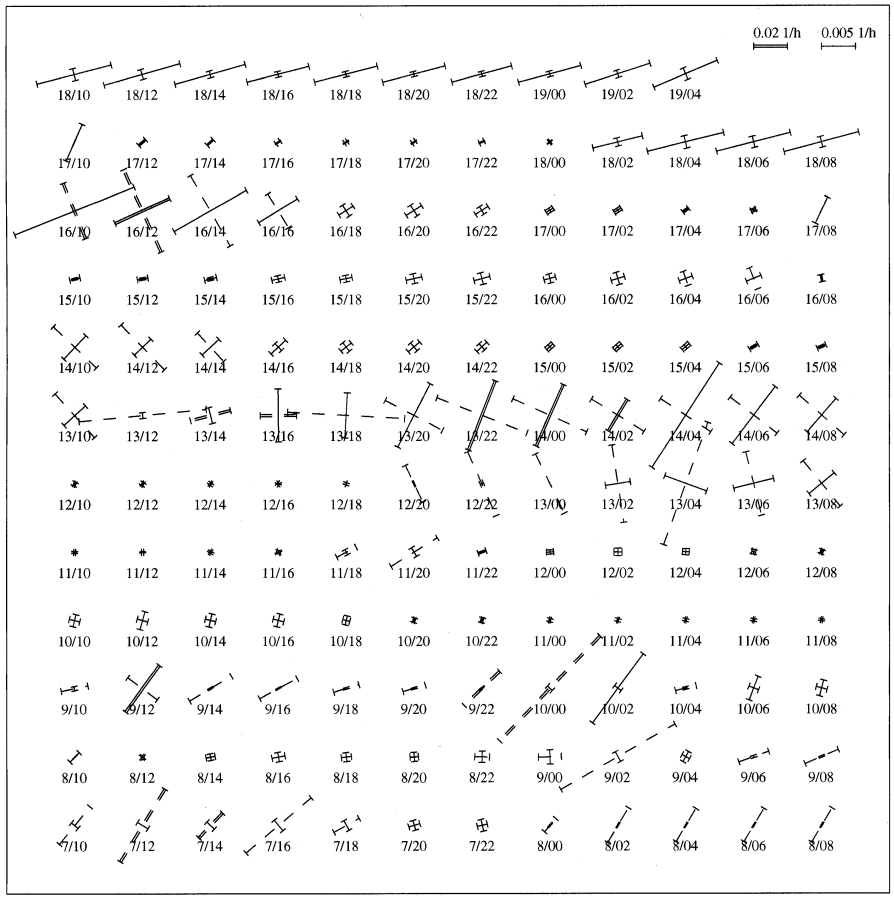

Notation 10/15 means 10 March 1997, 15:00 UTC

Figure 3.13 Time series of the 2-hourly, principal strain-rates in the coastal drift ice zone, Bay of Bothnia, in March 1997. The coastline is aligned vertically, and the notation 10/14 means 10 March at 14:00 hrs.

From Leppäranta et al. (2001).

In winter 1997 a special coastal boundary zone experiment was performed in the Baltic Sea (Leppäranta *et al.*, 2001; Goldstein *et al.*, 2001). Sea ice dynamics was examined using GPS drifters in a 10-km size array. Compared with central basins (Leppäranta, 1981b), the strain had more uniaxiality and was more stepwise (Figure 3.13). The deformation signal was seen to travel at $\sim 5\,\mathrm{m\,s^{-1}}$ across the array, and the time response indicated separate local- and basin-wide (100-km size) responses.

Another case from the northern Baltic Sea is shown in Figure 3.14, based on *Landsat* images. Ice velocities were obtained manually by identifying shifts in a number of ice floes, and these were then averaged into an 18.5-km grid. The resulting deformation field showed an overall level of 5% $\mathrm{day^{-1}}$ for both divergence and maximum shear (the length scale of the deformation field was some 50 km).

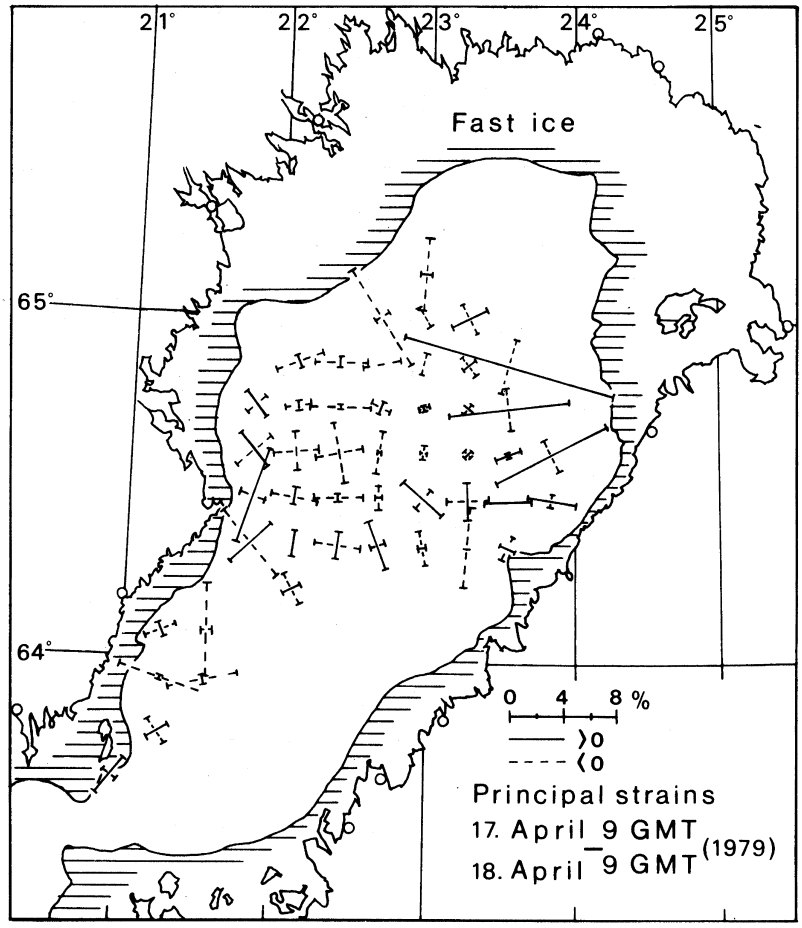

Figure 3.14 Principal axis strain field from consecutive *Landsat* images in the Baltic Sea. Satellite passes were 1 day apart. Solid (dashed) lines show tensile (compressive) strain. From Leppäranta (1982).

With sequential remote imaging of the ice pack, it is possible to determine spatial deformation fields. A coastal radar network has been utilized for research in sea ice kinematics in the Sea of Okhotsk since 1969 (Tabata, 1972). The system tracks deformed sea ice floes such as ridges, and consecutive radar images can be utilized to obtain sea ice kinematics information. Tabata (1971) and Tabata *et al.* (1980) followed several quadrangles in the coastal ice drift. The spatial scale of the deformation was about 20 km, and the magnitude of hourly strain and rotation was 1–5% or $10^{-5}\,s^{-1}$. The radar system was, however, closed down in 2005.

3.2.4 Deformation structures

As a result of mechanical deformation, ordered structures appear in sea ice cover. Figure 3.15 shows banding of drift ice as seen from the hills of the northern coast of Hokkaido. Deformation structures are identifiable in airborne and spaceborne remote-sensing imagery and can be used to observe kinematic events and to interpret their effect on the mechanical behaviour of the ice. For example, Erlingsson (1988) examined fracture geometry and the mesoscale plastic properties of drift ice.

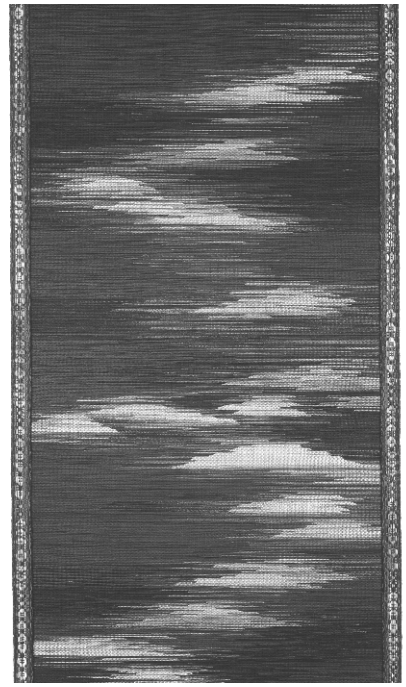

Figure 3.15 Drift ice bands in the Sea of Okhotsk shown in Yukara-ori weaving handicraft. This style was started by Ms Aya Kiuchi in the early 1960s; thereafter, she developed it with her son Kazuhiro.

Reproduced with permission from Yukara-ori Kougeikan [Yukara Weaving Museum], Asahikawa, Hokkaido.

Goldstein *et al.* (2000) examined Baltic Sea imagery and identified (a) a parallel system of faults under unidirectional tension, (b) a concentric system of radial faults, (c) coupled compression–tension structures, (d) broom-like shear structures, and (e) vortexes (Figure 3.16). Point (c) refers to ridge-lead structures, which is a typical and important deformation process, illustrating how in pure shear simultaneous lead opening and pressure ice formation occurs. The typicality is reflected in the opposite signs of the principal axes of strain shown in the previous sub-section. The classification was later refined for ice flow at the boundary of landfast ice as shown in Figure 3.16 (Goldstein *et al.*, 2009).

Cracks and leads in a sea ice cover are easily recognizable in remote-sensing imagery. Classification of cracks, and their formation and structure were deeply

Action type	**Boundary condition**	**Type of the structure**	**Structure scale (km²)**	**Region of probable occurrence**
1. Uniform uniaxial tension caused by wind	Free boundaries	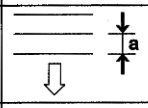 System of parallel faults a ~ const.	~10^4	Central Bay regions
	Displacement restrictions at the region boundary	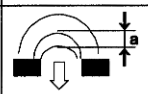 Arc-shaped faults a ~ const.	~10^3	Shore regions, islands of North part of the Bay
2. Bi-axial tension caused by wind	Free boundaries	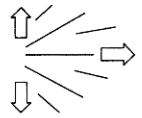 Concentric system of radial faults	~10^4	Region adjusting the central part of the Bay
3. Uniform compression caused by wind	Displacement restrictions in the compression direction	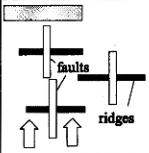 System of conjugated structures of compression-tension ridges (rafts) faults	~10^4	Region near the West Bank of the Bay
4. Local compression under motion of large mass or ice push on an obstacle	Displacement restrictions in the compression direction	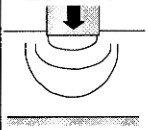 Arc-shaped structures of ridges	~10^2	The North region of the Bay
5. Local shear caused by wind	Displacement restrictions at the fast ice boundary	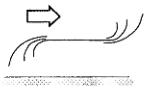 Shear with feathering "Broom" type structure	~10^3	East and North-East regions of the Bay
6. Tracing of flows		 Rotational stuctures of faults and ridging regions related to the structure of underice flows	~10^4	East and North regions of the Bay

Figure 3.16 Sea ice structures in the Bay of Bothnia, Baltic Sea, based on remote-sensing imagery. From Goldstein *et al.* (2000; 2009).

examined by Volkov *et al.* (2002). Lead formation structures in the Arctic were analyzed by Hibler (2001) for anisotropy of lead pattern and for development of an anisotropic sea ice model.

3.3 STOCHASTIC MODELLING

3.3.1 Two-dimensional motion using complex variables

Let us now carry out time series analyses of two-dimensional vectors using complex variables. We denote them like scalars, as in mathematics; they possess real and imaginary components oriented along the x- and y-axes, respectively (e.g., Ahlfors, 1966). Ice velocity is then expressed as $u = u_1 + \mathrm{i}u_2$, where $\mathrm{i} = \sqrt{-1}$ is the imaginary unit, and $u_1 = \mathrm{Re}u$ and $u_2 = \mathrm{Im}u$ are the real and imaginary components, which correspond to x- and y- components of two-dimensional vectors. For a complex variable u, the magnitude, or *modulus*, is $\sqrt{u\bar{u}} = \sqrt{u_1^2 + u_2^2}$, where $\bar{u} = u_1 - \mathrm{i}u_2$ is the complex conjugate of u. The direction, or *argument* (anticlockwise angle from the x-axis), of u is denoted as $\arg u$. The following elementary properties are very useful. For complex variables u and q and a real variable φ, we have:

(i) $|uq| = |u||q|$
(ii) $\arg(uq) = \arg u + \arg q$
(iii) $\exp(\mathrm{i}\varphi) = \cos\varphi + \mathrm{i}\sin\varphi$ (Euler's formula)

Example The covariance between two complex random variables u and q is given by $\mathrm{Cov}(u, q) = \langle (u - \langle u \rangle)\overline{(q - \langle q \rangle)} \rangle$ where the operator $\langle - \rangle$ stands for averaging, and their correlation coefficient is:

$$r = \frac{\mathrm{Cov}(u, q)}{\sqrt{\mathrm{Cov}(u, u)\,\mathrm{Cov}(q, q)}}$$

The modulus $|r|$ gives the total correlation between u and q, and the argument $\arg r$ gives the angle from u to q at which the quantities are correlated. Since the directions of ice drift, wind, and ocean current are different, it is convenient to study their correlations in complex form. In this way, the correlation coefficient provides both total and directional correlation.

A simple stochastic sea ice drift model is written:

$$\frac{du}{dt} = -\lambda u + F \tag{3.17}$$

where λ is the "memory" of the system, and F is an independent external forcing function. The spectrum of the velocity is then:

$$p(\omega) = \frac{p_F(\omega)}{|\lambda + \mathrm{i}\omega|^2} \tag{3.18}$$

For $|\omega| \ll |\lambda|$ ice velocity follows the forcing as $u = \lambda^{-1}F$ and its spectrum as $p(\omega) = \lambda^{-2}p_F(\omega)$, and for $|\omega| \gg |\lambda|$ the ice velocity spectrum is ω^{-2} times the forcing spectrum. The spectrum has a local maximum at $\omega = -\mathrm{Im}\,\lambda$, which is a singularity if $\mathrm{Re}\,\lambda = 0$. Wind and geostrophic ocean current can be taken as independent forcing functions, but oceanic boundary layer (OBL) dynamics is strongly coupled with the ice drift. Therefore Eq. (3.18) represents also the spectrum of ice–OBL system (with different λ). We shall return to the model coupled in Chapter 6.

3.3.2 Mean sea ice drift field in the Arctic Ocean

If we consider sea ice velocity as a random field, observations such as drifter data can be used to determine the field structure. This leads to interpolation of data into the mean ice velocity field. The first mean field was presented by Gordienko (1958) based on the drift of ships and manned stations. It was revised by Colony and Thorndike (1984) with large amounts of drift buoy data added and using optimum linear interpolation (Figure 3.17). More detailed structure of the Transpolar Drift Stream, the Beaufort Sea Gyre, and outflow through the Fram Strait then became evident.

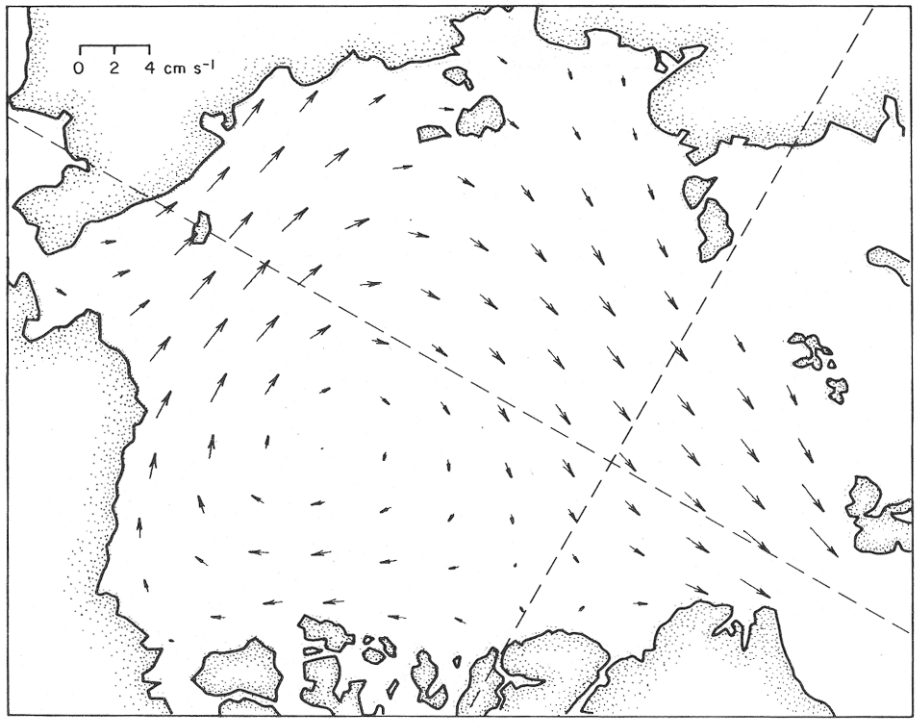

Figure 3.17 Annual mean of sea ice velocity in the Arctic Ocean.
Reproduced from Colony and Thorndike (1984), with permission of the American Geophysical Union.

According to Colony and Thorndike (1984), daily velocities average about $2\,\mathrm{km\,d^{-1}}$, with a standard deviation of $7\,\mathrm{km\,d^{-1}}$, and the integral timescale (time integral of the correlation coefficient) is 5 days. They also demonstrated that displacement variance increases with time, following a 1.4 power law. Inter-annual variations appear in annual mean fields as reflections of the variations in atmospheric pressure over the Arctic Ocean.

Thorndike (1986) examined spatial correlation structures in the large-scale longitudinal and transverse components of ice velocity, a view often taken in turbulence studies. Correlation lengths (the distance after which correlation has vanished) became 2,000 km for the longitudinal component and 800 km for the transverse component, close to the situation in the geostrophic wind field. This reflects that the ice drift follows atmospheric forcing in the large scale. The variance level over distances above the correlation length is $\sim 100\ (\mathrm{cm/s})^2$.

3.3.3 Diffusion

One way of examining the spatial variability of velocity is by looking at it from the diffusion viewpoint:

$$\frac{\partial \Theta}{\partial t} = K\nabla^2\Theta \tag{3.19}$$

where K is the diffusion coefficient and Θ is the quantity of concern. For tracer spots in the ocean, the diffusion coefficient depends on the length scale L as $K \propto L^{4/3}$ (Okubo and Ozmidov, 1970). Okubo and Ozmidov also showed that there are two separate regimes with a transition zone at 1–10 km; $K \sim 1\,\mathrm{m^2\,s^{-1}}$ and $K \sim 10\,\mathrm{m^2\,s^{-1}}$ at the length scale of 1 km and 10 km, respectively. In pure homogeneous diffusion the standard deviation of displacement (s) increases as $s = 2(Kt)^{1/2}$ (e.g., with $K = 10\,\mathrm{m^2\,s^{-1}} \approx 1\,\mathrm{km^2\,d^{-1}}$ and $t = 1$ d, we have $s = 2$ km, with $K = 1\,\mathrm{m^2\,s^{-1}}$ and $t = 1$ d, we have $s = 0.6$ km).

Gorbunov and Timokhov (1968) made a case study in the Chukchi Sea based on aerial photography. They estimated the diffusion coefficient from displacements Δl of ice floes over fixed time intervals Δt as $K = \langle \Delta l^2 \rangle / \Delta t$: for $A < 0.8$, the result was $K \approx 8.41 \times 10^{-4} L^{5/8}\,\mathrm{m^{11/8}\,s^{-1}}$. Compared with oceanic tracer spots, the magnitude was close at $L = 1$ km, illustrating that ice floes become well mixed when their compactness is lower than 0.8; however, length-scale dependence was weaker. Gorbunov and Timokhov (1968) further showed that the diffusion coefficient increased with decreasing compactness and decreasing floe size. Legen'kov *et al.* (1974) studied a 5-km area in which variation in ice velocity was within about $1\,\mathrm{cm\,s^{-1}}$ from the mean, with high sensitivity for ice compactness, which is in good agreement with Gorbunov and Timokhov (1968).

Diffusion models can be used to describe the spread and mixing of ice floes, but they have severe limitations. In the ice field itself there are no self-diffusive mechanisms, but the cause lies in atmospheric and oceanic forcing. Ice floes have a more or less random component in their motion due to their individual properties,

but these components are not always diffusive. Forcing may also collect floes together (i.e., cause "negative diffusion").

3.3.4 Random walk

A Markov chain model is written in general form as:

$$P(m; t + \Delta t) = \sum_{n} P(m \mid n; t) \tag{3.20}$$

where $P(m)$ is the probability that a particle is in cell m and $P(m \mid n)$ is the probability that a particle moves from cell n to cell m in one time step. In a two-dimensional random walk a particle is allowed to move only to one of the neighbouring cells in one time step (e.g., Feller, 1968). Dividing sea surface into N cells, transition probabilities can be obtained either from direct observations or using a Monte Carlo method[8] to define a Markov chain.

The random walk model was applied by Colony and Thorndike (1985) for drift ice. They divided the Arctic Basin into 111 cells, with sizes ranging within some hundreds of kilometres. Although the authors did not explain why the cells were fixed as they were, in practice a good choice must be based on data availability and resolution of interest. *Argos* buoy data were used for mean sea ice motion as a deterministic background and for displacement variance. The latter was estimated as $2.5 \times 10^4\,\mathrm{km}^2$ over 90-day time steps. The purpose of the study by Colony and Thorndike (1985) was to examine long-term statistical problems. They concluded that the model works well for questions such as the probability distributions for the path of pollutant transport by ice from a given source, ice renewal times in different basins, and statistical variability of ice conditions in a given climate. Figure 3.18 shows the resulting mean lifetime of an ice floe as a function of its location of birth.

3.3.5 Self-correcting simple forecasting

For a specific site, such as an oil platform or a lighthouse, ice conditions can be predicted on a length scale of the order of the size of grid cells with full basin numerical drift ice models. These models are continuum models, and therefore grid cells are usually much larger than the size of platforms and lighthouses. To predict the ice load at these structures, there are two approaches.

Firstly, a downscaling sub-model can be constructed for the ice stress produced in the continuum model grid. Then probability forecasts can be prepared for local peak loads. However, good data are not available to establish reliable relationships for the downscaling (see Section 4.5). Secondly, when ice compactness is low enough,

[8] The Monte Carlo method estimates ensemble properties by means of large-number simulations generated by random numbers (e.g., Korvin, 1992). Here they can be used for transition probabilities in a given space-time grid.

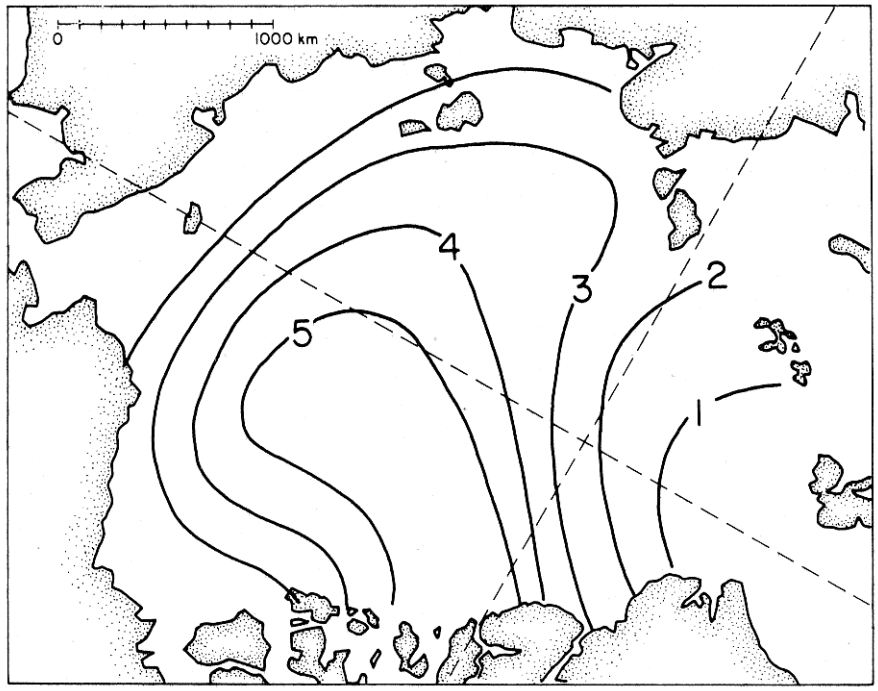

Figure 3.18 The mean lifetime (years) of an ice floe in the Arctic Basin based on a random walk model.
Reproduced from Colony and Thorndike (1985), with permission from the American Geophysical Union.

ice floes drift with their individual velocities, and a self-correcting forecasting system can be constructed. Then the simple stochastic model (3.17) can be applied. Its solution is

$$u(t) = u(0)\,\mathrm{e}^{-\lambda t} + \int_0^t \mathrm{e}^{-\lambda(t-t')}[cU_a(t') + \lambda U_w] \tag{3.21}$$

It is clear that the forcing consists of wind U_a and ocean current U_w; c is a floe-specific coefficient, as will be shown in Chapter 6, and current velocity is multiplied by λ since the drag from ice motion is taken as $-\lambda(u - U_w)$, see Eq. (3.17). Normally wind velocity is available at a local weather station and the velocity of the ice floe can be monitored from the platform. Thus the history of ice and wind velocity is usually known, and the remaining unknowns are λ, c and U_w.

For a fixed ice floe, we can consider λ and c to be constant. With an observation time series for u and U_a at times $t_1, t_2, \ldots, t_n$, we can solve the parameters λ, c and U_w from the integrated expression:

$$u(t_n) = u(0)\,\mathrm{e}^{-\lambda t_n} + \mathrm{e}^{-\lambda t_n} \sum_{k=0}^{n-1} (\mathrm{e}^{\lambda t_{k+1}} - \mathrm{e}^{-\lambda t_k})[\lambda^{-1} cU_a(t_k) + U_w(t_k)] \tag{3.22}$$

For the estimation problem to be solvable, the number of parameters cannot be larger than the number of equations. Therefore additional assumptions are needed to start: e.g., we can prescribe the current velocity for the first two steps based on *a priori* information, such as $U_w = 0$. Eq. (3.22) tells that velocity of ice is a weighted average of the initial velocity and the forcing history with weights decreasing exponentially toward past.

If the current velocity is assumed to vary slowly, getting new data points will lead to improving accuracy of the estimates of λ, c. When U_w can be assumed constant, a series of estimates with increasing accuracy (proportional to $\sqrt{n(t)}$) is obtained for λ, c and U_w. The optimized parameters at time t_n and wind forecast can be used to obtain the prediction of ice velocity at time t_{n+1}; at t_{n+1} parameter estimated can be updated for better accuracy, etc. This method allows prediction of whether a fixed ice floe will collide with a platform, based on the data that can be easily collected at site.

Example. Take $U_w \equiv 0$ and $t_n - t_{n-1} = \Delta t = \text{constant}$. We have after two time steps

$$u(\Delta t) = u(0)\,\mathrm{e}^{-\lambda\Delta t} + c\lambda(1 - \mathrm{e}^{-\lambda\Delta t})U_a(0)$$
$$u(2\Delta t) = u(0)\,\mathrm{e}^{-2\lambda\Delta t} + c\lambda(1 - \mathrm{e}^{-\lambda\Delta t})[\mathrm{e}^{-\lambda\Delta t}U_a(0) + U_a(\Delta t)]$$

These two equations can be used to estimate c and λ. It is easy to see from these equations that the weights of the initial velocity and wind-forced terms sum to one.

3.4 CONSERVATION OF ICE

Ice conditions in a given region, Ω, are modified by thermal and mechanical processes. The ice volume as well as ice-state variables in this region must obey conservation laws. For any property of the ice field (say, Θ) the conservation law is in general form:

$$\frac{\partial \Theta}{\partial t} + \boldsymbol{u} \cdot \nabla\Theta = \psi_\Theta + \phi_\Theta \tag{3.23}$$

where left-hand-side terms are the local rate of change and advection, and on the right-hand side ψ_Θ represents mechanical deformation and ϕ_Θ stands for thermodynamic changes. The left-hand side can be expressed briefly as $\mathrm{D}\Theta/\mathrm{D}t$, where $\mathrm{D}/\mathrm{D}t = \partial/\partial t + \boldsymbol{u} \cdot \nabla$ is the material or total time derivative operator, the rate of change in a particle following the motion. Here the properties of concern are the ice state components (i.e., basically the thicknesses of different ice categories or the thickness distribution of ice).

Mechanical deformation occurs as opening and closing of leads, rafting, hummocking, ridging, etc (Figure 3.19). Equation (3.23) includes two dynamical timescales: one for advection, $T_\Theta \sim L_\Theta/U$, and one for deformation, $|\dot{\varepsilon}|^{-1} \sim L_U/U$, where L_Θ and L_U are the length scales of the property Θ and velocity, respectively. Since $L_U \sim 100\,\mathrm{km}$ and $U \sim 10\,\mathrm{cm\,s^{-1}}$, the deformation timescale is typically 10 days, ranging from 1 to 100 days. We may also take $L_U \sim L_\Theta$ and the advection timescale

Figure 3.19 Mechanical deformation processes in drift ice.

would be the same. Ice growth/melting is obtained from the heat balance. It contains also a time scale via ice growth and melt rates being of the order of 1 cm day^{-1} – apart from thin ice the thermodynamic time scale of sea ice is thus quite long.

The conservation of ice mass $m = \rho\tilde{h}$ is a necessary condition for any ice state. Since $\rho = \text{constant}$, this is equivalent to the conservation of mean ice thickness, which may change due to the divergence of ice motion, and freezing or melting. Consequently:

$$\frac{\partial \tilde{h}}{\partial t} + \boldsymbol{u} \cdot \nabla \tilde{h} = -\tilde{h} \nabla \cdot \boldsymbol{u} + \Phi(\tilde{h}) \tag{3.24}$$

where Φ is the growth rate of ice. Apart from the thermodynamic term, the conservation law of mean thickness is derived as the mass conservation law in shallow water models. These models give an equation for sea level that exactly matches Eq. (3.24), with $\Phi = 0$ (e.g., Pond and Pickard, 1983). If $\tilde{h} = 0$, the mixed layer must be first cooled to freezing point for ice growth to start; if $\tilde{h} > 0$, it is assumed that the mixed layer is at freezing point.

The mechanical increase of ice thickness due to ridging is faster than the thermal increase. If $\tilde{h} > 1\,\text{m}$ and $\nabla \cdot \boldsymbol{u} \sim -10^{-6}\,\text{s}^{-1}$, the mechanical growth rate would be $\sim 10\,\text{cm}\,\text{day}^{-1}$. Mechanical growth events are very short, so that in the long run

thermal production of ice volume usually exceeds mechanical production. In regions of intensive ridging, such as off the northern coast of Greenland, the mean thickness of ice is more than twice the thermal equilibrium thickness of multi-year sea ice in the Arctic.

Thermal changes follow the heat conservation law

$$-\rho L \frac{dh}{dt} + \frac{d}{dt}(\rho c \tilde{T}) = Q_w + Q_n(h) \tag{3.25}$$

To a first approximation the left-hand side is governed by the latent heat term, and therefore external heat exchange provides directly ice thickness changes. In an area of variable ice thickness field, this equation does not hold for average thickness since ice sheet and atmospheric surface layer are thermally coupled during ice growth season. Thin ice grows much faster, in nonlinear manner, than thick ice, and the growth rate of mean thickness or ice volume depends on the thickness distribution. Thus for long-term investigations a multi-level ice state is preferable.

The ice conservation laws presented below deal with ice categories and ice thicknesses. A conservation law can be derived in a similar manner for floe size (Ovsienko, 1976). The advection and thermal growth of floes is straightforward, thermal growth being mainly due to lateral melting in summer. The break-up of floes as well as their merging together may be parameterized in terms of floe-size distribution parameters.

3.4.1 Ice states based on ice categories

The two-level ice state obeys the conservation law of ice thickness and compactness. The mean thickness law is as above (Eq. 3.24). For ice compactness, the conservation law can be derived similarly to that of thickness. The divergence of ice motion changes compactness mechanically, the one limitation being that compactness cannot be more than 1. The result can be expressed as:

$$\frac{\partial A}{\partial t} + \boldsymbol{u} \cdot \nabla A = |\dot{\varepsilon}| \chi_0(\varphi) + \Phi_A \quad (0 \leq A \leq 1) \tag{3.26}$$

where $\chi_0(\varphi)$ gives the opening of leads under different deformation modes φ, and Φ_A is thermodynamic change. For example, $\chi_0(0) = -1$ (pure divergence) and $\chi_0(\pi) = 1$ (pure convergence). When the mixed layer temperature is at freezing point, any heat loss would potentially freeze the surface over. Very thin ice is, however, insignificant in sea ice dynamics, and therefore a demarcation thickness h_0 is introduced to account only for ice thicker than that, $A = A(h_0)$ (see Eq. 2.48a). When the mixed layer temperature is at freezing point (as always when $A > 0$), it is assumed that, in the fractional area $1 - A$, ice thickness is uniformly distributed between zero and the demarcation thickness h_0. When $A < 1$, lateral melting of ice floes, Φ_H, may take place via absorption of solar radiation in leads and decrease the compactness (note that significant lateral growth does not take place, so $\Phi_H \leq 0$). Then:

$$\Phi_A = \frac{\Phi(h_0)}{h_0}(1 - A) + \Phi_H \tag{3.27}$$

When the mean ice thickness and compactness are known, the thickness of ice floes is obtained from $h_i = h/A$.

Example Take $h_0 = 10\,\text{cm}$ and assume that $\Phi(h_0) = 2\,\text{cm day}^{-1}$. For ice compactness $A(h_0) = 0.8$, we have $\Phi = 0.04\,\text{day}^{-1}$. It would take $h_0/\Phi(h_0) = 5$ days to reach full compaction $A(h_0) = 1$.

In multi-level cases different ice types and their volumes are included. The main question is then how the mechanical redistribution of ice is arranged in the case of compression of compact ice (i.e., how deformed ice is produced). Thin ice sheets (less than 10–20 cm) undergo rafting, and the consequence is local doubling of the ice thickness (Parmerter, 1975; Leppäranta, 1981a). By overriding, thicker ice breaks into blocks of size up to a few metres to form pressure ice: rubble fields, hummocks, and ridges.

The three-level case (A, h_u, h_i) has been used in the Baltic Sea (e.g., Leppäranta, 1981a; Haapala and Leppäranta, 1996), below the formulation is modified by inclusion of ridging and opening under shear. Ice compactness is treated in the same way as the two-level case. Undeformed ice thickness only changes by thermodynamics and advection, while also mechanical deformation may increase the thickness of deformed ice:

$$\frac{\partial h_u}{\partial t} + \boldsymbol{u}\nabla \cdot h_u = \Phi(h_u), \tag{3.28a}$$

$$\frac{\partial h_d}{\partial t} + \boldsymbol{u}\nabla \cdot h_d = -|\dot{\varepsilon}|\chi_d(\varphi, A)\tilde{h} + \Phi_d(h_d), \tag{3.28b}$$

where $\chi_d(\varphi)$ is the production of deformed ice as a function of the deformation mode, and Φ_d is the thermal growth rate of deformed ice. Deformed ice production depends on compactness since it occurs only in compact ice; for example, $\chi_d(\pi, 1) = -1$ (pure convergence of compact ice). The term $-|\dot{\varepsilon}|\chi_d(\varphi, A)\tilde{h}$, the gross term for the production of deformed ice, could be named the packing rate. Thermal changes in ice thickness are displayed as growth or melting at the upper and lower boundaries and in the interior (increase and decrease of brine pockets and voids between ice blocks). Therefore, the thickness of ice is understood as ice volume per unit area.

The mechanical deformation terms and Eqs. (3.26) and (3.28b) must be consistent with the conservation of total ice mass. In earlier approaches (Doronin, 1970; Hibler, 1979; Leppäranta, 1981a) lead opening and pressure ice formation in shear were ignored, meaning that changes due mechanical deformation in compactness and thickness of deformed ice were given, respectively, by $-A\nabla \cdot \boldsymbol{u}$ $(0 \le A \le 1)$ and $-h\nabla \cdot \boldsymbol{u}$ (if $A = 1$ and $\nabla \cdot \boldsymbol{u} < 0$).

Example With $h \sim 1\,\text{m}$ and a pure convergence of $-\nabla \cdot \boldsymbol{u} \sim U/L \sim 10^{-6}\,\text{s}^{-1}$ in compact ice, the packing rate is $\sim$0.36 cm/h. Such rapid packing events do not last long. In the Baltic Sea the thickness of ice that participates in ridging is 20–40 cm. Then for $\nabla \cdot \boldsymbol{u} \sim -10^{-6}\,\text{s}^{-1}$, the packing rate would be 1.7–3.5 cm per day. If there were one such deformation event every 10 days, the thickness of deformed ice would

grow to ~25 cm in one winter season, closely comparable with what has been actually observed (Lewis *et al.*, 1993). The magnitude 1.7–3.5 cm can also be compared with the mean equivalent thickness of 2.2 cm for one ridge per one kilometre in the Baltic Sea.

It is known that typically $h_d \sim h_u$ in mesoscale area averages (see Section 2.4). Thus, deformed ice is built up in short, intensive deformation events, while undeformed ice grows slowly but steadily through the whole cold season. An alternative formulation would be to replace $\tilde{h}$ by h_u in the mechanical deformation term of Eq. (3.28b), to allow only undeformed ice to build ridges. But then in the three-level model the mass conservation law (Eq. 3.24) would need to use $-h_u \nabla \cdot \boldsymbol{u}$ as well for the first term on the right-hand side.

The mass conservation law (Eq. 3.24) also allows us to examine vertical velocity. As the top and lower ice surfaces move farther from the sea surface with velocities w_t and w_b, respectively, we can ascertain the movement of a drift ice particle by:

$$w_t - w_b = -\tilde{h} \nabla \cdot \boldsymbol{u} + \Phi(\tilde{h}) \tag{3.29}$$

And if isostasy is assumed, $w_t/w_b = -(1 - \rho/\rho_w)$. The thermodynamic contribution to vertical motion is less than $5\,\mathrm{cm\,day^{-1}} \approx 5 \cdot 10^{-7}\,\mathrm{m\,s^{-1}}$. For $h \sim 1\,\mathrm{m}$ and $\nabla \cdot \boldsymbol{u} \sim 10^{-6}\,\mathrm{s^{-1}}$, we have $w_t - w_b \sim 10^{-6}\,\mathrm{m\,s^{-1}}$. All in all, the vertical motion of ice is weak and its integral is equivalent to changes in mean ice thickness (its details are not relevant here). Consequently, as stated at the beginning of this chapter, for the problem of sea ice drift it is sufficient to solve the horizontal velocity on the sea surface plane and the vertical dimension is taken care of by the mass conservation law.

3.4.2 Ice thickness distribution

The ice conservation law is obtained for thickness distribution in a similar fashion (recall Figure 2.20 for examples of thickness distributions). Freezing and melting advect the distribution in the thickness space, but additional assumptions are needed to specify how mechanics change the form of the thickness distribution. In general, thin ice is crushed and piled up into thicker, deformed ice. In discrete form the distribution is an N-category histogram$\{\pi_k, h_k, \Delta h_k\}$, and for any category a conservation law like that given in Eq. (3.23) is established. These categories interact as ice is transferred from one to another by mechanics and thermodynamics. Formally one may take the limit $\Delta h_k \to 0$ to obtain an almost continuous distribution, with delta peaks taking care of the singularities. This form of the conservation law is presented in Thorndike *et al.* (1975) and Rothrock (1986).

The way of working with the thickness distribution is not immediately clear. Therefore, the logic behind the derivation of the conservation law is shown below in detail for a simple two- to three-class distribution, and the generalization should then be clear. As such, the change in ice thickness distribution is easy to understand but technically complicated to formulate.

Derivation

The derivation of the conservation law is straightforward when using the thickness distribution function Π (see Eq. 2.37b) In general, consider a material (Lagrangian) element with spatial thickness distribution $S(h;t)$, in normalized form $\Pi(h;t) = S(h;t)/S_\infty$, $S_\infty = S(\infty;t)$. The change in Π due to mechanics is for a drift ice particle:

$$\frac{D\Pi}{Dt} = \frac{D}{Dt}\left[\frac{S(h;t)}{S(\infty;t)}\right] = \frac{1}{S_\infty}\frac{\partial S}{\partial t} - \frac{S}{S_\infty^2}\frac{dS_\infty}{dt} \tag{3.30}$$

This is the basic form in which the mechanical evolution of sea ice thickness distribution is normally presented. The reason is that this splits the evolution into rearrangement and net change parts. Indeed, the first term on the rightmost side of Eq. (3.30) states how the area coverages of different thickness categories change, defining *the thickness redistributor* as $\Psi = S_\infty^{-1}\partial S/\partial t$. The second term represents change of area of the particle, since $S_\infty^{-1}\, dS_\infty/dt = \nabla \cdot \boldsymbol{u}$ and $S/S_\infty = \Pi$. Thus we have:

$$\frac{D\Pi}{Dt} = \Psi - \Pi\nabla \cdot \boldsymbol{u} \tag{3.31}$$

In general the redistributor depends on the thickness distribution and strain-rate, $\Psi = \Psi(\pi, \dot{\varepsilon})$.

The thermodynamic change in thickness distribution also becomes clear from the distribution function Π. Since, clearly, by thermal growth $\Pi(h;t) = \Pi[h + \Phi(h)\delta t; t + \delta t]$ we have:

$$\Pi(h,t) = \Pi(h,t) + \frac{\partial \Pi}{\partial h}\,\Phi(h)\delta t + \frac{\partial \Pi}{\partial t}\,\delta t + O(\delta t^2) \tag{3.32}$$

Dividing by δt and letting $\delta t \to 0$, the change in the distribution function becomes $\partial\Pi/\partial t = -\Phi(h)\partial\Pi/\partial h$. This can be considered as advection of the spatial density by the growth rate $\Phi(h)$ in the thickness space.

Finally, by combining dynamics and thermodynamics together and taking the Eulerian frame, the conservation law of thickness distribution is (Thorndike *et al.*, 1975):

$$\frac{\partial \Pi}{\partial t} + \boldsymbol{u} \cdot \nabla\Pi = \Psi - \Pi\nabla \cdot \boldsymbol{u} - \Phi(h)\frac{\partial \Pi}{\partial h} \tag{3.33}$$

or, taking the derivative with respect to h, we have in terms of the spatial density of thickness:

$$\frac{\partial \pi}{\partial t} + \boldsymbol{u} \cdot \nabla\pi = \psi - \pi\nabla \cdot \boldsymbol{u} - \frac{\partial \Phi(h)\pi}{\partial h} \tag{3.34}$$

where $\Psi = d\Psi/dh$. The functions Π and π must satisfy the general conditions of spatial distribution and density (see Section 2.5), and the conservation law of ice volume or the mean ice thickness (Eq. 3.24). This means that for spatial density

$$\int_0^\infty \psi dh = \nabla \cdot \boldsymbol{u}, \quad \int_0^\infty h\psi dh = 0 \tag{3.35}$$

The first equation follows from the conservation of area, and the second states that mechanical rearrangement of thicknesses gives no net change.

Under the convergence of compact ice, the thinnest ice is broken and transformed into deformed ice. The thickness of the deformed ice may be spread into a certain range or simply transformed to a multiple of the original (say, from h to kh, $k > 1$). In purely mechanical processes there is a limitation that ice ridges have a maximum thickness of around 10–50 m depending on the thickness of the ice sheet used in building the ridge, but these thicknesses are very seldom reached.

In the following the formulation of mechanical deformation is examined from particular cases to a general case. A simple three-level case is used as an example. Ice thickness has three categories (Figure 3.20): open water ($h = 0$), undeformed ice

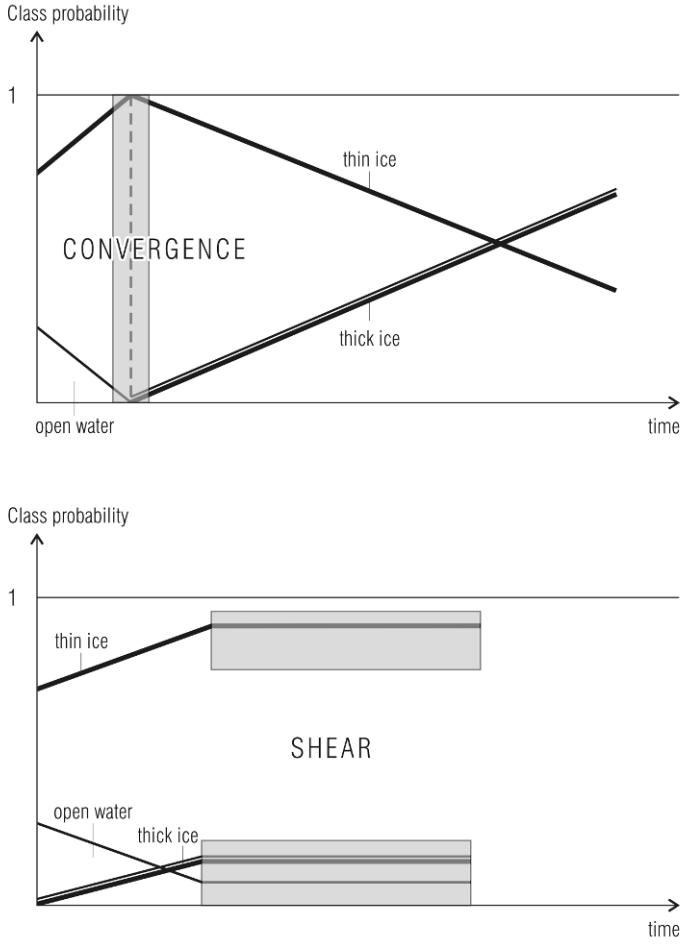

Figure 3.20 Convergence and pure shear for a three-level ice thickness distribution.

($h = h_1$) and deformed ice ($h = h_2 = kh_1$), and the corresponding areas are S_0, S_1 and S_2, $S_0 + S_1 + S_2 = S_\infty$. Recalling that H is the Heaviside function (Eq. 2.38b), redistributor for the distribution function Π can be written as:

$$\Psi = \frac{1}{S_\infty}\frac{\partial S_0}{\partial t} H(h) + \frac{1}{S_\infty}\frac{\partial S_1}{\partial t} H(h - h_1) + \frac{1}{S_\infty}\frac{\partial S_2}{\partial t} H(h - h_2) \tag{3.36a}$$

Equation (3.36a) transforms to the redistributor for spatial density when the Heaviside functions are replaced by delta functions:

$$\psi = \frac{1}{S_\infty}\frac{\partial S_0}{\partial t} \delta(h) + \frac{1}{S_\infty}\frac{\partial S_1}{\partial t} \delta(h - h_1) + \frac{1}{S_\infty}\frac{\partial S_2}{\partial t} \delta(h - h_2) \tag{3.36b}$$

Pure divergence and convergence

In pure divergence, the open water fraction increases while the relative coverage of non-zero thicknesses decreases (i.e., $\psi(0) = \nabla \cdot \boldsymbol{u}$ and $\psi(h) = 0$ for $h > 0$). The converse is true in pure convergence as long as the compactness of ice is less than unity (or less than a specified maximum). Consequently:

$$\frac{\partial \pi}{\partial t} + \boldsymbol{u} \cdot \nabla \pi = [\delta(h) - \pi] \nabla \cdot \boldsymbol{u} \tag{3.37}$$

Note that since $\pi_0 = 1 - A$, this equation is for π_0 exactly the same as Eq. (3.26) gives for mechanical changes in ice compactness under pure divergence or convergence.

Example Assume that $\nabla \cdot \boldsymbol{u} = \text{constant} = \lambda$, $|\lambda| = 0.1\,\text{day}^{-1}$, $A(t = 0) = 0.8$ and ignore thermodynamics and advection. Then:

$$\frac{d\pi_0}{dt} = \lambda(1 - \pi_0)$$

which gives $\pi_0 = 1 - 0.8\,\mathrm{e}^{-\lambda t}$. If $\lambda > 0$, the open water fraction approaches zero with an e-folding timescale $\lambda^{-1} = 10$ days; if $\lambda < 0$, the ice closes up and compactness is one at the time $-\lambda^{-1}\log(1/0.8) \approx -0.22 \times \lambda^{-1} = 2.2$ days.

Convergence in compact ice leads to redistribution of thicknesses by transforming thin ice to thick ice (i.e, undeformed ice to deformed ice). The area of thin ice decreases and the area of thick ice increases as the ice piles up. Becoming in thickness k-fold from the original, a spot ΔS must collect thin ice from area $(k - 1)\Delta S$ around. Consider the distributor of Eq. (3.36b). We have $S_\infty^{-1}\partial S_1/\partial t = k/(k - 1)\nabla \cdot \boldsymbol{u}$ and $S_\infty^{-1}\partial S_2/\partial t = -1/(k - 1)\nabla \cdot \boldsymbol{u}$, and then:

$$\frac{\partial \pi}{\partial t} + \boldsymbol{u} \cdot \nabla \pi = -\left[\left(\pi_1 - \frac{k}{k-1}\right)\delta(h - h_1) - \left(\pi_2 + \frac{1}{k-1}\right)\delta(h - h_2)\right]\nabla \cdot \boldsymbol{u} \tag{3.38}$$

Example Assume that $\nabla \cdot \boldsymbol{u} = \text{constant} = \lambda = -0.1\,\text{day}^{-1}$, ignore thermodynamics and advection (as in the previous example), and take initially $\pi = \delta(h - h_1)$.This ice is transformed into deformed ice with thickness kh_1 (Figure 3.20). Then

$$\frac{d\pi_1}{dt} = -\left(\pi_1 - \frac{k}{k-1}\right)\lambda, \quad \text{with the solution } \pi_1 = \frac{k - e^{-\lambda t}}{k-1}$$

Since $\lambda < 0$, the fractional area of thin ice decreases, and at time $\lambda^{-1} \log k$ the thin ice has totally disappeared; if $k = 5$, the time for this total deformation is $\approx$16 days.

Pure shear

Although divergence in shear deformation is zero, opening takes place in the first principal axis and closing in the second principal axis. In non-compact ice there is room enough for the ice floes to perform shear deformation without interaction, and the area density of ice is unchanged. This case corresponds to shear deformation of incompressible fluids. But in the case of compact ice, pressure ice forms and leads open along the principal axes, and being of different natures they cannot cancel each other. Consequently, thickness distribution may also change in pure shear.

Consider the redistributor in Eq. (3.36b). By opening leads at the rate of $\dot{\varepsilon}_0$, the same area of undeformed ice is taken and piled up as deformed ice (Figure 3.20). Clearly, the deformed ice area increases by $(k-1)^{-1}\dot{\varepsilon}_0$. The undeformed ice area must decrease by $k/(k-1)\dot{\varepsilon}_0$ to balance this. In pure shear $\dot{\varepsilon}_{\text{II}} = 2|\dot{\varepsilon}_{xy}|$, and one could then expect that $\dot{\varepsilon}_0 = \chi\dot{\varepsilon}_{\text{II}}$, $0 \le \chi \le \frac{1}{2}$ and χ decreases with decreasing compactness. Consequently:

$$\frac{\partial \pi}{\partial t} + \boldsymbol{u} \cdot \nabla \pi = \left[\delta(h) - \frac{k}{k-1}\,\delta(h-h_1) + \frac{1}{k-1}\,\delta(h-h_2)\right]\chi\dot{\varepsilon}_{\text{II}} \tag{3.40}$$

Thus, open water and deformed ice is formed here at the rate $\chi\dot{\varepsilon}_{\text{II}}$ even though divergence is zero.

General strain-rate

In general the mode of deformation is described by the angle φ, defined by $\tan\varphi = \dot{\varepsilon}_{\text{II}}/\dot{\varepsilon}_{\text{I}}$ (see Section 3.1). The pure divergence, convergence and shear correspond to $\varphi = 0$, π and $\pi/2$, respectively. For any mode φ, the amount of opening is given by a function $\chi_0(\varphi)$ and the amount of pressure ice formation is given by a function $\chi_d(\varphi)$ (Thorndike *et al.*, 1975). Figure 3.21 shows the AIDJEX form of lead opening and ridging functions. Then

$$\psi = |\dot{\varepsilon}|[\chi_0(\varphi)\delta(h) + \chi_d(\varphi)\psi'(h)] \tag{3.41}$$

where the function $\psi'(h)$ specifies the loss and gain of different thicknesses in ridging. It is commonly assumed that ψ' picks up the 0.15 lower tail from the thickness distribution (Thorndike *et al.*, 1975) and transfers it to k-multiple thicknesses. The original value was suggested as $k = 5$ (Thorndike, 1975), while later $k = 15$ was

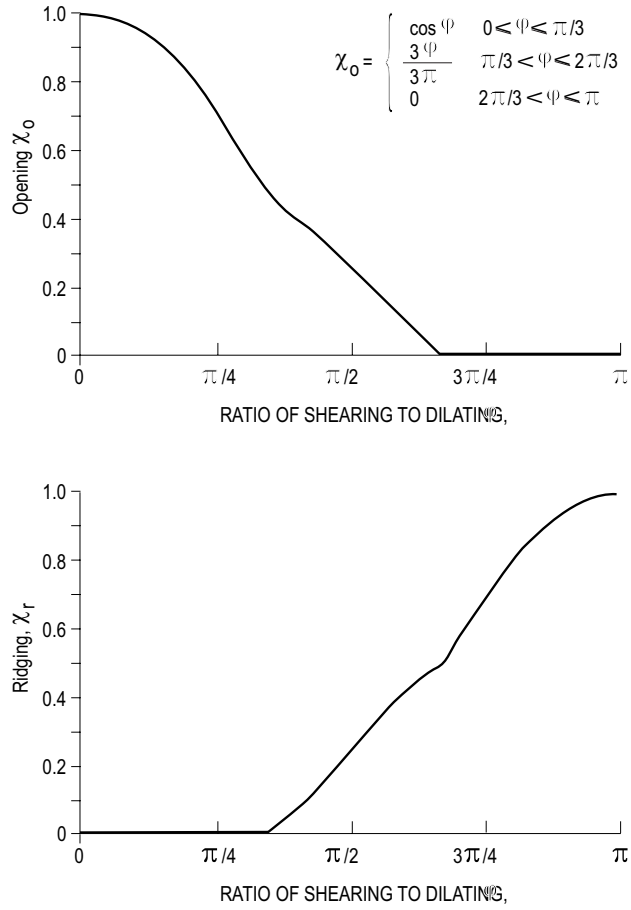

Figure 3.21 Opening and ridging as a function of the mode of deformation φ, $\tan\varphi = \dot{\varepsilon}_{II}/\dot{\varepsilon}_{I}$. Redrawn from Rothrock and Hall (1975), according to Pritchard (1981).

considered better at producing realistic thickness distributions (Pritchard, 1981; Rothrock, 1986). Flato and Hibler (1995) showed that $k = 5$ produces realistic thickness distributions up to 10-m thicknesses, but concluded that ψ' should rather pick up 0.05 thin-ice fractions and with a fixed k the resulting thickness distribution has a sawtooth shape.

It has also been suggested that the rafting process is significant in thin ice. This would be described by $k = 2$ (Leppäranta, 1981b; Bukharitsin, 1986; Babko *et al.*, 2002), or more generally rubble fields or hummocked ice fields where the parameter k is more than 2 but much less than for ridged ice.

Sea ice kinematics has been examined in this chapter for methods, theory, and data. Ice motion was taken as a continuum flow and analyzed using two-dimensional theory. The movement of a drift ice field was shown to consist of rigid displacement,

rotation, and strain. Stochastic models for ice drift were also introduced. In Section 3.4 the ice conservation law was derived for the ice state defined in Chapter 2. Chapter 4 is about the rheology of drift ice, examining how the internal ice stress is determined by the ice state and strain. The geophysical interpretation of stochastic models is given in Chapter 6, and the ice conservation law is combined with the equation of motion for fully closed ice drift models in Chapters 7 and 8.

4

Sea ice rheology

4.1 GENERAL

This chapter first explains the general concepts underlying the science of rheology. Then the usual drift ice rheology models are presented: viscous, plastic, and granular medium. There are two principal reasons for the inclusion of this chapter. First, drift ice is a very complicated medium and its rheology changes drastically as a function of ice state and deformation. The picture of this rheology is still far from complete. Second, for students and scientists in oceanography or meteorology, rheological problems are not so familiar, because the ocean and atmosphere are linear Newtonian fluids that obey the well-established Navier–Stokes equation.

To derive the two-dimensional drift ice rheology, it is necessary to begin in the three-dimensional world. In this way it is possible to analyze the three-dimensional effects of the rheology problem and determine the conditions when and how the two-dimensional approach is allowed for formulation of drift ice rheology. For clarity, three-dimensional vectors and tensors are underlined. The internal stress in a medium specifies the internal force field over its arbitrary internal surfaces. In three dimensions the stress has nine components, arising from three independent surface orientations and three independent force directions (Figure 4.1). In Cartesian form:

$$\underline{\boldsymbol{\sigma}} = \begin{bmatrix} \underline{\sigma}_{xx} & \underline{\sigma}_{xy} & \underline{\sigma}_{xz} \\ \underline{\sigma}_{yx} & \underline{\sigma}_{yy} & \underline{\sigma}_{yz} \\ \underline{\sigma}_{zx} & \underline{\sigma}_{zy} & \underline{\sigma}_{zz} \end{bmatrix} \tag{4.1}$$

Stress is thus a second-order tensor. Analogous to the strain and strain-rate tensors, the diagonal components are *normal (compressive or tensile) stresses* and off-diagonal components are *shear stresses*. The component $\underline{\sigma}_{xx}$ gives the normal stress in x-direction, the component $\underline{\sigma}_{yx}$ gives the shear stress across y-axis in the x-direction, etc. The stress tensor is necessarily *symmetric*, since otherwise there

M. Leppäranta, *The Drift of Sea Ice*, Springer Praxis Books,
DOI 10.1007/978-3-642-04683-4_4, © Springer-Verlag Berlin Heidelberg 2011

Tadashi Tabata (1923–1981), professor at the Institute of Low Temperature Science of Hokkaido University, founded the Sea Ice Research Laboratory in Mombetsu in 1967. He designed a coastal radar system, operational from 1969–2005, and largely advanced the understanding of the material properties and motion of sea ice. He also made major contributions to the study of the small-scale structure and mechanics of sea ice.
Reproduced with permission from the Institute of Low Temperature Science, Hokkaido University.

would be net internal torques that would not disappear when particle size approaches zero (e.g., Hunter, 1976). Thus $\underline{\sigma}_{xy} = \underline{\sigma}_{yx}$, $\underline{\sigma}_{xz} = \underline{\sigma}_{zx}$ and $\underline{\sigma}_{yz} = \underline{\sigma}_{zy}$ which reduces the number of independent stress components to six. At a given point, the force exerted by the stress on a unit area with normal $\underline{\boldsymbol{n}}$ is $\underline{\boldsymbol{\sigma}} \cdot \underline{\boldsymbol{n}}$. This vector has a normal stress component in the direction $\boldsymbol{n}$ and a shear stress component parallel to the surface.

Example Hydrostatic pressure is a stress $\underline{\boldsymbol{\sigma}} = -p\underline{\boldsymbol{I}}$, where $\underline{\boldsymbol{I}}$ is the unit tensor and $p > 0$ is scalar pressure; $\underline{\boldsymbol{\sigma}}$ is spherical (i.e., diagonal and equal in all directions) and compressive (i.e., $\underline{\sigma}_{xx} = \underline{\sigma}_{yy} = \underline{\sigma}_{zz} = -p < 0$). In seawater $p = p_a + \rho_w g D$, where p_a is the surface atmospheric pressure and D is the depth. In any direction, $\underline{\boldsymbol{n}} \cdot \underline{\boldsymbol{\sigma}} = -p\underline{\boldsymbol{n}}$ (i.e., hydrostatic pressure compresses the particle normal to the surface and is equal in all directions)

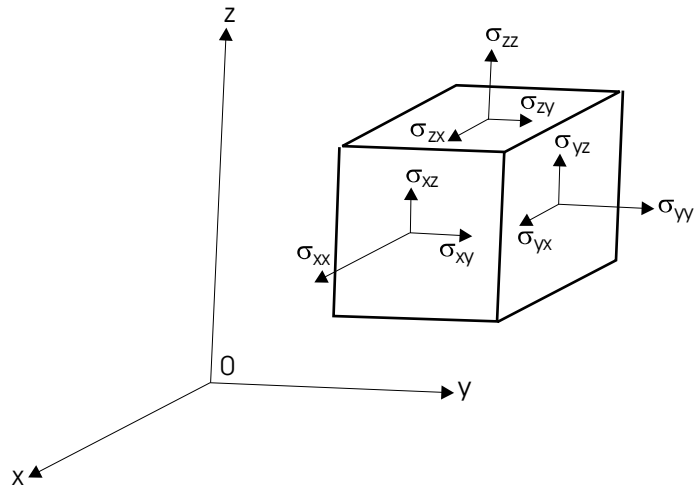

Figure 4.1 Stress σ on material element.

4.1.1 Rheological models

The science of rheology examines how the stress in a medium depends on its material properties and strain (with strain rate and possibly higher order strain derivatives). The basic models are *linear elastic* or Hooke's medium, *linear viscous* or Newton's medium, and *ideal plastic* or St Venant's medium. Linking a scientist's name to the rheology he or she has introduced is a common practice (e.g., Mase, 1970; Hunter, 1976). One-dimensional cases are illustrated in Figure 4.2. The linear elastic model assumes that stress is proportional to strain, while in the linear viscous model stress is proportional to the strain-rate (proportionality coefficients are, respectively, the elastic modulus or Young's modulus and viscosity). Rubber and water (in laminar flow) are good material examples of, respectively, linear elastic and viscous media. An ideal plastic medium collapses once the stress achieves yield strength (children's modelling wax serves as an example of a plastic medium). Mechanical analogues for these models include spring balance for linear elasticity, dashpot[1] for linear viscosity, and static friction for plasticity. Further analogies can be found in the refrigerator: sausage is elastic, jam is viscous, and gelatine is plastic.

Plastic rheology is normally presented in a stress–strain diagram as in Figure 4.2. It can also be formulated with a similar diagram for a stress–strain rate relation: when stress is below the yield stress, the medium is rigid; at the yield stress the medium flows and the stress is independent on the rate of strain.

Basic rheological models can be expanded for more complex ones (e.g., Mellor, 1986). First, linearities can be changed to general nonlinear laws in the elastic and viscous models. Second, models can be combined (e.g., linear elastic and linear

[1] Such as a door stroke compressor, which dampens or softens the movements of a door.

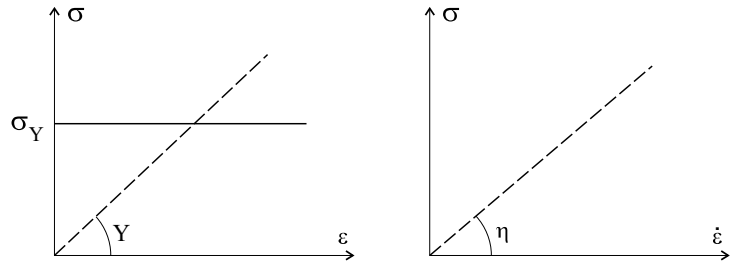

Figure 4.2 The basic rheology models (in one dimension) for the stress σ as a function of the strain ε and the strain-rate $\dot{\varepsilon}$; Y is elastic modulus, η is viscosity, and σ_Y is yield strength.

viscous models in series give a Maxwell medium while combining them parallel gives a Kelvin–Voigt medium). For a constant load, a Maxwell medium has an immediate elastic deformation and then flows in a linear viscous manner, while a Kelvin–Voigt medium flows in a viscous manner toward an asymptote determined by the elastic part.

An ideal plastic medium fails at yield stress, and the strain then depends on inertia and external forces acting on the system. In stable plastic medium strain hardening takes place. The yield strength increases under strain, and more stress is needed for further deformation. To continue the modelling wax example, more and more force would be needed to make a ball smaller (for a constant load a stationary steady state would result). In unstable plastic medium strain softening takes place, and even if forcing is lowered the strain may continue.

A difficulty with ideal plastic solution is often the lack of functional relationship $\varepsilon \rightarrow \sigma$: at $\varepsilon = 0$ the level of stress is indeterminate. A way to avoid this problem is to approximate ideal plasticity in the neighbourhood of $\varepsilon = 0$ by a convenient function $\sigma(\varepsilon)$, or by a function $\sigma(\dot{\varepsilon})$ if the strain-rate formulation is employed.

On a small scale, sea ice behaves in a linear elastic manner for short-term loading and in a general viscous manner for long-term low loading (Mellor, 1986). A typical Young's modulus is 2 GPa. The small-scale strength of first-year sea ice is lower than that of fresh water ice due to the presence of brine pockets. A convenient reference of strength of floating ice is flexural strength, because *in situ* tests can be easily performed in the specific natural temperature conditions where the bottom temperature is at the freezing point of seawater (Weeks, 1998a). The strength drops by one order of magnitude when the brine volume (ν_b) increases from $\nu_b = 0$ to $\nu_b = 0.15$, which is quite normal brine volume level for warm first-year sea ice (Figure 4.3). A typical level of the flexural strength is 0.5–1.0 MPa. Tensile strength is about the same as flexural strength, while compressive strength is 2–5 MPa. Multi-year ice has very low salinity and therefore much higher strength than first-year ice. In comparison with fresh water ice, Young's modulus and compressive strength are one order of magnitude larger for wood and two orders of magnitude larger for steel.

Example (*bearing capacity*) One of the fundamental problems in research of floating ice is the bearing capacity. This problem is approached using the theory of plate

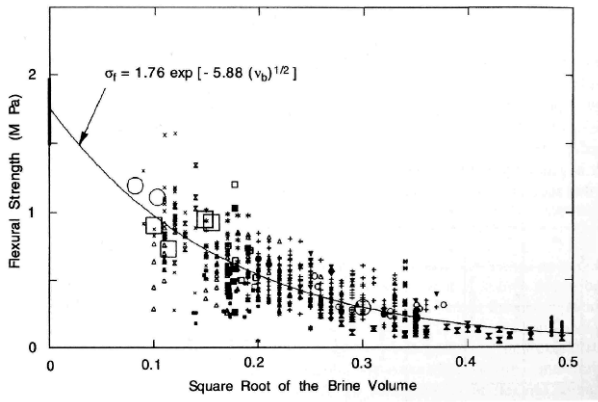

Figure 4.3 Flexural strength of sea ice as a function of brine content (ν_b).
Reproduced from Weeks (1998a), printed with permission from Helsinki University Press.

on elastic foundation from civil engineering. For a point load, the ice is forced down while it is supported by water pressure. The supporting pressure is $\rho g w$, where w is the deflection, and thus a liquid water body acts mathematically in the same way as an elastic foundation (i.e., response of the foundation is proportional to deflection). The general theory gives the equation of deflection as, for example Michel (1978):

$$\nabla^4 w = \rho_w g w$$

The load acts in the origin and is accounted for in the boundary conditions. Bending of the ice causes stresses, which eventually break the ice. This equation can be analytically solved using the Bessel functions. First-order approximation is obtained from the first term of the series solution; the ice can bear mass M, if $M < ah^2$, where the parameter a depends on the characteristic length of ice plate on water foundation l_c (Eq. 2.13) and on the strength of ice, $a \sim 5\,\mathrm{kg\,m^{-2}}$. The deflection takes the form of an exponentially damped wave with wavelength $2\pi l_c$. The radius of influence of a point load is $2l_c$ and consequently this is the safe distance between loads if the ice thickness is close to the critical level. For moving loads there is an additional danger when the speed of the load is close to the speed of a shallow water wave beneath the ice. Due to resonance in bending of the ice, the bearing capacity becomes in practice half that of static loads.

The viscous regime is more complicated. For a constant load, the strain history undergoes three consecutive regimes: I – sublinear, II – linear and III – superlinear (in that order).[2] In region I the ice is hardening while in region III it falls into an accelerating strain, and the strain inflection point is at about 1%-strain level (see Mellor, 1986). In the one-dimensional case a wide range of viscous rheologies can be written as a power law

$$\underline{\sigma} = \eta_{n-1} |\dot{\underline{\varepsilon}}|^{n-1} \dot{\underline{\varepsilon}} \tag{4.2}$$

[2] Law $y(x) = cx^a$ is sublinear for $a < 1$, linear for $a = 1$, and superlinear for $a > 1$.

where η_{n-1} is the viscosity of n-power law. Glacier flows are normally modelled by $n = 1/3$, known as Glen's law (Glen, 1958). Viscosities are dependent on ice temperature.

When going to the floe scale, the interaction between floes needs to be included into the stress-generating mechanisms, and further in the continuum scale these floe interactions dominate the physics and variations in small-scale properties become less important. This is the regime of drift ice.

4.1.2 Internal stress of drift ice

Floating at the air–sea interface, drift ice actually experiences hydrostatic pressure from seawater ($\rho_w gD$) and air (p_a) in addition to the stress $\boldsymbol{\sigma}$ due to the interaction between ice floes. The total internal stress is thus:

$$\underline{\Sigma} = \underline{\boldsymbol{\sigma}} - [p_a + \rho_w gD]\underline{\boldsymbol{I}} \tag{4.3}$$

The hydrostatic pressures of air and water have a role in the creation of the state of drift ice. But they can also have horizontal gradients that act as external forces on the ice, in much the same way as the horizontal pressure gradient works in dynamical oceanography. The influence of these surrounding media is straightforward and will be introduced in the derivation of the equation of motion in Chapter 5.

In this chapter the focus is on the stress σ, the most difficult and the least known factor in sea ice dynamics. The stress given in Eq. (4.1) is first split into three sub-fields:

$$\underline{\boldsymbol{\sigma}} = \begin{bmatrix} HH & HH & HV \\ HH & HH & HV \\ VH & VH & VV \end{bmatrix}, \quad \underline{\boldsymbol{\sigma}}_H = [HH] = \begin{bmatrix} \underline{\sigma}_{11} & \underline{\sigma}_{12} \\ \underline{\sigma}_{21} & \underline{\sigma}_{22} \end{bmatrix} \tag{4.4}$$

The left upper 2×2 stress (HH), denoted by $\underline{\sigma}_H$, is the horizontal stress due to horizontal interactions between ice floes. The left lower 1×2 stress (VH) is the vertical shear stress, which transfers air and water stress into the ice. The right side 3×1 stress (HV and VV) belongs to the vertical equation of motion, which becomes hydrostatic equation with ice floating on the sea surface. The partitioning of the stress tensor becomes clearer in the vertical integration of the momentum equation in the next chapter.

Integration of $\underline{\boldsymbol{\sigma}}_H$ through the ice thickness gives two-dimensional stress:

$$\boldsymbol{\sigma} = \int_{-h''}^{h'} \underline{\boldsymbol{\sigma}}_H \, dz \tag{4.5}$$

This is normally referred to as *internal ice stress* in sea ice dynamics. Note that the dimension of $\boldsymbol{\sigma}$ is force/length. The components σ_{xx} and σ_{yy} are normal stresses, and $\sigma_{xy} = \sigma_{yx}$ is the xy shear stress. The principal components, invariants, etc. for the stress tensor are found by a method similar for the two-dimensional strain-rate tensor in the previous chapter.

Drift ice forms a large field of ice broken into floes (Coon and Pritchard, 1974). There are several processes, which act continuously to break ice, and therefore the

broken appearance is persistent and means that drift ice cannot support tension. Cracks open and close due to long-period waves (Assur, 1963), thermal stresses (Evans and Untersteiner, 1971), and isostatic imbalance (Schwaegler, 1974). In closing drift ice fields, pressure ridges form of thin ice in the leads. This picture looks rather simple but, however, the rheology of drift ice is particularly complicated because qualitatively and quantitatively different laws apply to different ice states (particularly to the different packing densities and thicknesses of ice floes). The stress-generating mechanisms are:

(i) Floe collisions.
(ii) Floe break-up.
(iii) Shear friction between floes.
(iv) Friction between ice blocks in pressure ice formation.
(v) Potential energy production in pressure ice formation.

From observational evidence, we know the qualitative features of drift ice rheology are as follows (the numbering has no significance):

(1) Stress level ≈ 0 for $A < 0.8$ (weak floe contacts).
(2) Tensile strength ≈ 0 (nonzero but small for compact consolidated ice).
(3) Shear strength is significant.
(4) Shear strength $<$ Compressive strength.
(5) Yield strength > 0 for $A \approx 1$.
(6) No memory.

Items (1) and (2) mean that significant stresses are present only under compression of very close or compact drift ice. Item (6) means that stress may depend on both strain and strain-rate (i.e., the zeroth- and first-order time derivatives of the strain) but not on higher order time derivatives. Consequently, the rheological law of drift ice in general form is:

$$\boldsymbol{\sigma} = \boldsymbol{\sigma}(J, \boldsymbol{\varepsilon}, \dot{\boldsymbol{\varepsilon}}) \tag{4.6}$$

The material properties are included in the ice state J, and the deformation is specified by the strain $\boldsymbol{\varepsilon}$ and strain-rate $\dot{\boldsymbol{\varepsilon}}$. The form of the rheological equation is normally assumed, and its parameters are found from tuning a full large-scale or mesoscale model against ice state and kinematics data.

A one-dimensional illustration of drift ice rheology is given in Figure 4.4. The simplest rheology is the no-stress case ($\boldsymbol{\sigma} \equiv 0$) known as *free drift*. The main drawback of the free drift model is that coupling with the ice conservation law is lost and ice floes may accumulate without limitations. But it is applicable for $A < 0.8$ when stress levels are very small. In a way this is analogous to using the pure Ekman drift in ocean hydrodynamics, where piling of water is not controlled by hydrostatic pressure from sea level elevation or geostrophic adjustment (see Gill, 1982).

With increasing ice compactness, the significance of floe collisions increases and stress becomes a quadratic function of strain rate (Shen *et al.*, 1986). But still the level of stress is low. When compactness has increased above 0.7–0.8, shear friction between ice floes becomes important. Further on, when compactness approaches

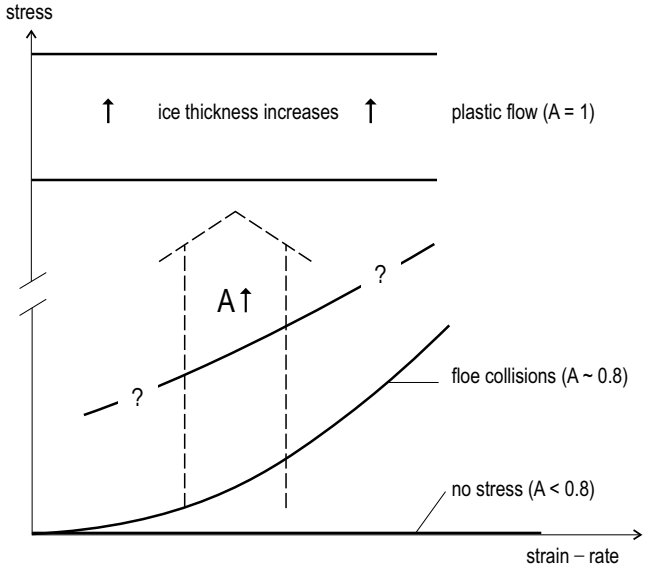

Figure 4.4 Schematic presentation of change in the quality of sea ice rheology as a function of ice compactness A and thickness h. The cut in the ordinate axis corresponds to a jump of several orders of magnitude.

unity, friction between ice blocks, inelastic dissipation and potential energy build-up in pressure ice formation result in plastic behaviour. How rheology changes from superlinear collision rheology to a plastic law is not known. In the plastic regime, yield strength increases with increasing ice thickness. Discrete particle models with detailed floe–floe interaction processes have been used to examine the closing up of drift ice (Løset, 1993; Hopkins, 1994; Savage, 1995), and the results are guiding the development of drift ice continuum rheologies.

In two dimensions shear strain and shear stress are also important. Their dependence is qualitatively similar to the case of normal stresses in the one-dimensional case, but the shear strength of drift ice is lower than its compressive strength. When shear strength is ignored, we have a *cavitating fluid* model (Flato and Hibler, 1990). Two-dimensional models were originally isotropic, but more recently anisotropic models due to directionality of lead patterns have been proposed (Coon *et al.*, 1998; Hibler and Schulson, 2000).

4.1.3 Internal friction

Spatial stress differences give rise to forces that step into the equation of motion. They smooth the velocity field, force the flow to satisfy boundary conditions, and may transmit momentum over large distances. The irrecoverable part of these forces is called *internal friction*. Apart from small elastic deformations, all changes due to stress differences are irrecoverable in drift ice mechanics. In dynamics of Newtonian

fluids, the internal stress consists of hydrostatic pressure and linear viscous friction. The storage of energy by the pressure can be returned for kinetic energy, but viscous friction dissipates mechanical energy to heat and is irrecoverable.

Consider a square $\delta x \times \delta y$ in a two-dimensional internal stress field σ. In the same way as in general continuum mechanics (e.g., Hunter, 1976), the net force comes to the x-direction from normal stress σ_{xx} and from shear stress $\boldsymbol{\sigma}_{xy}$, respectively:

$$\left(\sigma_{xx} + \frac{\partial \sigma_{xx}}{\partial x}\,\delta x - \sigma_{xx}\right)\delta y = \frac{\partial \sigma_{xx}}{\partial x}\,\delta x \delta y \tag{4.7a}$$

$$\left(\sigma_{xy} + \frac{\partial \sigma_{xy}}{\partial y}\,\delta y - \sigma_{xy}\right)\delta x = \frac{\partial \sigma_{xy}}{\partial y}\,\delta x \delta y \tag{4.7b}$$

Their sum is the total force in the x-direction from the internal stress. The force is obtained similarly for the y-direction. Summing together and dividing by the area $\delta x \delta y$, the total net force per unit area due to the interaction between ice floes is obtained. This becomes the divergence of the stress tensor $\nabla \cdot \sigma$:

$$[\nabla \cdot \boldsymbol{\sigma}]_x = \frac{\partial \sigma_{xx}}{\partial x} + \frac{\partial \sigma_{yx}}{\partial y}, \quad [\nabla \cdot \boldsymbol{\sigma}]_y = \frac{\partial \sigma_{xy}}{\partial x} + \frac{\partial \sigma_{yy}}{\partial y} \tag{4.8}$$

Dimension of the divergence of this two-dimensional stress σ is force per area. The three-dimensional case is analogous (i.e., the stress divergence gives the force per unit volume).

Example Hydrostatic pressure is given by $\boldsymbol{\sigma} = -p\boldsymbol{I}$, where p is the scalar pressure. Evaluating the pressure differences for an elementary volume gives $\nabla \cdot \boldsymbol{\sigma} = -\nabla p$, which is known as the pressure gradient term in fluid dynamics.

In sea ice dynamics, the internal ice stress σ is actually the vertically integrated three-dimensional stress (Eq. 4.5). Since the two-dimensional momentum equation of sea ice is obtained by vertical integration of the three-dimensional equation (see Section 5.1), the force due to the internal stress in sea ice dynamics is:

$$\boldsymbol{F}_{IF} = \int_{-h''}^{h'} (\underline{\nabla} \cdot \underline{\boldsymbol{\sigma}}_H) dz, \quad \sigma = \int_{-h''}^{h'} \underline{\boldsymbol{\sigma}}_H dz \tag{4.9}$$

How this is taken into sea ice dynamics needs special attention, because ice thickness is not constant in space (Nye, 1973). The partial derivative of a two-dimensional stress component σ_{ij} for a coordinate x_k is $(i, j, k = 1, 2)$:

$$\frac{\partial \sigma_{ij}}{\partial x_k} = \int_{-h''}^{h'} \frac{\partial \underline{\sigma}_{ij}}{\partial x_k}\, dz + \underline{\sigma}_{ij}(h')\,\frac{\partial h'}{\partial x_k} + \underline{\sigma}_{ij}(-h'')\,\frac{\partial h''}{\partial x_k} \tag{4.10}$$

Assuming isostatic balance, the freeboard and draft gradients can be combined for the thickness gradient. Then we have the desired form

$$\int_{-h''}^{h'} \frac{\partial \underline{\sigma}_{ij}}{\partial x_k}\, dz = \frac{\partial \sigma_{ij}}{\partial x_k} - \left[\underline{\sigma}_{ij}(h')\left(1 - \frac{\rho}{\rho_w}\right) + \underline{\sigma}_{ij}(h'')\,\frac{\rho}{\rho_w}\right]\frac{\partial h}{\partial x_k} \tag{4.11}$$

In other words, the vertical integral of forcing by the three-dimensional stress equals forcing by the two-dimensional stress minus the ice thickness gradient effect. If the thickness gradient is very small, its influence can be neglected, as is usually implicitly done in sea ice dynamics. In principle, we could use Eq. (4.11) to give the forcing correctly. However, to know the thickness gradient effect, one would need a full three-dimensional rheology of the ice sheet.

Assume the following scales: H and L_h for thickness and its length scale, and L_σ for length scale of stress variations. Taking $\underline{\sigma}_H$ vertically constant, the thickness gradient effect is $\sim\underline{\sigma}_H(H/L_h)$, and the two-dimensional stress gradient is $\sim\underline{\sigma}_H H/L_\sigma$. Therefore the thickness gradient effect is small when $L_\sigma \ll L_h$. In general, this condition holds since thermodynamics and dynamics tend to smooth variations in mean thickness (i.e., ice growth and mechanics transfer thin ice to thicker categories). However, melting treats all thickness categories equally but as a whole the strength of melting ice is not well understood yet. In a detailed study, Nye (1973) analyzed the linear viscous case and showed that for ice thickness gradients of 1 m per 20 km the thickness gradient correction becomes important. Such gradients would be exceptional in mesoscale averages, but the actual level is one order of magnitude less. In this book the condition for the pure two-dimensional approach – to ignore the thickness gradient in Eq. (4.11) – is assumed to be valid.

Sverdrup (1928) was the first author to formulate the internal friction. His form was $\boldsymbol{F}_{IF} = -k\rho\boldsymbol{u}$, where $k \sim \frac{1}{2}\,\mathrm{s}^{-1}$ is the friction coefficient. This was an empirical formulation of the effect of internal friction but it does not satisfy the physical requirement frame independence of the rheology.

4.2 VISCOUS LAWS

One approach is to consider drift ice as a fluid, and then viscous rheologies $\boldsymbol{\sigma} = \boldsymbol{\sigma}(J, \dot{\varepsilon})$ are employed. A general viscous model is provided by the *Reiner-Rivlin fluid model* (e.g., Hunter, 1976):

$$\boldsymbol{\sigma} = \alpha\boldsymbol{I} + \beta\dot{\boldsymbol{\varepsilon}} + \gamma\dot{\boldsymbol{\varepsilon}}^2 \tag{4.12}$$

where the coefficients α, β and γ may depend on the state variables of the medium and on the strain-rate invariants (e.g., Hunter, 1976). In drift ice dynamics the last term has not been accounted for, but since α and β may depend on strain-rate invariants non-linear rheologies are possible.

4.2.1 Linear viscous model

Linear viscous models are not very representative for drift ice. However, in the history of sea ice dynamics they were the first class of applied rheologies and were used throughout the 1960s. The first drift ice case was the Newtonian fluid model by Laikhtman (1958): $\boldsymbol{\sigma} = 2\eta\dot{\boldsymbol{\varepsilon}}$, where η is the shear viscosity. Newtonian fluids are linear, viscous and incompressible, such as water in laminar flow (viscosity gives the

resistance of the fluid to shear deformation). Linear viscous models, however, can satisfy realistic boundary conditions and provide first-order approximations for basin-wide ice circulation.

For a compressible fluid, bulk viscosity or second viscosity ζ is included to give the resistance to spherical deformation through compressive stress $\zeta(\nabla \cdot \boldsymbol{u})\boldsymbol{I}$. In principle, shear and bulk viscosities are independent. In the linear case they may depend on the material properties of the fluid but not on the strain-rate. Internal friction is then:

$$\nabla \cdot \boldsymbol{\sigma} = \zeta \nabla(\nabla \cdot \boldsymbol{u}) + \eta \nabla^2 \boldsymbol{u} + \nabla\zeta(\nabla \cdot \boldsymbol{u}) + \nabla\eta \cdot [\nabla \boldsymbol{u} + (\nabla \boldsymbol{u})^T - (\nabla \cdot \boldsymbol{u})\boldsymbol{I}] \qquad (4.13)$$

The third and fourth terms on the right-hand side are due to changing viscosity. Laikhtman (1958) had a constant shear viscosity and incompressible fluid, and consequently $\nabla \cdot \sigma = \eta \nabla^2 \boldsymbol{u}$.

The magnitude of the linear bulk and shear viscosities of drift ice is $10^8 - 10^{12}\,\mathrm{kg\,s^{-1}}$ (Laikhtman, 1958; Campbell, 1965; Doronin, 1970; Doronin and Kheysin, 1975; Hibler and Tucker, 1977; Leppäranta, 1981b). If the thickness of ice were 1 m, the corresponding three-dimensional viscosities would be $10^8 - 10^{12}\,\mathrm{kg\,m^{-1}\,s^{-1}}$. Hibler and Tucker (1977) further showed that there is a clear seasonal cycle in viscosities with winter and summer extrema at 10^{11} and $10^9\,\mathrm{kg\,s^{-1}}$, respectively, in the Arctic Basin. Since deformation rates are of magnitude $10^{-6}\,\mathrm{s^{-1}}$, the stress magnitude is 10 kPa for viscosity $10^{10}\,\mathrm{kg\,s^{-1}}$; thus at the geophysical scale the stress is about two orders of magnitude less than at the local scale. Campbell and Rasmussen (1972) introduced stepwise linear viscosities to separate opening and closing flows since, as known already, drift ice has no resistance to tension (see Section 4.1): $\zeta, \eta = 0$ for $\dot{\varepsilon}_\mathrm{I} > 0$ and $\zeta, \eta > 0$ for $\dot{\varepsilon}_\mathrm{I} < 0$.

Kinematic shear or bulk viscosity K is obtained from the corresponding dynamic viscosity ζ or η by dividing by ρh: $K \sim 10^7\,\mathrm{m^2\,s^{-1}} = 10^6\,\mathrm{km^2\,day^{-1}}$. This quantity includes time- and space-scale information, $K \sim L^2/T$. Thus in the viscous spreading of velocity we have $L \sim 200$ km at $T \sim 1$ h.

For comparison, viscosities of some materials are shown in Table 4.1. Small-scale viscosities can be determined in laboratory experiments and they vary in a very wide range. In geophysical flows, viscosities are estimated from kinematical data or model simulations. Glaciers flow in a nonlinear viscous manner (see Section 4.2.2); a linearized form for typical glacier strain-rates of $10^{-9}\,\mathrm{s^{-1}}$ gives a linear viscosity of

Table 4.1 The viscosity of some materials and horizontal eddy viscosity in turbulent flow.

Water (laminar flow, 0°C)	$1.8 \times 10^{-3}\,\mathrm{kg\,m^{-1}\,s^{-1}}$	Small scale
Wax, shoe makers (8°C)	$4.7 \times 10^{5}\,\mathrm{kg\,m^{-1}\,s^{-1}}$	Small scale
Pitch (0°C)	$5.1 \times 10^{9}\,\mathrm{kg\,m^{-1}\,s^{-1}}$	Small scale
Glacier	$\sim 10^{14}\,\mathrm{kg\,m^{-1}\,s^{-1}}$	Flow of glaciers
Oceanic turbulence	$\sim 10^{8}\,\mathrm{kg\,m^{-1}\,s^{-1}}$	Mesoscale ocean dynamics

Sources: Hunter (1976), Paterson (1995), Gill (1982).

the order of $10^{14}\,\mathrm{kg\,m^{-1}\,s^{-1}}$. In mesoscale or large-scale turbulence in ocean dynamics, in the first-order approximation turbulent stresses are represented in similar form as linear viscous stresses, and the "viscosity" is then called the eddy viscosity (e.g., Gill, 1982). Eddy viscosity of horizontal ocean currents is of the order of $10^7 - 10^9\,\mathrm{kg\,m^{-1}\,s^{-1}}$, at the lower end of the range for the linear viscosity of drift ice.

Linear models are too crude for quantitative ice velocity analysis and modelling. For example, Hibler *et al.* (1974a) found that in the Beaufort Sea the ice velocity could fit a linear model only by a stepwise viscosity or with a slip boundary condition. The stepwise model would need viscosities of $10^{12}\,\mathrm{kg\,s^{-1}}$ in the central pack but only $10^8\,\mathrm{kg\,s^{-1}}$ in the shear zone under convergence. Although this could be solved by matching coastal boundary layer and central basin flows together, drift ice dynamics has other characteristics, which do not favour a linear viscous approach. This is discussed further in Section 4.3.

Since sea ice floats on a (nearly) constant geopotential surface, there is no build-up of hydrostatic pressure. In some modelling approaches, a pressure term has been included in the rheology for the strong resistance of compact drift ice to convergence. Russian authors have also used a pressure term in linear viscous models (e.g., Doronin and Kheysin, 1975). This has been formulated as $p = k_p \delta A$, with $k_p = 0$ for $\delta A < 0$ and $k_p > 0$ for $\delta A > 0$, δA being compactness change. Thus, pressure becomes active under compression and, according to Kheysin and Ivchenko (1973), at $A \approx 1$ and $-\delta A \sim 10^{-3} - 10^{-2}$, $k_p \sim 10^5\,\mathrm{N\,m^{-1}}$.

The existence of the pressure term shows the general possibility of pressure waves in the system. Assuming that there is a constant compressibility k_p for small disturbances in the compactness, with symmetry for opening and closing, the speed of pressure waves would be $c_p = \sqrt{k_p/(\rho h)} \approx 10\,\mathrm{m\,s^{-1}}$. The existence of signal propagation in drift ice at speeds $\sim 10\,\mathrm{m\,s^{-1}}$ has been found in observations (Legen'kov, 1978; Goldstein *et al.*, 2001). Doronin and Kheysin (1975) also provide evidence of transverse waves, which propagate at speed $c_p/2$ perpendicular to the propagation of shear ridging. The physical mechanism for pressure waves in drift ice is, however, unclear. An interesting parallel can be made with underwater acoustics with waves propagating in the seabed (see Chapter 2 of Lurton, 2002).

4.2.2 Nonlinear viscous model

The general form of isotropic, homogeneous viscous law of Glen (1970), with the hydrostatic pressure p explicitly included, is:

$$\boldsymbol{\sigma} = \boldsymbol{\sigma}(\dot{\boldsymbol{\varepsilon}}, p; \zeta, \eta) = (-p + \zeta \operatorname{tr} \dot{\boldsymbol{\varepsilon}})\boldsymbol{I} + 2\eta\dot{\boldsymbol{\varepsilon}} \tag{4.14}$$

In nonlinear viscous laws, ζ and η are functions of strain-rate invariants and ice state, while the pressure term depends only on the ice state, $\zeta = \zeta(\dot{\varepsilon}_\mathrm{I}, \dot{\varepsilon}_\mathrm{II}, J)$, $\eta = \eta(\dot{\varepsilon}_\mathrm{I}, \dot{\varepsilon}_\mathrm{II}, J)$, $p = p(J)$. As there is no hydrostatic pressure build-up in the system, it would be clear to assume that $p \equiv 0$. However, in some rheological models the internal ice stress uses a technical hydrostatic pressure term in the formalism, and therefore this term is included in the general rheology.

It is generally assumed that the ratio of viscous compressive strength to viscous shear strength, ζ/η is constant and greater than 1, based on calibration of numerical models. This ratio is obtained as the ratio of viscous stress in pure compression to viscous stress in pure shear, with the same strain rate magnitude. Compressive strength $\zeta(\dot{\varepsilon}_{\mathrm{I}}, \dot{\varepsilon}_{\mathrm{II}}, J)$ as well as shear strength can be taken as a homogeneous function of strain rate in power m:

$$\zeta(c\dot{\varepsilon}_{\mathrm{I}}, c\dot{\varepsilon}_{\mathrm{II}}, J) = c^m \times \zeta(\dot{\varepsilon}_{\mathrm{I}}, \dot{\varepsilon}_{\mathrm{II}}, J) \tag{4.15}$$

Thus, taking $n = m + 1$, we have $|\sigma| \propto |\dot{\varepsilon}|^n$, and $n < 1$ results in a sublinear law while $n > 1$ gives a superlinear law. From physical basis we have $n \geq 0$. Close or compact drift ice is sublinear ($0 \leq n < 1$), but in more open ice where floe collisions are important, $n = 2$, as will be seen in Section 4.4. Applications of general nonlinear viscous models to drift ice did not really get started, since they were very soon superceded by plastic models, which will be discussed in Section 4.3.

Nonlinear viscous laws have been much used for glacier flow (e.g., Paterson, 1995). These models are three-dimensional and can be taken incompressible (in drift ice theory the compressibility is needed in general for opening and closing of ice fields and for compact ice because of two-dimensional treatment). Consequently, only the shear viscosity needs to be accounted for in glacier flow. The basic model can be written for uniaxial shear flow $u = u(z)$ as:

$$\sigma = \eta_{n-1} \left| \frac{du}{dz} \right|^{n-1} \frac{du}{dz} \tag{4.16}$$

where the z-coordinate is the local normal with the glacier surface. Viscosity is the main tuning parameter; it depends first of all on the temperature of the glacier. The case $n = 1/3$ is known as Glen's rheology (Glen, 1958). Then a typical value of viscosity would be $\eta \approx 10^5\,\mathrm{kPa\,s^{1/3}}$.

Glacier ice is taken incompressible in three dimensions, and the rheology is based on power law between the strain rate and deviatoric stress[3] magnitudes, $|\sigma'| \propto |\dot{\varepsilon}|^n$. Note that for incompressible medium $\varepsilon' = \varepsilon'^{1}$, and tensor magnitude is taken in the present work as the Frobenius norm $|B| = \sqrt{\Sigma_{i,j} B_{ij}^2}$, see Eq. 3.12). The three-dimensional deviatoric stress is expressed in tensor form as:

$$\boldsymbol{\sigma}' = \eta_{n-1} |\dot{\boldsymbol{\varepsilon}}|^{n-1} \dot{\boldsymbol{\varepsilon}} \tag{4.17}$$

Thus there are two parameters, η_{n-1} and n, and usually n is fixed to Glen's power law or Glen's law with power $n = 1/3$ with η_{n-1} tuned from data. Glacier flow can be obtained then from the equation of motion:

$$\rho \frac{D\underline{\boldsymbol{u}}}{Dt} = \nabla \cdot \underline{\boldsymbol{\sigma}} + \underline{\boldsymbol{F}} \tag{4.18}$$

[3] It is assumed that the spherical part of the stress gives no net forcing for glacier flow but rather the deviatoric stress $\sigma' = \sigma - \frac{1}{3} \operatorname{tr} \sigma \boldsymbol{I}$.

External forcing contains only gravity, and the acceleration terms can be usually neglected. Glacier flow is then determined by the topography of the terrain and the glacier.

Example Power law flows. Consider a gravity-forced flow of a glacier along a sloping surface where the flow depends only on the z-coordinate. The glacier surface is taken as the level $z = 0$, z-coordinate is positive downward, and the glacier bottom is at $z = h$. Using the rheology (4.16), we have the flow law and boundary conditions as:

$$\frac{d}{dz}\left(\eta_{n-1}\left|\frac{du}{dz}\right|^{n-1}\frac{du}{dz}\right) = -g\rho\sin\alpha$$

$$z = 0: \quad \sigma = 0; \quad z = h: \quad u = 0$$

where α is the slope angle. Glacier surface is taken stress-free, and at glacier bottom no sliding speed is assumed. This equation can be directly integrated into

$$u = \left(\frac{g\rho\sin\alpha}{\eta_{n-1}}\right)^{1/n}\frac{n}{n+1}[h^{(n+1)/n} - z^{(n+1)/n}] = c_n[h^{(n+1)/n} - z^{(n+1)/n}]$$

For $n = 1$ we have the linear viscous case and parabolic velocity profile as is well known from open channel solution for sloping channel in hydrodynamics. As n decreases from one, the bottom boundary layer of the glacier velocity becomes thinner. If $c_n \to c < \infty$ as $n \to 0$, we have $u \to cH(z)$, where H is the Heaviside function (see Eq. 2.38b). This is in fact a plastic flow where the bottom boundary layer is shrunk to a yield line. Thus plastic flow can come as a limiting case of nonlinear viscous laws.

4.3 PLASTIC LAWS

4.3.1 Plastic drift ice

Drift ice mechanics investigations in the early 1970s opened the way to plastic rheologies, which have been the state-of-art to the present (Coon, 1972; Coon and Pritchard, 1974; Coon *et al.*, 1974; Pritchard, 1975). Plastic failure flow is formulated in terms of dimensionless mode of strain or strain rate. The result was found in the Arctic Ice Dynamics Joint Experiment (AIDJEX) research programme, largely inspired by soil mechanics theory and models. In particular, two characteristics in the mechanical behaviour of compact ice cover favour plasticity:

- stresses in drift ice are rate independent;
- there is a finite yield limit for drift ice to deform.

Plastic rheologies are considered best at representing the physical behaviour of compact drift ice. The existence of finite yield strength is clear from observations, in

particular to people working in enclosed or semi-enclosed sea ice basins: compact ice is stationary until forcing exceeds a certain minimum level, the yield strength. The rate independence of stress on the strain-rate is less obvious but it has been verified in modelling of pressure ridging. A highly sublinear rheology is needed to produce narrow deformation zones, as found from the Beaufort Sea shear zone by Hibler *et al.* (1974a), among others. It was in the 1970s that the mathematical–physical basis for plastic drift ice models was constructed (Coon *et al.*, 1974), a major achievement of the AIDJEX programme. Then the concept of a granular medium was introduced for drift ice, and new ideas came from understanding the similarities between the mechanics of drift ice and soil. A soil mechanics approach was used for local processes such as pressure ridging and for basin-scale processes – dynamics of drifting ice.

Parmerter and Coon (1972) constructed a kinematic model of ridging, which is the main sink for kinetic energy in sea ice dynamics, and showed that ice stress appears to be independent of strain-rate magnitude, a strong characteristic feature of plasticity. They further examined the mechanical energy budget in ridging, and the results became the basis for the parameters of plastic drift ice rheologies (Rothrock, 1975a). This energy budget was later reworked with a discrete particle model (Hopkins and Hibler, 1991; Hopkins, 1994). The losses of kinetic energy in ridging are due to friction between ice blocks, creation of potential energy, inelastic deformation of ice blocks, and breakage of the ice sheet. Potential energy can be observed in the topography of ridges, while the other losses would be very difficult to track. Therefore, total loss is often assumed to be proportional to potential energy change. This is arguably questionable, since it has become clear that potential energy loss is one order of magnitude less than frictional losses (e.g., Leppäranta, 1981b; Hopkins, 1994).

The plastic properties of drift ice are up to the condition of high compactness (see Figure 4.4). However, when the compactness has decreased to 0.8 or so, stress levels are small and the resulting internal friction is not significant, whatever the rheology. Therefore, the state-of-the-art drift ice models possess a plastic rheology for compact ice and a parameterization, which loses the strength when the ice field has opened.

Example In Section 4.2 a nonlinear gravity-driven viscous simple shear flow was solved with power law rheologies $\sigma' = \eta_{n-1}|\dot{\boldsymbol{\varepsilon}}|^{n-1}\boldsymbol{\varepsilon}'$. As $n \to 0$, the rheology becomes a plastic rheology $\sigma' = \eta_\infty \dot{\varepsilon}*$, where the tensor $\dot{\varepsilon}*$ consists of dimensionless strain rates, scaled by the strain-rate magnitude. The stress is thus independent of the strain-rate but depends on the distribution of the strain into different components. Viscous flow has a finite bottom boundary layer, while in the plastic case the glacier stands still or flows down as a block with an infinitely thin boundary layer.

For one-dimensional plastic rheology just the yield strength values for compression and tension need to be specified. In two-dimensions, plastic rheologies have two fundamental yield elements: *yield curve* and *flow rule*. Yield curve is a function of the stress state and specifies the yield stress (i.e., it tells when the medium fails into

plastic deformation). For isotropic materials, the yield curve depends on two scalar invariants of the stress tensor[4]. In the principal stress space, the yield curve is written:

$$F(\sigma_1, \sigma_2) = 0 \tag{4.19}$$

A yield curve is a closed, convex curve in the principal stress space. Inside the yield curve $F < 0$ and the medium acts like a rigid body (i.e., there is no functional relation between stress and deformation). At $F = 0$ the principal stresses reach the yield level and the medium fails. Outside the yield curve $F > 0$ and these stress states are not allowed. The yield function is a property of the medium.

The flow rule defines how plastic deformation takes place once the stress has reached the yield curve. The one-dimensional case is again simple: compressive strain for compressive stress and tensile strain for tensile stress. In two dimensions we have to specify how the medium strains for a given yield stress. For example, if the medium fails at pure shear, how will the strain be? The plasticity theory does not automatically tell this. Drucker's postulate for stable materials states that the yield curve serves as the plastic potential, and consequently the failure strain is directed perpendicular to the yield curve (Drucker, 1950; see also Coon *et al.*, 1974). This is the *normal* or *associated flow rule*.

Plastic yielding is expressed in drift ice dynamics for the strain-rate as:

$$\dot{\varepsilon}_1 = \lambda \frac{\partial F}{\partial \sigma_1}, \quad \dot{\varepsilon}_2 = \lambda \frac{\partial F}{\partial \sigma_2} \tag{4.20}$$

where λ is a free parameter to be determined as a part of the solution. Strain-rates are then obtained for the xy-coordinate system, assuming that the alignments of the principal axes of stress and strain-rate are overlapping. Stresses in plastic media are independent of the absolute level of the strain-rate but, however, they do depend on the mode of strain rate (i.e., whether it is compression or tension and how much relative shear there is). The strain-rate is quantified by the external forcing of the system.

Example Take the yield curve as a circle $F(\sigma_1, \sigma_2) = \sigma_1^2 + \sigma_2^2 - \sigma_Y^2$. By definition, inside the yield curve ($F < 0$) the medium is rigid and fails at $\sigma_1^2 + \sigma_2^2 = \sigma_Y^2$. The associated flow rule gives $\dot{\varepsilon}_k = 2\lambda\sigma_k$, $k = 1, 2$, and λ derives from stress being equal to yield stress:

$$\left(\frac{\dot{\varepsilon}_1}{2\lambda}\right)^2 + \left(\frac{\dot{\varepsilon}_2}{2\lambda}\right)^2 = \sigma_Y^2$$

and thus $\lambda = \sqrt{\dot{\varepsilon}_1^2 + \dot{\varepsilon}_2^2}/2\sigma_Y$ and further:

$$\sigma_k = \frac{\dot{\varepsilon}_k}{\sqrt{\dot{\varepsilon}_1^2 + \dot{\varepsilon}_2^2}}\,\sigma_Y.$$

[4] Two-dimensional tensor has two independent invariants, and the yield curve needs to be independent of the coordinate system. The principal stresses can be taken as these invariants.

Clearly the stress is independent of the absolute level of the strain rate. For uniaxial (along x-axis) compressive strain rate $\dot{\varepsilon}_{xx} < 0$, $\dot{\varepsilon}_{xy} = \dot{\varepsilon}_{yx} = \dot{\varepsilon}_{yy} = 0$, and therefore we have $\dot{\varepsilon}_1 = 0$, $\dot{\varepsilon}_2 = \dot{\varepsilon}_{xx}$ (note that the principal components are taken here as $\varepsilon_1 > \dot{\varepsilon}_2$, by definition). The resulting stress is uniaxial, $\sigma_{xx} = -\sigma_Y$. For the circular symmetric yield curve in general, the principal strain rates and stresses are proportional to each other.

For the drift ice yield curve, the following additional requirements exist (based on the known qualitative properties listed in Section 4.1):

- As a broken field of floes, drift ice has (almost) no tensile strength, so the principal stresses must always be negative or zero, σ_1, $\sigma_2 \leq 0$, and this means that the yield curve must be located in the quadrant III of the principal axes co-ordinate system.
- The yield curve is symmetric with respect to the line $\sigma_1 = \sigma_2$ for isotropy.
- The yield curve is elongated in the $\sigma_1 = \sigma_2$ axis to give a compressive strength higher than shear strength.

Figure 4.5 shows the common yield curves for drift ice that will be derived in the following subsections. The main parameter in drift ice plastic rheologies is compressive strength P. It depends on the ice state $P = P(J)$; it also varies due to the

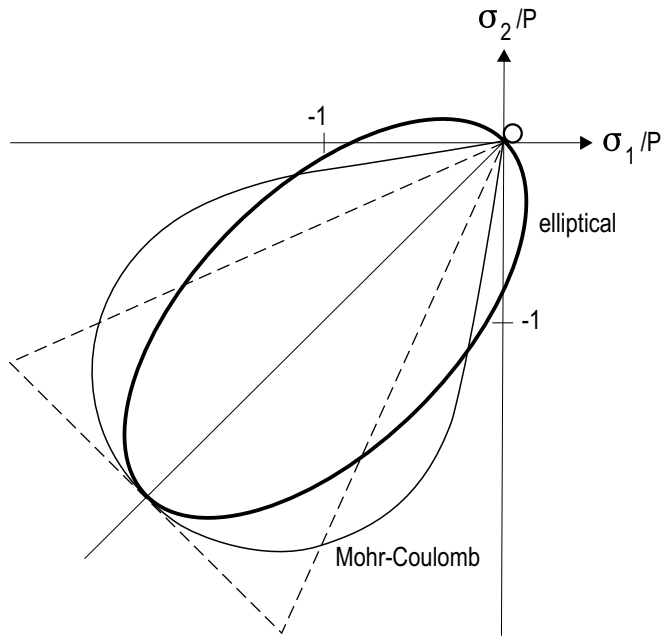

Figure 4.5 Plastic yield curves for drift ice: wedge or Mohr-Coulomb (Coon, 1974), teardrop (Rothrock, 1975a), and elliptic (Hibler, 1979).

mode of failure (i.e., crushing, buckling, or rafting) but this has not been accounted for drift ice strength parameterizations. In the yield curves of Figure 4.5, compressive strength is represented by the point farthest from the origin in the line $\sigma_1 = \sigma_2$. Other examples are (a) a square yield curve (bounded by the lines $\sigma_1 = 0$, $\sigma_2 = 0$, $\sigma_1 = -P/\sqrt{2}$, $\sigma_2 = -P/\sqrt{2}$) of Pritchard (1977), and (b) the cavitating fluid ($-P \leq \sigma_1 = \sigma_2 \leq 0$) of Flato and Hibler (1990).

The common hypothesis is that compressive strength can be written in the form $P = P^*\gamma(h)\alpha(A)$, with $\gamma(0) = 0$, $\alpha(0) = 0$, and $\alpha(1) = 1$. P^* is thought as a constant, and the normal values refer to the compressive strength in ridging process. Observations indicate that P^* is lower for rafting of thin ice (Leppäranta *et al.*, 1998). The level of P^* for pancake ice or frazil ice is not well known but would be of key importance in the Southern Ocean.

In the drift ice dynamics rheology problem, normal flow rule has been used to solve the failure strain. How fast the strain takes place then depends on the other forces in the system. The flow rule is therefore formulated in terms of the strain-rate, and the problem is closed for the absolute strain-rate level from the equation of motion. Other flow rules exist in plasticity theory but for the drift ice they have not been applied. This is logical since the detailed form of the yield curve itself has not been established; in fact, different reasonable yield curves with the normal flow rule have produced equally good ice velocities within the limits of the observational validation of ice velocity (e.g., Zhang, 2000).

The size of the yield curve is given by the yield strength, which increases with ice compactness and thickness. But the shape is invariant. In compressive deformation ($\dot{\varepsilon}_I < 0$), the compactness and thickness and consequently strength increase. Thus drift ice is *strain hardening* under compression. For a given forcing, drift ice compression may proceed only to a certain limit as ice thickness increases, obeying common sense. In pure shear the asymmetry of deformation – ridging and lead opening along the principal axes – leads the softening of the material or unstable material behaviour. Pure shear flow thus approaches free drift situation by opening leads parallel to the motion. In opening deformation ($\dot{\varepsilon}_I > 0$), the strength is zero and the opening may continue as a free drift without any limitation.

Example In one-dimensional case, let $A = 1$ and $P = P(h)$. Under compression, ice is packed thicker, and due to strain-hardening $dP/dh > 0$. Compressing an ice bar of unit width and thickness h from the left boundary by a force F, it continues failing until stress equals the yields stress at all points. At equilibrium, the condition $P(h) = F/h$ gives the resulting thickness.

For numerical modelling ideal plastic law is not always feasible, since there is no functional relationship between stress and strain rate (i.e., at zero strain rate the stress is indeterminate). Therefore this rigid (no deformation) mode is replaced by a "nearly rigid" mode. Two approaches have been taken: the Arctic Ice Dynamics Joint Experiment (AIDJEX) model (Coon *et al.*, 1974) used a linear elastic model, while Hibler (1979) chose a linear viscous model. Combined with yield behaviour, elastic–plastic and viscous–plastic rheologies result. There is no good observational

evidence to qualify and quantify the correct model for drift ice stresses below the yield level, and both these models can be considered just as approximations to the ideal plastic model. Elastic approach is a better approximation to rigid–plastic behaviour since elastic strains are small (within 10^{-3}) and recoverable, while viscous creep may increase to significant, unreal levels if the viscous state remains for a long time.

4.3.2 Mohr–Coulomb rheology

The first plastic drift ice model was by Coon (1974) using the Mohr-Coulomb medium model, for which failure shear stress σ_S is proportional the compressive stress σ_N:

$$\sigma_S = \sigma_N \tan \vartheta \tag{4.21}$$

where ϑ is the angle of friction between ice floes, taken as $\vartheta = 35^\circ$ from the repose angle of ice ridges. A cut-off stress for σ_N is provided by the ice strength, which depends on the mode of failure. This results in a wedge shaped yield curve (Figure 4.5). Coon (1974) adopted Drucker's postulate and consequently the normal flow rule.

According to Coon (1974), the cut-off stress in crushing failure is $\sigma_{cr}h$, where σ_{cr} is the crushing strength of ice sheet, and in buckling failure it is $\rho_w g l_0^2/(12h)$ where l_0

Figure 4.6 Field experiment into the strength of sea ice ridges in the Baltic Sea, winter 1987. The ridge keel is loaded with weights to examine the Mohr–Coulomb model.

is the smallest floe size in the loading area; if l_0 is taken as the size of pieces which break in rafting (see Section 2.2), the cut-off stress is:

$$\sigma_b = \frac{\pi^2}{192}\sqrt{\frac{Y\rho_w g h}{3(1-\nu^2)}} \tag{4.22}$$

For $h \sim 1$ m, the local magnitude levels of crushing failure and buckling failure are, respectively, 1 MPa and 100 kPa (i.e., the crushing failure stress is one order of magnitude larger). They are large but local; integrated over continuum length scales, the failure stresses become lower.

Example The Mohr–Coulomb model has also been used for sea ice ridges and hummocks in local scale problems with ice block accumulation (Figure 4.6). The shear strength of a pile of ice blocks is

$$\sigma_S = c + \sigma_N \tan\vartheta$$

where c is cohesion. The values of cohesion and angle of friction depend on the degree of consolidation of the ridge. With no frozen bonds between ice blocks $c = 0$ and $\phi \approx 6$ deg (Schaefer and Ettema, 1986). With more consolidated ridges, the strength is mainly due to cohesion (Leppäranta and Hakala, 1992).

4.3.3 AIDJEX elastic–plastic rheology

In the AIDJEX programme an elastic–plastic drift ice model was developed (Coon *et al.*, 1974; Coon and Pritchard, 1974; Pritchard, 1975). A *linear elastic model* is used inside the yield curve, where the stress is proportional to the strain:

$$\boldsymbol{\sigma} = 0, \quad \varepsilon_{\mathrm{I}} \geq 0; \quad \boldsymbol{\sigma}(\boldsymbol{\varepsilon}; M_1, M_2) = M_1(\mathrm{tr}\,\boldsymbol{\varepsilon})\boldsymbol{I} + 2M_2\boldsymbol{\varepsilon}', \quad \varepsilon_{\mathrm{I}} < 0 \tag{4.23}$$

where M_1 is the bulk modulus and M_2 is the shear modulus. Note that here, inside the yield curve, stresses are compressive and tensile stresses are not allowed ($M_1, M_2 = 0$ for $\varepsilon_{\mathrm{I}} > 0$). The magnitude of mesoscale elastic constants is 10–100 MN m^{-1} (Pritchard, 1980b), and they allow the ice to deform up to yield stresses. The original expressions for the bulk and shear modulus were $M_1 = 10^7 \tilde{h}$ N m^{-2}, $M_2 \approx \frac{1}{2}M_1$ (Coon and Pritchard, 1974). The compressive elastic strength is $\sigma_c \approx 0.1$ MN m^{-1} (Pritchard, 1980b), and therefore mesoscale elastic strains remain less than about 10^{-3} (i.e., less than 100 m across 100 km distances). Note that in small-scale sea ice mechanics the elastic constants and compressive strength are one to two orders of magnitude larger, in three dimensions: $M_1 \approx 3$ GN m^{-2}, $M_2 \approx 0.4$ GN m^{-2}, $\sigma_c \approx 2$ MN m^{-2} (Mellor, 1986). The landfast ice problem is a suitable area in which to apply the theory of elasticity.

The AIDJEX *plastic model* is based on the mechanics of ridging. Compressive strength is obtained by equating the plastic work done in ridging with the creation of potential energy and losses due to friction between ice blocks (Rothrock, 1975a). The rate of loss of energy in ridging is $R_p + R_f = \sigma_{\mathrm{I}}\dot{\varepsilon}_{\mathrm{I}} + \sigma_{\mathrm{II}}\dot{\varepsilon}_{\mathrm{II}}$, where R_p represents

the creation of potential energy and R_f represents friction. The potential energy portion comes from the redistribution of ice thickness as (see Eqs. 2.2 and 3.41):

$$R_p = \frac{dE_p}{dt} = c_p \int_0^\infty h^2 \psi' \, dh = |\dot{\varepsilon}| \chi_d(\varphi) P_p \tag{4.24}$$

where $P_p = c_p \int_0^\infty h^2 \psi' \, dh$ is potential energy produced per unit area and unit strain in pure convergence, $c_p = \frac{1}{2}\rho g(\rho_w - \rho)/\rho$, and ψ' gives thickness rearrangement in ridging (see Eq. 3.41), expressed as the sum of loss and gain as $\psi' = -\psi'_- + \psi'_+$. In the AIDJEX thickness distribution model, ridging transfers thin ice to ridged ice k times as thick. Therefore, $\psi'_-(h_1) = kh_1/(k-1)$ and $\psi_+(h_2) = h_2/(k-1)$, $h_2 = kh_1$ for those thicknesses h that take part in building ridges.

To ascertain the frictional losses in ridge building, a Coulomb model is used where the frictional force equals the weight of the ice times the coefficient of sliding friction μ (Rothrock, 1975a). In building a ridge, the frictional force per unit length is:

$$F_f = \mu\rho g \frac{h_s^2}{2\tan\varphi_s} + \mu_w(\rho_w - \rho)g \frac{h_k^2}{2\tan\varphi_k} \tag{4.25}$$

where h_s, φ_s, h_k, φ_k are the sail height, sail slope, keel depth and keel slope of ridges (see Figure 2.21), and μ and μ_w are the coefficients of dry and wet friction, respectively. Assuming isostatic balance and reasoning that $\mu \approx \mu_w$, the sail term becomes small compared with the keel term and can be neglected. Then for ridging ice of thickness h_1:

$$F_f = \frac{\mu(\rho_w - \rho)g}{2\tan\varphi_k} \left(\frac{\rho(k-1)}{\rho_w}\right)^2 h_1^2 = c_f h_1^2 \tag{4.26}$$

In the ridging process the loss of ice of thickness h_1 is $h_1 k/(k-1)$ (see Eq. 3.38), and consequently the frictional energy loss in ridging becomes:

$$R_f = |\dot{\varepsilon}| \chi_r(\varphi) P_f, \quad P_f = c_f \int_0^\infty \frac{k}{k-1} h^2 \psi'_-(h) dh \tag{4.27}$$

The compressive strength of drift ice is then obtained as the sum of work done to increase the potential energy and overcome the friction. In pure compression, $|\dot{\varepsilon}| = |\dot{\varepsilon}_1|$, $\chi_d = 1$ and $R_p + R_f = \sigma_1 \dot{\varepsilon}_1$, and since the loss and gain of ice must balance, the potential energy production can be written in terms of ψ'_-. We have:

$$P = P_p + P_f = \left(kc_p + \frac{k}{k-1} c_f\right) \int_0^\infty h^2 \psi'_-(h) \, dh \tag{4.28}$$

The ratio of frictional losses to potential energy is thus

$$\Gamma = \mu \frac{k-1}{\tan\varphi_k} \cdot \frac{\rho}{\rho_w} \tag{4.29}$$

If the thickness of ice consumed in ridging is constant (h_1), for $\psi'_-(h_1) = kh_1/(k-1)$, we have

$$P \propto h_1^2 \tag{4.30}$$

Closing of leads does not form ridges, and therefore, as long as that alone takes place in convergence, the strength of the ice field is zero. It is up to the thickness redistribution model to state when ridging is initiated; if the lower 15% tail is allowed to deform, ice strength starts to build up at $A = 0.85$.

The value of compressive strength can be estimated from Eq. (4.26), and the result using the original parameters is $P \approx 5\,\text{kPa}$ for $h_1 = 1\,\text{m}$. In the original work of Rothrock (1975a), the key parameters were chosen as $\mu = 0.1$ and $k = 5$ resulting in $\Gamma \approx 1$. Later, it has become clear from model tuning that $\Gamma \gg 1$ and both μ and k should be larger by a factor of about 3. Thus the original strength is one order of magnitude too small. Pritchard (1977) obtained $P = 40\,\text{kPa}$ based on fitting model simulations with kinematics data. The shape of the yield curve still depends on the form of the ridging function $\chi_r(\varphi)$, which is unknown. Rothrock (1975a) suggested two possibilities for the yield curve: a teardrop shape (Figure 4.5) and a lens shape. Pritchard (1977) used the AIDJEX model and concluded that a wedge-shaped (Figure 4.5) or a square yield curve $[(0,0),(0,-\sigma_s),(-\sigma_s,-\sigma_s),(0,-\sigma_s)]$ could better reproduce ice dynamics in the Beaufort Sea. Several theoretical or modelling studies have been performed about the yield curve with no clear conclusive results so far (e.g., Ukita and Moritz, 1995; Wang, 2007).

4.3.4 Hibler's viscous–plastic rheology

Hibler's (1979) approach to the plastic flow solution involved a viscous–plastic rheology. In essence, no new physics were introduced, but the solution was very elegant. It satisfies the qualitative requirements for a proper rheology of drift ice and is an excellent tool for numerical modelling since it allows an explicit solution for stress as a function of strain rate. Most numerical sea ice models basically use this rheology, and its parameters have been tuned for different basins and scales based on model simulations and field data (Figure 4.7).

The yield curve is an ellipse in the principal stress space (Figure 4.5), for reasons to be explained below. To locate in the III quadrant, the centre point of the ellipse must be shifted down there along the line $\sigma_1 = \sigma_2$, and fixing zero stress for pure divergence, the centre must be at $(-\frac{1}{2}P, -\frac{1}{2}P)$. With aspect ratio e, the elliptic yield curve is written:

$$F(\sigma_1,\sigma_2) = \left(\frac{\sigma_1+\sigma_2+P/2}{P/2}\right)^2 + \left(\frac{\sigma_1-\sigma_2}{P/(2e)}\right)^2 - \sigma_Y \tag{4.31a}$$

The associated flow rule gives:

$$\dot{\varepsilon}_1 = \lambda\frac{\partial F}{\partial \sigma_1} = \lambda\left[\frac{2(\sigma_1+\sigma_2+P/2)}{(P/2)^2} + \frac{2(\sigma_1-\sigma_2)}{[P/(2e)]^2}\right] \tag{4.31b}$$

$$\dot{\varepsilon}_2 = \lambda\frac{\partial F}{\partial \sigma_2} = \lambda\left[\frac{2(\sigma_1+\sigma_2+P/2)}{(P/2)^2} + \frac{2(\sigma_1-\sigma_2)}{[P/(2e)]^2}\right] \tag{4.31c}$$

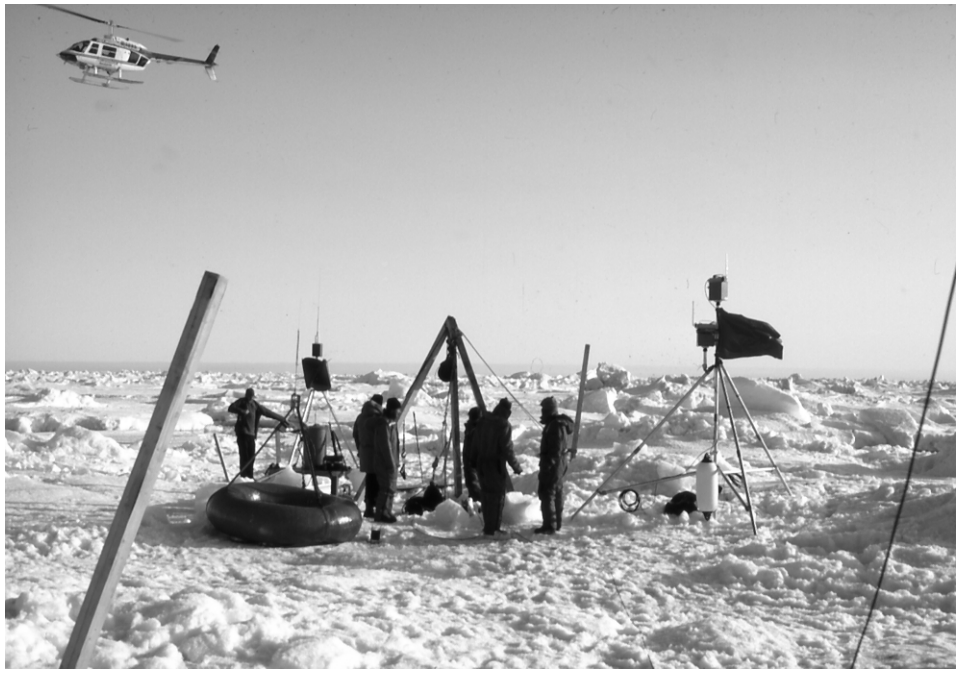

Figure 4.7 Field experiment data are used for high quality research of sea ice mechanical phenomenology and for tuning rheological parameters. Large-scale stresses cannot be measured directly, but examined from measurements of ice state and ice kinematics. The photograph shows an automatic drifting station in the MIZEX-83 experiment, Greenland Sea.

Solving Eq. (4.31) for σ_1 and σ_2 and transforming to a fixed coordinate system (to do this we need to assume that the principal stresses and principal strain-rates are parallel) gives the rheological law:

$$\boldsymbol{\sigma} = \frac{P}{2}\left(\frac{\dot{\varepsilon}_{\mathrm{I}}}{\Delta} - 1\right)\boldsymbol{I} + \frac{P}{2e^2\Delta}\dot{\boldsymbol{\varepsilon}}, \quad \Delta = \sqrt{\dot{\varepsilon}_{\mathrm{I}}^2 + e^{-2}\dot{\varepsilon}_{\mathrm{II}}^2} \tag{4.32}$$

Thus, with elliptic yield curves, the stress can be expressed as an explicit function of the strain-rate, which is a great advantage in analytic and numerical modelling. We also see that the plastic stress consists of unconfined pressure term $-P/2$ and yield terms for convergence and shear, which formally resemble viscous stresses with bulk and shear viscosities (see Eq. 4.14):

$$\zeta = \frac{P}{2\Delta}, \quad \eta = \frac{P}{4\Delta e^2} \tag{4.33}$$

respectively. But these viscosities are the limiting case of "plastic viscosities" and the resulting stresses are rate independent (the viscosities are homogeneous functions of order -1 of the strain rate invariants). In fact, as shown in Section 4.2, nonlinear

viscous power laws with $\zeta, \eta \propto \Delta^{n-1}$ would result in the Hibler plastic law as $n \to 0$. The size of the yield curve defines the overall ice strength:

$$P = P^* h \exp[-C(1 - A)] \tag{4.34}$$

where P^* and C are constants. The strength is directly proportional to ice thickness but highly sensitive to ice compactness. Comparing with the AIDJEX model ice strength (see Section 4.3.3), both are highly sensitive to ice compactness, with different formulations, but the main difference is in the thickness relationship, which is linear in the Hibler model and quadratic in the AIDJEX model.

This plastic rheology thus contains three parameters: the compressive strength, P^*, the strength reduction constant for lead opening, C, and the aspect ratio of the yield ellipse, e. In exact terms, P^* is the compressive strength of compact ice of unit thickness, the inverse of C gives the e-folding scale for ice strength as a function of compactness, and the aspect ratio is related to the ratio of compressive strength to shear strength (in pure shear flow, this ratio is $2e$).

Inside the yield curve a linear viscous law is employed. This is done by writing the viscosities as $\zeta = \frac{1}{2} P/\Delta_0$, $\eta = \zeta/e^2$ and including an unconfined pressure term $-P/2$:

$$\boldsymbol{\sigma} = \left(\frac{P}{2\Delta_0}\right)\dot{\varepsilon}_{\mathrm{I}}\boldsymbol{I} + 2\left(\frac{P}{4\Delta_0 e^2}\right)\dot{\boldsymbol{\varepsilon}} - \left(\frac{P}{2}\right)\boldsymbol{I} \tag{4.35}$$

Here Δ_0 is a fixed scaling parameter, which gives the viscous stress to be equal with the plastic stress, when $\Delta = \Delta_0$. This parameter represents the largest allowed value for the invariant Δ in the viscous regime, and can be called *the maximum viscous creep invariant*.

This rheology includes a notable artefact. The pressure term is enough to force expansion by slow creep for a stationary ice field with free boundaries (i.e., ice patch would have tendency to spread due to its own mass). However, this is not known to occur. The pressure term is necessary to put the ellipse into the right quadrant in the principal axes system and should be used with care inside the yield curve. A more recent formulation overcomes this problem by letting $\boldsymbol{\sigma} \to 0$ (instead of $-\frac{1}{2} P\boldsymbol{I}$) as $|\dot{\boldsymbol{\varepsilon}}| \to 0$ (Hibler, 2001).

A major advantage with viscous models is that they depend on the strain-rate and therefore are easily combined with strain-rate-formulated plastic flow rules Clearly, Eqs. (4.32) and (4.35) combined into

$$\boldsymbol{\sigma} = \frac{P}{2}\left[\frac{\operatorname{tr}\dot{\varepsilon}_{\mathrm{I}}}{\max(\Delta, \Delta_0)} - 1\right]\boldsymbol{I} + \frac{P}{2e^2 \max(\Delta, \Delta_0)}\,\dot{\boldsymbol{\varepsilon}} \tag{4.36}$$

At $\Delta = \Delta_0$, the viscous and plastic stresses meet. Eq. (4.36) presents Hibler's viscous–plastic rheology. In addition to the plastic law parameters, the creep rate Δ_0 is the fourth parameter of the rheology, but its role is technical rather than physical. The level of Δ_0 needs to be kept well below common strain rates to allow a good approximation for plastic flow.

Normal levels for the plastic parameters of Hibler (1979) rheology are $P^* = 25\,\text{kPa}$, $C = 20$, and $e = 2$ (Table 4.2). The strength constant P^* is the principal plastic rheology parameter. It has ranged from 5 to 50 kPa. In the original model paper (Hibler, 1979) it was 5 kPa (the low level was necessary because 8-day averaged winds were used). More recently, Arctic ice models have used the level of about 25 kPa. In the Baltic Sea, model outcome comparison with SAR ice kinematics has resulted in 10–40 kPa, with 27.5 kPa chosen as a working standard level (Leppäranta *et al.*, 1998). Comparisons with sea surface elevation in open water and compact ice cases have shown that the strength could be as high as 100 kPa (Zhang and Leppäranta, 1995). Parameters e and C are usually fixed to the original values. The aspect ratio e provides significant shear strength and the parameter C provides the sensitivity of the strength to compactness, but no serious efforts have been published for their quantification.

The maximum creep parameter Δ_0 must be taken much smaller than typical strain-rates to have a good approximation of plastic flow. In the Central Arctic, long-term strain rates are of the order of $10^{-7}\,\text{s}^{-1}$, which can be taken as an upper limit for the maximum creep. If $\Delta_0 \sim 10^{-5}\,\text{s}^{-1}$, then the solution is actually that for a linear viscous fluid.

Example The cavitating fluid (Flato and Hibler, 1990) model can be derived as a special case of the Hibler (1979) rheology where $e \to \infty$. The rheology then becomes:

$$\boldsymbol{\sigma} = \frac{P}{2}\left(\frac{\dot{\varepsilon}_\text{I}}{\max(\dot{\varepsilon}_\text{I0}, |\dot{\varepsilon}_\text{I}|)} - 1\right)\boldsymbol{I}$$

where $\dot{\varepsilon}_\text{I0}$ is the maximum allowed viscous convergence rate. The plastic flow is here given by[5] $\sigma = \frac{1}{2}[\text{sgn}(\dot{\varepsilon}_\text{I}) - 1]P$ for $|\dot{\varepsilon}_\text{I}| \geq |\dot{\varepsilon}_\text{I0}|$, while for viscous flow ($|\dot{\varepsilon}_\text{I}| < |\dot{\varepsilon}_\text{I0}|$), $\sigma = \zeta\dot{\varepsilon}_\text{I} - \frac{1}{2}P$ where the bulk viscosity is $\zeta = \frac{1}{2}P/|\dot{\varepsilon}_\text{I0}|$. The yield curve has thus shrunk into two points, origin for tensile stress and $(-P, -P)$ for compression.

Recently an anisotropic version of the viscous-plastic model has been developed to take into account the geometric structure of lead patterns (Hibler and Schulson, 2000).

Table 4.2 Parameters of the viscous-plastic ice rheology of Hibler (1979).

Parameter	Notation and standard	Range
Compressive strength	$P^* = 25\,\text{kPa}$	10–100 kPa
Yield ellipse aspect ratio	$e = 2$	$1 < e \ll \infty$
Compaction hardening	$C = 20$	$1 \ll C \ll \infty$
Maximum creep	$\Delta_0 = 2 \cdot 10^{-9}\,\text{s}^{-1}$	$\Delta_0 < 10^{-7}\,\text{s}^{-1}$

[5] sgn is the sign function: $\text{sgn}(x) = 1$ for $x > 0$, 0 for $x = 0$, or -1 for $x < 0$.

4.4 GRANULAR FLOE COLLISION MODELS

The idea of floe collisions as the basis for sea ice rheology was introduced in the 1970s (Ovsienko, 1976). The exact physical formulation was presented by Shen *et al.* (1986), who derived an analytical solution for rheology when spatial random fluctuations in ice velocity in shear flow give rise to floe collisions, which further transmit stresses within the ice field (Figure 4.8). Ice floes were taken as uniform size circular disks, diameter d, and thickness h, and the frequency of collisions depends on the level of velocity fluctuations and ice compactness. The nature of the collisions is described by the restitution or inelasticity coefficient κ ($0 \leq \kappa \leq 1$, with $\kappa = 1$ for perfect elasticity).

The stress generated by the collisions is dictated by the momentum transfer rate within the system. To close the system the level of random velocity fluctuations needs to be determined. This is done by means of the kinetic energy equation, which provides the fluctuation level on the basis of energy dissipation in the deformation of ice. Thus, the fluctuation level is zero if and only if deformation is zero. These collisions lead (via averaging) to the continuum rheology (see Shen *et al.*, 1986, 1987 for a detailed derivation):

$$\boldsymbol{\sigma} = m(1+\kappa)\frac{A^{3/2}}{\sqrt{A_0}-\sqrt{A}}\left(f_1\boldsymbol{I}+f_2\dot{\boldsymbol{\varepsilon}}'\right) \tag{4.37}$$

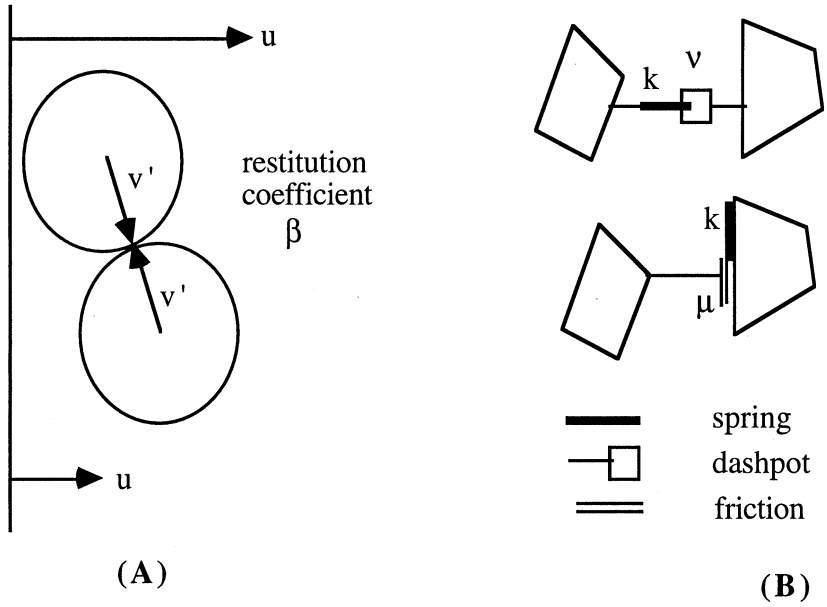

Figure 4.8 Floe–floe interaction: (a) the floe collision model; and (b) the discrete particle model. (a) From Shen *et al.* (1986) and (b) from Hopkins (1994).

where $m = \frac{1}{4}\pi\rho h d^2$ is the mass of an ice floe, $A_0 = \pi/(2\sqrt{3})$ is equal to the maximum compactness of uniform circular floes, and f_1 and f_2 are viscosities. These are expressed as:

$$f_1 = \frac{1}{4\pi}\frac{v}{d}\dot{\varepsilon}_{\mathrm{I}} - \frac{\sqrt{2}}{\pi^2}\left(\frac{v}{d}\right)^2, \quad f_2 = \frac{1}{6\pi}\frac{v}{d} \tag{4.38}$$

where v' is the velocity fluctuation level obtained from:

$$\begin{aligned} \frac{v'}{d} &= \sqrt{k_1^2 - k_2} - k_1, \\ k_1 &= \left(\frac{4\sqrt{2}}{\pi^2(1-\kappa)} - \frac{2\sqrt{2}}{\pi}\right)\dot{\varepsilon}_{\mathrm{I}} \\ k_2 &= \left(\frac{1}{4} - \frac{2}{\pi(1-\kappa)}\right)\dot{\varepsilon}_{\mathrm{I}}^2 + \left(\frac{1}{8} - \frac{2}{3\pi(1-\kappa)}\right)\dot{\varepsilon}_{\mathrm{II}}^2 \end{aligned} \tag{4.39}$$

The derivation is based on the assumption $v'/d \gg |\dot{\boldsymbol{\varepsilon}}|$. Note that v'/d is a first-degree homogeneous function of the strain-rate invariants. Then it can be concluded that the rheology is of the general viscous form (4.14) with $p = 0$, bulk and shear viscosities are finite and proportional to the strain-rate, and consequently stress is quadratic in the strain-rate. The material parameters, which show up in the rheology, are floe characteristics (ρ, h, d), ice compactness, and restitution coefficient $\kappa \sim 0.9$. Also note that the quadratic dependence is of the form $\sigma \propto \eta(\dot{\varepsilon}_{\mathrm{I}}, \dot{\varepsilon}_{\mathrm{II}})\dot{\varepsilon}$ not $\sigma \propto \dot{\varepsilon}^2$ as in the last term of the Reiner–Rivlin model (Eq. 4.12).

The collision model integrates kinematics within a drift ice particle into a large-scale stress field. It is in principle correct. The stress level is very low for compactness less than 0.9, but there is a singularity as $A \to A_0$. In reality, when the stress level has reached the strength of individual floes or the plastic yield strength, floes break and override, and the collision model is no longer valid. This supports the physical picture that ice stress only becomes important when an ice field becomes compact; stresses then arise due to friction between floes and formation of hummocks and ridges. There is another singularity when $\kappa \to 1$ (i.e., when ice floes become fully elastic) but this limit is mathematical rather than physical.

Inelastic floe collisions are incapable of transmitting large stresses. Lu *et al.* (1989) merged the floe collision model with a plastic model across the marginal ice zone's (MIZ) interior pack boundary, but the results did not reveal any new qualitative features about ice dynamics. However, collision rheology correctly represents the behaviour of drift ice at compactness levels up to *ca* 0.7–0.9, and its low stress levels explain why it is so easy for the ice pack to close up. Shen *et al.* (1987) examined observed kinematics during the Marginal Ice Zone Equipment (MIZEX-83) in the Greenland Sea and found a clear connection between predicted and observed velocity fluctuations (Figure 4.9).

Collision rheology gives a functional relationship between the strength of ice and ice compactness (Eq. 4.37): the factor is $B(A) = A^{3/2}/(\sqrt{A_0} - \sqrt{A})$. This becomes singular as $A \to A_0$ ($\approx$0.907 for uniform circular floes), and $B(0.7) \approx 5.1$, $B(0.85) \approx 25.8$, $B(0.9) \approx 231.9$. Thus closing to $A = 0.9$ the change is very sharp (Figure 4.10).

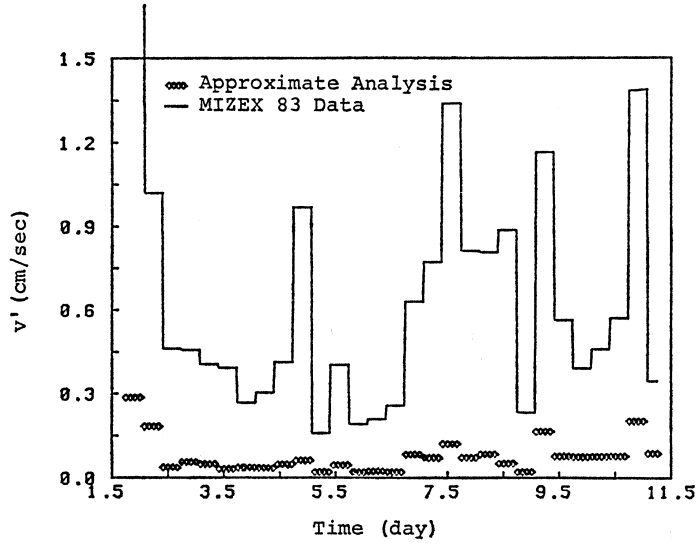

Figure 4.9 Velocity fluctuation level according to measurements and Monte Carlo simulations based on the measured strain rate. The field data are from MIZEX-83, Greenland Sea. From Shen *et al.* (1987).

Example Harr (1977) Consider the transmission of forces across a line of unit width. At any point a force $F' > 0$ is or is not experienced, depending on whether there is, respectively, material contact or a void. For N points, the probability distribution of the number of $F' > 0$ points is binomial with a probability $p^{(N)}$. Increasing N, the Poisson distribution results (e.g., Feller, 1968), and the number of n forces $F' > 0$ has the probability:

$$p_n = \frac{\Gamma^n}{n!} e^{-\Gamma}$$

where Γ is the Poisson distribution parameter, $\Gamma = \lim_{N\to\infty} Np^{(N)}$. Since the probability of void must be equal to the relative amount of open water, we have $p_0 = 1 - A = e^{-\Gamma}$ and consequently $\Gamma = -\log(1 - A)$. This becomes singular as $A \to 1$; however, somewhere at $A < 1$ the ice floes break and pressure ice formation begins. For $A = 0.7$ or 0.99, Γ is 1.2 or 4.6, respectively, and the singularity is therefore very sharp. Mean and variance are equal to Γ, so the stress level is proportional to $-\log(1 - A)$. Although stress increases with compactness, its relative variability decreases and the coefficient of variation (standard deviation divided by the mean) is $\Gamma^{-1/2}$. If the mean stress level is $\tilde{\sigma}$ and compactness is A, the range between the standard deviation and the mean is $\tilde{\sigma}(1 \pm \Gamma^{1/2})$ and the probability of $\sigma = n\tilde{\sigma}$ is $\Gamma^n e^{-\Gamma}/n!$. Overall, this reasoning does not hold when contacts between floes disappear, but the model illustrates how the stress field starts to change from a collisional system to a system, in which stress is transmitted between ice floes in contact. The stress level from loose to dense contact fields increases several times (Figure 4.10).

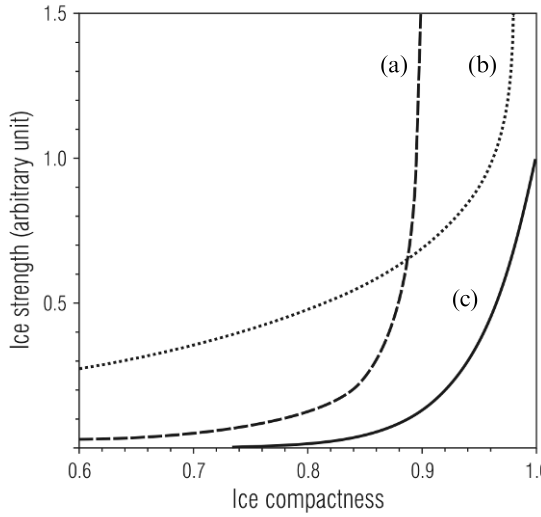

Figure 4.10 The stress level as a function of compactness for (a) floe collision models (Shen *et al.*, 1986), (b) floe contact models based on Harr (1977), and (c) standard version of Hibler (1979) sea ice rheology.

A more general approach to a floe–floe interaction system is provided by so-called *discrete particle models*, where a mechanical model is constructed for the interactions and a simultaneous solution for a large number (thousands) of floes is obtained numerically (Hopkins and Hibler, 1991; Løset, 1993; Hopkins, 1994). This has the potential to improve the understanding of the geophysics of sea ice dynamics and provide possibilities to parameterize continuum models from individual floe–floe interaction processes.

Hopkins (1994) constructed a model for ice blocks breaking from a parent ice sheet and accumulating into an ice ridge. Floe–floe interactions were modelled by a viscoelastic normal force (Kelvin–Voigt medium, Section 4.1) and Coulomb friction was used for the tangential force (Figure 4.9). The viscous part of the normal force takes care of the inelasticity of floe contacts in much the same way as did the restitution coefficient in the collision model. The tangential force initially has an elastic part for static friction but, once overcome, frictional sliding occurs.

The resulting ridges looked quite natural. Hopkins (1994) could also determine the mechanical energy budget to show that the potential energy created in ridge building is small compared with frictional losses. Figure 4.11 illustrates the result. The key parameter is the friction coefficient, and he used different dry (μ) and wet (μ_w) friction coefficients. Friction takes energy that is about one order of magnitude greater than that required to create potential energy. Comparable with potential energy are the inelastic losses in the deformation of ice blocks. Within the ranges $\mu \sim 0.4$–1.0 and $\mu_w \sim 0.3$–0.6 the energy budget was not much affected. Because potential energy and friction are correlated to some degree, the theory based on the potential energy is qualitatively good.

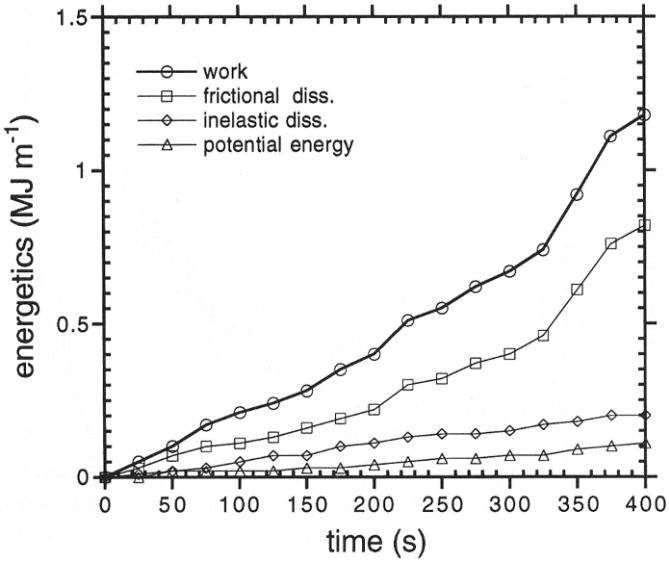

Figure 4.11 Energy budget in sea ice ridging as simulated by a discrete particle model. Ice thickness was 30 cm, the dry friction coefficient was 1.0, and the wet friction coefficient was 0.6.

From Hopkins (1994), printed by permission of the American Geophysical Union.

The results from discrete particle models have been good for local scale processes such as pressure ridge formation with its mechanical energy budget, which is key to understanding sea ice plastic rheology. Only recently have attempts been made to use them in full basin-scale sea ice dynamics problems. Comparison between continuum and discrete particle models for MIZ ice dynamics was made by Gutfraind and Savage (1997), giving similar results for both approaches. Rheem *et al.* (1997) used a mixed discrete particle–continuum approach for a study in the Sea of Okhotsk.

4.5 SCALING OF ICE STRENGTH

Scale questions have become a major issue in sea ice physics during the last 10 years. For cross-scale experiments, a particular campaign (SIMI, for Sea Ice Mechanics Initiative) was organized in the Beaufort Sea (e.g., Richter-Menge and Elder, 1998), and another took place in the Baltic Sea in 1997 (Haapala and Leppäranta, 1997b). In 2000, a dedicated symposium was organized around the scaling problem (Dempsey and Shen, 2001). Ice engineering has traditionally focused on the local scale (1–10 m), while in geophysical sea ice dynamics the scales of interest have been mesoscale to large scale (10^5–10^6 m). Between the engineering and geophysical scale there is the less known floe scale (10^2–10^3 m), through which the two main scales are interconnected (Figure 4.12).

In shallow regions interaction between ice and sea bottom and ice and shore must be considered. The forcing from drift ice fields causes scouring of the bottom and ice ride-up on shores (Figure 4.13).

In the length scales from 10^1 m to 10^5 m, there are bands where different material properties play the main role (Overland *et al.*, 1995; Weeks, 1998a): in the 10^1–10^2 m band these are fractures and thermal cracks; in the 10^2–10^3 m band these are individual ice floes; in the 10^3–10^4 m band these are floe assemblages and leads; and at larger scales the ice field becomes a continuum. Overland et al. (1995) proposed the concept of an hierarchical system to analyze sea ice over a wide range of scales (Figure 4.14). State variables at level $n+1$ vary smoothly and evolve slowly as compared with those at level n; they serve as constraints, driving forces, or boundary conditions on level n. The effect of $n-1$ level on level n, via interactions and averaging, is known as the aggregate problem. The hierarchy theory states that the levels $n+2$ or $n-2$ are on scales too large or too small to have a direct impact at level n.

The key quantity in the scaling problem is the ice stress or, rather, the ice strength. The local strength can be measured directly, while the mesoscale strength can only be derived from a mathematical model. It is known that, at its highest, the local strength is of the order of 1–10 MPa (Mellor, 1986), while the mesoscale strength is 10–100 kPa in compact ice. So, there is a difference of two orders of

Figure 4.12 Ice pressure has captured one ship in the Baltic Sea. The strength of the ship is known but it is very difficult to predict local scale ice forcing from geophysical scale sea ice dynamics.
From Ramsay (1949).

Figure 4.13 Ice ride-up on shore in the Bohai Sea. The diameter of the cylinders is about 1 m. In the front sediment-enriched ice floes are seen.
Photograph by Professor Zhijun Li, printed with permission.

magnitude. In a recent field study off the northern coast of Alaska, Richter-Menge *et al.* (2002) have shown clear connections between the small-scale and mesoscale internal stress fields in the ice.

Figure 4.15 presenting Sanderson's curve, gives a rough idea of how stress behaves as a function of the size of the loading area. Results from laboratory tests to large-scale drift ice models are included. A decrease in strength of two orders of magnitude from local scale to mesoscale is clearly seen in groups *C* and *D*. The form of dependence appears as a power law:

$$\sigma(L) \propto L^n \tag{4.40}$$

This power law is understandable when considering forcing by ice stress as a spatial Gaussian process $F = \tilde{F} + F'$, where the right-hand side shows mean and fluctuation with variance v^2. Taking the root-mean-square as a representative force, $F_{rms}(L) = \sqrt{\tilde{F}^2 + 4v^2 L}$, we have the stress over length scale as

$$\frac{F_{rms}}{L} = \sqrt{\left(\frac{\tilde{F}}{L}\right)^2 + \frac{4v^2}{L}} \tag{4.41}$$

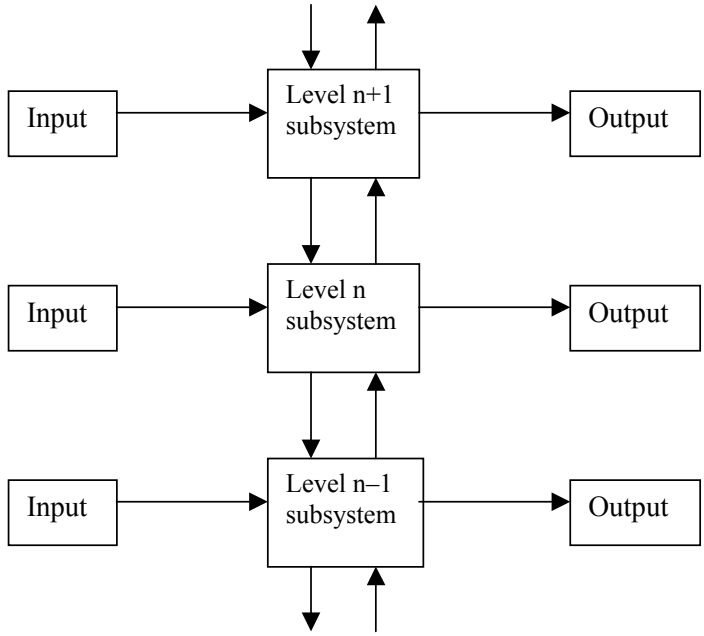

Figure 4.14 Structure of a hierarchical system.
Redrawn from Overland *et al.* (1995).

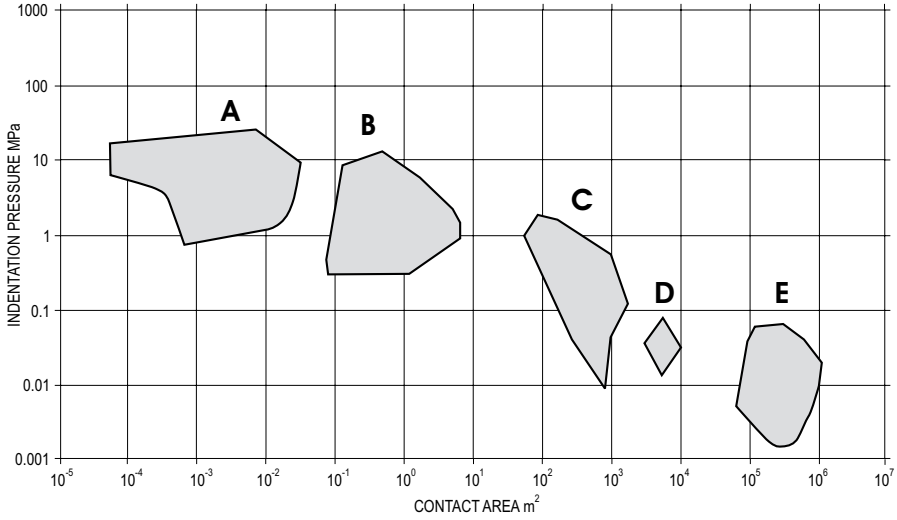

Figure 4.15 Sanderson's curve: the strength of sea ice vs. the loading area. A to C show local-scale tests, D shows Baltic Sea high-resolution ice drift models, and E shows Arctic Ocean mesoscale ice drift models.
From Sanderson (1988), but with Baltic Sea drift ice dynamics data (D) added.

Thus, if the fluctuation part is dominant, we have $\sigma(L) \propto L^{-1/2}$ but with no fluctuations the stress is scale independent. This scaling is discussed in more detail in the example below.

Example: stress as a spatial diffusion process (Harr, 1977). Consider the transmission of stress as a diffusion process due to the random interactions of ice floes. Start with the local stress σ_{yy} at origin and then progress along y-axis:

$$\frac{\partial \sigma_{yy}}{\partial y} = D \frac{\partial^2 \sigma_{yy}}{\partial x^2}$$

where D is the diffusion coefficient, its dimension is here length, and stress is considered dimensionless. Then $\sigma_{yy}(y)$ is a Gaussian process with zero mean and variance $2Dy$, and the probability density is:

$$p(x, y; D) = \frac{1}{\sqrt{4\pi D y}} \exp\left(-\frac{x^2}{4Dy}\right)$$

The peak stress is $(4\pi Dy)^{-1/2}$, and the width over which the stress acts is $(Dy)^{1/2}$, defined as the length scale when the stress is within one standard deviation from the peak value. Thus, the peak stress $\times$ width = constant; the peak stress decreases as $y^{-1/2}$, while width increases as $y^{1/2}$. One would anticipate that $D \propto d$ (floe size) since diffusion proceeds as floes interact, implying that one scale is the floe size in ice mechanics. The stress diffuses better the smaller the floe size, scaling in proportion to $d^{-1/2}$.

The relationship between mesoscale and local scale stresses was examined using a probabilistic approach by Kheysin (1978). He started from general relation for the stress in a region Ω:

$$\frac{1}{S}\int_{\Omega} (\nabla \cdot \boldsymbol{\sigma})\, d\Omega = \frac{1}{S}\int_{\partial\Omega} \boldsymbol{\sigma} \cdot \boldsymbol{n} dl = \frac{1}{S}\int_{\partial\Omega} \boldsymbol{t} dl \tag{4.42}$$

where S is the surface area of Ω and $\boldsymbol{t}$ is the outward force at the boundary of Ω. Taking Ω as a circle $\boldsymbol{C}$ with radius r and discretizing the integral, we have:

$$\tilde{\boldsymbol{\sigma}} = \frac{2}{nr}\sum_{m} \boldsymbol{t}^{(m)} \delta l^{(m)} = \frac{2}{r}\, Cov[\boldsymbol{t}, \boldsymbol{C}] = \frac{2}{r}\, Cor[\boldsymbol{t}, \boldsymbol{C}] \sqrt{\tilde{t}^2 \tilde{l}^2} \tag{4.43}$$

where Cov is covariance and Cor is correlation. Since $\bar{l}^2 = r/\sqrt{2}$, denoting by $\tau = \sqrt{\bar{t}^2}$ we have finally:

$$\sigma_{ij} = \sqrt{2}\, Cor[t_i, x_j]\tau \tag{4.44}$$

Kheysin (1978) proposed an exponential law for the spatial decay of correlation in the stress field, $\mathrm{Cor}[t_j, x_i] = \exp(-r/a_{ij})$, and reported on experimental data showing that the correlation radius (e-folding length) of normal stresses is of the order of magnitude of 10 km. It is clear that the correlation length is not a constant but varies

with the geophysical state of the ice. The exponential model differs in kind from the power law. It only gives small changes within the correlation radius and, thereafter, drops off faster than the power law.

In the geophysical regime, the main deformation processes involved in the convergence of compact ice are rafting and pressure ridge formation. They are quite different in kind and, consequently, the same similarity law is unlikely to be valid for both cases. The main internal resistance in rafting comes from the friction between rafting floes, while the accumulation of blocks in pressure ice formation has much larger friction, and a lot more potential energy has to be created. Leppäranta *et al.* (1998), in an effort to understand observed sea ice kinematics, showed that much lower resistance appeared in the rafting of thin ice (10–15 cm) than in the ridging of 30–40 cm thick ice. Using the Hibler (1979) viscous–plastic rheology, the compressive strength constant P^* was about 30 kPa for thick ice, but lower by nearly an order of magnitude for thin ice.

Hummocks and ridges normally form in ice thicker than 10–20 cm, while the thickest ice blocks found in ridges are around 1 m. Multi-year ice does not break down into pressure ice, but first-year ice and thinner ice in leads does. Consequently, empirical knowledge of mesoscale or large-scale sea ice mechanics is valid for thicknesses up to 1 m for the undeformed ice involved in deformation processes. Thin ice (thickness less than 10–15 cm) undergoes rafting in compression and the resulting internal friction is low. For thick ice, 10–100 cm, the internal stress in mesoscale dynamics, where hummocking and ridging cause the main loss of kinetic energy, follows the same rheological law. Compressive strength is proportional to the thickness raised to power n, $P \propto h^n$, with the exact value of n being an open question ($\frac{1}{2} \leq n \leq 2$). For a homogenous ice sheet, buckling failure would give $n = \frac{1}{2}$, crushing failure $n = 1$ (Coon, 1974), and in ridge formation $n = 2$ (Rothrock 1975a). In the continuum scales deformation events consist of a mixture of processes and the power can be taken as a tuning parameter.

The rheology question is now completed. The core is the plastic model, which is based on the yield curve with associated flow rule. The size of the yield curve corresponds to the overall strength of the ice, while its shape specifies the behaviour of different modes of deformation. Open drift ice fields can be treated with the free drift (no stress) approach. Between open and compact states rheology changes from stress free in a viscous manner. Rheology gives the internal stress tensor as a function of ice state, strain, and strain rate. Then, the divergence of stress steps into the equation of motion as a forcing term, as will be shown in Chapter 5.

5

Equation of drift ice motion

5.1 DERIVATION OF THE EQUATION OF MOTION

The law of conservation of momentum, or the equation of motion, is derived for drift ice from Newton's second law for a continuum in Section 5.1. By integrating through the thickness of ice, the two-dimensional equations can be obtained. Planetary boundary layers are presented in Section 5.2, and ice–ocean dynamic coupling is treated in Section 5.3. Scale analysis and dimensional analysis are studied in Section 5.4 to derive the magnitudes of the terms of the momentum equation and the key dimensionless quantities. Section 5.5 concerns the dynamics of a single ice floe based on rigid body mechanics.

5.1.1 Fundamental equation

In this chapter, the motion of drift ice is two-dimensional (as described in Chapter 3). Its equation of motion can now be derived using all three dimensions. For the sake of clarity, three-dimensional vectors and tensors are underlined (e.g., $\underline{\boldsymbol{u}} = (u, v, w)$, where w is the vertical velocity).

Figure 5.1 shows a photograph of ice motion past a lighthouse enclosed within drifting ice. In this case the ice is open and can drift without much interaction between ice floes. The general sea ice drift problem is schematically illustrated in Figure 5.2. The starting point is Newton's second law, $m\mathrm{d}\underline{\boldsymbol{u}}/\mathrm{d}t = \underline{\boldsymbol{F}}$, where $\underline{\boldsymbol{F}}$ represents the forcing acting on the ice. First, normal *continuum mechanics* modifications are introduced (e.g., Hunter, 1976):

(i) The mass field of continuum particles, or parcels, is given by mass per unit volume or density.
(ii) The forcing due to the internal stress field is $\underline{\nabla} \cdot \underline{\Sigma}$, where $\underline{\nabla} = (\partial/\partial x, \partial/\partial y, \partial/\partial z)$ (see Section 4.1.2).

M. Leppäranta, *The Drift of Sea Ice*, Springer Praxis Books,
DOI 10.1007/978-3-642-04683-4_5, © Springer-Verlag Berlin Heidelberg 2011

Vasilii Vladimirovich Shuleikin (1895–1979), Soviet oceanographer, sea ice physicist, and author of classic texts in the early development of the theory of sea ice drift. He was nominated Academician of the Soviet Academy of Sciences in 1946.
Reproduced with permission from the Russian State Museum of the Arctic and Antarctic, St Petersburg.

(iii) Choose an Eulerian or a Lagrangian frame – spatial or material grid – for the mathematical treatment of the dynamics.

In drift ice dynamics the Lagrangian frame is used with free drift theory and with observational techniques. But for the full problem with significant internal friction the Eulerian frame is normally taken.

The equation of motion for a continuum is the Cauchy equation:

$$\rho\left(\frac{\partial \underline{\boldsymbol{u}}}{\partial t} + \underline{\boldsymbol{u}} \cdot \underline{\nabla \boldsymbol{u}}\right) = \underline{\nabla} \cdot \underline{\Sigma} + \underline{F}_{ext} \tag{5.1}$$

where $\underline{F}_{\text{ext}}$ contains the external forcing on the ice in terms of force per unit volume. On the left side we have the local and advective acceleration.

Figure 5.1 Sea ice drifts pass the lighthouse Nahkiainen, northern Baltic Sea. The width of the lighthouse is about 5 m.

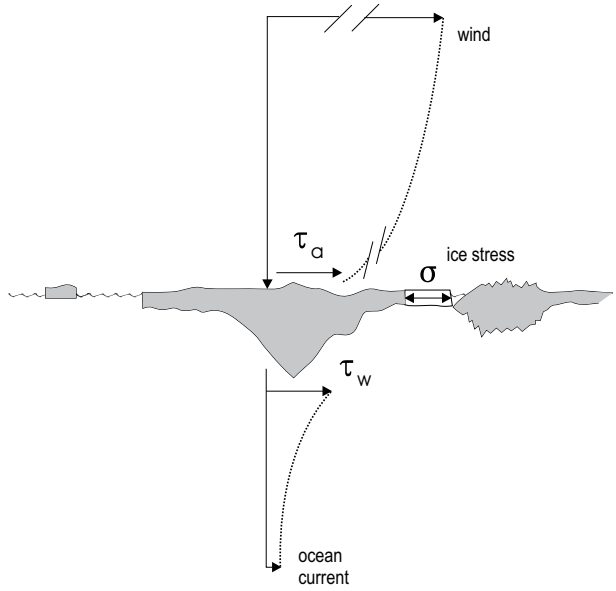

Figure 5.2 The ice drift problem. Ice is driven by atmospheric and oceanic flows and responds to forcing through its internal stress field.

Second, *geophysical effects* are introduced into the equation of motion:

(i) The Coriolis acceleration is added to the inertial term (e.g., Pond and Pickard, 1983; Cushman-Roisin, 1994).
(ii) Earth's gravity provides external body forcing, expressed as $\underline{\nabla}\Phi$, where Φ is the geopotential height of the sea surface.

Third, the *internal stress* of drift ice includes the stress due to interactions between ice floes, $\underline{\boldsymbol{\sigma}}$, and the pressure p from the surrounding air and water, $\underline{\Sigma} = \underline{\boldsymbol{\sigma}} - p\underline{\boldsymbol{I}}$, $p = p_a + \rho_w g D$ (see Eq. 4.3). Now we have the three-dimensional momentum equation for sea ice as:

$$\rho\left(\frac{\partial \underline{\boldsymbol{u}}}{\partial t} + \underline{\boldsymbol{u}} \cdot \nabla \underline{\boldsymbol{u}} + 2\underline{\boldsymbol{\Omega}} \times \underline{\boldsymbol{u}}\right) = \underline{\nabla} \cdot (-p\underline{\boldsymbol{I}} + \underline{\boldsymbol{\sigma}}) - \rho \underline{\nabla}\Phi \tag{5.2}$$

where $\underline{\boldsymbol{\Omega}} = (\Omega \cos\phi)\mathbf{j} + (\Omega \sin\phi)\mathbf{k}$ is the Coriolis vector, $\Omega = 7.292 \cdot 10^{-5}\,\mathrm{s}^{-1}$ is the angular velocity of the Earth, and ϕ is the latitude.

Example For an incompressible linear viscous fluid with constant viscosity η, the rheology reads $\underline{\boldsymbol{\sigma}} = -p\underline{\boldsymbol{I}} + 2\eta\underline{\dot{\boldsymbol{\varepsilon}}}$ (see Section 4.2). Then $\underline{\nabla} \cdot \underline{\boldsymbol{\sigma}} = \eta \underline{\nabla}^2 \underline{\boldsymbol{u}}$; that is, Eq. (5.2) becomes the Navier-Stokes equation on a rotating sphere:

$$\frac{\partial \underline{\boldsymbol{u}}}{\partial t} + \underline{\boldsymbol{u}} \cdot \underline{\nabla}\underline{\boldsymbol{u}} + 2\underline{\boldsymbol{\Omega}} \times \underline{\boldsymbol{u}} = -\frac{1}{\rho}\underline{\nabla} p + \nu \underline{\nabla}^2 \underline{\boldsymbol{u}} - \underline{\nabla}\Phi$$

where $\nu = \eta/\rho$ the kinematic viscosity of the fluid.

Let us take the sea surface as the zero reference surface, approximating it locally as a Cartesian xy-plane. Although this is not a fixed surface on the Earth, it is easy to see (e.g., by scale analysis) that forces due to vertical motion of the sea level are negligible in the dynamics of sea ice. The force due to the Earth's gravity or the gradient of the geopotential $\underline{\nabla}\Phi$ is then written as $\underline{\nabla}\Phi = g\underline{\nabla}'\xi$, where $\underline{\nabla}'$ is the three-dimensional gradient operator in the true horizontal–vertical coordinate system, and ξ is the sea surface elevation.

5.1.2 Vertical integration

The equation of motion (5.2) is next integrated through the thickness of the ice. The horizontal velocity of sea ice has no vertical structure, as discussed in Chapter 3. Therefore, integration of the acceleration terms, the left-hand side of Eq. (5.2), is straightforward: they are simply multiplied by the ice thickness h. Similarly, integration of the geopotential term results in multiplication by h.

Integration of the divergence of internal ice stress is more complicated. We have:

$$\int_{-h''}^{h'} \underline{\nabla} \cdot \underline{\Sigma}\, dz = -\int_{-h''}^{h'} \underline{\nabla} p\, dz + \int_{-h''}^{h'} \underline{\nabla} \cdot \underline{\boldsymbol{\sigma}}\, dz \tag{5.3a}$$

where h' is freeboard and h'' is draft. In component form:

$$\int_{-h''}^{h'} \begin{bmatrix} \dfrac{\partial \underline{\Sigma}_{xx}}{\partial x} + \dfrac{\partial \underline{\Sigma}_{yx}}{\partial y} + \dfrac{\partial \underline{\Sigma}_{zx}}{\partial z} \\ \dfrac{\partial \underline{\Sigma}_{xy}}{\partial x} + \dfrac{\partial \underline{\Sigma}_{yy}}{\partial y} + \dfrac{\partial \underline{\Sigma}_{zy}}{\partial z} \\ \dfrac{\partial \underline{\Sigma}_{xz}}{\partial x} + \dfrac{\partial \underline{\Sigma}_{yz}}{\partial y} + \dfrac{\partial \underline{\Sigma}_{zz}}{\partial z} \end{bmatrix} dz = -\int_{-h''}^{h'} \begin{bmatrix} \dfrac{\partial p}{\partial x} \\ \dfrac{\partial p}{\partial y} \\ \dfrac{\partial p}{\partial z} \end{bmatrix} dz + \int_{h''}^{h'} \begin{bmatrix} \dfrac{\partial \underline{\sigma}_{xx}}{\partial x} + \dfrac{\partial \underline{\sigma}_{yx}}{\partial y} + \dfrac{\partial \underline{\sigma}_{zx}}{\partial x} \\ \dfrac{\partial \underline{\sigma}_{xy}}{\partial x} + \dfrac{\partial \underline{\sigma}_{yy}}{\partial y} + \dfrac{\partial \underline{\sigma}_{zy}}{\partial z} \\ \dfrac{\partial \underline{\sigma}_{xz}}{\partial x} + \dfrac{\partial \underline{\sigma}_{yz}}{\partial y} + \dfrac{\partial \underline{\sigma}_{zz}}{\partial z} \end{bmatrix} dz \tag{5.3b}$$

The components of the three-dimensional stresses $\underline{\boldsymbol{\Sigma}}$ and $\underline{\boldsymbol{\sigma}}$ are underlined to differentiate them from the integrated stresses, which are used here to represent the two-dimensional stress (see Eq. 4.3).

Equation of motion on the sea surface plane

The first and second components, or the x- and y-components, of Eq. (5.3b) are first considered. They are for the sea surface plane. Since this plane is the zero reference plane, the horizontal pressure gradient ∇p integrates to zero in the water and thus becomes equal to the air pressure gradient ∇p_a. Then:

$$\int_{-h''}^{h'} \begin{bmatrix} \dfrac{\partial \underline{\Sigma}_{xx}}{\partial x} + \dfrac{\partial \underline{\Sigma}_{yx}}{\partial y} + \dfrac{\partial \underline{\Sigma}_{zx}}{\partial z} \\ \dfrac{\partial \underline{\Sigma}_{xy}}{\partial x} + \dfrac{\partial \underline{\Sigma}_{yy}}{\partial y} + \dfrac{\partial \underline{\Sigma}_{zy}}{\partial z} \end{bmatrix} dz = \int_{-h''}^{h'} \begin{bmatrix} \dfrac{\partial \underline{\sigma}_{xx}}{\partial x} + \dfrac{\partial \underline{\sigma}_{yx}}{\partial y} \\ \dfrac{\partial \underline{\sigma}_{xy}}{\partial x} + \dfrac{\partial \underline{\sigma}_{yy}}{\partial y} \end{bmatrix} dz + \Big|_{-h''}^{h'} \begin{bmatrix} \underline{\sigma}_{zx}(h) \\ \underline{\sigma}_{zy}(h) \end{bmatrix} - h \nabla \rho_a \tag{5.4}$$

Take the first term on the right-hand side. The two-dimensional internal ice stress $\boldsymbol{\sigma}$ is the vertical integral of the component $\boldsymbol{\sigma}_H$ in the three-dimensional stress (see Eq. 4.5). To get there the order of integration and derivation must be interchanged as was done for Eq. (4.11). Recalling this equation, we have for the x-component:

$$\begin{aligned} \int_{-h''}^{h'} \left(\frac{\partial \underline{\sigma}_{xx}}{\partial x} + \frac{\partial \underline{\sigma}_{yx}}{\partial y} \right) dz = {} & \frac{\partial \sigma_{xx}}{\partial x} + \frac{\partial \sigma_{xy}}{\partial y} - \left[\underline{\sigma}_{xx}(h') \left(1 - \frac{\rho}{\rho_w} \right) + \underline{\sigma}_{xx}(-h'') \frac{\rho}{\rho_w} \right] \frac{dh}{dx} \\ & - \left[\underline{\sigma}_{xy}(h') \left(1 - \frac{\rho}{\rho_w} \right) + \underline{\sigma}_{xy}(-h'') \frac{\rho}{\rho_w} \right] \frac{dh}{dy} \end{aligned} \tag{5.5}$$

Thus the integral is split into the x-component of the divergence of the two-dimensional stress $\nabla \cdot \boldsymbol{\sigma}$ and the x-component of the ice thickness gradient correction, denoted below by $\Theta_{h,x}$. The y-component is treated similarly.

The second term on the right-hand side of Eq. (5.4) comes from the surface boundary condition that the ice shear stress must match the shear stresses of air and water, respectively, τ_a and τ_w on ice:

$$\begin{bmatrix} \underline{\sigma}_{zx}(h') - \underline{\sigma}_{zx}(-h'') \\ \underline{\sigma}_{zy}(h') - \underline{\sigma}_{zy}(-h'') \end{bmatrix} = \boldsymbol{\tau}_a - (-\boldsymbol{\tau}_w) \tag{5.6}$$

Consequently, the integral of the divergence of the total stress $\underline{\Sigma}$ is in the sea surface plane:

$$\int_{-h''}^{h'} [\underline{\nabla} \cdot \underline{\Sigma}]_H \, dz = \nabla \cdot \boldsymbol{\sigma} - \boldsymbol{\Theta}_h + \boldsymbol{\tau}_a + \boldsymbol{\tau}_w - h \nabla p_a \tag{5.7}$$

where $\boldsymbol{\Theta}_h = \Theta_{h,x} \boldsymbol{i} + \Theta_{h,y} \boldsymbol{j}$. To evaluate the thickness gradient effect, one needs $\underline{\boldsymbol{\sigma}}(h')$ and $\underline{\boldsymbol{\sigma}}(h'')$ and, consequently, a full three-dimensional rheology of the ice sheet (see Section 4.1). But the thickness gradient is generally small enough for the correction term $\boldsymbol{\Theta}_h$ to be neglected, as is usually implicitly done in sea ice dynamics (e.g., Rothrock, 1975b; Coon *et al.*, 1980; Hibler, 1986; Leppäranta, 1998).

As in ocean dynamics, in the horizontal Coriolis acceleration the part arising from vertical motion, $w 2\Omega \cos\phi$, where ϕ is latitude, is very small compared with the part arising from horizontal motion. Consequently, in the horizontal motion the Coriolis acceleration is reduced to $f \boldsymbol{k} \times \boldsymbol{u}$, where $f = 2\Omega \sin\phi$ is the *Coriolis parameter*.

Denoting the coordinates of the true horizontal plane by (x', y'), the slope of the sea surface with respect to horizontal is:

$$\boldsymbol{\beta} = \boldsymbol{i} \frac{\partial \xi}{\partial x'} + \boldsymbol{j} \frac{\partial \xi}{\partial y'} \tag{5.8}$$

The geopotential gradient on the sea surface plane thus integrates into $\rho h \nabla \Phi = \rho h g \boldsymbol{\beta}$, usually called the *sea surface tilt*. Apart from shallow regions (depth less than the Ekman depth[1]), this term can be expressed in terms of the surface geostrophic current $\boldsymbol{U}_{wg}$ by (e.g., Pond and Pickard, 1983; Cushman-Roisin, 1994):

$$g \boldsymbol{\beta} = -f \boldsymbol{k} \times \boldsymbol{U}_{wg} \tag{5.9}$$

This is a convenient expression since geostrophic velocity is often also used as the reference in the ice–water friction law. In shallow waters the geostrophic approximation given by Eq. (5.9) does not hold due to the influence of bottom friction, but the explicit tilt expression must remain in the equation of motion. In fact, for deep basins this expression would also be preferable, but usually the non-geostrophic sea surface tilt is not known.

Finally, the general form of the equation of motion of sea ice on the sea surface plane is:

$$\rho h \left(\frac{\partial \boldsymbol{u}}{\partial t} + \boldsymbol{u} \cdot \nabla \boldsymbol{u} + f \boldsymbol{k} \times \boldsymbol{u} \right) = \nabla \cdot \boldsymbol{\sigma} + \boldsymbol{\tau}_a + \boldsymbol{\tau}_w - \rho h g \boldsymbol{\beta} - h \nabla p_a \tag{5.10}$$

Sometimes the factor ρh on the left-hand side is replaced by $\rho h(1 + \mu)$, where μ is the coefficient of added mass of water (e.g., Timokhov and Kheysin, 1987). This coefficient is, however, not used further below. Figure 5.3 shows a schematic force diagram of ice drift. Usually, wind is the driving force, and this is balanced by the ice–ocean drag and internal friction of the ice. Coriolis acceleration is smaller than

[1] The depth of the frictional influence of surface forcing in the ocean (e.g., Gill, 1982; Pond and Pickard, 1983); for sea ice it is typically 30–50 m.

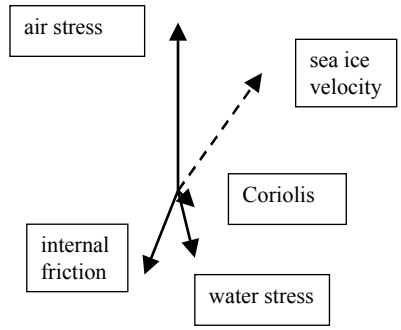

Figure 5.3 A typical diagram of major forces in drifting sea ice (northern hemisphere).

the three major forces and is always perpendicular to the ice motion. The other acceleration terms and sea surface tilt are smaller still and can influence in any direction.

Compared with vertically integrated ocean circulation models (see, e.g., Pond and Pickard, 1983), the following points are noted in the horizontal momentum equation: ice thickness corresponds to sea depth; ice–water friction corresponds to bottom friction; and the internal friction of ice corresponds to horizontal turbulent friction. In contrast to sea ice dynamics, in vertical integration the constancy of velocity does not hold in ocean circulation, resulting in a biased momentum balance due to the inaccuracy of the advection integral.

Vertical equation of motion

The vertical component of the integrated total stress divergence is from Eq. (5.3)

$$\int_{-h''}^{h'} \left(\frac{\partial \underline{\Sigma}_{xz}}{\partial x} + \frac{\partial \underline{\Sigma}_{yz}}{\partial y} + \frac{\partial \underline{\Sigma}_{zz}}{\partial z} \right) dz = \int_{-h''}^{h'} \left(\frac{\partial \underline{\sigma}_{xz}}{\partial x} + \frac{\partial \underline{\sigma}_{yz}}{\partial y} \right) dz + \Big|_{-h''}^{h'} (\underline{\sigma}_{zz} - p) \qquad (5.11)$$

The last term is equal to the hydrostatic pressure of water directly below sea ice, $\rho_w g h''$. By scaling analysis, it is seen that this pressure is much greater than the integral term on the right-hand side: since $(\underline{\sigma}_{xz}, \underline{\sigma}_{yz}) \sim \tau_a$, the integral is $\sim \tau_a h/L \sim 1$ Pa while $\rho_w g h'' \sim 10^4$ Pa.

The vertical geopotential gradient is $g_z \cong g$ since the sea surface is very close to horizontal. Thus, multiplied by the ice density it integrates to $\rho g h$, which is comparable with the pressure at the ice bottom. It is easy to see (e.g., by scale analysis) that other terms in the vertical momentum equation are negligible. Consequently, the *vertical momentum equation* becomes Archimedes' law

$$\rho_w g h'' - \rho g h = 0 \qquad (5.12)$$

or $h''/h = \rho/\rho_w$. This equation corresponds to the vertical hydrostatic equation in ocean dynamics. Archimedes' law defines which portions of ice sheet are above and below the sea surface, but otherwise it is not needed in sea ice dynamics problems.

Boundary conditions

Consider a sea ice field Ω with a boundary curve Γ (Figure 5.4). The field is bounded by open water and solid medium (land or landfast ice), and the configuration changes with time, $\Omega = \Omega(t)$ and $\Gamma = \Gamma(t)$. The boundary conditions are:

$$\boldsymbol{\sigma} \cdot \boldsymbol{n} = 0 \qquad \text{open water boundary} \tag{5.13a}$$

$$\boldsymbol{u} \cdot \boldsymbol{n} \leq 0 \qquad \text{solid boundary} \tag{5.13b}$$

At the open water boundary,the ice does not support normal stresses and the motion of ice changes the boundary configuration. At the land boundary, the ice is allowed to stay or move away into the drift ice basin, but it is not allowed to override the solid boundary out from the basin. As soon as the ice has moved away (lost contact with the solid boundary), the solid boundary changes to the open water boundary.

The boundary conditions (5.13) are often replaced by a simplified form:

$$\text{Open water} \equiv \text{Ice with zero thickness} \tag{5.14a}$$

$$\boldsymbol{u} = 0, \text{ solid boundary} \tag{5.14b}$$

Equation (5.14a) removes the question of the open water boundary, while Eq. (5.14b) is the usual no slip condition used for viscous flows.

5.1.3 Drift regimes

In general, sea ice dynamics phenomena can be divided into three categories: (i) *stationary ice*; (ii) *drift in the presence of internal friction*, or drift of interacting ice floes; and (iii) *free drift*, or drift of non-interacting ice floes. Cases (ii) and (iii) were named by Zubov (1945) and correspond to the fields of close drift ice and scattered drift ice, respectively. Figure 5.5 shows ice displacement fields between two SAR mappings in a semi-enclosed basin. The ice is stationary close to shore, drifting free in the north at the ice edge, and experiencing a strong frictional resistance at the coast in south where the basin becomes narrower.

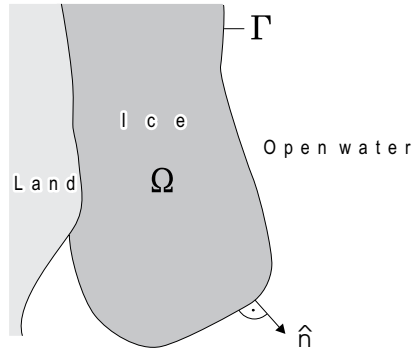

Figure 5.4 A sea ice field Ω with the boundary curve Γ consisting of open water and land sections.

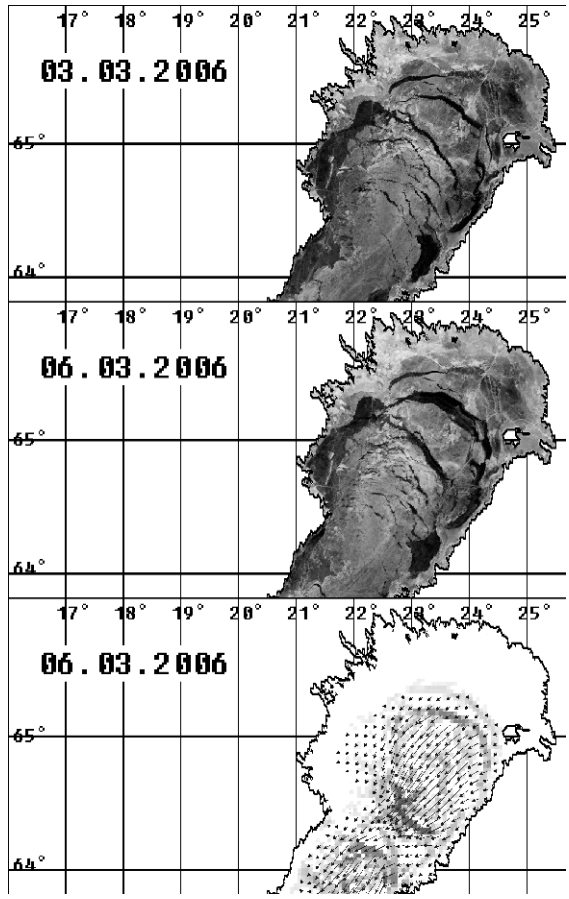

Figure 5.5 Two SAR images over the Bay of Bothnia, Baltic Sea (March 3rd and 6th, 2006), and the estimated motion vector field between the images.
Prepared by Dr. Juha Karvonen, Finnish Meteorological Institute, printed with permission (published in Finnish COSPAR report 2008, http://www.cospar.fi/Rep2008.pdf).

The drift ice dynamics problem can be approached in three ways: free drift solution, analytical zonal models of drift in the presence of internal friction, and full numerical models. These are the topics of Chapters 6, 7, and 8. In the present chapter, the momentum equation is further discussed and analyzed for external forcing, scales, and non-dimensional form.

5.1.4 Conservation of kinetic energy, divergence and vorticity

The conservation law of kinetic energy (per unit area) $q = \frac{1}{2}\rho h|\boldsymbol{u}|^2$ is obtained from the momentum equation by scalar multiplication by ice velocity (Coon and

Pritchard, 1979; Leppäranta, 1981b). This is quite straightforward, as done usually in fluid dynamics. For the internal friction term, the formula

$$\nabla \cdot (\boldsymbol{u} \cdot \boldsymbol{\sigma}) = \boldsymbol{u} \cdot \nabla \cdot \boldsymbol{\sigma} + \boldsymbol{\sigma} : \nabla \boldsymbol{u} = \boldsymbol{u} \cdot \nabla \cdot \boldsymbol{\sigma} + \mathrm{tr}(\boldsymbol{\sigma} \cdot \dot{\boldsymbol{\varepsilon}}) \tag{5.15}$$

is utilized, where the colon product is defined by $\boldsymbol{B}:\boldsymbol{C} = \Sigma_{ij} B_{ij} C_{ij}$ for two matrices $\boldsymbol{B}$ and $\boldsymbol{C}$. We have then the kinetic energy equation as:

$$\frac{\partial q}{\partial t} + \boldsymbol{u} \cdot \nabla q = -\mathrm{tr}(\boldsymbol{\sigma} \cdot \dot{\boldsymbol{\varepsilon}}) + \nabla \cdot (\boldsymbol{u} \cdot \boldsymbol{\sigma}) + \boldsymbol{u} \cdot \boldsymbol{\tau}_a + \boldsymbol{u} \cdot \boldsymbol{\tau}_w - \rho h g \boldsymbol{u} \cdot \boldsymbol{\beta} - h \boldsymbol{u} \cdot \nabla p_a \tag{5.16}$$

The left-hand side gives the local change and advection of kinetic energy, while the terms on the right-hand side are, respectively, (i) work done by the stress field including frictional dissipation, (ii) work done by the surrounding ice, (iii) input of kinetic energy from the atmosphere, (iv) exchange of kinetic energy with the ocean, (v) input of kinetic energy from the sea surface slope, and (vi) input from the atmospheric pressure gradient.

To illustrate term (ii), Gauss theorem says that for a region Ω with boundary Γ:

$$\int_\Omega \nabla \cdot (\boldsymbol{u} \cdot \boldsymbol{\sigma})\, \mathrm{d}\Omega = \int_\Gamma (\boldsymbol{u} \cdot \boldsymbol{\sigma}) \cdot \mathrm{d}\Gamma \tag{5.17}$$

This term can thus be understood as the transmission of stress across region boundaries.

Example: internal friction and kinetic energy balance a) For an ideal fluid, $\boldsymbol{\sigma} = -p\boldsymbol{I}$, $\mathrm{tr}(\boldsymbol{\sigma} \cdot \dot{\boldsymbol{\varepsilon}}) = p \nabla \cdot \boldsymbol{u}$ and $\nabla \cdot (\boldsymbol{u} \cdot \boldsymbol{\sigma}) = -\nabla \cdot (p\boldsymbol{u})$. There are no frictional losses, but the pressure field redistributes mechanical energy. If the fluid is incompressible, we have $\mathrm{tr}(\boldsymbol{\sigma} \cdot \dot{\boldsymbol{\varepsilon}}) = 0$ and $\nabla \cdot (\boldsymbol{u} \cdot \boldsymbol{\sigma}) = \boldsymbol{u} \cdot \nabla p$. b) For a linear viscous incompressible fluid, $\mathrm{tr}(\boldsymbol{\sigma} \cdot \dot{\boldsymbol{\varepsilon}}) = \eta \dot{\varepsilon}_{\mathrm{II}}^2$, which is the dissipation of kinetic energy due to viscous shear.

The input of kinetic energy from the wind is $\boldsymbol{u} \cdot \boldsymbol{\tau}_a = \rho_a C_a |\boldsymbol{U}_a| \boldsymbol{u} \cdot \boldsymbol{U}_a$. In purely wind-driven drift, ice velocity is approximately proportional to the wind velocity, and therefore input is proportional to the cube of the wind speed. The ice–water rate of exchange of kinetic energy is written as:

$$\boldsymbol{u} \cdot \boldsymbol{\tau}_w = \rho_w C_w |\boldsymbol{U}_w - \boldsymbol{u}| [\cos(\theta_w + \upsilon) |\boldsymbol{u}| \boldsymbol{U}_w| - |\boldsymbol{u}|^2] \tag{5.18}$$

where υ is the angle between ice motion and ocean current. If $\boldsymbol{U}_w = 0$, then $\boldsymbol{u} \cdot \boldsymbol{\tau}_w = -\rho_w C_w \cos\theta_w |\boldsymbol{u}|^3$; that is, the rate of energy loss to the ocean boundary layer is proportional to the cube of ice speed.

The mechanical energy budget evaluated from observations is illustrated in Table 5.1. The results show that the principal source is the wind and that energy is used to overcome ice–water friction and the internal friction of the ice. The ice thickness was about 50 cm and, therefore, the overall level of kinetic energy was 1–10 J/m^2. This is considerably less than the average gain and loss over 1 hour and, therefore, the timescale of the kinetic energy of sea ice is very short.

The energy budget has not been widely used in sea ice dynamics investigations, despite the fact that it would shed light on internal stress transfer and dissipation

Table 5.1 Kinetic energy budget of sea ice dynamics in the northern Baltic Sea (Leppäranta, 1981b). The values are in $\mathrm{mJ\,m^{-1}\,s^{-1}}$ and based on hourly data, acquired during a 2-week experiment.

	Mean	Standard deviation
Rate of change	0.3	1.6
Input from the wind	10.3	20.7
Input from the currents	2.3	5.7
Input from the sea surface tilt	0.1	0.5
Loss to the ocean boundary layer	8.4	29.3
Loss to the internal friction	6.0	13.8

mechanisms. Apart from short-term elastic events, drift ice does not store recoverable mechanical energy. A small fraction of the energy loss due to internal friction goes to potential energy of deformed ice but this energy is no more recoverable for ice motion.

The conservation laws of divergence $\dot{\varepsilon}_\mathrm{I}$ and vorticity $\dot{\omega}$ are obtained from the momentum equation by applying divergence and curl operators (respectively, $\nabla\cdot$ and $\nabla\times$):

$$\rho h\left[\frac{D\dot{\varepsilon}_\mathrm{I}}{Dt}+\nabla(\boldsymbol{u}\cdot\nabla)\cdot\boldsymbol{u}-f2\dot{\omega}\right]=\nabla\cdot(\nabla\cdot\boldsymbol{\sigma}+\boldsymbol{\tau}_a+\boldsymbol{\tau}_w-h\nabla p_a) \tag{5.19a}$$

$$\rho h\left[\frac{D2\dot{\omega}}{Dt}+(2\dot{\omega}+f)\nabla\cdot\boldsymbol{u}\right]=\nabla\times(\nabla\cdot\boldsymbol{\sigma}+\boldsymbol{\tau}_a+\boldsymbol{\tau}_w) \tag{5.19b}$$

Note that, in two-dimensional flow, vorticity is the vertical component of $\frac{1}{2}\nabla\times\boldsymbol{u}$. As in the case of kinetic energy, the inertial part or the left-hand sides are small and the main balance is between internal friction and surface stress terms.

Even though air and water are incompressible fluids, the Coriolis phenomenon causes divergence in surface stress. Therefore, the atmosphere and ocean are capable of producing divergence and vorticity in ice velocity. The physics are similar to the phenomenon known as "Ekman pumping" in the open ocean, where the divergence of surface stress sucks deeper water to the surface (e.g., Cushman-Roisin, 1994). In addition, the internal friction of ice and the inhomogeneity of the ice cover for surface roughness and thickness give rise to deformation and vorticity even in the presence of constant wind and ocean current.

5.2 ATMOSPHERIC AND OCEANIC BOUNDARY LAYERS

5.2.1 Planetary boundary layers

Sea ice lies between atmospheric and oceanic planetary boundary layers. These turbulent boundary layers comprise two main parts (e.g., Tennekes and Lumley,

1972): next to ice, a surface layer, where the stress is approximately constant, and an outer Ekman layer, where velocity rotates due to the Earth's rotation and stress decreases to zero with distance from the ice boundary. The full boundary-layer solution of velocity is constructed by matching the surface layer and Ekman layer solutions together, normally assuming steady-state conditions. The thickness of the planetary boundary layer[2] is ~1 km in the atmosphere and ~50 m in the ocean; this can also be referred to as the layer of frictional influence of the ice. In shallow seas, however, the Ekman layer is weak or lacking and the ice and bottom boundary layers must be matched together (this will be discussed more in Section 5.3).

Complex variable techniques are convenient for the planetary boundary layer velocities because of rotation effects (see Section 3.3). Horizontal and vertical velocity of fluid (air or seawater), $\hat{U} = \hat{U}_1 + \mathrm{i}\hat{U}_2$ and $\hat{W}$, respectively, are expressed in the Reynolds decomposition as:

$$\hat{U} = U + U', \quad \hat{W} = W + W' \tag{5.20}$$

where U and W are the time averages and U' and W' are the fluctuating components. The vertical shear stress is expressed as:

$$\tau = -\rho\langle U'W'\rangle = \rho K \frac{\partial U}{\partial z} \tag{5.21}$$

where $\langle\cdot\rangle$ is time averaging operator and K is kinematic eddy viscosity.

The steady state boundary layer equations are (e.g., Cushman-Roisin, 1994):

$$\mathrm{i}fU = \mathrm{i}U_g + \frac{1}{\rho}\frac{\partial \tau}{\partial z} \tag{5.22a}$$

$$\frac{\partial p}{\partial z} = -g\rho \tag{5.22b}$$

where U_g is geostrophic velocity and τ is vertical shear stress. The fluid at the outer boundary is assumed to be in geostrophic balance, and therefore the pressure gradient has been replaced by the geostrophic flow: $\nabla p = -\mathrm{i}\rho f U_g$. In shallow ocean waters this replacement cannot be done but the pressure gradient is taken as an external force. For the vertical direction the hydrostatic equation applies, and in barotropic flow the geostrophic velocity is independent of depth. At the top of the boundary layer, stress vanishes and, therefore, $U = U_g$, while, at the bottom of the boundary layer, velocity must be equal to the velocity of the boundary, $U = U_0$.

The atmospheric and oceanic planetary boundary layers have the following main differences:

(i) The densities of air and sea water differ (respectively, $\rho_a \approx 1.3\,\mathrm{kg\,m^{-3}}$ and $\rho_w = 1028\,\mathrm{kg\,m^{-3}}$ the density ratio being thus $\rho_a/\rho_w \approx 1.3 \cdot 10^{-3}$).

(ii) The velocities of air and water flows differ (respectively, $U_a \sim 10\,\mathrm{m\,s^{-1}}$ and $U_w \sim 10\,\mathrm{cm\,s^{-1}}$, the velocity ratio being $U_a/U_w \sim 10^2$).

[2] Planetary fluid boundary layer thicknesses scale as $f^{-1}(\tau/\rho)^{1/2}$ (e.g., Tennekes and Lumley, 1972).

(iii) The height of boundary layers differ (respectively $\delta_a \sim 1$ km and $\delta_w \sim 50$ m, the height ratio being $\delta_a/\delta_w \sim 20$).
(iv) Ridge sails are very small compared with the height of the atmospheric boundary layer but ridge keels are of the order of the oceanic boundary layer depth (respectively, $\delta_a \gg h_s$ and $\delta_w \sim h_k$).

In the presence of sea ice, its velocity ($\boldsymbol{u}$) serves as the boundary condition for both media. Since $U_a \gg u \sim U_w$, for the atmospheric boundary layer we may take $U_0 \cong 0$; but, for the oceanic boundary layer the condition must be $\boldsymbol{U}_0 = \boldsymbol{u}$. Thus, in pure dynamics ice and ocean form a coupled system, but wind stress acts as an external force.

The atmospheric boundary layer over sea ice has been extensively examined (Rossby and Montgomery, 1935; Brown, 1980; Joffre, 1984; Vihma, 1995; Andreas, 1998) (Figure 5.6). The oceanic boundary layer beneath sea ice is much less known (McPhee, 1986, 2008; Shirasawa and Ingram, 1991; Shirasawa and Leppäranta, 2009). This is partly due to greater observational difficulties, but more so to the uniqueness of the ice–water interaction. Atmospheric boundary layers have also been widely examined over land and open ocean and these results have been utilized in sea ice research as well.

Ekman layer

In the Ekman layer the eddy viscosity coefficient K can be taken as a constant and Coriolis acceleration is important. Consequently, velocity-turning takes place. We have:

$$if\,U = if\,U_g + K\frac{d^2U}{dz^2} \tag{5.23}$$

The general solution is $U = U_g + C_1\exp(\lambda_1 z) + C_2\exp(\lambda_2 z)$, where C_1 and C_2 are constants to be determined from the boundary conditions, and $\lambda_{1,2} = \pm\sqrt{if/(2K)}$. The boundary conditions are the no-slip condition ($U = U_0$) at the surface and the stress-free geostrophic velocity at the top. A more simple condition can be used for the upper boundary, $U \to U_g$ as $z \to \infty$, resulting in:

$$U = U_g + (U_0 - U_g)\exp\left\{-[1 + \mathrm{sgn}(f)i]\,\frac{\pi z}{D}\right\} \tag{5.24}$$

where $D = \pi\sqrt{2K/|f|}$ is the *Ekman depth*. At $z = D$, the latter term on the right-hand side has decreased to $\mathrm{e}^{-\pi} \approx 4\%$ from the boundary level and rotated the angle of π clockwise (anticlockwise) in the northern (southern) hemisphere.

Figure 5.7 illustrates the velocity distribution in the Ekman layers of the atmosphere and the ocean. For the atmosphere $U_0 \cong 0$. Starting from the top of the atmospheric boundary layer, velocity rotates to zero at the surface, counterclockwise in the northern hemisphere, and clockwise in the southern hemisphere. Surface stress now becomes:

$$\tau = \rho K\left.\frac{dU}{dz}\right|_{z=0} = \rho(U_g - U_0)[1 + i\,\mathrm{sgn}(f)]\,\frac{\pi}{D} \tag{5.25}$$

Figure 5.6 A mast (height 10 m) for atmospheric surface layer measurements. Velocity, temperature, and humidity are measured at several altitudes to determine the fluxes using the so-called profile method.

Surface layer

In the surface layer, the vertical shear stress is constant and velocity direction is constant. Here this direction is taken as the real axis. A velocity scale u_*, called the friction velocity, can be defined by:

$$\tau = \rho u_*^2 \tag{5.26}$$

and serves as the velocity scale for the surface layer. Comparing with the Ekman layer solution, we get the scaling relation $u_*^2 = K|U_g - U_0|2\pi/D$.

In neutral stratification, the length scale comes from Prandtl's *mixing length hypothesis* that states that the size of turbulent eddies scales with the distance from the boundary (i.e., the length scale is z; see Tennekes and Lumley, 1972). Therefore, $K \sim u_* z$ and, for the stress to be constant, the vertical velocity gradient is $\sim u_*/z$. In exact terms:

$$\frac{\partial U}{\partial z} = \frac{1}{\kappa} \cdot \frac{u_*}{z} \tag{5.27a}$$

where $\kappa \cong 0.4$ is the von Karman constant. A logarithmic velocity profile results:

$$U(z) - U_0 = \frac{u_*}{\kappa} \log\left(\frac{z}{z_0}\right) \tag{5.27b}$$

where z_0 is the roughness length. For undeformed sea ice, the roughness length is of the order of 0.1 cm, and characteristic friction velocities are $50\,\mathrm{cm\,s^{-1}}$ for the atmosphere and $2\,\mathrm{cm\,s^{-1}}$ for the ocean. For deformed sea ice, the effective aerodynamic roughness length is of the order of 1–10 cm, corresponding to hummocks and ridges that have geometrical extents of 1 m above the surface and 10 m below (see Section 2.5).

Stratification

The stability of stratification is described by the Richardson number (see Tennekes and Lumley, 1972):

$$Ri = \frac{g}{\Theta_0} \frac{\langle W'\theta' \rangle}{\langle W'U' \rangle (\partial U/\partial z)} = \frac{Ag}{K\Theta_0} \frac{\partial\theta/\partial z}{(\partial U/\partial z)^2} \tag{5.28}$$

where $\hat{\theta} = \theta + \theta'$ is the Reynolds decomposition of potential temperature, Θ_0 is reference temperature, and K and A are the turbulent viscosity and thermal diffusivity, respectively. The Richardson number describes the ratio of buoyant production to shear production of turbulence, and $Ri > 0$ for stable stratification (potential temperature decreases with elevation) and $Ri < 0$ for unstable stratification. According to observations, stabilizing buoyancy will damp the turbulence if $Ri > 0.2$ (Tennekes and Lumley, 1972).

Using Eq. (5.28) and defining $\langle W'\theta' \rangle = -u_*\theta_*$, it is seen that Richardson number contains a length scale L_{MO}, the Monin-Obukhov length:

$$Ri = \frac{z}{L_{\mathrm{MO}}}, \quad L_{\mathrm{MO}} = -\frac{u_*^2}{\kappa b \theta_*} \tag{5.29}$$

where $b = g/T_v$ is a buoyancy parameter, and T_v is virtual temperature[3]. In neutral conditions, $L_{\mathrm{MO}} = \infty$ and $z/L_{\mathrm{MO}} = 0$. In stable conditions, the heat flux is negative (toward the boundary) and then $z/L_{\mathrm{MO}} > 0$. In unstable conditions the opposite is true.

[3] The temperature, which dry air would need to have the same density as moist air (i.e., $T_v = T(1 + 0.6078q)$, where q is specific humidity, see Gill, 1982).

In general, in non-neutral conditions Eq. (5.27a) is replaced by (e.g., Andreas, 1998):

$$\frac{\mathrm{d}U}{\mathrm{d}z} = \frac{u_*}{\kappa z}\,\phi_m\left(\frac{z}{L_{\mathrm{MO}}}\right) \tag{5.30}$$

where ϕ_m is "universal function" for momentum transfer. For $z/L_{\mathrm{MO}} = 0$, we have $\phi_m(0) = 1$.

Buoyancy depends on temperature and humidity (atmosphere) or salinity (ocean). Therefore, additional equations to Eq. (5.30) are needed. For the temperature:

$$\frac{\mathrm{d}\theta}{\mathrm{d}z} = \frac{\theta_*}{\kappa z}\,\phi_{\mathrm{H}}\left(\frac{z}{L_{\mathrm{MO}}}\right) \tag{5.31}$$

and similar for the humidity or salinity. Here ϕ_H is universal function of temperature distribution. The velocity–temperature–humidity structure or the velocity–temperature–salinity structure is interconnected via the Monin-Obukhov length, and therefore the three boundary-layer equations must be simultaneously solved. This question goes beyond the scope of this book; details about the methods with expressions for the universal functions can be found in Andreas (1998) and McPhee (2008).

When the velocity profile with the friction velocity has been solved, the surface stress is directly obtained. However, such detailed knowledge is not usually available, and different parameterization schemes are employed in terms of fluid velocity and drag coefficient.

Drag force formulae

Based on dimensional analysis, the drag force of the fluid on a solid plate is $\tau = \rho_0 C_D U^2$, where ρ_0 is the density of the fluid, U is the velocity of the fluid relative to the plate, and C_D is the (dimensionless) drag coefficient (e.g., Li and Lam, 1964). In general, we have:

$$C_D = C_D(Re, \gamma, Ri) \tag{5.32}$$

Re is the Reynolds number:

$$\mathrm{Re} = \frac{UL}{\nu} \tag{5.33}$$

where ν is the kinematic viscosity of the fluid. For non-stratified fluids, the drag coefficient depends on the Reynolds number and surface roughness (γ). In laminar flow, $C_D \propto \mathrm{Re}^{-1}$ and therefore $\tau \propto U$. But in turbulent flow the Reynolds number becomes very large and the drag coefficient is then independent of it, $C_D = C_D(\gamma)$ and $\tau \propto U^2$. Note also that the velocity and drag coefficient have reference elevation or depth, and they could be written as C_{Dz} and U_z for clarity.

For planetary boundary layers, geostrophic flow serves as the natural, undisturbed reference velocity. Surface geostrophic velocities are usually good approximations for velocities immediately above boundary layers, i.e., above the

frictional layer of influence. In planetary boundary layers the Coriolis effect causes the flow to turn, and therefore a second stress law parameter is required: the *turning angle*, *or Ekman angle*, between the geostrophic flow and the surface stress (see Figure 5.7). This angle also depends on surface roughness and stratification.

By using the quadratic drag laws, the necessary parameters of which are the drag coefficient and boundary-layer turning angle (e.g., Brown, 1980; McPhee, 1982), the atmospheric and oceanic drag laws can then be written in general form as:

$$\tau_a = \rho_a C_a |U_{ag}| \exp(i\theta_a) U_{ag} \tag{5.34a}$$

$$\tau_w = \rho_w C_w |U_{wg} - u| \exp(i\theta_w)(U_{wg} - u) \tag{5.34b}$$

where ρ_a and ρ_w are air and water densities, C_a and C_w are air and water drag coefficients, and θ_a and θ_w are boundary layer turning angles in air and water. Note that to ascertain wind stress exactly there should be $(U_a - \boldsymbol{u})$ instead of U_a, but since $U_a \gg \boldsymbol{u}$ the approximation used is good. The factors $\exp(i\theta_a)$ and $\exp(i\theta_w)$ simply rotate the velocity vectors by the angles θ_a and θ_w. In the northern hemisphere the angles are positive, turning counter-clockwise, and vice versa in the southern hemisphere. Drag coefficients consist of skin friction and form drag due to ridges, $C_D = C_D^S + C_D^F$. For the air–ice interface they arguably are of similar magnitude (Arya, 1975), as seems to be case for the ice–water interface.

The drag law parameters depend on the altitude of the reference velocity. If the velocity profile and the stratification are known, then transformation of these parameters between different levels is straightforward. Although geostrophic flow is a natural reference velocity, other references are also used. In measurement campaigns, instrumentation altitudes can fix the reference level. In some freezing seas there is a good meteorological station network with surface wind (10 m altitude) data, which provide more accurate surface stress estimates and are therefore preferable in modelling applications. The turning angle is zero for the surface wind, and the surface wind drag coefficient is $C_{D10} = (U_g/U_{10})^2 C_{Dg}$ or about twice the geostrophic wind drag coefficient. When using atmospheric model output for the wind field, the surface wind or the surface stress directly is available. Similarly, in coupled ice–ocean modelling, oceanic top-layer velocity is used as the reference, with drag parameters depending on the thickness of this top layer.

Most research on sea ice boundary layers has been made in Arctic seas. The representative geostrophic drag coefficients and turning angles of $C_a = 1.2 \times 10^{-3}$, $\theta_a = 25^\circ$, $C_w = 5 \times 10^{-3}$, and $\theta_w = 25^\circ$, are the result of AIDJEX field studies in the Beaufort Sea (Brown, 1980; McPhee, 1982). In the Baltic Sea the drag coefficients are 25–50% smaller than in the Arctic due to the roughness of the ice. But, in the Weddell Sea the water drag coefficient seems to be as low as 1.6×10^{-3} while the air drag coefficient is close to the Arctic value (Martinson and Wamser, 1990). This may be because the bottom of Antarctic sea ice is smoother or the frictional oceanic boundary layers are thinner than those in the Arctic or even those in the Baltic Sea.

As for geostrophic reference velocities, in Arctic seas $C_a/C_w \approx 0.24$; this happens to be about the ratio of the scales in the top and bottom topography of deformed ice. Because the geometries of top and bottom ice surfaces are well correlated, the ratio

C_a/C_w should not vary much between different regions. In the Baltic $C_a/C_w \approx 0.19$ (Leppäranta and Omstedt, 1990). But, in the Antarctic the ratio C_a/C_w turns out to be larger, since the ice bottom is relatively smoother; Martinson and Wamser (1990) data give $C_a/C_w \approx 0.8$.

Note that the air and water stresses are written in vector form as:

$$\tau_a = \rho_a C_a U_{ag}(\cos\theta_a + \sin\theta_a \boldsymbol{k}\times)\boldsymbol{U}_{ag} \tag{5.34c}$$

$$\tau_w = \rho_w C_w |\boldsymbol{U}_{wg} - \boldsymbol{u}|(\cos\theta_w + \sin\theta_w \boldsymbol{k}\times)(\boldsymbol{U}_{wg} - \boldsymbol{u}) \tag{5.34d}$$

Quadratic water stress introduces nonlinearity to the ice drift problem. Despite not being very robust, *linear models* can be useful in several cases. To preserve the approximate linearity between ice and wind velocities, it is convenient to linearize wind stress too. The linear forms are expressed as:

$$\tau_a = \rho_a C_{a1} \exp(i\theta_a) U_a \tag{5.35a}$$

$$\tau_w = \rho_w C_{w1} \exp(i\theta_w)(U_w - u) \tag{5.35b}$$

where the linear drag law coefficients can be estimated from the quadratic ones using fixed scaling speeds (subscript 0): $C_{a1} = C_a|U_{a0}|$ and $C_{w1} = C_w|(U_w - \boldsymbol{u})_0|$. Another way is to take the Ekman spiral down (or up) to the surface and from $\tau = \rho_0 K dU/dz|_{z=0}$ we have $C_1 = \sqrt{Kf}$. The turning angle becomes $\mathrm{sgn}(f)\pi/4$ in the Ekman model. Since the linear laws come out from the Ekman boundary layer solution, they were widely used in the past.

5.2.2 Atmospheric drag force on sea ice

A key atmospheric parameter in sea ice dynamics research is the speed ratio U_{as}/U_{ag} between the surface wind U_{as} and the geostrophic wind U_{ag}. Its modulus and argument, the so-called cross-isobar angle, are, respectively:

$$R_g = \left|\frac{U_{as}}{U_{ag}}\right|, \quad \theta_a = \arg\left(\frac{U_{as}}{U_{ag}}\right) \tag{5.36}$$

These parameters depend on the stability of stratification and their relevance comes from the fact that wind is often known for its geostrophic value only from atmospheric pressure data (especially so in the polar regions), $if\, U_{ag} = \rho^{-1}\nabla p_a$. In near-neutral conditions over polar sea areas, the ratio of surface wind speed to geostrophic wind speed is 0.5–0.7 and the cross-isobar angle is 10–30°. During AIDJEX the average wind speed ratio and turning angle were found to be 0.59 and 25.9° in the Beaufort Sea (Albright, 1980; Brown, 1980). Joffre (1985) investigated the diurnal cycle of the ratio R_g for two different campaigns of about three weeks in the Baltic Sea. The resulting R_g displayed a maximum of 0.9 at about 23:00 h (local time) and a minimum of 0.55 at about 8:00 h. Joffre (1982b) also found that the cross-isobar angle varied between 15° and 30°.

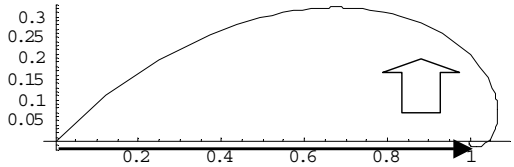

Wind velocity rotates counterclockwise down from the geostrophic wind to the surface. Surface stress is 45° to the left from the geostrophic wind.

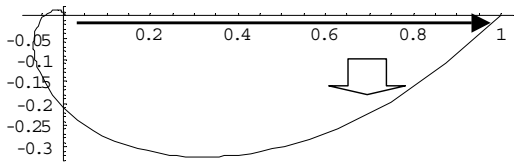

Surface flow is 45° to the right from the wind stress. Ocean current rotates clockwise down from the surface.

Figure 5.7 Theoretical form of the atmospheric and oceanic Ekman layers above and beneath sea ice (northern hemisphere). Note that oceanic velocities are two orders of magnitude less than atmospheric velocities.

Measurements of atmospheric surface layers over sea ice have been widely made using profiling masts (Figure 5.7) and aircraft. The roughness length of the top surface of undeformed sea ice is of the order of 0.1 cm. Joffre (1982a) examined the surface layer over northern Baltic Sea ice. The roughness length ranged between 0.04 cm and 0.08 cm, and data-fitting resulted in:

$$z_0 = mu_*^2 \tag{5.37}$$

where $m = 1.5 \times 10^{-3}\,\mathrm{s^2\,m^{-1}}$, for $\boldsymbol{u}_* \geq 0.35\,\mathrm{m\,s^{-1}}$, in good agreement with a compilation of various snow and ice data by Chamberlain (1983), resulting in $m = 1.6 \times 10^{-3}\,\mathrm{s^2\,m^{-1}}$. Note also that Eq. (5.37) indicates that the sea ice roughness is grossly equivalent to the average roughness of the sea surface as determined by Charnock's formula (Charnock, 1955) with the same numerical coefficient m (e.g., Stull, 1988, p. 265) for non-gale situations. For instance, Garratt (1977) reviewed a wide range of sea surface roughness data that yielded $z_0 = 0.0144u_*^2/g = 1.47 \times 10^{-3}\boldsymbol{u}_*^2\,\mathrm{s^2\,m^{-1}}$. Although roughness parameter z_0 is in general considered to represent only geometric surface characteristics, it can also depend on flow conditions such as hydrostatic stability (e.g., Joffre, 1982a).

Neutral stratification

Local mast measurements provide surface wind drag coefficients, which are representative for undeformed ice surfaces (Table 5.2). The normal reference altitude of surface wind is 10 m (WMO recommendation for wind measurements), where the turning angle is zero. Variations are from 1.4×10^{-3} to 1.9×10^{-3}, and a representative drag coefficient is 1.5×10^{-3}.

Table 5.2 The drag coefficient for surface wind (measured at the standard altitude of 10 m) for neutral atmospheric stratification.

Region	Drag coefficient	Method	Reference
Gulf of St. Lawrence	1.4×10^{-3}	Mast	Smith (1972)
Beaufort Sea	1.6×10^{-3}	Sonic anemometer	Banke *et al.* (1980)
Weddell Sea	1.9×10^{-3}	Mast	Andreas and Claffey (1995)
Baltic Sea	1.5×10^{-3}	Mast	Joffre (1982a)

In neutral stratification the drag coefficient depends on surface roughness. Banke *et al.* (1980) modelled the air–ice surface drag coefficient for the surface wind as:

$$C_a = 1.10 + 0.072\gamma^2 \tag{5.38a}$$

where γ is the root-mean-square (r.m.s.) elevation defined as the square root of the variance of the surface elevation for wavelengths less than 13 m (the best correlation was found when the variance was taken over short wavelengths only). Their data covered r.m.s. elevations from 4 to 14 cm corresponding to drag coefficients from 1.2×10^{-3} to 2×10^{-3} or roughness lengths z_o from 0.01 cm to 0.2 cm.

The surface wind drag parameters can be transformed into geostrophic drag coefficients using the wind speed ratio and cross-isobar angle (Eqs. 5.36). Thus the ratio between the drag coefficients for geostrophic wind and the surface wind should be $C_{aw}/C_{ag} \approx 2$–4. In the AIDJEX experiment this ratio was 2.9 (Albright, 1980).

Sea ice drift, taking place in scales of ice floes and larger, integrates the roughness to such scales. Rossby and Montgomery (1935) examined the air–ice and ice–water stresses using the data of Sverdrup (1928) and Brennecke (1921), and obtained a floe-scale air drag coefficient of 2.5×10^{-3}, close to modern values. Their roughness parameter was 3.68 cm, which corresponds to a physical roughness of the order of 1 metre (explained by the presence of pressure ridges). Thus surface topography features such as floe edges, snowdrifts and hummocks and ridges add to the drag. Results by Andreas and Claffey (1995) suggest that snowdrifts may add about 50% to the drag coefficient but, however, they tend to deform into streamlined shape and reduce the drag coefficient; therefore Eq. (5.38a) oversimplifies the air–ice coupling effects.

Due to pressure differences on both sides of ridges an additional *form drag* results, and attempts have been made to relate the atmospheric form drag coefficient to ridge statistics. In Arya's (1975) model the form drag coefficient is proportional to the product of ridge density μ and mean sail height $\tilde{h}_s$, later confirmed by Banke *et al.* (1980) as[4]:

$$C_a^F = \tfrac{1}{2} C_F \mu \tilde{h}_s \tag{5.38b}$$

[4] In this formula the cut-off height of sails is not specified leaving some uncertainty for its application.

where C_F is the form drag coefficient for a single ridge sail of unit height, $C_F = 0.012 + 0.012\phi_s$ (ϕ_s being the sail slope angle in degrees). Thus, $C_F \approx 0.4$ for $\phi_s = 30°$. For $h_s \sim 1\,\text{m}$ and $\mu \sim 5\,\text{km}^{-1}$, $C_a^F \sim 1.0 \times 10^{-3}$ (i.e., close to the skin friction drag coefficient). This result has been found to be valid in the Baltic Sea as well (Joffre, 1983). Including the form drag effect, Joffre (1983, 1984) found that the overall roughness is approximately between 20% and 70% larger than local skin roughness. For heavily ridged ice the drag coefficient may be as high as 4×10^{-3}.

The present standard for the geostrophic drag coefficient is about 1.2×10^{-3} for both polar regions, corresponding to a surface wind drag coefficient of 3.5×10^{-3} (Brown, 1980; Martinsen and Wamser, 1990). Being independent of the frictional influence of the ice, the geostrophic wind represents the real atmospheric force that is driving the ice.

In the open ocean, the drag coefficient of surface wind depends on the wind speed. According to Smith (1980), it is 1.1×10^{-3} for weak winds and $(0.61 + 0.063U_a) \times 10^{-3}$ for winds from 6 to 22 m s^{-1}. Therefore, air–ice drag is normally larger than air–water drag. For strong winds (about 15 m s^{-1}) these drags are equal over undeformed ice but over deformed ice the drag may be twice as much.

Non-neutral stratification

In a stratified fluid the drag parameters also depend on the stability of the stratification. According to the Monin–Obukhov similarity theory, they are functions of the Monin–Obukhov length. Figure 5.8 presents the geostrophic drag parameters for the atmosphere (Andreas, 1998). The neutral values are $C_a = 1.2 \times 10^{-3}$ and $\theta_a = 15°$. In very stable conditions $C_a \approx 10^{-4}$ and $\theta_a \approx 35°$ while in unstable conditions $C_a \approx 1.5 \times 10^{-3}$ and $\theta_a \to 0$.

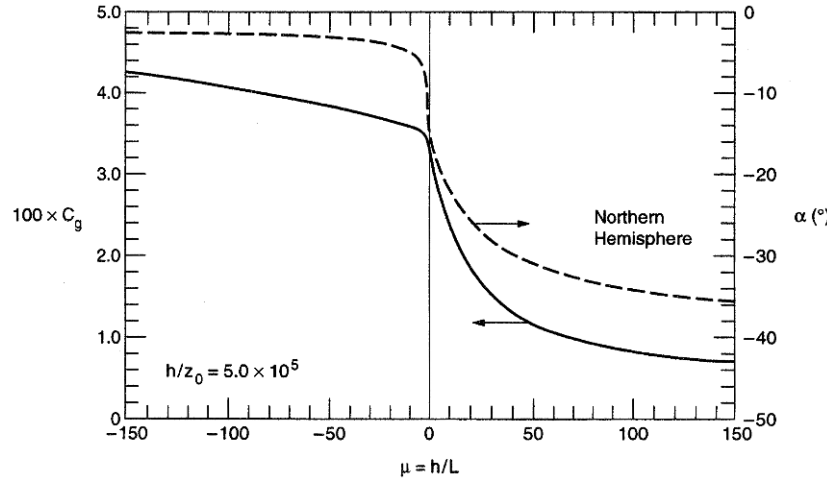

Figure 5.8 Geostrophic drag coefficient $C_{ag}(= C_g^2)$ and turning angle as functions of boundary layer height h scaled using the Monin–Obukhov length L.
From Andreas (1998), printed with permission of the University of Helsinki Press.

Joffre (1982a) examined the surface wind drag coefficient over a wide range of stability conditions ($-1 < z/L_{MO} < 10$) in the Baltic Sea. He found that C_a is strongly modulated by thermal stability (shown also in Stull, 1988, p. 268), decreasing from about 2×10^{-3} under unstable conditions to close to zero for strong stratification. His formulae read:

$$\frac{1}{\sqrt{C_a}} = 70.51 \frac{z}{L_{MO}} + 24.56, \quad \frac{z}{L_{MO}} > 0, \tag{5.39a}$$

$$\frac{1}{\sqrt{C_a}} = 2.98 \frac{z}{L_{MO}} + 25.55, \quad \frac{z}{L_{MO}} < 0 \tag{5.39b}$$

The fit was especially good under stable condition.

Overland (1985) reviewed the air–sea drag coefficient for first-year ice from aircraft measurements and reconciled the range of observed drag coefficients of $10^3 C_a \approx 1.2$–3.7 for the surface wind (referenced at an altitude of 10 m) for all sea ice types, based on ice roughness and seasonal meteorology. For sea ice dynamics investigations it is necessary to define an effective drag coefficient that relates regional stress to regional wind, because sea ice is heterogeneous. Regional stress is influenced by the distribution of surface roughness, the buoyancy flux from quasi-periodic leads, and external atmospheric conditions, principally the inversion height. For wind speeds greater than $5\,m\,s^{-1}$ and air temperatures below freezing, the effective drag coefficient is $10^3 C_a \approx 2.5$–3.0 for nearly continuous pack ice, such as first-year ice in seasonal ice zones and the central Arctic basin. The range of values of $10^3 C_a$ is 3.0–3.7 for unstable boundary layers typical of off-ice winds in the MIZ or even greater if the ice has been broken by a recent storm. The effective drag coefficient when there is just a small concentration of sea ice is generally greater than the oceanic value.

5.3 SEA ICE–OCEAN INTERACTION

5.3.1 Oceanic boundary layer beneath drifting ice

Sea ice is intensively and continuously interacted with the ocean waters, and the depth of its immediate influence[5] is of the order of 50 m. The presence of the phase boundary forces the temperature of the ice bottom to be at the freezing point of the surface water. But since sea ice is a changing ice–brine mixture with no fixed melting point, the interfacial ice–water boundary has finite thickness, forming what is referred to as the skeleton layer. The ice grows at the bottom when the released latent heat can be transmitted through the ice to the atmosphere. The ice–ocean heat flux from the liquid water body into the bottom of the ice sheet reduces the growth rate or may cause the ice to melt at the bottom. The salinity of the surface layer is

[5] This depth of frictional influence (Ekman depth) is about the same under sea ice as in open water conditions.

influenced by salt rejection from growing ice and by freshwater flux from melting ice (see, e.g., Weeks, 1998a). The mechanical ice–ocean interaction is due to the drag force where the faster moving body is driving the other, usually parameterized as a quadratic drag law. The exchanges of heat and salt/freshwater are approached by similar bulk exchange formulas. The strength of the exchange depends on the stratification of the surface layer, and consequently the exchanges of momentum, heat and salt/freshwater are interdependent. An excellent presentation of the physics of the oceanic boundary layer (OBL) beneath sea ice is provided by a recent book (McPhee, 2008). Other publications on the OBL beneath sea ice are by e.g., McPhee (1986, 1990), Shirasawa and Ingram (1991a), and Shirasawa and Leppäranta (2009).

The velocity difference between sea ice and geostrophic ocean current can be used to classify the ice–ocean dynamics cases. There are three possibilities:

(a) If $|\boldsymbol{U}_{wg}| \gg |\boldsymbol{u}|$, then there is rotation in the oceanic boundary layer from the surface to the bottom, but with reversed directions compared with the atmosphere case.
(b) If $|\boldsymbol{U}_{wg}| \ll |\boldsymbol{u}|$, the Ekman spiral (e.g., Cushman-Roisin, 1994) results.
(c) If $|\boldsymbol{U}_{wg}| \sim |\boldsymbol{u}|$, the faster moving medium drives the slower one; when also $|\boldsymbol{U}_{wg} - \boldsymbol{u}| \sim 0$, the Ekman spiral is less sharp.

Ice is an excellent platform for oceanic boundary layer investigations. OBL beneath drift ice represents the pure shear stress forcing case with no disturbances from surface waves and provides a stable site for measurements. Ekman himself made observations in the winter of 1901 on the ice of Oslo Fjord and was the first to record the Ekman profile in the ocean. It took a long time for the Ekman theory to be validated in open ocean conditions.

OBL field investigations consist of measurements of ice thickness, hydrography and currents. Ice bottom roughness would be very desirable to have but there are many practical difficulties. Current meters are used to measure the current speed and direction at the reference depth or current profiles, and Conductivity–Temperature–Depth (CTD) sounders are used to measure the temperature and salinity (Figure 5.9). Turbulence meters are also used for direct mapping of the turbulent transfer of momentum, heat and salts based on eddy correlation technique; this is the direct method to estimate the turbulent fluxes.

An example of time series records of the current velocity, water temperature, and salinity measured at a fixed depth at the central area of the Saroma-ko lagoon offshore Hokkaido, Japan is shown in Figure 5.10. The period of observations with freeze-up and break-up dates is included. Ice freeze-up started in late January, and almost the entire surface of the lagoon was covered with sea ice until the onset of ice break-up in early April. The current speed was as high as $10\,\mathrm{cm\,s^{-1}}$ before freeze-up and reduced to $2–3\,\mathrm{cm\,s^{-1}}$ during the ice-covered period. The solid ice cover caused significant reduction of vertical mixing of the water under the ice, and thus there was not much momentum transfer from the wind to the water body. The main forcing of the circulation comes from the two inlets and rivers, heating of the water body by the heat flux from the bottom sediments, and from the solar heating as soon as the snow has melted.

Figure 5.9 Current measurements by a three-dimensional electromagnetic current meter (Model ACM32M, Alec Electronics Co., Ltd., Japan). One person lowers the current meter through a drill hole and fixes it with a tripod at the depth of 1 m (as the reference level) below the ice bottom in the oceanic boundary layer.
Photograph by Dr Kunio Shirasawa, printed with permission.

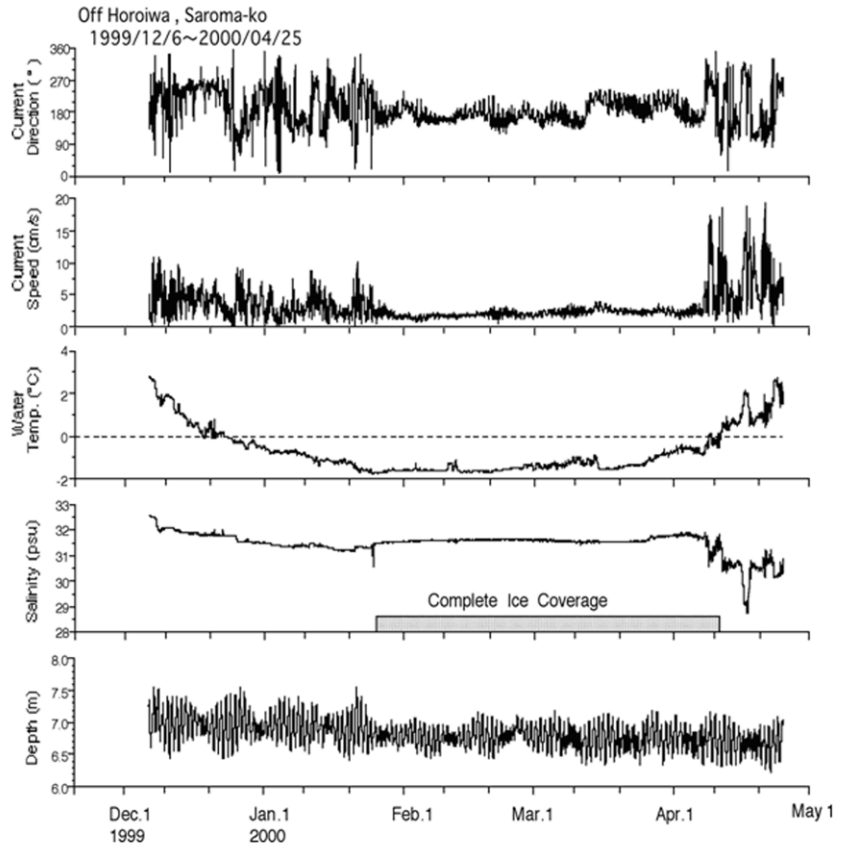

Figure 5.10 Time series of currents, temperature and salinity obtained from the mooring station at the central area of Saroma-ko lagoon during the period from 6 December 1999 through 25 April 2000.
From Shirasawa and Leppäranta (2006).

Oceanic flow regime may be laminar, turbulent or in transition between laminar and turbulent flows. Reynolds number is used to distinguish between these flow regimes: flow is laminar for $Re < 10^3$, turbulent for $Re > 10^4$, and in between in the transition zone. Since the kinematic viscosity of water is $\nu \approx 10^{-6}\,\mathrm{m^2\,s^{-1}}$, only in extreme situations laminar or transition zone flows are found in oceanic waters, such as under landfast ice in shallow waters. However, a very thin viscous sublayer exists in turbulent boundary layers next to a solid boundary where the water velocity is taken to match the boundary velocity and where kinetic energy is dissipated into heat.

Using the complex variable techniques and Reynolds decomposition as denoted in Section 5.2, the ocean boundary layer velocity, temperature[6] and salinity are

[6] In OBL the potential temperature is approximately equal to the actual temperature.

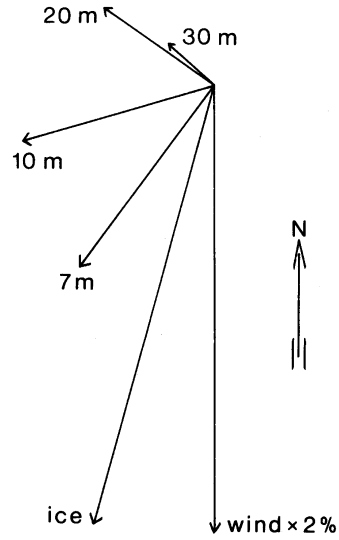

Figure 5.11 Averaged velocities of wind, sea ice, and currents (depths 7, 10, 30, and 40 m), 8–15 April 1975 in the Baltic Sea. For the velocity scale, the ice velocity averaged 3.1 cm s^{-1} (at maximum it was 35 cm s^{-1}).
From Leppäranta (1990).

expressed as $\hat{U}_w = U_w + U'_w$, $\hat{W}_w = W_w + W'_w$, $\hat{T}_w = T_w + T'_w$, $\hat{S}_w = S_w + S'_w$. The oceanic boundary layer equations are written:

$$\frac{\partial U_w}{\partial t} + \mathrm{i}f U_w = if U_g + \frac{\partial}{\partial z}\langle U'_w W'_w \rangle \tag{5.40a}$$

$$\frac{\partial T}{\partial t} = -\frac{\partial}{\partial z}\langle T' W'_w \rangle + \kappa Q_s e^{-\kappa z} \tag{5.40b}$$

$$\frac{\partial S}{\partial t} = -\frac{\partial}{\partial z}\langle S' W'_w \rangle \tag{5.40c}$$

In general, temperature and salinity depend on depth, and the evolution of the boundary layer is an interconnected temperature–salinity–velocity process. Sverdrup (1928) emphasized the role of stratification in the planetary boundary layers. He claimed that in the Siberian shelf in summer there is a 25–40 m low-density upper layer, which moves almost uniformly with the ice and with a very weak momentum transfer to the deeper water. Rossby and Montgomery (1935) examined the air–ice and ice–water stresses using the data of Sverdrup (1928) and Brennecke (1921). They criticized Sverdrup's assumption for the bulk drift of the upper ocean with ice and, instead, showed that there is always a shear layer beneath the ice; but they agreed with Sverdrup in that the presence of a stable shear layer in summer reduces significantly the ice–water friction.

Assuming that the geostrophic flow U_{wg} is steady, Eq. (5.40a) can be written as

$$\frac{\partial(U_w - U_{wg})}{\partial t} + \mathrm{i}f(U_w - U_{wg}) = -\frac{\partial}{\partial z}\langle U'_w W'_w \rangle \tag{5.40d}$$

Thus the full solution can be constructed by adding U_{wg} to the solution with $U_{wg} = 0$.

The thickness of Ekman layer scales as $u_* f^{-1} \sim 50\,\mathrm{m}$, and the layer structure is characterized by the roughness Rossby number (e.g., McPhee, 2008):

$$Ro_* = \frac{u_*}{z_0 f} \tag{5.41}$$

The Ekman layer solution is presented in Eq. (5.24). Figure 5.11 shows the Ekman spiral recorded beneath drifting sea ice in the Baltic Sea (based on 1-week velocity records) showing averaged velocities of wind, sea ice and currents (depths 7, 10, 30 and 40 m), April 1975 in the Baltic Sea (Leppäranta, 1990). Here the ice velocity is much larger than the geostrophic current.

5.3.2 Monin-Obukhov model

As discussed above, planetary turbulent boundary layers consist of a surface layer (wall layer) and an Ekman layer. Turbulent fluxes of momentum (τ), heat (Q_w) and salt (Ξ) are:

$$\tau = -\rho\langle U'_w W'_w \rangle = \rho u_*^2 \tag{5.42a}$$

$$Q_w = -\rho c_w \langle W' T' \rangle \tag{5.42b}$$

$$\Xi = -\langle w' S' \rangle \tag{5.42c}$$

where c_w is the specific heat of seawater.

Introducing roughness as the length scale and friction velocity as the velocity scale, we have the roughness Reynolds number characterizing wall layers:

$$Re_* = \frac{u_* z_0}{\nu} \tag{5.43}$$

The roughness length can be estimated as $z_0 \approx \gamma/30$, where the roughness parameter γ is taken as the root-mean-square of the surface elevation. There is not much data available for the roughness of the ice bottom (see McPhee, 2008). For undeformed sea ice the roughness length is of the order of $z_0 \sim 0.1$–$1\,\mathrm{cm}$, and characteristic OBL friction velocity is $2\,\mathrm{cm\,s^{-1}}$. Shirasawa (1986) obtained $z_0 \approx 0.5$–$2.0\,\mathrm{cm}$ and Shirasawa and Ingram (1997) had $z_0 \approx 0.3$–$0.4\,\mathrm{mm}$ for smooth landfast sea ice sheet from turbulence measurements near the bottom of landfast ice in the Canadian Arctic archipelago. For deformed sea ice the effective roughness length is of the order of 1–10 cm corresponding to the hummocks and ridges; McPhee (1986) obtained $z_0 \approx 20\,\mathrm{cm}$ for deformed ice in the Arctic Ice Dynamics Joint Experiment (AIDJEX) in the Beaufort Sea.

Table 5.3 The parameters of the quadratic water–ice drag laws for neutral oceanic stratification (GSC = geostrophic current).

Region	Drag coefficient	Turning angle (deg)	Level	Reference
Barrow Strait	5.4×10^{-3}	0°	1 m	Shirasawa and Ingram (1997)
Beaufort Sea	5.0×10^{-3}	25°	GSC	McPhee (1982)
Baltic Sea	3.5×10^{-3}	17°	GSC	Leppäranta and Omstedt (1990)
Weddell Sea	1.6×10^{-3}	15°	GSC	Martinson and Wamser (1990)

The wall layer is treated with the Monin–Obukhov theory (see Section 5.2.1). The steady state distributions of velocity, temperature and salinity are:

$$\frac{\mathrm{d}U}{\mathrm{d}z} = \frac{u_*}{\kappa z}\,\phi_m\left(\frac{z}{L_{\mathrm{MO}}}\right) \tag{5.44a}$$

$$\frac{\mathrm{d}T}{\mathrm{d}z} = \frac{T_*}{\kappa z}\,\phi_H\left(\frac{z}{L_{\mathrm{MO}}}\right) \tag{5.44b}$$

$$\frac{\mathrm{d}S}{\mathrm{d}z} = \frac{S_*}{\kappa z}\,\phi_S\left(\frac{z}{L_{\mathrm{MO}}}\right) \tag{5.44c}$$

where ϕ_m, ϕ_T and ϕ_S are the so-called universal functions, T_* and S_* are characteristic temperature and salinity scales in the surface layer, and L_{MO} is the *Monin–Obukhov length*. In the wall layer the fluxes are constant and water velocity takes a logarithmic profile as shown by Eq. (5.27b). Since the wall layer stress provides the shear stress between sea ice and water underneath, the viscous sub-layer needs not usually be considered when the turbulent ice–ocean transfer is examined.

The ice–ocean fluxes need to be parameterised for the mean quantities. The usual approach is to employ *bulk formulas*, i.e., for the flux F_P of a property P, we have:

$$F_P = \rho C_P(z)[\,P(z) - P(0)] \cdot |U_w(z) - U_w(0)| \tag{5.45}$$

where C_P is the transfer coefficient and z is depth. For the momentum transfer, the exchange coefficient is called the drag coefficient (see Eq. 5.34b).

In general the drag coefficient and turning angle may be defined for an arbitrary velocity reference level, and their values would then depend on the chosen level. If the velocity profile and stratification are known, then transformation of the drag law parameters between different levels is straightforward. Taking the logarithmic profile for the surface layer, in neutral conditions the roughness length and drag coefficient are related by:

$$C_w(z) = \left(\frac{\kappa}{\log(z/z_0)}\right)^2 \tag{5.46}$$

Table 5.3 shows a collection of oceanic drag parameters for several regions. The reference depth of 1 m has been often used in turbulence measurements beneath sea ice. The study of Shirasawa and Ingram (1997) gives a local drag coefficient of

smooth ice, while the others refer to the geostrophic flow and include the form drag by hummocks and ridges.

Representative Arctic – the best known region – values for the geostrophic drag coefficient and turning angle are $C_w = 5 \times 10^{-3}$, and $\theta_w = 25°$, resulting from the AIDJEX field experiments in the Beaufort Sea (McPhee, 1982). Due to the roughness of the ice in the Baltic Sea the drag coefficients are 25–50% smaller than in the Arctic. But in the Weddell Sea the water drag coefficient seems to be as low as 1.6×10^{-3} (Martinson and Wamser, 1990). The most likely explanation is that the bottom of Antarctic sea ice is smooth or the frictional oceanic boundary layer is thin as compared with that in the Arctic or even in the Baltic Sea.

Analyzing ice drift based on the Ekman theory, Shuleikin (1938) assumed $\theta_w \approx 30°$, a constant. Early investigations as this employed linear drag laws, which result from Ekman profiles. These drag coefficients are therefore not directly comparable with quadratic ones, but the wind-driven ice speed is proportional to the ratio of drag coefficients, whether linear or quadratic as will be shown later. This ratio came out well in Shuleikin's (1938) work and in many others. Nansen (1902) stated that floating ice increases the velocity of the OBL because no energy is needed for wave formation and ice is rougher than open water to absorb more energy from the wind – if the internal ice resistance to motion is not too strong. There is a natural variation of $\pm 50\%$ in the drag coefficients due to the stability of the stratification and roughness variations.

A specific case is the so-called *dead water* (Ekman, 1904), where a large amount of ice momentum is used to generate internal waves. This necessitates the existence of a shallow, stable surface layer, on the bottom of which the internal waves form. The representative drag coefficient may be then five times the normal ice–ocean drag coefficient (Waters and Bruno 1995).

5.3.3 Second order turbulence model

A more direct way is to employ a second order turbulence model directly. Svensson (1979) prepared a $k\varepsilon$-model for marine boundary layer applications, and this model has been used for several ice–ocean dynamics applications (Omstedt, 1990; Leppäranta and Omstedt, 1990; Omstedt *et al.*, 1996; Omstedt, 1998). This approach includes the equations of turbulent energy (k) and its dissipation rate (ε) and, therefore, avoids the need for drag law parameters. However, this model is one-dimensional and its applicability is consequently limited to local boundary-layer problems only.

The boundary layer equations for velocity, temperature and salinity are shown in Eqs. (5.40a–c). The turbulent fluxes are expressed using the eddy diffusivities, which depend on k and ε. The momentum flux is:

$$-\langle U'W' \rangle = K \frac{\partial U}{\partial z} \tag{5.47a}$$

$$K = C_\mu \frac{k^2}{\varepsilon}$$

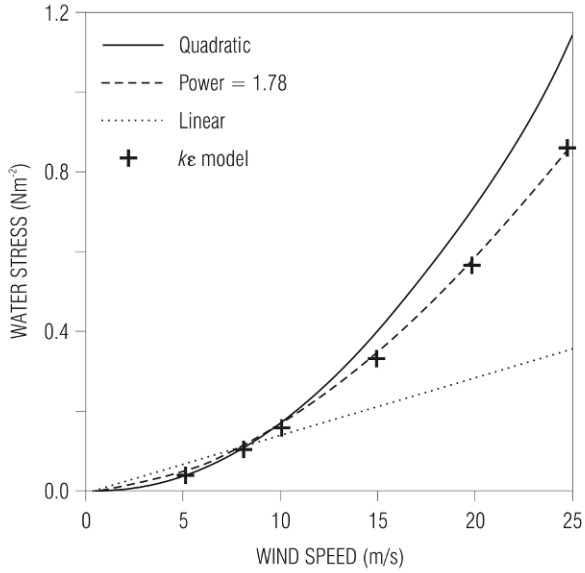

Figure 5.12 Ice–ocean stress according to linear drag law, quadratic drag law, McPhee (1986) drag law (power 1.78), and $k\varepsilon$-turbulence model.
From Omstedt *et al.* (1996).

where C_μ is a model constant. The temperature and salinity fluxes are obtained with similar formulation. To close the system the diffusion coefficients are obtained from the level and dissipation rate of turbulent kinetic energy:

$$\frac{\partial k}{\partial t} = \frac{\partial}{\partial z}\left(\frac{K}{\sigma_k}\frac{\partial k}{\partial z}\right) + P_s + P_b - \varepsilon \tag{5.47c}$$

$$\frac{\partial \varepsilon}{\partial t} = \frac{\partial}{\partial z}\left(\frac{K}{\sigma_\varepsilon}\frac{\partial k}{\partial z}\right) + \frac{\varepsilon}{k}\left(c_{\varepsilon 1}P_s + c_{\varepsilon 3}P_b - c_{2\varepsilon}\varepsilon\right) \tag{5.47d}$$

Here $\sigma_k = K/K_T$ and $\sigma_\varepsilon = K/K_S$ are the turbulent Prandtl and Schmidt numbers,

$$P_s = K\left[\left(\frac{\partial v_1}{\partial z}\right)^2 + \left(\frac{\partial v_2}{\partial z}\right)^2\right] \quad \text{and} \quad P_b = \frac{K}{\sigma}\cdot\frac{g}{\rho_0}\cdot\frac{\partial \rho}{\partial z} \tag{5.47e}$$

are the turbulence productions due to shear and buoyancy, and $c_{1\varepsilon}$, $c_{2\varepsilon}$ and $c_{3\varepsilon}$ are model constants and σ is the Prandtl number. The $k\varepsilon$ model has thus six parameters, and with their standard values they are: $C_\mu = 0.09$, $c_{1\varepsilon} = 1.44$, $c_{2\varepsilon} = 1.92$, $c_{3\varepsilon} = 0.8$, $\sigma_k = 1.0$ and $\sigma_\varepsilon = 1.3$. The most uncertain part of this system is the equation for the dissipation of turbulent kinetic energy (Eq. 5.47d), which involves several parameters.

In all, the upper layer physics comes out fairly well in the model for central basins, but deeper horizontal processes become more significant, relatively speaking,

and so-called "deep mixing" functions have been added into the model. The turbulence model provides eddy viscosity K, which can then be used to determine the stress.

The one-dimensional approach has limitations in that advection cannot be properly accounted for and interactions between the coastal zone and central basins are not solved. However, for several central basin problems good results have been obtained with this approach (Leppäranta and Omstedt, 1990; Omstedt *et al.*, 1996), and furthermore a group of one-dimensional models has been used as the basis of connected box-model network (Omstedt, 1990). Omstedt et al. (1996) examined also the drag formulations as compared with the surface stress obtained directly from the turbulence model (Figure 5.12). The drag law of McPhee (1986) with $\tau \propto |\boldsymbol{U}_w - \boldsymbol{u}|^{1.78}$ gave a good fit with the turbulence model.

5.3.4 Shallow waters

In shallow waters, where the depth is much less than the Ekman depth, the oceanic boundary layer covers the whole water body, and then the drag coefficient depends on the depth of the water and the turning angle can be ignored. Taking the vertical coordinate $z = 0$ at the sea bottom, the velocity solution can be written (e.g., Leppäranta and Myrberg, 2009):

$$U_w(z) = U_{ws}\frac{\sinh(\lambda z)}{\sinh(\lambda D)}, \quad U_{ws} = \frac{\tau}{\rho K\lambda}\tanh(\lambda D), \quad \lambda = \frac{(1+\mathrm{i})}{2}\sqrt{\frac{f}{2K}} \tag{5.48}$$

where U_{ws} is surface velocity and D is sea depth. Integrating this for the vertical mean velocity we have:

$$\tilde{U}_w = -\mathrm{i}\,\frac{\tau_a}{\rho f D}\left[\frac{1}{\cosh(\lambda D)}\right] \tag{5.49}$$

Thus the factor in brackets presents the correction due to finite depth to the Ekman transport. For $|\lambda D| \ll 1$, Couette flow is obtained with:

$$U_{ws} = \frac{\tau_a}{\rho K}\cdot D, \quad \tilde{U}_w = \frac{1}{2}U_{ws} \tag{5.50}$$

The velocity is thus parallel to the wind and decreases proportional to the depth when the depth decreases.

In an open, sloping channel, the velocity is obtained from the Chezy-Manning relationship (e.g., Li and Lam 1964):

$$\tilde{U}_w = \frac{0.67}{n}R^{2/3}\beta \tag{5.51}$$

where n is Manning's coefficient, which depends on the quality of the sea bottom, R is hydraulic radius and β is the channel slope. Since $R \to D$ as the channel width $L \to \infty$, the velocity is proportional to $D^{2/3}$.

5.4 SCALE ANALYSIS

5.4.1 Magnitudes

The ice variables in the momentum equation are thickness, velocity, and stress, all of which depend on time and space. The magnitudes of their scales are now rather well known from the long-term database built up over the years by manned and automatic drifting station programmes (Figure 5.13 and Table 5.4).

Figure 5.13 The Soviet Union North Pole [Severnyj Poljus] drifting station programme was commenced in 1937, continuing regularly until 1991. It was restarted in 2003. The photograph shows the first station SP-1, under the leadership of Ivan Papanin, who wrote the book *Life on an Ice Floe* about SP-1 (Papanin, 1939).
Reproduced with permission from the Russian State Museum of the Arctic and Antarctic, St Petersburg.

Table 5.4 Typical and extreme levels from the long-term database.

	Typical	Low	High
Thickness, H	1 m	0.1 m	10 m
Velocity, U	0.1 m/s	0	1 m/s
Strength, P	10 kPa	0	100 kPa
Time, T	10^5 s	10^3 s	∞
Length, L	100 km	10 km	1,000 km

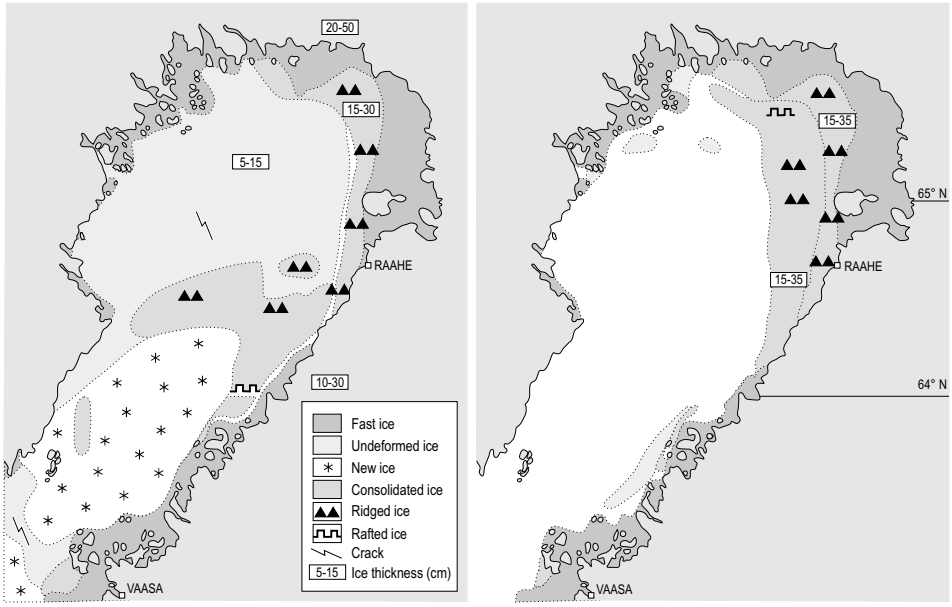

Figure 5.14 Ice situation in the Bay of Bothnia, Baltic Sea on 20 and 26 February 1992. Strong southerly to westerly winds drove the ice to the northeast corner of the basin (the basin length is 320 km).

Very thin ice is the term used for ice 0.1 m thick and deformed ice that for 10 m thick ice. Velocity is zero for stationary ice, and strength is zero for open drift ice. The timescale for velocity changes is typically 1 d $\approx 10^5$ s and in stationary flows it is ∞. For compact ice the length scale is 100 km in mesoscale dynamics. It has been known to go down to 10 km in shear and marginal ice zones, while in the general ice circulation of the polar oceans it can reach lengths of 1,000 km. Thin ice can show extreme behaviour (Figure 5.14): due to wind forcing, the whole ice cover in the Bay of Bothnia, Baltic Sea was driven in six days into the north-east corner (into an area 20% of its initial value).

Magnitude analysis of the momentum equation is performed using Table 5.4. The derivatives are estimated as $\partial \boldsymbol{u}/\partial t \sim U/T$, etc. The internal friction of ice is the most open term because there are still unsolved phenomenological problems; thereafter the key parameters are air–ice and ice–water drag coefficients, and the Coriolis parameter. Atmospheric and oceanic boundary-layer angles do not much influence the magnitude level of drag forces.

As for air and water velocity, typical scales in geostrophic flows are $U_{ag} \sim 15\,\mathrm{m\,s^{-1}}$ and $U_{wg} \sim 5\,\mathrm{cm\,s^{-1}}$. The air pressure effect is related to geostrophic wind since $f\boldsymbol{k} \times \boldsymbol{U}_{ag} = -\rho_a^{-1}\nabla p_a$, and therefore the ratio of the direct pressure effect to the wind drag is of the order of 10^{-2}. The governing background scales are the atmospheric cyclones and ocean circulation systems (10–1,000 km) and oceanic eddies (10–100 km).

Table 5.5 Scaling of the terms of the momentum equation of drift ice: standard case. Representative elementary scales are: $H = 1\,\mathrm{m}$, $U = 10\,\mathrm{cm\,s^{-1}}$, $P = 10\,\mathrm{kPa}$, $U_{ag} = 15\,\mathrm{m\,s^{-1}}$, $U_{wg} = 5\,\mathrm{cm\,s^{-1}}$, $T = 1$ day, and $L = 100\,\mathrm{km}$. The "Value" column gives the base-ten logarithm of the scale in pascals (i.e., -3 corresponds to 10^{-3} Pa).

Term	Scale	Value (^{10}log [in Pa])	Comments
Local acceleration	$\rho HU/T$	-3	-1 for rapid changes ($T = 10^3$ s)
Advective acceleration	$\rho HU^2/L$	-4	Long-term effects may be significant
Coriolis acceleration	ρHfU	-2	Mostly < -1
Internal friction	PH/L	-1 ($\ll -1$)	Compact ice, $A > 0.9$ ($A < 0.8$)
Wind stress	$\rho_a C_a U_{ag}^2$	-1	Mostly significant
Water stress	$\rho_w C_w \lvert \boldsymbol{U}_{wg} - \boldsymbol{U} \rvert^2$	-1	Mostly significant
Sea surface tilt	ρHfU_{wg}	-2	Mostly ≤ -2
Air pressure	$H\rho_a f U_a$	-3	Minor term

Typical scales

Table 5.5 shows the outcome based on typical scales. The governing terms are wind and water stresses and internal friction, their level being 10^{-1} Pa. The significance of internal friction is limited to compact ice fields, while in open ice fields the free drift situation prevails. Coriolis acceleration and sea surface tilt are an order of magnitude smaller, and local and advective acceleration are smaller still. The air pressure term is minor and will be excluded from further analysis. It is not commonly listed in the equation of motion of drift ice, but may if necessary be absorbed into the sea surface tilt term.

The ice–water stress deserves specific attention. If $|\boldsymbol{U}_{wg} - \boldsymbol{U}| \gg 0$, the magnitude of the ice–water stress is 10^{-1} Pa as shown in Table 5.5 and the interpretation in the previous paragraph holds. But if $\boldsymbol{U} \sim \boldsymbol{U}_{wg}$, the stress becomes small, and also the Coriolis term and sea surface tilt balance each other. Then wind stress and internal friction must balance each other for a steady state, otherwise acceleration is important and the ice field is undergoing adjustment toward a new steady state.

Scale ranges

Consider the cases of low and high levels of the scales in ice variables shown in Table 5.4. In the case of thin-ice cover (0.1 m), compared with the standard situation (Table 5.5) the air and water stresses are unchanged, but the other terms are proportional to the ice thickness and drop down by one order of magnitude; this results in a governing balance between the air and water stresses. In the case of thick-ice cover (10 m), the internal friction is dominant in compact ice, while the Coriolis and pressure gradient terms become comparable with the air and water stresses. Absence of ice strength automatically implies the free drift condition, while high ice strength makes the internal friction dominant.

However, because of nonlinearities in sea ice drift, the secondary term may have an important role. For example, if the wind forcing is close to the direction of coastline, whether including Coriolis acceleration or not may be critical for the ice drift to be onshore or offshore. The consequences to the ice conditions in onshore and offshore motion cases would be drastically different. This was reported by Stössel (2008 and corrigendum in 2010) of his model simulations in the Weddell Sea.

In the case of *stationary ice*, internal friction balances any external force acting on the ice. Due to the plasticity of compact ice, a stationary situation is true of any forcing lower than yield stress. In the case of *rapidly moving ice* ($1\,\mathrm{m\,s^{-1}}$), the acceleration terms increase, but the question is which force drives the ice. If it is air stress, then air and water stresses increase by two orders of magnitude and form the dominant balance; if it is water stress, the geostrophic current velocity is also $\sim 1\,\mathrm{m\,s^{-1}}$ and the magnitude of water stress may be up to 10^{-1} Pa. It is unlikely that internal friction or sea surface tilt would cause such high ice velocities.

Acceleration terms are not important in the standard case. Local acceleration disappears in the steady state ($T = \infty$) and rises to 0.1 Pa when the timescale is shortened to 10^3 s; this is the inertial timescale of drift ice. The ratio of advective to local acceleration is UT/L, equal to 10^{-1} in the standard case. In the case of a short length scale and high ice velocity the advective term is comparable to local acceleration. However, high ice velocity scale increases also the surface stresses and short length scale increases the internal friction.

The length scale becomes important in internal friction and advection. In the case of short length scales they both increase and, in compact drift ice, internal friction becomes the governing term. In compact ice a short length scale increases internal friction, which suppresses the role of advection. Consequently, in sea ice dynamics advective acceleration may only become important in a rapid free drift with a short length scale (e.g., under low wind conditions when the ice is just tracking the ocean surface layer currents).

In vertically integrated shallow-water models, the wind and bottom stresses are highly important (analogous to wind stress and water stress here). But, instead of internal friction in the ice case, the Coriolis term and pressure gradient are important in the shallow-water case. This difference is due to the large difference between the thicknesses of sea ice and the shallow water layer and between the rheologies of ice and water.

Parameters

It is interesting also to look into the role of parameters of the drift ice dynamics in the determination of scales of forces. These parameters are (i) planetary parameters (acceleration due to gravity and Coriolis parameter), (ii) ice parameters (ice density and strength), and (iii) drag parameters (air and water drag coefficients).

The planetary parameters show up in the Coriolis term and sea surface tilt. The force due to sea surface tilt is $-\rho h g \beta$, and there is an apparent proportionality between the force and gravitational acceleration. However, in ocean physics external forcing produces the product $g\beta$, and therefore changes in gravity would be

compensated by changes in the sea surface tilt without changing the drift of sea ice. The Coriolis effect shows up in the pressure gradient and Coriolis acceleration, which can be combined into $\rho hf(\boldsymbol{U}_{wg} - \boldsymbol{u})$. With increasing planetary rotation rate, the role of this term increases and $\boldsymbol{u} \to \boldsymbol{U}_{wg}$ as $f \to \infty$. In addition, f^{-1} introduces a time scale. Compared with the Earth, increasing the Coriolis parameter brings the Coriolis time scale toward the inertial time scale of drift ice.

The role of ice density is first of all in that how the ice floats, and this has further consequences to ice deformation and drag forces. As such, the density influences the acceleration terms and body forces, which are not among the leading terms. Ice strength depends on ice density implicitly, since resistance to deformation is less for less dense material. In all, increasing density slows down the dynamics and vice versa. Ice strength shows up only in the internal friction, and therefore implications of changing strength are straightforward. Similar conclusions can be made for changes in drag parameters.

5.4.2 Dimensionless form

For a more quantitative approach to the scaling problem, the momentum equation is examined in dimensionless form. Let the scaling factors be H, U, P, T and L as in Section 5.4.1 for the thickness, velocity and stress of ice and for the time and horizontal length scales. We denote dimensionless quantities with asterisks (e.g., $\boldsymbol{u}^* = \boldsymbol{u}/U$). Assuming $U \neq 0$, a convenient scaling of the momentum equation is made by the ice-water stress magnitude $\rho_w C_w U^2$:

$$\begin{aligned}
&\frac{\rho}{\rho_w C_w}\left(\frac{H}{UT}\, h^* \frac{\partial \boldsymbol{u}^*}{\partial t^*} + \frac{H}{L}\, h^* \boldsymbol{u}^* \cdot \nabla^* \boldsymbol{u}^* + \frac{fH}{U}\, h^* \boldsymbol{k} \times \boldsymbol{u}^*\right) = \\
&\frac{1}{C_w} \cdot \frac{PH}{\rho_w U^2 L}\, \nabla^* \cdot \sigma^* + \frac{\rho_a C_a}{\rho_w C_w}\, (\cos\theta_a + \sin\theta_a \boldsymbol{k}\times) U_a^* \boldsymbol{U}_a^* \qquad (5.52) \\
&\quad + (\cos\theta_w + \sin\theta_w \boldsymbol{k}\times)|\boldsymbol{U}_{wg}^* - \boldsymbol{u}^*|(\boldsymbol{U}_{wg}^* - \boldsymbol{u}^*) - \frac{\rho}{\rho_w C_w} \cdot \frac{gH}{U^2}\, h^* \beta
\end{aligned}$$

The scaling was done by the ice–water stress emphasizing the very close link between drift ice dynamics and the dynamics of the ocean boundary layer. The ocean has a firm grip on the ice, and many of the characteristics of sea ice drift are oceanic: ice transfers momentum from the wind to the ocean and receives part of it back as modified by the ocean. However, it is also clear that ice itself has an active role to play in the interaction between the atmosphere and the ocean. Consequently, we have $0 \ll C_w \ll \infty$.

When $C_w \to \infty$, drift ice follows the ocean surface current exactly and it only influences by transferring the air drag force into the ocean. When $C_w \to 0$, the dynamics would be governed by the balance $\rho hf \boldsymbol{k} \times \boldsymbol{u} = \nabla \cdot \boldsymbol{\sigma} + \boldsymbol{\tau}_a$. With no internal friction, the result would then be the Ekman transport $\rho h \boldsymbol{u} = -f^{-1} \boldsymbol{k} \times \boldsymbol{\tau}_a$ (i.e., ice motion is perpendicular to the wind and $|\boldsymbol{u}| \infty |\boldsymbol{U}_a|^2$; $|\boldsymbol{u}| \sim 2\,\mathrm{m\,s^{-1}}$ for $|\boldsymbol{U}_a| \sim 10\,\mathrm{m\,s^{-1}}$).

With strong internal friction, the influence of Coriolis acceleration reduces and ice adjusts to the wind field by rearranging its state. This situation is sometimes close to reality when wind-driven drift is strongly slowed down by the internal friction. Scaling also included the velocity U, which can be assumed non-zero. For $U \to 0$, we have a stationary ice cover held together by a plastic yield limit.

The following fundamental dimensionless quantities arise to characterize the importance of the different terms:

- Density ratio $\gamma = \dfrac{\rho}{\rho_w}$
- Local acceleration: *Strouhal number* $Sr = \dfrac{UT}{H}$
- Advective acceleration: *draft aspect ratio* $\delta_A = \dfrac{H}{L}$
- Coriolis acceleration: *Rossby number* $Ro = \dfrac{U}{fH}$
- Internal friction: *friction number* $X = \dfrac{1}{\rho_w C_w U^2} \dfrac{PH}{L}$
- Wind stress: *Nansen number* $Na = \sqrt{\dfrac{\rho_a C_a}{\rho_w C_w}}$
- Pressure gradient: *Froude number* $Fr = \dfrac{U}{\sqrt{gH}}$

The dimensionless equation of motion is then:

$$\frac{\gamma}{C_w Sr} h^* \frac{\partial \boldsymbol{u}^*}{\partial t^*} + \frac{\gamma\delta}{C_w} h^* \boldsymbol{u}^* \cdot \nabla^* \boldsymbol{u}^* + \frac{\gamma}{C_w Ro} h^* \boldsymbol{k} \times \boldsymbol{u}^* =$$

$$X \nabla^* \cdot \boldsymbol{\sigma}^* + Na^2 (\cos\theta_a + \sin\theta_a \boldsymbol{k} \times) U_a^* \boldsymbol{U}_a^* \tag{5.53}$$

$$+ (\cos\theta_w + \sin\theta_w \boldsymbol{k} \times) |\boldsymbol{U}_{wg}^* - \boldsymbol{u}^*| (\boldsymbol{U}_{wg}^* - \boldsymbol{u}^*) - \frac{\gamma}{C_w Fr^2} \cdot h^* \boldsymbol{\beta}$$

In ice–water stress just the normalized ice–ocean velocity difference remains and the magnitude is one. Wind velocity is naturally scaled by the Nansen number down to $\mathrm{Na}\boldsymbol{U}_a^*$ for a representative wind-driven ice velocity. If other terms are small, $|\boldsymbol{U}_{wg}^* - \boldsymbol{u}^*| \sim \mathrm{Na} U_a^*$ and the direction between $\boldsymbol{U}_{wg}^* - \boldsymbol{u}^*$ and $\boldsymbol{U}_a^*$ will depend on boundary-layer angles. The ratio $\Gamma_{iw} = u^*/U_{wg}^*$ tells us whether the ice is driving the oceanic boundary layer ($\Gamma_{iw} > 1$) or vice versa ($\Gamma_{iw} < 1$). Wind and the geostrophic water current are outer boundary velocities between which the ice and water velocities lie. Consequently, the ratio $\Gamma_{aw} = \mathrm{Na} U_a / U_{wg}$ tells us whether the ice motion is dominantly wind-driven ($\Gamma_{aw} > 1$) or driven by oceanic circulation ($\Gamma_{aw} < 1$).

The influence of sea surface tilt is described by the Froude number. Since $C_w Fr^2 \sim 10^{-5}$, a very steep sea surface slope ($\beta \sim 10^{-5}$) would be needed for

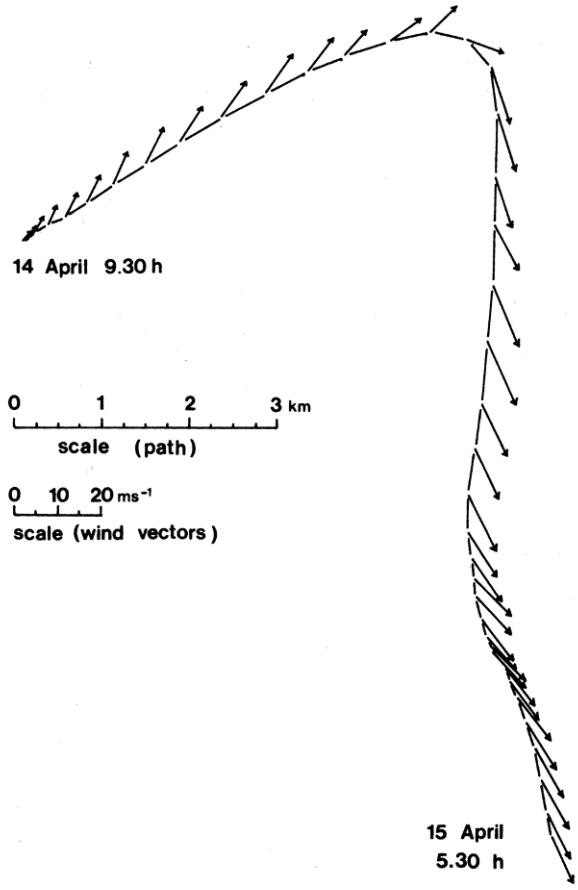

Figure 5.15 Observed path of a drifting station and wind in the Baltic Sea, April 1979. The time interval between trajectory points and wind vectors is 30 min.
From Leppäranta (1981b).

the pressure gradient to become important. Rewriting the tilt term by using the geostrophic current, the dimensionless form would be

$$\frac{\rho f h \boldsymbol{k} \times \boldsymbol{U}_{wg}}{\rho_w C_w U^2} = \frac{\gamma}{C_w Ro} h^* \boldsymbol{k} \times \boldsymbol{U}^*_{wg} \tag{5.54}$$

The influence of the pressure gradient can be compared with the influence of the Coriolis acceleration, as their ratio becomes U_{wg}/u.

The internal friction looks more complicated. It is seen that the coefficient X contains a length scale equal to the ratio between ice strength and ice-water stress:

$$L = \frac{P^* H}{\rho_w C_w U^2} \tag{5.55}$$

When $X \sim 1$, internal friction smooths the ice motion over these length scales. E.g., for $P^* \approx 10\,\text{kPa}$, $H \approx 1\,\text{m}$, and $\tau_w \approx 0.1\,\text{Pa}$ we have $L \approx 10\,\text{km}$. When $X \ll 1$, free drift situation results with no internal length scales, and when $X \gg 1$, ice velocity becomes very small approaching a stationary state.

The inertial timescale is included in the Strouhal number (Sr) and equals:

$$T_\text{I} = \frac{\gamma H}{C_w U} \tag{5.56}$$

Thus for $H \sim 1\,\text{m}$ and $U \sim 10\,\text{cm}\,\text{s}^{-1}$, $T_\text{I} \sim 2 \times 10^3\,\text{s} \sim \frac{1}{2}\,\text{h}$ (a short timescale is seen in Figure 3.9). Figure 5.15 shows in detail a case in which sea ice drift followed a sudden large change in the direction of strong wind. This is very short in comparison with the timescale of ice advection and deformation (typically 1–100 days, see Section 3.4). Since the timescales of forcing are usually much longer than the inertial timescale of ice, a quasi-steady approach can often be taken. This means solving the steady-state form of the momentum equation first, allowing the advection and deformation of ice with the obtained velocity field, and thereafter returning to the steady-state momentum equation with a new ice state field, etc.

The influence of advection is given by $\delta_A \gamma / C_w$. Thus, increasing the value of velocity for intensive dynamics does not help advection because ice-water friction increases at the same rate; only over a very short length scale ($H/L \sim \rho_w C_w / \rho \sim 10^{-3}$) may momentum advection may be important. Using the advective time scale $T_D = L/U$ (see Section 3.4), the influence of advection can be expressed as:

$$\frac{\gamma}{C_w} \cdot \frac{H}{L} = \frac{T_\text{I}}{T_D} \tag{5.57}$$

The Coriolis term contains the Rossby number, which includes the Coriolis period $f^{-1} \sim 10^4\,\text{s}$ (a fundamental timescale in geophysical fluid dynamics). The influence of Coriolis acceleration can be expressed as:

$$\frac{\gamma}{C_w Ro} = T_\text{I} f \tag{5.58}$$

Thus the Coriolis term becomes important when the inertial timescale is comparable to the Coriolis period – a very high ice thickness would be needed for this.

As a consequence, in drift ice dynamics the internal timescales satisfy in general:

$$T_\text{I} \ll f^{-1} \ll T_D \tag{5.59}$$

Stationary ice

In the case of a stationary ice field the momentum equation is reduced to the static case $\boldsymbol{u} \equiv 0$. A convenient scaling is obtained using the internal friction of ice, PH/L. Then we have

$$\nabla^* \cdot \boldsymbol{\sigma}* + \frac{L}{PH} \boldsymbol{F} = 0 \tag{5.60}$$

Table 5.6 Comparison between the characteristics of sea ice drift in Arctic, Antarctic and Baltic Sea waters. The velocity scale is $10\,\mathrm{cm\,s^{-1}}$ in all cases.

		Arctic	Antarctic	Baltic
Ice thickness	H	2–5 m	0.5–2 m	0.1–1 m
Free drift	Na	2%	3%	2%
Internal length scale	PH/F	250 km	100 km	50 km
Inertial timescale	$H/C_{\mathrm{w}}U$	2 h	1.5 h	0.5 h
Adjustment timescale	L/U	30 d	10 d	5 d

where $\boldsymbol{F} = \boldsymbol{\tau}_a + \boldsymbol{\tau}_w - \rho g h \boldsymbol{\beta}$ is the forcing. Now, both surface stresses $\boldsymbol{\tau}_a$ and $\boldsymbol{\tau}_w$ are independent of the ice (apart from surface roughness), but the pressure gradient is proportional to the ice thickness. The key dimensionless number is $X_0 = PH/FL$. When $X_0 > 1$ the forcing is below the strength of the ice and the stationarity condition holds; but when $X_0 < 1$ the opposite is true.

5.4.3 Basin scales

The theory of drift ice dynamics has been applied to a wide range of basins. At the upper bound, the length scale of polar oceans is up to 3,000 km. Large Arctic and subarctic seas (e.g., the Barents Sea and Okhotsk Sea) are at the 1,000 km size. Further down there are small mediterranean and marginal seas with size 100–300 km (e.g., the Baltic Sea and the Gulf of St Lawrence). There are also large lakes in this size band that have drift ice (e.g., the Great Lakes in North America, see Wake and Rumer, 1983, and Lakes Ladoga and Vänern in Europe). Small bays of freezing seas and lakes, 10–30 km in size, exist with occasional drift ice conditions. Even ice flows in large rivers can be modelled using the present drift ice dynamics theory (e.g., ice flows in the Niagara River in North America, see Shen *et al.*, 1990). As shown in the previous section, an ice covered basin is a drift ice basin when $X_0 < 1$ or $FL > PH$.

Two widely investigated areas for sea ice dynamics are the Arctic Ocean and the Baltic Sea. In the former the ice thickness and the size of the basins are one order of magnitude larger than in the latter. This scaling applies to the ice morphology as well (see Table 2.1). The stability ratio h/L is about the same.

The Baltic Sea belongs to the seasonal sea ice zone. The size of its basins is 100–300 km, the thickness of undeformed ice can reach 1 m, and ice ridges are typically 5–15 m thick. The extent of the fast ice zone is largely influenced by the formation of grounded ridges, in the Baltic extending to sea depths of 5–15 m. The motion of ice ranges between zero and the free drift state, depending on the forcing and thickness of the ice. Compact, thick-ice fields may remain stationary. When drifting the geometry of the fast ice boundary has a strong aligning influence on ice motion. In fact, the whole ice field belongs to the coastal boundary layer. Compact ice fields show plastic behaviour with a yield strength of 10–100 kPa and

significant shear strength, while slight opening in the ice fields transforms the flow to a viscous regime.

Table 5.6 shows the characteristics of sea ice dynamics in the polar seas and in the Baltic Sea. The principal reason for the difference in values is ice thickness (forcing and characteristic ice velocity are about the same in all these areas). The ice–water drag coefficient is relatively low in Antarctica (apparent in the free drift level and inertial timescale).

5.5 DYNAMICS OF A SINGLE ICE FLOE

A single ice floe (say, Ω) has three degrees of freedom in its movement: the translational velocity $\boldsymbol{U}$ and angular velocity around the vertical axis. For a point at distance $\boldsymbol{r}$ from the mass centre of the floe, the velocity is (see Figure 3.1):

$$\boldsymbol{u} = \boldsymbol{U} + \dot{\omega}\boldsymbol{k} \times \boldsymbol{r} \tag{5.61}$$

By definition of the mass centre $\int_\Omega hr d\Omega = 0$. The motion of the floe must satisfy the conservation of linear and angular momentum (e.g., Landau and Lifschitz, 1976):

$$\rho\tilde{h}\left(\frac{d\boldsymbol{u}}{dt} + f\boldsymbol{k} \times \boldsymbol{u}\right) = \frac{1}{S_f}\int_\Omega (\boldsymbol{\tau}_a + \boldsymbol{\tau}_w - \rho h \nabla\Phi)\, d\Omega \tag{5.62a}$$

$$\rho\tilde{h}r_{\mathrm{I}}^2 \frac{d\dot{\omega}}{dt} = \frac{1}{S_f}\boldsymbol{k} \cdot \int_\Omega \boldsymbol{r} \times (\boldsymbol{\tau}_a + \boldsymbol{\tau}_w - \rho h \nabla\Phi)\, d\Omega \tag{5.62b}$$

where $\tilde{h}$ is mean ice thickness, S_f is the floe area and r_{I} is the radius of gyration defined by:

$$r_{\mathrm{I}}^2 \int_\Omega \rho h d\Omega = \int_\Omega \rho h r^2 d\Omega \tag{5.63}$$

Note that the right-hand side is the moment of inertia of the floe about the vertical axis. Translational motion is determined from the mean floe thickness, but for rotation the radius of gyration also needs to be known. The point of action of inertial and body forces is the mass centre of the floe, while surface forces act on the geometric centre, which is located at the distance $\boldsymbol{r}^* = S_f^{-1}\int_\Omega \boldsymbol{r} d\Omega$ from the mass centre. The quantity $\boldsymbol{r}^*$ measures floe inhomogenuity; for $h =$ constant we have $\boldsymbol{r}^* = 0$. In general:

$$\rho\tilde{h}\left(\frac{d\boldsymbol{u}}{dt} + f\boldsymbol{k} \times \boldsymbol{u}\right) = \boldsymbol{\tau}_a - \rho\tilde{h}\nabla\Phi + \frac{1}{S_f}\int_\Omega \boldsymbol{\tau}_w\, d\Omega \tag{5.64a}$$

$$\rho\tilde{h}r_{\mathrm{I}}^2 \frac{d\dot{\omega}}{dt} = \boldsymbol{k} \cdot (\boldsymbol{r}^* \times \boldsymbol{\tau}_a) + \frac{1}{S_f}\boldsymbol{k} \cdot \int_\Omega \boldsymbol{r} \times \boldsymbol{\tau}_w d\Omega \tag{5.64b}$$

The integrals of ice–water stress cannot be directly evaluated since they depend quadratically on the ice–water velocity difference. Note that the rotation of an

ice floe affects the resistance to translation. Linearizing the ice–water stress $\boldsymbol{\tau}_{w1} = \rho_w C_{w1}[\cos\theta_w + \sin\theta_w \boldsymbol{k}\times](\boldsymbol{U}_w - \boldsymbol{u})$, Eqs. (5.64) become

$$\rho\tilde{h}\left(\frac{d\boldsymbol{u}}{dt} + f\boldsymbol{k}\times\boldsymbol{u}\right) = \boldsymbol{\tau}_a + \boldsymbol{\tau}_{w1} - \rho\tilde{h}\nabla\Phi - \rho_w C_{w1}\dot{\omega}(\cos\theta_w + \boldsymbol{k}\times\sin\theta_w)\boldsymbol{r}^* \tag{5.65a}$$

$$\rho\tilde{h}r_1^2\frac{d\dot{\omega}}{dt} = \boldsymbol{k}\cdot[\boldsymbol{r}^*(\boldsymbol{\tau}_a + \boldsymbol{\tau}_{w1})] - \rho_w C_{w1}\dot{\omega}\cos\theta_w\tilde{r}^2 \tag{5.65b}$$

where $\tilde{r}^2$ is the mean square radius of the floe. For a homogeneous floe, $\boldsymbol{r}^* = 0$; the floe rotation effect disappears from the translatory motion in the linear case (it would be there for quadratic water stress) but remains as a damping term in rotation. Since then $\tilde{r}^2 = r_1^2$, the timescale of this damping is

$$t_d = \frac{\rho\tilde{h}}{\rho_w C_{w1}\cos\theta_w} \tag{5.66}$$

The timescale is proportional to ice thickness and equals about 1 hour for $h = 1\,\text{m}$. Thus, if a rotation is initiated by floe shear or collision, its lifetime will be short. For an extreme case, a very low drag coefficient would allow relatively long relaxation times.

The derivation and analysis of the equation of motion of drift ice is now complete. Together with the ice conservation law (Section 3.4) and ice rheology (Chapter 4), it forms the closed system used to solve the dynamics of drift ice with a given definition of state (Section 2.6). In the following three chapters, the solution to the drift ice dynamics problem is presented using three different approaches.

6

Free drift

6.1 STEADY STATE SOLUTION

This chapter presents the free drift solution of sea ice dynamics. It is based on the momentum equation only. There is no internal stress, and the ice conservation law is not normally solved since it would eventually lead to an unrealistic ice-state field. The solution describes the velocity at one point or along the path of one ice floe, easily obtained for both steady state (Section 6.1) and unsteady (Section 6.2) situations. The free drift case is analogous to the pure Ekman drift case in ocean dynamics. In Section 6.3 a linear ice–ocean coupled free drift model is presented, and the following section analyzes the frequency spectrum of ice drift. Spatial aspects of free drift are briefly discussed in Section 6.5.

Free drift is defined as the drift of sea ice in the absence of internal friction of ice. The term was introduced by McPhee (1980), although the situation itself has been known from the times of Fridtjof Nansen and Vagn Walfrid Ekman and the *Fram* expedition (1893–1896). Free drift is a good approximation for individual, separate ice floes and for ice fields with low compactness, less than about 0.8 (e.g., McPhee, 1980; Leppäranta and Omstedt, 1990). One may follow the motion in either a Lagrangian frame, in which there is no advective acceleration, or in a Eulerian frame, in which advective acceleration remains. In free drift theory, utilization of a complex number technique is particularly useful (see Section 3.3 for notation, etc.).

Consider the momentum equation of sea ice drift (Eq. 5.10). In free drift theory the following simplifications are made. In the right-hand side, the first term – internal friction ($\nabla \cdot \boldsymbol{\sigma}$) – is neglected as the basic assumption of free drift, and the last term – air pressure gradient – is in general a minor term in sea ice drift as discussed in Chapter 5. In the left-hand side, advective acceleration is always small as shown by the scale analysis in Section 5.4. Thus we have the basic equation of free drift as:

$$\rho h\left(\frac{du}{dt} + \mathrm{i}fu\right) = \tau_a + \tau_w - \rho h g \beta \tag{6.1}$$

M. Leppäranta, *The Drift of Sea Ice*, Springer Praxis Books,
DOI 10.1007/978-3-642-04683-4_6, © Springer-Verlag Berlin Heidelberg 2011

Vagn Walfrid Ekman (1874–1954) was born in Sweden. He was a student of Vilhelm Bjerknes and Fridtjof Nansen, and in his doctoral thesis (1902) presented his theory of ocean currents, including the theoretical explanation of Nansen's observations of the drift of the vessel *Fram* in the Arctic Ocean. He later became a professor at the University of Lund (Sweden). This photograph was taken in 1902.
Reproduced from the V.W. Ekman Family Photo Album, with courtesy of Dr Artur Svansson.

Since the time scale of ice dynamics is short, local acceleration can be ignored when the time scale of interest is more than hours (time scale is proportional to ice thickness, with 1 hour for 1-m thick ice). For this steady state case, an algebraic equation results from Eq. (6.1).

The ice–water stress and sea surface tilt term can be written in terms of the geostrophic current (see Eqs 5.34b and 5.9):

$$\tau_w = \rho_w C_w |U_{wg} - u| \exp(\mathrm{i}\theta_w)(U_{wg} - u) \tag{6.2a}$$

$$\mathrm{i}fU_{wg} = -g\beta \tag{6.2b}$$

Expressing wind stress in general form $\tau_a = \rho_a C_a \exp(\mathrm{i}\theta_a)|U_a|U_a$ (see Eq. 5.34a), we have the algebraic equation:

$$\rho_a C_a \exp(\mathrm{i}\theta_a)|U_a|U_a + \rho_w C_w \exp(\mathrm{i}\theta_w)|U_{wg} - u|(U_{wg} - u) + \mathrm{i}\rho h f (U_{wg} - u) = 0 \tag{6.3}$$

Note that the Coriolis parameter and turning angles are positive in the northern hemisphere and negative in the southern hemisphere.

There are three velocities in the momentum equation. Let their representative scales be: U_a for wind velocity, U for ice velocity, and U_{wg} for geostrophic water velocity. The ratio $\Gamma_{iw} = U/U_{wg}$ tells us whether the ice is driving the ocean ($\Gamma_{iw} > 1$) or vice versa ($\Gamma_{iw} < 1$), and the ratio $\mathrm{Na}\,U_a/U_{wg}$ tells us whether the wind or the current is the dominant force. The solution is determined by boundary-layer parameters and the Coriolis parameter (i.e., Nansen number, Rossby number and the Ekman angles).

In Eq. (6.3) the ice velocity appears always in connection with the geostrophic flow as the difference $U_{wg} - u$. Thus we can solve first the wind-driven ice drift as $u - U_{wg}$ and then add the geostrophic current for the full solution.

Geostrophic sea ice drift

Let us assume there is no wind. In such a case, we can clearly see that, irrespective of drag law parameters and ice thickness, the only solution is $u = U_{wg}$. Sea ice follows the geostrophic flow together with the ocean surface layer. Thus the pressure gradient provides the correct limiting behaviour and continuity with the surface layer and, though small, is therefore important in coupled ice-ocean modelling.

Note that in the case of sea ice the balance between the Coriolis acceleration and sea surface tilt β reads $\mathrm{i}\rho hfu = -\rho gh\beta$ (see Eq. 5.9), which gives $u = \mathrm{i}gf^{-1}\beta$, exactly the same solution as for the surface geostrophic current in the ocean (e.g., for $\beta \sim 10^{-6}$ we have $|u| \sim 0.1\,\mathrm{m\,s^{-1}}$).

6.1.1 Classical case

Free drift of thin ice

Next, wind is added. When ice thickness is small, the Coriolis and pressure gradient terms are small and the solution is easily obtained as:

$$u = Na\exp(-\mathrm{i}\theta_0)U_a + U_{wg} \tag{6.4}$$

where the Nansen number $Na = \sqrt{\rho_a C_a/\rho_w C_w}$ equals the wind factor, and $\theta_0 = \theta_w - \theta_a$ is the deviation angle from the wind-driven ice drift direction to wind direction.

The ratio C_a/C_w is key to determining the free drift speed. The roughnesses of the upper and lower surfaces are to some degree correlated, and therefore the ratio C_a/C_w is not very sensitive to the ice type. A representative value for Arctic Ocean ice cover is $Na \approx 1.7\%$ for the geostrophic references and $Na \approx 2.5\%$ for the surface wind, while in Antarctica these values are much greater (e.g., the surface wind $Na \approx 3.5\%$) due to the low ice–water drag coefficient (see Section 5.3).

Positive rotation is counter-clockwise. The angle θ_w is positive in the northern hemisphere, and as $\theta_a = 0$ for the surface wind, we have $\theta_0 = \theta_w > 0$ and the minus

sign in Eq. (6.4) turns rotation clockwise (i.e., "ice drift is to the right from the wind direction"). In the southern hemisphere $\theta_w < 0$ and rotation is opposite. In the case of geostrophic wind, $\theta_w \approx \theta_a$. Thus the deviation angle is $\theta_0 \approx 0$ for the geostrophic wind or 25° (−25°) for surface wind in the northern (southern) hemisphere.

Example: Zubov's (1945) isobaric drift rule For the geostrophic wind, $\theta_0 \approx 0$. If $U_{wg} = 0$, then $u = NaU_{ag}$ (i.e., ice drifts along the isobars of atmospheric pressure with the speed of 1.7% times the geostrophic wind speed). This law was earlier used as the rule of thumb, easily applied when atmospheric pressure charts are available.

General solution

The general solution can be written in the form:

$$u = \alpha \exp(-\mathrm{i}\theta) U_a + U_{wg} \tag{6.5}$$

where α and θ are the general (scalar) wind factor and the deviation angle: they depend on boundary layer parameters and the Rossby number (Figure 6.1).

The solution of the wind-driven ice drift is obtained from Eq. (6.3) as follows. Let $U_{wg} = 0$. First, rewrite the equation as:

$$\exp(i\theta_a)|U|U = \exp(i\theta_w)|u|u + iRu; \quad R = \frac{\gamma}{C_w Ro}, \quad Ro = \frac{U}{Hf}, \tag{6.6}$$

where the velocity scale is $U = Na|U_a|$. Dividing Eq. (6.6) by $|U|^2$ and taking the modulus and argument of both sides gives us:

$$\alpha^4 + 2\sin\theta_w RNa\alpha^3 + R^2 Na^2\alpha^2 - Na^4 = 0 \tag{6.7a}$$

$$\theta = \arctan\left(\tan\theta_w + \frac{RNa}{\alpha\cos\theta_w}\right) - \theta_a \tag{6.7b}$$

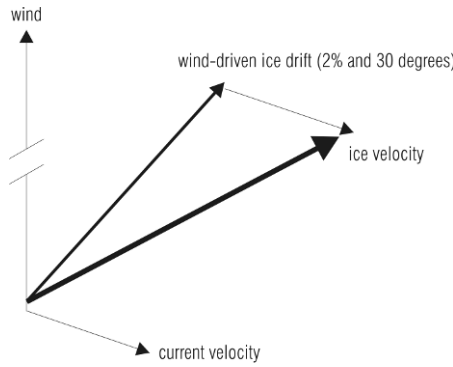

Figure 6.1a Free sea ice drift obtained as a vector addition of wind-driven drift and geostrophic ocean current.

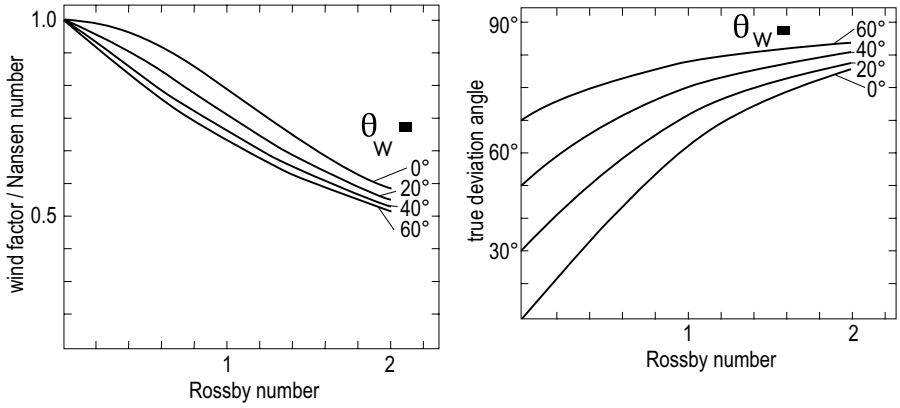

Figure 6.1b The free drift solution: wind factor α (left) and deviation angle θ (right) as a function of a modified Rossby number $R = \gamma/(C_w Ro) = (\rho H f)/(\rho_w C_w \mathrm{Na}|U_a|)$ in the northern hemisphere (the signs of θ_w and θ are reversed in the southern hemisphere).

Note that R, θ_a and θ_w are negative in the southern hemisphere, following the sign of the Coriolis acceleration. The first equation is a fourth-order polynomial of α, which in principle can be solved in closed form; however, this is quite cumbersome and does not allow a simple general expression for α. A numerical iteration scheme provides us an easier way. Figure 6.1 shows the solution in graphical form. It is directly seen that $\alpha \leq Na$ and $|\theta| \geq |\theta_0|$, and

$$\alpha \to Na \text{ and } \theta \to \theta_0 \text{ as } R \to 0 \ (Ro \to \infty) \tag{6.7c}$$

For $|R| \ll 1$, the first correction term to Na is $-\frac{1}{2}\sin|\theta_w|R$. But the accuracy of the thin-ice solution ($R \to 0$) is good for $|R| < 0.2$: α is within 10% below Na and θ is within 10° above θ_0. At the other extreme, $|R| > 2$, the solution is asymptotically:

$$\alpha = Na\sqrt{\sqrt{\frac{R^4}{4}+1}-\frac{R^2}{2}} \approx \frac{Na}{R} \tag{6.8a}$$

$$\theta \approx \arctan\left(\tan\theta_w + \frac{R^2}{\cos\theta_w}\right) - \theta_a \tag{6.8b}$$

In the Arctic, the usual surface wind parameters are 2% for the wind factor and 30° for the deviation angle (Nansen, 1902; Ekman, 1902), as confirmed with drift buoy data later (Thorndike and Colony, 1982). High wind factors have been found in Antarctica. Brennecke (1921) obtained the averages of $\alpha \approx 2.8\%$ and $\theta = -34°$, and Martinson and Wamser (1990) report $\alpha \approx 3\%$ for surface wind in the Weddell Sea. The ratio of the drag coefficients C_a/C_w must therefore be larger in the Weddell Sea than in the Arctic; as discussed in Sections 5.2–5.3, this is due to the hydrodynamically smoother lower surface of ridges and hummocks in the south. The air drag coefficient is about the same in both polar seas. However, Rossby and Montgomery (1935) attributed the high wind factor in Antarctica to hydrographic

conditions in the water beneath the ice but now this looks less likely. The wind factor in the Baltic Sea is 2–2.5% (Leppäranta, 1981b, 1990), while in the Okhotsk Sea it is more than 3% (Fukutomi, 1952).

Example Kinematics data can be utilized to obtain information about the air–ice and ice–water drag parameters (Leppäranta, 1981b). The wind factor and deviation angle approach Na and θ_0 as $R \to 0$; thus, for a drifter on a fixed ice floe, asymptotically $|u - U_{wg}|/U_a \to Na \propto \sqrt{C_a/C_w}$ and $\theta \to \theta_0$ as $R \to 0$. Often C_a is much better known than C_w, and particularly in the case of surface wind $\theta \to \theta_w$ as $R \to 0$.

The theory behind our general solution is best applicable in summer conditions, when there are free paths between floes and open-water areas do not freeze (Figure 6.2). Shuleikin (1938) solved the wind-driven ice–ocean flow problem using the Ekman theory. He used the balance between the air and water stresses and the Coriolis term, resulting in Eq. (6.3) with $U_{wg} = 0$ and exact expressions for the wind factor and deviation angle.

Figure 6.2 "In summer in the Arctic Ocean" by Gunnar Brusewitz, 1980. Gunnar Brusewitz (1924–2004) is an author and artist from Sweden, best known for his drawings of birds. This picture is from the Ymer-80 expedition in the European sector of the Arctic Ocean.
Reproduced from Gunnar Brusewitz, Arktis sommar, 1980, with permission from Wahlström & Widstrand, Stockholm.

At low wind speeds the straight free drift model is questionable, since the stratification of air and water may play a major role. When the wind speed is less than $2\,\mathrm{m\,s^{-1}}$ there is no longer any clear connection between ice motion and wind (Rossby and Montgomery, 1935), since the local wind is overcome by the wind field over a larger area and by ocean currents as well. At $|U_a| = 3$–$4\,\mathrm{m\,s^{-1}}$, there is a rapid decrease in the wind factor as then the stable layer disappears from beneath the ice.

In shallow waters (depth considerably less than the Ekman depth), turning angle and Coriolis acceleration can be ignored, and the solution is in principle easily obtained from $\rho_w C_w |u| u = \tau_a - \rho g h \beta$, where β is sea surface tilt. Since the whole water column is in the frictional boundary layer, the reference depth for the ocean velocity can be taken as the sea bottom, $U_w = 0$, and water drag force becomes depth-dependent. This question has not been addressed in sea ice dynamics investigations, probably because shallow coastal areas are normally covered by landfast ice. But there is now a clear motivation to work on this problem, much due to practical questions related to ice forces.

6.1.2 One-dimensional channel flow

One-dimensional flow models are useful in sea ice dynamics. In free drift it is the external friction coefficients that have the dominant role, while for drift in the presence of internal friction much of the resistance comes from compression. Consequently, first-order physics can be taken as non-rotational. The mathematics becomes much more simple and the solutions easy to interpret. The one-dimensional free drift equation comes from Eq. (6.3) as:

$$\tau_a + \rho_w C_w |U_w - u| (U_w - u) - \rho g h \beta = 0 \tag{6.9a}$$

All variables are now real. If $\tau_a - \rho g h \beta > 0$, then $u > U_w$, and the solution is

$$u = \sqrt{N a^2 |U_a| U_a - \frac{g h'' \beta}{C_w}} + U_w \tag{6.9b}$$

where h'' is the draft.

Consider an open channel of finite depth H and bottom slope $-\beta$ (Figure 6.3). The coupled momentum equations for the ice and water are:

$$\tau_a + \tau_w + \rho g h \beta = 0 \tag{6.10a}$$

$$\left.\begin{aligned} &\frac{d}{dz}\left(K_w \frac{dU_w}{dz}\right) + g\beta = 0 \\ &z = 0: \quad U_w(0) = 0 \\ &z = H: \quad K_w \frac{dU_w}{dz} = \frac{\tau_w}{\rho_w} \end{aligned}\right\} \tag{6.10b}$$

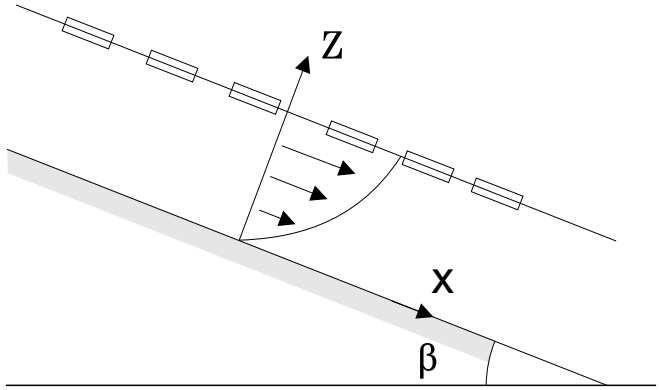

Figure 6.3 Schematic picture of open channel flow.

where K_w is the eddy viscosity coefficient of water, and the vertical coordinate z is taken up from the channel bottom. With $K_w = \text{constant}$, this system can be directly integrated, and the solution for velocity is:

$$U_w = \frac{g\beta}{K_w}\left(H + \frac{\rho}{\rho_w}h - \frac{z}{2}\right)z + \frac{\tau_a}{\rho_w K_w}z \tag{6.11}$$

and by continuity $u = U_w(H)$. Fixing the total volume of water (solid + liquid), we may write $H_0 = H + h'' = \text{constant}$, where H is the depth of liquid water and $h'' = (\rho/\rho_w)h$ is the draft, which corresponds to the volume of water stored in the ice. The surface velocity is then (cf. Figure 6.3):

$$U_w(H) = \frac{g\beta}{2K_w}(H_0^2 - h''^2) + \frac{\tau_a}{\rho_w K_w}(H_0 - h'') \tag{6.12}$$

This shows that the more ice is formed and consequently the less liquid water there is, the smaller the surface velocity will be. The reason is that when the thickness of ice increases, the depth of liquid water decreases and the bottom friction becomes relatively more important. In wind-driven channel flow ($\beta = 0$), the ice velocity is proportional to the depth of the liquid water, while in gravity-driven flow the dependence is quadratic (when $h'' \ll H_0$).

Example In classical hydraulics the Chezy formula[1] is applied for flow calculations (e.g., Li and Lam, 1964). The flow is driven by gravity alone and is assumed uniform, and the mean velocity is:

$$\tilde{U}_w = \sqrt{\frac{8gm\beta}{\mu}}$$

[1] Classical formula in river hydraulics, describing the steady state flow velocity balancing the bottom friction and gravity forces (see, e.g., Li and Lam, 1964).

where m is the hydraulic radius and μ is the friction coefficient, which can be determined from the Manning's formula[2] $\sqrt{8g/\mu} = 0.262\sqrt{g}\, m^{1/6} n^{-1}$ where n is the Manning coefficient. For a channel with a half-circle cross-section $m = \frac{1}{2}H$, while a rectangular cross-section gives $m = \frac{1}{2}H(1+\delta)$, where δ is the channel aspect ratio. The Manning coefficient is $n \approx 0.020\,\mathrm{m}^{1/6}$ for soil material. Thus, $U_w \propto \sqrt{\beta}$ and $U_w \propto H^{2/3}$, while in Eq. (6.12) $U_w \propto \beta$ and $U_w \propto H^2$. The difference is due to the different treatment of friction. Chezy's model has quadratic friction and includes also the vertical sides of the channel. For $\beta \sim 10^{-4}$ and $m = 5\,\mathrm{m}$ we have $U_w \sim 1.2\,\mathrm{m\,s^{-1}}$. Assuming that the ice drifts with the Chezy flow, the result agrees with the surface velocity from Eq. (6.9) when the eddy viscosity is $K_w = 0.041\,\mathrm{m^2\,s^{-1}}$, which is a realistic number (e.g., Cushman-Roisin, 1994).

In a channel with a closed end, a surface slope develops under wind forcing. In the steady state the slope balances the surface stress, so that the vertical mean velocity of water is zero. The coupled ice–water model is thus:

$$\tau_a - \rho_w C_w |u| u - \rho g h \beta = 0 \tag{6.13a}$$

$$\rho_w C_w |u| u - \rho_w g H \beta = 0 \tag{6.13b}$$

where for simplicity τ_a, $u > 0$ has been assumed. The solution is $u = Na U_a \sqrt{H/(H+h'')}$. In shallow seas the influence of depth shows up in the water drag coefficient in Na and in the square root factor. The free drift assumption, however, breaks down when the ice starts to pack at the end of the channel. This case will be examined in the Chapter 7.

6.1.3 Shallow waters

In shallow water, where the sea depth is less than the Ekman depth ($\sim$30 m), the Earth's rotation can be ignored for ice and water. There is no geostrophic water current to stand for the drag reference, and the bottom friction of the water body must be taken into account. Then, for a coupled ice–ocean steady-state model, with complex variables:

$$\rho_a C_a |U_a| U_a + \rho_w C_w |U_w - u| (U_w - u) - \rho g h \beta = 0 \tag{6.14a}$$

$$-\rho_w C_w |U_w - u| (U_w - u) - \rho_w C_b |U_w| U_w - \rho_w g H \beta = 0 \tag{6.14b}$$

where U_w is the water velocity at mid-depth and C_b is the bottom drag coefficient. Both ice–water and bottom drag coefficients depend on depth.

Assume an infinite ocean with constant wind. In such a case there is no build-up of sea surface slope, $\beta = 0$, and the solution is:

$$u = \sqrt{\frac{\rho_a C_a}{\rho_w C_w}}\, U_a + U_w, \quad U_w = \sqrt{\frac{\rho_a C_a}{\rho_w C_b}}\, U_a \tag{6.15}$$

[2] Classical formula in river hydraulics for the friction coefficient (see, e.g., Li and Lam, 1964).

Assuming that $C_w \sim C_b$, we have $|u/U_w| \sim 2$. As the sea depth decreases, both water and bottom drag coefficients increase with $|u/U_w| \approx$ constant and u, $U_w \to 0$. Since the sea surface tilt term is independent of the velocities, the case $\beta \neq 0$ is easy to treat.

We can then define a semi-infinite ocean as the complex half-plane $\{z: Rez < 0\}$ and take the wind blowing toward the shore. At steady state, the mean water velocity U_w must be zero, and the solution is the same as that in the channel model, $u = NaU_a\sqrt{H/(H+h'')}$.

6.1.4 Linear model

Quadratic water stress introduces nonlinearity to the free drift system. However, this nonlinearity is not very strong and a linear model is sufficiently good for several cases. To preserve the approximate linearity between ice and wind velocities, it is convenient to linearize the wind stress as well. The linear forms are expressed as:

$$\tau_a = \rho_a C_{a1} \exp(\mathrm{i}\theta_a) U_a \tag{6.16a}$$

$$\tau_w = \rho_w C_{w1} \exp(\mathrm{i}\theta_w)(U_w - u) \tag{6.16b}$$

where linear drag law coefficients may be estimated from quadratic ones using fixed scaling speeds: $C_{a1} = C_a|U_{a0}|$ and $C_{w1} = C_w|(U_w - u)_0|$; this is essentially the same drag law that results from the classical Ekman solution, with $C_a|U_a| = \sqrt{K_a f}$ and $C_w|U_w| = \sqrt{K_w f}$ and the boundary layer angle changed to θ_a and θ_w from 45°. Defining the number Na_1 for the linear drag law as:

$$Na_1 = \frac{\rho_a C_{a1}}{\rho_w C_{w1}}, \tag{6.17}$$

the resulting steady state solution is:

$$u = a_1 U_a + U_w, \quad a_1 = \frac{\rho_a C_{a1} \exp(\mathrm{i}\theta_a)}{\rho_w C_{w1} \exp(\mathrm{i}\theta_w) + \mathrm{i} f\rho h} = \frac{\exp(\mathrm{i}\theta_a)}{\exp(\mathrm{i}\theta_w) + \mathrm{i}\gamma f h / C_{w1}}\, Na_1 \tag{6.18}$$

where the coefficient a_1 includes the linear wind factor $\alpha_1 = |a_1|$ and the linear deviation angle $\theta_1 = \arg a_1$. It depends on the boundary-layer parameters and ice thickness, but in contrast to the quadratic solution it is independent of the velocity scale.

Example: Ekman solution In his PhD thesis, Ekman (1902) was the first to devise linear friction laws. He obtained $C_{a1} = \sqrt{K_a f}$, $C_{w1} = \sqrt{K_w f}$ and $\theta_a = \theta_w = 45°$, and he neglected the geostrophic current. The solution was therefore for the wind-driven ice drift:

$$u = \frac{\rho_a \sqrt{K_a f}(1 + \mathrm{i})}{\rho_w \sqrt{K_w f}(1 + \mathrm{i}) + \mathrm{i}\rho h f}\, U_a$$

For $h \to 0$, the wind factor becomes $\rho_a\sqrt{K_a}/(\rho_w\sqrt{K_a})$.

6.2 NON-STEADY CASE

The small amount of inertia of drift ice was clearly illustrated in historical data; consequently, not much attention was paid to it. Shuleikin (1938) analysed the free drift case and noted inertial oscillations due to the Coriolis term and the short response time of about 1 h. Zubov (1945) also reported the quick (a few hours) response of ice to wind. An example of the rapid response of ice drift to changes in wind is shown in Figure 5.15.

6.2.1 One-dimensional flow with quadratic surface stresses

The full, nonlinear, free drift equation does not allow for a general analytical solution. The one-dimensional case can be easily solved for constant forcing. The equation reads:

$$\rho h \frac{\mathrm{d}u}{\mathrm{d}t} = \rho_a C_a \,\mathrm{sgn}(U_a) U_a^2 + \rho_w C_w \,\mathrm{sgn}(U_w - u)(U_w - u)^2 \tag{6.19a}$$

If the wind and current velocities are constant, the analytical solution can be obtained. Without loss of generality we can assume that $U_a \geq 0$, $U_w = 0$, and $u \geq 0$ (as usual, the solution for $U_w \neq 0$ is obtained by adding U_w to the solution with $U_w = 0$. The time scale and the steady state solution are given by:

$$T_\mathrm{I} = \frac{\gamma h}{C_w U}, \quad U_F = NaU_a \tag{6.19b}$$

where U is the velocity scale. Eq. (6.19a) is separable and integrates into (Leppäranta, 1981b; Goldstein *et al.*, 2009):

$$u(t) = \frac{u_0}{1 + t/T_\mathrm{I}}, \quad U_a = 0, \quad U = |u_0| \tag{6.20a}$$

$$u(t) = U \tanh\left[\left(\frac{t}{T_\mathrm{I}}\right) + \operatorname{arctanh}\left(\frac{u_0}{U}\right)\right], \quad U_a > 0, \quad u_0 < U_F = U \tag{6.20b}$$

$$u(t) = U \coth\left[\left(\frac{t}{T_\mathrm{I}}\right) + \operatorname{arccoth}\left(\frac{u_0}{U}\right)\right], \quad U_a > 0, \quad u_0 > U_F = U \tag{6.20c}$$

For $h \sim 1$ m and $U \sim 0.1$m/s the timescale is $\sim \frac{1}{2}$h. In (6.20b, c) the time scale can be written in the form:

$$T_\mathrm{I} = \frac{\rho h}{U\sqrt{\rho_a C_a \rho_w C_w}} \tag{6.21a}$$

Thus, when $U_a \neq 0$ the response time is proportional to $1/\sqrt{C_a C_w}$, decreasing with both air and water drag coefficients, while the steady-state velocity is proportional to $\sqrt{C_a/C_w}$. Since surface and bottom roughnesses are positively correlated, rougher

ice responds faster but, however, the steady-state velocity is not very sensitive to roughness. In relaxation to rest ($U_a = 0$), the timescale can be expressed as:

$$T_{\mathrm{I}} = \frac{\rho h}{U \rho_w C_w} \tag{6.21b}$$

6.2.2 Linear two-dimensional model

The two-dimensional non-steady problem can be analytically examined using the linear model. This model possesses the strong property of superposition, which allows us to construct general solutions from simple elementary solutions. The linear model is written:

$$\rho h \frac{du}{dt} = (\rho_w C_{w1} \, \mathrm{e}^{\mathrm{i}\theta_w} + \mathrm{i}\rho h f)(U_{wg} - u) + \tau_a \tag{6.22a}$$

The steady-state system is described by Nansen (Eq. 6.17) and Rossby numbers, and for the unsteady part the Strouhal number (see Section 5.4.2) is taken. There are two time scales, relaxation time and Coriolis period:

$$T = \frac{\rho h}{\rho_w C_{w1}}, \text{ and } f^{-1} \tag{6.22b}$$

Eq. (6.22a) is a linear non-homogeneous equation, and the solution is directly integrated from:

$$u(t) = u_0 \, \mathrm{e}^{-\lambda_i t} + \int_0^t \left(\lambda_i U_{wg} + \frac{\tau_a}{\rho h} \right) \mathrm{e}^{-\lambda_i (t-s)} ds \tag{6.23}$$

where $\lambda_{\mathrm{i}} = \exp(\mathrm{i}\theta_w) T^{-1} + \mathrm{i}f$. Furthermore, $\mathrm{Re}\,\lambda_i$ is the inverse response time and $\mathrm{Im}\,\lambda_i$ is the oscillation frequency of the system. If they are both non-zero, a damping oscillatory solution results for constant forcing.

For constant forcing we have:

$$u(t) = u_0 \, \mathrm{e}^{-\lambda_i t} + (1 - \mathrm{e}^{-\lambda_i t})(U_{wg} + a_1 U_a) \tag{6.24}$$

where a_1 is the steady state complex wind factor given in Eq. (6.18). Thus, the ice adjusts from the initial velocity to the steady state velocity with adjustment time scale $\lambda_{\mathrm{i}}^{-1}$. For $U \sim 0.1\,\mathrm{m\,s^{-1}}$ and $h \sim 1\,\mathrm{m}$, we have $|\lambda_{\mathrm{i}}^{-1}| \sim \frac{1}{2}\,\mathrm{h}$. Note that the oscillation frequency is different from the Coriolis frequency; this bias is an artefact left over from using a passive ocean in this model and will be removed when using a coupled ice-ocean model in Section 6.3.

Tidal ice flow

The periodic forcing case can be applied to the tidal problem. Tidal currents can be taken independently of the ice appearing as a periodic forcing in Eq. (6.20a). Oceanic velocity is fixed by $U_w = U_0 \exp(\mathrm{i}\omega t)$ where U_0 and ω are the tidal velocity amplitude

and frequency. Let us take a simple approach by ignoring wind. The transient term can also be left out, and then:

$$u(t;\omega) = \int_0^t \lambda_i U_0 \, \mathrm{e}^{\mathrm{i}\omega s} \, \mathrm{e}^{-\lambda_i (t-s)} ds \tag{6.25}$$

The solution becomes:

$$u(t;\omega) = \Gamma(\omega) U_0 \, \mathrm{e}^{\mathrm{i}\omega t}, \quad \Gamma(\omega) = \frac{\lambda_i}{\lambda_i + \mathrm{i}\omega} \tag{6.26a}$$

The frequency of ice velocity thus follows the tidal current. The transfer function $\Gamma(\omega)$ is, ignoring Ekman angle, written:

$$\Gamma(\omega) = \frac{1 - f(f+\omega)T^2 - \mathrm{i}\omega T}{1 + [(f+\omega)T]^2} \tag{6.26b}$$

For $f = 0$ the phase is delayed by ωT radians and amplitude is damped by $1/\sqrt{1+(\omega T)^2}$. Since $T \sim \frac{1}{2}$h for $h \sim 1$ m, in semi-diurnal tides the phase lag is $\sim\frac{1}{2}$h and the amplitude is 97% of the amplitude of the tidal current. Allowing for Coriolis acceleration changes the situation to some degree. For semi-diurnal tides $|\omega| \approx |f|$ in high polar regions. If $\omega = -f$, the tidal and inertial currents rotate in the same direction and then $\Gamma(\omega) = 1 - \mathrm{i}\omega T$ (i.e., the lag remains but the amplitude is strengthened by the factor of $\sqrt{1+(\omega T)^2}$. If $\omega = f$, the amplitude weakens and phase lag decreases with increasing time scale. When $|\omega T| \ll 1$ the solution is symmetric to ω, to the first order; but for $|\omega T| = 1/\sqrt{2}$, which requires thick ice ($h \sim 3$ m), we have $\Gamma = -\mathrm{i}/(3\sqrt{2})$ or damping factor of $\frac{1}{4}$ and phase delay of 3 hours.

Thus for first-year ice the tidal period is much longer than the inertial response time of drift ice, and consequently the transfer function Γ is not much different from unity. Therefore, a quasi-steady model would also be applicable. Because of the linearity of the system, ice follows the tide in a free drift tidal flow and the wind-driven drift component can be superposed on top. In multi-year ice, significant modification of the tidal cycle takes place when the tide rotates opposite to the inertial oscillation. A half-day cycle for divergence-convergence of an ice drift had already been reported by Nansen (1902) and Sverdrup (1928). They suggested it to be a tidal phenomenon. However, in polar oceans the semi-diurnal tidal period and inertial period are very close.

6.2.3 Drift of a single floe

Drifting stations have sometimes been installed on large ice floes or islands (Figure 6.4), and observations about their movements as a rigid body exist. In particular, the path of inhomogeneous floes is affected by the geometry of the floe via rotational motion.

Let us now return to the normal vector formulation of two-dimensional quantities and equations. A single ice floe drifts with three degrees of freedom:

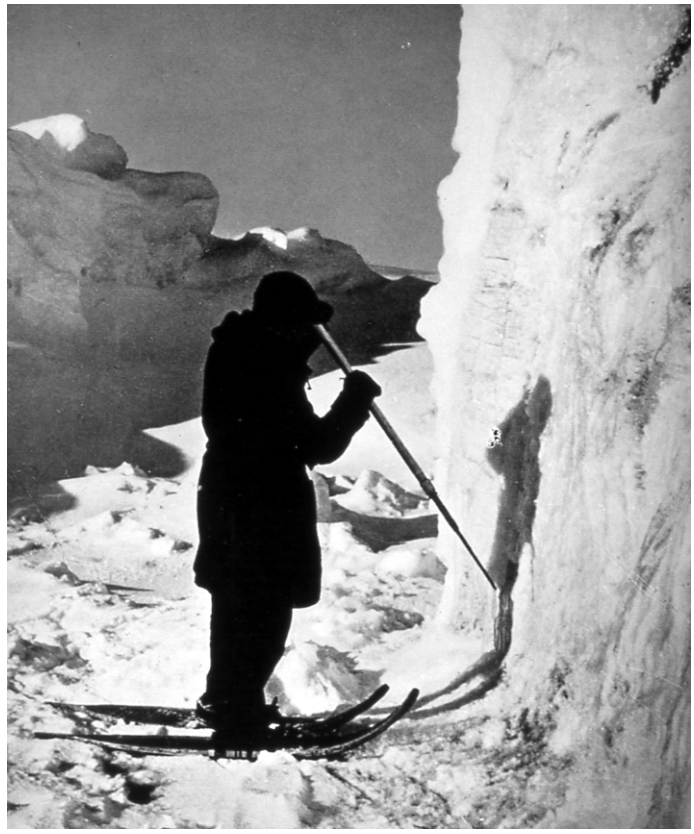

Figure 6.4 Fletcher's ice island, or ice island T-3, in the Beaufort Sea, a widely used base for ice drift studies in the 1950s.
From Rodahl (1954).

translational velocity u and angular velocity $\dot{\omega}$ around the vertical axis obtained from the conservation laws of momentum and angular momentum (see Section 5.5). These conservation laws were given by Eqs. (5.65) for linear ice–water stress. For homogeneous floes the inertial timescale of rotation is $T \sim \rho h/(\rho_w C_{w1})$ (Eq. 5.66), equal to the inertial timescale of the translational motion. High ice thickness or a low ice–water drag coefficient would allow relatively long relaxation times.

Inhomogeneous floes possess a nonzero distance $\boldsymbol{r}^* \neq 0$ between the mass centre and the geometric centre. Surface stresses act on the geometric centre, while inertial and body forces act on the mass centre, and the resulting couple influences on the orientation of ice floes with respect to the direction of forcing. Rotation causes an additional ice–water stress term for the translational motion, but its magnitude is normally small; for example, for $\dot{\omega} \sim 1$ cycles per day, $|\boldsymbol{r}^*| \sim 100\,\mathrm{m}$ and $|\boldsymbol{U}_w - u| \sim 10\,\mathrm{cm\,s^{-1}}$, and the relation between the translational and rotational stress terms is $\sim 10^{-1}$.

In the inhomogeneous case, rotation equation obtains a forcing term. Write first $\boldsymbol{k} \cdot [\boldsymbol{r}^* \times (\boldsymbol{\tau}_a + \boldsymbol{\tau}_{w1})] = |\boldsymbol{r}^*|(\Delta\tau_x \cos\omega + \Delta\tau_y \sin\omega)$, where $\Delta\boldsymbol{\tau} = \boldsymbol{\tau}_a + \boldsymbol{\tau}_{w1}$, $\boldsymbol{\tau}_{w1}$ is the ice–water stress from translational motion, and ω is the direction of $\boldsymbol{r}^*$. Let us then assume that $\Delta\boldsymbol{\tau} \approx$ constant and align the x-axis with it. Then the orientation angle of the floe satisfies the equation:

$$\rho\tilde{h}r_{\mathrm{I}}^2 \frac{d^2\omega}{dt^2} + \rho_w C_{w1} \cos\theta_w \tilde{r}^2 \frac{d\omega}{dt} + \Delta\tau \mathrm{r}^* \sin\omega = 0 \tag{6.27}$$

When ω is small, $\sin\omega \approx \omega$ and we have a linear second-order equation that represents pure damping or oscillatory damping whether the discriminant of this equation is positive or negative, respectively. The pure damping case takes place if:

$$\frac{(\tilde{r}^2)^2}{hr_{\mathrm{I}}^2 r^*} > \frac{4\rho\Delta\tau}{(\rho_w C_{w1} \cos\theta_w)^2} \tag{6.28}$$

The left-hand side is $\sim d/(r^*\delta)$, where d and δ are the size and aspect ratio of the floe. The right-hand side is $\sim 4\rho U^2/\Delta\tau$. Simple scale considerations tell us that Eq. (6.28) is usually true. Taking $d \sim 1\,\mathrm{km}$, $\delta \sim 10^{-3}$ and $\boldsymbol{r}^* \sim 100\,\mathrm{m}$, the left-hand side becomes $\sim 10^4$; and with $U \sim 10\,\mathrm{cm/s}$ and $\Delta\tau \sim 10^{-1}\,\mathrm{Pa}$, the right-hand side becomes $\sim 4 \cdot 10^2$. This means that floe rotation normally obeys the pure damping solution: once the forcing changes, the floe orientation moves steadily to the new equilibrium position, and the angular velocity is:

$$\dot{\omega} \approx \frac{r^* \sin\theta_w \Delta\tau}{\rho_w C_{w1} \cos\theta_w \tilde{r}^2} \tag{6.29}$$

A damping oscillator solution could result for strongly inhomogeneous floes ($r^* \sim d$) or for low ice–water friction C_{w1}.

Example (*Leppäranta, 1981b*) One large ice floe was mapped in a Baltic Sea field experiment with the following resulting measures: characteristic diameter 3.3 km, thickness 0.5 m, radius of gyration 1.3 km, and radius of inhomogeneity $r^* = 0.24\,\mathrm{km}$. Then

$$\frac{(\tilde{r}^2)^2}{\tilde{h}r_{\mathrm{I}}^2 r^*} \approx 1 \cdot 10^5$$

where the approximation $\tilde{r}^2 \sim d/2$ has been used. It is very difficult to break the inequality expressed in Eq. (6.28), and a pure damping solution results. The angular velocity is of the order of $10^{-6}\,\mathrm{s}^{-1}$. Interestingly, floe geometry can cause similar rotation rates as the external forcing does.

The ratio of rotational kinetic energy to translational kinetic energy is $\frac{1}{2}(\dot{\omega}r_{\mathrm{I}}/|u|)^2$. Usually, $\dot{\omega}r_{\mathrm{I}} < 1\,\mathrm{cm\,s}^{-1}$, and so the kinetic energy is nearly all translational. In practice, the surface stress resultant $\Delta\tau$ varies in timescales of 0.1–1 day. In such periods floe rotations are within a few degrees and appear as aperiodic adjustments to the changing forcing.

6.3 LINEAR COUPLED ICE–OCEAN MODEL

In the non-steady case a prescribed oceanic velocity can be a limiting assumption; therefore, a coupled model should be used. Consequently, a vertically integrated mixed-layer model is employed for the ocean. Now, U_w represents the mean velocity of the mixed layer and H is the thickness of the mixed layer. The resulting equation for the mixed layer velocity is:

$$\rho_w H \frac{dU_w}{dt} = -(\rho_w C_{w1} e^{i\theta_w} + i\rho_w H f) U_w + \rho_w C_{w1} e^{i\theta_w} u \tag{6.30}$$

which includes on the right-hand side ice–ocean coupling (first and third terms) and Coriolis acceleration.

In April 1975 an almost ideal free drift situation occurred in the northern Baltic Sea (Figure 6.5) where there was a drift ice field 100 km across without any contact with the fast ice boundary. The correlation between the velocities of ice and wind was about 0.9, and the spectra showed good correspondence with each other (Figure 6.6). Due to the shallowness of the basin and weak stratification in winter (the mean depth is 43 m), inertial oscillation is weak.

6.3.1 General solution

The coupled model (Eqs 6.22a and 6.30) is a pair of linear first-order equations with constant coefficients that can be solved by standard techniques. The coupled system

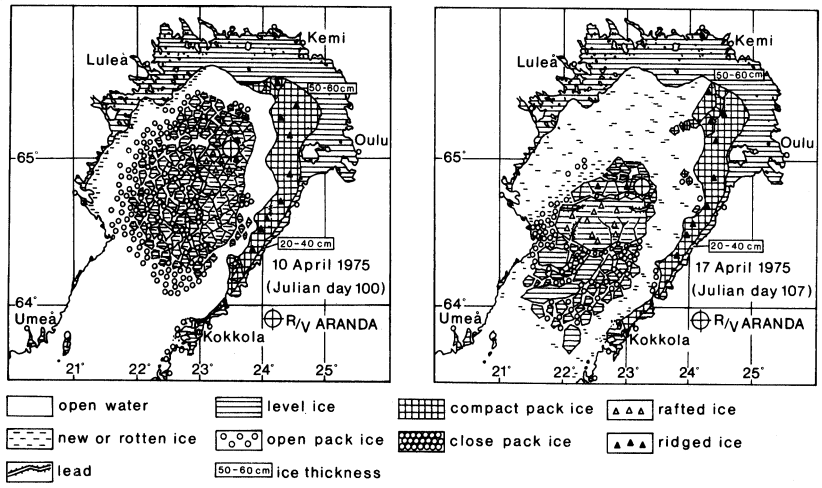

Figure 6.5 Drift of an ice patch, 100 km across and free from any contact with solid boundaries. (April 1975, Bay of Bothnia, Baltic Sea). *R/V Aranda* was the base.
From Leppäranta (1990).

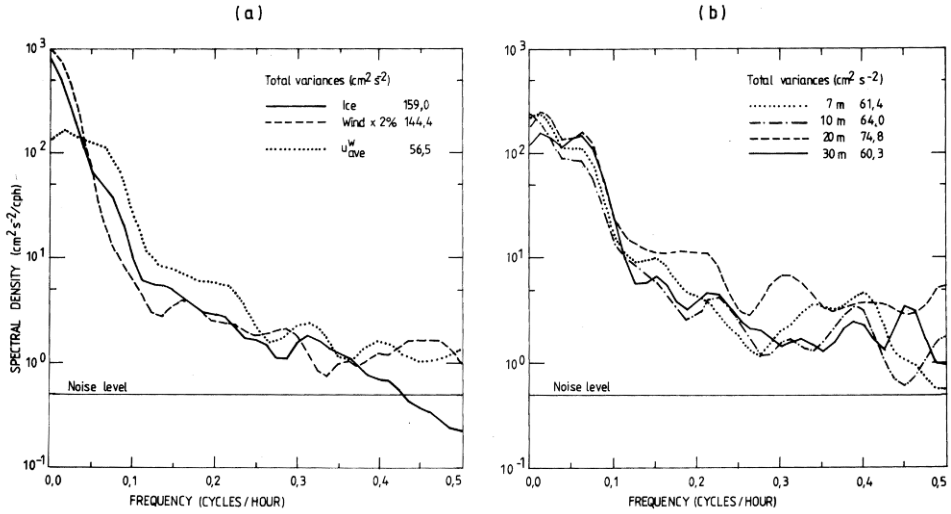

Figure 6.6 Spectra of wind, ice drift and mixed layer velocities in the near-free drift situation shown in Figure 6.5. On the right plot the spectra for current velocities at 7 m, 10 m, 20 m, and 30 m depths are shown, while u_w^{ave} on the left plot is the mean mixed layer velocity estimated from them.
From Leppäranta and Omstedt (1990).

includes three internal frequencies: the Coriolis frequency f, the ice response λ_i, and the mixed layer response λ_w:

$$\lambda_i = \frac{\rho_w}{\rho} \cdot \frac{C_{w1}}{h} e^{i\theta_w}, \quad \lambda_w = \frac{C_{w1}}{H} e^{i\theta_w} \tag{6.31a}$$

The corresponding timescales are:

$$|\lambda_i|^{-1} \sim 10^3 \text{ s} \ll |\lambda_w|^{-1}, \quad |f|^{-1} \sim 10^4 \text{ s} \tag{6.31b}$$

Additionally, the forcing may have its own timescales.

The coupled model is easily rewritten, with velocity terms multiplied by inverse timescales, in the form:

$$\frac{du}{dt} = -(\lambda_i + if)u + \lambda_i U_w + \lambda_a U_a \tag{6.32a}$$

$$\frac{dU_w}{dt} = -(\lambda_w + if)U_w + \lambda_w u \tag{6.32b}$$

where

$$\lambda_a = \frac{\rho_a C_{a1}}{\rho h} e^{i\theta_a} = Na_1 \lambda_i e^{i(\theta_a - \theta_w)} \tag{6.32c}$$

If $f \neq 0$, Eqs. (6.32) have a steady-state solution

$$\begin{aligned} \hat{u} &= \left[\frac{\lambda_i (f - \mathrm{i}\lambda_w)}{(\lambda_i + \lambda_w) f + \mathrm{i} f^2} \right] N a_1 \, \mathrm{e}^{\mathrm{i}(\theta_a - \theta_w)} U_a \\ \hat{U}_w &= \frac{\lambda_w}{\lambda_w + \mathrm{i} f} u \end{aligned} \tag{6.33}$$

If $f = 0$, the steady-state solution becomes infinite. A finite solution is then possible if bottom friction is added into the mixed-layer momentum equation (Eq. 6.32b).

The general solution is obtained by the elimination method (consult basic analysis textbooks for this, such as Adams, 1995). Briefly, U_w is eliminated from Eqs. (6.32), and a second-order equation is obtained for u. The roots of the characteristic polynomial are $r_1 = -\mathrm{i}f$, $r_2 = -(\lambda_i + \lambda_w + \mathrm{i}f)$, and the general solution is then:

$$u = A \, \mathrm{e}^{r_1 t} + B \, \mathrm{e}^{r_1 t} + u_p \tag{6.34a}$$

where the terms A and B describe the general solution to the homogeneous case, and $u_p = u_p(t)$ is a particular integral of the full equation. The solution for U_w then results from Eq. (6.32a) as:

$$U_w = A \, \mathrm{e}^{r_1 t} \frac{\lambda_w}{\lambda_i} \, B \, \mathrm{e}^{r_2 t} + \frac{1}{\lambda_i} \frac{du_p}{dt} + \left(1 + \frac{f}{\lambda_i} \right) u_p + \frac{\lambda_a}{\lambda_i} U_a \tag{6.34b}$$

Example Estimation of water drag parameters from velocity data using the momentum integral method (Hunkins, 1975). Vertical integration of ocean boundary-layer equations gives:

$$\frac{dU_w}{dt} + \mathrm{i} f U_w = -\frac{\tau_w + \tau_b}{\rho_w H}$$

where τ_b is the stress on the bottom of the boundary layer. Stresses τ_w and τ_b influence the evolution of momentum. If current measurements are available across the boundary layer, the sum of these stresses can be evaluated. If the sea depth is more than the Ekman depth, one may assume $\tau_b \approx 0$ and obtain the ice–water stress τ_w. Once we know the ice velocity, the drag parameters can be obtained from $\tau_w = \rho_w C_w \exp(\mathrm{i}\theta_w) |U_{w0} - u| (U_{w0} - u)$, where U_{w0} is the chosen reference velocity.

6.3.2 Inertial oscillations

Inertial oscillation is one of the fundamental frequencies in the dynamics of the upper ocean (e.g., Gill, 1982). The period of this oscillation equals $T_f = 2\pi / |f| = \pi / (\Omega |\sin \phi|)$, clockwise in the northern hemisphere and anticlockwise in the southern hemisphere. At the poles the period is 12 hours and then it increases toward the equator, for $|\phi| > 74^\circ$ it is still below 12.5 hours. Consequently, in high polar regions, inertial frequency is not easily distinguishable from the semi-diurnal tidal frequency with same sign for rotation. In the subarctic seas of the seasonal sea ice zone (e.g., Sea of Okhotsk and Gulf of St Lawrence) the latitude goes down to 45° where $T_f = 17$ h (Figure 6.7). The inertial signal has been found from drifting sea ice (Hunkins, 1967;

McPhee, 1978; Ono, 1978) when near-free drift conditions exist. However, the internal friction of ice seems to depress the signal (Leppäranta, 1981b). In shallow seas the loss of stratification in winter also increases the influence of bottom friction on the damping of the inertial oscillation (Leppäranta and Omstedt, 1990).

In the absence of wind, Eqs (6.32a, b) show that the ice and ocean velocities must be equal (apart from possible transient terms from the initial conditions). Then, they can be simply added together for the solution (McPhee, 1978):

$$\frac{dM}{dt} = -\mathrm{i}Mf, \quad M = \rho_w H U_w + \rho h u \tag{6.35}$$

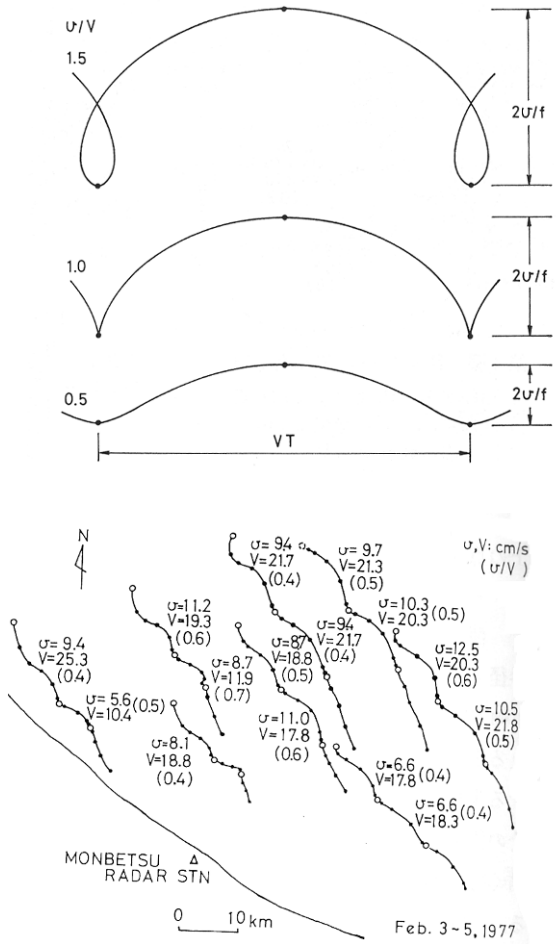

Figure 6.7 Inertial motion of sea ice superposed on alongshore translational ice motion. **Upper graph**: theoretical, u/V is relative magnitude of inertial motion. **Lower graph**: Observations in the Sea of Okhotsk.

Reproduced from Ono (1978), with permission from Hokkaido University.

where M is the total mass transport of ice and water. The solution is $M = M_0 \exp(-\mathrm{i}ft)$, where M_0 is the initial transport, similarly to the mass transport in the dynamics of ice-free upper ocean. Inertial motion draws a clockwise (anticlockwise) circle in the northern (southern) hemisphere, and the radius of this circle is $|U_{iw}|/f$, where $U_{iw} = M/m_{iw}$, m_{iw} is the total mass of mixed layer ($m_w = \rho_w H$) and ice ($m = \rho h$), $m_{iw} = m_w + m$, and U_{iw} is the ice–ocean joint velocity that is equal to a weighted average of ice and ocean velocities, weighted by the ice and mixed layer masses; for $|U_{iw}| \sim 0.1\,\mathrm{m\,s^{-1}}$ the radius is $\sim 1\,\mathrm{km}$.

Now, let us consider the coupled model (Eqs. 6.32) in the homogeneous case. With initial conditions $u = u_0$ and $U = U_0$ at $t = 0$, the solution is:

$$u = U_{iw}\,\mathrm{e}^{-\mathrm{i}ft} + \left(1 - \frac{\rho h}{m_{iw}}\right)(u_0 - U_{w0})\,\mathrm{e}^{-(\lambda_i + \lambda_w + \mathrm{i}f)t} \tag{6.36a}$$

$$U_w = U_{iw}\,\mathrm{e}^{-\mathrm{i}ft} + \frac{\rho h}{m_{iw}}\,(U_{w0} - u_0)\,\mathrm{e}^{-(\lambda_i + \lambda_w + \mathrm{i}f)t} \tag{6.36b}$$

The ice and ocean approach a state of persistent inertial (Coriolis) oscillation, and the transient terms are needed to adjust the equalization of ice and ocean velocities. The adjustment timescale is $\mathrm{Re}(\lambda_i + \lambda_w)^{-1} \sim 1\,\mathrm{h}$, primarily determined by the ice response.

If a constant wind stress is included in Eq. (6.32), the particular integral can be evaluated as the steady-state solution (Eq. 6.33). The full solution can now be obtained from Eqs. (6.34), and the initial conditions will determine the constants A and B. With $u = U_w = 0$ at $t = 0$, the solution is (ignoring transient terms):

$$\begin{gathered} u = \hat{u} + U_{iw}\,\mathrm{e}^{-\mathrm{i}ft}, \quad U_w = \hat{U}_w + U_{iw}\,\mathrm{e}^{-\mathrm{i}ft} \\ U_{iw} = -\mathrm{i}\,\frac{\tau_a}{m_{iw} f} \end{gathered} \tag{6.37}$$

That is, ice and ocean have individual steady-state components and together undergo inertial oscillation of the same amplitude, frequency, and phase.

The amplitude of inertial oscillation compared with the steady-state velocity is small, $\sim m_{iw} f/|\rho_w C_{w1}| \sim 1\%$. The uncoupled steady-state of velocity is:

$$\hat{u} = \frac{\lambda_i}{\lambda_i + \mathrm{i}f}\,Na_1\,\mathrm{e}^{\mathrm{i}(\theta_a - \theta_w)}\,U_a \tag{6.38}$$

It has a slightly larger magnitude and slightly smaller deviation angle than the coupled solution.

A friction term for the mixed layer, due to bottom friction or internal friction, could be added to the coupled model in the form $-\mu U_w$, $\mu \sim \rho_w C_b |U_{w0}|$; this would damp inertial motion out; in the solution both roots of the characteristic polynomial would have non-zero real components taking care of damping. Frictional dissipation is small in deep water, $[\mu/(\rho_w H)]^{-1}$ being of the order of days, and inertial oscillations are clearly observable. But as soon as the depth is less than Ekman depth, mixed layer friction corresponds to bottom friction, $\mu/(\rho_w H) \sim \lambda_w$, λ_w^{-1} being of the

order of hours, and the damping takes place rapidly, as has been reported in observations (Leppäranta, 1990). Using a similar linear friction law for the internal friction of ice, rapid damping would also result; this is reflected in the fact that inertial signal in ice drift is much clearer in summer than in winter.

6.4 FREQUENCY SPECTRUM OF FREE DRIFT

6.4.1 Periodic forcing

Wind forcing on sea ice drift is purely external in that it is independent of ice velocity. To examine the spectral response of ice drift to a periodic wind, let us choose:

$$U_a = U_{a0}\,\mathrm{e}^{\mathrm{i}\omega t} \tag{6.39}$$

where U_{a0} is the amplitude and ω the frequency of wind velocity. The particular integral can be directly obtained by the integrating factor method, and the result is:

$$u_1 = a_1 U_{a0}\,\mathrm{e}^{\mathrm{i}\omega t} \tag{6.40}$$

where the transfer function $a_1 = a_1(\omega)$ is:

$$a_1 = N a_1\,\mathrm{e}^{\mathrm{i}(\theta_a - \theta_w)}\,\frac{\lambda_i(\omega + f) - \mathrm{i}\lambda_i\lambda_w}{(\lambda_i + \lambda_w)(\omega + f) + \mathrm{i}(\omega + f)^2} \tag{6.41}$$

That is, ice follows wind with a wind factor of $|a_1|$ and deviation angle $\arg a_1$, which is in this case the lag in a cycle as well. The solution is illustrated by the gain and phase shift of ice motion with respect to the wind (Figure 6.8). As $\omega \to 0$, the steady-state solution results; and as $\omega \to \pm\infty$, the wind factor slowly decreases with increasing $|\omega|$ except for peaking at the Coriolis frequency $\omega = -f$. There is no observational

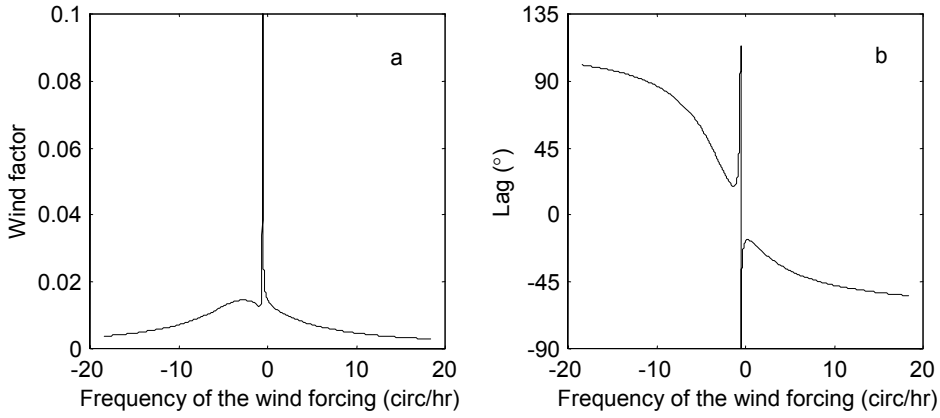

Figure 6.8 The geostrophic wind factor (left) and lag (right) in a wind-driven non-steady ice drift as functions of the frequency of wind forcing.

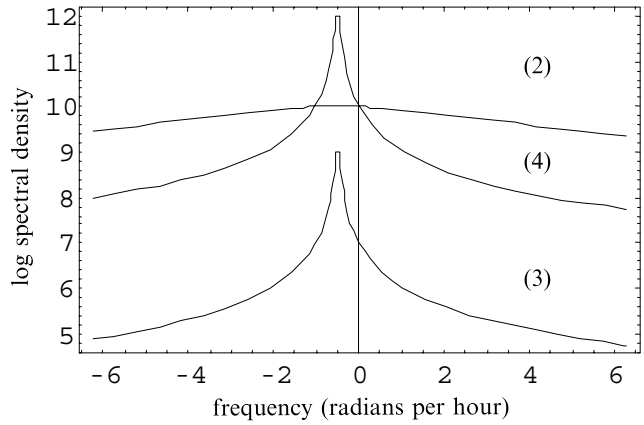

Figure 6.9 Sea ice velocity spectra normalized by forcing: (1) ice–ocean coupled model, (2) ice-only model, and (3) locked ice–ocean model.

evidence for this peak but it also occurs in advanced turbulence modelling of the ocean beneath the ice (Omstedt *et al.*, 1996). As $\omega \to \pm\infty$, the transfer function a_1 asymptotically becomes $-\mathrm{i}\lambda_a/\omega$, which means that $|a_1|$ asymptotically vanishes as $|\lambda_a|/\omega$, and $\arg a_1$ asymptotically approaches to $\arg \lambda_a - \pi/2$ or ice follows the surface wind ($\arg \lambda_a = 0$) one-quarter of a cycle behind.

6.4.2 Free drift velocity spectrum

Observed sea ice velocity spectra (Figure 3.10) are governed by wind forcing at frequencies below one cycle per day. At higher frequencies, the inertial peak is commonly observed (as are tidal frequencies in places), but otherwise the high-frequency spectra are red noise. However, available observations only provide coverage up to about 5 cycles per day because of measurement noise problems. The free drift solution with periodic forcing allows us to construct the theoretical frequency spectrum of sea ice velocity.

Denote the spectrum of wind as $p_a = p_a(\omega)$. The linear coupled free ice drift–ocean model can be analytically solved as shown in Section 6.3. Since ice velocity is then a linear transformation of the wind velocity, ice velocity spectrum is directly obtained from the wind velocity spectrum (e.g., Jenkins and Watts, 1968). The resulting spectrum of sea ice velocity is:

$$p_i(\omega) = \frac{\lambda_i^2 + f^2 + \omega^2}{[(\lambda_i + \lambda_w)^2 + (\omega + f)^2](\omega + f)^2}\, p_a(\omega) \tag{6.42}$$

This has the following properties:

(i) $$p_i(0) = \frac{\lambda_i^2 + f^2}{[(\lambda_i + \lambda_w)^2 + f^2]f^2}\, p_a(0)$$

(ii) There is a delta peak at the inertial frequency $\omega = -f$.
(iii) Asymptotically $p(\omega) \to p_a(\omega)/\omega^2$ as $\omega \to \pm\infty$.

The form normalized by dividing by the forcing spectrum is shown in Figure 6.9. This fully coupled free drift spectrum is then compared with two specific cases: (a) ice-only, where the ocean is passive; and (b) locked ice–ocean, where the ice and mixed layer flow together.

In the ice-only case (Eq. 6.22a), ocean velocity is external and the ice velocity spectrum becomes:

$$p_i(\omega) = \frac{p_a(\omega)}{\lambda_i^2 + (\omega + f)^2} \tag{6.43}$$

This equals $p_a(0)/(\lambda_i^2 + f^2)$ at $\omega = 0$, peaks to $p_a(-f)/\lambda_i^2$ at $\omega = -f$, and asymptotically reaches $p_a(\omega)/\omega^2$ as $\omega \to \pm\infty$ (Figure 6.9). The ice response time dominates the form of the spectrum. For the locked ice–ocean system (McPhee, 1978), adding the forcing $\tau_a' = \tau_a m/m_{iw}$ into Eq. (6.35) produces the joint ice and ocean velocity spectrum:

$$p_{iw}(\omega) = \left(\frac{m}{m_{iw}}\right)^2 \cdot \frac{p_a(\omega)}{(\omega + \lambda)^2} \tag{6.44}$$

which equals $(m/m_{iw})^2 p_a(0)/f^2$ at $\omega = 0$, has a delta peak at $\omega = -f$, and asymptotically $p_{iw}(\omega) \to p_a(\omega)/\omega^2$ as $\omega \to \pm\infty$ (Figure 6.9). Since $m/m_{iw} \sim 0.05$, the locked system shows a much lower level than the fully coupled system.

A particular ice model with inertial embedding was presented by Heil and Hibler (2002). In this approach, sea ice velocity is extracted from the joint ice and ocean boundary layer velocity by assuming a drag coefficient and a turning angle. The stationary solution is correct, and therefore low frequencies reproduce very well in the ice velocity spectrum, as does the inertial peak. However, at higher frequencies the spectrum falls off too quickly. Using the present linear model, inertial embedding is carried out by replacing the ice mass ρh in the acceleration term of Eq. (6.22) by $\rho h - \mathrm{i}\rho_w C_{w1}/f$. If we work through the analytic model with this modified ice inertia, the main features of Heil and Hibler (2002) model would become apparent.

6.4.3 Nonlinear questions

The linear free drift model is just a linear filter for forcing where amplitude and phase are modified but frequencies are unchanged. The true free drift model contains nonlinearities in the ice–water stress and advection but, however, their influence to the free drift spectrum is small.

Let us first consider the quadratic ice–water stress with passive ocean. Take $U_w = 0$ and $u = u_0\, \mathrm{e}^{\mathrm{i}\omega t}$. The ice–water drag can be written as:

$$\tau_w = -\rho_w C_w |u_0\, \mathrm{e}^{\mathrm{i}\omega t}|\, \mathrm{e}^{\mathrm{i}\theta_w} u_0\, \mathrm{e}^{\mathrm{i}\omega t} = -\rho_w C_w u_0^2\, \mathrm{e}^{\mathrm{i}(\theta_w + \omega t)} \tag{6.45}$$

Thus forcing frequencies transfer as such into ice velocity but due to the nonlinearity the form of cycles is modified. Ocean currents beneath the boundary layer vary at frequencies lower than the inertial time scale of the ice drift, and frequency conservation is apparent from the form of the quasi steady-state solution $u = U_{wg} + \alpha e^{-i\theta} U_a$ (Eq. 6.5). Thus ocean current and wind velocity frequencies appear unchanged in the ice motion. The parameters α and θ depend on wind speed, and thus the transformation is not exactly linear. The situation is clearly illustrated by numerical solution (Figure 6.10).

A study using a coupled free drift and second order turbulence model (see Section 5.3.3) forced by the wind did not indicate any frequency change in the ice

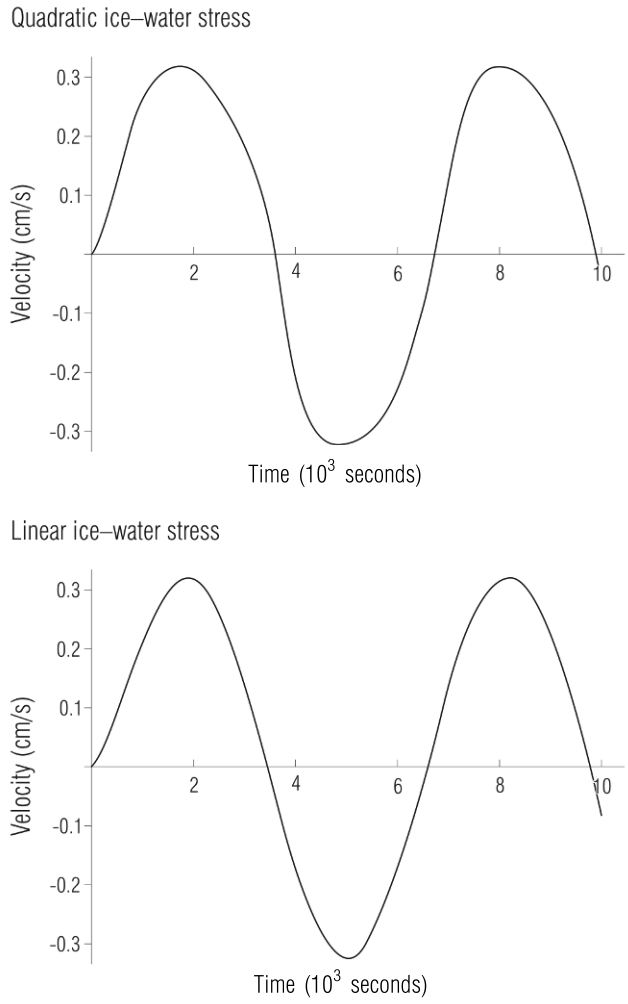

Figure 6.10 Numerical solution of the free drift with quadratic (above) and linear (below) ice–water stress.

motion (Omstedt *et al.*, 1996). Figure 6.11 compares the analytical solution (given in Eq. 6.34a for ice) and the turbulence model outcome. The results only differ at very high frequencies, basically because the drag formulation in terms of the mean mixed layer velocity does not follow rapid changes well. But strong nonlinearities could arise if the ice was forced by wind and ocean currents equally from both sides and at frequencies above the inertial scale (not a likely scenario, though).

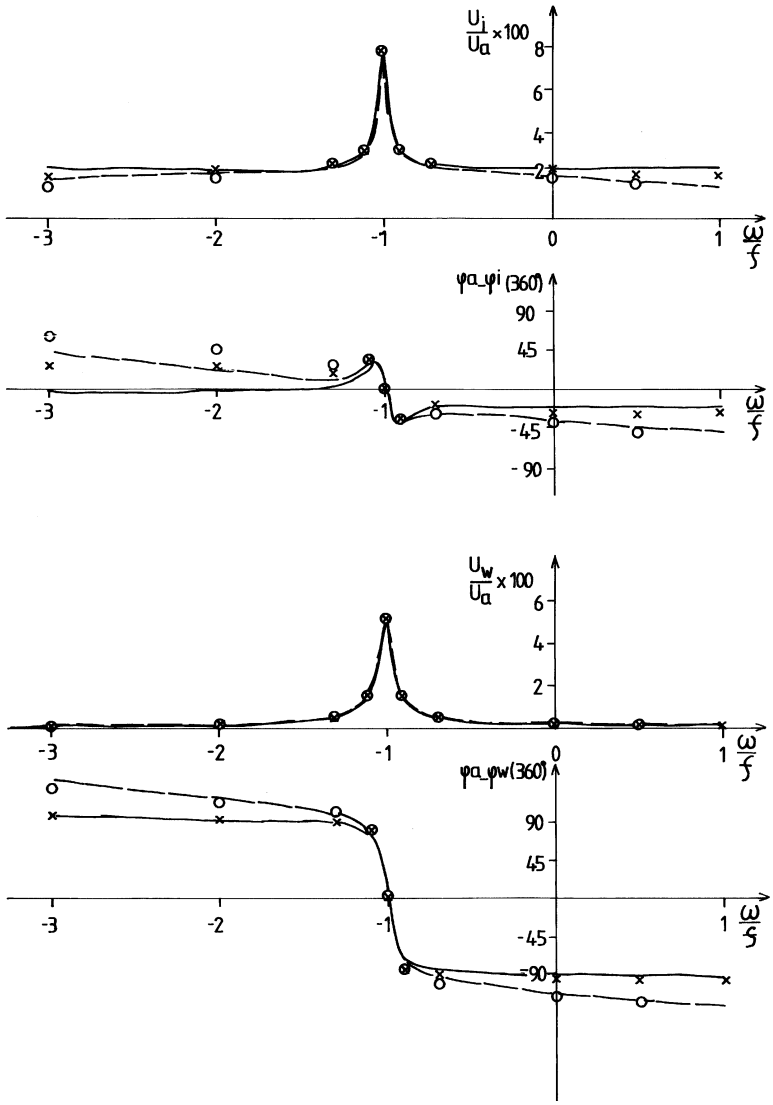

Figure 6.11 Speed and direction of ice drift (u_i, φ_i) and mixed layer (u_w, φ_w) scaled with wind (u_a, φ_a), as functions of forcing frequency ω scaled with Coriolis frequency f. Analytical two-body model: solid line for $h = 0.5$ m, dashed line for $h = 3$ m; ice model coupled with second-order turbulence model: $\times$ for $h = 0.5$ m and $\circ$ for $h = 3$ m. The angles φ_a, φ_i, and φ_w are positive anticlockwise.

From Omstedt *et al.* (1996).

Momentum advection transfers energy to higher frequencies. This holds in general for Newtonian fluids and leads to the energy cascade down to the Kolmogorov microscale regime, where the energy is dissipated due to viscosity. However, advection is a minor term in sea ice drift. Instead of energy cascade in the ice cover, the following takes place: ice drift transfers kinetic energy to the ocean, where frequency transfer takes place toward higher frequencies. Then high frequencies can be fed into the ice drift.

6.5 SPATIAL ASPECTS OF FREE DRIFT

The free drift solution has severe limitations. As it is only valid for compactness less than about 0.8, ice deformation may invalidate the free drift state by driving compactness over the critical limit (e.g., when two ice floes 10 km apart approach each other at 2.5 cm s^{-1}, the compactness between them would increase from 0.6 to 0.8 in 24 h).

An even more severe limitation is that the ice drift problem cannot be closed with a free drift model. The ice would eventually pile up on shore. A similar case is the Ekman surface current model: it must be combined with the pressure gradient and mass conservation law to obtain the circulation over the whole study basin. The internal friction force combined with the ice conservation law enable the ice problem to be closed. Because of its limitations in treating ice deformation properly, the ice conservation law is not usually analyzed in free drift theory.

6.5.1 Advection

Let us give a simple example to illustrate the role of the advective acceleration in sea ice drift. Take the steady-state one-dimensional free drift equation:

$$\rho h u \frac{\mathrm{d}u}{\mathrm{d}x} = \tau_{ax} - \rho_w C_w u^2 \tag{6.46}$$

where $u > 0$ has been assumed. Writing $u\mathrm{d}u/\mathrm{d}x = \frac{1}{2}\mathrm{d}u^2\mathrm{d}x$, we have a linear equation for u^2. The general solution then becomes:

$$u^2 = A\exp(-2\lambda x) - \int_0^x \frac{2\tau_{ax}(x')}{\rho h}\exp[-2\lambda(x-x')]dx' \tag{6.47}$$

where $\lambda = \rho_w C_w/(\rho h)$ and A is integration constant. Advection transfers momentum over distances of $l = (2\lambda)^{-1} \sim 100$ m for $h \sim 1$ m, much smaller than normal forcing length scale. Because the ice is thin, advection cannot transport much momentum. Consequently, the advective term is very small in the equation of motion.

Example Take wind stress $\tau_{ax} = \tau_0 x/L$. The solution is:

$$u^2 = \left(\mathrm{u}_0^2 + \frac{\tau_0 l}{\rho_w C_w L}\right)\mathrm{e}^{-x/l} + \frac{\tau_0(z-l)}{\rho_w C_w L}$$

Without advection the solution would be $u^2 = \tau_0 x/(\rho_w C_w L)$. Thus, due to advection the square of ice velocity lags spatially proportional to l/L, and spatial memory of boundary conditions has the length scale of l.

6.5.2 Divergence and vorticity

In this subsection, the velocities are taken as normal vectors, i.e. $\boldsymbol{u} = u\boldsymbol{i} + v\boldsymbol{j}$, etc. The free drift solution (Eq. 6.5) can then be written as $\boldsymbol{u} = (\alpha_1 + \alpha_2 \boldsymbol{k}\times)\boldsymbol{U}_a + \boldsymbol{U}_w$, where α_1 and α_2 are scalars. Assuming α_1 and α_2 to be constant, we have:

$$\nabla \cdot \boldsymbol{u} = \alpha_1 \nabla \cdot \boldsymbol{U}_a + \alpha_2 \nabla_z \times \boldsymbol{U}_a + \nabla \cdot \boldsymbol{U}_w \tag{6.43a}$$

$$\nabla_z \times \boldsymbol{u} = \alpha_1 \nabla_z \times \boldsymbol{U}_a + \alpha_2 \nabla \cdot \boldsymbol{U}_a + \nabla_z \times \boldsymbol{U}_w \tag{6.43b}$$

where ∇_z stands for the vertical component of vorticity. For surface wind the deviation angle between ice drift and wind is about 30°, $\alpha_1 \approx 2\%$, and $\alpha_2 \approx 1\%$. For geostrophic wind, Zubov's (1945) rule would give ice drift parallel to the isobars of atmospheric pressure (i.e., incompressible drift). However, this rule is exactly valid as $h \to 0$, and with finite ice thickness the cross-isobar parameter α_2 would be nonzero.

If the horizontal wind and water flow are incompressible, the vorticity of wind alone may drive the divergence of ice drift. This is similar to the Ekman pumping phenomenon in atmosphere–ocean dynamics. For wind vorticity of $10^{-4}\,\mathrm{s}^{-1}$, typical ice drift divergence level of $10^{-6}\,\mathrm{s}^{-1}$ would result. In the northern hemisphere anticlockwise wind vorticity gives opening and clockwise vorticity gives closing of the ice. The vorticity of ice is driven by both wind and current vorticities, with free ice drift vorticity two orders of magnitude below wind vorticity and of equal magnitude as the oceanic vorticity.

In addition to this, variations in ice thickness or roughness may affect free drift parameters sufficiently to produce divergence and vorticity under constant wind (e.g., $\nabla \cdot (\alpha_1 \boldsymbol{U}_a) = \boldsymbol{U}_a \cdot \nabla \alpha_1$ for $\boldsymbol{U}_a = \text{constant}$). The free drift solution shows that we may have $\nabla \alpha_1 \sim 0.001/10\,\mathrm{km}$ and therefore $\nabla \cdot (\alpha_1 \boldsymbol{U}_a) \sim 10^{-6}\,\mathrm{s}^{-1}$ for $|\boldsymbol{U}_a| \sim 10\,\mathrm{m\,s}^{-1}$.

Example: floe clustering (Leppäranta and Hibler, 1984) Free drift velocity depends on ice thickness, with thicker floes drifting slower and more to the right of the wind. Leppäranta and Hibler (1984) used this mechanism to show that faster floes catch up with slower ones and form clusters, one possible mechanism for the banding together of ice floes in the marginal ice zone (MIZ). A similar reasoning was used by Zubov (1945) for the drift of scattered ice, illustrating how dynamics depends on ice compactness. As floes have individual velocities, this may lead to collisions and consequently grouping of floes. In case of low ice concentration, ice strips converge with small floes (moving faster) on the wind side. When wind ceases, these strips diverge due to inertia.

The conservation law of kinetic energy (Eq. 5.16) is easily understood in free drift: energy is transferred to the ocean after a short time lag, and energy storage within the ice is very low. The rate of this energy transfer is mainly determined by drag coefficients.

In this chapter the free drift solution was presented for sea ice drift: the steady-state case resulted in an algebraic equation, while the non-steady-state case was solved using a linearized form of the momentum equation. The free drift solution is fairly realistic when ice compactness is less than 0.8. But this is a severe limitation, since ice compactness changes easily and levels about 1 are usual. In Chapter 7 the internal friction of ice is added into the free drift model, and its influence on sea ice drift characteristics is examined by analytical modelling.

7

Drift in the presence of internal friction

7.1 THE ROLE OF INTERNAL FRICTION

In this chapter the drift of ice in the presence of internal friction is examined using analytical methods. The role of internal friction is discussed with examples in Section 7.1, and Sections 7.2–7.4 present simple analytical models, which include internal friction of ice and which are useful for understanding its physical implications. Section 7.5 introduces the mathematical modelling of tests in ice tanks where a properly scaled drift ice-type medium is used, and the last section discusses time–space aspects of ice drift in the presence of internal friction.

7.1.1 Consequences of internal friction

In compact ice fields there is large internal resistance to motion, and it is even possible for stationary ice conditions to prevail under considerable forcing. A fundamental problem exists in that the system of sea ice dynamics equations cannot be properly closed under conditions of free drift because it is ice stress that controls the mechanical accumulation of ice material. The ice cannot go ashore or pile up to arbitrary thicknesses, as would result in free drift in a basin with land boundaries or anywhere that has variable forcing fields.

The situation can be compared with that of ocean dynamics. Ekman's theory of wind-driven currents provides a good estimate for local surface-layer currents and transport, but for a whole basin it does not give a realistic circulation. To achieve this goal, the hydrostatic pressure gradient is needed to control the piling up of water and to keep all the water in the basin. Thus, hydrostatic pressure has a similar role in ocean dynamics to that of ice stress in ice dynamics. But since sea ice as a material is essentially different from liquid seawater and since the mechanical energy used for deformation is irrecoverable in sea ice dynamics, the ice and water circulation systems are very different.

M. Leppäranta, *The Drift of Sea Ice*, Springer Praxis Books,
DOI 10.1007/978-3-642-04683-4_7, © Springer-Verlag Berlin Heidelberg 2011

Malcolm Mellor (1933–1991), a classic figure in snow and ice science, in particular in sea ice mechanics. He was born in England, studied at Melbourne University, Australia, and from 1961 he worked in the U.S. Army Cold Regions Research and Engineering Laboratory, in Hanover, New Hampshire.

The inclusion of internal friction necessitates a formulation of drift ice rheology (see Chapter 4). This tells us how ice resists different kinds of deformation, and thus in general how spatial interactions of ice floes step into the picture. The presence of internal friction in drift ice has the following main consequences:

(i) The overall level of drift speed is lowered since part of the input of mechanical energy goes into the ice deformation.
(ii) Ice is motionless if external forcing does not reach the yield limit.
(iii) Spatial variations of forcing show up smoother in the ice velocity, because ice is more rigid than the atmosphere and ocean.
(iv) Narrow deformation zones occur, in particular at land (or fast ice) boundaries.
(v) The internal stress field in the ice is capable to transfer mechanical energy over long distances in the ice cover.

7.1.2 Examples

First, let us give a few examples to illustrate the influence of internal friction on the dynamics of sea ice.

Example: drift speed vs. ice compactness Figure 7.1 shows some observations of ice drift speed in different ice compactness conditions (Shirokov, 1977). When compactness reaches about 0.8 and increases further, the mean wind factor decreases and the variance of the wind factor increases sharply (i.e., the wind factor becomes sensitive to small compactness changes and becomes less predictable by free drift theory). The reason can only be in the internal friction of the ice.

Example: sea level elevation and ice fields in a closed bay In a bay closed at one end, at dynamic equilibrium the wind stress τ_0 on the surface and sea surface slope β are balanced; that is:

$$\tau_0 - \rho_w g H \beta = 0$$

where H is the depth of the bay. In open sea $\tau_0 = \tau_a$, while in an ice-covered sea $\tau_0 = \tau_a + \rho g h \beta$ in free drift conditions. Therefore, sea surface slopes in open water and ice conditions are:

$$\text{open water}: \quad \frac{\tau_0}{\rho_w g H_0}, \qquad \text{ice}: \quad \frac{\tau_0}{\rho_w g H_1 + \rho g h}$$

where H_0 and H_1 are the depths of open water and ice-covered basins. Since the ice is formed from water in the bay, $\rho_w H + \rho h = \text{constant} = \rho_w H_0$ for all realizable (H, h) pairs and, consequently, sea surface slope is the same, if only τ_0 is the same.

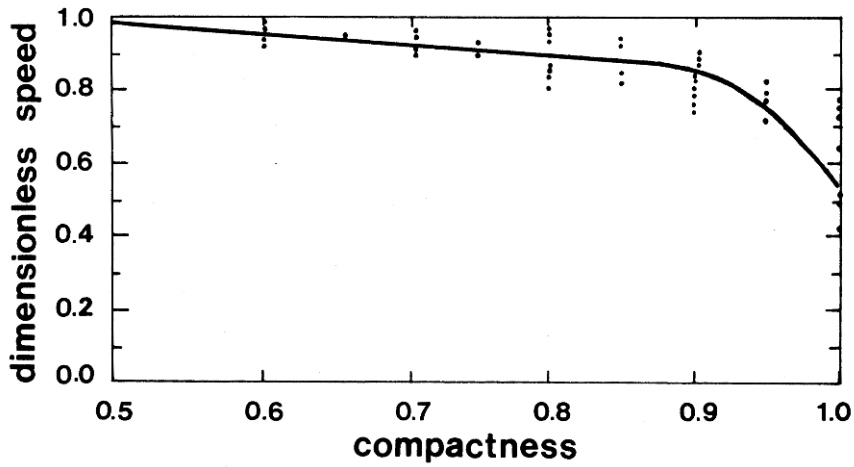

Figure 7.1 Empirical data of ice drift speed scaled with the theoretical free drift speed as a function of ice compactness.
Redrawn from Shirokov (1977).

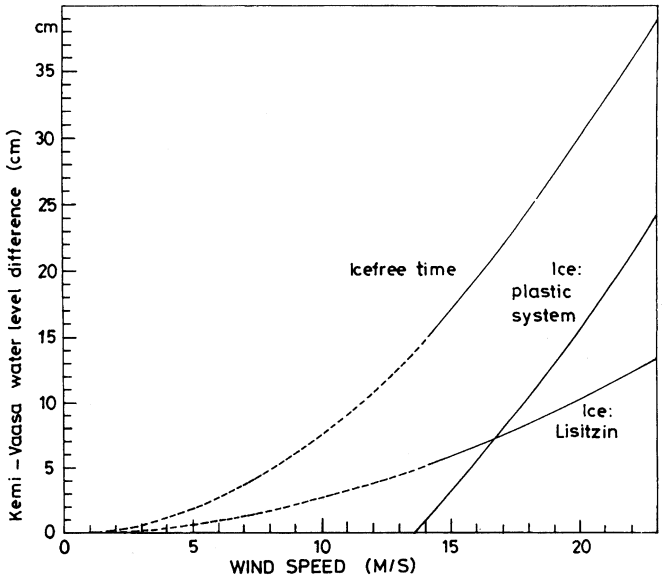

Figure 7.2 Sea surface slope vs. wind speed in the Bay of Bothnia, Baltic Sea in ice and ice-free cases. Also shown is the fit of a one-dimensional plastic ice model on the data.
From Zhang and Leppäranta (1995), modified from Lisitzin (1957).

Here it is assumed that the drag coefficients over ice and open water are equal, which is close to the truth in the Baltic Sea for rough (high-wind) sea surfaces. Sea level records from the Bay of Bothnia, Baltic Sea show (Figure 7.2), however, that sea surface slope is smaller under ice conditions than under ice-free conditions with the same wind forcing (Lisitzin, 1957). Therefore, wind forcing is reduced through compact ice fields due to internal friction of the ice, and in synoptic timescales the reduced surface stress is on average about one-third that of the open-water case. The reduction in sea surface slope was later reproduced by a numerical ice–ocean model (Zhang and Leppäranta, 1995).

Example: ice–ocean differential motion In the free drift of ice the ice velocity gradient equals the ocean velocity gradient plus a linear transformation of the wind velocity gradient (see Eq. 6.5, with α and θ constants). In the Marginal Ice Zone Experiment (MIZEX-83), Greenland Sea ice kinematics and ocean current data were collected at four sites in a 10-km area (Leppäranta and Hibler, 1987). Differential motion was at a much smaller level in the ice than in the oceanic surface layer and variance spectra were similar in form but an order of magnitude less in the ice (Figure 7.3). The obvious explanation for this is the internal friction of the ice.

Example: nonlinear internal friction of ice Several experiments have been performed in the Bay of Bothnia, the northernmost basin of the Baltic Sea. The bay is ca

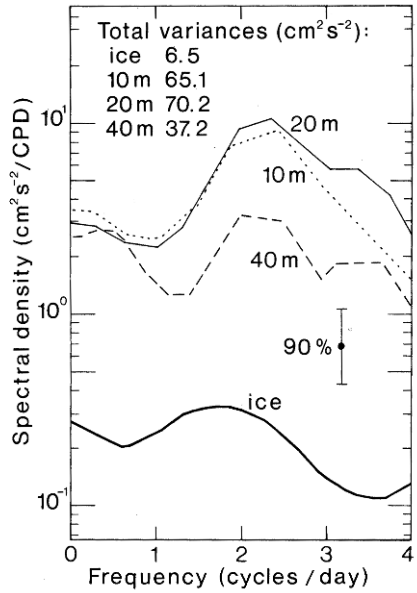

Figure 7.3 Spectra of the strain rate of ice motion and ocean currents beneath the ice in MIZEX-83 in the Greenland Sea for a 10-km area.
From Leppäranta and Hibler (1987).

300 km × 120 km in area. In February 1992 (Leppäranta and Zhang, 1992a), the ice was thin (10–20 cm) and strong southwesterly winds (10–20 m s^{-1}) packed the ice cover into an area 20% of the original in six days (Figure 5.14). Whereas, in February 1985 (Leppäranta, 1987), the ice thickness was 50 cm and similar winds did not cause any motion during 14 days, at least within the positioning accuracy of ~100 m (Figure 7.4). A further case from this same basin was used to examine the free drift problem when drift ice was not in contact with fast ice boundaries (Figure 6.5).

The presence of significant internal friction has been known since the advent of sea ice drift research. Nansen (1902) observed differences in the wind factor and explained them as the influence of ice compactness on the freedom of ice to move. Sverdrup (1928) collected ice drift observations on the Siberian Shelf between 1922 and 1924. He wrote that, "resistance arising from ice meeting ice in a different state of motion" was the most important factor in ice drift. He also showed that there is a strong seasonal cycle in the wind factor and deviation angle due to internal friction: between March and May they were 0.014 and 17°, between July and September they were 0.023 and 42°, respectively.

Analyzing his data Sverdrup (1928) assumed the existence of a simple kinetic friction law and replaced $(\rho h)^{-1}\nabla\cdot\boldsymbol{\sigma}$ by $-\kappa\boldsymbol{u}$. This form is not a physically acceptable rheology but rather an empirical model for the study area. His estimate

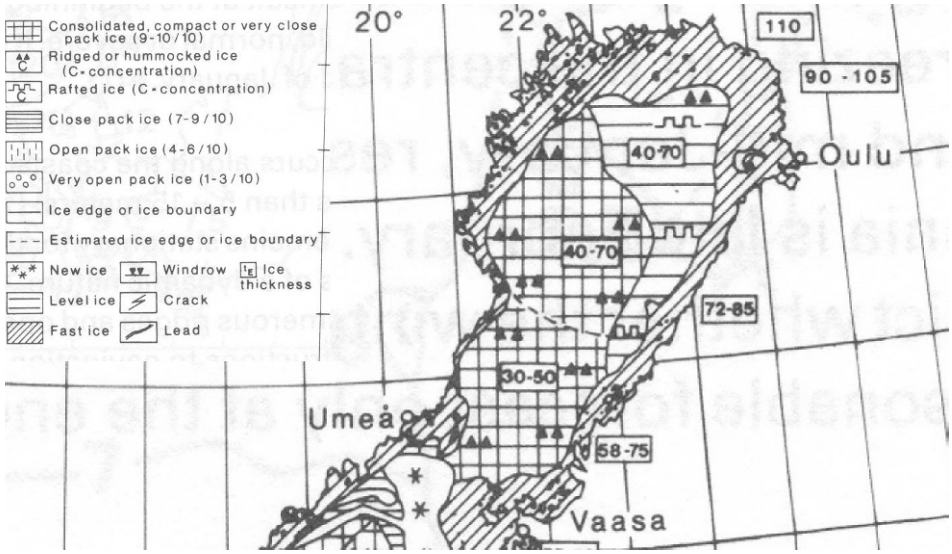

Figure 7.4 Ice conditions in the Bay of Bothnia, 4 March 1985. The ice situation was stationary for February–March 1985, but there was thickness growth of 5–10 cm. The size of the basin is about 300 km × 120 km.
Redrawn from operational ice chart by the Finnish Institute of Marine Research.

for the friction coefficient was $\kappa \approx 5 \times 10^{-4}\,\mathrm{s}^{-1}$ between March and May and $\kappa \approx 1.5 \times 10^{-4}\,\mathrm{s}^{-1}$ between July and September. The magnitude can be compared with the linear ice–water stress law (Eq. 6.16b): $(\rho h)^{-1}\boldsymbol{\tau}_w = -\kappa' \boldsymbol{u}$, where $\kappa' = (\rho h)^{-1} C_{w1} \approx 5 \times 10^{-4}\,\mathrm{s}^{-1}$ (i.e., in the Arctic seas in winter the water drag and internal friction are comparable but in summer the latter is smaller). The truth of this is confirmed by present knowledge. In addition, Sverdrup (1928) qualitatively connected high internal friction to ridging events. Zubov (1945) also showed that the different nature of ice drift between seasons is due to freezing of leads and evolution of ridges.

In general, the free drift assumption is good as long as the compactness of ice is less than about 0.8. This level of 0.8 is based on empirical knowledge, such as shown in Figure 7.1, and has agreed with numerical model simulations. However, compactness may change considerably in a short time (e.g., for a 1-cm s^{-1} difference in the normal speed between two sites 10 km apart, the total contraction would be 10% in 1 day). In an ice field with free boundaries, internal friction resists internal deformation. But when a drift ice field is in contact with a solid boundary, the influence of internal friction can be dramatic.

The formation of a proper rheological equation is needed to introduce a nonlinear internal friction term with spatial derivatives into the momentum equation. The ice drift problem then becomes difficult to examine analytically, but some simple cases can be solved. In this chapter analytical models are used to examine the drift of sea ice in the presence of internal friction. A two-level (mean

thickness and ice compactness being the state variables) purely dynamic system (no thermodynamics) is employed:

$$\rho h\left(\frac{\partial \boldsymbol{u}}{\partial t}+\boldsymbol{u}\cdot\nabla\boldsymbol{u}+f\boldsymbol{k}\times\boldsymbol{u}\right)=\nabla\cdot\boldsymbol{\sigma}+\boldsymbol{\tau}_a+\boldsymbol{\tau}_w-\rho hg\beta \tag{7.1a}$$

$$\frac{\partial h}{\partial t}+\boldsymbol{u}\cdot\nabla h=-h\nabla\cdot\boldsymbol{u},\quad \frac{\partial A}{\partial t}+\boldsymbol{u}\cdot\nabla A=-A\nabla\cdot\boldsymbol{u}\quad (0\le A\le 1) \tag{7.1b}$$

7.1.3 Landfast ice problem

Landfast ice is a solid sheet supported by islands, shoreline, and grounded ridges (Figure 7.5). Thus, by definition, $\boldsymbol{u}\equiv 0$, and we have the static equation:

$$\nabla\cdot\boldsymbol{\sigma}+\boldsymbol{F}=0 \tag{7.2}$$

where $\boldsymbol{F}=\boldsymbol{\tau}_a+\boldsymbol{\tau}_w-\rho hg\beta$ is the forcing; for $\boldsymbol{u}=0$ this is nearly independent of ice because ice shows up only in the sea surface slope term, which is small.

Consider a one-dimensional channel aligned with the x-axis, closed at $x=L$ and initially filled with ice of uniform thickness h_0 from $x=0$ to L. The landfast condition $\boldsymbol{u}\equiv 0$ gives:

$$\frac{\partial\sigma}{\partial x}+F=0 \tag{7.3}$$

Figure 7.5 Winter roads on landfast sea ice are used in the Finnish Archipelago in the Baltic Sea. This photograph shows the road to Hailuoto Island in the north.
Photograph by Kyösti Marjoniemi, Oulu, Finland, reproduced with his permission.

where $F = \tau_{ax} + \rho_w C_w \,\mathrm{sgn}(U_w) U_w^2 - \rho h g \beta_x$. If $F \neq 0$ somewhere, the rheology must include an elastic or a plastic property. The solution is:

$$\sigma(x) = -\int_0^x F(x')dx' \tag{7.4}$$

For the landfast ice condition to hold, stress everywhere must be beneath the yield level, $-\sigma_c < \sigma(x) < \sigma_t$, where $\sigma_c = \sigma_c(h) \leq 0$ and $\sigma_t = \sigma_t(h) \geq 0$ are the compressive and the tensile yield strengths, respectively.

Example Let us assume constant forcing $F > 0$. Then $\sigma(x) = -Fx$ and the maximum compressive stress occurs at the end of the basin, $\sigma(L) = -FL$. The ice is immobile as long as $FL < \sigma_c$. If $\sigma_c = \underline{\sigma}_c h$, where $\underline{\sigma}_c$ is the three-dimensional compressive strength, the landfast ice condition is

$$\frac{h}{L} > \frac{F}{\underline{\sigma}_c}$$

It is known that $h/L < 10^{-5}$ in drift ice basins (see Table 2.1), and since $F < 1\,\mathrm{Pa}$ we have $\underline{\sigma}_c < 10^5\,\mathrm{Pa}$. As the local or "engineering"-scale compressive strength is $\sim 10^6\,\mathrm{Pa}$ (Mellor, 1986), it is seen that the mesoscale or geophysical scale compressive strength is at least one order of magnitude less.

In general, the stability of a solid ice sheet or the solution of the fast ice problem depends on ice thickness, size of the basin, and the limiting forcing, which is normally a representative maximum wind stress τ_{aM}. The minimum thickness of landfast ice in a given basin is obtained from:

$$h_{\min} = \min\{h; |\sigma_Y(h)| > \tau_{aM} L\}\,. \tag{7.5}$$

where σ_Y is the yield strength of ice. Usually wind stress is the critical factor. The length scale of wind forcing is much more than the length scale of ocean forcing, and therefore the force obtained from integration of surface stress over its length scale becomes much more for wind stress than for ice–water stress.

Analysis of the stability of fast ice in the Baltic Sea was performed by Palosuo (1963), and he found that the breakage of fast ice could be presented as straight lines $U_a = bh$ in a given region surrounded by islands, with b depending on the size of the basin, $b = b(L)$. The whole data set was then combined into a relationship $h/U_a = b^{-1}$ for the fast ice condition (Figure 7.6). Taking $|\sigma_Y(h)| \propto h^\gamma$, Eq. (7.5) tells that the fast ice condition is of form:

$$\frac{h}{U_a} \propto h^{1-\gamma/2} L^{1/2} \tag{7.6}$$

For $\gamma = 2$, the condition would be $h/U_a \propto L^{1/2}$; however, the range in the thickness data is too narrow for a good estimate of the exponent. On the other hand, it is known that a compact ice cover is normally stationary in the Baltic Sea, with $h \sim 50\,\mathrm{cm}$ and $L \sim 100\,\mathrm{km}$, and, consequently, in Figure 7.6 the ordinate should be about 3 at $l = 100\,\mathrm{km}$ (i.e., close to the value at $L = 10\,\mathrm{km}$). Consequently, the

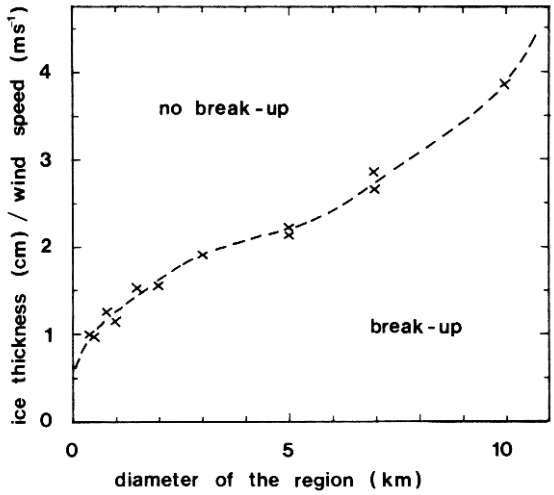

Figure 7.6. The stability of fast ice in the Baltic Sea.
From Leppäranta (1981b), after Palosuo (1963).

quality of the phenomenon changes and with increasing basin size the ice becomes more easily unstable. The strength of ice was in fact shown to decrease with length scale in Chapter 4 (see Figure 4.15).

Grounded deep ridges provide support points for the fast ice sheet. Keel depths follow exponential distribution (see Section 2.5), and the spatial density of ridges deeper than, say, H is $\mu_H = \mu \exp[-\lambda(H - h_c)]$, where μ is the ridge density, h_c is cut-off depth, and the inverse of λ is the average keel depth in excess of the cut-off size. The relationship between the density of ridges and the density of grounded ridges, μ_G is not very clear, but one may argue that $\mu_G \sim \mu_H$, when H is the depth of the region in consideration. For example, if $\mu \sim 5\,\mathrm{km}^{-1}$, $\lambda^{-1} \sim 5\,\mathrm{m}$, $h_c \sim 3\,\mathrm{m}$ and $H \sim 20\,\mathrm{m}$, then $\mu_H \sim 0.17\,\mathrm{km}^{-1}$ or, in other words, the spacing of large, 20 m ridges would be 6.0 km. Whether this spacing is enough to hold the fast ice together depends on ice thickness.

7.2 CHANNEL FLOW OF SEA ICE

In this instance the channel is aligned on the x axis and closed at $x = L$ (Figure 7.7). The boundary conditions are $u = 0$ at $x = L$ and $\sigma = 0$ at the free ice edge. The channel flow is examined using a quasi-steady-state momentum equation and the two-level ice state $J = \{h, A\}$. The system of equations is written as:

$$\frac{\partial \sigma}{\partial x} + \tau_a + \rho_w C_w |U_w - u|(U_w - u) - \rho h g \beta = 0 \tag{7.7a}$$

$$\frac{\partial h}{\partial t} + \frac{\partial}{\partial x}(uh) = 0, \quad \frac{\partial A}{\partial t} + \frac{\partial}{\partial x}(uA) = 0 \quad (0 \le A \le 1) \tag{7.7b}$$

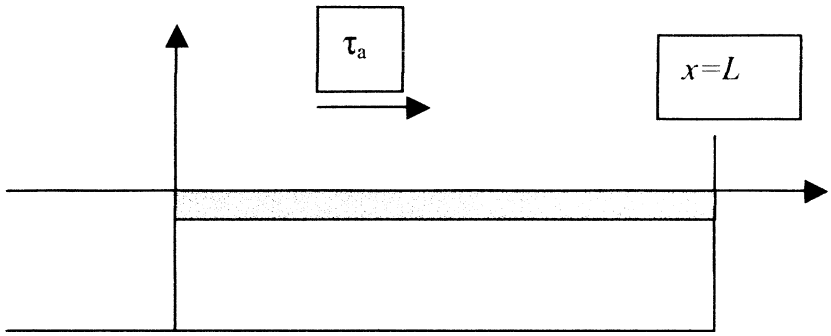

Figure 7.7 The geometry of the channel flow problem.

If the landfast ice condition is broken, ice drift commences. Without loss of generality we can assume that the forcing is toward the positive x-axis, $\tau_a - \rho g h \beta > 0$. The free drift solution is directly obtained as:

$$u_F = U_w + \sqrt{\frac{\tau_a - \rho g h \beta}{\rho_w C_w}} \tag{7.8}$$

It is clear that ice velocity must also be positive in the quasi-steady-state model. The steady-state solution of Eq. (7.7b) shows that uA and uh are constant across the ice field, and thus if the ice field is in contact with a rigid boundary the velocity solution is $u \equiv 0$. For the remainder of this section, we assume that the ice field is in contact with a rigid boundary and vertical average water velocity is zero. If the ice is moving, it will drag surface water with it, but then there is a return flow at a deeper layer because of the continuity; a zero reference current for ice–water stress is therefore a reasonable assumption.

7.2.1 Creep

Whether a slow-creep regime exists in drift ice flow is an open question. It is, however, used in viscous–plastic sea ice models (e.g., Hibler, 1979). Consider a slow-creep case, where the ice velocity is small enough for ice–water stress to be negligible and, for simplicity, surface slope is also ignored (it can absorbed into the wind stress, though). Then we have:

$$\frac{d}{dx}\left(\zeta \frac{du}{dx}\right) + \tau_a = 0 \tag{7.9}$$

where ζ is the bulk viscosity coefficient. For $\zeta =$ constant and taking a free edge at $x = 0$, the solution is:

$$u = \frac{\tau_a}{2\zeta}(L^2 - x^2) \tag{7.10}$$

For $\tau_a \sim 0.1\,\text{Pa}$, $\zeta \sim 10^{12}\,\text{kg s}^{-1}$, and $L = 100\,\text{km}$, the ice velocity distribution would be parabolic and at its maximum at ice edge, $\text{u} = \frac{1}{2}\tau_a L^2/\zeta \sim 0.5\,\text{mm s}^{-1} \approx 43\,\text{m day}^{-1}$. For the ice velocity to remain small, viscosity should not be less than $10^{12}\,\text{kg s}^{-1}$ (as used here) if the length scale of the ice cover is of the order of 100 km. Creep with ice–water stress included will be examined in later sections.

In this creep process, velocity divergence is $-\tau_a x/\zeta$, which means that the ice accumulation rate due to convergence increases linearly toward the end of the channel. The rate is of the order of $10^{-3}h$ per day at the channel end. The steady-state solution is that all the ice becomes squeezed into the end of the channel. If viscosity were to increase with thickness as $\zeta \propto h$ or thereabouts, the change would be very slow and integration could be made stepwise in time.

The solution can be easily expanded to allow for a general nonlinear viscous flow. Let us assume the power law rheology similar to Eq. (4.16), $\sigma = \zeta_{n-1}|\dot{\varepsilon}_{xx}|^{n-1}\dot{\varepsilon}_{xx}$, $n \geq 0$, which has been used widely for shear viscous glacier flow, normally $n = 1/3$ (Paterson, 1995). The creep solution is:

$$\boldsymbol{u} = \left(\frac{\tau_a}{\zeta_{n-1}}\right)^n \frac{(L^b - x^b)}{b} \tag{7.11}$$

where $b = (n+1)/n$. The parabolic distribution in the linear case ($n = 1$) is reproduced, and as n increases the deformation zone becomes increasingly concentrated in the channel end.

7.2.2 Plastic flow

In plastic flow, rheology is given by the yield criterion $\sigma_Y = \sigma_Y(A, h)$. In the present case our concern is compressive strength. Remember that ice continues to flow as long as internal stress overcomes the yield level. The solution of the quasi-steady-state momentum equation is formally:

$$u = \sqrt{\frac{\tau_a}{\rho_w C_w} + \frac{1}{\rho_w C_w}\frac{\text{d}\sigma}{\text{d}x}} \tag{7.12a}$$

where the expression under square root must be positive, $\tau_a \geq -\text{d}\sigma/\text{d}x$. At the end of the channel the ice must stop and there $\text{d}\sigma/\text{d}x = -\tau_a$.

Let us start with an ice field that ranges from $x = 0$ to $x = L$, with $h = h_0 = \text{constant}$ and $A = 1$. Let us further assume $\sigma_c = -P^* q(A) r(h)$, where q is the influence of ice compactness, $q(0) = 0$ and $q(1) = 1$, and r is the influence of ice thickness on the strength. Wind stress is taken as a constant $\tau_a > 0$. The solution to the fast ice problem shows that motion starts when $\tau_a L > \sigma_c$.

Plastic rheology allows a steady-state solution $u \equiv 0$ with a finite ice field. It is known that q is highly sensitive to compactness. Ice stress goes down one order of magnitude when compactness drops from about 1 to 0.8–0.9 and furthermore thereafter. This means that a very sharp ice edge, less than 1 km wide, forms at on-ice forcing (see Leppäranta and Hibler, 1985). Let us call this the ice edge zone. Beyond

the edge zone, $A \approx 1$ and thickness increases by $\mathrm{d}r(h)/\mathrm{d}x = \tau_a/P^*$. Ignoring ice in the edge zone, the conservation of ice volume tells us that for linear r:

$$h_0 L = \tfrac{1}{2}(h_L + h_0)(L - x_0) \tag{7.12b}$$

where h_L is ice thickness at the channel end and x_0 is location of the ice edge.

In the steady state, wind stress must exactly balance ice strength at the channel end: $\tau_a(L - x_0) = P^* r(h_L)$. For the linear form $r(h) = h$, the ice thickness in the channel end, the location of the ice edge, and the friction number are:

$$\left.\begin{aligned} h_L &= h_0\left(\sqrt{\tfrac{1}{4} + 2X_0} - \tfrac{1}{2}\right) \\ x_0 &= L\left(1 - X_0 \frac{h_L}{h_0}\right) \\ X_0 &= \frac{\tau_a L}{P^* h_0} \end{aligned}\right\} \tag{7.13}$$

For $X_0 \to 1$, $h_L \to h_0$ and $x_0 \to 0$ or, in words, the fast ice condition is obtained consistently. Thus the excess of X_0 above 1 states how much deformation will take place during the adjustment process. For $\tau_a \sim 0.1$ Pa and $P^* \sim 10^4$ Pa, $\mathrm{d}h/\mathrm{d}x \sim 10^{-5}$ or, in words, ice thickness increases by 1 m over 100 km.

Adjustment to the steady state proceeds along the following lines. The motion of ice starts to change at the boundaries. At the free boundary the ice edge zone develops by outward opening (i.e., the compactness of ice decreases to satisfy the no-stress condition). Ice build-up begins from the channel end, where the thickness slope becomes $\partial h/\partial x = \tau_a/P^*$. Then the edge zone remains static and the deformation zone spreads out from the boundary, with compactness equal to 1 and thickness gradient approaching τ_a/P^* throughout the ice field. This interpretation is consistent with the results of the numerical solution of Leppäranta and Hibler (1985), using a Lagrangian model to avoid numerical diffusion problems at the ice edge.

This steady-state solution can be generalized to spatially variable winds and other types of yield strength formulations. The steady-state compactness and thickness profile is obtained from:

$$\sigma(x; A, h) = -\int_{x_0}^{x} \tau_a(x')\,\mathrm{d}x', \tag{7.14}$$

which is valid as long as stress is negative. Thus, the ice compactness and thickness profile adjust to the forcing distribution. In places where stress vanishes, new free boundaries form and set drifting zones free from the pack.

Example In general, if the compressive yield strength of compact ice is $\sigma_c = \sigma_c(h)$, the steady-state ice thickness profile $h = h(x)$ provides the functional form of σ_c. Thus, the linear ice thickness profile gives $\sigma_c \propto h$, while the square-root thickness profile gives $\sigma_c \propto h^{1/2}$. The same principle holds also for the dependence of ice strength on ice compactness or on ice compactness and thickness together.

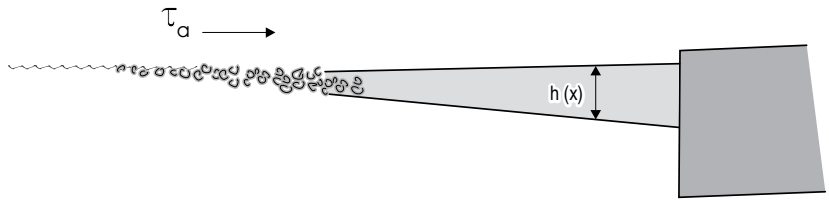

Figure 7.8 Accumulation of wind-driven frazil ice in a polynya. Typical scale is $L = 10\,\text{km}$ for the width of the polynya and $h = 10\,\text{cm}$ for the thickness of the accumulated frazil.

Example: wind-driven frazil ice in leads or polynyas Consider a lead of width L where frazil ice is forming and wind stress τ_a is constant across the lead (Figure 7.8). Frazil ice drifts and accumulates at a thickness profile $h = h(x)$. In equilibrium, the ice is stationary and covers the lead. The thickness profile can be obtained from:

$$\sigma_c(h) = \tau_a x$$

In particular, if $\sigma_c = -P^* h$, then the thickness profile is linear, $h = (\tau_a/P^*)x$. For $P^* \sim 10\,\text{kPa}$, $\tau_a \sim 0.1\,\text{Pa}$, and $L \sim 10\,\text{km}$, the thickness at the right side of the lead is 10 cm.

Consider an ice field forced by periodic forcing at the boundary

$$\rho h \frac{\partial u}{\partial t} = \frac{\partial \sigma}{\partial x} - \rho_w C_w |u| u \tag{7.15}$$

with $u = u_0$ $(-u_0)$ for $0 \le t/T \bmod 2\pi \le \pi$ $(\pi \le \boldsymbol{t/T} \bmod 2\pi \le 2\pi)$. If timescale T is much longer than the inertial timescale, the quasi-steady-state approach can be applied. In a stationary cycle, ice must move left and right by the same amount. Since internal ice stress is asymmetric (i.e., high stress for compression and low stress for opening), it must vanish for the stationary cycle to develop. Then, $|u| = u_0$ and ice compactness must be low enough for stresses to be small. Thus close to coast, tidal cycles move ice back and forth in the water but for shore pile-up wind blowing toward the shore is needed.

Ice–ocean coupling

The steady-state solution of a coupled ice–ocean model for constant forcing is straightforward. In the channel of depth H, closed at one end, the coupled system is

$$\frac{\partial \sigma}{\partial x} + \tau_a + \rho_w C_w |U_w - u|(U_w - u) - \rho h g \beta = 0 \tag{7.16a}$$

$$-\rho_w C_w |U_w - u|(U_w - u) - \rho_w C_b |U_w| U_w - \rho H g \beta = 0 \tag{7.16b}$$

where U_w is chosen as the vertical average mean current. Wind stress on the system is balanced by ice stress, sea surface tilt and bottom friction. At the equilibrium, $u \equiv 0$ and $U_w \equiv 0$, and Eq. (7.16b) implies that $\beta = 0$. In the absence of ice, the equilibrium condition would be $\tau_a = \rho H g \beta$.

Thus, in the steady state internal ice stress totally removes the effects of the surface pressure gradient, and the steady-state solution is the same as in the ice-only channel model. However, to reach the equilibrium takes a long time. As shown in Section 7.1 for the Bay of Bothnia (Figure 7.2), the wind-driven sea surface slope for ice-covered basin is about 1/3 of that of ice-free conditions in synoptic time scales.

7.3 ICE DRIFT ALONG COASTAL BOUNDARY

7.3.1 Influence of the boundary

In a bounded sea area the dynamics of drift ice is to a large extent related to the interaction of the moving ice and the solid boundary, i.e., the shoreline or the boundary of landfast ice, depending on the morphology of the basin in question. The specific form of this interaction is dependent on the relationship between the normal and shear components of loading along the contact zone (Goldstein *et al.*, 2009). Here we shall consider the shear motion along the coastal zone in the neighbourhood of the fast ice boundary. In the presence of internal friction, the boundary conditions are essential: no normal stress at the free boundaries and no motion across the solid boundaries out from the basin. The presence of the boundary influences the ice dynamics up to distances of $l \sim 10^5 \times$ ice thickness.

Figure 7.9 shows experimental data of the Bay of Bothnia coastal ice zone based on satellite and airborne remote-sensing data as well as ground observations. The forces of the contact friction adjust the ice massif motion. Large-scale variations in the structure occur along the contact line and in the nearby ice field during the relaxation period. A system of faults is formed, and an intermediate zone of geometric structures is formed in the contact region.

The ice motion was determined using drifters (Leppäranta *et al.*, 2001). Figure 7.10 illustrates the drift histories. The motion of the ice pack at the fast ice boundary decelerated and was lined along the orientation of the fast ice boundary. The local variations in ice velocity were small. The drifter data show cases of short-term and long-term relaxation (Figure 7.10). The peak ice velocities were 10–15 $\mathrm{cm\,s^{-1}}$. A specific case of long-term relaxation was observed during March 14–17. The wind was first from the southwest and then turned north, with velocities up to 10–15 $\mathrm{m\,s^{-1}}$. The drifter velocity became very small, approximately 0.2 $\mathrm{cm\,s^{-1}}$ and the rate of spin-down was 0.1 $\mathrm{cm\,s^{-1}}$ per day. The rapid decrease in ice drift speed, despite the preservation of the wind action level, shows that other sources of retardation exist in addition to the ice–water friction. In particular, friction in the drift ice-fast ice contact zone can serve as such source.

7.3.2 Dynamics of the relaxation process

We assume that the ice field moves in a fixed direction at the boundary. The time-dependent free drift solution was derived for this case in Section 6.2.1 (Eq. 6.20),

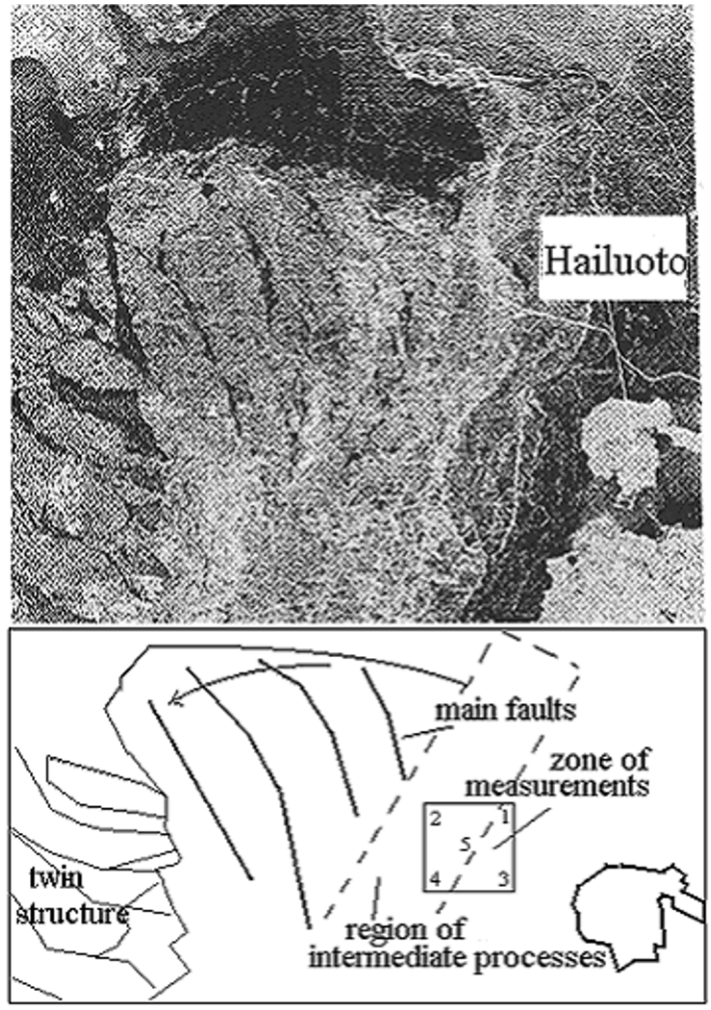

Figure 7.9 Structure of the ice cover formed as a result of its shear interaction with fast ice, shown on a section of Radarsat image. Drifters were placed at the four corners of the testing area (1 Northeast – NE drifter, 2 Northwest – NW drifter, 3 Southeast – SE drifter, 4 Southwest – SW drifter) and in the centre of the area (central drifter). Image width is 100 km. From Goldstein *et al.* (2009).

with $f = 0$ and $\theta_w = 0$. Inertial time scale was obtained as $T_I = \rho h/(\rho_w C_w U) = \rho h/(\sqrt{\rho_a C_a \rho_w C_w} U_a) \sim 1$ h where the velocity scale is $U = NaU_a$.

Take now the wind field pushing the drift ice towards the boundary (Figure 7.11). The ice drift forms an angle γ with the boundary, and the angle between the wind and ice drift is θ; it is clear that for feasible solutions the wind is more on-shore than the ice motion. Note that the ice drift is not parallel to the wind, due to the coastal friction, but there is a deviation angle θ. For the Coulomb friction model,

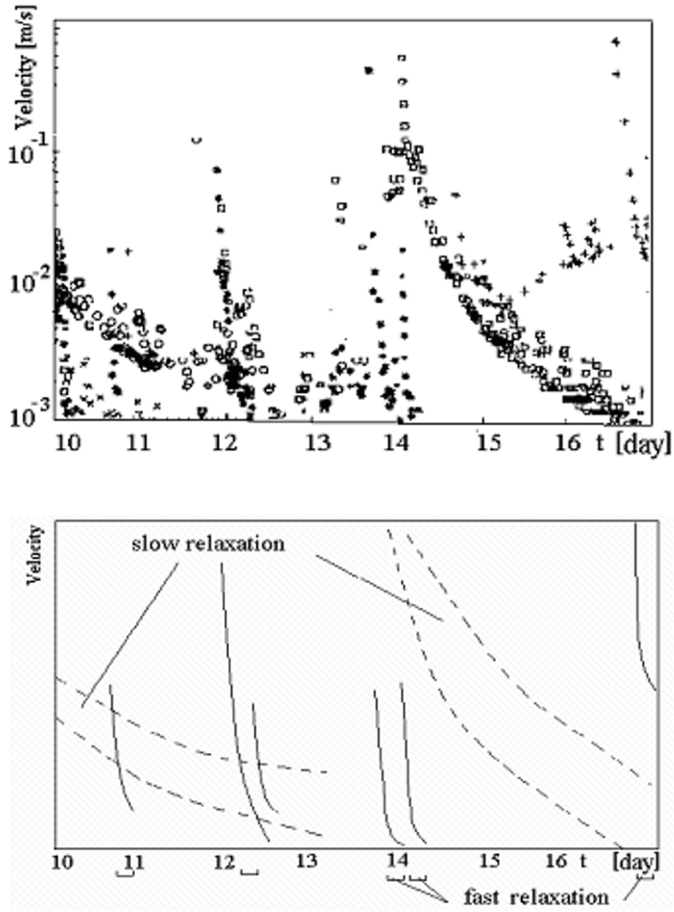

Figure 7.10 Upper part: the velocity of the drifters ($\circ$ = central drifter, $\times$ = NE drifter, $+$ = NW drifter, * = SE drifter) during March 10–17, 1997. Lower part: schematic illustration of the slow and fast relaxation, based on the data in the upper part.
From Goldstein *et al.* (2009).

the wind field is analogous to gravity, and therefore the friction against wind forcing is $\mu \sin(\theta + \gamma)$ where μ is the boundary friction coefficient. This is projected to the ice motion as:

$$F = -\tau_a S \mu \sin(\theta + \gamma) \cos\gamma \tag{7.17}$$

where S is surface area of the ice field. The Coulomb friction can be added to the wind force in the free drift equation (Eq. 6.19a) for the coastal drift dynamics. Assuming that U_a, $u \geq 0$ (no loss of generality in doing so) we have:

$$\frac{\mathrm{d}u}{\mathrm{d}t} + \frac{\rho_w C_w}{\rho h} u^2 = \frac{\rho_a C_a}{\rho h} U_a^2 [\cos\theta - \mu \sin(\theta + \gamma) \cos\gamma] \tag{7.18}$$

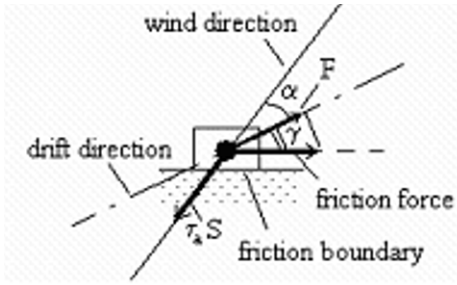

Figure 7.11 Geometry of ice drift and friction at the landfast ice boundary.
From Goldstein *et al.* (2009).

Compared with the free drift case, the influence of friction modifies the wind forcing by the factor $b = \cos\theta - \mu\sin(\theta+\gamma)\cos\gamma$; denote $B^2 = |b|$. There is no scaling effect, since B is dependent only on the friction coefficient and the angles θ and γ. For $\gamma \to 0$, $B \to 0$ when $\tan\theta \to \mu^{-1}$. In this case, the wind approaches $\arctan\mu^{-1}$ onshore and the ice motion parallel to the coastline ceases.

When the friction is stronger than the wind force, the ice motion stops. This means that $b < 0$, i.e., the net forcing is against the ice motion. The solution of the equation of motion is then:

$$u(t) = BU_F \tan\left[\arctan\left(\frac{u_0}{BU_F}\right) - \frac{t}{t_c}\right] \tag{7.20a}$$

where $t_c = B^{-1}t_I$ is the time scale and $u_0 = u(0)$ is the initial velocity at time $t = 0$. Ice velocity decreases and when the argument of the tangent becomes zero the motion stops. The time of this spin-down is

$$t_s = t_c \arctan\left(\frac{u_0}{BU_F}\right) \tag{7.20b}$$

The transition to the stoppage of moving ice cover may be even more rapid than in the free drift, depending on the loading situation and the initial ice velocity. Note that the characteristic relaxation times in free drift and drift in the presence of Coulomb friction are not dependent on the drifting ice area. This result is related to proportionality of the acting forces of the wind drift and Coulomb friction to the area of the moving ice cover in translational motion of the centre of mass.

Goldstein *et al.* (2009) obtained the estimate $\mu \sim 0.7$ based on field data. In a viscous-plastic sea-ice model for the coastal zone, similar results were obtained with the friction coefficient replaced by the ratio of shear strength to compressive strength (Leppäranta and Hibler, 1985). This ratio is often taken as equal to $\frac{1}{2}$ in plastic sea-ice models, suggesting that the Coulomb friction coefficient should also be that much.

If $b \to 0$, the spin-down approaches the spin-down of free drift when the forcing has ceased. If $b > 0$, the friction slows down the ice drift to move at a reduced speed, compared with the free drift case. The solution then follows the free drift solution

with wind stress modified by coefficient B; the steady state is then $u = Na \cdot BU_a$ and the time scale is $t_I B^{-1}$.

The situation becomes qualitatively different if the conditions at the fast ice boundary are changed into occurrence of a certain fracture mechanism (Goldstein *et al.*, 2009). This case can occur if the average shear loads at the contact of the fast ice and drifting ice attain a level sufficient for violation of the structure or strength of one of the bodies in contact. Let us consider an asymptotic variant of such interaction for which (e.g., resulting from ridging) the condition of the shear stress constancy is fulfilled, $\tau \sim \tau^* = \text{const}$. Other assumptions remain unchanged. The right side of Eq. (7.18) then becomes:

$$F_a = \tau_a S \cos\theta - \tau^* hL \cos\gamma \tag{7.20c}$$

where L is the length of the rectilinear boundary of contact along which the condition of constancy of the average shear stresses is fulfilled. Ice velocity is then

$$u(t) = NaU_a\sqrt{B^* \cos\gamma - \cos\theta} \times \tan\left[\frac{\sqrt{\rho_a C_a \rho_w C_w}}{\rho h} U_a \sqrt{B^* \cos\gamma - \cos\theta}(C + t)\right] \tag{7.21}$$

where a new dimensionless number has been introduced:

$$B^* = \frac{\tau^* hL}{\tau_a S} \tag{7.22}$$

This number equals the ratio of friction to wind forcing in the fracture mechanism case. The relaxation time then equals

$$t_f = \frac{\rho h}{\rho_w C_w u_F}\sqrt{\frac{1}{B^* \cos\gamma - \cos\theta}} = t_I\sqrt{\frac{1}{B^* \cos\gamma - \cos\theta}} \tag{7.23}$$

The ice cover velocity and relaxation time are dependent on the parameter (L/S), embedded in B^*, which represents the ratio of the contact zone length to the area of the moving ice. With increasing L/S, B^* increases and consequently the time scale decreases. Physically this means that the friction along the contact line becomes larger relative to the area of the ice field and can stop the ice motion more effectively.

7.4 ZONAL SEA ICE DRIFT

The longitudinal boundary-zone flow offers excellent possibilities for the analysis of sea ice drift (Figure 7.12). This zone may physically represent the coastal shear zone or the marginal ice zone (MIZ), where one may anticipate transverse changes much larger than longitudinal changes. Mathematically, the y-axis is aligned along the longitudinal direction, and the situation is assumed invariant in y: $\partial/\partial y \equiv 0$ (Leppäranta and Hibler, 1985). For the ice state, the two-level description $J = \{A, h\}$ is employed.

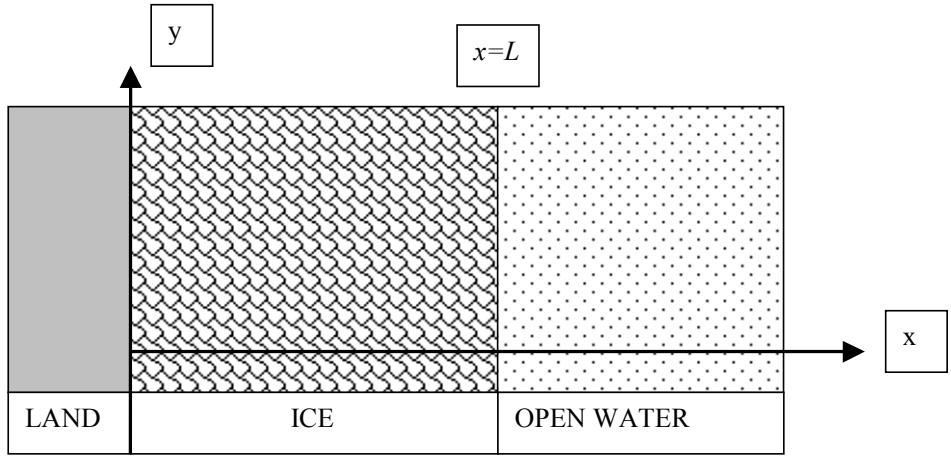

Figure 7.12 Boundary-zone configuration. The width is typically of the order of 100 km.

The general solution is first derived. The y-invariant equations of ice dynamics are directly obtained from the full form: the equation of motion from Eq. (5.10), ice rheology from Eq. (4.6) and the ice conservation law from Eqs. (3.24 and 3.26). The resulting model is:

$$\rho h\left(\frac{\partial u}{\partial t}+u\,\frac{\partial u}{\partial x}-fv\right)=\frac{\partial \sigma_{xx}}{\partial x}+\tau_{ax}+\tau_{wx}-\rho h g\,\frac{\partial \xi}{\partial x} \tag{7.24a}$$

$$\rho h\left(\frac{\partial v}{\partial t}+u\,\frac{\partial v}{\partial x}+fu\right)=\frac{\partial \sigma_{xy}}{\partial x}+\tau_{ay}+\tau_{wy} \tag{7.24b}$$

$$\left.\begin{aligned}\sigma &= \sigma(h, A, \dot{\varepsilon})\\ \dot{\varepsilon}_{xx} &= \frac{\partial u}{\partial x}\\ \dot{\varepsilon}_{xy} &= \dot{\varepsilon}_{yx}=\frac{1}{2}\,\frac{\partial v}{\partial x}\\ \dot{\varepsilon}_{yy} &= 0\end{aligned}\right\} \tag{7.24c}$$

$$\frac{\partial\{A,h\}}{\partial t}+\frac{\partial u\{A,h\}}{\partial x}=0\ (0\le A\le 1) \tag{7.24d}$$

Note that the sea surface slope is taken as zero along the y-axis that lines the geostrophic current into alongshore directions. The atmospheric pressure gradient has been ignored in the momentum equation and also the elastic part of the rheology. The boundary conditions can be taken as stationary at the land boundary and zero stress at a long distance from the land:

$$x=0:\quad u=0;\quad x=L:\quad \sigma=0 \tag{7.24e}$$

Eqs. (7.24) can be solved for free drift as shown in Chapter 6. Taking $\sigma = 0$, the free drift equation is obtained, and the solution is formally $u = u_F = u'_a + U_{wg}$, where u'_a is the wind-driven component of speed equal to a fraction α of the wind speed, and with a direction deviating by angle θ from the wind direction (see Eq. 6.5 and Figure 6.1).

7.4.1 Steady-state velocity: wind-driven case

Purely wind-driven drift is first considered (i.e., $U_{wg} = 0$ and $\beta = 0$). Free drift velocity (speed u_F, deviation angle h) can be obtained from Eqs. (7.24a, b). If $u_F > 0$, then ice will drift away from the coast with free boundaries and in free drift state (see Figure 7.10) and u_F will be the true solution; the boundary condition $u = 0$ would also no longer be valid. In the case of pure wind-driven sea ice dynamics, the off-coast free drift solution results when the direction[1] of the wind stress vector (or the surface wind vector), ϑ, satisfies:

$$-90^\circ + \theta < \vartheta < 90^\circ + \theta \tag{7.25}$$

(see Figure 7.10). In the northern hemisphere $\theta \sim 30^\circ$, and therefore the wind direction must be approximately between -60° and 120°; in the southern hemisphere $\theta \sim -30^\circ$ and the range is from -120° to 60°.

Otherwise, if condition (7.25) is not satisfied, the ice will stay in contact with the coast and internal stress will spread the friction from the coast deeper into the drift ice zone. Then, either a boundary zone shear flow will develop or the ice will reach a stationary state (as in the channel flow case).

To solve on-shore-forced steady zonal flow, the ice conservation law states that for a steady state uA and uh must be constant, and then the boundary condition implies $u \equiv 0$. The ice conservation law is then satisfied, leaving the momentum equation and rheology for the longitudinal component of ice velocity and for the ice stress:

$$\frac{\mathrm{d}\sigma_{xx}}{\mathrm{d}x} + \tau_{ax} + \rho_w C_w \sin\theta_w |v| v + \rho h f v = 0 \tag{7.26a}$$

$$\frac{\mathrm{d}\sigma_{xy}}{\mathrm{d}x} + \tau_{ay} - \rho_w C_w \cos\theta_w |v| v = 0 \tag{7.26b}$$

$$\left.\begin{aligned} \sigma &= \sigma(h, A, \dot{\varepsilon}) \\ \dot{\varepsilon}_x &= 0 \\ \dot{\varepsilon}_{xy} &= \dot{\varepsilon}_{yx} = \frac{1}{2}\frac{\partial v}{\partial x} \\ \dot{\varepsilon}_{yy} &= 0 \end{aligned}\right\} \tag{7.26c}$$

[1] Vector directions are taken according to the normal mathematical standard: zero direction is toward east and positive directions turn anticlockwise.

In this case, for quite general conditions:

$$\left| \frac{\sigma_{xy}}{\sigma_{xx}} \right| = \gamma = \text{constant} \tag{7.27}$$

For example, in the viscous-plastic rheology used by Hibler (1979) $\gamma = e^{-1}$, when the strain-rate is given by Eqs. (7.26c). Then, the ice stress derivatives can be eliminated from Eqs. (7.26a, b), an algebraic equation is obtained for v, and the solution can be easily found (Figure 7.13) (see Leppäranta and Hibler, 1985). But care must be taken with the signs, since the sign of shear stress σ_{xy} depends on which side the solid boundary is and the sign of ice–water stress depends on the direction of motion. Stress σ_{xx} is negative (compressive) in all cases.

Let us first assume that the ice drifts north, $v \geq 0$ and then also $\sigma_{xy} > 0$. Equation (7.26a) can be multiplied by γ and then added to Eq. (7.26b). The result is:

$$\tau_{ay} - \rho_w C_w \cos\theta_w v^2 + \gamma(\tau_{ax} + \rho_w C_w \sin\theta_w v^2 + \rho h f v) = 0 \tag{7.28}$$

This is a quadratic equation, whose solution is:

$$v = \sqrt{\frac{\tau_{ay} + \gamma\tau_{ax}}{C_N} + \left(\frac{\gamma\rho h f}{2C_N}\right)^2} - \frac{\gamma\rho h f}{2C_N}, \tag{7.29}$$

where $C_N = \rho_w C_w(\cos\theta_w - \gamma \sin\theta_w)$. In the northward on-shore forcing $\tau_{ay} > 0$ and $\tau_{ax} < 0$, and thus the coastal friction cuts the portion $\gamma\tau_{ax}$ out of the alongshore momentum input. Setting $v \equiv 0$ in Eq. (7.29) we get the condition $\tau_{ay} + \gamma\tau_{ax} = 0$. For a positive velocity solution, the reduced stress must be positive, that is:

$$\tau_{ay} + \gamma\tau_{ax} > 0 \tag{7.30}$$

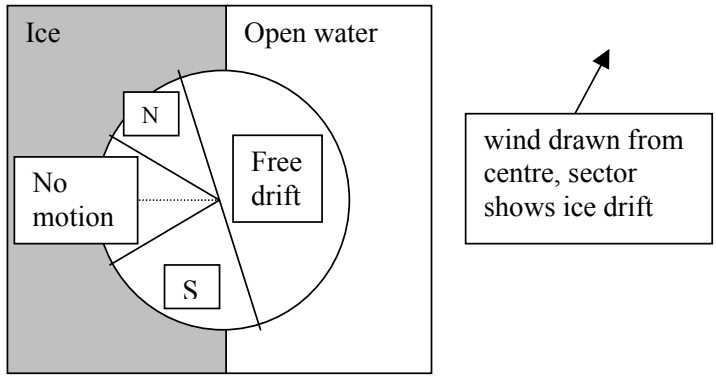

Figure 7.13 Steady-state solution of wind-driven zonal flow, northern hemisphere. The wind vector is drawn from the centre of the circle to the perimeter, and the resulting ice velocity is free drift, northward or southward boundary flow, or no motion, depending on ice strength and wind direction.
From Leppäranta and Hibler (1985).

This means that the northward component τ_{ay} must be larger than $\gamma|\tau_{ax}|$ or the on-ice direction of the wind stress must be less than $\arctan(\gamma)$. Otherwise, a stationary ice field results in the steady state (as in the channel flow case). The following conclusion can now be presented for northward wind stress forcing:

$$\begin{aligned} 0 \le \vartheta &\le 90^\circ + \theta && \text{(free drift)} \\ 90^\circ + \theta \le \vartheta &\le 180^\circ - \arctan(\gamma) && \text{(northward flow } v > 0\text{, see Eq. 7.29)} \\ 180^\circ - \arctan(\gamma) \le \vartheta &\le 180^\circ && \text{(stationary ice } v \equiv 0\text{)} \end{aligned}$$

If $\gamma = \frac{1}{2}$, then $\arctan(\gamma) = 27^\circ$. Thus the northward flow results from a 33° wide wind direction sector in the northern hemisphere. The deviation angle between wind and ice drift is simply equal to the on-ice angle of the wind speed; therefore, it is between 30° and 63°.

Example The characteristics of the shear flow become clearer when Coriolis and boundary-layer angle effects are ignored. Then $u_F > 0$ if $\tau_{ax} > 0$. The northward flow solution can be written as:

$$v = Na\sqrt{\sin\vartheta + \gamma\cos\vartheta}\,|U_a|$$

where wind direction is in the range $90^\circ + \theta \le \vartheta < 180^\circ - \arctan(\gamma)$. Thus $v \propto |U_a|$; however, the proportionality factor is affected by the wind direction and the strength parameter γ in addition to the drag coefficients.

Second, assume that the ice drifts south, $v \le 0$ and then also $\sigma_{xy} < 0$. The solution is found as in the northward case, and the result is:

$$v = -\sqrt{\frac{-\tau_{ay} + \gamma\tau_{ax}}{C_s} + \left(\frac{\gamma\rho hf}{2C_s}\right)^2} + \frac{\gamma\rho hf}{2C_s}, \tag{7.31}$$

where $C_s = \rho_w C_w(\cos\theta_w + \gamma\sin\theta_w)$. And furthermore, the following conclusion can be presented for southward forcing by the wind stress:

$$\begin{aligned} 180^\circ \le \vartheta &\le 180^\circ + \arctan(\gamma) && \text{(stationary ice } v = 0\text{)} \\ 180^\circ + \arctan(\gamma) \le \vartheta &\le 270^\circ + \theta && \text{(southward flow } v < 0\text{, see Eq. 7.31)} \\ 270^\circ + \theta \le \vartheta &\le 360^\circ && \text{(free drift)} \end{aligned}$$

The stationary sector is as in the northward case, but the flow zones are changed so that now it is narrow in the southern hemisphere and wide in the northern hemisphere.

The general solution is illustrated in Figures 7.13 and 7.14 for the northern hemisphere case. The southern case is symmetric (i.e., the northward flow zone is wide and the southward flow zone is narrow).

It is striking that the velocity solution is independent of the exact form of the rheology and even of the absolute magnitude of the stresses as long as Eq. (7.27) holds. The only rheology parameter present is γ, which describes the ratio of shear strength to compressive strength. Taking the plastic part of the viscous-plastic rheology of

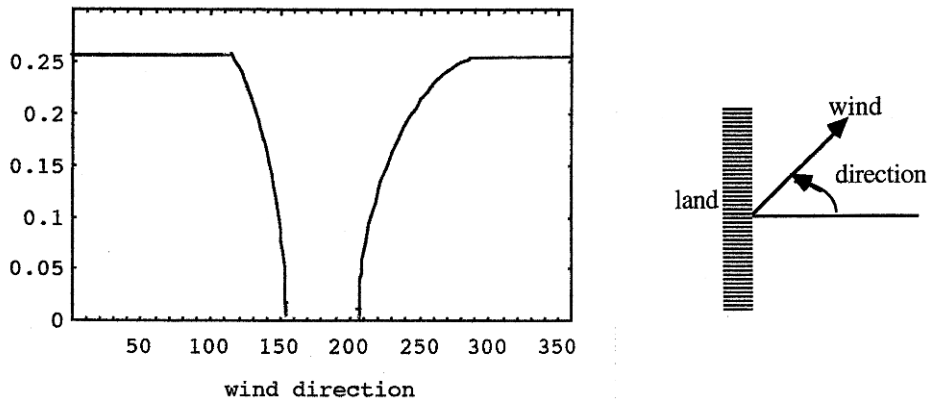

Figure 7.14 The zonal flow speed (m/s) as a function of wind direction when the coastal boundary is in the east, northern hemisphere. Wind speed is $10\,\mathrm{m\,s^{-1}}$ and the strength parameter is $\gamma = \frac{1}{2}$.

Hibler (1979) (Eq. 4.32), we have $\gamma = e^{-1}$ for all shear flows, with the standard level $\gamma = \frac{1}{2}$. In the floe collision model of Shen *et al.* (1987) (Eq. 4.37) we have:

$$\gamma = \frac{12}{\pi}\sqrt{\frac{4}{3\pi(1-\kappa)} - \frac{1}{4}} \tag{7.32}$$

with $\gamma = 0.13$ for the restitution coefficient $\kappa = 0.9$.

Note also that the zonal flow solution is valid for spatially variable wind constant in time. The spatial variability must, however, be consistently in a fixed zone shown in Figure 7.13. Thus, ice adjusts to the wind field with the wind factor reduced from the free drift factor, while direction is parallel to the coast. The time evolution of zonal flow was examined using numerical modelling by Leppäranta and Hibler (1985).

7.4.2 Steady-state with ocean currents

Steady ocean currents can be added to the wind-driven steady zonal flow still allowing analytical solutions. In the zonal model the geostrophic ocean current is longitudinal, $\boldsymbol{U}_{wg} = V_{wg}\mathbf{j}$. The steady-state equations read, taking the geostrophic current for the reference water velocity: ($V_w = V_{wg}$)

$$\frac{\mathrm{d}\sigma_{xx}}{\mathrm{d}x} + \tau_{ax} - \rho_w C_w \sin\theta_w |V_w - v|(V_w - v) - \rho h f (V_w - v) = 0 \tag{7.33a}$$

$$\frac{\mathrm{d}\sigma_{xy}}{\mathrm{d}x} + \tau_{ay} + \rho_w C_w \cos\theta_w |V_w - v|(V_w - v) = 0 \tag{7.33b}$$

$$\sigma = \sigma(h, A, \dot{\varepsilon}), \quad \dot{\varepsilon}_{xx} = 0, \quad \dot{\varepsilon}_{xy} = \dot{\varepsilon}_{yx} = \frac{1}{2}\frac{\partial v}{\partial x}, \quad \dot{\varepsilon}_{yy} = 0 \tag{7.33c}$$

This is a model for the relative velocity $v - V_w$, derived exactly as the wind-driven (zero ocean current) model for v. The longitudinal velocity is therefore:

$$v = V_w + v_0 \tag{7.34}$$

where v_0 is the wind driven velocity component. Note that the solution (7.34) is valid for any $V_w = V_w(x)$. It is noteworthy that even though sea ice drift is highly nonlinear in the presence of internal friction, steady zonal flow allows superposition of wind-driven and ocean current-driven components.

7.4.3 Steady-state ice thickness and compactness profiles

During the time evolution of zonal sea ice flow, the ice state evolves to allow steady-state conditions to be satisfied. When longitudinal velocity has been solved, the ice stress components σ_{xx} and σ_{xy} can be solved from the momentum equation, $\sigma_{yx} = \sigma_{xy}$ holds for symmetry, and ice rheology provides the component σ_{yy}. The ice state can then be obtained from the stress distribution.

If a stationary ice field results in the steady state, integration of Eqs. (7.26) is straightforward and proceeds similarly to the channel flow problem. Otherwise, the steady-state velocity profile also influences the stress field. The y-component of the momentum balance gives:

$$\sigma_{xy}(x) = \sigma_{xy}(0) - \int_0^x (\tau_{ay} - \rho_w C_w \cos\theta_w |v| v)\, \mathrm{d}x' \tag{7.35}$$

The second boundary condition states that at the ice edge, $x = L$, the stress must vanish. The shear stress at the coast is $\sigma_{xy}(0) = \int_0^L (\tau_{ay} - \rho_w C_w \cos\theta_w |v| v)\, \mathrm{d}x'$.

With the present two-level ice state, ice strength depends on ice compactness and thickness. Starting at the ice edge, ice compactness first increases from 0 to 1 and thereafter a ridging zone follows. The geometric profiles of the edge zone and ridging zone depend on functional relationships between ice compactness and strength and ice thickness and strength, formally[2]:

$$|\sigma_{xy}(x)| = \sigma^* q(A) r(h) \tag{7.36}$$

where σ^* is a strength constant, $0 \leq q \leq 1$ and $q(0) = 0$, $q(1) = 1$, and $r(h)$ tells to us to what degree the strength of compact ice depends on ice floe thickness. The inner boundary of the edge zone can be ascertained from the location where the shear stress in Eq. (7.35) is in absolute value equal to $\sigma^* r(h_0)$.

Example In the plastic rheology of Hibler (1979), shear stress is shown in the steady state as:

$$\sigma_{xy} = sgn\left(\frac{\partial v}{\partial x}\right) \frac{P^* h}{e} \exp[-C(1 - A)]$$

[2] In the ice strength expressions ice compactness and thickness show up in separate factors that serves thus as a general hypothesis.

Assume a constant wind stress toward the sector where the steady-state solution is the northward zonal flow. Ignoring the Coriolis and oceanic turning angle, we have:

$$\tau_{ay} - \rho_w C_w v^2 = -\gamma\tau_{ax}$$

and, consequently, from Eq. (7.35) we have $\sigma_{xy}(x) = \sigma_{xy}(0) + \gamma\tau_{ax}x$. The shear stress at the fast ice boundary is $-\gamma\tau_{ax}L$. Let us assume that initially the ice cover consists of homogeneous floes of thickness h_0. The ridging condition is $-\tau_{ax}L > P^*h_0$. If it is satisfied, then ice builds up at the coast and the ice thickness at the boundary will be $h(0) = -\tau_{ax}L/P^*$. Ridging takes place in the zone $-\tau_{ax}(L - x) > P^*h$, while beyond that ice floe thickness is constant h_0 and ice compactness is limited from below by $-\tau_{ax}(L - x) = P^*h_0 \exp\{-C[1 - A]\}$ and by the initial conditions. Then, integration of the ice state out from the coast proceeds exactly as in the one-dimensional case. Consequently, the channel model and shear flow give similar ice thickness and compactness profiles, but in the shear zone there may be a steady state, non-zero longitudinal velocity. Adding Coriolis and boundary-layer turning angle effects would modify the profiles, but qualitatively the result would be similar.

The full solution of the time evolution of ice thickness and compactness is shown in Figure 7.15. The ice edge zone draws a very sharp ice compactness profile because of the high sensitivity of ice strength to ice compactness. The adjustment time is quite long as it is governed by the viscous creep and therefore it is not necessarily realistic.

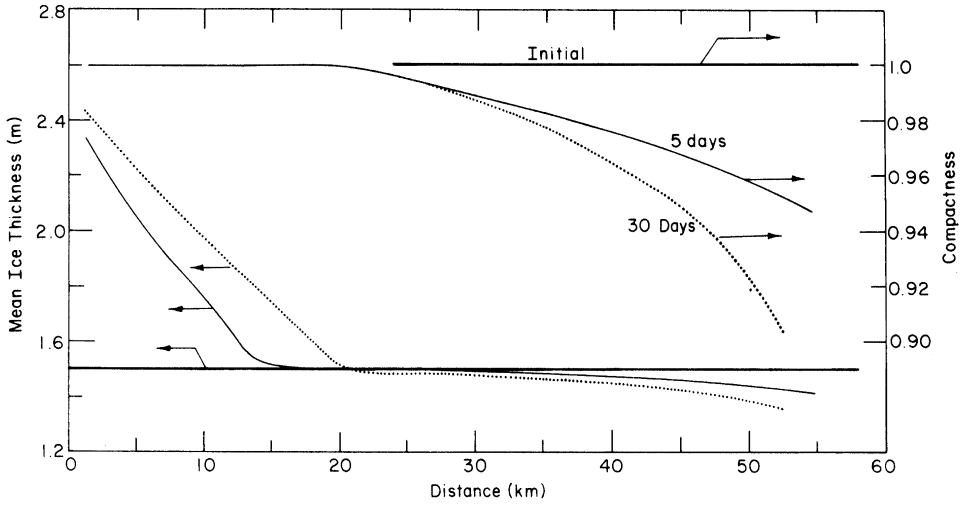

Figure 7.15 The profile of ice thickness and ice compactness from the fast ice boundary to the ice edge. Numerical solution of time evolution, the solution at 30 days is close to the steady state. From Leppäranta and Hibler (1985).

7.4.4 Viscous models

The general viscous model was given by Eq. (4.14): $\sigma = \sigma(\dot{\varepsilon}, p; \zeta, \eta) = (-p + \zeta \operatorname{tr} \dot{\varepsilon})\boldsymbol{I} + 2\eta\dot{\varepsilon}$. In the steady-state zonal flow, $\operatorname{tr} \dot{\varepsilon} = 0$ and:

$$\left.\begin{aligned} \frac{\partial \sigma_{xx}}{\partial x} &= -\frac{\partial p}{\partial x} \\ \frac{\partial \sigma_{xy}}{\partial x} &= \frac{\partial}{\partial x}\left(\eta \frac{\partial v}{\partial x}\right) \end{aligned}\right\} \tag{7.37}$$

Here pressure depends on ice-state variables and viscosity additionally depends on strain-rate invariants.

Consider the steady-state zonal flow problem (Eq. 7.26). Ignoring the Coriolis and the oceanic turning angle:

$$\left.\begin{aligned} \frac{dp}{\mathrm{d}x} + \tau_{ax} &= 0 \\ \frac{d}{dx}\left(\eta \frac{dv}{dx}\right) + \tau_{ay} - \rho_w C_w |v| v &= 0 \end{aligned}\right\} \tag{7.38}$$

A pressure gradient is therefore needed to balance on-ice forcing. If it does not exist, the true steady state is never achieved, but the ice continues to creep toward the shore and the wind stress is balanced by the bulk viscous stress. The longitudinal equation allows a general solution if ice–water stress can be ignored similarly to the channel flow case (Eq. 7.9).

Example: the Laikhtman model A historical landmark in sea ice dynamics is the work of Laikhtman (1958), who presented the first frictional sea ice model. He used a linear viscous model for the zonal flow at a land boundary. He took constant viscosity, ignored the Coriolis and turning angle, and assumed the wind and water stresses to be linear. The momentum equation in the y-direction is then:

$$\eta \frac{dv^2}{dx^2} - \rho_w C_{w1} v + \rho_a C_{a1} V_a = 0$$

With the boundary conditions $v = 0$ at $x = 0$ and $v \to v_\infty = Na_1 V_a$ (free drift) as $x \to \infty$, the solution is:

$$\left.\begin{aligned} v &= v_\infty \left[1 - \exp\left(-\frac{x}{L}\right)\right] \\ L &= \sqrt{\frac{\eta}{\rho_w C_w}} \end{aligned}\right\}$$

where L is a length scale for the coastal boundary layer. For $C_{w1} \sim C_w$, $v_\infty \sim 0.5\,\mathrm{m\,s^{-1}}$ and $\eta \sim 10^{10}\,\mathrm{kg\,s^{-1}}$, the width is $L \sim 140\,\mathrm{km}$.

Under constant forcing the linear viscous case thus gives a gently sloping coastal boundary zone, while in plastic flow the steady-state boundary is a sharp slip line

although, during the adjustment process, plastic flow has a spatial structure. When viscous rheology becomes increasingly sublinear, the plastic solution is approached.

7.4.5 Marginal ice zone

The marginal ice zone (MIZ) is located along the open ocean edge of sea ice cover, its width usually referred to as 100 km (Figure 7.16). In the MIZ, ice dynamics has a number of qualitative features:

- off-ice forcing results in ice edge dispersion;
- formation of ice bands, parallel to the MIZ;
- oceanic eddies form and ice tracks them;
- on-ice forcing gives a compact ice edge;
- little ridging takes place;
- intensive air–ice–sea interaction takes place.

On-ice and off-ice forcing cases are therefore highly dissimilar. Ice compactness and thickness increase inward from the ice edge. Because of the looseness of its ice, the outermost MIZ can move for short periods at high velocity compared with the bulk zone flow. Sometimes these high-velocity cases have been termed "ice edge jets".

Figure 7.16 An ice edge in the Greenland Sea.

The zonal flow problem also applies to MIZ ice dynamics. If the free drift solution is off-ice, the MIZ will diffuse into a free drifting, open ice field, where ice velocity consists of the wind effect superposed on the current field. For on-ice forcing, the steady-state solution is a stationary ice field or a longitudinal flow, which runs parallel to the ice edge and moves at a velocity reduced from free drift. In such conditions, disturbances in the ice floes at the ice edge could give rise to transient ice edge jets.

Integrating the shear stress (Eq. (7.26b) from the ice edge, we have:

$$\sigma_{xy}(x) = \int_x^L (\tau_{ay} - \rho_w C_w \cos\theta_w |v| v)\, \mathrm{d}x' \tag{7.39}$$

Then $A = 1$ at $x = L_1$; the inner boundary of the MIZ can be taken as $\sim L_1$ since little ridging occurs closer to the ice edge. Let us take the plastic rheology of Hibler (1979). Further, let us assume that initially the ice cover consists of homogeneous floes of thickness h_i. Starting at the ice edge, ice compactness is first obtained from the equation:

$$\mathrm{sgn}\left(\frac{\partial v}{\partial x}\right) \frac{P^* h}{e} \exp[-C(1-A)] = \int_x^L (\tau_{ay} - \rho_w C_w \cos\theta_w |v| v)\, dx' \tag{7.40a}$$

This is integrated to $A = 1$ where $x = L_1$. Thereafter $A \equiv 1$ and h is obtained from:

$$h = h_i + \mathrm{sgn}\left(\frac{\partial v}{\partial x}\right) \frac{e}{P^*} \int_{LI}^x (\tau_{ay} - \rho_w C_w \cos\theta_w |v| v)\, dx' \tag{7.40b}$$

Taking a northward flow and ignoring the Coriolis and turning angle, we have $L_1 = L + P^* h_i / \tau_{ax}$ (note: $\tau_{ax} < 0$). A sharp ice edge results because of the exponential factor in the strength–compactness relation. If $P^* = 10\,\mathrm{kPa}$, $e = 2$, $h_i = 1\,\mathrm{m}$, $C = 20$, and $\tau_{ay} - \rho_w C_w \cos\theta_w |v| v = 0.1\,\mathrm{Pa}$, compactness is equal to 0.8 at a distance of 0.7 km from the ice edge. A sharp ice edge under steady on-ice wind is well known from observations (i.e., here the compactness increased from 0 to 0.8 over the first 0.7 km). But to go from 0.8 to 1.0 an additional distance of 49.3 km is needed. A linearly increasing ice thickness profile results starting at point L_1 and extending inwards to the ice pack, the thickness slope being equal to $-\tau_{ax}/P^*$.

Since an ocean current field parallel to the ice edge can be superposed on the wind-driven MIZ solution, any jet in the ocean beneath the ice at the ice edge is added to the ice velocity. Ice drift strongly interacts with atmospheric and oceanic boundary layers in the MIZ. In particular, with compact ice edges there is a very rapid change in surface characteristics. The surface roughness of sea ice is different from the surface roughness of the open ocean, the drag coefficient usually being larger over sea ice. Surface temperature also changes across the ice edge. As far as ocean forcing is concerned, there is a seasonal difference in the forcing of the ocean across the ice edge, giving rise either to divergence or convergence. In winter, freezing and ice growth cause brine formation and reduce the stability of stratification in the water, while in summer ice melt yields the opposite effect. As a consequence, an ice edge front may form where dynamic instabilities appear, resulting in ice edge eddies.

Table 7.1 Upwelling (+) and downwelling (−) at the ice edge.

MIZ location		Ice friction	
Arctic seas	Antarctica	Large	Small
Left from wind	Right from wind	+	−
Right from wind	Left from wind	−	+

Example: upwelling at the ice edge Assume a constant wind toward north that is parallel to the ice edge. Ekman transport in the ocean surface layer is $\mathbf{i}\tau_{0y}/f$ (e.g., Cushman-Roisin, 1994), where $\boldsymbol{\tau}_0 = \mathbf{j}\tau_{0y}$ is surface stress. Now the surface stress is:

$$\text{Over open ocean: } \tau_{0y} = \rho_a C_{aw} V_a^2, \quad \text{Over ice: } \tau_{0y} = \rho_a C_{ai} V_a^2 + \frac{\mathrm{d}\sigma_{xy}}{\mathrm{d}x}$$

where C_{aw} and C_{ai} are the air drag coefficients over open water and sea ice, respectively. Since usually $C_{aw} < C_{ai}$, the wind stress transmitted to the ocean is larger over ice if $|d\sigma_{xy}/dx|$ is small. But when $|\mathrm{d}\sigma_{xy}/\mathrm{d}x|$ is large enough, wind stress will be larger over open water, resulting in divergence and consequent upwelling at the ice edge.

Consequently, we can compile Table 7.1 for upwelling (+) and downwelling (−) at the ice edge. It works for either hemisphere, whether the ice is to left or right of the wind, and whether the internal friction of ice is large or small. The large ice friction case also applies to the fast ice edge.

7.4.6 Circular ice drift

A y-invariant ice flow can be closed into a circle (termed a "circular ice drift"), and then it is natural to use spherical coordinates. Let us consider a polar cap and choose spherical coordinates $\boldsymbol{r} = (r_e, Z, \lambda)$ (Figure 7.17). The steady-state momentum equation is:

$$\frac{1}{r_e \sin Z}\frac{\partial \sigma_{\lambda\lambda}}{\partial \lambda} + \frac{1}{r_e}\frac{\partial \sigma_{Z\lambda}}{\partial Z} + \frac{2}{r_e}\sigma_{Z\lambda}\cot Z + \tau_{a\lambda} + \tau_{w\lambda} + \rho h 2\Omega \cos Z u_Z - \rho h g \beta_\lambda = 0 \tag{7.41a}$$

$$\frac{1}{r_e \sin Z}\frac{\partial \sigma_{Z\lambda}}{\partial \lambda} + \frac{1}{r_e}\frac{\partial \sigma_{ZZ}}{\partial Z} + \frac{1}{r_e}(\sigma_{ZZ} - \sigma_{\lambda\lambda})\cot Z + \tau_{aZ} + \tau_{wZ} - \rho h 2\Omega \cos Z u_\lambda - \rho h g \beta_Z = 0 \tag{7.41b}$$

The y-coordinates that transform into circles correspond to zenith angle circles $Z =$ constant (or latitude circles), and for the situation to be invariant along these circles we have $\partial/\partial\lambda \equiv 0$. When the ice state is fully adjusted and the ice conservation

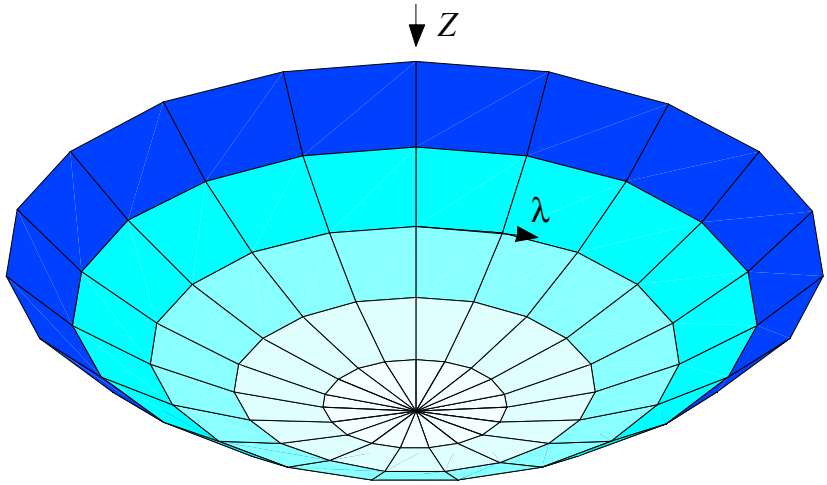

Figure 7.17 Configuration of zonal flow on a southern polar cap.

law has also achieved a steady state, the zenith angle velocity component is $u_Z \equiv 0$, as the east component became 0 in the Cartesian system. The ice conservation law is then automatically satisfied, and the equilibrium momentum equation becomes:

$$\frac{1}{r_e}\frac{d\sigma_{Z\lambda}}{dZ} + \frac{2}{r_e}\sigma_{Z\lambda}\cot Z + \tau_{a\lambda} + \tau_{w\lambda} = 0 \tag{7.42a}$$

$$\frac{1}{r_e}\frac{d\sigma_{ZZ}}{dZ} + \frac{1}{r_e}(\sigma_{ZZ} - \sigma_{\lambda\lambda})\cot Z + \tau_{aZ} + \tau_{wZ} + \rho h 2\Omega \cos Z(u_\lambda - U_{w\lambda}) = 0 \tag{7.42b}$$

Now the strain-rate components are:

$$\dot{\varepsilon}_{ZZ} = 0, \quad \dot{\varepsilon}_{\lambda\lambda} = 0 \text{ and } \dot{\varepsilon}_{Z\lambda} = \frac{1}{2}\left(\frac{1}{r_e}\frac{\mathrm{d}u_\lambda}{\mathrm{d}Z} - \frac{u_\lambda}{r_e}\cot Z\right) \tag{7.43}$$

This problem is then solved using the plastic rheology of Hibler (1979) and, as a result, $\sigma_{ZZ} = \sigma_{\lambda\lambda} = -P/2$ and $\sigma_{Z\lambda} = \frac{1}{2}\,\mathrm{sgn}(\dot{\varepsilon}_{Z\lambda})P/e$. Equations (7.42) then become:

$$\mathrm{sgn}(\dot{\varepsilon}_{Z\lambda})\frac{1}{2er_e}\frac{\mathrm{d}P}{\mathrm{d}Z} + \frac{2}{r_e}\,\mathrm{sgn}(\dot{\varepsilon}_{z\lambda})\,\frac{P}{2e}\cot Z + \tau_{a\lambda} + \tau_{w\lambda} = 0 \tag{7.44a}$$

$$-\frac{1}{2r_e}\frac{\mathrm{d}P}{\mathrm{d}Z} + \tau_{aZ} + \tau_{wZ} - \rho h 2\Omega \cos Z(u_\lambda - U_{w\lambda}) = 0 \tag{7.44b}$$

Let us now ignore the Coriolis and oceanic turning angle. For a westerly wind $\tau_{a\lambda} > 0$, $\tau_{aZ} = 0$, we have $P =$ constant from Eq. (7.44b). Equation (7.44a) now gives:

$$\mathrm{sgn}(\dot{\varepsilon}_{Z\lambda})\,\frac{P}{r_e e}\cot Z + \tau_{a\lambda} - \rho_w C_w u_\lambda^2 = 0 \tag{7.45}$$

The cotangent term geometrically restricts the motion of ice. Approaching the poles, $|\cot Z| \to \infty$, therefore, there must be a rigidly rotating polar cap. Since

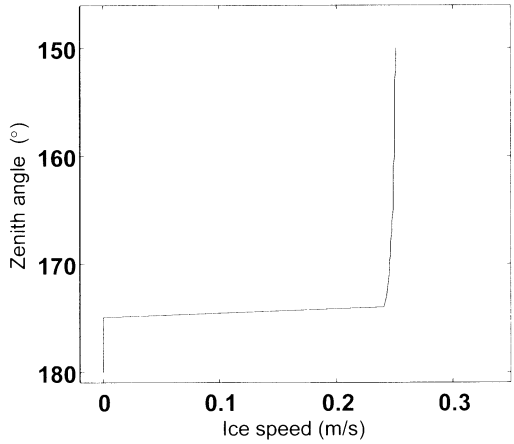

Figure 7.18 The steady-state solution of circular ice drift.

$P/(r_e e) \sim 10^{-3}$ Pa, usually we need $|\cot Z| < 100$ or the width of the rigid cap is $\sim 2r_e|\text{arccot}\, Z| \sim 100$ km. As the strength of ice increases with thickness, the width of the rigid cap must also increase with ice thickness.

In the general case, the pressure gradient is eliminated and the resulting equation is:

$$\text{sgn}(\dot{\varepsilon}_{Z\lambda})\frac{P}{r_e e}\cot Z + \tau_{a\lambda} + \frac{\tau_{aZ}}{e} - \rho_w C_w u_\lambda^2 - \frac{\rho h 2\Omega \cos Z u_\lambda}{e} \tag{7.46}$$

This equation gives $u_\lambda = u_\lambda(Z)$. Then ice compactness and thickness can be integrated using the Z-momentum equation. The solution for ice velocity is schematically shown in Figure 7.18.

Example Antarctic drift The Antarctic ice drift problem (Figure 7.19) can be idealized as a continent symmetric around the pole, with $-90^\circ \le Z \le Z_0$, an east wind zone $Z_0 \le Z \le Z_1$, and a west wind zone $Z_1 \le Z \le Z_2$. Because Coriolis acceleration is to the left of the motion in the southern hemisphere, west wind drift is diffusive while east wind drift is compressive. Therefore the west wind drift zone is in a near-free drift state, but a significant friction is present in the east wind drift zone. In the latter zone $\tau_{a\lambda} < 0$, $\tau_{aZ} = 0$ and $\text{sgn}(\dot{\varepsilon}_{Z\lambda}) = -1$. Elimination of the pressure gradient from the momentum equations gives:

$$\frac{P}{r_e e}\cot Z - \tau_{a\lambda} - \rho_w C_w\left(\cos\theta_w + \frac{\sin\theta_w}{e}\right)u_\lambda^2 - \rho h 2\Omega \cos Z\, e^{-1} u_\lambda = 0$$

Ignoring the Coriolis and the oceanic turning angle, we have:

$$\frac{P}{r_e e}\cot Z - \tau_{a\lambda} - \rho_w C_w u_\lambda^2 = 0.$$

A non-zero shear flow solution exists if:

$$|\tau_{a\lambda}| r_e e/P > |\cot Z|.$$

Figure 7.19 Sea ice cover in the Antarctic is more divergent than in the Arctic, characteristic features being the presence of polynyas and the co-existence of icebergs inside the pack ice. Reproduced with permission from Professor Hardy B. Granberg, Sherbrooke, Quebec.

When the velocity has been resolved, the compactness and thickness profiles are integrated similarly as in the rectangular case. When Coriolis acceleration is added, the right-hand side of the above equation increases and a stronger wind is needed to initiate ice motion.

The circular ice drift model also serves as an analytic tool for examining sea ice flows on other Earth configurations (e.g., the distribution of land and water surfaces) and other (theoretical) planetary bodies[3] as well.

Example: circular drift in polar coordinates. The case can be also worked through in polar coordinates (r, ϕ), and the steady-state equations are then:

$$\frac{\mathrm{d}\sigma_{rr}}{\mathrm{d}r} + \frac{\sigma_{rr} - \sigma_{\phi\phi}}{r} + \tau_{ar} + \tau_{wr} - \rho h f (u_\phi - U_{w\phi}) = 0$$

$$\frac{\mathrm{d}\sigma_{r\phi}}{\mathrm{d}r} + \frac{2}{r}\,\sigma_{r\phi} + \tau_{a\phi} + \tau_{w\phi} = 0$$

[3] Planetary bodies with similar "sea ice" dynamics to those on Earth are not known. However, the ice on Europa, the sixth moon of Jupiter, may be a floating glacier.

Ignoring the Coriolis and Ekman angle, the viscous–plastic model provides the velocity from:

$$\operatorname{sgn}(\varepsilon_{r\phi})\,\frac{P}{er}+\tau_{a\lambda}-\rho_w C_w u_\phi^2=0$$

A rigid (or rigidly rotating) disc around the origin is thus needed to obtain a non-zero shearing velocity field. The radius of this disc is $r\sim P/(e\tau_a)\sim 100\,\text{km}$.

7.5 MODELLING OF ICE TANK EXPERIMENTS

The calibration and validation of continuum models have been based on full-scale observations, mainly encompassing the extent, compactness and kinematics of drift ice. As to whether small-scale tank experiments could be useful has not been much examined. Such experiments might be used to investigate questions like the re-distribution of drift ice thickness, drift ice rheology, and the dependence of the yield function on the state of the drift ice field. But, how well can ice tank tests be reproduced using mathematical sea ice models? An effort was made by Ovsienko *et al.* (1999b) to model ice tank experiments using a numerical model. The result was quite promising in that an elastic–plastic drift ice model could reproduce the outcome of the tank test.

7.5.1 Drift ice dynamics in a tank

An ice tank is a small, elongated rectangular basin, in which the x-axis is aligned with its major axis. Mathematical modelling of tank ice dynamics is based on a two-level system $J=\{A,h\}$ using the equations of ice dynamics given in Eqs. (7.1). In tanks the Coriolis term can be ignored, and forcing and motion are longitudinal along the x-axis:

$$\rho h\left(\frac{\partial u}{\partial t}+u\,\frac{\partial u}{\partial x}\right)=\frac{\partial \sigma_{xx}}{\partial x}+\frac{\partial \sigma_{yx}}{\partial y}+\tau_{ax}+\rho_w C_w|U_w-u|(U_w-u)-\rho h g\beta_x \qquad (7.47a)$$

$$\frac{\partial\{A,h\}}{\partial t}+\frac{\partial u\{A,h\}}{\partial x}=0\quad(0\le A\le 1) \qquad (7.47b)$$

The boundary conditions depend on the experiment configuration. The initial conditions are usually $u(x,0)=0$, $J(x,0)=J_0(x)=\{A_0(x),h_0(x)\}$. The difference from the channel flow model is the inclusion of shear friction, which may be important for narrow tanks (Hopkins and Tuhkuri, 1999). The system can be forced by wind, water flow, or from the boundary. We will now analyze the boundary forcing case, mainly because ice tank experimental data exist for this case.

In the boundary forced case, an ice field is compressed by being pushed at velocity u_b by a moving boundary toward a fixed boundary (Figure 7.20). Then,

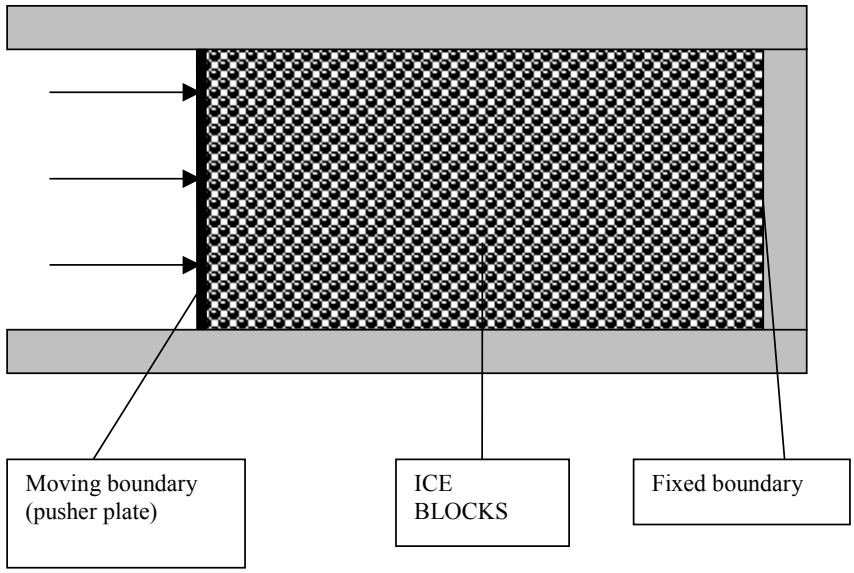

Figure 7.20 Ice tank experiment with boundary forcing.

wind stress, water surface slope, and water flow velocity are all zero, and the momentum equation is

$$\rho h\left(\frac{\partial u}{\partial t}+u\,\frac{\partial u}{\partial x}\right)=\frac{\partial \sigma_{xx}}{\partial x}+\frac{\partial \sigma_{yx}}{\partial y}-\rho_w C_w|u|u \tag{7.48}$$

Let us assume that the ice field is initially homogeneous, $J_0 = \text{constant}$, and its length is L_0. The origin is at the fixed boundary, and the x-coordinate increases toward the moving boundary located at $L = L(t)$, $dL/dt = u_b$. Momentum advection and ice–water stress scale as U^2 and their ratio is $h/(C_w L) \sim 1$ for $h \sim 10\,\text{cm}$, $C_w \sim 10^{-2}$ and $L \sim 10\,\text{m}$. In fast-velocity experiments they are both important, while in slow-velocity experiments they become very small. The local acceleration is small if the velocity of the moving boundary is held constant.

Consequently, in the simplest experiment – slow, fixed boundary speed, and enough tank width for low shear friction – compressive stress is the dominant factor, and Eq. (7.48) gives the solution $\sigma_{xx} \approx \text{constant}$. Then, according to the boundary condition of a moving boundary:

$$\sigma_{xx} = -\frac{F}{b}\,, \tag{7.49}$$

where b is the width of the tank and $F = F(t)$ is the pushing force required at the moving boundary.

For a general rheology, let us take the power law as $\sigma_{xx} = \zeta \mathrm{d}u/\mathrm{d}x$ where $\zeta = \zeta_n(A,h)|\mathrm{d}u/\mathrm{d}x|^{n-1}$ is the bulk viscosity. The cases $n = 2$, $n = 1$ and $n = 0$ correspond, respectively, to floe collision rheology (Shen *et al.*, 1986), linear viscous

rheology, and plastic rheology. In these cases it is natural to assume that ice velocity is monotonously decreasing with x, $u(0) = 0$ and $u(L) = u_b < 0$, and thus $\mathrm{d}u/\mathrm{d}x < 0$. We have

$$\zeta_n \left| \frac{\mathrm{d}u}{\mathrm{d}x} \right|^n = -\frac{F}{b} \tag{7.50}$$

The case $n = 0$ corresponds to plastic ice rheology with ζ_0 as the compressive yield strength σ_c. Then, under compressive deformation, the internal ice stress corresponds to the minimum yield strength $\sigma_c = \sigma_c(J)$ in the tank, $\sigma_{xx} = -\min\{\sigma_c(x) \mid 0 \le x \le L\}$. Since the ice state is initially homogeneous, stress equals yield stress everywhere. Ice fails in a uniform manner, and the resulting uniform deformation necessitates a linear velocity profile. For $n \neq 0$, a linear velocity profile $u = -u_b x/L$ also results if the ice state is constant in space. Therefore the solution is continuous for $n \to 0$.

As regards the linear velocity profile, the ice conservation law is:

$$\frac{\partial J}{\partial t} + u_b \frac{x}{L} \frac{\partial J}{\partial x} = -J \frac{u_b}{L} \quad (0 \le A \le 1) \tag{7.51}$$

If the ice state is constant in space, then by $\partial J/\partial t = -Ju_b/L$ it remains to be so (i.e., $J = J(t)$). Consequently, boundary forcing of an ice field with its state constant in space results in a rubble field that thickens evenly (no particular pressure ridge features can form). This result is quite general with all viscous power laws, including the plastic flow. If the initial condition were changed to some $J_0 \neq$ constant, the weakest points would fail first and eventually the situation $J(t_1) =$ constant would be faced. This is clear by the principle of minimizing the work for additional deformation. A uniformly growing rubble field would result after time t_1.

Ice volume conservation requires that $hL = h_0 L_0$ at any time. Deformation of the ice field proceeds first by compacting to the maximum packing A^*, and thereafter rubble formation takes place and the actual ice thickness increases. We have for the compaction and rubble growth phases:

$$A(t) = \frac{AL_0}{L_0 + u_b t} \le A^*, \quad h = h_i A, \quad 0 \le t \le t^* \tag{7.52a}$$

$$h(t) = \frac{h_i L^*}{L^* + u_b t}, \quad A = A^*, \quad t > t^* \tag{7.52b}$$

where $h_i = h_0/A_0$ is the initial ice floe thickness and $L^* = L_0 A_0/A^*$ is the length of the ice field at the time t^* when the free paths in the ice floe field have all closed up.

If the time evolution of the forcing is known, it is possible to obtain information on rheology. Since the ice state depends on time, so does the strength. Therefore these tank experiments do not provide a unique solution for the viscosity ζ_n and power n. Instead, if n is given, viscosity together with its functional form can be determined. With the plasticity assumption, $\sigma_c(A, h) = F/b$ and the yield function can be examined for the dependence of σ_c on A in the compaction phase and on h in the rubble growth phase.

7.5.2 Case study

Let us take the tank experiments of Tuhkuri and Lensu (1997) for a case study. The tank was 40 m × 40 m with a depth of 2.8 m. It was first frozen, then test areas 6 m × 20 m were cut into the ice sheet, and the ice in each test area was broken into floes with a fixed thickness (h_i), diameter, and shape. In one experiment, the ice floe field was forced from one boundary by a pusher plate set to a fixed velocity u_b (Figure 7.20). The initial compactness was $A_0 = 0.7$, with 10% of the ice being brash. The only measured data concerned the force history at the pusher plate. The water flow velocity U_w was zero, and since the test regions were inside a large tank it is assumed that no significant surface slope was built up. These experiments have been simulated by a discrete particle model with good agreement (Hopkins and Tuhkuri, 1999). The continuum modelling approach is also very useful since it is the standard means of addressing the sea ice dynamics problem.

The outcome of 17 tests is presented in Tuhkuri and Lensu (1997). Nine tests were carried out with a variable ice thickness (28–54 mm) and velocity of the pusher plate (15–52 mm s^{-1}), while the shape and size of the ice floes were fixed (circular and diameter 400 mm). In eight tests the velocity of the pusher plate was nearly the same (10–13 mm s^{-1}), and ice floes had variable thickness (36 or 57 mm), shape (square or irregular), and diameter (300–600 mm). The force at the pusher plate was 50–200 N at $A = 1$, which increased up to 300–1,500 N at $h \approx 8h_i$ at the time the tests drew to a close.

Thus the relevant scales were $u \sim 30$ mm s^{-1} and $h \sim 50$ mm. The inertial force is much less than $\frac{1}{2}bL\rho h\Delta u/\Delta t \sim 40$ N; this would result if half of the test area would change the velocity in 1 s by half the maximum u_b used in the tests. By using a similar magnitude analysis, advective acceleration and ice–water stress are found to be less than 10 N. Consequently, the slow model with weak ice–water interaction is realistic. Also friction effects at the channel edges are relatively small for these cases, but they would become significant at half of the present channel width (Hopkins and Tuhkuri, 1999).

The outcome of each experiment shows two phases. First comes the compaction phase, which lasts until the time $t^* = (A^* - A_0)L_0/u_b$; for $A^* = 1$ and $u_b = 50$ mm s^{-1} this is 120 s. The second phase is the piling up of the ice floes into a rubble field right up to the end of the experiment, when the rubble thickness is nearly ten times the floe thickness. The experiment outcome agrees with the mathematical model in that, for boundary-forced deformation, no pressure ridges form and the rubble thickens evenly. Figure 7.21 shows one experiment, the essential features of which are adequately repeated in the other experiments as well.

The basic statistics of experiments with uniform circular ice floes is shown in Table 7.2. In the compaction phase the force at the pushing plate and also the compactness increase almost linearly. The stress level is half of that at $A = 1$ when the compactness is within 0.8–0.9. This is different from common sea ice rheologies, where the strength increases quickly with compactness (see Figure 4.10). In the widely used strength formulation of Hibler (1979) $\sigma_c \propto \exp[-C(1 - A)]$, $C = 20$, which means one order of magnitude strength increase for an increase of 0.15 in

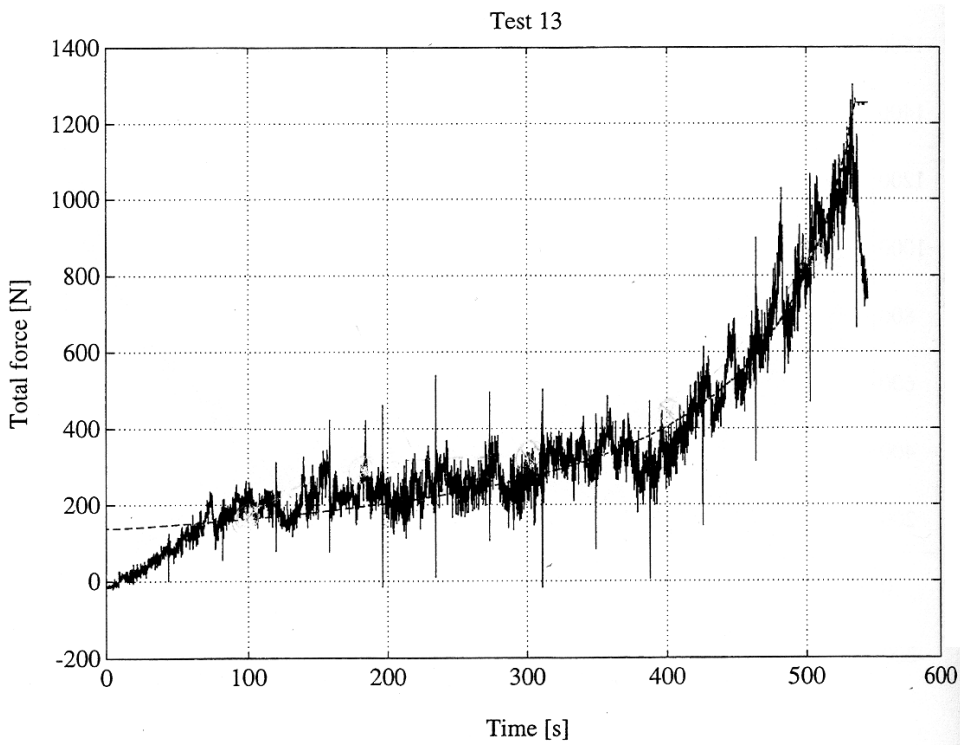

Figure 7.21 The force at the pusher plate in ice tank test #13 with pusher plate velocity $u_b = 33\,\mathrm{mm\,s^{-1}}$; the dashed line shows the fit of the analytical interpretation model.
Reproduced from Tuhkuri and Lensu (1997), with permission from Helsinki University of Technology.

Table 7.2 The measured force (in Newtons) at the pusher plate at $A = 1$ (F_1) and at $h_+ = 4h_i$ (F_4). The diameter of the circular ice floes was 400 mm and the pusher plate velocity was 15–52 mm s^{-1}.

	Ice thickness					
	28 mm		38 mm		54 mm	
Pusher plate speed	F_1	F_4	F_1	F_4	F_1	F_4
15 mm s^{-1}	80	300	150	450	230	1000
33 mm s^{-1}	50	170	140	330	280	830
52 mm s^{-1}	50	180	70	240	100	600
Mean	60	220	120	340	200	810

the compactness. In addition, the floe collision rheology of Shen *et al.* (1986) has a singularity at $A = A^*$ and therefore a very high sensitivity to compactness as the maximum packing density is approached.

In the rubble growth phase, the force at the pusher plate depends on the thickness of the rubble and the speed of the pusher plate. In the cases $h_i = 28\,\text{mm}$ and 54 mm, strength increases in proportion to the thickness of the accumulated rubble field, but for $h_i = 38\,\text{mm}$ the increase in strength is a little slower. But a remarkable feature is that a decrease in strength is seen when the speed of the pusher plate is increased. This was explained by Tuhkuri and Lensu (1997) as a decrease in the floe–floe friction coefficient.

Let us now assume a general power law for ice strength at $\zeta_n = \zeta_{n\kappa} h^\kappa$, where $\zeta_{n\kappa}$ is a constant. The strain rate is $\dot{\varepsilon} = u_b/L$, and thus Eq. (7.50) gives:

$$\zeta_{n\kappa} \frac{(L_0 h_i)^\kappa |u_b|^n}{(L_0 + u_b t)^{\kappa+n}} = -\frac{F}{b} \tag{7.53}$$

The form of the experimental curves is in very good agreement with this law when we take $\kappa + n = 1$ (see Figure 7.21).

In the plastic law $n = 0$ and therefore $\kappa = 1$. Averaging over the different pusher plate speeds for a representative plastic flow gives a yield function of compact ice in agreement with Hibler (1979), $\sigma_e = -P^* h$. The estimate for P^* becomes 0.35 kPa for $h_i = 28\,\text{mm}$, 0.45 kPa for $h_i = 38\,\text{mm}$, and 0.62 kPa for $h_i = 54\,\text{mm}$; the overall average is $P^* = 0.47 \pm 0.29\,\text{kPa}$. Including the pusher plate speed, the data suggest that $n \approx -\frac{1}{2}$ and therefore $\kappa = 3/2$. This tells of a strain-rate weakening property of the ice field. The strain is here pure compression, and the ice hardening effect due to thickness increase (power = 3/2) overcomes the weakening due to more rapid compression (power = −1/2). Therefore the result is a stable material behaviour.

The potential energy of the rubble is given as $\frac{1}{2} g[\rho(\rho_w - \rho)/\rho_w]h^2 \sim 10\,\text{Nm}$ (Rothrock, 1975). This is very small in comparison with the work done by the pusher plate. Consequently, the resistance of the ice field to the rubble formation is almost purely due to friction. According to Hopkins and Tuhkuri (1999), the failing of this ice field is due to floe underturning and rafting, and more pushing force is needed when the ice–ice friction coefficient increases or the aspect ratio of floes increases. With fixed floe diameter, the aspect ratio is proportional to ice thickness. Therefore, part of the 3/2 power of κ is due to the increase in aspect ratio.

Experiments with different kinds of floes were made at low speed (10–13 mm s^{-1}) and then compared with the lowest speed in the fixed floe cases. The results show good correspondence. Further inspection of the experiment results did not indicate any systematic changes in ice strength with the size and shape of the floes. However, the range of floe diameters and therefore aspect ratios was not large. Scaling of tank experiments to nature is partly open to question. Ice strength constant P^* in these experiments was in the order of magnitude of 0.3–0.6 kPa, while in nature it is 10–50 kPa.

The evolution of ice thickness distribution is unnatural in the confines of a tank since the system is forced from a boundary rather than by a distributed forcing as in nature. For constant forcing over the whole ice field, stress would peak at one

boundary where pressure ridge formation would begin. Nevertheless, the tank results show the feasibility of ice tank experiments for the progress of knowledge in sea ice dynamics and for parameterization of sea ice dynamics models. The design of further experiments should be based on setting hypotheses and questions from sea ice dynamics science.

In these tank tests real floating ice blocks were used, although the ice is not the same as in nature. In ice tank technology, solid ice is softened by using dissolved substances in the water, which freezes for the tank ice (see Tuhkuri and Lensu, 1997). One line of research could be physical analogue experiments (Philippe Blondel, personal communication). For example, layers of sand, mixed with honey and engine oil, are used as scaled-down versions of tectonic plates (e.g., to model the collision of India with the Eurasian continent and creation of the Himalayas).

7.6 TIME–SPACE SCALING OF ICE DRIFT

7.6.1 Frequency spectrum of sea ice drift

The free drift velocity spectra were analyzed in Section 6.4 using a coupled ice–ocean model. For a general forcing $F/(\rho h)$, of spectrum $p_F = p_F(\omega)$, the resulting spectrum of sea ice velocity was obtained as (Eq. 6.42):

$$p_i(\omega) = \frac{(\lambda_i^2 + f^2 + \omega^2)}{[(\lambda_i + \lambda_w)^2 + (\omega + f)^2](\omega + f)^2}\, p_F(\omega)$$

In the free drift model, forcing included the wind stress and the sea surface slope (or geostrophic current). Let us try to examine spectral characteristics arising from the internal friction F_I by formally replacing F by $F + F_\mathrm{I}$.

In the one-dimensional case, a general viscous model gives $\sigma \propto |\partial u/\partial x|^m$. Since $F_\mathrm{I} = \partial\sigma/\partial x \sim U^m L^{m-1}$, for a spectral velocity component $u = \hat{u}(x.\, y)\exp(-\mathrm{i}\omega t)$, we get:

$$F_\mathrm{I} \propto \left|\frac{\partial \hat{u}}{\partial x}\right|^{m-1} \frac{\partial^2 \hat{u}}{\partial x^2}\, \mathrm{e}^{-im\omega t} \tag{7.54}$$

Acceleration gives rise to a velocity component of frequency $m\omega$. In the linear case ($m = 1$) there is no frequency change, in the sublinear ($m < 1$) case there is frequency transfer toward lower frequencies, and in the superlinear case ($m > 1$) the transfer is toward higher frequencies (as is well known in turbulent flows).

For internal friction of drift ice, floe collision models (see Section 4.4) are superlinear and then kinetic energy is transferred toward higher frequencies. However, collisional stresses are small and the frequency transfer has not much significance. When large stresses are found, the ice rheology is sublinear, which would transfer energy toward lower frequencies. But these sublinear drift ice rheologies have a distinct asymmetry: during closing the stress may be very high but during opening it

is nearly zero. By coupling the ice conservation and momentum equations a new dominant feature is introduced: opening and closing frequencies are passed on to the ice velocity spectrum. Then, whatever the value of m, ice velocity is forced into the deformation frequency.

Deeper investigation of the spectral response in the presence of internal friction needs a numerical model. A three-level viscous-plastic model tuned for the Baltic Sea was used by Leppäranta *et al.* (2009). This model employs the Hibler (1979) viscous-plastic rheology and ice state consisting of compactness, thickness of undeformed ice and thickness of deformed ice. A series of numerical experiments was performed in the presence of internal friction of ice. Figure 7.22 shows for one case the wind forcing spectrum and the resulting ice speed spectrum. The wind forcing peaks at the frequency of 2/3 cycles per day (i.e., period is 1.5 days), and the peak shows up in the ice at the same frequency. Inertial peak also appears in the ice motion. The result is similar to the observations in the Arctic Ocean by Heil and Hibler (2002), where it was interpreted by inertial imbedding. However, the relatively low amplitude in the present ice speed spectrum suggests that high frequency energy could be due to numerical noise as well. The phase lag of ice velocity with respect to the wind forcing varies with the frequency of wind. It is about two hours in this case (Figure 7.23).

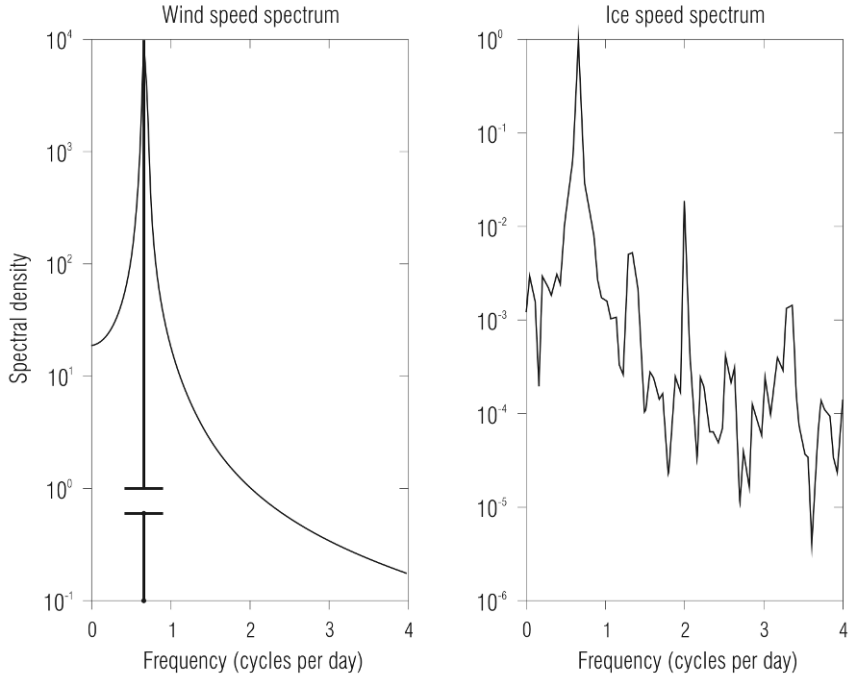

Figure 7.22 Wind speed spectrum and the resulting ice speed spectrum in numerical viscous-plastic model simulations. Wind case was a delta peak resulting as a sharp form in estimation from finite time series.
From Leppäranta *et al.* (2009).

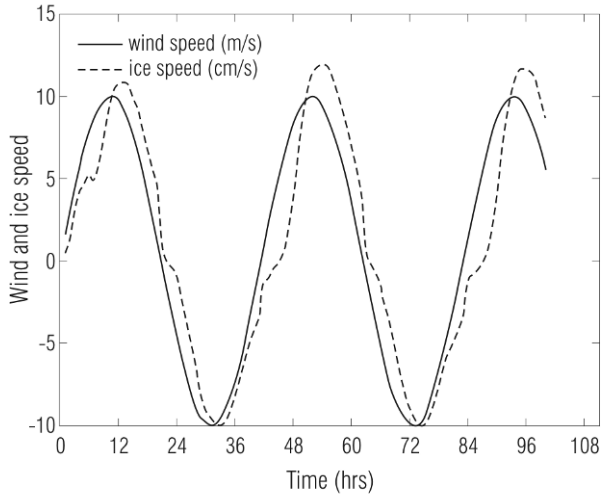

Figure 7.23 A section of wind velocity and ice velocity in numerical viscous-plastic model simulations.
From Leppäranta *et al.* (2009).

Thus the results from numerical modelling in a semi-enclosed or closed basin indeed show that, in cyclic external forcing, frequency is passed on to deformation and then further to ice velocity (Leppäranta *et al.*, 2009). If the stress was taken symmetric for small disturbances, straight sublinear behaviour could appear in compact drift ice leading to frequency transfer toward lower frequencies. However, so far no observational evidence has been found of such frequency transfer.

In all, the momentum equation of drift ice has three nonlinear terms: advection, ice–water stress, and internal ice stress. Advection is practically always small. Ice–water stress is a dominant force and source for damping and phase shift ice drift but does not influence the frequency. Internal ice stress also influences amplitude and phase but its main part does not cause frequency transfer due to the asymmetry of the stress for opening and closing.

7.6.2 Spatial structures

The Bay of Bothnia in the Baltic Sea has been widely investigated for sea ice physics. The size of the basin is about 300 km × 120 km, with a narrow open water boundary in the south (Figure 7.24). In March 1997 an experiment ZIP-97 (Zooming of Ice Physics, 1997) was performed there, based in the island of Hailuoto in the north (Haapala and Leppäranta, 1997b). The scale of the basin is close to the dynamical length scale of drift ice dynamics, and therefore the coastal boundary layers cover the whole basin.

The characteristics of ice motion are strongly influenced by the presence of the boundary. The plasticity of drift ice shows up clearly in that ice moves or is

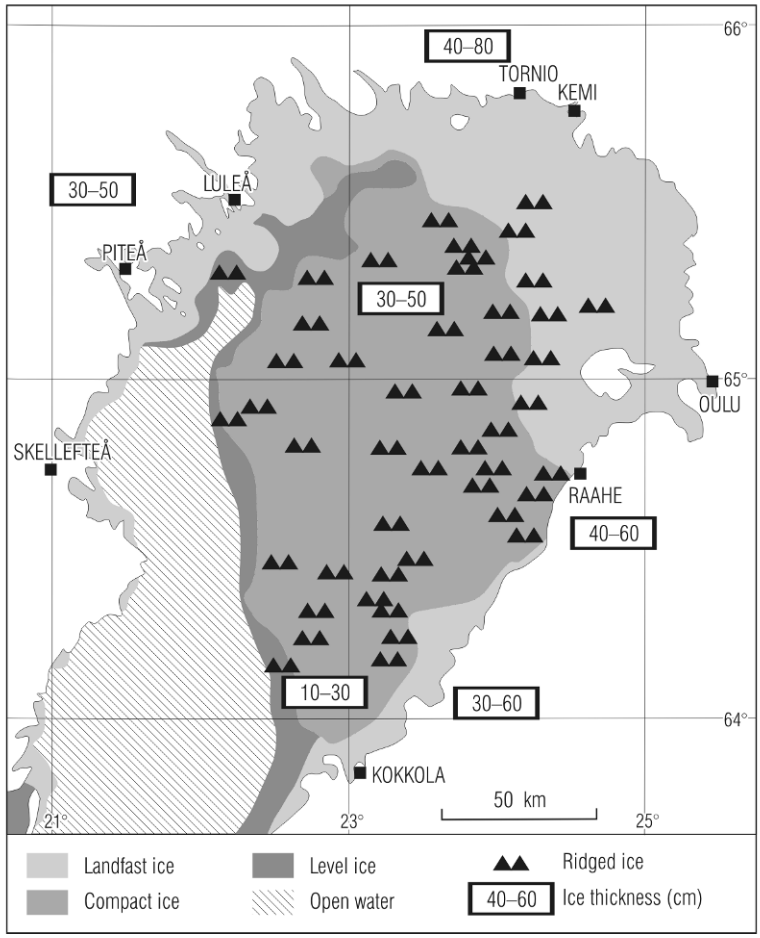

Figure 7.24 Ice situation in the Bay of Bothnia on March 10, 1997.
From Leppäranta and Haapala (1997).

stationary, depending on the forcing. Coastal alignment is strong, which is seen in asymmetry in deformation parallel and perpendicular to the coastline (Figure 7.25). Ice motion history showed two relaxation time scales: local inertial time scale of $\sim$1 h and basin-wide time scale of the order of one day when the ice cover adjusts to the external forcing (Goldstein *et al.*, 2001, 2009).

Coupling the ice conservation and momentum equations may also produce "sound" waves as a result of the connection between ice strength and thickness, similarly to sound waves in compressible fluid flow. The speed of sound waves is $c^2 = \partial p/\partial\rho$ (e.g., Li and Lam, 1964). For sea ice dynamics it would read $c^2 = \rho^{-1}\partial P/\partial h$. For $P = P^*h$, $c \sim 1$–$10\,\mathrm{m\,s^{-1}}$. Such velocities have been occasionally observed in sea ice fields for progressing signals (e.g., Doronin and Kheysin, 1975;

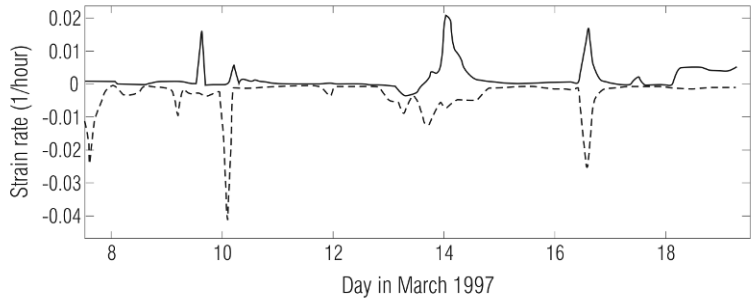

Figure 7.25 Deformation of drift ice in the coastal boundary zone; principal strain rates are shown for a 10-km square.
From Leppäranta *et al.* (2001).

Goldstein *et al.*, 2001). For example, wind-forced momentum may travel faster in ice than the speed at which the wind field moves. As a consequence, ice motion may commence prior to the arrival of the wind.

7.6.3 Downscaling

In a drifting sea ice field local ice forces due to the internal ice stress can be very large and a historical case was the destruction of Tainio lighthouse in the Gulf of Finland in 1967 (unpublished report by Erkki Palosuo, Finnish Institute of Marine Research). During the night between February 6 and 7, 1967, the lighthouse was pushed 14 m east by wind-driven ice. The wind speed was 13 m s^{-1}, fetch was some 200 km, ice thickness was 30–50 cm, and the width of the lighthouse was 3.5 m at the water surface level. It was estimated that the loading force was 4.7 MN, assuming that the ice–lighthouse friction coefficient was equal to 0.6. The thickness of rubble became 3.5 m on the wind side and 1 m on the lee side of the lighthouse. A few similar events have occurred in the Baltic Sea, where outer lighthouses must be constructed in drift ice areas.

A major motivation in scaling research is to find connections between the ice stress in mesoscale drift ice dynamics models or "geophysical stress" (scale 1–10 km) and local forces at lighthouses and ships or "engineering stress" (scale 10–100 m). This would make it possible to produce short-term forecasts for ice forces on marine constructions. As discussed in Chapter 4, the general level of geophysical stress is 1–2 orders of magnitude lower than the level of engineering stress (see Figure 4.15).

There have been several experiments on the *in situ* engineering stress but, however, much of the material is unpublished. Construction of Confederation Bridge from the continent to Prince Edward's Island in Gulf of St Lawrence, Canada was a major engineering problem due to the presence of drift ice in the Northumberland Strait (Figure 7.26). Frederking *et al.* (2006) examined a ice loading case on April 4, 2003. A large piece of landfast ice (5 km × 10 km, thickness 1 m with many ridges) broke free, failing against the bridge piers. It was spring and ice was soft resulting in the maximum force determined on the two piers only in the order of 2 MN.

Figure 7.26 *Confederation Bridge* across Northumberland Strait in the Gulf of St Lawrence. The bridge is 13 km long connecting Prince Edward Island and New Brunswick in Canada. Photograph by Dr. Simon Prinsenberg (http://www.mar.dfo-mpo.gc.ca/science/ocean/seaice/public.html), printed with permission.

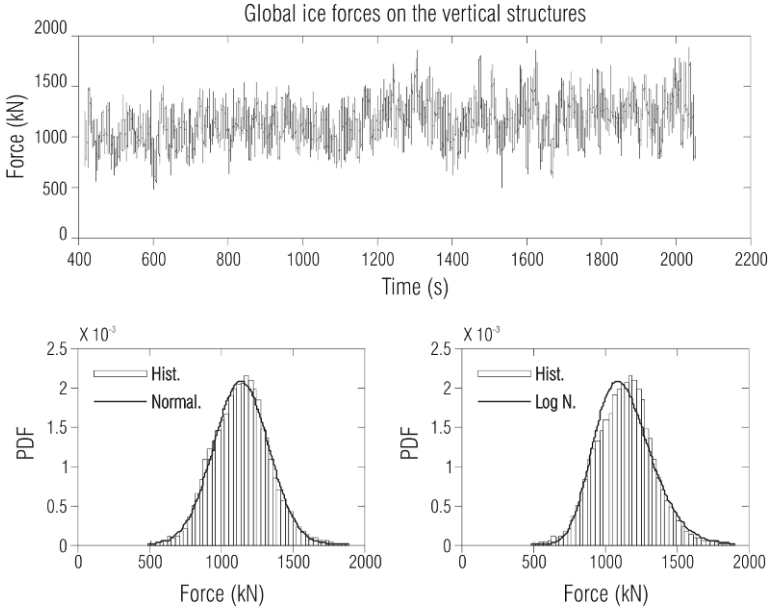

Figure 7.27 Ice forcing at lighthouse Nordstömsgrund, Baltic Sea. The width of the lighthouse is 8.0 m.
Redrawn from Kärnä and Qu (2005).

Ice forces on fixed marine constructions have been measured in the Baltic Sea (Løset *et al.*, 2003; Kärnä and Qu, 2005) and Bohai Sea (Yue *et al.* 1996). Figure 7.27 shows a 35-minute time series of ice forcing at a lighthouse in the northern Baltic Sea. The measurements were made using force panels. The global force is defined as $F_G = p_G wh$, where p_G is global pressure, w is structure width, and h is ice thickness (Kärnä *et al.*, 2006). The level of global force was 1.0–1.5 MN, and the distribution of forces is quite close to Gaussian distribution. Ice force varied randomly with time in each event, and continuous ice crushing was a wide band random process (Kärnä and Qu, 2005). The largest energy of the force variation occurred in the frequency range of around 0.1 Hz. Maximum pressures are sometimes expressed by using some characteristic values that are defined using the parent distribution of a single event (Kärnä and Qu, 2005). This method can be expressed as

$$p^{\max} = \mu_p + k\sigma_p$$

where μ_p and σ_p are the mean level and the standard deviation of the measured pressure. The parameter k is conventionally taken as $k = 2$ to obtain the 98% cumulative distribution function value. The data analysis showed that the measured peak values of the panel pressures correspond to a k-value value of $k \approx 4.0$.

The advantage of analytical modelling is its ability to provide a full picture of the physical problem. Because of necessary simplifications, the outcome is not quantitatively exact, but the main qualitative characteristics and their physical background become understandable. In addition, analytical solutions serve as excellent validation cases for the numerical model technology. Having learned the analytical methods, the next step is to go into the world of numerical models.

8

Numerical modelling

8.1 NUMERICAL SOLUTIONS

This chapter contains methods and solutions in numerical modelling of sea ice drift. The idea is to introduce the numerical technology used in sea ice modelling in Sections 8.1–8.2 and present standard-type cases of model applications for short-term ice forecasting in Sections 8.3–8.4 and climate investigations in Section 8.5. The reader with an understanding of the fundamental laws of sea ice dynamics, together with the free drift solution and analytical 1- and 1.5-dimensional models for ice flow in the presence of internal friction, will be able to interpret properties and outcomes of numerical models. From the perspective of our present knowledge, continuum numerical models provide the best quantitative solution to ice drift, up to the highest spatial resolution the floe size allows.

Numerical modelling of sea ice dynamics began in the 1960s in the Soviet Union and in the USA (Campbell, 1965; Doronin, 1970). The first models were linear and matched the computational technology of the time. During the 1970s the modern theory of sea ice dynamics was developed, and at the end of the decade continuum sea ice models were close to what they are now, at least in terms of the description of physical processes. Thereafter, coupled ice–ocean models have been developed, and spatial resolution has been continuously improving as well. The main applications of these models have been short-term ice forecasting for shipping and oil drilling and transportation, recently also for weather forecasting, and for long-term simulations in climate research.

8.1.1 System of equations

In a way, the classical Nansen–Ekman drift law is already a simple model. But numerical models are normally understood as *full models* (i.e., closed system models), which can solve the sea ice circulation problem for the whole basin under

M. Leppäranta, *The Drift of Sea Ice*, Springer Praxis Books,
DOI 10.1007/978-3-642-04683-4_8, © Springer-Verlag Berlin Heidelberg 2011

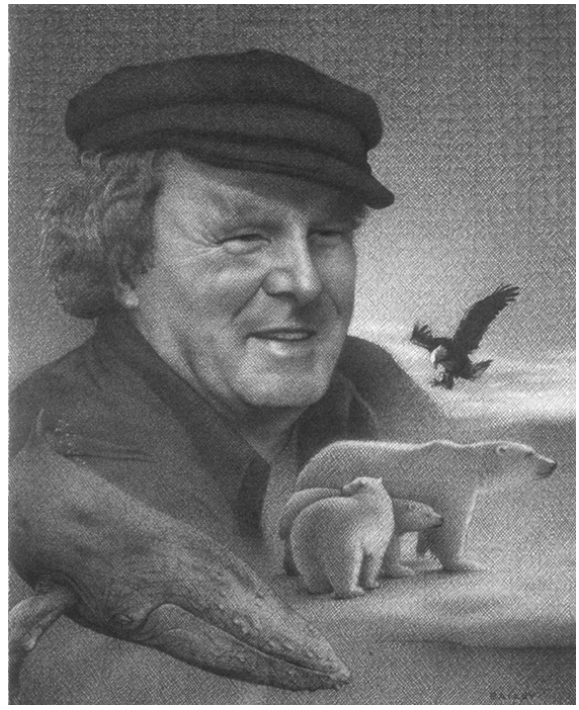

William J. Campbell (1930–1992) was a pioneer in numerical modelling of sea ice dynamics. His PhD thesis at the University of Washington (Campbell, 1965) showed the first Arctic Ocean numerical sea ice drift model. He then worked with the US Geological Survey, focusing his research in the 1970s on remote sensing of sea ice.
Courtesy of Puget Sound Magazine, Puget Sound, WA.

consideration. The modeller chooses the ice state and rheology, and the conservation laws for the ice state and momentum close the system. A full drift ice model thus consists of four basic elements:

Sea ice state $$J = \{J_1, J_2, J_3, \ldots\} \tag{8.1a}$$

Sea ice rheology $$\boldsymbol{\sigma} = \sigma(J, \boldsymbol{\varepsilon}, \dot{\boldsymbol{\varepsilon}}) \tag{8.1b}$$

Conservation of momentum $$\rho h \frac{D\boldsymbol{u}}{Dt} = \nabla \cdot \boldsymbol{\sigma} + \boldsymbol{F}_{ext} \tag{8.1c}$$

Conservation of ice $$\frac{DJ}{Dt} = \psi + \phi \tag{8.1d}$$

Elements (8.1a) and (8.1b) constitute the heart of a sea ice model and are reflected in the model attributes: one speaks of a three-level ($\dim(J) = 3$) viscous plastic sea ice model, multi-level ($\dim(J) \gg 2$) elastic-plastic model, etc. Thus a modeller has to make three key choices:

1 The choice of ice state (i.e., how many different thickness or other morphological categories of the ice pack are needed).
2 With a given ice-state definition, the ice conservation law must be split into as many equations as there are ice-state variables and a choice needs to be made on how the ice state is redistributed in mechanical deformation.
3 The choice of the rheology depends on what features need to be solved by the model. A realistic rheology is necessary for closure of the model (e.g., the free drift approach could give reasonable velocities in a central basin, but would produce seriously biased ice conditions at the coast).

When ice state, its redistribution function, and ice rheology have been chosen, the conservation laws for ice and momentum obtain their specific forms and can be solved for evolution of ice conditions.

The full sea ice dynamics problem includes three unknowns: ice state, ice velocity, and ice stress. The number of independent variables is $N = j + 2 + 3$, where $j = \dim(J)$ is the number of levels in the ice state. Any proper ice state has at least two levels, $j \geq 2$ and thus $N \geq 7$. In principle, instead of ice state a modeller could take a family of distributions and then j would represent the number of independent parameters of this family. Such efforts have not been made, however.

The first numerical methodology choice would be between *discrete particle models* and *continuum models*. In mesoscale and large-scale sea ice dynamics all workable models are still in the continuum world, while discrete particle models have been used in local scale process model (see Hopkins, 1994). The present chapter therefore focuses on the continuum models. An effort to construct a compromise model between continuum and discrete particle models was made by Rheem *et al.* (1997), for the purpose of trying to solve ice drift and ice forcing on structures with the same model.

The inertial timescale of 1 m thick ice is of the order of 1 hour, much less than the advective timescale, and therefore a quasi-steady-state approach for the momentum equation is feasible in the seasonal sea ice zone. In the Central Arctic basin, and consequently in full Arctic Ocean sea ice models, the inertial term should be included.

The model parameters can be grouped into four categories:

(i) Drag parameters of the atmospheric and oceanic boundary layers.
(ii) Sea ice rheology parameters.
(iii) Ice-state redistribution parameters.
(iv) Numerical design parameters.

The primary *geophysical parameters* of sea ice dynamics models are the air and water drag coefficients and the compressive strength of ice. Drag coefficients together with Ekman angles tune the free drift velocity of thin ice or for strong winds, while compressive strength tunes the length scale of the ice flow in the presence of internal friction. Secondary geophysical parameters come from the chosen sea ice rheology – what more is required than compressive strength – and from the ice-state

redistribution scheme. Ice-state redistribution is a very important process in drift ice dynamics, but its proper formulation suffers from lack of good data. One parameter needed in low-level ice states is the demarcation thickness h_0: "mechanically active ice" is defined as ice with thickness equal to or thicker than h_0 (see Eq. 2.48), while ice thinner than h_0 experiences only thermal changes (otherwise the term "mean thickness" would not represent the mechanical strength of ice well).

A numerical model includes *numerical design parameters*, which include artificial practical formulations due to limitations of numerical approximation and methodological parameters to fix the resolution and to keep the numerical solution stable. The first task is to choose the grid and its size. The system to be solved is highly nonlinear and the stability of the solution may require smoothing techniques in order to keep the solution stable. In a way, the demarcation thickness is a numerical design parameter, as it is required due to limited resolution of the ice thickness.

Sea ice dynamics–thermodynamics models also have heat budgets, which lead to ice growth and melting and temperature changes. Sea ice temperature does not explicitly show in ice properties in sea ice dynamics models, but ice thickness changes influence the volume and strength of the ice. The thermodynamics can be solved from full heat budget or a prescribed growth function $f = f(t, h)$ for each grid cell. Although sea ice has salt inclusions, the salinity level is much less than in ocean water. Only very recently, sea ice models with salt budgets have been developed (Vancoppenolle *et al.*, 2009). Earlier it was always assumed that in freezing all salts are rejected into seawater and the meltwater is fresh.

There is a numerical modelling line, which is based on the free drift theory but also includes the ice conservation law. These models have singularities, the influence of which is made smaller by using properly smoothed forcing fields. A model based on free drift with semi-empirical corrections on the coast was presented by Nikiforov *et al.* (1967), and the incompressible inviscid solution was presented by Rothrock (1975c). However, because of the high level of the internal friction of sea ice and because it is not possible to properly close the ice motion without internal friction, these non-friction models are not further discussed in this chapter.

8.1.2 Numerical technology

In the continuum approach, there are different steps along which to proceed. The first step is the choice between the finite element and finite difference approaches. The latter has by far been the dominant technique in sea ice dynamics, and only that will be used below. Finite element models could be preferable in small time- and space-scales, when the geometry of boundaries has a pronounced influence on dynamics.

Eulerian/Lagrangian frames

The next step is between *Eulerian* and *Lagrangian* frames (i.e., respectively, whether the numerical grid is fixed in space or medium). The former has been most frequently

used in sea ice dynamics models. But the ice drift problem has the peculiarity of moving boundaries that are difficult to take care of in a Eulerian system. In common numerical techniques it is assumed that the medium (and ice state) is evenly spread within each grid cell, and this leads to strong numerical diffusion at open boundaries, when the usual first- or second-order approximations are used for spatial derivatives. In particular, a diffuse ice edge results, which may cause serious mistakes when the location of the boundary is important.

Consequently, more advanced methods have been used for the ice conservation law. The solution to the ice edge is significantly improved if the location of the ice edge is kept as a variable in the model. It is then advected by the velocity field and boundary conditions are precisely taken care by this real ice edge. Ovsienko (1976) employed a Eulerian–Lagrangian technology. He solved the momentum equation in a Eulerian[1] grid and the ice conservation law in a Lagrangian grid using the *particle-in-cell* method (Harlow, 1964). The ice field is represented by a large number of particles with given thickness and size. For each Eulerian grid cell they are summed for compactness and mean thickness, and then the momentum equation can be solved. Interpolating an individual velocity for each particle, these can be advected in space for a new configuration and state distribution of the ice field. Then the new ice state is obtained for the Eulerian grid by summing from the advected configuration. The particles are virtual; with their large number they may represent a sea ice continuum, but they do not interact mechanically as is the case with discrete particle models. A similar approach was taken by Flato (1993) for a short-term model in the Beaufort Sea and Shen *et al.* (1993) for an ice dynamics model in the Niagara River.

Grid

The suitability of the continuum approach for drift ice was discussed in Section 2.2, and the length scale hierarchy was set as $d \ll D \ll \Lambda$, where d is the floe size, D is the continuum particle size, and Λ is the gradient scale. The grid size of numerical models fits in as:

$$d \ll D \sim \Delta x \ll \Lambda \tag{8.2}$$

Below D, continuum physics are no more valid, so choosing $\Delta x \ll D$ would introduce artefacts. This problem has not been well examined in drift ice modelling; but it is now of major concern since the grid size in ocean models has become much smaller than D (in other words, we need to find way of constructing high-resolution, coupled ice–ocean models). On the other hand, $\Delta x > D$ is allowed but since D is relatively large there is normally enough computational power to work with $\Delta x \sim D$. There is not much freedom to choose a proper grid size, and in practice this has been 10–100 km. In ocean dynamics, on the other hand, the choice of Δx is mainly determined from the computational power available and from the resolution required for the model outcome – and the problem is to develop a solution in these conditions (e.g., Kowalik and Murty, 1993).

[1] A Eulerian grid is fixed in space, while a Lagrangian grid is fixed in the medium.

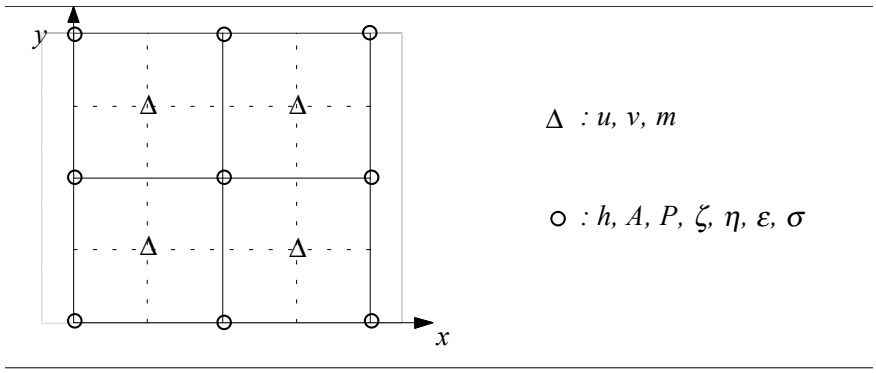

Figure 8.1 Spatial grid (Arakawa B type) normally employed in the numerical modelling of sea ice dynamics.

In each grid cell, ice-state variables are taken as averages, as by definition are the spatial occurrences of the classes of ice thickness distribution. If spatial distribution is strongly non-uniform in a grid cell, additional effects could arise that are not included in the thickness distribution theory: cracks and leads may have a preferred orientation; how a given percentage of open water is distributed in a grid cell could make a difference; different ice types may occur in patches; etc.

In principle, a grid can have any geometry but, in practice, most sea ice models by far use a regular rectangular grid, the use of which makes the construction of numerical algorithms straightforward. In the very first models all quantities were calculated in the same grid points, but since then staggered grids have been employed (Figure 8.1). Triangular grids would be more flexible and could follow the solid and open boundaries of sea ice fields better.

The time steps are determined by the stability criterion set by the required resolution and method of numerical time integration. In practice, time steps have been from half an hour to 1 day. From the physics point of view, since the timescale of ice inertia is $T_1 = \rho h/(\rho_w C_w U)$ (see Section 5.4), approximately $10^3\,\mathrm{s}\,h\,\mathrm{m}^{-1}$, a safe time step would be $10^2\,\mathrm{s}\,h\,\mathrm{m}^{-1}$ to resolve acceleration and deceleration events. However, in most cases this high temporal resolution is not needed. The highest frequency of interest is the Coriolis frequency, where ice drift follows inertial oscillations together with the mixed layer of the ocean. In high polar regions the Coriolis period is about 12 hours; this takes the necessary time step down to 1–2 hours. At such time steps the inertia of thick multi-year ice may be significant, and the inertial term consequently needs to be included in the model; whereas in the seasonal sea ice zone the quasi-steady-state approach works well.

Initial and boundary conditions

Initial ice-state conditions are needed in purely dynamic cases. However, because the inertial timescale of sea ice is small, in non-steady-state models initial ice velocity

can be taken as zero. In quasi-steady-state models the steady-state solution of the momentum equation for the given initial ice state and forcing serves as the initial field.

For boundary conditions there are two approaches. First, the more physical approach is to define the ice region by $\Omega = \Omega(t)$ and its boundary curve by $\Gamma = \Gamma(t)$ (e.g., Ovsienko, 1976). Along Γ, we have:

Free boundary: $$\boldsymbol{\sigma} \cdot \mathbf{n} = 0 \tag{8.3a}$$

Solid boundary: $$\boldsymbol{u} \cdot \mathbf{n} \leq 0; \text{ if } \boldsymbol{u} \cdot \mathbf{n} < 0 \text{ then } \boldsymbol{\sigma} \cdot \mathbf{n} = 0 \tag{8.3b}$$

Boundary curve: $$\frac{d\Gamma}{dt} = \boldsymbol{u} \cdot \mathbf{n} \tag{8.3c}$$

Thus, at free boundary – ice edge – the normal stress is zero. At solid boundary, the ice cannot cross the boundary but may move away from it towards the central basin and then the boundary becomes free. The movement of ice changes continuously the boundary configuration (Eq. 8.3c).

The second approach, which is more practical, is to define open water as ice with zero thickness and then this "generalized" ice fills the whole basin avoiding the existence of the free boundary. At a solid boundary the no-slip condition $\boldsymbol{u} = 0$, normal for viscous fluids, is employed.

Open boundaries, where ice may flow in or out from the model basin, are kept small or far from the ice pack. Transmission of ice stress across an open boundary would cause difficulties. Therefore open boundaries with ice exchange are preferably narrow straits where the stress transmission is unlikely.

Numerical integration

The numerical solution progresses by solving the momentum equation and the ice conservation law in turn. First, with a fixed ice state, the momentum equation is solved. Because of the high ice strength and inclusion of inertia, direct, explicit (Euler) time marching would require a very short time step. Therefore, more advanced methods are used. In the quasi-steady-state approach this problem is avoided.

But, in any case, because the momentum equation is nonlinear, a series of iterations is normally needed. With a given ice velocity, the equation of motion is linearized and a new, corrected velocity field is obtained by a matrix algorithm, such as the over-relaxation method (Ames, 1977). Then the corrected velocity is inserted for a new linearized equation and the matrix algorithm is used again. The whole cycle is repeated until the desired accuracy is obtained.

When ice velocity has been solved, the ice conservation law is integrated for temporal change in ice state. Different kinds of techniques have been employed in this integration. Doronin (1970) took upstream spatial derivatives (i.e., one-sided derivatives based on the direction from which ice was entering the grid cell). Hibler (1979) integrated the ice conservation law explicitly with centred spatial derivatives

resulting in a second-order differencing scheme. Ovsienko (1976) used the particle-in-cell method (i.e., a Lagrangian scheme), which efficiently tracks the location of the ice edge and the internal boundaries of the ice field.

With explicit time stepping of the ice conservation law, the principal stability condition for the whole system comes from the Courant–Friedrichs–Lewy criterion:

$$\frac{\Delta x}{\Delta t} \geq \sqrt{2}\,|\boldsymbol{u}| \tag{8.4}$$

This puts the time step below 1 day for a 100-km grid or below 3 hours for a 10-km grid.

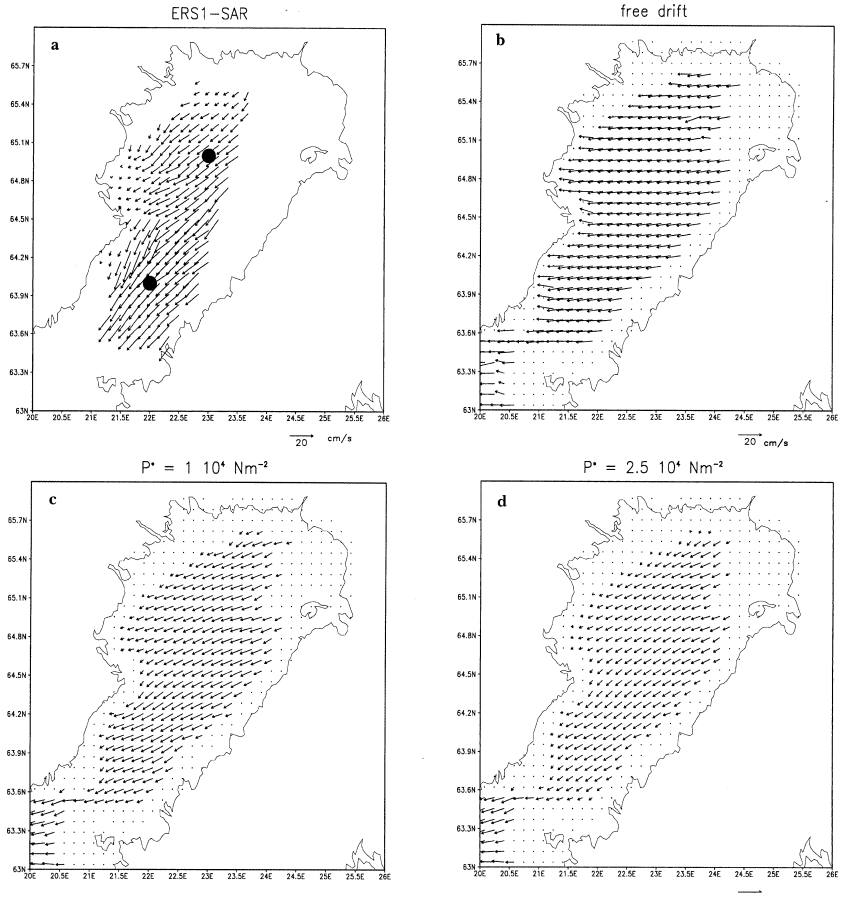

Figure 8.2 Calibration runs for ice strength against ice velocity fields obtained from ERS-1 SAR data in the Bay of Bothnia, Baltic Sea. The ice is thin (10–50 cm) and has low strength. The black dots here have no relevance.
From Leppäranta *et al.* (1998).

8.1.3 Calibration/validation

The calibration and validation of sea ice models has been made based on ice concentration, ice thickness, and ice velocity. The best validation data exist for concentration, since it can be easily detected by satellite remote sensing. Velocity data are also available from drifter station time series and from sequential satellite mapping (Figure 8.2). The thickness of ice is the main problem; suitable information contains only statistical mean fields. An essential improvement would be to run sea ice models against high-resolution changes of ice thickness fields, since they integrate the mechanical growth of ice thickness and could tell us how the ice state is redistributed in mechanical deformation.

Satellite remote sensing provides excellent velocity fields, which could serve the redistribution problem directly. By using observed velocities directly, ice-state integration would progress without systematic errors in velocity. However, validation would still require thickness data.

8.2 EXAMPLES OF SEA ICE DYNAMICS MODELS

8.2.1 Campbell and Doronin models

The first models in the 1960s were linear viscous. Campbell (1965) presented a steady-state circulation model of ice and water for the whole Arctic Basin, while Doronin (1970) presented a prognostic short-term sea ice dynamics model for the Kara Sea. Campbell (1965) was able to reproduce the Transpolar Drift Stream and the Beaufort Sea Gyre (Figure 8.3). The result was significantly different from earlier free drift approaches. There was too much convergence in the Beaufort Sea Gyre, as noted by Campbell himself (a problem that arises from using a linear viscous rheology). Air–ice and ice–water stresses were determined from Prandtl-type boundary-layer models. The viscosity of sea ice was formulated as $\eta = \rho h K_i$, where K_i is the eddy viscosity coefficient of ice floes; the best fit resulted in $K_i = 3 \times 10^8\,\mathrm{m^2\,s^{-1}}$, corresponding to dynamic viscosity of about $1 \times 10^{12}\,\mathrm{kg\,s^{-1}}$ for 3 m thick multi-year ice in the Central Arctic Ocean. A total of 260 grid points covered the Central Arctic Ocean, corresponding to a grid size of about 150 km. The conjugate gradient method was used to iterate for the solution of two ice velocity components and the stream function of water flow.

The Doronin (1970) model was a two-level, linear viscous quasi-steady model:

$$J = \{h, A\} \tag{8.5a}$$

$$\boldsymbol{\sigma} = 2\eta\dot{\boldsymbol{\varepsilon}}, \quad \eta \propto A \tag{8.5b}$$

$$f\mathbf{k} \times \boldsymbol{u} = \nabla \cdot \boldsymbol{\sigma} + \boldsymbol{\tau}_a + \boldsymbol{\tau}_w - \rho h g \beta \tag{8.5c}$$

$$\frac{Dh}{Dt} = \Phi(h), \quad \frac{DA}{Dt} = -A\nabla \cdot \boldsymbol{u} + \Phi_A(A) \tag{8.6d}$$

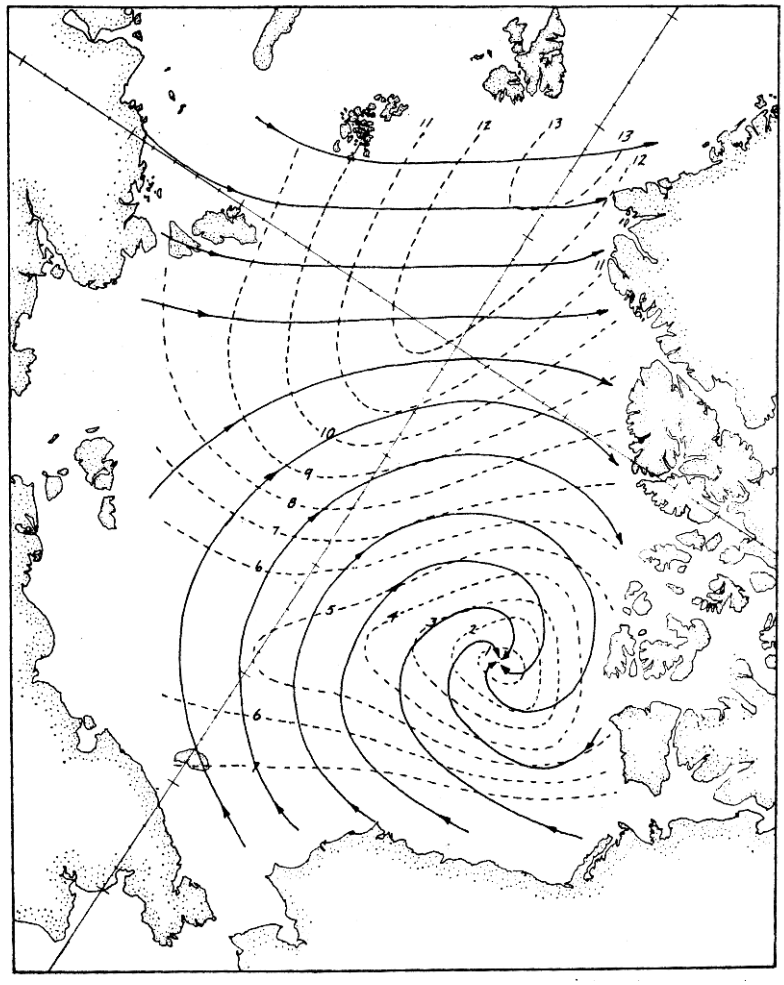

Figure 8.3 Steady-state ice circulation in the Arctic Basin according to the linear viscous model of Campbell (1965). Solid lines show ice drift streamlines, and dashed lines show ice drift speed isolines (in cm/s).
Reproduced with permission from the American Geophysical Union.

Atmospheric and oceanic drag forces were taken linear, like the solutions from Ekman velocity profiles. Boundary-layer parameters could be fixed so that the solutions agreed with usual free drift conditions when internal friction became small. The best-fit linear viscosity of sea ice was obtained as $3 \times 10^8\,\mathrm{kg\,s^{-1}}$ for $A = 1$. The viscosity is relatively low, partly because the simulations were made for summer ice conditions but mainly because the Kara Sea lies throughout in the drift ice coastal boundary layer where much smaller viscosity is needed than in a large-scale central pack (see Section 4.2.1).

The numerical solution of ice velocity and compactness was obtained simultaneously by the over-relaxation technique. Then the thickness of ice was determined by thermal changes plus advection (advection for a given grid point was taken by the upstream spatial derivative). The grid size was 100 km and the time step was 1 day. The model was applied for summer conditions in the Kara Sea, the ice state changing due to melting, advection, and dynamic opening and closing. This model structure introduced the first full sea ice model as a closed system.

8.2.2 AIDJEX model

The AIDJEX model is the product of the extensive AIDJEX programme performed in the 1970s (Coon, 1980). The new features introduced by the AIDJEX group were an elastic–plastic rheology (Coon *et al.*, 1974) and the concept of thickness distribution (Thorndike *et al.*, 1975). The system of equations reads:

$$J = \Pi \tag{8.6a}$$

$$\left.\begin{aligned} &F(\sigma_{\mathrm{I}}, \sigma_{\mathrm{II}}, P^*) \le 0, \quad P^* = c_p(1+\Gamma)\int_0^\infty h^2 \psi' \, dh \\ &F < 0 : \boldsymbol{\sigma} = (M_1 - M_2)(\operatorname{tr}\boldsymbol{\varepsilon})\mathbf{I} + 2M_2\boldsymbol{\varepsilon}', \quad \dot{\boldsymbol{\varepsilon}} - \dot{\boldsymbol{\Omega}}\cdot\boldsymbol{\varepsilon} + \boldsymbol{\varepsilon}\cdot\dot{\boldsymbol{\Omega}} = \dot{\boldsymbol{\varepsilon}} - \dot{\boldsymbol{\varepsilon}}_p \\ &F = 0 : \dot{\boldsymbol{\varepsilon}}_p = \lambda \frac{\partial F}{\partial t} \end{aligned}\right\} \tag{8.6b}$$

$$\rho h\left(\frac{D\boldsymbol{u}}{Dt} + f\boldsymbol{k}\times\boldsymbol{u}\right) = \nabla\cdot\boldsymbol{\sigma} + \boldsymbol{\tau}_a + \boldsymbol{\tau}_w - \rho h g \boldsymbol{\beta} \tag{8.6c}$$

$$\frac{D\Pi}{Dt} + \Phi(h)\frac{\partial \Pi}{\partial h} = \Phi - \Pi\nabla\cdot\boldsymbol{u} \tag{8.6d}$$

Ice state is defined as ice thickness distribution. The yield function F has the shape of a teardrop. Its size is defined by strength P^*, which depends on the ridging function ψ', buoyancy parameter $c_p = \frac{1}{2}g\rho(\rho_w - \rho)/\rho_w$ and the parameter Γ equal to the ratio of frictional losses to the production of potential energy in ridging (see Section 4.3.3). Inside the yield curve, rheology gives elastic behaviour, while on the yield curve plastic deformation $\dot{\varepsilon}_p$ takes place according to the associated flow rule. The magnitude of mesoscale elastic constants is 10–100 MN m^{-1}, $M_1 \approx 2M_2$ (Pritchard, 1980b). The elastic part necessitates tracking any change from the reference configuration, which makes the numerical solution quite complicated. The momentum equation is solved in its full form, and the ice conservation law is integrated for the whole thickness distribution. Note that the ice state as ice thickness distribution is taken in finite-dimensional form (i.e., as a histogram presentation).

The boundary-layer parameters were based on the AIDJEX results and are basically as in Hibler (1979). Ice strength is integrated directly from the thickness redistribution by determining the work needed to form new ridges. The coefficient Γ

is equal to zero if all energy sink at ridging is due to potential energy increase. However, with frictional losses added, we have $\Gamma > 0$. The thickness redistribution function has the following parameters: the band used for ridging and how large ridges will form. The usual solution is to take the lower 15% of the thickness distribution and transform them to k-multiple ice thicknesses; originally k was 5 (Coon, 1974) but later it was increased to 15 (Pritchard, 1981). The grid size was 50–100 km in the original application in the Beaufort Sea.

8.2.3 Hibler model

Most present drift ice dynamics models are based on Hibler's (1979) model. It is therefore a very good benchmark for other models. The Hibler model is a two-level viscous–plastic model, with ice state as given in the Doronin (1970) model. The full momentum equation is solved. The original model application was to study seasonal ice conditions in the Arctic Ocean:

$$J = \{h, A\} \tag{8.7a}$$

$$\left.\begin{aligned} \boldsymbol{\sigma} &= \left(\zeta \operatorname{tr}\dot{\varepsilon} - \frac{P}{2}\right)\boldsymbol{I} + 2\eta\dot{\boldsymbol{\varepsilon}} \\ P &= P^* h \exp[-C(1-A)] \\ \zeta &= \frac{P}{2\max(\Delta, \Delta_0)}, \quad \eta = \frac{\zeta}{e^2}, \quad \Delta_0 = \sqrt{\dot{\varepsilon}_{\mathrm{I}}^2 + \left(\frac{\dot{\varepsilon}_{\mathrm{II}}}{e}\right)^2} \end{aligned}\right\} \tag{8.7b}$$

$$\rho h\left(\frac{D\boldsymbol{u}}{Dt} + f\boldsymbol{k}\times\boldsymbol{u}\right) = \nabla\cdot\boldsymbol{\sigma} + \boldsymbol{\tau}_a + \boldsymbol{\tau}_w - \rho g h\boldsymbol{\beta} \tag{8.7c}$$

$$\frac{Dh}{Dt} = -h\nabla\cdot\boldsymbol{u} + \Phi(h) + D_1\nabla^2 h + D_2\nabla^4 h \tag{8.7d}$$

$$\frac{DA}{Dt} = -A\nabla\cdot\boldsymbol{u} + \Phi_A + D_1\nabla^2 A + D_2\nabla^4 A \quad (0 \le A \le 1) \tag{8.7e}$$

When the elliptic yield curve is assumed, the plastic flow rule can be analytically solved, written in viscous law form. Then the whole viscous–plastic rheology can be expressed in the compact form (8.7b) (see Section 4.3.2) and the full momentum equation is solved, including both local and advective acceleration. In the ice conservation law two additional terms are introduced: harmonic and biharmonic diffusion with their corresponding diffusion coefficients D_1 and D_2, respectively. These diffusion terms are needed for the numerical stability of the solution, the stability problem being created by the highly nonlinear form of the momentum equation.

The original model parameters are shown in Table 8.1. The boundary-layer parameters were based on Arctic Ice Dynamics Joint Experiment (AIDJEX) results (Brown, 1980; McPhee, 1982) and are representative for the Central Arctic Ocean.

Table 8.1 Parameterization of the viscous–plastic sea ice model of Hibler (1979). The parameter groups are: I – atmospheric and oceanic drag parameters; II – rheology parameters; III – ice-state redistribution parameters; and IV – numerical design parameters.

	Parameter	Value	Comments
I	Air–ice drag coefficient, C_a	$1.2 \cdot 10^{-3}$	geostrophic wind
	Air–ice Ekman angle, θ_a	25°	geostrophic wind
	Air–water drag coefficient, C_w	$5.5 \cdot 10^{-3}$	geostrophic current
	Air–water Ekman angle, θ_w	25°	geostrophic current
II	Compressive strength constant, P^*	25 kPa	5 kPa in the original model
	Aspect ratio of yield ellipse, e	2	
	Strength constant for opening, C	20	
	Maximum viscous creep rate, Δ_0	$2 \cdot 10^{-9}\ \mathrm{s}^{-1}$	
III	Demarcation thickness, h_0	50 cm	
IV	Spatial grid size, $\Delta x = \Delta y$	125 km	
	Time step, Δt	1 day	
	Harmonic diffusion coefficient, D_1	$500\ \mathrm{m}^2\ \mathrm{s}^{-1}$	
	Biharmonic diffusion coefficient, D_2	$7.81 \cdot 10^{12}\ \mathrm{m}^4\ \mathrm{s}^{-1}$	

For geostrophic wind the thin ice wind factor (Na) and deviation angle are 1.7% and zero, corresponding to 2.8% and 25º for the surface wind.

There are four rheology parameters. The compressive strength constant is the main tuning parameter. It defines the internal length scale L of sea ice dynamics by $FL \sim P^*h$, where F is the forcing. In the original model (Hibler, 1979), P^* was tuned low, 5 kPa, because 8-day average winds were used for the forcing; later the level was found to be higher, 25 kPa representing a typical level. There are variations through 10–50 kPa due to model tuning in different basins. The aspect ratio e and the strength reduction constant for opening C have almost always been fixed to the original values. Physically, e is the ratio of compressive stress to shear stress in pure shear, and it would be possible to estimate it from ice kinematics data close to a coastline. Even though e has an important role in ice dynamics, attempts to examine its level and variability have not been made; it looks clear that $1 < e \ll \infty$ (i.e., shear strength is significant but less than compressive strength).

The inverse of parameter C, C^{-1}, is the e-folding value of strength of changes in compactness. It is quite clear that $C \gg 1$ (i.e., ice strength is very sensitive to the compactness of ice). The standard value is $C^{-1} = 0.05$, and to estimate its value from data would require highly accurate time series data of ice compactness, more than is possible from present satellite data. The question of this parameter is also connected to the maximum compactness of a given ice field, which depends on the floe size distribution. To know the actual compactness would be important in the cold season since openings are very effective ice producers then.

The fourth parameter of the viscous–plastic rheology is the maximum creep invariant Δ_0 or the transition between viscous and plastic states. This rheology attempts to approximate a plastic medium, and the viscous part is there to make strain-rates solvable at sub-yield stresses. There is no physical support for linear viscous behaviour at very small strain rates; therefore, viscous strain rates need to be much lower than typical strain rates. The level $\Delta_0 = 2 \times 10^{-9}\,\mathrm{s}^{-1}$ is low enough (see Section 3.2.3) and corresponds to extension/contraction of 1 m over a distance of 20 km in 1 day. The small deformation rheology question has not been examined from field data, largely because signals would be within measurement noise. Actually we should regard the rheology as plastic and take the viscous sub-model as a numerical design parameter.

With a two-level ice state, redistribution is straightforward; only the demarcation thickness is needed as a model parameter. It is taken as 50 cm, much less than typical ice thicknesses in the model basin, as it should. The ice conservation law (Eqs. 8.7d, e) ignored ridging and opening under pure shear (see Section 3.4.1).

The grid size was taken as 125 km, sufficiently large for continuum modelling and not too large to resolve the main features of ice circulation in the central Arctic Basin. The smallest geometry to be resolved is the outflow of ice through the Fram Strait. In fact, a realistic grid size here should be within a factor of about ½ up to 2 from that used. The time step was 1 day, small enough for stability, and since the time step of the forcing data was 8 days, a shorter time step would not provide much more new information. The ratios of the diffusion terms to the mechanical deformation term are $D_1/(U\Delta x) \approx 0.04$ and $D_2/[U(\Delta x)^3] \approx 0.04$ for $U \sim 10\,\mathrm{cm\,s}^{-1}$. Thus for low ice velocities the diffusion terms are comparable with the deformation terms. More exactly, Eulerian time differencing gives the change in ice thickness due to harmonic diffusion as:

$$\frac{h_{ij}(t+\Delta t) - h_{ij}(t)}{\Delta t} \approx D_1 \frac{[\Delta^2 h]_{ij}}{(\Delta x)} = D_1 \frac{h_{i-1,j-1} + h_{i-1,j+1} + h_{i+1,j-1} + h_{i+1,j+1} - 4h_{i,j}}{(\Delta x)^2} \tag{8.8}$$

where Δ^2 is the second-order spatial difference operator, $[\Delta^2 Q]_{ij}$ being equal to the mean of the differences $Q_{i\pm1,j\pm1} - Q_{ij}$ for a quantity Q. For $\Delta x = 125\,\mathrm{km}$ and $\Delta t = 1\,\mathrm{d}$, Eq. (8.8) gives,

$$h_{ij}(t+\Delta t) - h_{ij}(t) = 2.76 \times 10^{-3} \Delta^2 h \tag{8.9}$$

Thus, at each time step, thickness and compactness are smoothed by the factor of 2.76×10^{-3} toward the mean of the values in the surrounding grid points, which means that the timescale for homogenization of a stationary ice field is ≈360 d. The biharmonic smoothing operator is analogous, with $D_2 \Delta t/(\Delta x)^4 \approx 2.76 \times 10^{-3}$ (in other words, the smoothing is equally effective).

To prevent instabilities, also a minimum value was specified for nonlinear viscosities in the original model (Hibler, 1979): $\zeta > \zeta_{\min} = 4 \times 10^8\,\mathrm{kg\,s}^{-1}$ and $\eta = \zeta/e^2$ holding. This limit is much lower than the normal level of bulk viscosity. This, however, does not seem to be a necessary feature.

One time step proceeds as follows. The momentum equation is solved repeatedly from linearized equations by over-relaxation until the desired accuracy is obtained. Then the ice conservation equation is integrated for a new ice state. The original model was validated against observed average thickness and velocity fields: the Transpolar Drift Stream and the Beaufort Sea Gyre come out well but, more importantly, the mean ice thickness field is good. An independent comparison for ice velocity which gave a good result was made by Zwally and Walsh (1987). Sensitivity studies of ice model dynamics have been made by Holland *et al.* (1993), among others.

The stability of the numerical solution has been examined by Gray and Killworth (1995). They illustrate cases when the non-zero tensile strength contained in the elliptic yield curve, although small, may lead to instabilities. In these cases, ice–water stress was ignored; but, had it been included, the instabilities would not form. Consequently, the instability problem may exist only in the most extreme situations. Instabilities could be totally avoided by limiting the whole yield curve to the third quadrant in the principal stress space (Gray and Killworth, 1995). Later, Gray (1999) analyzed the case of uniaxial divergent flow and showed that compactness distribution develops into a deepening finger-shaped form, but does not actually become unstable.

Further developments of the model include the use of a multi-level thickness distribution for ice state (Hibler, 1980a). The rheology is inconsistent in having stress for an ice field at rest, but this has been removed: the original rheology gives $\sigma = -\frac{1}{2}P$ for $\dot{\varepsilon} = 0$, evidently incorrect, and the revised form has $\sigma \to 0$ as $\dot{\varepsilon} \to 0$ (Hibler, 2001). Flato and Hibler (1990) designed a cavitating fluid version in which the shear stresses are ignored, $e = \infty$, leading to computationally less expensive solutions. An anisotropic extension was developed by Hibler and Schulson (2000) to examine the dynamics of oriented lead and fracture systems.

The model has been used for climate studies and short-term regional ice forecasting. It has been shown to be feasible with about the same parameterization over a wide range of time and space scales. Hunke and Dukewicz (1997) developed an elastic–viscous–plastic scheme for the numerical solution of Hibler's (1979) model. It is easily applicable to parallel computing, in particular.

8.2.4 Baltic Sea model

Sea ice model development in the Baltic Sea has progressed in Finland parallel to work in the Arctic. The first model was a linear viscous four-level model, used initially for short-term sea ice forecasting (Leppäranta, 1981a). In the late 1980s, modelling collaboration was commenced with Chinese scientists, working in the Bo Hai Sea. A three-level viscous–plastic model was designed for both seas (Wu and Leppäranta, 1990; Leppäranta and Zhang, 1992b). All modelling until then had forecasting as its purpose. Haapala and Leppäranta (1996) developed a dynamic–thermodynamic regional sea ice climate model, where the dynamic part was as in the one used by Leppäranta and Zhang (1992b).

The present Baltic Sea ice dynamics model differs from the Hibler (1979) model in that a three-level ice state is included, and the momentum equation is quasi-steady-state with sea surface tilt ignored. The system of equations reads:

$$J = \{h_u, h_d, A\} \tag{8.10a}$$

$$\left.\begin{aligned} \boldsymbol{\sigma} &= \left(\zeta \operatorname{tr}\dot{\boldsymbol{\varepsilon}} - \frac{P}{2}\right)\boldsymbol{I} + 2\eta\dot{\boldsymbol{\varepsilon}}, \quad P = P^* h e^{-C(1-A)} \\ \zeta &= \frac{P}{2\max(\Delta, \Delta_0)}, \quad \eta = \frac{\zeta}{e^2}, \quad \Delta = \sqrt{\dot{\varepsilon}_{\mathrm{I}}^2 + \left(\frac{\dot{\varepsilon}_{\mathrm{II}}}{e}\right)^2} \end{aligned}\right\} \tag{8.10b}$$

$$\rho h f \boldsymbol{k} \times \boldsymbol{u} = \nabla \cdot \boldsymbol{\sigma} + \boldsymbol{\tau}_a + \boldsymbol{\tau}_w \tag{8.10c}$$

$$\left.\begin{aligned} \frac{Dh_u}{Dt} &= \Phi(h_u) + D_1 \nabla^2 h_u, \quad \frac{Dh_d}{Dt} = \psi_d + \Phi_d(h_d) + D_1 \nabla^2 h_d \\ \frac{DA}{Dt} &= -A\nabla \cdot \boldsymbol{u} + \Phi_A(A) + D_1^2 A \quad (0 \le A \le 1) \end{aligned}\right\} \tag{8.10d}$$

where h_u and h_d are the thicknesses of undeformed and deformed ice, respectively, ψ_d is the ridging function:

$$\psi_d = \begin{cases} -(h_u + h_d)\nabla \cdot \boldsymbol{u}, & \text{if } \nabla\cdot\boldsymbol{u} < 0 \text{ and } A = 1 \\ 0, & \text{otherwise} \end{cases} \tag{8.11}$$

and Φ_d is the thermodynamic change of deformed ice. The early four-level version split the thickness of deformed ice into mean ridge size and ridge density, but since observations showed that the mean ridge size varied very little it was possible to go down to three levels (Leppäranta, 1981b). It has been possible to validate the model outcome of the volume of ridged ice against observations with good results.

The model parameters were determined from Baltic Sea field data and model experiments (Table 8.2), while the boundary-layer parameters were based on field experiment results (Joffre, 1984; Leppäranta and Omstedt, 1990). Both drag coefficients are in essence larger in the Arctic, by factors of 1.3 for the air drag coefficient and 1.6 for the water drag coefficient, due to the greater roughness of Arctic ice. For the surface wind the asymptotic thin-ice wind factor is 2.6% and the deviation angle is 17°; this wind factor is a little less than in the Arctic, but because the ice is much thinner in the Baltic the real (observed) wind factor is higher.

Compressive strength was tuned to 25 kPa, and the range in different numerical experiments against field data was 10–50 kPa (Zhang and Leppäranta, 1995; Leppäranta *et al.*, 1998). The aspect ratio e and the strength reduction constant for opening were equal to the original values (Hibler, 1979). The demarcation thickness was 10 cm, less than typical ice thicknesses. There was also a physical background in that ice thinner than about 10 cm underwent rafting under compression and offered much less resistance to deformation, as validated from basin-wide ice kinematics data (Leppäranta *et al.*, 1998).

Table 8.2 Parameterization of the Baltic Sea viscous–plastic sea ice model (Leppäranta and Zhang, 1992; Haapala and Leppäranta, 1996). The parameter groups are I – atmospheric and oceanic drag parameters, II – rheology parameters, III – ice state redistribution parameters, and IV – numerical design parameters.

	Parameter	Value
I	Air–ice drag coefficient, C_a	$1.8 \cdot 10^{-3}$ (surface wind)
	Air–ice Ekman angle, θ_a	0 (surface wind)
	Air–water drag coefficient, C_w	$3.5 \cdot 10^{-3}$ (vertically averaged current velocity)
	Air–water Ekman angle, θ_w	17° (vertically averaged current velocity)
II	Compressive strength constant, P^*	25 kPa (based on observed data)
	Aspect ratio of yield ellipse, e	2
	Strength constant for opening, C	20
	Maximum viscous creep rate, Δ_0	$2 \cdot 10^{-9}\ \mathrm{s}^{-1}$
III	Demarcation thickness, h_0	10 cm
	Upper limit for rafting	
IV	Spatial grid size, $\Delta x = \Delta y$	18 km (Present version 5 km)
	Time step, Δt	6 hours
	Harmonic diffusion coefficient, D_1	$500\ \mathrm{m}^2\ \mathrm{s}^{-1}$
	Biharmonic diffusion coefficient, D_2	0

This model was recently examined in detail for dynamics in different basins, in particular for scaling and the influence of coastal geometry and islands (Leppäranta and Wang, 2002; Wang *et al.*, 2003). It worked well down to a bay size of 15 km with thin ice (10 cm) moving under strong winds ($25\ \mathrm{m\ s}^{-1}$).

8.3 SHORT-TERM MODELLING APPLICATIONS

In short-term modelling the timescale ranges from 1 hour to 10 days. The approach is often purely dynamic (i.e., thermodynamics is neglected). The initial field of ice state must therefore be given. The objective of short-term modelling includes basic research into drift ice dynamics, coupled ice–ocean–atmosphere modelling, simulations to examine the influence of ice dynamics on planned marine operations (Figure 8.4), and ice forecasting.

8.3.1 Research work

The knowledge of sea ice dynamics can be improved by numerical experiments. This is especially true of rheology and thickness redistribution problems. Direct evidence is in short supply for these questions. However, with accurate indirect information, model simulations may provide information about background physics: as an

Figure 8.4 Shipping in ice-covered seas has penetrated deeper and deeper into the ice pack. The first ship to reach the North Pole was the Soviet nuclear icebreaker *Arktika* in summer 1977.

Reproduced with permission from the Russian State Museum of the Arctic and Antarctic, St Petersburg.

example, sea level variations in the Gulf of Bothnia in ice conditions can provide data on the losses of kinetic energy in mechanical deformation (Figure 8.5).

The question of ice–tide interaction has been investigated using short-term ice–ocean dynamics models. In the presence of internal friction, ice introduces an additional damping effect on tides. Kowalik (1981) examined the situation in the Arctic Ocean using a nonlinear sea ice model, and results showed good overall agreement between the tides in the real and ice-free Arctic Ocean. The influence of ice was mostly seen in coastal regions. Between the ice and water velocities there is a time lag, which is a complicated function of internal ice friction and ice–water stress parameters. Tidal amplitude appears damped in the ice and, due to the nonlinearity of sea ice rheology, a residual ice drift results from the tidal cycle. Kowalik and Proshutinsky (1995) examined the topographic influence on tides in the Barents Sea, and the model predicted trapping of ice dynamics at Bear Island by the residual tidal flow (basically in agreement with observations).

A large amount of short-term sea ice modelling work has been done in the marginal ice zone (MIZ). In the neighbourhood of the ice edge, an intensive air–ice–ocean interplay takes place and the location of the ice edge introduces a discontinuity in the characteristics of the air–sea interface, together with velocity and temperature.

The situation allows a 1.5-dimensional approach[2] that assumes alongshore, or longitudinal, variations to be much less than transverse variations and, consequently,

[2] In these 1.5-dimensional models there are two space co-ordinates, but the dependent variables are allowed to vary only along one of the co-ordinates

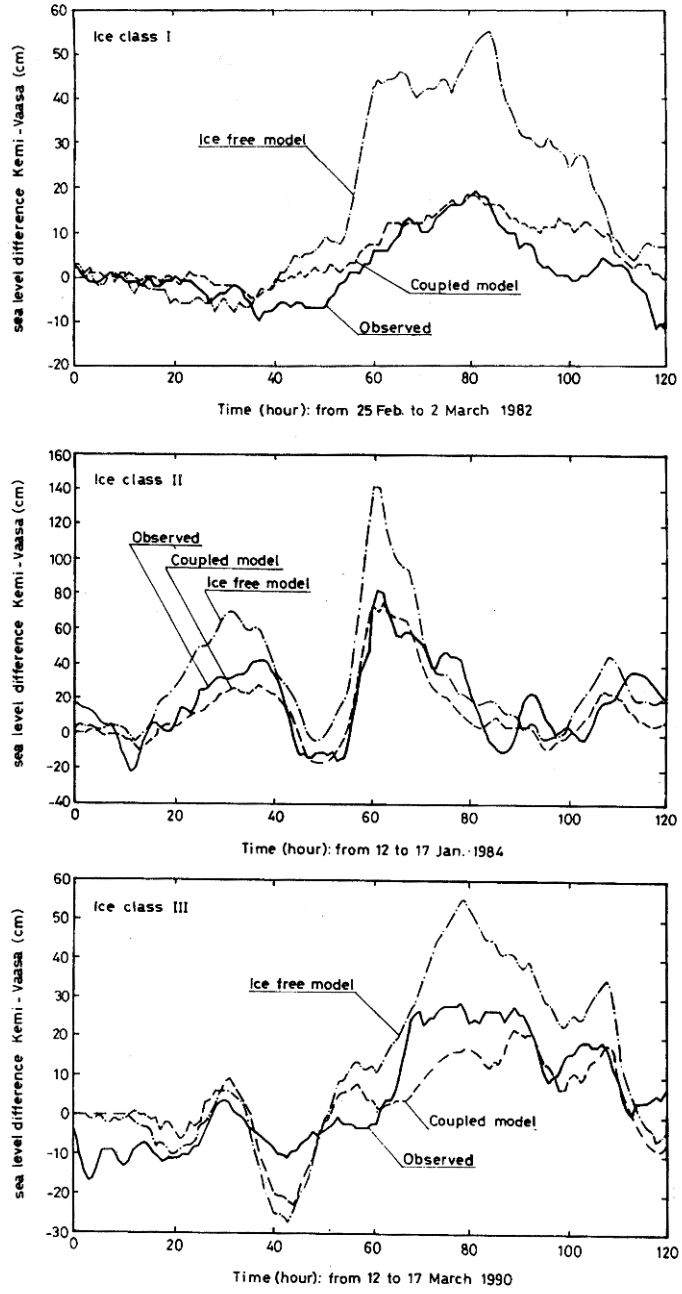

Figure 8.5 Simulated sea level elevation in the Gulf of Bothnia, Baltic Sea. Ice-free model and viscous–plastic coupled iceocean model have been employed. Ice classes: I – severe, II – normal, III – mild.

From Zhang and Leppäranta (1995).

alongshore derivatives can be ignored (see Section 7.4). The two-level viscous–plastic model was solved analytically for steady-state conditions and numerically for non-steady-state cases by Leppäranta and Hibler (1985). Comparison between the continuum viscous–plastic model and a discrete particle model was made by Gutfraind and Savage (1997), and the best agreement was obtained when the Mohr–Coulomb yield criterion was used in the viscous–plastic model. This is to be expected since the physical basis is similar in the Mohr–Coulomb and discrete particle models.

Similar 1.5-dimensional coupled ice–ocean models have been used to further examine the MIZ and coastal dynamics. A general coupled model for coastal seas was presented by Overland and Pease (1988) with a barotropic ocean. One major topic is upwelling at the ice edge. The problem can be approached by analytical modelling of the steady state (see Section 7.4), where the surface stress difference across the ice edge may have either sign, resulting in upwelling or downwelling analogous to coastal ocean dynamics. A more detailed oceanic case allowing an analytical solution was studied by Van Hejst (1984). Other ice edge process models include banding (Häkkinen, 1986) and ice edge eddies.

Regional coupled ice–ocean modelling has been one major question, aiming at research and forecasting purposes. The Baltic Sea and the Bo Hai Sea are discussed below. In other regions, models for the Sea of Okhotsk have been presented by Rheem *et al.* (1997), for the Labrador Sea by Ikeda (1985), Keliher and Venkatesh (1987), and Fissel and Tang (1991), and for Hudson Bay by Wang *et al.* (1994).

Example (*Lehmuskoski and Mäkinen, 1978*) Sea ice is a good platform for gravity measurements over the ocean. This has been utilized by the Finnish Geodetic Institute in the Baltic Sea. However, because of Coriolis acceleration, the eastward component of sea ice velocity affects the apparent local gravity. Therefore, short-term ice dynamics simulations have been made to correct gravity measurements.

8.3.2 Sea ice forecasting

Sea ice conditions can change over short timescales due to dynamics. Leads up to 20 km wide may open and close in a single day, and heavy pressure may build up in the compression of compact ice. These processes have a strong influence on shipping, oil drilling, and other marine operations. Changes in ice conditions, such as the location of the ice edge, are important for weather forecasting over a few days. Consequently, short-term ice forecasts are crucial for ice-covered seas, in particular in the seasonal sea ice zone when human activities are at their height.

Sea ice drift has long been predicted using wind factor and deviation angle rules (e.g., Vasiliev, 1985). However, it is only with numerical models that the full sea ice problem can be solved for realistic basin-wide dynamics. The first prognostic sea ice model was a two-level linear viscous ice model for the Kara Sea (Doronin, 1970), applicable to sea ice forecasting. The Hibler and AIDJEX models (Coon, 1980; Hibler, 1979) have also been applied to the ice-forecasting problem.

The key areas of short-term modelling research are now ice thickness distribution and evolution, and the use of satellite synthetic aperture radars (SARs) for ice kinematics. The scaling problem, and in particular the downscaling of stress from geophysical to local (engineering) scale, is examined by combining scientific and engineering knowledge and developing ice load calculation and forecasting methods. The physics of drift ice is quite well represented in short-term ice-forecasting models, in the sense that other questions are more critical for their further development. In particular, the data assimilation problem has not been much examined for sea ice models.

Baltic Sea

In the Baltic Sea the main harbours have been kept open all year since 1970. Winter shipping has been assisted by 20–25 icebreakers, and even then transportation systems have suffered from delays. This was the catalyst for an extensive research

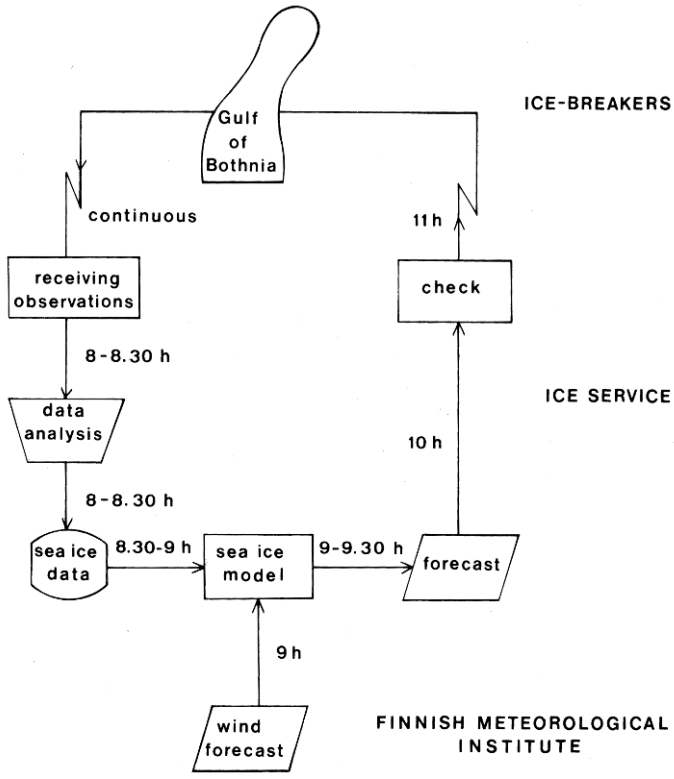

Figure 8.6 The structure of the Finnish ice-forecasting system in winter 1977 in the Finnish Institute of Marine Research.
From Leppäranta (1981a).

programme in the 1970s in Finland and Sweden, organized by a joint winter navigation research board. One of the research aims was to develop an ice-forecasting system based on mathematical modelling (Udin and Ullerstig, 1976; Leppäranta, 1981a). The first real ice-forecasting season was winter 1977 (Figure 8.6), based on a four-level extension of the Doronin (1970) model (Leppäranta, 1981a). Initially, the forecast period was 30 hours, limited by the period of available wind forecasts. The grid size was 27 km and the time step was 6 hours, the same as the time step in the wind forecast. The ice forecast, which was sent to the icebreakers by fax, contained ice speed, direction of ice drift, change in ice concentration, and qualitative pressure field.

The outcome in the first winter was marginally positive (Leppäranta, 1981a). Comparison with real ice conditions showed satisfactory results and, in answer to a questionnaire, the icebreaker personnel concluded that the most important quantity was ice drift velocity and its direction with respect to the fast ice boundary. This is understandable since the opening and closing of leads at the fast ice boundary is the process that is key to shipping (Figure 8.7).

The system was continued for subsequent winters along with model improvement and, as a result, lengthening of the forecast period. A viscous–plastic three-level model was first adopted for operational ice forecasting in 1992 (Leppäranta and Zhang, 1992b). This model was also integrated into the ice-forecasting system in

Figure 8.7 Convoy of ships assisted by an icebreaker in the Baltic Sea. Ice dynamics determines the length of a convoy.

Sweden (Omstedt *et al.*, 1994). With the progress of satellite remote-sensing techniques, initial ice compactness became better mapped. However, the thickness of ice has continued to be a difficult quantity, with updates coming from occasional ship reports. From the outset any new initial ice thicknesses were constructed from a hindcast combined with new observations.

Bo Hai Sea

Another region subject to modelling has been the Bo Hai Sea, China (Wu *et al.*, 1998). A three-level dynamic–thermodynamic sea ice model has been employed for 3–5-day sea ice forecasting since 1990 by the National Research Centre for Marine Environment Forecasts, Beijing. The model is linked to numerical weather forecasting. Its dynamics is similar to the Baltic Sea ice model (Wu and Leppäranta, 1990). The principal motivation behind the Bo Hai Sea ice model is to serve the oil-drilling operation of the Bo Hai Oil Corporation in the basin.

Ice motion in the Bo Hai Sea is forced by strong, cold winds from the north and strong tides of up to 1 m/s (Wu *et al.*, 1998). The ice is fairly thin, typically 25 cm. The model is initialized by a composite analysis of NOAA satellite images, aerial reconnaissance, and ground data as well as real-time data from an oil-drilling platform in Liaodong Bay. The grid size is about 10 km. Ice forecasts are sent to users by fax and email (Figure 8.8). Between 1991 and 1996, some 30–80 ice forecasts were prepared each winter, and verification showed that error in location of the ice edge was within 10 km in 80–90% of all cases for 3-day forecasts and in 50–80% of all cases for 5-day forecasts.

Arctic seas

In Canada, the Atmospheric Environment Service started ice forecasting in 1979, initially in the Beaufort Sea (Neralla *et al.*, 1988). The grid size was then 42 km, with a time step of 3 hours and total length of forecast period 48 hours. At the moment, this is taken care of by the Canadian Ice Service (CIS), a branch of the Meteorological Service of Canada (MSC) (`http://ice-glaces.ec.gc.ca/`). The ice forecasting service is needed by shipping, commercial fishing, offshore resource development, hunting and fishing, tourism and recreation, and local weather questions. The Canadian Arctic is divided into four regions and, in addition, the Great Lakes of North America are included as one more region (Figure 8.9).

The Arctic and Antarctic Research Institute (AARI), St Petersburg, has investigated the ice-forecasting problem since its establishment in the 1920s, and presently a numerical model-based forecast is prepared for the Arctic seas on a regular basis (see `http://www.aari.nw.ru/`). The web site contains ice charts and ice forecasts over the Arctic Ocean.

In large lakes drift ice also occurs, and requirements for ice forecasting service are sometimes similar as for small marine basins. An ice-forecasting system based on an ice dynamics model was developed for Lake Erie in the USA in the early 1980s (Chieh *et al.*, 1983).

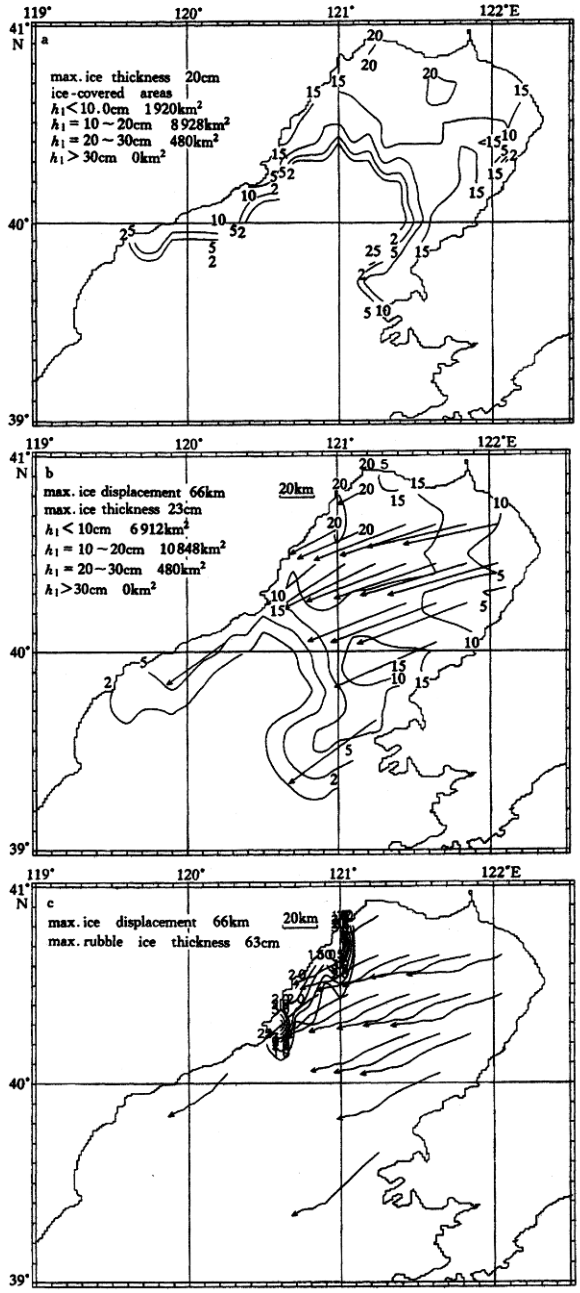

Figure 8.8 Five-day ice forecast for the Liaodong Bay, Bo Hai Sea, from 13 January 1993: (a) initial ice state; (b) ice thickness and velocity forecast; and (c) ice rubble thickness and track forecast.

From Wu *et al.* (1998).

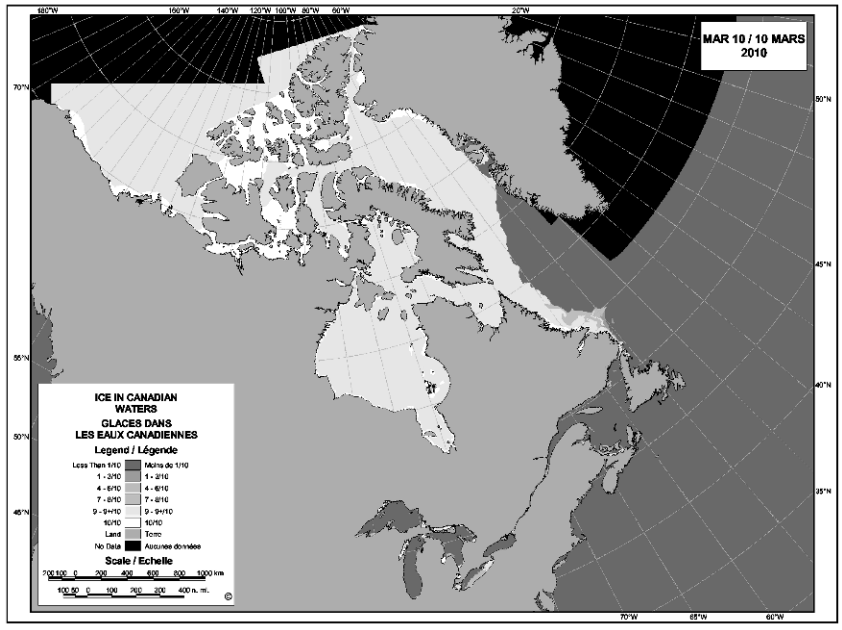

Figure 8.9 Ice monitoring and forecasting regions of the Canadian Ice Service.
Source: Canadian Ice Service web site (http://ice-glaces.ec.gc.ca/).

Local forecasting

For a given local site, such as a drilling platform or a ship, simple models can be applied for local forecasting. These models are based on physical principles of sea ice drift and statistical techniques (see Section 3.3.5). Especially, the method works well in a scattered field of ice floes, when the free drift theory is applicable. The unsteady free drift equation is written as (in complex form):

$$\rho h\left(\frac{du}{dt}+\mathrm{i}fu\right)=\tau_a+\tau_w-\rho hg\beta \tag{8.12}$$

If $U_{wg}\approx 0$, with local observations of ice and wind velocity and ice thickness, non-dimensional key parameters (Na, θ_w) can be estimated, and prediction for the ice floe displacement can be made for the next time-step. The estimates of the parameters can be updated at every new time-step into an improved accuracy. If geostrophic current is slowly varying, that can also be added into the list of parameters; another possibility is to measure the geostrophic current at site.

This forecasting system is thus self-correcting. For example, taking U_{wg} as an unknown constant, with an observation time series for u and U_{a} at times $t_1, t_2, \ldots$, we can solve α and U_{wg} by linear regression:

$$u(t_k)=\alpha U_a(t_k)+U_{wg}+e_k,\quad k=1,2,\ldots \tag{8.13}$$

where e_k is error term. Starting with initial values, say, $|\alpha(0)| = 2\%$, $\arg \alpha = 30^\circ$ and $U_{wg} = 0$, a series of estimates with increasing accuracy, proportional to $\sqrt{n(t)}$ where n is the number of observations, is obtained for α and U_{wg}. This method allows prediction of whether a fixed ice floe will collide with a platform, based on the data that can be easily collected from the platform.

This kind of approach applies for any floating objects on the sea surface. In iceberg drift forecasting a self-correcting forecasting system was developed by Garrett (1985) in the Canadian Eastern Arctic.

8.4 OIL SPILLS IN ICE CONDITIONS

8.4.1 General

Oil spills are difficult problems under normal circumstances but in ice conditions they are particularly so (Figure 8.10). Effective oil spill-cleaning methods do not exist in sea ice conditions, and it is difficult to keep track of drift and dispersion of oil. Oil may penetrate into the ice sheet and drift with the ice, drift on the surface in open

Figure 8.10 Oil spill in the Gulf of Finland.
Photograph by Jouko Pirttijärvi, reproduced with permission from the Finnish Environment Centre, Helsinki.

water spots, and drift beneath sea ice. For drifting beneath the ice, the bottom roughness is important since oil may be trapped between roughness elements. In addition, the quality of ice-ocean dynamics is highly significant. Under landfast ice oil basically stays just beneath the stationary ice, but under drifting ice oil drifts and spreads with the oceanic surface layer dynamics.

Venkatesh *et al.* (1990) state that, for ice compactness greater than 30%, oil practically drifts with the ice, and that in slush or brash the thickness of the oil film can be much larger than in open cold water. When compactness reaches the 80% level the oil is trapped between ice floes and at above 95% the oil is forced beneath the ice.

A simple modelling approach is an oil advection model with ice and surface current, with random diffusion superposed, using a Monte Carlo method. An advanced, physical model treats oil as a viscous medium with density and viscosity dependent on the type of oil (e.g., Venkatesh *et al.*, 1990). Modelling the boundaries of an oil spill calls for an advanced advection scheme. Ovsienko *et al.* (1999a) used the particle-in-cell technique in their model, which has been applied to several areas of Arctic seas.

8.4.2 *Runner-4* oil spill in the Gulf of Finland

An oil spill case is presented from the Gulf of Finland; for more details see Wang *et al.* (2008). This basin is one of the densest oil transport routes in freezing seas. There are major oil terminals in the basin, and risks are large due to shallow topography and dense sea traffic (Figure 8.11). The Gulf of Finland is an elongated basin with a smooth salinity gradient from 6–7 per mille on the west to fresh water in the Neva Bay in the east (Soomere *et al.*, 2008). The long-term circulation is counterclockwise with eastward flow on the Estonian coast and westward flow on the Finnish coast.

The ship *Runner-4* sank in the eastern basin of the Gulf of Finland on 5 March 2006, which caused a major oil spill event. During the first days the oil was either beneath the ice cover or mixed with the broken ice. Oil-spill cleaning operations started when the wind pushed the ice floes away and spill was observed in open patches. The ice conditions were quite severe due to the presence of ridged ice. In some areas the oil-spill cleaning vessel *Seili* was not able to pass through the ridged ice zones. It was also observed that the drifting oil tended to accumulate on ice edges.

On 12 March, the Estonian Border Service reported two oil slicks off the northern coast of the Parispea peninsula, possibly oil spills #4 and #5 (Figure 8.12). At noon on 15 March 2006, a combined observation of the oil spills was made by using aerial surveillance and oil-spill cleaning vessels (Source: Pollution Observation Log, Helsinki Commission, Helsinki). The patches #1 and #2 were rather close to the site of the wrecked *Runner 4*. Oil spill #1 was seen in the open water as rainbow-coloured (thickness of rainbow-coloured oil is 0.3–5.0 μm, quantity 0.30–5.0 $m^3\,km^{-2}$), whereas all the other patches were seen as brown oil mixed with ice. The size of

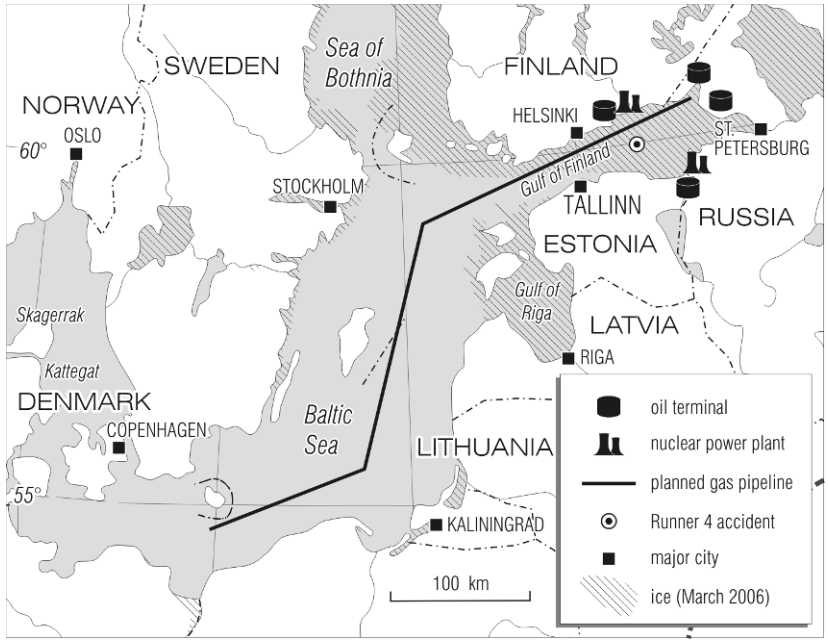

Figure 8.11 An ice chart of the Gulf of Finland in a normal winter. The major oil terminals are also shown.

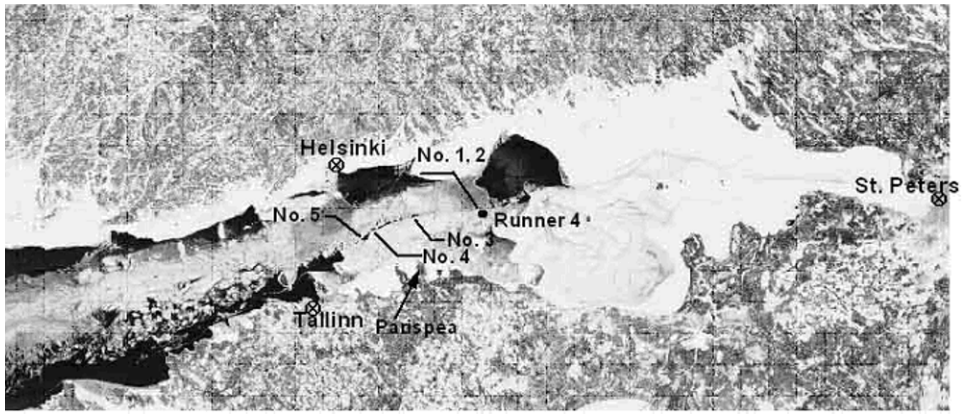

Figure 8.12 Oil spill observations on 15 March 2006 in the Gulf of Finland, with the ice conditions on 13 March, image courtesy of MODIS Rapid Response Project at NASA/GSFC, modified by Keguang Wang. Patches No. 1 and No.2 were very close to the wrecked site of *Runner-4*. Patches No. 4 and No. 5 were in ship channels and No. 3 indicates much oil around in ship channels and in brash ice.

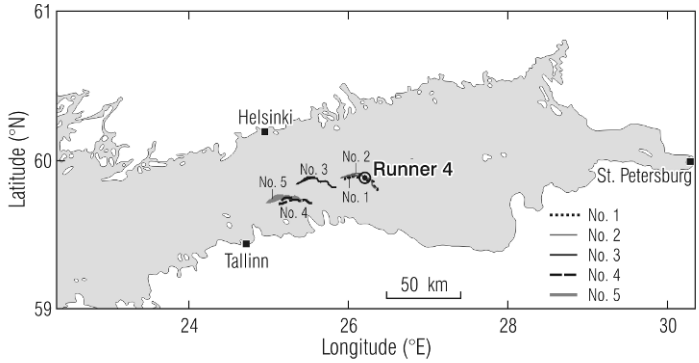

Figure 8.13 Simulated drift of the ice floes whose locations are the same as oil spills Nos.1–5. From Wang *et al.* (2008).

oil-covered areas of patches #s1–4 was all around 0.01 km^2, while that of #5 was about 0.09 km^2.

The development of the ice conditions in the Gulf of Finland was simulated with the Baltic Sea ice model. On the west part, the simulated thin ice cover originally close to the Finnish Coast on 15 March gradually moved to the Estonian coast; whereas the thicker ice cover on the east part moved just a little. The drift trajectories of the ice particles starting from the same locations as the oil spills #s1–5 are shown in Figure 8.13. The simulated drift of the ice goes to the east of Tallinn. This is different from the actual oil spills, which finally reached Tallinn Bay. There may be several reasons causing this difference. First, oil spills #s3–5 were mostly in the ship channel where they can drift almost freely under the wind and currents, whereas the simulated ice drift was based only on wind forcing. Second, the wind drag coefficient may be underestimated, thus underestimating the drift of the sea ice. Third, the spreading of the oil may contribute to its finally reaching the Tallinn Bay. Further study is therefore needed to get a more reliable conclusion.

8.4.3 Oil spill modelling in ice-covered waters

There is not yet a good model for oil spill in ice conditions available. There are good sea ice models and good oil spill models. Drift ice dynamics is independent of drift and dispersion of oil spill but not vice versa. The behaviour of oil depends on the bottom roughness, dynamic state of the ice, fine scale porosity of the ice, and floe size distribution. The last item makes the modelling task difficult, since floe size distribution changes are time-dependent and not provided by existing drift ice models. Also there is a downscaling problem in that oil spill scale is initially less than the size of grid cells of drift ice models.

Formally the floe size distribution $p(d)$ follows a conservation law:

$$\frac{\partial p}{\partial t} = -\boldsymbol{u} \cdot \nabla p + \Xi \tag{8.14}$$

where Ξ represents the thermo-mechanical changes. In a short time scale we may take $\Xi = 0$ and just advect the floe size distribution with a normal drift ice model, once the initial situation has been observed.

When size of spill is not large in comparison with typical size of ice floes, as at initial stage of spill or for large ice floes, it can be treated as problem of gravity-driven current with rigid (possibly moveable) boundaries. The "open-water" particle-in-cell technique can be effectively adopted for this task. Examples of numerical solutions are shown in Figures 8.14 and 8.15. At later spill stages, as for large spills, this technique becomes more difficult to use because of enormous calculation needs: the

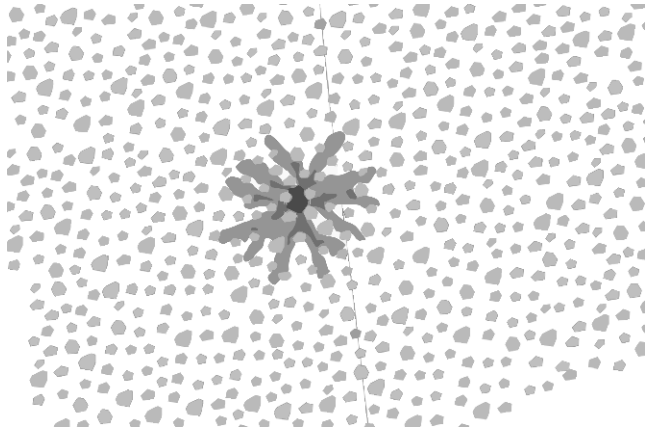

Figure 8.14 Oil spill, 1500 t/h in broken ice. $T = 3$ min.
From Leppäranta *et al.* (2008).

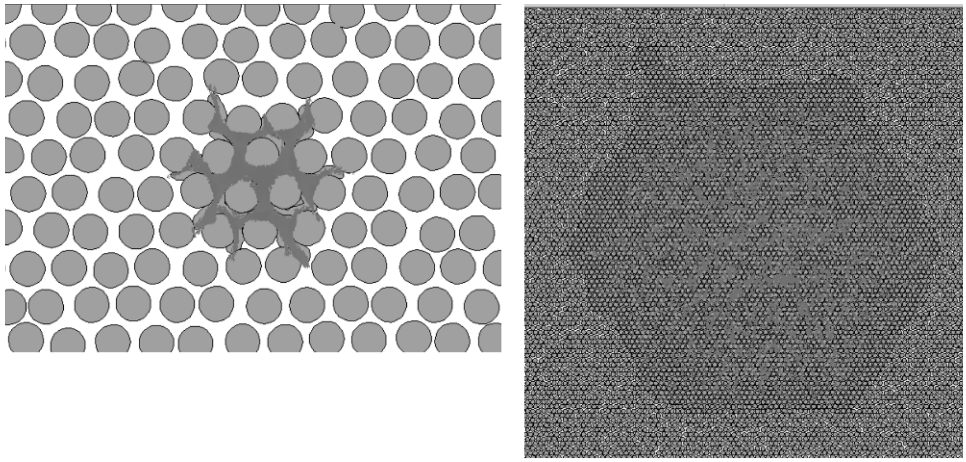

Figure 8.15 Two stages of oil spill spreading on simplified ice-like structure.
From Leppäranta *et al.* (2008).

grid resolution is still related to characteristic ice floe size, whereas size of domain is persistently increasing. Then the only way to overcome difficulties in model simulations and forecasting is to treat oil spreading as an idealized, quasi-two-dimensional regular medium with a net drag force proportional to the square of the local velocity, also depending on ice compactness and mean floe size.

8.5 CLIMATE MODELS

In long-term modelling the timescale ranges from 1 month to 100 years. The approach is dynamic–thermodynamic, and sometimes even the dynamics is ignored. Initial conditions are arbitrary in very long timescales, but relevant for ice state in monthly problems. The objective of long-term modelling includes basic research into drift ice geophysics, ice climatology investigations, and coupled ice–ocean–atmosphere climate modelling.

The role of ice dynamics in the climatology problem is to provide transport of ice to regions where it would not be formed. This transport modifies the ice boundary and, therefore, the air–sea fluxes of momentum, heat, and matter. It also transports latent heat and freshwater. Equally important is differential ice drift: leads open and close, resulting in major changes to air–sea heat fluxes, and the mechanical accumulation of ice blocks, like ridging, adds large amounts to the total volume of ice.

Long-term sea ice modelling has increased as a result of climate research, giving computational possibilities to have more realistic coupled ice–ocean and atmosphere–ice–ocean models. Initially, only thermodynamic models were available for forecasting the times of freezing and ice break-up and for the evolution of ice thickness. But it became rapidly clear that realistic ice dynamics are needed for ice transport and for the opening and closing of leads. Large amounts of heat are transmitted through leads from the ocean to the atmosphere. By freezing and melting the ice has a major influence on the hydrographic structure of the ocean. Therefore, the motion of ice has an important role since ice often melts in a different region from the one in which it forms.

8.5.1 Arctic regions

The first realistic sea ice climate model for the Arctic Ocean was that by Hibler (1979). The mean annual velocity from the simulation together with the mean thickness field corresponded well when validated against submarine data[3] (Figure 8.16; see also Figures 2.19 and 3.17). The model predicted that there is always at least a small amount of open water or thin ice present in the central Arctic Ocean and, further, that with dynamics the annual cycle of mean thickness has about the same

[3] Hibler (1979) used submarine data received from L.A. LeSchack by private communication; some of these data are reported in LeSchack *et al.* (1971).

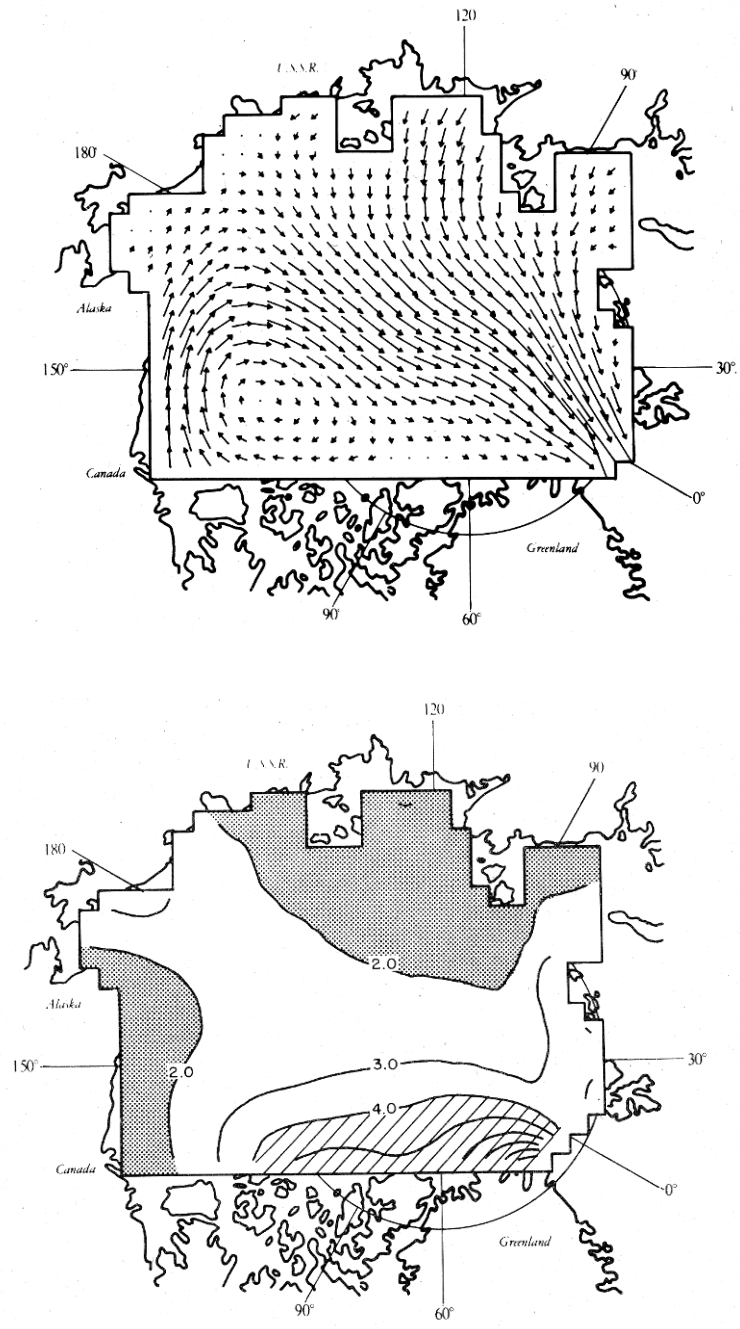

Figure 8.16 The average annual ice velocity (top) and April thickness contours (bottom) produced by Hibler's model (1979).

Reproduced from Hibler (1979), with permission from the American Meteorological Society.

amplitude as it does without dynamics, but the level drops by about 1 m. Maximum ice thicknesses were 5–8 m due to mechanical deformation off the northern coast of Greenland.

Almost ten years later, coupled ice–ocean climate models with full dynamic-thermodynamic ice physics were introduced and the seasonal ice cycle was improved in a diagnostic model (Hibler and Bryan, 1987). In more recent models, resolution, numerical technology, and coupling have all been improved, but the ice physics itself is not much different from what it was in the ice-only models of the 1980s. Better model bases have also improved the outcome for ice state and motion (e.g., Zhang *et al.*, 1998; Arberter *et al.*, 1999; Hunke and Zhang, 1999).

8.5.2 Antarctica

Sea ice models in Antarctic seas have been basically free drift models or viscous–plastic Hibler-type models. Hibler and Ackley (1983) applied the Arctic model to Antarctic regions, with the essential changes of much greater strength, $P^* = 27.5\,\text{kPa}$, and higher demarcation thickness, $h_0 = 1\,\text{m}$. The high strength was explained by temporal spacing of the wind data, while the higher demarcation thickness, which may seem strange, was explained on the basis of the large amounts of frazil ice in the Antarctic and, therefore, a large demarcation thickness would be required by thermodynamics. But this means that the internal friction of ice thinner than 1 m does not influence model ice dynamics. The grid size used by the model was 222 km. Stössel *et al.* (1990) used the model for the entire Southern Ocean.

Timmermann *et al.* (2002) employed the Hibler model for long-term simulations in the Weddell Sea. The boundary-layer parameters were the following: the ice–air drag coefficient was 1.32×10^{-3} for the surface wind, the ice–ocean drag coefficient was 3×10^{-3}, and the turning angle was -10° for the upper layer velocity in the ocean model. The thickness of the upper layer was 8–40 m, thinner in shallow areas. The thin-ice wind factor then becomes 2.4%; this is a bit low for the Antarctic, as is the deviation angle, but it can be to some degree explained by the fact that the upper layer water current was the reference for water stress, not the geostrophic flow. The compressive strength constant was taken as $P^* = 20\,\text{kPa}$. The model grid size was about 165 km, and the model sea ice outcome was calibrated with drift buoy data for ice velocity (Kottmeier and Hartig, 1986) and upward-looking sonar data for ice thickness (Strass and Fahrbach, 1998) (Figure 8.17). There is a strong convergence region in the southwest part of the basin, and advection of the ice shows up in larger ice thickness northward along the Antarctic Peninsula. The width of the compressive region east of the Peninsula is around 500 km.

8.5.3 Baltic Sea

A dynamic–thermodynamic model was developed for the Baltic Sea for investigations into the ice climatology of the region (Haapala and Leppäranta, 1996).

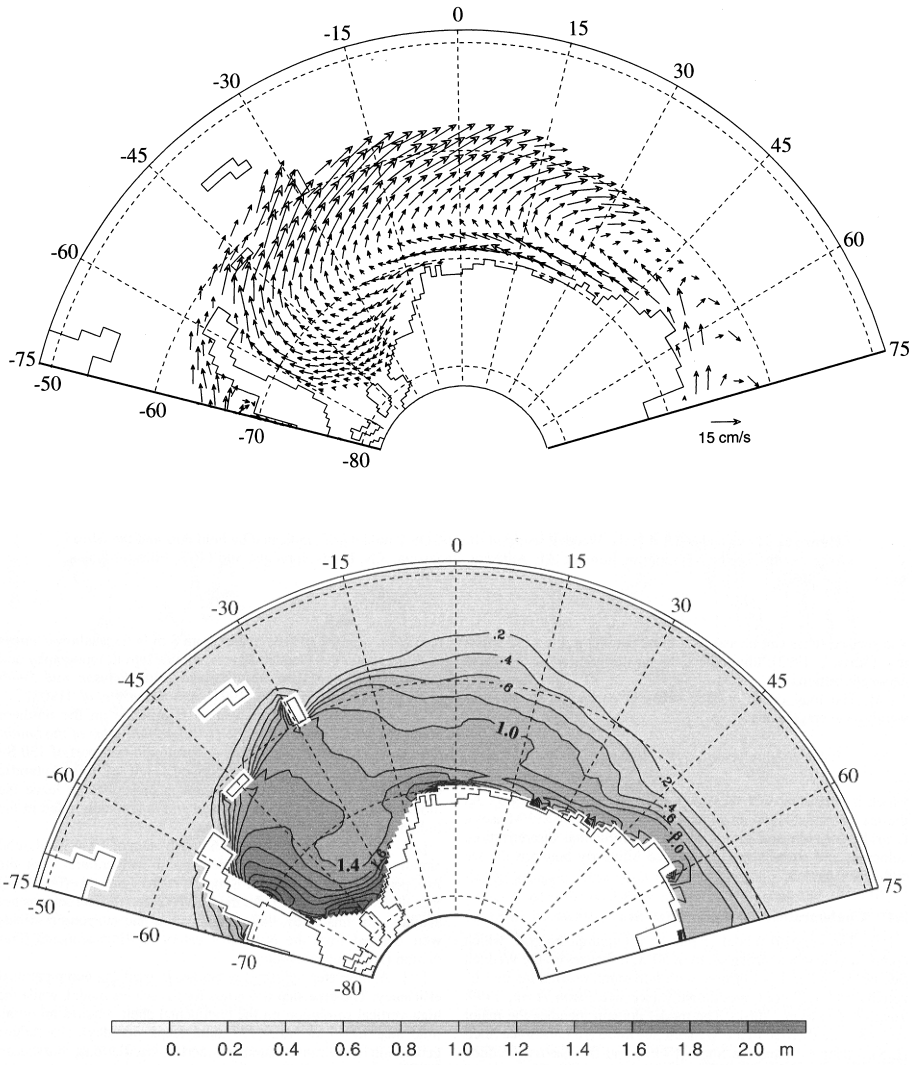

Figure 8.17 Climatological (top) sea ice velocity and (bottom) sea ice thickness in the Weddell Sea.

From Timmermann *et al.* (2002), with permission from the American Geophysical Union.

Its dynamics differs from that of the Hibler model: a three-level ice description is included, the momentum equation is quasi-steady-state, and the surface pressure gradient is ignored. It is a Hibler-type, three-level (compactness, undeformed ice, deformed ice), dynamic–thermodynamic ice model coupled to an ocean model with shallow-water circulation and four-layer, vertical heat transfer. The model was forced by prescribed atmospheric evolution and had a grid size of 18 km. It was calibrated using three different winter categories (mild, normal, and severe) and was used for

simulations of future ice seasons under different atmospheric climate scenarios (with an end date of 2100).

Figure 8.18 gives an example of the outcome, in which model calibration is shown for the normal ice season of 1983/1984. It shows total ice thickness, the thickness of deformed ice, and their comparison with an operational ice chart at the time of the maximum ice extent. Overall agreement is quite good; the main discrepancy is at latitudes 61–62°N where there was an open-water region in the

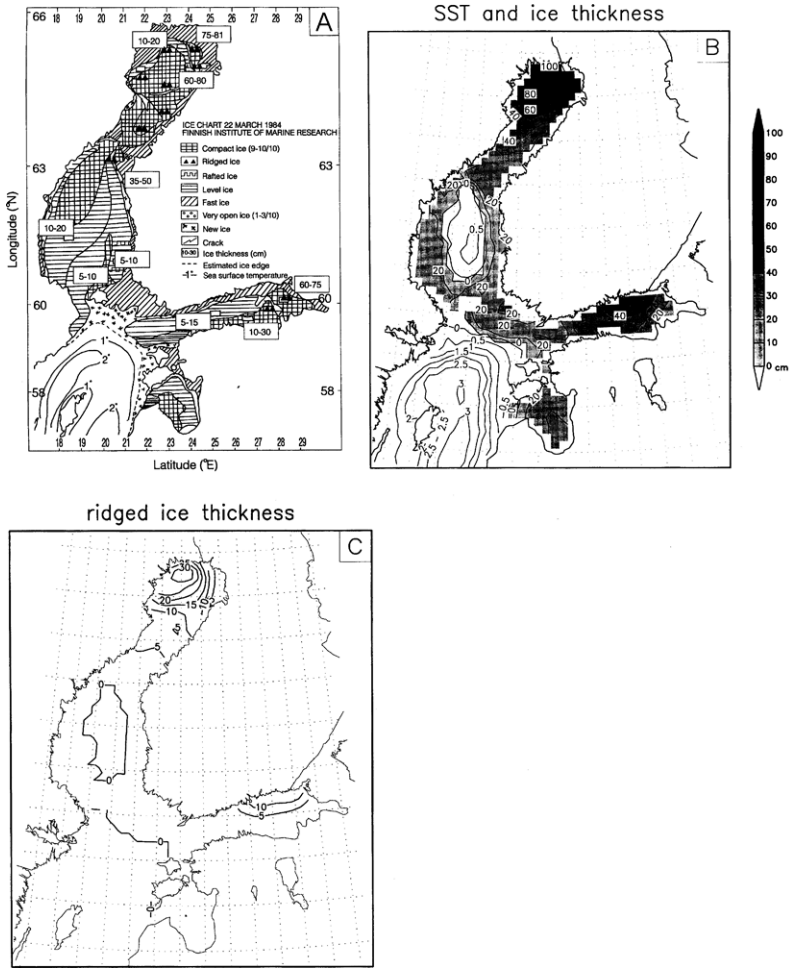

Figure 8.18 Ice conditions and sea surface temperature (SST) on 22 March 1984 in the Baltic (normal winter): (a) observed situation according to an operational chart; (b) modelled SST (°C) in open sea (white area) and total ice thickness (cm); and (c) modelled thickness of deformed ice.

From Haapala and Leppäranta (1996).

model result (due to excessive vertical convection in the model). A thermodynamic-only model would give smoothly increasing thicknesses from the ice edge to 60–90 cm in the eastern and northern corners of the Baltic.

In the open-water region mentioned above the real ice thickness was only 5–10 cm, and so model bias was not too bad. Deformed ice comes out well in the model. Significant values are shown north of 63°N and east of 26°E; these correspond to the ridged areas shown qualitatively by the black triangles in the operational ice chart. Numerical values cannot be compared with quantitative data from the same season, but they correspond to the volume of ridged ice in the basin observed in another winter (Lewis *et al.*, 1993). Comparison with the amount and distribution of deformed ice is sensitive to the sea ice dynamics representation in a model.

8.5.4 Future projections with sea ice climate models

In polar regions sea ice forms together with ocean and atmosphere to form a coupled system, where changes in the three media are strongly interconnected. An hypothesis of warming climate is expected to give less ice but it is less clear how so. Much research is devoted presently on this problem (Figure 8.19).

Figure 8.19 Research vessel *Xue Long* [Snow Dragon] of Polar Research Institute of China in her expedition in the Chukchi Sea, summer 2008. The length of the ship is 167 m.
Photograph by Yuan Shaohong (The Album of Photograph 2008 Chinese Arctic Research Expedition. China Ocean Press, Beijing, 97 p.). Printed with permission.

After 1990 the ice cover in the Arctic Ocean has shown dramatic changes with thinning of ice and a reduction in the multi-year ice area (Rothrock *et al.*, 1999; Wadhams and Davis, 2000; Comiso, 2002). Over the course of the modern satellite record (1979 to present), sea ice extent has declined significantly in all months, with the decline being most pronounced in September. Especially in summer the ice extent has been very small in several years (Figure 8.20). A new record low summer minimum was set in 2007. Monthly ice extent for September 2007 was 4.28×10^6 km^2, 23% smaller than the previous benchmark of 5.56×10^6 km^2 set in September 2005 (Stroeve *et al.*, 2008). The linear trend in ice extent over the satellite record now stands at -10.7% per decade. On the basis of an extended time series from Hadley Centre (Rayner *et al.*, 2002), ice extent in September 2007 was 50% lower than conditions in the 1950s to the 1970s (Stroeve *et al.*, 2005).

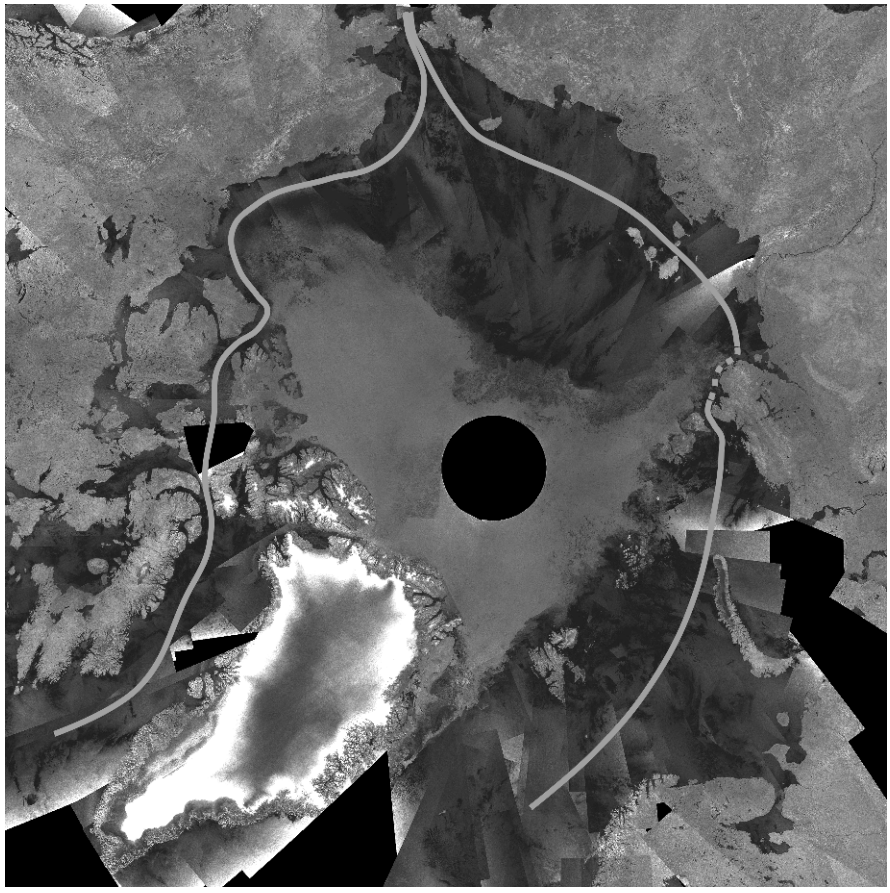

Figure 8.20 Ice conditions in September 2007 in the Arctic Ocean. Ice is shown by the strong backscatter (white) in the Central Arctic. This is a mosaic of ENVISAT ASAR images over the Arctic Ocean with land mask. Northeast and northwest passages are also illustrated. Ice is absent from the Eastern Arctic Ocean. © European Space Agency. Printed with permission.

It has been suggested that the Arctic ice cover is at the edge of a rapidly decreasing trend. However, the considerable natural variability in the Arctic ice conditions makes it difficult to judge whether a (Holland *et al.*, 2006). It is hypothesized that observed changes are due to anthropogenically driven climate change (Vinnikov *et al.*, 1999; Johannessen *et al.*, 1999) and climate models predict the change to continue in the future (Houghton *et al.*, 2001; Zhang and Walsh, 2006). This would mean the Arctic Ocean becoming a basin with a basically seasonal ice cover, much as the ice is in the Southern Ocean. Consequently, the physics of the evolution and of the ice conditions would become different, and a critical question is that how good the present models would be for such an Arctic ice pack.

Summer retardation of the Arctic sea ice cover is an interconnected atmosphere–ice–ocean dynamic-thermodynamic process. The decrease of summer ice extent in recent years was due to ice melting and also due to a favourable pattern of

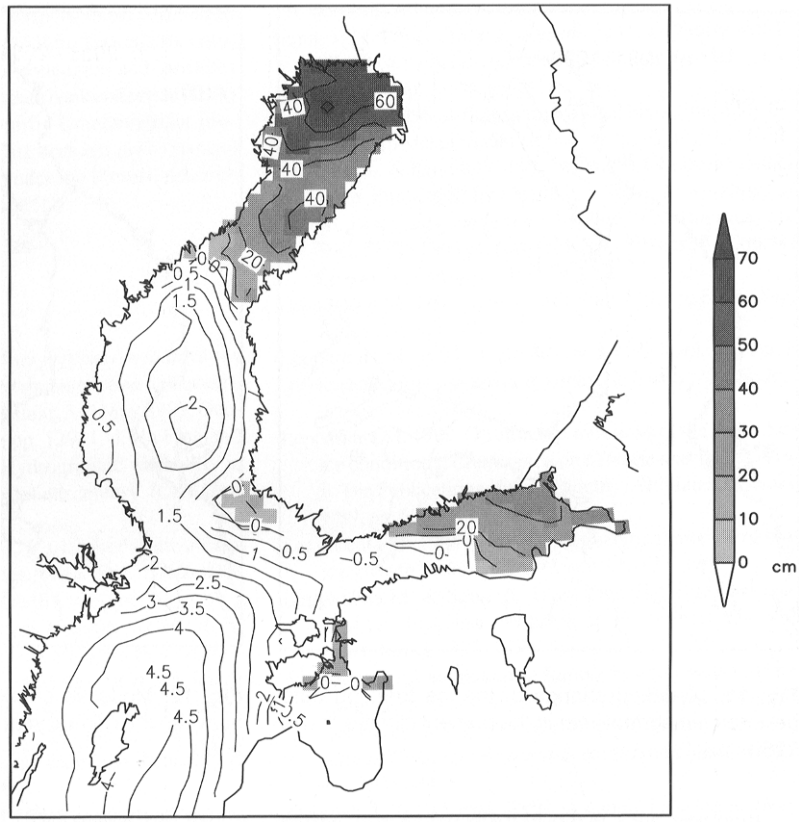

Figure 8.21 Average ice situation at the annual maximum in the Baltic Sea, 2050 ± 15 years, based on a regional sea ice model forced by an expected climate-warming scenario. Grey tones show ice thicknesses, and the white area is the open sea with numbers showing the surface temperature (°C).

From Haapala and Leppäranta (1997a).

atmospheric circulation. An anticyclonic pattern over the central Arctic Ocean was coupled with low pressures over central and western Siberia (Maslanik *et al.*, 2007). The sky was relatively clear over the Arctic Ocean increasing the ice melt rate by solar radiation, and the wind pattern speeded up the ice transport. Along with a possible systematic decrease of the Arctic sea ice cover, positive albedo feedback would strongly support that the trend will continue. The possibility of abrupt transitions in the future Arctic sea ice has consequences for the entire Arctic system.

Small basins in the seasonal sea ice zone are simpler. The thickness and extent of ice are highly correlated with regional air temperature. Figure 8.21 shows the Baltic Sea ice climate model outcome for the year 2050 forced by a weather generator with suggested climate warming as the input. It is seen that predicted ice coverage is less than half the true normal winter level between 1960 and 1990 (Figure 8.21).

This completes our review of the current status of the numerical modelling of sea ice drift. Although the solution is rather good, there still are some open questions regarding its physics, numerical technology, and coupling with atmosphere and ocean. Interesting research topics for the modelling problem as well as for the whole sea ice drift problem are outlined in Chapter 9.

9

Use and need for knowledge on ice drift

9.1 SCIENCE

The ice drift problem contains interesting basic research questions. It is a two-dimensional problem in the branch of mechanics called geophysical fluid dynamics. The medium is a compressible fluid, whose dynamic characteristics are its largely variable strength (low to very high), low inertia, and the irreversibility of mechanical deformation processes. In ice-only dynamics, adjustment of the ice mass to external forcing takes place, ruled by the strength of ice and the forcing characteristics. As ice is relatively thin, the direct Coriolis effect on it is rather weak, in contrast to the atmosphere and ocean, and gives second-order modifications. However, indirect influence of Coriolis acceleration is important as it modifies the directions of wind and water stresses on the ice.

The principal open questions in sea ice dynamics are the drift ice rheology, redistribution of ice in deformation, and scaling. Rheology seems to be an ever-lasting topic, such as turbulence in fluid dynamics. As far as thickness distribution is concerned, many theories and models exist, but the lack of good data is a major barrier to progress. The thickness-mapping problem is common to most sea ice research. The scaling of sea ice dynamics is becoming better understood and is closely connected to the rheology and redistribution of ice (Figure 9.1). The theory and models of sea ice dynamics have been utilized for ice dynamics in large lakes and rivers, the essential feature being that floating ice breaks into floes and then drifts (Wake and Rumer, 1983; Shen *et al.*, 1993; Leppäranta and Wang, 2008).

The dynamics of sea ice is intimately coupled with the upper ocean. The dynamic ice–ocean interaction is dictated by skin friction and form drag due to hummocks and ridges at the ice–water interface. At extremes the ice may drift along with surface currents or may act as a stationary lid providing frictional resistance to surface currents. In the adjustment of ice–ocean dynamics, atmospheric kinetic energy is transferred through drifting ice to the ocean, where it is modified by ocean dynamics, and a part is returned to the ice.

M. Leppäranta, *The Drift of Sea Ice*, Springer Praxis Books,
DOI 10.1007/978-3-642-04683-4_9, © Springer-Verlag Berlin Heidelberg 2011

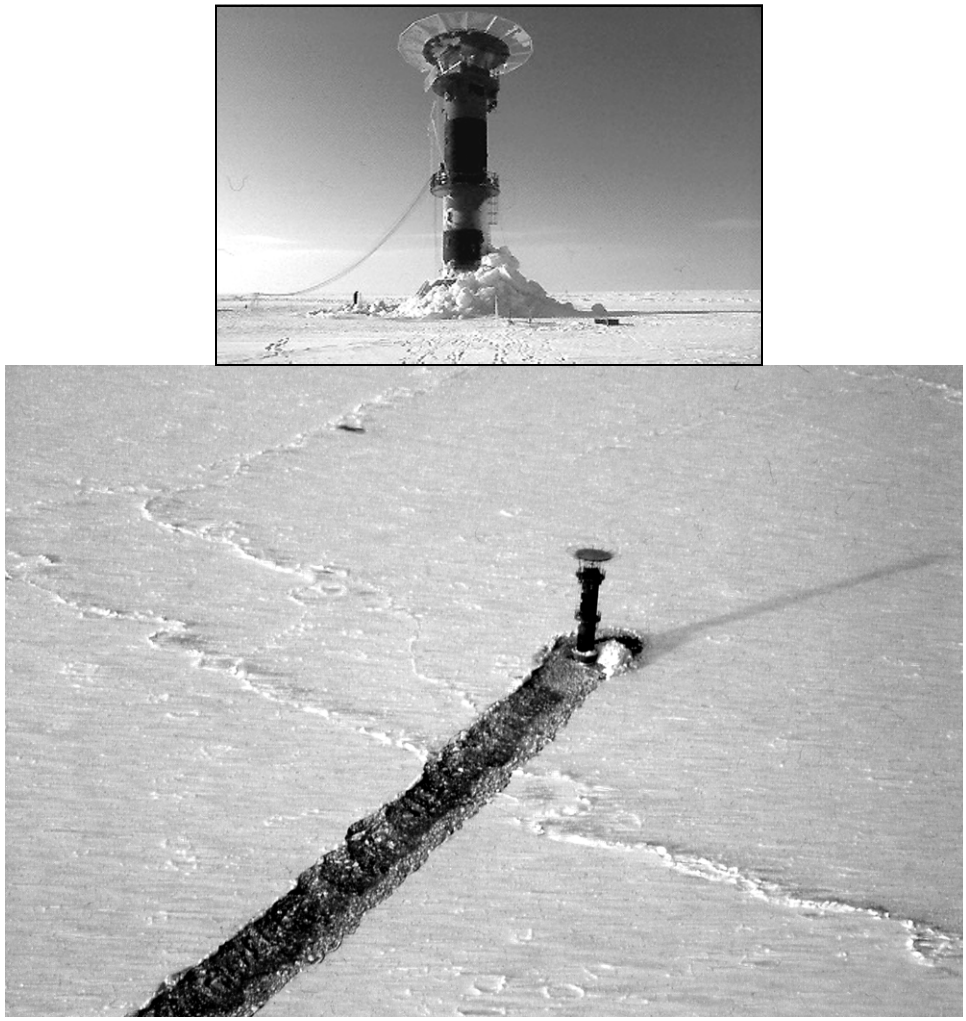

Figure 9.1 Illustration of the geophysics–engineering scaling question: the local ice forcing on the lighthouse is an ice engineering problem, while the mesoscale drift of ice past the lighthouse is a geophysical problem. The photographs are of the Baltic Sea. The topmost photograph was taken by Dr Tuomo Kärnä. It is reproduced with permission from the VTT Technical Research Centre of Finland.

So, the drift of sea ice receives many of its characteristic features from atmospheric and oceanic boundary layers in the interplay of the three media. The principal problem in this interplay is the parameterizing of the ice–ocean drag force; it is much less understood than the atmospheric drag force on the ice. In ice–ocean modelling the question of spatial resolution has yet to be answered: How can we construct high-resolution models when the continuum physics basis breaks down for sea ice?

Another interaction problem that has only recently been considered is that between sea ice and icebergs. The large-scale drift of compact sea ice forces the drift of icebergs (Lichey and Hellmer, 2001), while icebergs act as moving islands for sea ice drift. Modelling of coupled sea ice–iceberg dynamics would be highly desirable both for short- and long-term questions.

But the underlying scientific motivation for the examination of sea ice dynamics is indirect: to understand the entire atmosphere–ocean interface and consequently the physics of the atmosphere–ocean system at high latitudes. The exchange of momentum, heat, and freshwater between the atmosphere and the ocean takes place in sea ice fields, where the interface experiences changes in location and in structure due to ice motion.

Sea ice has an important role in the evolution of hydrographical conditions in the upper ocean. In the presence of ice the ocean surface temperature is locked into the freezing point, and the amplitude of the annual surface temperature cycle is small. The salinity of new ice is about half that of seawater and the salinity of multi-year ice is around 1% (e.g., Weeks, 1998a). Therefore, as sea ice grows, brine is absorbed by the surface layer, which decreases the stability of the stratification, while as sea ice melts the surface layer becomes more fresh and stable.

The location of the sea ice edge introduces a discontinuity in the air–ice–ocean interface and, consequently, particular dynamic and thermodynamic phenomena follow. In polar oceans the ice edge and oceanic polar front location constitute a coupled problem, just like the one in the austral winter in Antarctica. Whereas in small basins the location of the ice edge is basically controlled by seasonal atmospheric conditions, in the Baltic Sea the winter ice extent is well correlated with the North Atlantic Oscillation (Tinz, 1996).

The transport of ice takes sea ice to regions where it would not be formed by thermodynamic processes alone. Good examples are the southward flows of ice in the East Greenland Current and in the Labrador Current. Within the ice pack, ice transport influences the local age of ice and thus the distribution of first-year and multi-year ice. Along the whole Siberian Shelf, ice drifts north and the local ice is therefore predominantly first-year ice, much thinner than it would be without the ice motion.

The Fram Strait is the main channel of ice outflow from the central Arctic Ocean (e.g., Rudels, 1998). Ice transport is $0.1 \times 10^6\,\mathrm{m^3\,s^{-1}}$, about equal to river run-off into the basin. Ice outflow is about 5% of the outflow of polar water, but with its latent heat the ice has more influence on the heat exchange between the central Arctic Ocean and the Greenland Sea. The flow integrates to about $3 \times 10^3\,\mathrm{km^3}$ of ice in a year. The fresh water flux due to ice melting in an area of 3,000 km × 1,000 km would correspond to precipitation of 1,000 mm per year.

Due to differential sea ice drift, leads open and close, and hummocks and ridges form: this is crucially important and makes the sea ice drift problem a serious challenge, since differential motion is difficult to solve with good accuracy. Drift ice also plays a role in the life history of polynyas, as thin ice and frazil ice are easily transported due to their low strength.

Leads and polynyas constitute an extremely sensitive element in the atmosphere–ocean physics in polar seas. For the transfer of momentum, the strength of ice and therefore its mobility and stiffness are highly sensitive to leads. Heat flux in winter through open water may be up to 100 times as effective as through the ice, and in summer open-water surfaces absorb solar radiation up to 10 times as effectively as the ice cover. Consequently, heat flux is extremely sensitive to sea ice dynamics. Similarly, leads and polynyas also play an important role in the exchange of moisture between the atmosphere and the ocean.

Ridges and hummocks are thick accumulations of sea ice blocks, and with scales of 100 km their mean thickness may be two or three times as much as that of thermally grown ice. These accumulations have high strength and are no longer deformable; due to their large volume they provide thermal inertia for the melting of ice. The principal problem with our understanding of ridging and hummocking is to discover how ice is broken and rearranged into a new configuration (in particular, how the thickness distribution changes during deformation). Research on this problem is severely limited by the inadequacy of existing technical methodologies to map the thickness of sea ice.

The global sea ice cover is an important factor in the climate system. Atmosphere–ocean heat exchange is to a great extent directly affected by sea ice area and compactness at high latitudes. The summer heat budget is also present in the cryospheric albedo problem, with changes in snow and ice surface area having a positive feedback. Growth of the snow and ice area decreases the absorption of solar radiation by the Earth, which leads to further cooling and further growth of snow and ice area, etc.; the opposite is true when snow and ice area decreases. Sea ice extent can be changed by thermodynamic or dynamic forcing, while other components of the cryosphere are influenced by thermodynamics only. The drift of ice involves the transport of latent heat and freshwater; freshwater flux into the oceanic surface layer has major consequences. Corresponding to considerable precipitation, the melting of sea ice increases the stability of stratification and polar deep convection slows down. This is potentially a serious problem in the northern part of the North Atlantic Ocean and has led scientists to closely monitor the Atlantic Conveyor.

Sea ice is an important topic in the *environmental research* of ice-covered seas (Thomas and Dieckmann, 2003). During freezing and ice growth, impurities are taken by the ice sheet from the seawater, sea bottom and atmospheric fallout (Pfirman *et al.*, 1995; Lange and Pfirman, 1998). These impurities are transported with the ice and released into the water column during the short melting season. The drifting of sea ice may transport ice and these impurities over long distances, as takes place in the Arctic Ocean from the Siberian coast to the northern part of the North Atlantic Ocean (e.g., Volkov *et al.*, 2002).

Sea ice provides a unique habitat for polar microbial assemblages in ice-covered waters (e.g., Arrigo, 2003). The ice–ocean interface is an optimal habitat for algal communities, where light is sufficient for net growth. The light transfer through sea ice is a complex processes where light is absorbed and scattered back from snow and ice, a fraction penetrating into the oceanic boundary layer. The location of the ice edge with the ice melting processes is a fundamental boundary condition for the

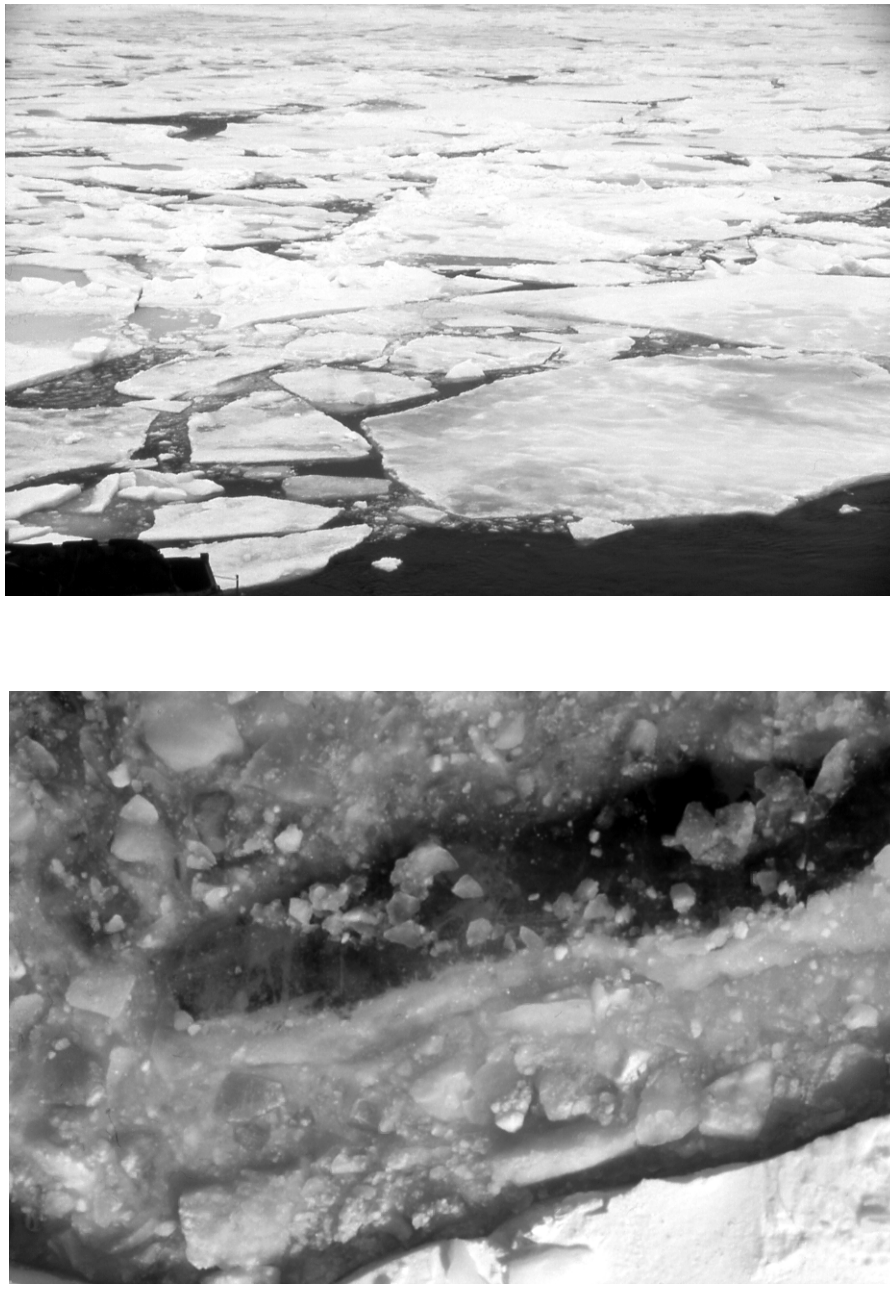

Figure 9.2 High algae productivity exists in the ocean close to the sea ice edge. (Top) Diatoms in Antarctica imparting a brownish–greenish colouring to the ice pack. (Bottom) Close-up of sea ice algae.

Reproduced with permission from Dr Johanna Ikävalko.

summer productivity (e.g., Gradinger, 1995). It has appeared that hydrographical and light conditions for primary production are excellent in the ocean surface layer close to the ice edge, and consequently the dynamics of sea ice in the MIZ is crucial for the marine biology in the region (Figure 9.2). Sea ice has also an internal biota in the brine pockets, less critically connected to the ice dynamics.

A recent research area for sea ice dynamics is palaeoclimatology and palaeoceanography (Bischof, 2000). The data archive of drift ice and icebergs exists in marine sediments and the influence of drift ice on ocean circulation has been shown to be an active agent in global climate history.

9.2 PRACTICE

In the practical world there are three major concerns connected with sea ice dynamics. First, sea ice models have been applied to aid navigation by providing short-term forecasts of ice conditions (e.g., Leppäranta, 1981a). Second, ice forcing on ships and fixed structures is affected by the dynamic behaviour of the ice (e.g., Sanderson, 1988). Third, the question of pollutant transport by drifting sea ice has become an important issue (Pfirman *et al.*, 1995; Lange and Pfirman, 1998). In particular, assessment of the risk of oil spills and the need for oil clean-up operations require proper oil transport and dispersion models for ice-covered seas (e.g., Ovsienko *et al.*, 1999a).

Sea ice information services are operational routine systems to support shipping and other marine operations, such as the drilling of oil wells in ice-covered seas. Figure 9.3 shows some modern ice information products, based on satellite information, overlain on a marine chart. Ice information services exist in all countries with seasonal sea ice zones (e.g., the Arctic and Antarctic Research Institute, St Petersburg for the Eurasian Arctic and the Canadian Ice Service, Ottawa for the American Arctic). Due to the drift of sea ice, ice conditions can change quickly; therefore ice charts need to be updated on a daily basis. Updating is done on the basis of remote sensing and occasional surface observations. However, with a proper sea ice model it should be possible to assimilate a model outcome using real data. Closely connected to real-time ice charting is short-term (1–10 days) ice forecasting. With today's ice chart as the initial situation, ice forecasts may be produced using a mathematical model up to the time limit in the available weather forecast (i.e., up to about a week). Such a forecasting model could also be applied to the assimilation problem.

Ice forecasting has become a routine activity for ice information services, and the demand for these forecasting systems is increasing. The development of the Northern Sea Route along the Eurasian coast of the Arctic Ocean will increase the shipping there, and the drilling of oil wells is expanding in the seasonal sea ice zone in the Sea of Okhotsk, the Barents Sea, and the Kara Sea.

The field of *ice engineering* attempts to evaluate forces on fixed structures and ships in an ice-covered sea. These are connected to the mobility and motion of sea ice, and thus the problem is closely linked to sea ice dynamics (Figure 9.1). Recently,

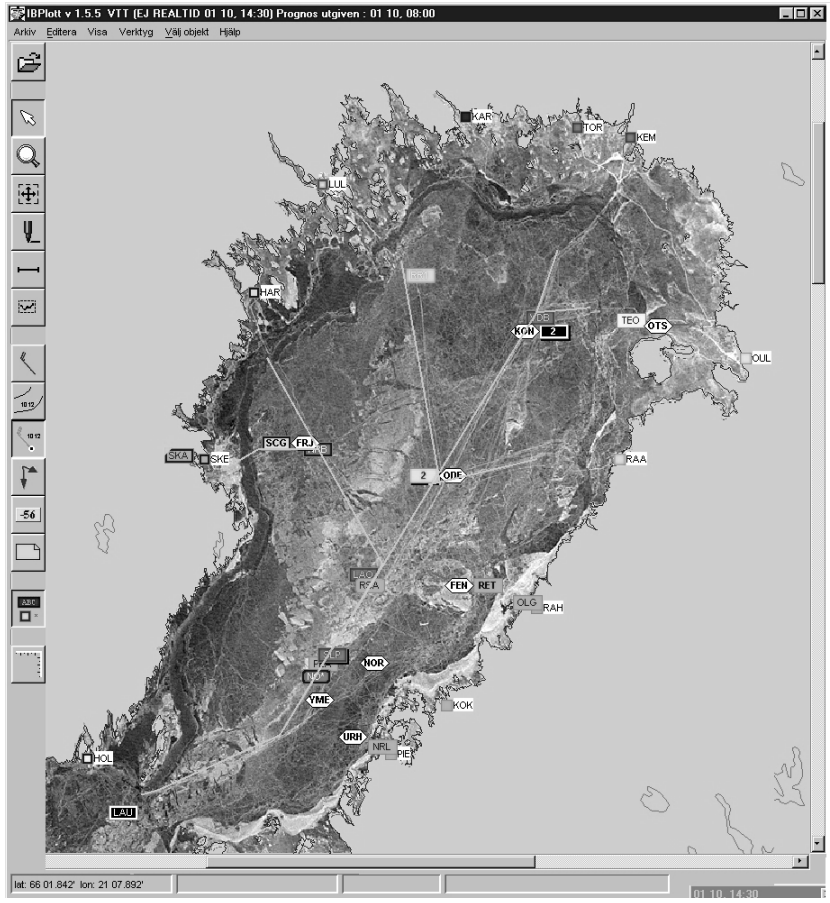

Figure 9.3 Modern sea ice information products include navigation data (depth contours, ship routes, lighthouses, ships) overlain on ice information. The picture shows the ice conditions (Radarsat image) and traffic situation in the Bay of Bothnia on 10 January 2003. Merchant ships and icebreakers are displayed as symbols on top of a radar image, and the recommended routes determined by the icebreakers are indicated. This IBPlott application is part of the distributed traffic information system IBNet used by Swedish and Finnish icebreakers.

great strides have been taken in understanding the scaling between engineering and geophysical – local scale and mesoscale – sea ice mechanics. Large loads are connected with hummocks and ridges, particularly in the seasonal sea ice zone, and progress there is still suffering from the inadequate knowledge of geophysical, full-scale processes.

Sea ice formation and evolution, including its dynamics, have seen great progress in regional oceanographic knowledge of ice-covered seas in recent years, as

reflected in the book about the Kara Sea by Volkov *et al.* (2002). For a long time, an ice-covered sea was something to avoid in observational programmes because of major practical difficulties and in oceanographic research because of the large difference between the physics of ocean waters and sea ice.

9.3 FINAL COMMENTS

The first chapter of this book gave a brief historical overview of sea ice dynamics research and an introduction to the problem of sea ice drift with its applications. Chapters 2–4 presented the drift ice medium, material properties, kinematic properties, and rheology. Chapter 5 investigated external forcing from the atmosphere and ocean, and Newton's second law was applied to obtain the equation of motion for sea ice. Chapters 6–8 pondered solutions to the sea ice drift problem for three different circumstances: free drift, analytical modelling in the presence of internal friction, and numerical modelling.

Chapter 2 provided a description of drift ice material, ice floes, and ice thickness, leading to the concept of *ice state*, a set of relevant quantities for the mechanical behaviour of drift ice. Chapter 3 dealt with ice velocity observations and proposed a theoretical framework for ice kinematics analysis. Then, the *ice conservation law* was derived for ice state. Chapter 4 treated the *drift ice rheology*, a difficult but necessary question to understand the motion of drift ice. It was recognized that the medium possesses a significant internal stress field, which influences its dynamics as an internal force field. Chapter 5 derived the *momentum equation* of ice dynamics and then went on to discuss the principal external forcing from the atmosphere and ocean, as well as magnitude and dimension analyses of the momentum equation. Altogether, ice state, ice conservation law, ice rheology and equation of motion constitute the physical basis for the closed system of equations for the sea ice drift problem.

Chapter 6 examined free drift, or drift in the absence of internal friction, leading to simple drift rules: ice velocity is equal to the wind-driven drift superposed on the ocean current beneath the layer of frictional influence of ice. Chapter 7 studied ice drift in the presence of internal friction, based on analytical 1- and 1.5-dimensional models and application of plastic rheology. Chapter 8 gave the modern-numerical modelling solution to sea ice drift, starting with an introduction to numerical modelling techniques. Chapters 6–8 considered the idea of stepwise progression to derive solutions for increasingly complicated systems. The reader following this line will be able to understand the whole solution, how it reflects the behaviour of real sea ice, and how one should interpret the outcome of numerical sea ice dynamics models. Finally, Chapter 9 briefly discussed some consequences of the ice drift phenomenon. Chapter 10 gives a collection of study problems. Chapter 11 lists the references.

The drift of sea ice is an essential element in the dynamics of polar oceans, those essential and fragile components of the world's climate system. The drift transports sea ice over long distances, even to regions where ice is not formed by thermodynamic processes. At the same time the ice transports latent heat and freshwater;

the influence of icemelt on the salinity of the mixed layer is equivalent to considerable precipitation. The ice cover forms a particular airsea interface, which is modified drastically by differential ice motion. Consequently, sea ice dynamics is a key factor in air–sea interaction processes in the polar oceans. This is of renewed interest owing to the increasingly growing concern about man-made global warming.

The drift of ice is also a major ecological and environmental factor. Ice margin regions are known for their high biological productivity because of favourable light and hydrographical conditions. Therefore, their location – to some degree determined by the drift of ice – is of deep concern in marine ecology. Pollutants accumulate in the ice sheet, originating from the water body, sea bottom, and atmospheric fallout, and they are transported within the ice over long distances. A particular pollutant question is oil spills.

Sea ice has always been a barrier to winter shipping. For the purpose of sea ice monitoring and forecasting, ice information services collect and distribute ice charts and forecasts. The drift of ice shifts the ice edge, opens and closes leads, and forms pressure zones, all of which are key to ice navigation. The timescale of remarkable changes is 1 day. Presently, expansion of the Northern Sea Route requires further development in sea ice-mapping and forecasting services.

All in all, the reading of Chapters 1–8 provides a complete overview of the problems associated with measuring, geophysics, and the modelling of sea ice drift. The principal idea has been to include the whole story of sea ice dynamics in a single book, from material state through dynamics laws to mathematical models. The first edition of this book – *The Drift of Sea Ice* – satisfied a crying need for a synthesis of these research endeavours, as sea ice dynamics applications had been increasing and, apart from review papers, there was no book dedicated to this topic in English. Now, after five years, the second edition presents an update of knowledge in sea ice dynamics with corrections of some shortcomings and technical details in the first edition.

10

Study problems

10.1 PROBLEMS

CHAPTER 1

1 If all the sea ice melted, how would the sea surface level be affected?

2 Assume that the sea ice melt rate is cuT_w, where c is a heat exchange coefficient, u is ice velocity and T_w is water temperature. An ice floe with thickness h_0 starts to drift with constant speed from the origin along the x-axis. How far would it get if the water temperature increases linearly with space, $T_w = ax$? What is the optimum speed? Work through the numerical example: $h_0 = 1\,\text{m}$, $c = 10^{-6}\,^\circ\text{C}^{-1}$, $a = 1^\circ\text{C}/100\,\text{km}$, $u = 10\,\text{cm/s}$.

3 A strong wind blows across a basin totally covered by 1-m thick sea ice and drives the ice to drift by 20 cm/s. How wide wil the lead open on the lee side in six hours? On the opposite side, how thick will the deformed ice zone be at the same time, if its width is 1 km and the ice is evenly packed?

CHAPTER 2

1 With an ice thickness is 50 cm, how large would an ice floe need to be for you to stand on it with dry feet?

2 For uniform circular ice floes, and where floes are locked together, show that the most open and dense packings are $\pi/4 \approx 0.79$ and $\pi/(2\sqrt{3}) \approx 0.91$.

3 Show that the median, mean, and root-mean-square values are $\lambda^{-1}\log 2$, λ^{-1}, and $\lambda^{-1}\sqrt{2}$, respectively, for a random variable with exponential distribution; the probability density is $p(x;\lambda) = \lambda\exp(-\lambda x)$, $x \geq 0$. What is the 95% fractile $x_{0.95}$, defined by $\text{Prob}(x \leq x_{0.95}) = 0.95$?

M. Leppäranta, *The Drift of Sea Ice*, Springer Praxis Books,
DOI 10.1007/978-3-642-04683-4_10, © Springer-Verlag Berlin Heidelberg 2011

4 Assume that the surface temperature is negative and averages to Θ during nine winter months, and for three summer months the radiation balance is $(1-\alpha)Q_s + Q_{nL} > 0$, where α is the albedo, Q_s is the mean incoming solar radiation, and Q_{nL} is the mean net long-wave radiation. The ice grows according to the Stefan's law in winter and melts by the solar radiation in summer.
(a) Determine the conditions for the survival of the ice over summer and the equilibrium thickness of multi-year ice.
(b) What is the sensitivity of the multi-year ice thickness to Θ and α?
(c) Work through the numerical example: $\Theta = -20°\text{C}$, $\alpha = 0.4$, $Q_s = 150\,\text{W/m}^2$, and $Q_{nL} = -50\,\text{W/m}^2$.

5 The ratio of sail height to keel depth is 1:5 and 1:3 for first-year and multiyear sea ice ridges. How is the difference explained from geometry?

CHAPTER 3

1 (a) An ice floe is drifting along the latitude ϕ with speed u. How long does it take to complete the full latitude cycle? Work through the numerical example: $\phi = 70°\text{S}$, $u = 10\,\text{cm/s}$.
(b) An ice floe starts from the North Pole at velocity v along the zero meridian on the 1st of January. When does it meet the polar front with warm waters at 75°N, $v = 5\,\text{cm/s}$?

2 (a) Derive the mathematical expressions of eigenvalues and eigenvectors for two-dimensional symmetric tensor.
(b) Show that the sum of squared components of a two-dimensional symmetric tensor is invariant.

3 Analyze strain-rate tensor of the zonal flow: full expression, eigenvalues and eigenvectors, and invariants. How does a 10-km square, oriented in xy coordinate axes, change in one day, if $\partial u/\partial x = 10^{-6}\,\text{s}^{-1}$ and $\partial v/\partial x = 5 \cdot 10^{-6}\,\text{s}^{-1}$.

4 Consider a stochastic ice drift model $\text{d}u/\text{d}t = -\lambda(u - U_w) + \varepsilon$, where λ is constant, u and U_w are ice and ocean current velocities, and ε is white noise with variance σ^2. Examine the spectrum of ice velocity for periodic ocean currents.

5 Derive the conservation law for ice compactness in spherical coordinates on the Earth's surface.

CHAPTER 4

1 Lake Ladoga is a lake in North Europe of size $150\,\text{km} \times 100\,\text{km}$. In principle, it is possible to put all the people in the world on the ice of the lake by allocating each person a 1-m^2 spot. But under what conditions would this be physically possible?

2 How long can an icicle with a uniform cross-section grow? Take the tensile strength of ice to be equal to 1 MPa.

3 Show that for an incompressible Newtonian viscous fluid, $\boldsymbol{\sigma} = -p\mathbf{I} + \eta\dot{\boldsymbol{\varepsilon}}$, where p is hydrostatic pressure and $\eta =$ constant is viscosity, the stress divergence consists of a pressure gradient and internal friction as $\nabla \cdot \boldsymbol{\sigma} = -\nabla p + \eta\nabla^2\boldsymbol{u}$.

4 Derive the relationship between stress and strain for a square yield curve with corner points $(0, \sigma_2)$, (σ_1, σ_y), (σ_y, σ_2), and $(\sigma_1, 0)$, where $\sigma_y < 0$ is the uniaxial compressive yield strength.

CHAPTER 5

1 Gravity measurements are normally difficult to perform in the open ocean. Lehmuskoski and Mäkinen (1978) have made gravity measurements on drifting ice in the Baltic Sea. The drifting platform introduces a change in the apparent gravity via the Coriolis effect. Estimate the magnitude of this effect (called the Eötvös effect in gravimetry) when the ice velocity is 10 cm/s.

2 Derive the sea surface tilt term with horizontal surface as the zero reference.

3 Show that the following relationship holds between the roughness length and drag coefficient: $z_0/z = \exp(\kappa/\sqrt{C_z})$.

4 Estimate the magnitudes of the forces in the ice equation of motion by scaling analysis as well as possible, when
(a) Wind speed = 20 m/s, ice velocity = 40 cm/s;
(b) Wind speed = 10 m/s, ice velocity = 10 cm/s; and
(c) Wind = 2 m/s, ice velocity = 1 cm/s.
The geostrophic current is 5 cm/s and ice thickness is 1 or 3 m.

5 Examine the ice drift problem and assume that $C_w = 0$. What are the dominant forces and key dimensionless numbers?

CHAPTER 6

1 An ice floe, thickness 1 m, is drifting free in the Antarctic circumpolar current at 60°S. The ocean current is 10 cm/s eastward along the latitude circle and the wind is 10 m/s from the west. Determine the total displacement of the floe in one month.

2 In a horizontal channel, ice is moving at a steady state speed u driven by the wind stress. When the wind ceases, how far will the floe traavel before stopping?

3 Assume an open channel flow, water depth H and channel inclination β. How is the total discharge affected when part of the water is frozen into a sea ice lid of thickness h which drifts freely?

4 For a perturbation approach, let $U = \tilde{U} + E$ where $\tilde{U}$ is the mean level of the drift and E is the first order perturbation. Derive the free drift solution including the first order terms. How does it compare with the linear solution?

5 The Newton-Raphson iteration scheme for a pair of nonlinear equations $F(X, Y)$ is written

$$(X, Y)^{(n+1)} = (X, Y)^{(n)} - F^{(n)}[(\mathrm{DF})^{(n)}]^{-1},$$

where DF is the gradient 2×2 matrix of F. Use this to solve the wind factor and deviation angle from the wind-driven free drift equation.

(a) Write the iteration scheme in explicit form.

(b) Work through the numerical example: wind = 3, 5, 10, 15 m/s and ice thickness = 0.1, 0.5, 1, 2, 3, 6 m.

CHAPTER 7

1 Construct the solution of the one-dimensional channel drift forced by a constant current velocity. The channel is closed for ice drift at $x = L$ and in the beginning the ice covers the region from 0 to L with compactness equal to 1 and thickness equal to 1 m.

2 (Laikhtman problem) Solve the coastal ice drift subject to viscous rheology:

$$\eta \frac{\mathrm{d}^2 v}{\mathrm{d}x^2} - c_1 v + c_a V_a = 0$$

where $\eta \approx 10^8$–10^{10} kg/s, v is the alongshore ice velocity, x is the distance from the shore, c_1 and c_a are linear drag coefficients, and V_a is wind speed. The boundary conditions are zero velocity (no slip) at coast and free drift as $x \to \infty$. Take $V_a = 10$ m/s and find suitable values for c_1 and c_a.

3 Solve the coastal steady state plastic ice flow problem when the ice–ocean interaction is ignored.

4 Assume a 30° on-ice surface wind in the northern hemisphere, with the marginal ice zone (MIZ) on the left of the wind. Solve the steady state plastic flow with the thickness and compactness distribution, when initially ice thickness is 1 m, concentration is 80%, and width of the MIZ is 200 km:

(a) wind speed is 10 m/s;

(b) wind speed increases from zero to 20 m/s across the MIZ.

5 Solve the steady-state plastic circular flow in polar coordinates. Compare the solution of the East wind drift in Antarctica between polar and spherical coordinates.

CHAPTER 8

1 Write a consistent, discrete formula for the internal friction of drift ice assuming the plastic flow with elliptic yield curve. Use the Taylor's polynomial to obtain approximations for the derivatives. Note: consistency means that the original differential form results when the grid size approaches zero.

2 Write numerical model equations for a one-dimensional plastic channel flow including ice thickness conservation law and momentum equation. Integrate the model for one day when the channel length is 200 km and the grid size is 10 km. The wind speed is 10 m/s on-ice, and initially ice thickness is 1 m and ice concentration is 100%. The quasi-steady approach may be taken.

3 Take a rectangular basin 200 km 100 km, and ignore the Coriolis acceleration, Ekman angle in the ocean, and the geostrophic ocean current. Solve numerically the steady-state plastic flow for ice thickness equal to 1 m and ice concentration 100%, wind speed 10 m/s along the major axis of the basin, and a yield curve that is (a) square and (b) elliptic.

4 Solve numerically the ice drift pass a circular island of radius r using a linear viscous and a plastic rheology. Choose the grid size equal to $r/3$.

10.2 INSTRUCTIONS AND SOLUTIONS

CHAPTER 1

1 No change in the sea level elevation.

2 The distance is $\sqrt{\frac{2h_0}{ca}}$, independent of the velocity. In the numerical example the distance is 447 km.

3 The lead width is 5 km and the thickness of the deformed ice zone is 6 m.

CHAPTER 2

1 The floating condition is $Ah(\rho_w - \rho) \geq m$, where A is floe area, h is ice thickness, ρ_w and ρ are water and ice densities, and m is your mass.

2 A circle in square takes relative volume of $\pi/4$, which corresponds to the most open packing; when circle rows are displaced by half radius from each other the densest packing is obtained.

3 Mean and root-mean-square are integrals of $xp(x;\lambda)$ and $x^2p(x;\lambda)$, respectively, from 0 to infinity. Median and 95% fractile are obtained from $P(x^*;\lambda) = 0.5$ and 0.95, respectively, where $P(x^*;\lambda) = \int_0^{x^*} p(x;\lambda)\mathrm{d}x$.

4 Multiyear equilibrium thickness (H) is obtained from

$$H = \frac{at_F(\Theta - T_f)}{2\Delta H} - \frac{\Delta H}{2}, \quad \Delta H = \frac{(1-\alpha)Q_s + Q_{nL}}{\rho L}\, t_M, \quad H \geq 0$$

where $a \approx 11\,\mathrm{cm^2\,d^{-1}\,^\circ C}$, $t_F = 9$ months, T_f is freezing point of sea water, ρ is ice density, L is latent heat of freezing, and t_M is three months. (a) The condition for existence of multiyear ice is that $H > 0$. (b) The sensitivity is obtained from partial derivatives:

$$\delta H|_\Theta = \frac{\partial H}{\partial \Theta}\,\delta\Theta = \frac{at_F}{2\Delta H}\,\delta\Theta, \quad \delta H|_{\Delta H} = -\left\lfloor \frac{at_F}{2(\Delta H)^2} + \frac{1}{2} \right\rfloor \delta(\Delta H)$$

The latter form provides the sensitivity for α and Q_{nL}. (c) 3.6 m.

5 Floating ridges satisfy Archimedes law:

$$\frac{\nu_s \cot\phi_s h_s^2}{\nu_k \cot\phi_k h_k^2} = \frac{\rho_w - \rho}{\rho} \approx \frac{1}{9}$$

where ν is porosity, ϕ is slope angle, h thickess, and subscript s and k refer to sail and keel. If porosity and slopes are equal, the ratio $h_s : h_k$ is 1:3, with different slopes 1:5 can be obtained.

CHAPTER 3

1 (a) 4.3 years
(b) 22 January in the following year.

2 (a) See Eqs. (3.10)
(b) Take matrix $\boldsymbol{A}$; rotate the matrix to a new cocordinate system by $\boldsymbol{A}' = \boldsymbol{Q}^T\boldsymbol{A}\boldsymbol{Q}$, where

$$\boldsymbol{Q} = \begin{pmatrix} \cos\vartheta & \sin\vartheta \\ -\sin\vartheta & \cos\vartheta \end{pmatrix}$$

Upper index T stands for transpose and ϑ is the angle between the coordinate systems. Show then that the sum of squares of $\boldsymbol{A}$ and $\boldsymbol{A}'$ are equal.

3 As 2(a) with matrix

$$\dot{\varepsilon} = \begin{pmatrix} \dfrac{\partial u}{\partial x} & \dfrac{1}{2} \cdot \dfrac{\partial v}{\partial x} \\ \dfrac{1}{2} \cdot \dfrac{\partial v}{\partial x} & 0 \end{pmatrix}$$

A 10 km square along xy axes is stretched by 864 m in one day for $\partial u/\partial x = 10^{-6}\,\mathrm{s}^{-1}$ and the square angles change by 24.8° in one day for $\partial v/\partial x = 5 \cdot 10^{-6}\,\mathrm{s}^{-1}$

4 The spectrum is

$$p(\omega) = \frac{p_w(\omega)}{|1 + \mathrm{i}(\omega/\lambda)|^2}$$

where $p_w(\omega)$ is the ocean current spectrum. If ocean current is periodic with frequency ω^*, it appears equally strong in sea ice if $\omega^* \ll \lambda$ and disappears when $\omega^* \gg \lambda$. The relaxation time scale λ^{-1} is of the order of one hour.

CHAPTER 4

1 There are two conditions: floating and strength. For floating, the buoyancy of 1 m thick ice of 1 m^2 horizontal area is enough for 90 kg (see Task 1, Chapter 2). The bearing capacity of 1 m ice is 50 tons (see Section 4.1.1) corresponding to 550 persons weighing 90 kg each, distributed into a square of 24 m. The radius of influence is 30 m for a point load for 1-m thick ice, and therefore the bearing capacity is close to the limit.

2 110 m.

3 Straight mathematical manipulation: $\nabla \cdot (p\mathbf{I}) = -\nabla p$ and $\nabla \cdot (\eta\dot{\varepsilon}') = \eta\nabla^2\boldsymbol{u}$ using the condition $\nabla \cdot \boldsymbol{u} = 0$ for incompressible fluids.

4 When one principal stress reaches the yield curve, uniaxial failure takes place directed normal to the yield curve.

CHAPTER 5

1 Coriolis acceleration is $2\underline{\Omega} \times \underline{\boldsymbol{u}}$, its vertical component is thus $u2\Omega\cos\phi$. Taking the latitude 60°N corresponding to the Baltic Sea, the Eötvös effect becomes $7.3 \times 10^{-6}\,\mathrm{m\,s}^{-2}$.

2 This comes out from the vertical integration of the momentum equation by changing the level $z = 0$ from sea surface to horizontal plane.

3 Use definitions of surface stress and logarithmic velocity profile.

4 Estimate magnitudes of wind stress from wind velocity, pressure gradient from geostrophic current, Coriolis acceleration from ice velocity, and ice–water stress from ice velocity (note that the ice–water differential velocity is within ice velocity $\pm$ geostrophic current leaving some uncertainty). Local and advective accelerations cannot be estimated but they can be assumed small. Then internal friction comes as a residual term from the others. The case becomes more strict when directions are assumed for the velocities.

CHAPTER 6

1 The wind factor is taken as 3% and the direction of wind-driven drift is 30° to the left from the wind direction. In one month displacement is 1010 km directed to 22.6° to the left from the wind.

2 Integration of the spin-down solution under quadratic ice–water stress gives distance $= \infty$.

3 Start from Eq. (6.11).

5 Use Figure 6.1b to verify the result.

CHAPTER 7

1 We can assume that $U_w \geq u \geq 0$ and $A \equiv 1$. Take ice strength as $P = P^*h$. Quasi-steady system is given as

$$u = U_w - \sqrt{\frac{P^*}{\rho_w C_w}\frac{dh}{dx}}$$

$$h_{i,j+1} = h_{ij}[1 - c(u_{i+1,j} - u_{i-1,j})] - cu_{ij}[h_{i+1,j} - h_{i-1,j}]c = \frac{\Delta t}{2\Delta x}$$

where lower index i refers to x-axis and j refers to time. Then u and h are solved in turn from these equations.

2 This is a linear second order equation with constant coefficients, and it integrates directly into

$$v = \left\lfloor 1 - \exp\left(-\sqrt{\frac{c_1}{\eta}}x\right)\right\rfloor \frac{c_2}{c_1} V_a$$

We must have $c_2/c_1 \approx 2\%$ and $\sqrt{\eta/c_1} \approx 50\,\text{km}$ for realistic free drift and length scales. Taking $\eta = 10^9\,\text{kg s}^{-1}$, then $c_1 = 0.40\,\text{kg m}^2\,\text{s}^{-1}$ and $c_2 = 0.0080\,\text{kg m}^2\,\text{s}^{-1}$, for $V_a = 10\,\text{m s}^{-1}$, the velocity approaches $20\,\text{cm s}^{-1}$ far from the coast.

3 Free drift solution is $u = \tau_{ay}/(\rho h f)$, $v = -\tau_{ax}/(\rho h f)$. It is offshore, and here a valid solution is when $\tau_{ay} > 0$. For coastal shear flow, thus $\tau_{ay} \leq 0$. Then we have

$$v = -\frac{\tau_{ax} \pm e^{-1}\tau_{ay}}{\rho h f}$$

where in $\pm$, the $+$ sign is taken for southward flow and the $-$ sign for northward flow; inconsistent solutions are taken as $v = 0$.

4 Velocity is obtained from Eq. (7.29) and thickness and compactness profiles from Eq. (7.35).

5 The solutions are given in Section 7.3.6, from where the comparison can be made directly.

CHAPTER 8

The problems concern preparation of simple numerical models.

11

References

Adams, R.A. (1995) *Calculus: A Complete Course*, 3rd edn. Addison-Wesley, Don Mills, Ontario.

Agnew, T.A., Le, H. and Hirose, T. (1997) Estimation of large scale sea ice motion from SSM/I 85.5 GHz imagery. *Annals of Glaciology* **25**, 305–311.

Ahlfors, L.V. (1966) *Complex Analysis*. McGraw-Hill, New York.

Albright, M. (1980) Geostrophic wind calculations for AIDJEX. In: R.S. Pritchard (ed.), *Sea Ice Processes and Model* (pp. 402–409). University of Washington Press, Seattle.

Ames, W.F. (1977) *Numerical Methods for Partial Differential Equations,* 2nd edn. Academic Press, New York.

Andreas, E.L. (1998) The atmospheric boundary layer over polar marine surfaces. In: M. Leppäranta (ed.), *Physics of Ice-Covered Seas* (Vol. II, pp. 715–773). Helsinki University Press, Helsinki.

Andreas, E.L. and Claffey, K.J. (1995) Air-ice drag coefficients in the western Weddell Sea: 1. Values deduced from profile measurements. *Journal of Geophysical Research* **100**, 4821–4831.

Andreas, E.L., Tucker, W.B., III, and Ackley, S.F. (1984) Atmospheric boundary layer modification, drag coefficient, and surface net heat flux in the Antarctic marginal ice zone. *Journal of Geophysical Research* **89**, 649–661.

Appel, I.L. (1989) Variability of thickness of ice and snow in Arctic seas and its parametrization. *Meteorologiya i Gidrologiya* **3**, 80–87.

Arberter, T.E., Curry, J.A., and Maslanik, J.A. (1999) Effects of rheology and ice thickness distribution in a dynamic-thermodynamic sea ice model. *Journal of Physical Oceanography* **29**, 2656–2670.

Armstrong, T., Roberts, B., and Swithinbank, C. (1966) *Illustrated Glossary of Snow and Ice*. Scott Polar Research Institute, Cambridge, UK.

Arrigo, K.R. (2003) Primary production in sea ice. In: D.N. Thomas and G.S. Dieckmann (eds.). *Sea Ice: An Introduction to its Physics, Chemistry, Biology, and Geology*, pp. 143–183, Blackwell Publishing, Oxford, UK.

Arya, S.P.S. (1975) A drag partition theory for determining the large-scale roughness parameter and wind stress on the Arctic pack ice. *Journal of Geophysical Research*, **80**(24), 3447–3454.

M. Leppäranta, *The Drift of Sea Ice*, Springer Praxis Books,
DOI 10.1007/978-3-642-04683-4, © Springer-Verlag Berlin Heidelberg 2011

Assur, A. (1963) Breakup of pack ice floes. In: Kingery, W.D. (ed.), *Ice and snow* (pp. 335–347). MIT Press.

Babko, O., Rothrock, D.A. and Maykut, G.A. (2002) Role of rafting in the mechanical distribution of sea ice thickness. *Journal of Geophysical Research* **107**(C8), 27.

Banke, E.G., Smith, S.D., and Anderson, R.J. (1980) Drag coefficients at AIDJEX from sonic anemometer measurements. In: R.S. Pritchard (ed.), *Sea Ice Processes and Models* (pp. 430–442). University of Washington Press, Seattle.

Belchansky, G.I. and Douglas, D.C. (2002) Seasonal comparisons of sea ice concentration estimates derived from SSM/I, OKEAN, and RADARSAT data. *Remote Sensing of Environment* **81**, 67–81.

Belliveau, D.J., Bugden, G.L., Eid, B.M., and Calnan, C.J. (1990) Sea ice velocity measurements by upward-looking Doppler current profilers. *Journal of Atmospheric and Oceanic Technolog,* **7**, 596–602.

Bischof, J. (2000) *Ice Drift, Ocean Circulation and Climate Change*. Springer-Praxis, Chichester, UK.

Bjerkås, M., Moslet, P.O., Jochmann, P., and Løset, S. (2003) Global ice loads on the lighthouse Norströmsgrund in the winter 2001. *Proceedings of the 17th International Conference on Port and Ocean Engineering under Arctic Conditions (POAC '03)*. Trondheim, Norway, June 16–19, 2003.

Blondel, P. and Murton, B.J. (1997) *Handbook of Seafloor Sonar Imagery*. Wiley-Praxis, Chichester, UK.

Bourke, R.H. and Garret, R.P. (1987) Sea ice thickness distribution in the Arctic Ocean. *Cold Regions Science and Technology* **13**, 259–280.

Brennecke, W. (1921). Die ozeanographischen Arbeiten der Deutschen Antarktischen Expedition 19111912. *Archiv der Deutschen Seewarte*, **XXXIX** Jahrgang, Nr. 1. Hamburg.

Brown, R.A. (1980) Boundary-layer modeling for AIDJEX. In: R.S. Pritchard (ed.), *Sea Ice Processes and Models* (pp. 387401). University of Washington Press, Seattle.

Bukharitsin, P.I. (1986) Calculation and prediction of rafted ice thickness in navigable regions of the northwestern Caspian Sea. *Meteorologiya i Gidrologiya* **4**, 87–93.

Bushuyev, A.V., Volkov, N.A., Gudkovich, Z.M., and Loshchilov, V.S. (1967) Rezul'taty ekspeditsionnykh issledovanii dreifa I dinamiki ledianogo pokrova Arkticheskogo Basseina Vesnoi, 1961g. [Results of expedition investigations of the drift and dynamics of the ice cover of the Arctic Basin during the spring of 1961]. *Trudy. Arkticheskii i Antarkticheskii Nauchno-issledovatel'skii Institut* **257**, 26–44. Leningrad. [Engl. summary AIDJEX Bulletin **3**, 1–21]

Campbell, W.J. (1965) The wind-driven circulation of ice and water in a polar ocean. *Journal of Geophysical Research* **70**, 3279–3301.

Campbell, W.J. and Rasmussen, L.A. (1972) A numerical model for sea ice dynamics incorporating three alternative ice constitutive laws. In: T. Karlsson (ed.), *Sea Ice: Proceedings of an International Conference* (pp. 176–187). National Research Council, Reykjavik.

Carsey, F. (ed.) (1992) *Microwave Remote Sensing of Sea Ice* (Geophysical Monograph 68). American Geophysical Union, Washington, DC.

Cavalieri, D., Gloersen, P., and Zwally, J. (1999 updated regularly) Near real-time DMSP SSM/I daily polar gridded sea ice concentrations. Edited by J. Maslanik and J. Stroeve. NSIDC. Boulder, CO. (`http://nsidc.org/`)

Chamberlain A.C. (1983) Roughness lengths of sea, sand and snow. *Boundary Layer Meteorology* **25**, 405409.

Charnock, H. (1955) Wind stress on water surface. *Quarterly Journal of Royal Meteorological Society* **81**, 639.

Chieh, S.-H., Wake, A., and Rumer, R.R. (1983) Ice forecasting model for Lake Erie. *Journal of Waterway, Port, Coastal and Ocean Engineering* **109**(4), 392–415.

Colony, R. and Thorndike, A.S. (1984) An estimate of the mean field of Arctic sea ice motion. *Journal of Geophysical Research* **89**(C6), **10**, 623–10, 629.

Colony, R. and Thorndike, A.S. (1985) Sea ice motion as a drunkard's walk. *Journal of Geophysical Research,* **90**(C1), 965–974.

Comiso, J. C. (2002) A rapidly declining perennial sea ice cover in the Arctic. *Geophysical Research Letters* **29**(20), 1956, doi:10.1029/2002GL015650.

Coon, M.D. (1974) Mechanical behaviour of compacted Arctic ice floes. *Journal of Petroleum Technology* **257**, 466–479.

Coon, M.D. (1980) A review of AIDJEX modeling. In: R.S. Pritchard (ed.), *Proceedings of ICSI/AIDJEX Symposium on Sea Ice Processes and Models* (pp. 12–23). University of Washington, Seattle.

Coon, M.D. and Pritchard, R.S. (1974) Application of an elastic-plastic model of Arctic pack ice. In: J.C. Sater and J.C. Reed (eds.), *The Coast and Shelf of the Beaufort Sea* (pp. 173–193). Arctic Institute of North America, Washington, D.C.

Coon, M.D. and Pritchard, R.S. (1979) Mechanical energy considerations in sea-ice dynamics. *Journal of Glaciology* **24**(90), 377–389.

Coon, M.D., Maykut, G.A., Pritchard, R.S., Rothrock, D.A., and Thorndike, A.S. (1974) Modeling the pack ice as an elastic-plastic material. *AIDJEX Bulletin* **24**, 1–105.

Coon, M.D., Knoke, G.S., Echert, D.C., and Pritchard, R.S. (1998) The architecture of an anisotropic elastic-plastic sea ice mechanics constitutive law. *Journal of Geophysical Research* **103**(C10), **21**, 915–21, 925.

Crow, E.L. and Shimizu, K. (eds.) (1988) *Logarithmic Normal Distribution: Theory and Application*. Marcel Dekker, New York.

Curry, J.A. and Webster, P.J. (1999) *Thermodynamics of Atmospheres and Ooceans*. Academic Press, San Diego, CA.

Cushman-Roisin, B. (1994) *Introduction to Geophysical Fluid Dynamics*. Prentice-Hall, Englewood Cliffs, NJ.

Dempsey, J.P. and Shen, H.H. (eds.) (2001) *IUTAM Symposium on Scaling Laws in Ice Mechanics*. Kluwer Academic, Dordrecht, the Netherlands.

Dierking, W. (1995) Laser profiling of the ice surface topography during the Winter Weddell Gyre Study 1992. *Journal of Geophysical Research* **100**(C3), 4807–4820.

Divine, D.V. (2003) Peculiarities of shore-fast ice formation and destruction in the Kara Sea. PhD thesis, University of Bergen, Norway.

Doble, M. (2008) Simulating pancake and frazil ice growth in the Weddell Sea: A process model from freezing to consolidation. *Journal of Geophysical Research* **114**(C09003), doi: 10.1029/2008JC004935.

Doronin, Yu.P. (1970) On a method of calculating the compactness and drift of ice floes. *Trudy Arkticheskii i Antarkticheskii Nauchno-issledovatel'skii Institut* **291**, 5–17 [English transl. 1970 in AIDJEX *Bulletin* **3**, 22–39].

Doronin, Yu.P. and Kheysin, D.Ye. (1975) *Morskoi led [Sea Ice]* (318 pp.). Gidrometeoizdat, Leningrad [English transl. 1977 by Amerind, New Delhi].

Drucker, D.C. (1950) Some implications of work hardening and ideal plasticity. *Quantitative Applied Mathematics* **7**, 411–418.

Dulière, V. and Fichefet, T. (2007) On the assimilation of ice velocity and concentration data into large-scale sea ice models. *Ocean Science Discussions,* **4**, 265–301.

Eicken, H. and Lange, M. (1989) Development and properties of sea ice in the coastal regime of the southern Weddell Sea. *Journal of Geophysical Research* **94**, 8193–8206.

Ekman, V.W. (1902) Om jordrotationens inverkan på vindströmmar i hafvet. *Nyt Magasin för Naturvidenskab B* **40**, 1.

Ekman, V.W. (1904) On dead water. In: F. Nansen (ed.), *The Norwegian North Polar Expedition 1893–1896: Scientific Results* (Vol. V, pp. 1–152). Copp, Clark, Mississauga, Ontario.

Erlingsson, B. (1988) Two-dimensional deformation patterns in sea ice. *Journal of Glaciology* **34**(118), 301–308.

Evans, R.J. and Untersteiner, N. (1971) Thermal cracks in floating ice sheets. *Journal of Geophysical Research,* **76**, 694–703.

Feller, W. (1968) *An Introduction to Probability Theory and Its Applications* (Vol. 1). John Wiley & Sons Inc., New York.

Fily, M. and Rothrock, D.A. (1987) Sea ice tracking by nested correlations. *IEEE Transactions on Geoscience and Remote Sensing* **GE-24**(6), 570–580.

Fissel, D.B. and Tang, C.L. (1991) Response of sea ice drift to wind forcing on the north-eastern Newfoundland Shelf. *Journal of Geophysical Research* **96**(C10): 18,397–18,409.

Flato, G.M. (1993) A particle-in-cell method sea-ice model. *Atmosphere-Ocean* **31**(3), 339–358.

Flato, G.M. and Hibler, W.D., III (1990) On a simple sea-ice dynamics model for climate studies. *Annals of Glaciology* **14**, 72–77.

Flato, G.M. and Hibler, W.D., III (1995) Ridging and strength in modelling the thickness distribution of Arctic sea ice. *Journal of Geophysical Research* **100**(C9), 18611–18626.

Frederking, R., Kubat, I., and Prinsenberg, S. (2006) Response of two piers on Confederation Bridge to ice loading event of April 4, 2003. *Proceedings of the 18th International Symposium on Ice, IAHR'06,* Vol. 1, pp. 231–238. Sapporo, Japan.

Frolov, I.E., Gudkovich, Z.M., Radionov, V.R., Shirochkov, A.V., and Timokhov, L.A. (2005) *The Arctic Basin. Results from Russian Drifting Stations*. Springer-Praxis, Chichester, UK.

Frolov, I.E., Gudkovich, Z.M., Karklin, V.P., Kovalev, E.G., and Smolyanitsky, V.M. (2009) *Climate Change in Eurasian Arctic Shelf Seas: Centennial Ice Cover Observations*. Springer-Praxis, Chichester, UK.

Fukamachi, Y., Shirasawa, K., Polomoshnov, A.M., Ohshima, K.I., Kalinin, E., Nihashi, S., Melling, H., Mizuta, G., and Wakatsuchi, M. (2009) Direct observations of sea-ice thickness and brine rejection off Sakhalin in the Sea of Okhotsk. *Continental Shelf Research* **29**, 1541–1548.

Fukutomi, T. (1952). Study of sea ice (the 18th report): Drift of sea ice due to wind in the Sea of Okhotsk, especially in its southern part. *Low Temperature Science* **9**, 137–144.

Garratt J.R. (1977) Review of drag coefficients over oceans and continents. *Monthly Weather Review* **105**, 915–929.

Garrett, C. (1985) Statistical prediction of iceberg trajectories. *Cold Regions Science and Tecnology* **11**, 255–266.

Gill, A.E. (1982) *Atmosphere-Ocean Dynamics*. Academic Press, New York.

Glen, J.W. (1958) The flow law of ice. *International Association of Scientific Hydrology* **47**, 171–183.

Glen, J.W. (1970) Thoughts on a viscous model for sea ice. *AIDJEX Bull*etin **2**, 18–27.

Gloersen, P., Zwally, H.J., Chang, A.T.C., Hall, D.K., Campbell, W.J., and Ramseier, R.O. (1978) Time dependence of sea ice concentration and multi-year ice fraction in the Arctic Basin. *Boundary Layer Meteorology* **13**, 339–359.

Goldstein, R., Osipenko, N., and Leppäranta, M. (2001) On the formation of large scale structural features. In: J.P. Dempsey and H.H. Shen (eds.), *IUTAM Symposium on Scaling Laws in Ice Mechanics and Ice Dynamics* (pp. 323–334). Kluwer Academic, Dordrecht, The Netherlands.

Goldstein, R.V., Osipenko, N.M. and Leppäranta, M. (2009) Relaxation scales and the structure of fractures in the dynamics of sea ice. *Cold Regions Science and Technology* **58**, 29–35.

Gorbunov, Yu.A. and Timokhov, L.A. (1968) Investigation of ice dynamics. *Izvestiya Atmospheric and Oceanic Physics* **4**(10), 623–626.

Gordienko, P. (1958) Arctic ice drift. *Proceedings of Conference on Arctic Sea Ice* (Publication No. 598, pp. 210–220. National Academy of Science, National Research Council, Washington, D.C.

Gordon, A.L. and Lukin, V.V. (1992) Ice Station Weddell #1. *Antarctic Journal of the United States* **27**(5), 97–99.

Gothus, Olaus Magnus (1539) *Carta Marina*. Original published in Venice [available at Geenimap Oy, Vantaa, Finland (`http://www.genimap.fi/kuluttajatuotteet/`)].

Gradinger, R. (1995) Climate change and the biological oceanography of the Arctic Ocean. *Philosophical Transactions of the Royal Society of London* **A352**, 277–286.

Granberg, H.B. and Leppäranta, M. (1999) Observations of sea ice ridging in the Weddell Sea. *Journal of Geophysical Research* **104**(C11), 25,735–25,745.

Gray, J.N.M.T. (1999) Loss of hyperbolicity and ill-posedness of the viscous-plastic sea ice rheology in uniaxial divergent flow. *Journal of Physical Oceanography* **29**, 2920–2929.

Gray, J.N.M.T. and Killworth, P. (1995) Stability of viscous-plastic sea ice rheology. *Journal of Physical Oceanography* **25**, 971–978.

Gray, J.N.M.T. and Morland, L.W. (1994) A two-dimensional model for the dynamics of sea ice. *Philosophical Transactions of the Royal Society of London* **A, 347**, 219–290.

Gudkovic, Z.M. and Romanov, M.A. (1976) Method for calculation the distribution of ice thickness in the Arctic seas during the winter period. *Ice Forecasting Techniques for the Arctic Seas*, pp. 1–47.

Gudkovic, Z.M. and Doronin, Yu.P. (2001) *Dreif morskikh l'dov*. Gidrometeoizdat, St. Petersburg [in Russian].

Gutfraind, R. and Savage, S.B. (1997) Marginal ice zone rheology: Comparison of results from continuum-plastic models and discrete particle simulations. *Journal of Geophysical Research* **102**(C6), 12,647–12,661.

Haapala, J. (2000) On the modelling of ice-thickness distribution. *Journal of Glaciology* **46**(154), 427–437.

Haapala, J. and Leppäranta, M. (1996) Simulations of the Baltic Sea ice season with a coupled ice-ocean model. *Tellus* **48A**, 622–643.

Haapala, J. and Leppäranta, M. (1997a) The Baltic Sea ice season in changing climate. *Boreal Environment Research* **2**, 93–108.

Haapala, J. and Leppäranta, M. (eds.) (1997b) *ZIP-97 Data Report*. (Report Series in Geophysics, No. 37, 123 pp). University of Helsinki, Department of Geophysics, Helsinki.

Haas, C. (1998) Evaluation of ship based electromagnetic-inductive thickness measurements of summer sea ice in the Bellingshausen and Amundsen seas, Antarctica. *Cold Regions Science and Technology* **27**, 1–6.

Häkkinen, S. (1986) Ice banding as a response of the coupled iceocean system to temporally varying winds. *Journal of Geophysical Research* **91**(C4), 5047–5053.

Harlow, F.H. (1964) The particle-in-cell computing method for fluid dynamics. *Methods in Computational Physics* **3**, 319–343.

Harr, M.E. (1977) *Mechanics of Particulate Media. A probabilistic approach*. McGraw-Hill, New York.

Heil, P. and Hibler, W.D., III (2002) Modeling the high-frequency component of Arctic sea ice drift and deformation. *Journal of Physical Oceanography* **32**(11), 3039–3057.

Hibler, W.D., III (1979) A dynamic-thermodynamic sea ice model. *Journal of Physical Oceanography* **9**, 815–846.

Hibler, W.D., III (1980a) Modelling a variable thickness sea ice cover. *Monthly Weather Review* **108**(12), 1943–1973.

Hibler, W.D., III (1980b) Sea ice growth, drift and decay. In: S. Colbeck (ed.), *Dynamics of Snow and Ice Masses* (pp. 141–209). Academic Press, New York.

Hibler, W. D., III (1986) Ice dynamics. In: N. Untersteiner (ed.), *Geophysics of Sea Ice* (pp. 577–640). Plenum Press, New York.

Hibler, W.D., III (2001) Sea ice fracturing on the large scale. *Engineering Fracture Mechanics* **68**, 2013–2043.

Hibler, W.D., III and Ackley, S.F. (1983) Numerical simulation of the Weddell Sea pack ice. *Journal of Geophysical Research* **88**(C5), 2873–2887.

Hibler, W.D., III and Bryan, K. (1987) A diagnostic iceocean model. *Journal of Physical Oceanography* **17**, 987–1015.

Hibler, W.D., III and Schulson, E.M. (2000) On modeling the anisotropic failure and flow of flawed sea ice. *Journal of Geophysical Research* **105**(C7), 17105–17120.

Hibler, W.D., III and Tucker, W.B., III (1977) Seasonal variations in apparent sea ice viscosity on the geophysical scale. *Geophysical Research Letters* **4**(2), 87–90.

Hibler, W.D., III, Weeks, W.F., and Mock, S.J. (1972) Statistical aspects of sea-ice ridge distributions. *Journal of Geophysical Research* **77**, 5954–5970.

Hibler, W.D., III, Weeks, W.F., Ackley, S.F., Kovacs, A., and Campbell, W.J. (1973) Mesoscale strain measurements on the Beaufort Sea pack ice (AIDJEX 1971). *Journal of Glaciology* **12**(65), 187–206.

Hibler, W.D., III, Ackley, S.F., Crowder, W.K., McKim, H.L., and Anderson, D.M. (1974a) Analysis of shear zone ice deformation in the Beaufort Sea using satellite imagery. In: J.C. Reed and J.E. Sater (eds.), *The Coast and Shelf of the Beaufort Sea* (pp. 285–296). The Arctic Institute of North America, Arlington, VA.

Hibler, W.D., III, Mock, S.J. and Tucker, W.B., III (1974b) Classification and variation of sea ice ridging in the Western Arctic basin. *Journal of Geophysical Research* **79**(18), 2735–2743.

Hibler, W.D., III, Weeks, W.F., Kovacs, A. and Ackley, S.F. (1974c) Differential sea-ice drift. I. Spatial and temporal variations in sea ice deformation. *Journal of Glaciology* **13**(69), 437–455.

Hibler, W.D., III, Tucker, W.B., III and Weeks, W.F. (1975) Measurement of sea ice drift far from shore using Landsat and aerial photograph imagery. *Proceedings of 3rd International Symposium on Ice Problems* (pp. 541–554). IAHR Committee on Ice Problems, Hanover, NH.

Holland, D., Mysak, L.A., and Manak, D.K. (1993) Sensitivity study of a dynamic thermodynamic sea ice model. *Journal of Geophysical Research* **98**(C2), 2561–2586.

Holland, M.M., Bitz, C.M. and Tremblay, B. (2006) Future abrupt reductions in the summer Arctic sea ice. *Geophysical Research Letters* **33**, L2353, doi:10.1029/2006GL028024.

Hopkins, M. (1994) On the ridging of intact lead ice. *Journal of Geophysical Research* **99**(C8), 16,351–16,360.

Hopkins, M. and Hibler, W.D., III (1991) On the ridging of a thin sheet of lead ice. *Journal of Geophysical Research* **96**, 4809–4820.

Hopkins, M.A. and Tuhkuri, J. (1999) Compression of floating ice fields *Journal of Geophysical Research* **104**(C7), 15,815–15,825.

Houghton, J. T. (ed.) (2001) *Climate Change 2001: The Scientific Basis*. Cambridge University Press, New York.

Hunke, E. and Dukewicz, J.K. (1997) An elastic-viscous-plastic model for sea ice dynamics. *Journal of Physical Oceanography* **27**, 1849–1847.

Hunke, E. and Zhang, Y. (1999) A comparison of sea ice dynamics models at high resolution. *Monthly Weather Review* **127**, 396–408.

Hunkins, K. (1967) Inertial oscillations of Fletcher's Ice Island (T-3). *Journal of Geophysical Research* **72**(4), 1165–1173.

Hunkins, K. (1975) The oceanic boundary-layer and stress beneath a drifting ice floe. *Journal of Geophysical Research* **80**(24), 3425–3433.

Hunter, S.C. (1976) *Mechanics of Continuous Media*. Ellis Horwood, Chichester, UK.

Ikeda, M. (1985) A coupled ice-ocean model of a wind-driven coastal flow. *Journal of Geophysical Research* **90**(C5), 9119–9128.

Jakkila, J., Leppäranta, M., Kawamura, T., Shirasawa, K., and Salonen, K. (2009) Radiation transfer and heat budget during the melting season in Lake Pääjärvi. – *Aquatic Ecology* **43**(3), 609–616.

Jenkins, G.M. and Watts, D. (1968) *Spectral analysis and its applications*. Holden-Day, San Fransisco, CA.

Joffre S.M. (1982a) Momentum and Heat Transfers in the Surface Layer over a Frozen Sea. *Boundary Layer Meteorology* **24**, 211–229.

Joffre S.M. (1982b) Assessment of the Separate Effects of Baroclinicity and Thermal Stability in the Atmospheric Boundary Layer over the Sea. *Tellus* **34**(6), 567–578.

Joffre S.M. (1983) Determining the Form Drag Contribution to the Total Stress of the Atmospheric Flow over Ridged Sea Ice. *Journal of Geophysical Research* **88**(C7), 4524–4530.

Joffre S.M. (1984) *The Atmospheric Boundary Layer over the Bothnian Bay: A Review of Work on Momentum Transfer and Wind Structure* (Report No. 40). Styrelsen för Vintersjöfartsforskning [Winter Navigation Research Board], Helsinki.

Joffre S.M. (1985) Effects of Local Accelerations and Baroclinity on the Mean Structure of the Atmospheric Boundary Layer over the Sea. *Boundary-Layer Meteorology* **32**(3), 237–255.

Johannessen, O. M., Shaline, E.V., and Miles, M.W. (1999) Satellite evidence for an Arctic sea ice cover in transformation. *Science* **286**, 1937–1939.

Johannessen, O.M., Alexandrov, V.Y., and Frolov, I.Y. (2007) *Remote Sensing of Sea Ice in the Northern Sea Route*. Springer-Praxis, Chichester, UK.

Jurva, R. (1937) Über die Eisverhältnisse des Baltischen Meeres an den Küsten Finnlands nebst einem Atlas [On the ice conditions in the Baltic Sea at the Finnish coastal area]. *Merentutkimuslaitoksen Julkaisu/Havsforskningsinstitutets Skr.* **114** (Finnish Institute of Marine Research) [in German].

Kankaanpää, P. (1998). Distribution, morphology and structure of sea ice pressure ridges in the Baltic Sea. *Fennia* **175**(2)

Kärnä, T. and Qu, Y. (2005) Pressure area relationships based on enhanced-quality data. *Proceedings of the 18th International Conference on Port and Ocean Engineering under Arctic Conditions (POAC'05)*. Potsdam, NY, USA, 26–30 June 2005, Vol. 3.

Kärnä, T. and Qu, Y., and Yue, Q.-J. (2006) An equivalent lateral force for continuous crushing. *Proceedings of OMAE2006 – 25th International Conference on Offshore Mechanics and Arctic Engineering*, Paper 2006–92648. June 4–9, 2006. Hamburg, Germany.

Karvonen, J., Similä, M., Hallikainen, M., Haas, C. (2005) Estimation of equivalent deformed ice thickness from Baltic Sea ice SAR Imagery. *Proceedings of the International Geoscience and Remote Sensing Symposium 2005 (IGARSS'05)*, Vol VII, pp. 5165–5167.

Keliher, T.E. and Venkatesh, S. (1987) Modelling of Labrador Sea pack ice, with an application to estimating geostrophic currents. *Cold Regions Science and Technology* **13**, 161–176.

Ketchum, R.D., Jr. (1971) Airborne laser profiling of the Arctic pack ice. *Remote Sensing of Environment* **2**, 41–52.

Kheysin, D.Ye. (1978) Relationship between mean stresses and local values of internal forces in a drifting ice cover. *Oceanology* **18**(3), 285–286.

Kheysin, D.Ye. and Ivchenko, V.O. (1973) Numerical model of tidal drift of ice allowing for interaction between ice floes. *Izvestiya AN SSSR Series Fizyki Atmosfery i Okeana* **9**(4), 420–429.

Kirillov, A.A. (1957) Calculation of hummockness in determining ice volume. *Problems of the Arctic*, **2**, 53–58 [in Russian].

Kolmogorov, A.N., 1941. Über das logaritmisch normale Verteilungsgesetz der Dimensionen der Teilchen bei Zerstückelung. *Doklady Academy of Sciences of USSR* 31, 99.

Kondratyev, K., Johannessen, O.M., and Melentyev, V.V. (1996) *High Latitude Climate and Remote Sensing*. Wiley-Praxis, Chichester, UK.

Korvin, G., 1992. *Fractal Models in the Earth Sciences*. Elsevier, Amsterdam.

Kottmeier, C. and Hartig, R. (1990) Winter observations of the atmosphere over Antarctic sea ice. *Journal of Geophysical Research* **95**, 16551–16560.

Kovacs, A. (1971) On pressured sea ice. *Proceedings of International Sea Ice Conference*. National Research Council of Iceland, Reykjavik.

Kovacs, A. and Holladay, J.S. (1990) Airborne sea ice thickness sounding. In: S.F. Ackley and W.F. Weeks (eds), *Sea Ice Properties and Processes* (CRREL Monograph 90–1, pp. 225–229). Cold Regions Research and Engineering Laboratory, Hanover, NH.

Kovacs, A. and Mellor, M. (1974) Sea ice morphology and ice as a geological agent in the southern Beaufort Sea. In: J.J. Reed and J.E. Sater (eds), *The Coast and Shelf of the Beaufort Sea* (pp. 113–161). Arctic Institute of North America, Arlington, VA.

Kowalik, Z. (1981) A study of the M_2 tide in the ice-covered Arctic Ocean. *Modeling, Identification and Control* **2**(4), 201–223.

Kowalik, Z. and Murty, T.S. (1993) *Numerical Modeling of Ocean Dynamics* (Advanced Series in Ocean Engineering, 481 pp.). World Scientific, Singapore.

Kowalik, Z, and Proshutinsky, A.Yu. (1995) Topographic enhancement of tidal motion in the western Barents Sea. *Journal of Geophysical Research* **100**(C2), 2613–2637.

Kuznetsov, I.M. and Mironov, E.U. (1986) Studying anomalously high ice drift velocities in Arctic seas. *Meteorologiya i Gidrologiya* **1**, 70–75.

Kwok, R. (1998) The Radarsat geophysical processor system. In: G. Tsatsoulis and R. Kwok (eds), *Analysis of SAR Data of the Polar Oceans* (pp. 235–257). Springer-Verlag, Berlin.

Kwok, R. (2001) Deformation of the Arctic Ocean sea ice cover between November 1996 and April 1997: A qualitative survey. In: J.P. Dempsey and H.H. Shen (eds), *IUTAM Symposium on Scaling Laws in Ice Mechanics and Ice Dynamics* (pp. 315–322). Kluwer Academic, Dordrecht, The Netherlands.

Kwok, R., Curlander, J.C., McConnell, R., and Pang, S.S. (1990) An ice-motion tracking system at the Alaska SAR facility. *IEEE Journal of Oceanic Engineering* **15**(1), 44–54.

Kwok, R., Rignot, E., Holt, B. and Onstott, R. (1992) Identification of sea ice types in spaceorne SAR data. *Journal of Geophysical Research* **97**(C2), 2391–2402.

Kwok, R., Schweiger, A., Rothrock, D.A., Pang, S., and Kottmeier, C. (1998) Sea ice motion from satellite passive microwave imagery assess with ERS SAR and buoy motion. *Journal of Geophysical Research* **103**(C4), 8191–8214.

Laikhtman, D.L. (1958) O vetrovom dreife ledjanykh poley. *Trudy Leningradskiy Gidrometmeteorologicheskiy Institut* **7**, 129–137.

Landau, L.D. and Lifschitz, E.M. (1976) *Mechanics*, 3rd edn.. Pergamon Press, Oxford, UK.

Lange, M. and Pfirman, S. (1998) Arctic sea ice contamination: major characteristics and consequences. In: M. Leppäranta (ed.), *Physics of Ice-Covered Seas* (Vol. 2, pp. 651–682). Helsinki University Press.

Legen'kov, A.P. (1977) On the strains in the drifting sea ice in the Arctic Basin. *Izvestiya, Atmospheric and Oceanic Physics* **13**(10), 728–733.

Legen'kov, A.P. (1978) Ice movements in the Arctic Basin and external factors. *Oceanology* **18**(2), 156–159.

Legen'kov, A.P., Chuguy, I.V., and Appel, I.L. (1974) On ice shifts in the Arctic basin. *Okeanology* **14**(6), 807–813.

Lehmuskoski, P. and Mäkinen, J. (1978) Gravity measurements on the ice of the Bothnian Bay. *Geophysica* **15**(1).

Lensu, M. (2003) *The Evolution of Ridged Ice Fields* (Report M-280, 140 pp). Helsinki University of Technology, Ship Laboratory, Espoo, Finland.

Leppäranta, M. (1981a) An ice drift model for the Baltic Sea. *Tellus* **33**(6), 583–596.

Leppäranta, M. (1981b) On the structure and mechanics of pack ice in the Bothnian Bay. *Finnish Marine Research* **248**, 3–86.

Leppäranta, M. (1982) A case study of pack ice displacement and deformation field based on Landsat images. *Geophysica* **19**(1), 23–31.

Leppäranta, M. (1983) A growth model for black ice, snow ice and snow thickness in subarctic basins. *Nordic Hydrology* **14**(2): 59–70. 1983

Leppäranta, M. (1987) Ice observations: Sea Ice-85 experiment. *Meri* **15**.

Leppäranta, M. (1990) Observations of free ice drift and currents in the Bay of Bothnia. *Acta Regiae Societatis Scientiarum et Litterarum Gothoburgensis, Geophysica* **3**, 84–98.

Leppäranta, M., 1993. A review of analytical modelling of sea ice growth. *Atmosphere- Ocean* **31**(1), 123–138.

Leppäranta, M. (1998) The dynamics of sea ice. In: M. Leppäranta (ed.), *Physics of Ice-Covered Seas* (Vol. 1, pp. 305–342). Helsinki University Press.

Leppäranta, M. (2005) *The Drift of Sea Ice*. Springer-Praxis, Chichester, UK.

Leppäranta, M. and Hakala, R. (1992) The structure and strength of first-year ice ridges in the Baltic Sea. *Cold Regions Science and Technology* **20**, 295–311.

Leppäranta, M. and Hibler, W.D., III (1984) A mechanism for floe clustering in the marginal ice zone. *MIZEX Bulletin* **3**, 73–76.

Leppäranta, M. and Hibler, W.D., III (1985) The role of plastic ice interaction in marginal ice zone dynamics. *Journal of Geophysical Research* **90**(C6), 11,899–11,909.

Leppäranta, M. and Hibler, W.D., III (1987) Mesoscale sea ice deformation in the East Greenland marginal ice zone. *Journal of Geophysical Research* **92**(C7), 7060–7070.

Leppäranta, M. and Lewis, J.E. (2007) Observations of ice surface temperature in the Baltic Sea. International *Journal of Remote Sensing* **28**(17), 3963–3977.

Leppäranta, M. and Myrberg, K. (2009) *Physical Oceanography of the Baltic Sea*. Springer-Praxis, Chichester, UK.

Leppäranta, M. and Omstedt, A. (1990) Dynamic coupling of sea ice and water for an ice field with free boundaries. *Tellus* **42A**, 482–495.

Leppäranta, M. and Palosuo, E. (1981) Studies of Sea Ice Ridging with a Ship-Borne Laser Profilometer. *Proceedings of 6th International Conference on Port and Ocean Engineering under Arctic Conditions (POAC'81)*, Québec City, Vol. 2, pp. 1031–1038.

Leppäranta, M. and Palosuo, E. (1983) Use of ship's radar to observe two-dimensional ridging characteristics. *Proceedings of 7th International Conference on Port and Ocean Engineering under Arctic Conditions (POAC'83)*, Helsinki (Vol. I, pp. 138–147).

Leppäranta, M. and Wang, K. (2002) Sea ice dynamics in the Baltic Sea basins. *Proc. 15th IAHR Ice Symposium*, Dunedin, New Zealand

Leppäranta, M. and Wang, K. (2008) The ice cover on small and large lakes: Scaling analysis and mathematical modelling. *Hydrobiologica* **599**, 183–189.

Leppäranta, M. and Zhang, Z. (1992a) Use of ERS-1 SAR data in numerical sea ice modeling. *Proceedings of the Central Symposium of the "International Space Year" Conference, Munich, 30 March–4 April 1992* (pp. 123–128, ESA SP-341, July 1992).

Leppäranta, M. and Zhang, Z. (1992b) *A viscous-plastic test model for Baltic Sea ice dynamics* (Internal Report 1992(3)). Finnish Institute of Marine Research, Helsinki.

Leppäranta, M., Lensu, M., and Lu, Q.-m. (1990) Shear flow of sea ice in the marginal ice zone with collision rheology. *Geophysica* **25**(1–2), 57–74.

Leppäranta, M., Lensu, M. Kosloff, P., and Veitch, B. (1995) The life story of a first-year sea ice ridge. *Cold Regions Science and Technology* **23**, 279–290.

Leppäranta, M., Sun, Y., and Haapala, J. (1998) Comparisons of sea-ice velocity fields from ERS-1 SAR and a dynamic model. *Journal of Glaciology* **44**(147), 248–262.

Leppäranta, M., Zhang, Z., Haapala, J., and Stipa, T. (2001) Sea ice mechanics in a coastal zone of the Baltic Sea. *Annals of Glaciology* **33**, 151–156.

Leppäranta, M. Ovsienko, S. and Wang, K. (2008) Modelling drift and dispersion of oil in ice conditions in the Gulf of Finland. Project Report to Nessling Foundation, Helsinki, Finland (unpublished).

Leppäranta, M., Wang, K. and Oikkonen, A. (2009) Modelling studies of the frequency spectrum of sea ice velocity. *Proceedings of the 20th International Conference on Port and Ocean Engineering under Arctic Conditions,* Paper #8. Luleå University of Technology, Sweden.

Lewis, J.E., Leppäranta, M., and Granberg, H.B. (1993) Statistical properties of sea ice surface topography in the Baltic Sea. *Tellus* **45A**, 127–142.

Li, S., Cheng, W., and Weeks, W.F. (1995) A grid based algorithm for the extraction of intermediate-scale sea ice deformation descriptors from SAR ice motion products. *International Journal of Remote Sensing* **16**(17), 3267–3286.

Li, W.H. and Lam, S.H., 1964. *Principles of Fluid Mechanics*. Addison-Wesley, Reading, MA.

Lichey, C. and Hellmer, H.H. (2001) Modeling giant-iceberg drift under the influence of sea ice in the Weddell Sea, Antarctica. *Journal of Glaciology* **47**(158), 452–460.

Lisitzin, E., 1957. On the reducing influence of sea ice on the piling-up of water due to wind stress. *Commentationes Physico-Mathematicae, Societas Scientarum Fennica* **20**(7), 1–12.

Liu, A.K. and Cavalieri, D.J. (1998) On sea ice drift from the wavelet analysis of the Defense Meteorological Satellite Program (DMSP) Special Sensor Microwave Imager (SSM/I) data. *International Journal of Remote Sensing* **19**(7), 1415–1423.

Løset, S. (1993) Some aspects of floating ice related sea surface operations in the Barents Sea. Ph.D. thesis, University of Trondheim, Norway.

Lu, P. and Li, Z. (2010) A method of obtaining ice concentration and floe size from shipboard oblique sea ice images. *Transactions on Geoscience and Remote Sensing* **48**(7), 2771–2880.

Lu, Q.-m., Larsen, J. and Tryde, P. (1989) On the role of ice interaction due to floe collisions in marginal ice zone dynamics. *Journal of Geophysical Research* **94**(C10), 14,525–14,537.

Lu, Q.-m., Larsen, J. and Tryde, P. (1990) A dynamic and thermodynamic sea ice model for subpolar regions. *Journal of Geophysical Research* **95**(C8), 13,433–13,457.

Lurton, X. (2002) *An Introduction to Underwater Acoustics* (347 pp.). Springer-Praxis, Chichester, UK.

Lyon, W.K. (1961) Ocean and sea-ice research in the Arctic Ocean via submarine. *Transactions of the New York Academy of Sciences, Series A* **23**(8), 662–674.

Lytle, V.I. and Ackley, S.F. (1991) Sea ice ridging in the eastern Weddell Sea. *Journal of Geophysical Research* **96**(C10), 18411–18416.

Makshtas, A.P. (1984) *The Heat Budget of Arctic Ice in the Winter*. Gidrometeoizdat, Leningrad [English language version by International Glaciological Society, Cambridge, UK, 1991].

Martinson, D.G. and Wamser, C. (1990) Ice drift and momentum exchange in winter Antarctic pack ice. *Journal of Geophysical Research* **95**(C2), 1741–1755.

Mase, G.E. (1970) *Continuum Mechanics* (Schaum's outline series). McGraw-Hill, New York.

Maslanik, J., Drobot, S., Fowler, C., Emery, W., and Barry, R. (2007) On the Arctic climate paradox and the continuing role of atmospheric circulation in affecting sea ice conditions. *Geophysical Research Letters* 34, L03711, doi:10.1029/2006GL028269.

Massom, R., Scambos, T., Lytle, V., Hill, K., Lubin, D., and Giles, B. (2003) Fast ice distribution and its interannual variability in East Antarctica, determined from satellite data analysis. *Proceedings of the 16th International Symposium on Ice* (Vol. 3, p. 271). IAHR and University of Otago, New Zealand.

Maykut, G.A. and Untersteiner, N. (1971) Some results from a time-dependent, thermodynamic model of sea ice. *Journal of Geophysical Research,* **76**, 1550–1575.

McPhee, M.G. (1978) A simulation of the inertial oscillation in drifting pack ice. *Dynamics of Atmospheres and Oceans* **2**, 107–122.

McPhee, M.G. (1980) An analysis of pack ice drift in summer. In: R.S. Pritchard (ed.), *Proceedings of ICSI/AIDJEX Symposium on Sea Ice Processes and Models* (pp. 62–75). University of Washington, Seattle.

McPhee, M.G. (1982) *Sea ice drag laws and simple boundary layer concepts, including application to rapid melting* (Report 82–4). US Army Cold Regions Research and Engineering Laboratory, Hanover, NH.

McPhee, M.G. (1986) The upper ocean. In: N. Untersteiner (ed.), *Geophysics of Sea Ice* (pp. 339–394). Plenum Press, New York.

McPhee, M.G. (2008) *Air–Ice–Ocean Interaction: Turbulent Ocean Boundary Layer Exchange Processes*. Berlin, Germany: Springer.

Mellor, M. (1986) The mechanical behavior of sea ice. In: N. Untersteiner (ed.), *Geophysics of Sea Ice* (pp. 165–281). Plenum Press, New York.

Michel, B. (1978) *Ice Mechanics*. Laval University Press, Québec city, Québec, Canada.

Mironov, Ye.U. (1987) Estimation of the volume of sea ice in the Arctic Ocean taking pressure ridges into account. *Polar Geography and Geology* **11**(1), 69–75.

Mock, S.J., Hartwell, A. and Hibler, W.D., III (1972) Spatial aspects of pressure ridge statistics. *Journal of Geophysical Research* **77**, 5945–5953.

Muench, R.D. and Ahlnäs, K. (1976) Ice movement and distribution in the Bering Sea from March to June 1974. *Journal of Geophysical Research* **81**(24): 4467–4476.

Muench, R., Martin, S., and Overland, J.E. (eds) (1987) Marginal ice zone research. *Journal of Geophysical Research* **92**(C7), 7225 pp. (special MIZEX issue).

Multala, J., Hautaniemi, H.., Oksama, M., Leppäranta, M., Haapala, J., Herlevi A., Riska, K., and Lensu, M. (1996) Airborne electromagnetic mapping of sea ice thickness in the Baltic Sea. *Cold Regions Science and Technology* **24**(4), 355–373.

Nansen, F. (1897) *Fram över Polarhavet*. Aschehoug, Kristiania, Norway.

Nansen, F. (1902) The Oceanography of the North Polar Basin. *Norwegian North Polar Expedition 1893–1896. Scientific Results* (Vol. III, No. 9,). Longman Green & Co., Kristiania, Norway.

Neralla, V.R., Jessup, R.G., and Venkatesh, S. (1988) The Atmospheric Environment Service regional ice model (RIM) for operational applications. *Marine Geodesy* **12**, 135–153.

Nikiforov, E.G. (1957) Changes in the compactness of the ice cover in relation to its dynamics. *Problemy Arktiki* (Vyp. 2). Morskoi Transport Press, Leningrad [in Russian].

Nikiforov, E.G., Gudkovich, Z.M., Yefimov, Yu.N., and Romanov, M.A. (1967) Principles of a method for calculating the ice redistribution under the influence of wind during the navigation period in Arctic seas. *Trudy Arkticheskii i Antarkticheskii Nauchno-issledovatel'skii Institut* **257**, 5–25 [English Translation in *AIDJEX Bulletin* **3**, 40–64].

Oda, M. and Iwashita, K. (eds.) (1999) *Mechanics of Granular Materials*. Balkema, Rotterdam.

Okubo, A. and Ozmidov, R.V. (1970) Empirical dependence of the coefficient of horizontal turbulent diffusion in the ocean on the scale of the phenomenon in question. *Izvestiya Atmospheric and Oceanic Physics* **6**(5), 534–536.

Omstedt, A. (1990) Modelling the Baltic Sea as thirteen sub-basins with vertical resolution. *Tellus A,* **4**, 286–301.

Omstedt, A. (1998) Freezing estuaries and semi-enclosed basins. In: M. Leppäranta (ed.), *Physics of Ice-Covered Seas* (Vol. 2, pp. 483516). Helsinki University Press.

Omstedt, A., Nyberg, L., and Leppäranta, M. (1994) A coupled ice-ocean model supporting winter navigation in the Baltic Sea. Part 1. Ice dynamics and water levels. *Styrelsen för Vintersjöfartsforskning [Winter Navigation Research Board]* Rep. No. 47, 17 pp. Board of Navigation, Norrköping, Sweden.

Omstedt, A., Nyberg, L. and Leppäranta, M. (1996) The role of ice inertia in ice-ocean dynamics. *Tellus* **48A**, 593–606.

Ono, N. (1978) Inertial period motions of drifting ice. *Low Temperature. Science* **A37**, 107–113.

Overgaard, S., Wadhams, P., and Leppäranta, M. (1983) Ice properties in the Greenland and Barents Seas during summer. *Journal of Glaciology* **29**(101), 142–164.

Overland, J.E. (1985) Atmospheric boundary layer structure and drag coefficients over sea ice. *Journal of Geophysical Research,* **90**(C5), 9029–9049.

Overland, J.E. and Pease, C.H. (1988) Modeling ice dynamics of coastal seas. *Journal of Geophysical Research* **93**, 15,619–15,637.

Overland, J.E., Walter, B.A., Curtin, T.B., and Turet, P. (1995) Hierarchy in sea ice mechanics: A case study from the Beaufort Sea. *Journal of Geophysical Research* **100**(C3), 4559–4571.

Ovsienko, S. (1976) Numerical modeling of the drift of ice. *Izvestiya, Atmospheric and Oceanic Physics* **12**(11), 1201–1206

Ovsienko, S., Zatsepa, S. and Ivchenko, A. (1999a) Study and modelling of behaviour and spreading of oil in cold water and in ice conditions. *Proceedings of 15th Conference on Port and Ocean Engineering under Arctic Conditions, Espoo, Finland.*

Ovsienko, S., Leppäranta, M., Zatsepa, S., and Ivchenko, A. (1999b) The use of ice tank experiment results for mesoscale sea ice modelling. *Proceedings of 15th Conference on Port and Ocean Engineering under Arctic Conditions, Espoo, Finland* (Vol 2, pp. 480–487).

Palosuo, E. (1953) A treatise on severe ice conditions in the Central Baltic. *Merentutkimus-laitoksen Julkaisu/Havsforskningsinstitutets Skrift* **156**.

Palosuo, E. (1963) The Gulf of Bothnia in winter. II. Freezing and ice forms. *Merentutkimuslaitoksen Julkaisu/Havsforskningsinstitutets Skrift* **209**.

Palosuo, E. (1970) The structure of an ice ridge in the Baltic. *Proceedings of IAHR Symposium of Ice and Its Action on Hydraulic Structures*, 13 p. Reykjavik, Iceland.

Papanin, I. (1939) *Life on an ice floe*. Julian Messner, New York [translated from Russian].

Parmerter, R.R. (1975) A model of simple rafting in sea ice. *Journal of Geophysical Research* **80**(15), 1948–1952.

Parmerter, R.R. and Coon, M.D. (1972) Model for pressure ridge formation in sea ice. *Journal of Geophysical Research* **77**, 6565–6575.

Paterson, W.S.B. (1995) *The Physics of Glaciers* (3rd edn). Pergamon Press, Oxford, UK.

Perovich, D. (1998) The optical properties of sea ice. In: M. Leppäranta (ed.), *Physics of Ice-covered Seas*, (Vol. 1, pp. 195–230). Helsinki University Press.

Perovich, D., Grenfell, T., Richter-Menge, J., Light, B., Tucker, III, W. and H. Eicken, H. (2003) Thin and thicker: Sea ice mass balance measurements during SHEBA, *Journal of Geophysical Research* **108**(C3*)*, 8050, doi:10.1029/2001JC001079.

Pfirman, S.L., Eicken, H., Bauch, D., and Weeks, W.F. (1995) The potential transport of pollutants by Arctic sea ice. *Science of the Total Environment* **159**, 129–146.

Pond, S. and Pickard, G.L. (1983) *Introductory Dynamical Oceanography* (2nd edn). Pergamon Press, Oxford, UK.

Pritchard, R.S. (1975) An elastic-plastic constitutive law for sea ice. *Journal of Applied Mechanicsc* **42E**, 379–384.

Pritchard, R.S. (1977) The effect of strength on simulations of sea ice dynamics. *Proceedings of the 4th International Conference on Port and Ocean Engineering under Arctic Conditions* (12 pp.). Memorial University of Newfoundland, St. John's, Canada.

Pritchard, R.S. (ed.) (1980a) *Proceedings of ICSI/AIDJEX Symposium on Sea Ice Processes and Models*. University of Washington, Seattle.

Pritchard, R.S. (1980b) Simulations of nearshore winter ice dynamics in the Beaufort Sea. In: R.S. Pritchard (ed.), *Proceedings of ICSI/AIDJEX Symposium on Sea Ice Processes and Models* (pp. 49–61). University of Washington, Seattle.

Pritchard, R.S. (1981) Mechanical behaviour of pack ice. In: A.P.S. Selvadurai (ed.), *Mechanics of Structured Media* (Part A, pp. 371–405). Elsevier, North-Holland.

Ramsay, W. (1949) *Jääsaarron murtajat [The Breakers of the Ice Barrier]*. K.F. Puromiehen kirjapaino, Helsinki.

Rayner, N. A., Parker, D.E., Horton, E.B., Folland, C.K., Alexander, L.V., Rowell, D.P., Kent, E.C., and Kaplan, A. (2003) Global analyses of sea surface temperature, sea ice, and night marine air temperature since the late nineteenth century. *Journal of Geophysical Research* **108**(D14), 4407, doi:10.1029/2002JD002670.

Rheem, C.K., Yamaguchi, H., and Hiroharu, K. (1997) Distributed mass/discrete floe model for pack ice rheology computation. *Journal of Marine Science and Technology* **2**, 101–121.

Richter-Menge, J.A. and Elder, B.C. (1998) Characteristics of ice stress in the Alaskan Beaufort Sea. *Journal of Geophysical Research* **103**(C10), 21,817–21,829.

Richter-Menge, J., McNutt, S.L., Overland, J.E., and Kwok, R. (2002) Relating arctic pack ice stress and deformation under winter conditions. *Journal of Geophysical Research* **107**(C10), SHE 15 (doi:10.1029/2000JC000477).

Rodahl, K. (1954) *T3*. Gyldendal, Oslo.

Rossby, C.G. and Montgomery, R.G. (1935) *Frictional Influence in Wind and Ocean Currents*. Papers in Physical Oceanography and Meteorology Vol. 3, No. 3. Massachusetts Institute of Technology and Woods Hole Oceanographic Institute, Cambridge, M.A.

Rossiter, J.R. and Holladay, J.S. (1994) Ice thickness measurement. In: S. Haykin, E.O. Lewis, R.K. Ramey, and J.R. Rossiter (eds), *Remote Sensing of Sea Ice and Icebergs* (pp. 141–176). John Wiley & Sons, N.Y.

Rossiter, J.R., Butt, K.A., Gamberg, J.B., and Ridings, T.F. (1980) Airborne impulse radar sounding of sea ice. *Proceedings of Sixth Canadian Symposium on Remote Sensing* (pp. 187–194).

Rothrock, D.A. (1975a) The energetics of the plastic deformation of pack ice by ridging. *Journal of Geophysical Research* **80**(33), 4514–4519.

Rothrock, D.A. (1975b) The mechanical behavior of pack ice. *Ann. Rev. Earth Planet. Sci.* **3,** 317–342.

Rothrock., D.A. (1975c) The steady drift of an incompressible Arctic ice cover. *Journal of Geophysical Research* **80**(3), 387–397.

Rothrock, D.A. (1986). Ice thickness distribution – measurement and theory. In: N. Untersteiner (ed.), *The Geophysics of Sea Ice* (pp. 551–575). Plenum Press, New York.

Rothrock, D.A. and Hall, R. (1975) Testing the redistribution of sea ice thickness from ERTS photographs. *AIDJEX Bulletin* 19, 1–19.

Rothrock, D.A. and Thorndike, A.S. (1980) Geometric properties of the underside of sea ice. *Journal of Geophysical Research* **85**(C7), 3955–3963.

Rothrock, D.A. and Thorndike, A.S. (1984) Measuring the sea ice floe size distribution. *Journal of Geophysical Research* **89**(C4), 6477–6486.

Rothrock, D. A., Yu, Y., and Maykut, G.A. (1999) Thinning of the Arctic sea-ice cover. *Geophysical Research Letters* **26**, 3469–3472.

Rudels, B. (1998) Aspects of Arctic oceanography. In: M. Leppäranta (ed.), *Physics of Ice-covered Seas* (Vol. 2, pp. 517–568). Helsinki University Press.

Saloranta, T. (2000) Modeling the evolution of snow, snow ice and ice in the Baltic Sea. *Tellus* **52A**, 93–108.

Sanderson, T.J.O. (1988) *Ice Mechanics. Risks to Offshore Structures* (253 pp.). Graham & Trotman, Boston.

Savage, S.B. (1995) Marginal ice zone dynamics modelled by computer simulations involving floe collisions. In: E. Guazelli and L. Oger (eds), *Mobile, Particulate Systems (*pp. 305–330). Kluwer Academic, Norwell, MA.

Schaefer, J.A. and Ettema, R. (1986) Experiments on freeze-bonding between ice blocks in floating ice rubble. *Proceedings of 8th IAHR Ice Symposium, Iowa City, IA* (Vol. 1, pp. 401–413).

Schwaegler, R. T. (1974) Fracture of sea ice sheets due to isostatic imbalance. *Ocean74: IEEE International Conference on Engineering in the Ocean Environment*, Vol. 1, pp. 77–81, IEEE, New York.

Schwarz, J. and Weeks, W.F. (1977) Engineering properties of sea ice. *Journal of Glaciology* **19**(81), 499–531.

Semtner, A. (1976) A model for the thermodynamic growth of sea ice in numerical investigations of climate. *Journal of Physical Oceanography* **6**(3), 379–389.

Shen, H.H., Hibler, W.D., III, and Leppäranta, M. (1986) On applying granular flow theory to a deforming broken ice field. *Acta Mechanica* **63**, 143–160.

Shen, H.H., Hibler, W.D., III, and Leppäranta, M. (1987) The role of ice floe collisions in sea ice rheology. *Journal of Geophysical Research* **92**(C7), 7085–7096.

Shen, H.T., Shen, H.H., and Tsai, S.M. (1990) Dynamic transport of river ice. *Journal of Hydraulic Research* **28**(6), 659–671.

Shen, H.T., Chen, Y.C., Wake, A., and Crissman, R.D. (1993) Lagrangian discrete parcel simulation of two-dimensional river ice dynamics. *International Journal of Offshore and Polar Engineering* **3**(4), 328–332.

Shevchenko, G.V., Rabinovich, A.B., and Thomson, R.E. (2004) Sea-ice drift on the northeastern shelf of Sakhalin island. *Journal of Physical Oceanography* **34**, 2470–2491.

Shimoda, H., Endo, T., Muramoto, K., Ono, N., Takizawa, T., Ushio, S., Kawamura, T., and Ohshima, K. (1997) Observations of sea-ice conditions in the Antarctic coastal region using ship-borne video cameras. *Nankyoku Shiryô* [*Antarctic Records*] **41**, 355–365 (in Japanese, with English abstract).

Shirasawa, K. (1986) Water stress and ocean current measurements under first-year sea ice in the Canadian Arctic. *Journal of Geophysical Research* **91**(C12), 14305–14316.

Shirasawa, K. and Ingram, R.G. (1991) Characteristics of the turbulent oceanic boundary layer under sea ice. Part 1: A review of the iceocean boundary layer. *Journal of Marine Systems* **2**, 153–160.

Shirasawa, K., Ingram, R. G. (1997) Currents and turbulent fluxes under the first-year sea ice in Resolute Passage, Northwest Territories, Canada *Journal of Marine Systems* **11**, 21–32.

Shirasawa, K. and Leppäranta, M. (2009) Measurements and modelling of the ice–ocean interaction. In: H. Eicken, R. Gradinger, M. Salganek, K. Shirasawa, D. Perovich and M. Leppäranta (eds.), *Field Techniques for Sea Ice Research*. University of Alaska Press.

Shirasawa, K., Leppäranta, M., Saloranta, T., Polomoshnov, A., Surkov, G. and Kawamura, T. (2005) The thickness of landfast ice in the Sea of Okhotsk. *Cold Regions Science and Technology* **42**, 25–40.

Shirasawa, K., Leppäranta, M., Kawamura, T., Ishikawa, M. and Takatsuka, T. (2006) Measurements and modelling of the water–ice heat flux in natural waters. *Proceedings of the 18th IAHR International Symposium on Ice* pp. 85–91. Hokkaido University, Sapporo, Japan.

Shirasawa, K., Ebuchi, N., Leppäranta, M., Ishikawa, M., and Takatsuka, T. (2010) Ice edge dynamics from C-band radar and HF radar coastal stations. *Proceedings of the 25th International Symposium on Okhotsk Sea & Sea Ice, 21–25 February 2010, Mombetsu, Japan*.

Shirokov, K.P. (1977) Vliyanie splochennosti na vetrovoj dreif l'dov [On the influence of ice concentration on the drift of ice]. *Sbornik Rabot Leningraskoye* Gidrometeorologicheskoye Obsestvo 9, 46–53 [in Russian].

Shuleikin, V.V. (1938) Drift of ice fields. *Doklady Academy of Sciences USSR* **19**(8), 589–594.

Smith, S.D. (1972) Wind stress and turbulence over a flat ice floe. *Journal of Geophysical Research* **77**, 3886–3901.

Smith, S.D. (1980) Wind stress and heat flux over the ocean in gale force winds. *Journal of Physical Oceanography* **10**, 709–726.

Soomere, T., Myrberg, K., Leppäranta, M. and Nekrasov, A. (2008) Progress in physical oceanography of the Gulf of Finland, Baltic Sea. *Oceanologia* **50**(3), 287–362.

Squire, V. (1998) The marginal ice zone. In: M. Leppäranta (ed.), *Physics of Ice-Covered Seas* (Vol. 1, pp. 381–446). Helsinki University Press.

Squire, V.A., Dugan, J., Wadhams, P., Rottier, P.J., and Liu, A.K. (1995) Of ocean waves and sea ice. *Annual Review of Fluid Mechanics* **27**, 115–168.

Stefan, J. (1891) Über die Theorie der Eisbildung, insbesondere über Eisbildung im Polarmeere. *Annalen der Physik*, 3rd Ser. 42, 269–286.

Steffen, K. and Lewis, J.E. (1988) Surface temperatures and sea ice typing for northern Baffin Bay. *International Journal of Remote Sensing* **9**(3), 409–422.

Stern, H.L. and Moritz, R.E. (2002) Sea ice kinematics and surface properties from RADARSAT synthetic aperture radar during SHEBA drift. *Journal of Geophysical Research* **107**(C10), 8028, doi:10.1029/2000JC000472.

Stössel, A., Lemke, P., and Owens, W.P. (1990) Coupled sea ice–mixed layer simulations for the Southern Ocean. *Journal of Geophysical Research* **95**(C6), 9539–9555.

Stössel, A. (2008) Employing satellite-derived sea-ice concentration to constrain upper-ocean temperature in a global ocean GCM. *Journal of Climate* **21**(17), 4498–4513. (with corrigendum by Stössel in 2010, submitted to *Journal of Climate*) **23**(9), 2450–2451.

Strass, V.H. and Fahrbach. E. (1998) Temporal and regional variation of sea ice drift and coverage in the Weddell Sea obtained from upward-looking sonars. In: M.O. Jeffries,

(ed.), *Antarctic Sea Ice: Physical Processes, Interactions and Variability* (Antarctic Research Series No. 74, pp. 123139). American Geophysical Union, Washington, DC.

Stroeve, J., Serreze, M., Drobot, S., Gearheard, S., Holland, M., Maslanik, J., Meier, W., and Scambos, T. (2008) Arctic sea ice extent plummets in 2007. *Eos* **89**(2), 13–20.

Strübing, K. (2009) Charting the Baltic Sea – a historical review. *Report Series in Geophysics* 61, pp. 11–27. Department of Physics, University of Helsinki.

Stull R.B. (1988) *An Introduction to Boundary-layer Meteorology*. Kluwer Academic Publishers, Dordrecht, the Netherlands, 666 p.

Sun, Y. (1996) Automatic ice motion retrieval from ERS-1 SAR images using the optical flow method. *International Journal of Remote Sensing* **17**(11), 2059–2087.

Sverdrup, H. U. (1928). The winddrift of the ice on the North Siberian Shelf. *The Norwegian North Polar Expedition with the "Maud" 19181925. Scientific Results* **4**(1), 1–46.

Tabata, T. (1971) Measurements of strain of ice field off the Okhotsk Sea Coast of Hokkaido [in Japanese, with English summary]. *Low Temperature Science* **A29**, 199–211.

Tabata, T. (1972) Radar network for drift ice observations in Hokkaido. In: T. Karlsson (ed.), *Sea Ice: Proceedings of International Conference* (pp. 67–71). National Research Council, Reykjavik.

Tabata, T., Kawamura, T., and Aota, M. (1980) Divergence and rotation of an ice field off Okhotsk Sea coast off Hokkaido. In: R.S, Pritchard (ed.), *Sea Ice Processes and Models* (pp. 273–282). University of Washington Press, Seattle.

Tennekes, H. and Lumley, J.L. (1972) *A First Course in Turbulence* (300 pp.). MIT Press, Cambridge, MA.

Thomas, D.N. and Dieckmann, G.S. (2003) *Sea Ice: An Introduction to Its Physics, Chemistry, Biology and Geology* (402 pp). Blackwell Publishing, Oxford, UK.

Thorndike, A.S. (1986) Kinematics of sea ice. In: N. Untersteiner (ed.), *Geophysics of Sea Ice* (pp. 489–549). Plenum Press, New York.

Thorndike, A.S. and Colony, R. (1980) Large-scale ice motion in the Beaufort Sea. In: R.S, Pritchard (ed.), *Sea Ice Processes and Models* (pp. 249–260). University of Washington Press, Seattle.

Thorndike, A.S. and Colony, R. (1982) Sea ice response to geostrophic winds. *Journal of Geophysical Research* **87**, 5845–5852.

Thorndike, A.S., Rothrock, D.A., Maykut, G.A., and Colony, R. (1975) The thickness distribution of sea ice. *Journal of Geophysical Research* **80**, 4501–4513.

Timco, G.W. and Burden, R.P. (1997) An analysis of the shapes of sea ice ridges. *Cold Regions Science and Technology* **25**, 65–77.

Timmermann, R., Beckmann, A., and Hellmer, H.H. (2002) Simulations of ice–ocean dynamics in the Weddell Sea 1. Model configuration and validation. *Journal of Geophysical Research* **107**(C3), 10.

Timokhov, L.A. and Kheysin, D.Ye. (1987) *Dynamika Morskikh L'dov*. Gidrometeoizdat, Leningrad.

Timokhov, L.A. (1998) Ice Dynmics Models. In: M. Leppäranta (ed.), *Physics of Ice-Covered Seas* (Vol. 1, p. 343–380). Helsinki University Press.

Tuhkuri, J. and Lensu, M. (1997) *Ice tank tests on rafting of a broken ice field* (Report M-218). Helsinki University of Technology, Ship Laboratory.

Udin, I. and Ullersig, A. (1976) *A numerical model for the forecasting of ice motion in the Bay and Sea of Bothnia*. (Styrelsen för Vintersjöfartsforskning [Winter Navigation Research Board] Rep. No. 18). Board of Navigation, Norrköping, Sweden.

Ukita, J. and Moritz, R. (1995) Yield curves and flow rules of pack ice. *Journal of Geophysical Research* **100**(C3), 4545–4557.

UNESCO, Tenth Report of the Joint Panel on Oceanographic Tables and Standards (1981) The Practical Salinity Scale 1978 and the International Equation of State of Seawater 1980. Technical Papers in Marine Science 36.

Untersteiner, N. (1984) The cryosphere. In: J.T. Houghton (ed.), *The Global Climate* (pp. 121–140). Cambridge University Press, New York.

Uusikivi, J., Ehn, J. and Granskog, M.A. (2006) Direct measurements of turbulent momentum, heat, and salt fluxes under landfast ice in the Baltic Sea. *Annals of Glaciology* **44**, 42–46.

Vancoppenolle, M., Fichefet, T., and Goosse, H. (2009) Simulating the mass balance and salinity of Arctic and Antarctic sea ice. 2. Importance of sea ice salinity variations. *Ocean Modelling* **27**, 54–69.

Van Hejst, G.J.F. (1984) An analytical model for ice-edge upwelling. *Geophysical and Astrophysical Fluid Dynamics* **29**, 155–177.

Vasiliev, K.P. (1985) *Sea-ice forecasting. Marine Meteorology and Related Oceanographic Activities* (Report No. 14, pp. 50–59. Scientific Lectures at CMMIX). WMO, Geneva.

Venkatesh, S., El-Tahan, H., Comfort, G., and Abdelnour, R. (1990) Modelling the behaviour of oil spills in ice-infested waters. *Atmosphere–Ocean* **28**(3), 303–329.

Vesecky, J.F., Samadani, R., Smith, M.P., Daida, J.M., and Bracewell, R.N. (1988) Observation of sea-ice dynamics using synthetic aperture radar images: automated analysis. *IEEE Transactions on Geosciences and Remote Sensing* **GE-26**(1), 38–48.

Vihma, T. (1995) Atmosphere-surface interactions over polar oceans and heterogeneous surfaces. *Finnish Marine Research* **264**, 41pp + 7 articles, Finnish Institute of Marine Research, Helsinki. (PhD Thesis)

Vinje, T. and Berge, T. (1989) *Upward looking sonar recordings at 75°N–12°W from 22 June 1987 to 20 June 1988*. (Data report Nr. 51). Norsk Polarinstitutt Rapportserie, Oslo.

Vinnikov, K. Y., Robock, A., Stouffer, R.J., Walsh, J.E., Parkinson, C.L., Cavalieri, D.J., Mitshell, J.F.B., Garrett, D., and Zakharov, V.F. (1999) Global warming and Northern Hemisphere sea ice extent. *Science* **286**, 1934–1937.

Wadhams, P. (1978) Wave decay in the marginal ice zone measured from a submarine. *DeepSea Research* **25**, 23–40.

Wadhams, P. (1980a). A comparison of sonar and laser profiles along corresponding tracks in the Arctic Ocean. In: R.S. Pritchard (ed.), *Sea Ice Processes and Models* (pp. 283–299). University of Washington Press, Seattle.

Wadhams, P. (1980b) Ice characteristics in the seasonal sea ice zone. *Cold Regions Science and Technology* **2**, 37–87.

Wadhams, P. (1981) Sea-ice topography of the Arctic Ocean in the region 70°W to 25°E. *Philosophical Transactions of the Royal Society of London* **A302**, 45–85.

Wadhams, P. (1998) Sea ice morphology. In: M. Leppäranta (ed.) *Physics of Ice-covered Seas* (Vol. 1, pp. 231–287). Helsinki University Press.

Wadhams, P. (2000) *Ice in the Ocean*. Gordon & Breach Science, Amsterdam.

Wadhams, P. and Davis, N.R. (2000) Further evidence of ice thinning in the Arctic Ocean. *Geophysical Research Letters* **27**, 3973–3975.

Wadhams, P. and Davy, T. (1986) On the spacing and draft distributions for pressure ridge keels. *Journal of Geophysical Research*, **91**, 10,697–10,708.

Wadhams, P., Martin, S., Johannessen, O.M., Hibler, W.D., III and Campbell, W.J. (eds.) (1981) MIZEX. A program for mesoscale air–ice–ocean experiments in the Arctic marginal ice zones. I. Research strategy. (CRREL Special Report 81–19, 20 p.). Cold Regions Research and Engineering Laboratory, Hanover, NH.

Wadhams, P. Lange, M.A., and Ackley, S.F. (1987) The ice thickness distribution across the Atlantic sector of the Antarctic Ocean in midwinter. *Journal of Geophysical Research* **92**(C13), 14,535–14,552.

Wake, A. and Rumer, R.R. (1983) Great Lakes ice dynamics simulation. *Journal of Waterway, Port, Coastal and Ocean Engineering* **109**, 86–102.

Wang, J., Mysak, L.A., and Ingram, R.G. (1994) A numerical simulation of sea ice cover in the Hudson Bay. *Journal of Physical Oceanography* **24**, 2515–2533.

Wang, K. (2007) Observing the yield curve of compacted pack ice. *Journal of Geophysical Research* **112**, C05015, doi: 10.1029/2006JC003610.

Wang, K., Leppäranta, M., and Kouts, T. (2003) A model for sea ice dynamics in the Gulf of Riga. *Proceedings of Estonian Academy of Sciences, Engineering*, **9**(2), 107–125.

Wang, K., Leppäranta, M., Gästgifvars, M., Vainio, J. and Wang, C. (2008) The drift and spreading of Runner-4 oil spill and the ice conditions in the Gulf of Finland, winter 2006. *Estonian Journal of Earth Sciences,* **57**(3), 181–191.

Waters, J.K. and Bruno, M.S. (1995) Internal wave generation by ice floes moving in stratified water: results from a laboratory study. *Journal of Geophysical Research* **100**(C7), 13635–13639.

Weeks, W.F. (1980) Overview. *Cold Regions Science and Technology* **2**, 1–35.

Weeks, W.F. (1998a) Growth conditions and structure and properties of sea ice. In: M. Leppäranta (ed.), *Physics of Ice-covered Seas* (Vol. 1, pp. 25–104). Helsinki University Press.

Weeks, W.F. (1998b) The history of sea ice research. In: M. Leppäranta (ed.), *Physics of Ice-covered Seas* (Vol. 1, pp. 1–24). Helsinki University Press.

Weeks, W.F. and Ackley, S.F. (1986) The growth, structure and properties of sea ice. In: N. Untersteiner (ed.), *Geophysics of Sea Ice* (pp. 9–164). Plenum Press, New York.

Weeks, W.F., Kovacs, A., and Hibler, W.D., III (1971) Pressure ridge characteristics in the Arctic coastal environment. *Proceedings of Conference on Port and Ocean Engineering under Arctic Conditions*. Trondheim, Norway.

Weyprecht, K. (1879) *Die Metamorphosen des Polareises* [The metamosphosis of polar ice]. The Austro–Hungarian Polar Expedition of 1872–1874. 284 pp. Moritz Perles, Vienna.

Williams, E., Swithinbank, C.W.M., and Robin, G. de Q. (1975) A submarine sonar study of Arctic pack ice. *Journal of Glaciology* **15**(73), 349–362.

Wittman, W.J. and Schule, J.J., Jr. (1966) Comments on the mass budget of Arctic pack ice. *Symposium on Arctic Heat Budget and Atmospheric Circulation* (pp. 215–246). RAND Corporation, Santa Monica, CA.

WMO (1970) *The WMO Sea-Ice Nomenclature*. (WMO No. 259, TP 145 (with later supplements). WMO, Geneva.

WMO (2000) *Sea-Ice Information Services in the World*. (WMO No. 574). WMO, Geneva.

Worby, A.P., Massom, R.A., Allison, I., Lytle, V.I., and Heil, P. (1998) East Antarctic sea ice: a review of structure, properties and drift. In: M.O. Jeffries (ed.), *Antarctic Sea Ice: Physical properties, interactions and variability* (Antarctic Research Series 74, pp. 41–67). American Geophysical Union, Washington, DC.

Worby, A.P., Geiger, C. A., Paget, M. J., Van Woert, M.L., Ackley, S.F., and DeLiberty, T.L. (2008) Thickness distribution of Antarctic sea ice. *Journal of Geophysical Research* **113**, C05S92, doi:10.1029/2007JC004254.

Wright, B., Hnatiuk, J., and Kovacs, A. (1978) Sea ice pressure ridges in the Beaufort Sea. *Proceedings of IAHR Ice Symposium*, Luleå, Sweden.

Wu, H.-D. and Leppäranta, M. (1990) Experiments in numerical sea ice forecasting in the Bohai Sea. *Proceedings of IAHR Ice Symposium 1990*, Espoo, Finland (Vol. III, pp. 173–186).

Wu, H., Bai, S. and Li, G. (1997) Sea ice conditions and forecasts in China. *Proceedings of 12th International Symposium on Okhotsk Sea and Sea Ice* (pp. 164–174). Okhotsk Sea & Cold Ocean Research Association, Mombetsu, Hokkaido, Japan.

Wu, H., Bai, S. and Zhang, Z. (1998) Numerical sea ice prediction in China. *Acta Oceanologica Sinica*, **17**(2), 167–185.

Yue, Q., Bi, X., Sun, B., Zhang, T., and Chen, X. (1996) Full scale force measurement on JZ20–2 platform. *Proceedings of the IAHR Ice Symposium (IAHR'96)*, Beijing, August 27–30, pp. 282–289.

Zhang, J., Thomas, D.B., Rothrock, D.A., Lindsay, R.W., and Yu, Y. (2003) Assimilation of ice motion observations and comparisons with submarine ice thickness data. *Journal of Geophysical Research* **108**(C6), 3170, doi: 10.1029/2001JC001041.

Zhang, J. Hibler, W.D., III, Steele, M., and Rothrock, D.A. (1998) Arctic iceocean modeling with and without climate restoring. *Journal of Physical Oceanography* **28**, 1745–1748.

Zhang, X. and Walsh, J.E. (2006) Toward a seasonally ice-covered Arctic Ocean: Scenarios from the IPCC AR4 model simulations. *Journal of Climate* **19**, 1,730–1,747.

Zhang, Z. (2000) Comparisons between observed and simulated ice motion in the northern Baltic Sea. *Geophysica* **36**(1–2), 111–126.

Zhang, Z. and Leppäranta, M. (1995) Modeling the influence of ice on sea level variations in the Baltic Sea. *Geophysica* **31**(2), 31–46.

Zubov, N.N. (1945) *L'dy Arktiki [Arctic Ice]*. Izdatel'stvo Glavsermorputi, Moscow [English translation 1963 by US Naval Oceanographic Office and American Meteorological Society, San Diego].

Zwally, H.J. and Walsh, J.E. (1987) Comparison of observed and modelled ice motion in the Arctic Ocean. *Annals of Glaciology* **9**, 1–9.

Index

Note: Page numbers in *italics* refer to illustrations